N° d'ordre : H547

UNIVERSITÉ DES SCIENCES ET TECHNOLOGIES DE LILLE

HABILITATION À DIRIGER DES RECHERCHES
EN SCIENCES PHYSIQUES

SYNTHÈSE DES TRAVAUX

INSTABILITÉS ET CHAOS DÉTERMINISTE : MODÉLISATION ET CARACTÉRISATION DANS DES SYSTÈMES EXPÉRIMENTAUX, EN OPTIQUE OU AILLEURS

présentée par

Marc LEFRANC

Laboratoire de Physique des Lasers,
Atomes et Molécules (UMR 8523)

Soutenue le 1er décembre 2006 devant le jury composé de :

Thomas ERNEUX	Maître de Recherche au FNRS	Rapporteur
Robert GILMORE	Professeur, Drexel University	Rapporteur
Jorge TREDICCE	Professeur, Université de Nice	Rapporteur
Pierre GLORIEUX	Professeur, USTL	Dir. de Recherche
Claude FABRE	Professeur, Université P. et M. Curie	Examinateur
Jean-Marc GAMBAUDO	Directeur de Recherche au CNRS	Examinateur
Bernard VANDENBUNDER	Directeur de Recherche au CNRS	Examinateur

Remerciements

On avance difficilement tout seul, et ce n'est pas une révélation que plus on avance, et plus on se retrouve redevable envers toutes sortes de gens pour toutes sortes de raisons. Écrire des remerciements est donc un exercice délicat, tant est grand le risque d'omettre quelqu'un qui aura compté à une étape ou à une autre. Que ceux qui se sentiront oubliés ne m'en veuillent pas et n'attribuent ma négligence qu'au peu de temps consacré à écrire cette page.

Mes remerciements vient bien sûr d'abord à mes parents et à mes professeurs, qui m'ont transmis le goût d'apprendre et de comprendre, et m'ont donné les bases qui m'ont permis un jour d'approcher le monde mystérieux de la recherche, et ce dans les meilleures conditions dont on puisse rêver.

Je remercie ensuite ceux qui m'ont fait entrer dans ce monde, et bien sûr tout particulièrement Pierre Glorieux, qui m'a accueilli en thèse au Laboratoire de Spectroscopie Hertzienne, alors dirigé par Bruno Macke, et a guidé mes premiers pas dans le domaine fascinant du chaos déterministe, à un moment où celui-ci était en plein essor. On sait que l'art d'un général est de savoir choisir son champ de bataille, et c'est là quelque chose qui passe généralement au-dessus de la tête d'un « bleu ». J'éprouve donc la plus profonde gratitude à tous ceux qui ont su m'orienter dans la bonne direction, à mes débuts et plus tard.

Dont bien sûr Robert Gilmore, qui a posé les bases d'une méthode d'analyse du chaos incroyablement féconde, et qui a dessiné un programme extrêmement ambitieux pour l'étude des systèmes dynamiques chaotiques, reliant celle-ci à ces joyaux des mathématiques que sont la théorie des singularités et la théorie des groupes. La lecture de ses articles, puis les échanges directs, et enfin la rédaction commune d'un ouvrage ont été pour moi une source inépuisable d'enrichissement, et j'espère un jour pouvoir rendre un peu de ce que j'ai reçu, en contribuant à la réalisation de ce programme, et notamment par l'extension de ces méthodes aux systèmes de dimension supérieure.

Plus récemment, je pense également à Bernard Vandenbunder, chargé de mission pour l'Institut de Recherches Interdisciplinaires, qui, avec beaucoup de patience et de générosité, a oeuvré sans relâche pour que s'enracine à Lille un dialogue entre biologie, mathématiques,

physique,... et pour que les talents conjugués permettent d'aller plus loin et de capturer un peu plus de l'intimidante complexité du vivant. Alors que nos efforts dans ce domaine vont commencer à porter leurs fruits, je lui suis infiniment reconnaissant de ses conseils toujours éclairants et pertinents, et je le remercie d'avoir pris le temps de nous aider à choisir des questions où nous pourrions nous montrer utiles. J'espère sincèrement que le futur bâtiment de l'IRI sera bientôt une ruche active, et je compte y contribuer de mon mieux.

La plupart des travaux décrits dans ce mémoire n'auraient pas vu le jour sans les collègues avec lesquels ils ont été réalisés, et je les remercie du fond du coeur pour le travail réalisé avec passion et bonne humeur, et pour tous les moments partagés, dans le travail et dans la vie. Au Laboratoire, je pense bien évidemment d'abord à Serge Bielawski, Dominique Derozier, Christophe Szwaj, Jaouad Zemmouri, avec qui j'ai interagi depuis si longtemps, mais également à Daniel Hennequin et Didier Dangoisse pour mes premiers pas dans le chaos, et à Quentin Thommen qui vient de nous rejoindre. Merci également aux collègues d'autres laboratoires : Ennio Arimondo, Francesco Papoff (Pise), Thomas Erneux , Michel Nizette, (Bruxelles), ainsi que plus récemment François-Yves Bouget (Banyuls-sur-mer) et Juan Carlos Martìn (Saragosse) pour les collaborations et les échanges passionnants que nous avons tissés.

J'aurais pu les remercier en tant que collègues, mais j'ai voulu leur réserver une place à part. Je veux dire ici merci à tous les étudiants que j'ai eu la chance d'encadrer ou de co-encadrer, et leur dire à quel point j'ai été fier d'accompagner leurs premiers pas, et que si j'espère leur avoir été utile, ils m'ont également beaucoup apporté par leur vitalité et leur enthousiasme, leur courage et leur intelligence. Cela a toujours une grande satisfaction pour moi de les voir un jour se retourner et être fiers de leur travail. C'est bien sûr aux thésards que je pense d'abord : Guillaume Boulant, Jérôme Plumecoq, Pierre Suret, Axelle Amon, Pierre-Emmanuel Morant et maintenant plus récemment Constant Vandermoere, mais également à Michel Nizette et Claudiu Giuraniuc, qui passèrent un an ici, respectivement en post-doc et en DEA. C'est parce que l'on vit tous les jours le fait que notre métier fait toujours rêver les jeunes qu'il a un sens.

Mais on n'interagit pas qu'avec ses collaborateurs, et on travaille tellement mieux dans une ambiance gaie et amicale... Merci donc à tous les autres collègues du Laboratoire (je ne chercherai pas à les nommer tous) pour les échanges et les moments de vie commune que nous avons eus pendant toutes ces années. Merci aussi aux techniciens et aux secrétaires pour leur aide toujours efficace et leur gentillesse.

Merci aussi à tous ceux qui, par des pressions amicales répétées, m'ont régulièrement rappelé l'importance de cette étape qu'est l'habilitation : ce mémoire leur doit forcément quelque chose...

Le respect et l'admiration que j'ai pour eux me rendent très sensible à l'honneur que m'ont fait Thomas Erneux, Robert Gilmore, Jorge Tredicce, qui ont bien voulu être rapporteurs de ce travail, ainsi que Claude Fabre, Jean-Marc Gambaudo et Bernard Vandenbunder, qui ont accepté de participer au jury de soutenance, et je les en remercie très sincèrement, en espérant être à la hauteur de leurs attentes.

Pour conclure par le plus important, je finirai par une pensée à ceux qui partagent ma vie, ma femme Catherine et mes enfants Clara et Martin, et à qui j'ai volé tant d'instants communs, détournés vers les divagations décrites dans ce mémoire. Et pourtant, il ne m'aurait servi à rien d'apprendre à être un chercheur s'ils ne m'avaient pas appris à être un homme.

Table des matières

1 Introduction

1.1 PREMIERS PAS DANS LE CHAOS

Ce mémoire retrace brièvement les travaux que j'ai menés dans les domaines de l'optique et de la dynamique non linéaires au Laboratoire de Spectroscopie Hertzienne, puis au Laboratoire de Physique des Lasers, Atomes, Molécules, né en 1998 de la fusion du LSH avec le Laboratoire de Dynamique Moléculaire et Photonique. Arrivé en 1988 dans le groupe de Pierre Glorieux, j'y ai préparé une thèse de doctorat intitulée « Caractérisation du chaos dans les lasers CO_2 », que j'ai soutenue en 1992. Après une formation initiale purement théorique, et des premiers pas dans le monde de la recherche consacrés à la construction de théories de supercordes, j'ai pris beaucoup de plaisir au cours de ma thèse à découvrir et explorer le monde du chaos déterministe et, surtout, à pouvoir mener coinjointement analyse théorique, où intervenaient des notions mathématiques surprenantes et paradoxales, expériences au laboratoire, où des lasers pourtant réputés stables se laissaient aller à d'apparentes extravagances, et simulations numériques, qui me permettaient de relier les deux. Ce fut là que je compris que ce qui m'avait attiré vers la physique était précisément le fait de pouvoir se placer au carrefour où se rencontrent l'esprit humain, avec ses abstractions cristallines, et le monde réel, avec ses lois inflexibles mais pourtant domesticables.

1.2 ANALYSE TOPOLOGIQUE DU CHAOS

Recruté au CNRS en 1993, mon activité de recherche s'est tout d'abord développée dans la voie initiée vers la fin de ma thèse, à savoir le développement de méthodes topologiques d'analyse du chaos déterministe, basées sur la théorie des noeuds [1–4], ainsi que leur application à des systèmes expérimentaux, au premier rang desquels les lasers chaotiques du Laboratoire. Mes travaux de thèse avaient essentiellement visé à confirmer la faisabilité expérimentale de cette approche [5]. Je me suis donc ensuite intéressé aux applications de cette approche à deux problèmes distincts : d'une part, la classification des différents types de régimes chaotiques et leur organisation dans l'espace des paramètres [6–9], d'autre part la

construction explicite de codages des trajectoires par des séquences binaires (« dynamique symbolique »), ces codages permettant d'extraire de manière robuste les invariants de la dynamique [10–12]. Dans les deux cas, ces méthodes d'analyse ont été conçues de manière à pouvoir caractériser des signaux expérimentaux.

Les travaux expérimentaux concernant la classification des régimes chaotiques furent remarqués par le théoricien américain Robert Gilmore, car nos observations nous avaient mené à des conclusions qui étaient en parfait accord avec des prédictions qu'il avait publiées peu avant [13, 14], et en fournissaient une confirmation expérimentale. Il nous proposa alors de collaborer avec lui pour relever un défi passionnant : étendre l'analyse topologique du chaos à des systèmes à nombre de degrés de liberté arbitrairement grand. Huit ans plus tard, nous ne sommes pas encore parvenus à ce résultat, même si des résultats récents ouvrent des pistes tout à fait prometteuses. Mais cette collaboration aura cependant donné naissance à un ouvrage ("The Topology of Chaos : Alice in Stretch and Squeezeland", [4]), où nous passons en revue les succès des techniques actuelles et les ingrédients que nous pensons être essentiels pour les étendre en dimension arbitraire. Par ailleurs, l'approche topologique a connu récemment des développements originaux, où nous avons montré qu'elle pouvait être mise à profit pour mettre en évidence la présence de chaos déterministe dans un système non stationnaire, où la dérive de paramètres rendait inopérantes les méthodes de caractérisation usuelles [15]. Enfin, j'ai récemment proposé un nouveau formalisme pour l'analyse topologique du chaos, basé sur des considérations géométriques dont on espère qu'elles pourront s'étendre en dimension supérieure [16].

1.3 DYNAMIQUE SPECTRO-TEMPORELLE DES LASERS FORTEMENT MULTIMODES

Parallèlement à ce projet de longue haleine, je me suis impliqué dans deux thèmes de recherche au carrefour de l'optique et de la dynamique non linéaire. Le premier a concerné l'étude de la dynamique spectro-temporelle des lasers fortement multimodes, thème de recherche initié par mes collègues Serge Bielawski, Dominique Derozier et Christophe Szwaj, et qui illustre de manière frappante les ponts que la dynamique non linéaire permet de jeter entre des domaines a priori aussi différents que l'optique et l'hydrodynamique. Lorsqu'un laser oscille simultanément sur des dizaines de milliers de modes, et que la portée effective du couplage entre modes de fréquences voisines est suffisamment petite, le spectre d'émission peut être assimilé à un milieu continu dans lequel les perturbations se transmettent préférentiellement de proche en proche [17]. On observe alors des phénomènes qui sont caractéristiques d'un milieu étendu, comme par exemple la propagation d'ondes ou l'apparition d'une onde stationnaire en réponse à une modulation globale [18].

Les travaux qui sont rassemblés dans l'appendice E ont mené à la mise en évidence dans ce dispositif de cascades d'instabilités paramétriques [19] ansi que d'instabilités induites par la présence de non uniformités, plus précisément par la variation d'une des propriétés du système le long de l'espace ainsi constitué [20]. De manière remarquable, cette non uniformité est directement liée à la dépendance en fréquence du gain laser et est donc intrinsèque. Ce fut à ma connaissance le premier travail à évoquer la pertinence de ce scénario dans un système optique, et fut suivi de près par un travail montrant que des effets similaires peuvent apparaître en raison de l'inhomogénéité du profil transverse de la pompe [21].

J'ai fait le choix dans ce mémoire de ne pas développer cette partie, malgré son grand intérêt, renvoyant directement le lecteur intéressé aux articles de l'appendice E ainsi qu'au mémoire d'habilitation de Serge Bielawski. Par rapport aux autres thèmes, j'y ai en effet joué un rôle plus secondaire, ma contribution principale à ces travaux ayant été de concevoir la partie du dispositif expérimental qui permit avec un PC de 1996 d'acquérir 67000 spectres laser complets par seconde, et donc d'avoir un suivi en temps réel de la dynamique spectro-temporelle. Acquérir en régime permanent 20 Moctets par seconde avec une mémoire limitée à 30 Mo/s au niveau matériel le plus bas, tout en faisant simultanément tourner un système d'exploitation multi-tâches pour la partie traitement, avait notamment exigé de détourner les routines de gestion mémoire du noyau du système linux qui pilotait l'expérience, de manière à effectuer des transferts directs en mémoire en court-circuitant tous les mécanismes de protection. Cela nous avait permis de gagner plus de trois ordres de grandeur en cadence d'acquisition par rapport aux solutions fournies par le constructeur de la carte d'acquisition.

1.4 DYNAMIQUE DES OSCILLATEURS PARAMÉTRIQUES OPTIQUES

Le deuxième axe de recherche a été consacré à l'étude de la dynamique des oscillateurs paramétriques optiques, sources de lumière cohérente présentant l'avantage d'être facilement accordables [22–25]. Comme les lasers, ces dispositifs sont basés sur une interaction non linéaire et sont donc susceptibles de présenter une dynamique riche et variée. Le constat que leur dynamique avait été relativement moins explorée que celles des lasers, ainsi que leur intérêt pratique, m'ont amené en 1997 à me lancer dans leur étude avec mes collègues Jaouad Zemmouri, Serge Bielawski et Dominique Derozier. L'objectif fixé initialement à ce projet était d'observer expérimentalement l'apparition de structures spatiales non triviales dans le profil transverse du faisceau émis par l'OPO, ainsi que le prévoyaient un certain nombre d'études théoriques [26–31]. Nous espérions également observer expérimentalement la bifurcation de Hopf menant à des oscillations périodiques dans le modèle champ moyen d'un OPO triplement résonant monomode [32].

Les non-linéarités optiques sont généralement exacerbées lorsque les intensités lumineuses sont importantes, et c'est donc à puissance de pompe élevée que l'on s'attend à rencontrer des comportements dynamiques intéressants, instabilités diverses ou chaos. Mais les densités d'énergie alors en jeu peuvent induire d'autres effets, et notamment des effets thermiques. C'est ainsi que la réalité expérimentale nous a détourné de notre but initial vers l'étude d'instabilités opto-thermiques. Ces dernières sont tout à fait remarquables car de très faibles variations de température peuvent entraîner une modulation de l'intensité de sortie de l'OPO par tout ou rien [33, 34]. Nous avons également mis en évidence des régimes multimodes aux propriétés intéressantes [35], avec notamment de beaux exemples d'« oscillations en rafale » qui n'ont rien à envier en complexité à ce qu'on peut rencontrer dans les systèmes biologiques [36], et nous avons réalisé ce qui est à notre connaissance la première observation de chaos déterministe dans un oscillateur paramétrique optique [15]. Enfin, nous avons pu mettre à jour un propriété particulièrement intéressante des régimes bimodes observés dans l'oscillateur paramétrique optique : ils peuvent apparaître même lorsque les modes concernés ne sont pas résonants dans la cavité, à condition que le désaccord d'un mode compense celui de l'autre [36]. Il en résulte qu'à forte puissance, les régimes bimodes peuvent être observés dans un nombre de configurations bien plus important que ne le prévoit un simple calcul de coïncidences [37].

1.5 RÉSEAUX DE RÉGULATION GÉNÉTIQUE

Enfin, nous nous sommes lancés très récemment dans une voie tout à fait nouvelle pour nous, à l'interface entre physique et biologie : la dynamique non linéaire des réseaux de régulation génétique [38–42]. Nul n'ignore que chacune de nos cellules renferme dans son noyau une molécule qui est devenue au cours des cinquante ans qui se sont écoulés depuis sa découverte l'objet central de la biologie moderne : l'acide désoxyribonucléique (ADN) [43]. Constituée chez l'Homme d'une longue chaîne de près de deux milliards de nucléotides, choisis parmi seulement quatre espèces (adénine, cytosine, guanine et thymine), elle porte les informations essentielles au fonctionnement de tout être vivant. On sait l'effort considérable qui a été consenti ces dernières années pour détermininer la séquence d'un certain nombre d'organismes vivants, dont l'homme [44]. Un des buts principaux de cet effort était d'identifier au sein de la séquence complète un certain de nombre de sous-séquences dont le rôle est fondamental : les gènes, qui renferment l'information nécessaire pour produire les protéines, qui sont les briques élementaires de la machinerie moléculaire de la Vie.

Mais il est de plus en plus évident que les données fournies par le séquençage du génome ne sont pas suffisantes pour appréhender toute la complexité des phénomènes biologiques. La séquence décrivant la structure d'une molécule d'ADN est un objet statique : elle n'explique pas pourquoi neurones, fibres musculaires, globules rouges ou toute autre cellule du corps humain ont des comportements aussi différents alors qu'elles partagent exactement la même information génétique, ni pourquoi l'état de ces cellules peuvent varier dans le temps. En fait, le niveau d'activité d'un gène varie en fonction de nombreux facteurs, et notamment de la concentration de protéines régulatrices (elles-mêmes produites par d'autres gènes), qui, en se fixant en amont de la zone codante du gène, modulent son activité. Gènes et protéines en interaction mutuelle forment donc un gigantesque système dynamique, capable d'une complexité que nous pouvons admirer même chez le plus simple des êtres vivants. Ce système dynamique est fortement non linéaire, comme le montre le fait que la multistabilité est généralement la règle [38, 41, 42]. On peut donc espérer que les outils de la dynamique non linéaire soient pertinents pour le comprendre et l'analyser.

Une grande partie de la recherche actuelle dans ce domaine est fondée sur l'espoir que l'extraordinaire réseau ainsi formé puisse être, au moins de manière approchée, décomposé en modules élémentaires associés à des fonctions bien précises. Nous avons choisi de nous intéresser plus particulièrement à une classe bien particulière de modules : celles des horloges moléculaires responsables de l'existence des oscillations circadiennes, qui rythment la physiologie de la plupart des organismes vivants sur une période de 24 heures et leur donnent une mesure interne du temps [45, 46]. Si l'existence de ces oscillations et leur caractère endogène sont connus depuis plus de deux siècles, ce n'est que depuis relativement récemment que l'on sait que les rouages de ces horloges sont constitués de réseaux de gènes et protéines en interaction. L'enjeu est ici de parvenir à un modèle théorique qui rende compte des observations expérimentales, et ainsi d'identifier les acteurs moléculaires impliqués dans l'horloge, et déterminer les voies de transduction qui couplent cette dernière aux autres fonctions cellulaires.

1.6 CONCLUSION

Nous avons maintenant décrit les grandes lignes des travaux que nous présentons dans ce mémoire, et il est maintenant temps de passer à une description plus détaillée dans les chapitres suivants, qui sont consacrés à nos premiers travaux sur le chaos, aux méthodes d'analyse topologique du chaos, à la dynamique des oscillateurs paramétriques optiques et à la dynamique des réseaux de régulation génétique. Afin de permettre une lecture à plusieurs niveaux, le lecteur trouvera au début de chaque chapitre une section introductive reprenant brièvement l'ensemble des travaux du thème considéré, puis une description détaillée des différents travaux.

2

Caractérisations qualitative et quantitative du chaos déterministe

2.1 INTRODUCTION

Ce chapitre est consacré à mes deux premiers articles dans le thème du chaos déterministe, qui ont été écrits avant que je m'intéresse aux méthodes d'analyse topologique du chaos dans lesquelles je me suis par la suite investi, et qui seront reprises dans le prochain chapitre. Ce sera donc l'occasion de rappeler brièvement ce qu'on entend par chaos déterministe, en préambule au chapitre suivant, où des techniques plus élaborées seront développées. Ces deux articles nous permettront d'illustrer deux approches complémentaires du chaos déterministe :

1) ***Une approche qualitative***, où l'on cherche, à partir des comportements observés dans une certaine région de l'espace des paramètres, à prédire ceux que l'on rencontrera dans d'autres régions. La notion importante est ici celle de *scénario*, c'est-à-dire de séquence de régimes dynamiques apparaissant dans un ordre bien précis lorsqu'on modifie un paramètre de contrôle. Les *routes vers le chaos* constituent une classe particulièrement importante de scénarios chaotiques, et correspondent aux transitions que peut subir un système lorsqu'il bascule d'un état parfaitement ordonné vers un état chaotique. L'exemple de la célèbre cascade de doublements de période, où un régime périodique devient apériodique en doublant sa période de base un nombre infini de fois, vient naturellement à l'esprit. En ce qui nous concerne, nous nous intéresserons dans la section 2.3 à ce qu'on appelle le *chaos homocline*, parfois par abus de langage, et qui se caractérise dans l'espace des paramètres par une accumulation de fenêtres périodiques de périodes croissantes.

2) ***Une approche quantitative***, où l'on s'efforce d'associer des chiffres aux régimes chaotiques observés, de les *quantifier*, non seulement pour pouvoir affirmer que ces régimes sont bien chaotiques, mais aussi pour estimer à quel point ils le sont. Deux mesures classiques du chaos sont la dimension fractale de l'attracteur chaotique et les exposants de Lyapunov. Les différents types de dimensions fractales permettent de mettre en évidence la complexité de la région de l'espace des états visitée par le système au cours du temps : cette dernière est-elle une simple courbe fermée, comme dans le cas d'un régime périodique (dimension 1), un tore, comme dans le cas d'un régime quasi-périodique à plusieurs fréquences

incommensurables (dimension 2, ou plus généralement entière), ou bien un attracteur chaotique, présentant une structure fractale caractérisé par une dimension non entière, signe d'une géométrie intermédiaire entre celles d'une surface et d'un volume ? Les exposants de Lyapunov, quant à eux, quantifient la vitesse avec laquelle des trajectoires proches se séparent en raison de l'instabilité de la dynamique chaotique, et par conséquent caractérisent l'imprédictibilité du système aux temps longs. Dans ce mémoire, nous présentons un travail consacré à l'évaluation de la dimension fractale d'un attracteur chaotique. Nous y avons montré que, contrairement à ce qui est généralement admis, cette mesure peut dépendre de la variable mesurée lorsque les données expérimentales sont inhomogènes et en quantité limitée, et n'est donc pas aussi fiable qu'on pouvait l'espérer.

2.2 LE CHAOS DÉTERMINISTE ET SA CARACTÉRISATION

2.2.1 Reconstruction dans un espace des états

Les premiers indices mathématiques suggérant qu'un système déterministe simple pouvait présenter une dynamique complexe et irrégulière furent rencontrés par Poincaré il y a plus d'un siècle [47], mais ce n'est que depuis une trentaine d'années que cette idée a commencé à être largement diffusée, et une bonne partie du grand public n'ignore plus que les battements d'un papillon en un point du globe est susceptible d'influer sur le déclenchement d'une tempête en un autre point diamétralement opposé, selon l'analogie imaginée par Edward Lorenz [48].

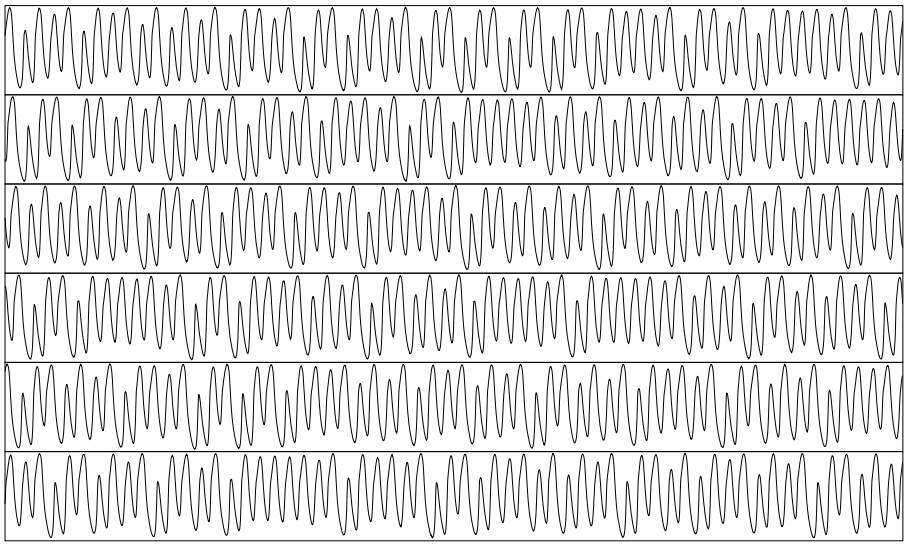

FIG. **2.1 –** *Signal chaotique délivré par un laser CO_2 guide d'onde, dont les pertes sont modulées à une fréquence d'environ 380 kHz. C'est une approximation du logarithme de l'intensité laser qui est ici enregistrée, au moyen d'un détecteur et d'un amplificateur logarithmique.*

Ce paradoxe apparent n'est pas qu'une expérience de pensée. Sans compter les nombreux phénomènes naturels où une dynamique chaotique est à l'oeuvre, de tels régimes ont été observés dans une multitude d'expériences de laboratoire à travers le monde. Les signaux de la figure 2.1 en fournissent en exemple particulièrement frappant, car le laser qui les a

délivrés se caractérise par une stabilité exemplaire et un rapport signal sur bruit exceptionnel. La nature irrégulière de la dynamique ne saurait être donc être attribuée à de quelconques imperfections techniques, d'autant plus que si le signal n'est jamais tout à fait le même tout au long de la série temporelle, il n'est pas non plus tout à fait un autre : le début et la fin de la série présentent des visages tout à fait semblables, et l'on pressent que cette dynamique changeante est engendrée par des lois invariantes, déterministes.

Comment mettre en évidence la caractère déterministe d'une telle dynamique ? C'est une description géométrique de celle-ci qui apporte la réponse [4, 49]. Un système déterministe possède par définition un certain nombre de variables d'état, dont les valeurs à un instant donné déterminent entièrement l'évolution future du système. L'idée est donc de se donner un espace des états dans lequel on trace la trajectoire associée à une série temporelle, et de s'assurer que la propriété de déterminisme est vérifiée. On voit ainsi à la figure 2.2 la trajectoire suivie par le laser de la figure 2.1 dans un espace des états reconstruit à partir des valeurs de la série temporelle, et dont on peut montrer qu'il est sous certaines conditions équivalent à l'espace des états original (intensité, inversion de population,...) [50].

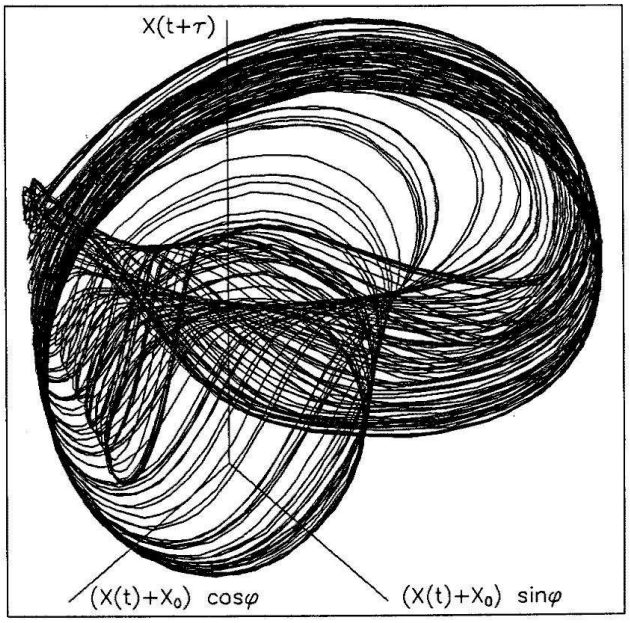

FIG. ***2.2*** – *Trajectoire reconstruite à partir du signal de la figure 2.1 dans un espace des états* $(X(t),X(t+\tau),\phi)$*, où* τ *est un délai temporel égal à environ un cinquième de la période de modulation, et* ϕ *est la phase de la modulation. La trajectoire s'enroule autour d'un attracteur étrange.*

On constate que cette trajectoire n'est pas disposée au hasard mais qu'elle est au contraire strictement organisée par la dynamique, et s'enroule sur un objet géométrique tout à fait particulier, que l'on appelle un « attracteur étrange ». C'est le fait que cet attracteur soit invariant dans le temps qui signe la nature déterministe de la dynamique. On remarque que des points proches dans l'espace des états ont localement des trajectoires semblables, et en particulier parallèles : à un point de cet espace correspond bien une et une seule trajectoire.

Caractériser la dynamique chaotique, c'est donc généralement caractériser l'attracteur reconstruit dans un espace des états convenablement choisi. Dans le chapitre 3, nous ex-

plorerons en détail une approche topologique basée sur la propriété de déterminisme, et notamment sur le fait que deux trajectoires ne peuvent se croiser en un point, à moins d'admettre que ce point a deux futurs différents. Dans ce chapitre, nous rappellerons le principe du calcul de dimension fractale, qui permet d'exprimer le fait qu'un attracteur comme celui de la figure 2.2 est un objet géométrique intermédiaire entre une surface et une volume, et est donc caractérisé par une dimension non entière comprise entre 2 et 3 [51–53].

2.2.2 Étirement et repliement

La représentation géométrique de la dynamique nous donne non seulement accès aux invariants de la dynamique, mais nous permet également de mieux comprendre les mécanismes à l'origine de la dynamique chaotique, comme nous allons l'illustrer avec l'attracteur expérimental de la figure 2.3.

Pour cela, on utilise la technique des sections de Poincaré, en intersectant l'attracteur par une séries de plans de sections, et en s'intéressant à l'évolution des sections lorsqu'on fait un tour autour de l'attracteur (c'est-à-dire lorsqu'on parcourt une période de modulation). Comme on le voit sur la figure 2.3, deux mécanismes géométriques distincts agissent sur les trajectoires dans l'espace des phases : *l'étirement*, qui sépare inexorablement les trajectoires proches, et est donc responsable de l'instabilité de la dynamique, et *le repliement* qui permet de les maintenir dans une région bornée de l'espace des états [4, 49, 54]. C'est donc un processus semblable à celui par lequel le boulanger fabrique une pâte feuilletée qui explique les propriétés fondamentales du chaos déterministe.

Les mécanismes d'étirement et de repliement peuvent être formalisés par la transformation géométrique dite du "fer à cheval" [4, 49, 54, 55], qui étire un carré dans une direction, le contracte dans une autre, avant de le replier pour qu'il intersecte le carré original en deux bandes (figure 2.4). Ce modèle mathématique élémentaire permet de décrire simplement les propriétés les plus importantes du chaos déterministe grâce à l'existence d'un codage symbolique obtenu en associant à chaque itéré un symbole 0 et 1 selon l'indice du rectangle dans lequel il tombe. En effet, on montre que les points de l'ensemble invariant, c'est-à-dire les points du plan dont toutes les images ou préimages sont contenues dans le carré, sont en bijection avec les séquences bi-infinies de 0 et de 1 : chaque point est associé à une séquence unique, et réciproquement. De plus, cette bijection est un homéomorphisme, ce qui veut dire que des points codés par des séquences proches seront proches dans le plan. En d'autres termes, une mesure grossière de l'état du système nous permet de localiser la condition initiale avec une précision arbitrairement grande si on la répète suffisamment souvent.

Cette correspondance permet de montrer que des points arbitrairement proches vont se retrouver tôt ou tard aux deux bouts du carré, qu'il existe une infinité de solutions périodiques plongées dans l'ensemble invariant, qu'il existe une orbite passant arbitrairement près de tous les points de l'ensemble invariant, etc. L'analyse topologique que nous développerons au chapitre 3 peut être vue comme une méthode systématique pour caractériser les fers à cheval sous-jacents à une dynamique chaotique.

2.2.3 Bifurcations et diagrammes de bifurcation

Nous nous sommes intéressés jusqu'ici aux comportements observés dans un système à paramètres fixés, et nous avons vu que dans un système chaotique, les trajectoires n'étaient pas organisées au hasard, malgré l'apparente irrégularité de la série temporelle. De même,

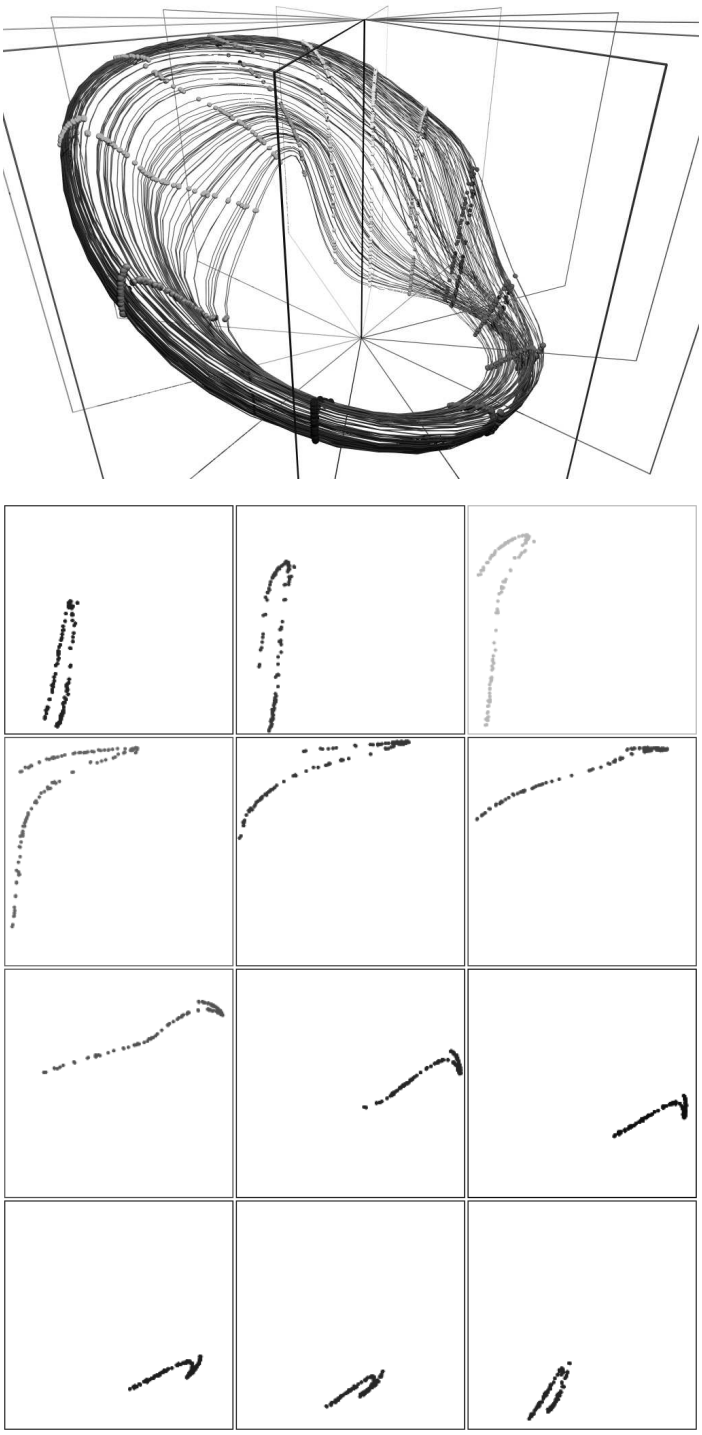

FIG. ***2.3 –*** *Haut : Sections de Poincaré d'un attracteur chaotique reconstruit à partir de signaux délivrés pas un laser CO_2 à modulation de pertes. Bas : Les sections de Poincaré de la figure du haut (parcourues dans le sens trigonométrique). On distingue parfaitement les mécanismes d'étirement (surtout visibles dans la première moitié), et de repliement (principalement dans la deuxième moitié) qui façonnent l'attracteur étrange.*

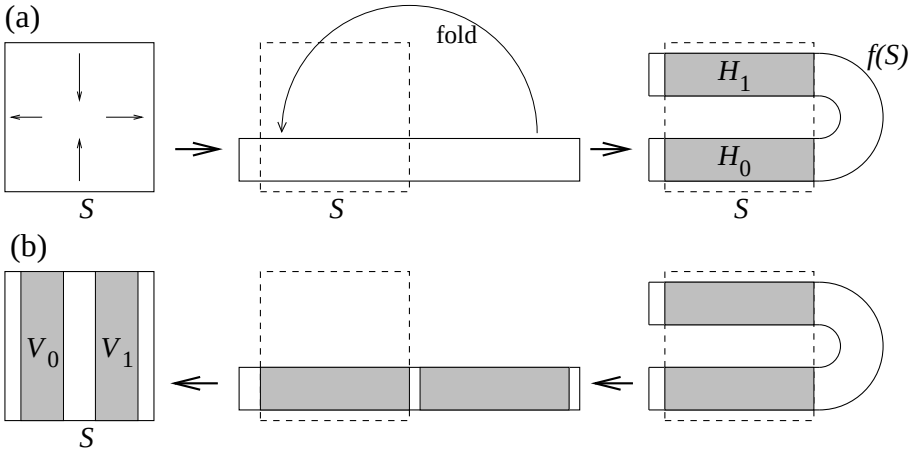

FIG. **2.4 –** *Représentation de l'action de l'application du fer à cheval sur le plan. Le carré unité est tout d'abord étiré selon la direction horizontale et comprimé selon la direction verticale. Une des moitiés du long ruban ainsi obtenu est ensuite repliée sur l'autre. L'ensemble invariant de l'application peut être codé symboliquement au moyen de la partition de ce dernier en deux bandes horizontales* $\{H_0,H_1\}$ *ou, de manière équivalente, en deux bandes verticales* $\{V_0,V_1\}$.

les changements qualitatifs par lesquels passe un système chaotique lorsqu'on fait varier un paramètre de contrôle suivent une logique rigoureuse, que la théorie des systèmes dynamiques peut nous aider à comprendre. L'observation de certains scénarios lorsqu'on balaye un paramètre permet ainsi d'identifier les mécanismes à l'oeuvre dans le système étudié. Inversement, le comportement observé en un jeu de paramètres donnés peut renseigner sur ceux observés dans un voisinage de l'espace des paramètres.

De manière générale, on désigne par bifurcation tout changement qualitatif dans le comportement d'un système qui fait que le système avant la bifurcation n'est pas équivalent au système après la bifurcation [56–58]. Un certain nombre de bifurcations sont rencontrées de manière générique quand on fait varier un paramètre de contrôle, et on peut notamment citer parmi celles que nous rencontrerons dans ce mémoire : la *bifurcation noeud-col*, ou *tangente*, qui voit l'apparition simultanée de deux états stationnaires ou de deux orbites périodiques, *le doublement de période*, où une orbite périodique se déstabililise en donnant naissance à une orbite de période double, et la *bifurcation de Hopf* qui connecte un régime stationnaire et une solution périodique confondus à la bifurcation. Ces bifurcation sont dites *locales*, car elles ne concernent que les propriétés du système dynamique étudié en un point de l'espace des phases. Dans la section 2.3, nous verrons un exemple de bifurcation *globale* – une bifurcation homocline – qui met en jeu la structure globale d'un flot dans l'espace des états [57, 58].

Afin d'illustrer le concept de *diagramme de bifurcation*, qui nous sera utile dans la section 2.3 consacrée au chaos homocline, nous présentons dans la figure 2.5 celui de la célèbre suite logistique $x_{n+1} = ax_n(1 - x_n)$, qui rassemble dans un même graphe les différentes bifurcations rencontrées et donc les différents comportements dynamiques observables selon la valeur de a. Il fournit l'exemple le plus simple de la route vers le chaos connue sous le nom de *cascade de doublement de période*, où la transition vers un régime chaotique s'effectue après que la solution périodique de base a subi un nombre infini de doublements

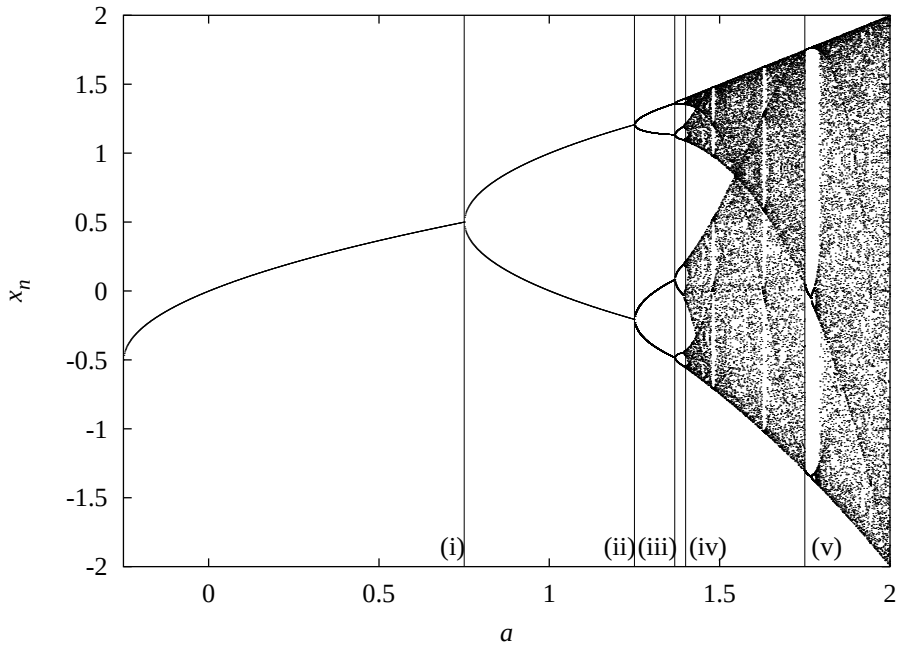

FIG. ***2.5 –*** *Diagramme de bifurcation de la suite logistique $x_{n+1} = ax_n(1 - x_n)$. Pour un certain nombre de valeurs entre $a = -0.25$ et $a = 2.0$, on a tracé en ordonnée 50 valeurs prises successivement par la suite après avoir laissé passer le transitoire. De gauche à droite, les lignes verticales indiquent les créations (i) d'une orbite de période 2 , (ii) d'une orbite de période 4 , (iii) d'une orbite de période 8; (iv) le point d'accumulation de la cascade de doublement de période ; (v) le début d'une fenêtre périodique de période 3.*

de périodes [4, 49]. L'enchevêtrement de zones claires et sombres que l'on voit sur la figure indique l'alternance de régimes périodiques et chaotiques lorsqu'on fait varier un paramètre.

2.3 CHAOS HOMOCLINE DANS LE LASER À ABSORBANT SATURABLE

– "Homoclinic chaos in a laser containing a saturable aborber", M. Lefranc, D. Hennequin, and D. Dangoisse, *J. Opt. Soc. Am. B* **8**, (1991) (appendice C, page 137).

2.3.1 Introduction

Un attracteur étrange tel que celui de la figure 2.2 n'est pas le seul objet invariant d'une dynamique chaotique. On verra ainsi plus loin que sont plongées dans cet attracteur une infinité d'orbites périodiques instables. Un point fixe est également un ensemble invariant, le plus simple qui soit.

Tout ensemble invariant $\mathcal{I}$ est inséré dans des variétés (ou surfaces) invariantes, sa *variété stable* $W^s(\mathcal{I})$ et sa *variété instable* $W^u(\mathcal{I})$, qui correspondent respectivement aux points de l'espace des états dont les orbites convergent vers $\mathcal{I}$ pour $t \to +\infty$ et $t \to -\infty$. Les variétés stable et instable de $\mathcal{I}$ se recontrent bien évidemment en $\mathcal{I}$, mais elles peuvent également se croiser en d'autres points de l'espace des états. On appelle orbite *homocline* toute orbite appartenant à une telle intersection. Une orbite homocline présente la particularité d'être asymptotique à $\mathcal{I}$ à la fois dans le futur et dans le passé [57, 58].

Le concept d'homoclinicité est absolument central dans la théorie des systèmes dynamiques. Ainsi, c'est quand Poincaré entrevit que l'existence d'intersections transverses entre les variétés stable et instable d'une orbite périodique impliquait une dynamique complexe et irrégulière que naquit ce que l'on appellerait plus tard chaos déterministe [47]. L'application du fer à cheval discutée précédemment fut inventée par Smale pour analyser la dynamique dans le voisinage d'une orbite homocline [55], et prouver l'existence de chaos dans une telle configuration. Très récemment, il a été montré que tout difféomorphisme peut être approché par un difféomorphisme de Morse-Smale[1], à la dynamique triviale, ou un difféomorphisme présentant des intersections homoclines transverses [59]. L'existence d'orbites homoclines est donc synonyme de chaos [60].

Il peut donc paraître redondant de parler de « chaos homocline », à moins que l'on n'ait quelque chose de plus précis en tête. Dans le contexte qui nous intéresse, les auteurs ont souvent associé ce terme à un théorème de Shilnikov montrant l'existence d'une dynamique compliquée dans le voisinage d'une bifurcation homocline autour d'un point d'équilibre d'un flot tridimensionnel [61,62]. Dans ces conditions, les deux variétés invariantes du point fixe, qui sont de dimensions 2 et 1, ne peuvent s'intersecter qu'en étant tangentes (une intersection transverse aurait deux trajectoire possibles, une dans chaque variété).[2] L'apparition de l'orbite homocline correspondante ne se produit alors que de manière ponctuelle lorsqu'on fait varier un seul paramètre de contrôle, d'où le nom de bifurcation homocline.

Shilnikov s'est plus précisément intéressé au cas d'un foyer-selle pour lequel l'orbite homocline quitte le point d'équilibre en spiralant dans une variété instable bidimensionnelle et y revient selon une variété stable uni-dimensionnelle. Il a montré en utilisant des modèles géométriques que lorsque le foyer-selle est moins répulsif qu'il n'est attractif, une dynamique chaotique est observée dans un voisinage de la bifurcation, et l'approche de cette dernière est caractérisée par une série de bifurcations où sont crées des orbites périodiques dont la période augmente d'une unité à chaque nouvelle bifurcation. Le chaos observé est extrêmement développé car il correspondrait à celui engendré par une transformation du fer à cheval où l'image du carré initial intersecterait ce dernier suivant une infinité de rectangles [61–64]. Le « chaos de Shilnikov » a donc frappé les esprits, et ses manifestations ont donc été recherchées dans plusieurs expériences.

2.3.2 Résultats

Afin de démontrer la présence de chaos de Shilnikov dans leur système expérimental, les chercheurs se sont généralement appuyés sur les indices suivants, dont on peut montrer qu'ils découlent du scénario prédit par Shilnikov : trajectoires spiralant de manière prolongée autour d'un point fixe dans l'espace des phases (signalant donc la proximité d'une bifurcation homocline), série de bifurcations voyant apparaître des orbites périodiques de périodes augmentant à chaque fois d'une unité et séparées par des zones chaotiques, et enfin structure en plusieurs branches des application de premier retour dans une section de Poincaré située

1. Un système est dit de Morse-Smale quand sa dynamique asymptotique n'implique qu'un nombre fini de points fixes ou d'orbites périodiques.
2. Les intersections homoclines transverses du paragraphe précédent étaient relatives à une orbite périodique. Dans un espace de dimension d, la somme des dimensions des variétés stable et instable est alors $d_u + d_s = d + 1$ est les intersections sont structurellement stables. Pour un point fixe, par contre $d_u + d_s = d$, ce qui rend les intersections non génériques, compte tenu de la contrainte d'unicité du champ de vecteur en un point.

dans la boucle de réinjection, loin des spirales autour du point fixe [63–67]. On voit qu'il s'agit de méthodes qualitatives, à contraster donc avec la méthode quantitative que nous présenterons brièvement dans la prochaine section.

Dans l'article cité au début de cette section, nous avons mis en évidence du « chaos homocline » dans le laser à absorbant saturable, en retrouvant les signatures mentionnées ci-dessus dans les signaux expérimentaux (figure 2.6). Les simulations numériques d'un modèle simple de ce laser ont permis de retrouver les comportements observés expérimentalement (figure 2.7) et de localiser le phénomène dynamique à l'origine du scénario observé, à savoir une région de l'espace des paramètres où deux surfaces invariantes de l'espace des états deviennent tangentes.

Bien que cet article ait recueilli un excellent accueil, avec plus de 50 citations depuis 1991, je suis forcé de constater rétrospectivement qu'il souffre de quelques contresens même s'il est sur l'essentiel correct. Ces défauts ne me sont malheureusement apparus qu'après avoir travaillé quelques années plus tard sur les aspects topologiques de la dynamique chaotique (voir le chapitre 3), et acquis les concepts permettant de mettre ces résultats en perspective.

En fait, le chaos observé dans notre laser n'est pas celui discuté par Shilnikov (bien qu'il lui soit apparenté car basé également sur une bifurcation homocline) : le scénario homocline que nous avions décrit, et qui a d'ailleurs également été décrit par de nombreuses autres équipes comme du chaos de Shilnikov, ne présente aucune différence au niveau topologique avec le chaos de type « fer à cheval » de la figure 2.4, et qui est par exemple à l'oeuvre dans la suite logistique ou le système de Rössler. C'est le chaos qui apparaît lors d'une bifurcation homocline impliquant une orbite périodique ou un point fixe *où la dynamique spiralante s'effectue selon la variété stable et non instable*. C'est alors le degré d'instabilité de l'orbite périodique ou du point fixe impliqué dans la bifurcation homocline qui fait qu'apparaît clairement ou non une série de fenêtres périodiques dont les périodes augmentent d'une unité à chaque fois, c'est-à-dire le diagramme de bifurcation caractéristique qui est généralement utilisé comme signature. Mais qu'elle saute à l'oeil ou non, cette série d'orbites périodiques est dans tous les cas présente dans le diagramme de bifurcation d'une cascade de doublement de période tel que celui de la figure 2.5.

Le véritable chaos de Shilnikov est en fait plus rare, car le type de point fixe autour duquel il se déploie ne peut se rencontrer dans un attracteur tridimensionnel (la variété instable est de dimension trop grande!). Il faut donc pour l'observer qu'un tel point fixe se retrouve sur la frontière d'un attracteur, comme on peut l'observer dans le système de Rössler pour des valeurs bien particulières des paramètres (c'est l'explication de ce qu'on appelle le « chaos entonnoir », c.f. [64]). A ma connaissance, les signatures topologiques les plus convaincantes de ce scénario ont été données par Letellier, Dutertre et Maheu grâce aux méthodes d'analyse topologique décrites dans le chapitre 3 [68].

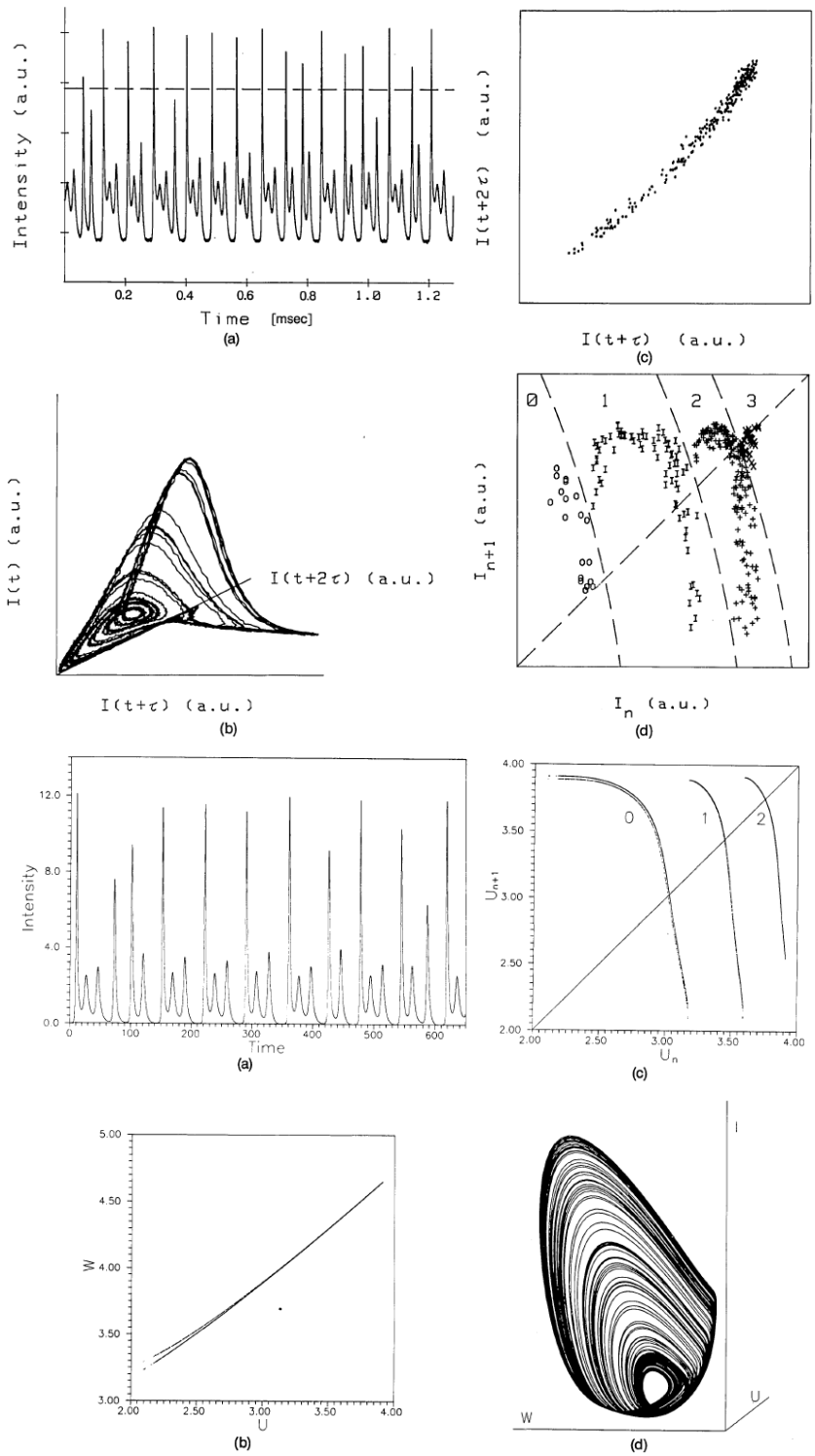

FIG. ***2.6*** – *Signatures de chaos homocline dans des séries temporelles du laser à absorbant saturable (en haut) et dans des simulations numériques d'un modèle de ce laser (en bas). Dans les deux cas sont montrés : le signal, l'attracteur, une section de Poincaré coupant ce dernier loin du centre des petites oscillations, et l'application de premier retour dans cette section, montrant une structure en plusieurs branches caractéristique du chaos homocline.*

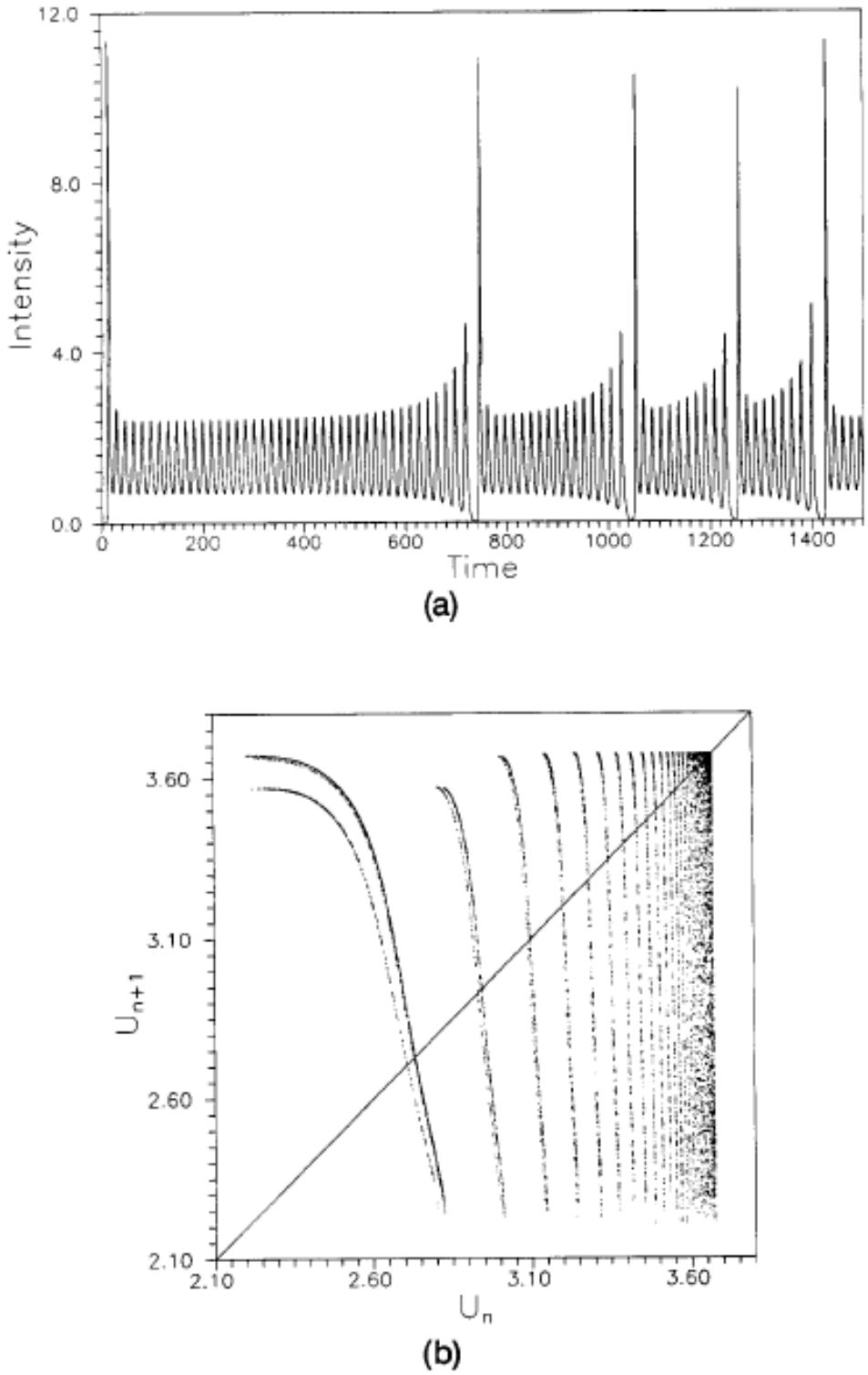

FIG. ***2.7 –*** *Signal et application de premier retour dans une situation quasi-homocline du modèle théorique. Chaque branche de l'application correspond dans les signal à un nombre donné de petites oscillations. Le nombre maximal de petites oscillations entre deux grands pics tend vers l'infini au voisinage de la bifurcation homocline.*

2.4 CALCUL DE DIMENSIONS FRACTALES DANS LE LASER CO_2

– "Improved correlation dimension estimates through change of variable", M. Lefranc, D. Hennequin, and P. Glorieux, *Phys. Lett.* A **163**, 269–274 (1992). (appendice C, page 151).

2.4.1 Introduction

Le deuxième article de ce chapitre concerne le calcul de dimensions fractales à partir de signaux délivrés par le laser CO_2 à modulation de pertes. Il y a dix ans, cette approche était probablement la reine des méthodes de caractérisation du chaos déterministe, notamment après la publication par Grassberger et Procaccia de leur célèbre algorithme [51]. Le principe en est le suivant : au cours du temps, le point représentant l'état du système à un instant donné parcourt une région bien définie de l'espace des états, l'attracteur (figure 2.2). Comme on l'a mentionné plus haut, cette région peut être caractérisée par sa dimension : s'agit-il d'une surface, d'un volume ou encore d'une structure intermédiaire, un objet fractal? De manière générale, la dimension topologique d'un objet géométrique peut être définie en s'intéressant au nombre $N(\epsilon)$ de boules de rayon ϵ qu'il faut utiliser pour le recouvrir. Si on observe que dans la limite $\epsilon \to 0$,

$$N(\epsilon) \sim \frac{1}{\epsilon^D},$$

alors D est la dimension topologique, qui vaut 1 pour une ligne, 2 pour une surface, etc. La mesure d'une dimension non entière est alors censée apporter la preuve qu'une dynamique chaotique est à l'oeuvre [51, 53, 69]. Le calcul de dimensions fractales peut également en principe aider à quantifier le nombre de degrés de liberté actifs dans un système, et donc à écarter la possibilité que la dynamique irrégulière observée soit produite par un système stochastique de dimension infinie.

La dimension fractale généralement calculée à partir de données expérimentales est la dimension de corrélation introduite par Grassberger et Procaccia [51]. Soit un ensemble de points échantillonnés sur un attracteur chaotique, on estime la probabilité $\mathcal{P}(r)$ que deux points pris au hasard aient une distance inférieure à une distance donnée r. On définit alors la dimension de corrélation par la loi d'échelle :

$$\mathcal{P}(r) \sim r^{D_2}$$

L'objectif expérimental est donc de mettre en évidence cette loi d'échelle dans l'analyse des séries temporelles et d'obtenir une estimation fiable de l'exposant.

Un des principaux attraits du calcul de dimensions fractales est, en principe, son invariance par rapport aux changement de coordonnées. On peut en effet montrer que deux ensembles de points reliés par un difféomorphisme (c'est-à-dire une application continue et différentiable, dont l'inverse existe et possède les mêmes propriétés) sont caractérisés par la même dimension fractale. Cette propriété assure de manière rigoureuse qu'une valeur unique de la dimension fractale puisse être obtenue, quelle que soit la variable d'état que l'on mesure pour reconstruire un attracteur chaotique, à condition toutefois que l'on dispose d'une série temporelle de longueur infinie, et parfaitement exempte de bruit. Il est évidemment impossible de garantir ces deux conditions dans des expériences réelles.

2.4.2 Résultats

Nous avons cherché à évaluer la robustesse du calcul de dimension en l'appliquant à des séries temporelles d'un laser CO_2 guide d'onde à modulation de pertes. Ces enregistrements présentaient l'avantage d'être relativement longs (en 1992) et extrêmement peu bruyants même si ils étaient entachés d'une erreur de quantification non négligeable, étant enregistrés au moyen d'un oscilloscope numérique d'une résolution de 8 bits. Il étaient donc exempts de la plupart des sources d'erreurs systématiques alors répertoriées dans la littérature, excepté le fait que le quantum de numérisation fixait une distance limite en dessous de laquelle il était illusoire de chercher la loi d'échelle dont l'exposant est censé fournir la dimension fractale. Ce dernier point est cependant moins une limitation qu'il n'y paraît, car la reconstruction de l'attracteur chaotique dans des espaces de plongement de dimensions de plus en plus grandes s'accompagne d'une augmentation systématique des distances entre points.

Notre étude a clairement mis en évidence un biais systématique lié à l'inhomogénéité de la densité de probabilité sur l'attracteur, conséquence directe du fait que des données réelles sont nécessairement en quantité finie, et ne permettent donc que d'explorer une petite partie de l'intervalle de distances où la loi de puissance est censée se manifester. En effet, les signaux laser présentent en général de longs intervalles de temps où l'intensité reste proche de zéro, pendant que le milieu actif reconstitue une inversion de population suffisante pour compenser les pertes de la cavité et donner à nouveau lieu à une émission laser. Ces longs passages à zéro font que l'attracteur reconstruit présente une forte concentration de points dans la région située autour du point de l'espace des états correspondant à une intensité nulle à tout temps.

Plus précisément, nous avons comparé les résultats obtenus d'une part à partir des séries temporelles de l'intensité, d'autre part à partir de celles enregistrées en introduisant un amplificateur logarithmique entre le détecteur et l'oscilloscope numérique. Nous avons observé des différences significatives, en contradiction directe avec la supposée invariance par rapport aux changements de coordonnées, avec dans tous les cas un bien meilleur comportement pour les données associées au logarithme de l'intensité. Pour un premier groupe de régimes correspondant à du chaos moyennement développé, une même valeur de la dimension fractale était obtenue pour les deux signaux à des dimensions de plongement suffisamment grandes, même si la convergence était bien plus rapide pour le logarithme. Pour des enregistrements correspondant à un degré de chaos plus élevé, la différence fut encore plus claire : le calcul convergeait vers des valeurs complètement différentes (1.50 et 2.09 !) de la dimension fractale, quelle que soit la dimension de l'espace de reconstruction (figure 2.8). Il fallait donc conclure qu'une estimation de la dimension fractale peut dépendre de manière importante de la variable mesurée, ce que confirmaient de manière particulièrement nette les simulations numériques accompagnant ces expériences. Il est intéressant de noter que les systèmes de Lorenz et Rössler, qui sont très majoritairement utilisés pour engendrer des séries temporelles synthétiques dans le but de tester les méthodes de caractérisation, présentent une structure extrêmement homogène et ne mettent donc pas en évidence ce problème.

Ces résultats mettaient donc en doute la fiabilité des estimations de dimensions fractales à partir de séries temporelles finies, entachées de bruit, en un mot provenant d'expériences réelles. Bien qu'ils furent mentionnés dans un article de revue de James Theiler [69], à ce moment l'un des meilleurs experts du sujet, ils ne connurent pas un très grand retentissement, probablement parce que le message délivré ne correspondait pas aux attentes de l'époque,

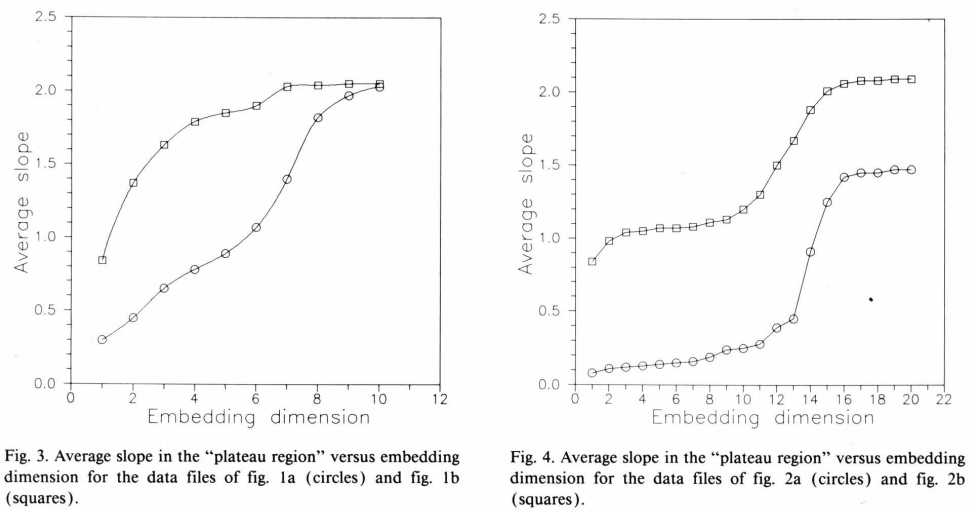

Fig. 3. Average slope in the "plateau region" versus embedding dimension for the data files of fig. 1a (circles) and fig. 1b (squares).

Fig. 4. Average slope in the "plateau region" versus embedding dimension for the data files of fig. 2a (circles) and fig. 2b (squares).

FIG. ***2.8 –*** *Estimation de la dimension fractale en fonction de la dimension de plongement. En principe, ces courbes doivent saturer à une valeur qui est la dimension recherchée. Dans chaque figure, on a représenté les résultats obtenus en utilisant l'intensité et son logarithme comme variables. A gauche, on observe que les deux courbes convergent vers la même valeur, mais que la convergence de la courbe obtenue avec le logarithme est beaucoup plus rapide. A droite, on s'aperçoit que les mesures obtenues avec l'intensité et le logarithme ne convergent même pas vers la même valeur, au moins pour des dimensions de plongement inférieures à 20.*

qui voulait croire à l'existence de méthodes de caractérisation solides. Quoiqu'il en soit, l'analyse du chaos grâce aux dimensions fractales semble avoir aujourd'hui complètement disparu de la littérature actuelle, probablement parce qu'un grand nombre d'investigateurs sont parvenus indépendamment aux mêmes conclusions. C'est ce constat qui m'avait alors convaincu de me tourner vers des méthodes de caractérisation plus robustes, et notamment celle proposée peu avant par l'équipe du théoricien américain Robert Gilmore, et qui est basée sur des concepts de topologie, et en particulier sur la théorie des noeuds.

3

L'Analyse Topologique du Chaos

3.1 INTRODUCTION

3.1.1 Les mécanismes du chaos : étirement et repliement

Comme on l'a vu au chapitre 6, c'est par des arguments géométriques et topologiques que s'explique de manière naturelle l'existence de régimes « chaotiques », à la fois déterministes et imprédictibles, comme l'illustre la transformation du fer à cheval [4, 49, 70]. Les lois d'évolution, qui déterminent la succession des états visités à partir d'une condition initiale donnée, peuvent être vues comme une transformation de l'espace des états dans lui-même. Dans le cas d'une dynamique chaotique, ces transformations sont caractérisées par deux mécanismes géométriques très simples : l'*étirement* et le *repliement* [3, 4, 70]. L'étirement, qui éloigne sans relâche les trajectoires voisines, est reponsable de l'instabilité et de l'imprédictibilité des régimes chaotiques, qui se manifeste par une croissance exponentielle de tout écart par rapport à une trajectoire de référence. Cette amplification continue serait incompatible avec le maintien dans une région bornée de l'espace des états sans la présence du repliement, effet intrinséquement non linéaire, qui ramène des régions éloignées de l'espace des états l'une sur l'autre (figure 2.3). Ce sont donc les principes que suit le boulanger pour réaliser une pâte feuilletée qui sont responsables de l'apparition du chaos dans un système dynamique, avec les mêmes propriétés de mélange.

Un des systèmes chaotiques les plus dépouillés qui soient, le paradigmatique « fer à cheval » imaginé par le mathématicien Stephen Smale dans les années 60 [55], et dont étirement et repliement sont les deux ingrédients essentiels, montre on ne peut plus clairement que ces deux mécanismes sont au coeur de la dynamique chaotique (figure 2.4). Il est donc logique que les premières méthodes quantitatives de caractérisation du chaos, apparues dans les années 80, aient été basées de manière plus ou moins directe sur l'existence des mécanismes d'étirement et de repliement. Ainsi, les calculs d'exposants de Lyapunov mesurent le taux moyen d'étirement des trajectoires de l'attracteur, tandis que les dimensions fractales mettent en évidence la structure feuilletée de l'attracteur chaotique résultant des effets combinés de

l'étirement et du repliement [49, 52] Cependant, ni l'une ni l'autre ne sont très robustes par rapport aux différentes imperfections dont peut souffrir une série temporelle expérimentale (bruit, inhomogénéité, longueur insuffisante, non stationnarité, etc.). Par ailleurs, elles ne permettent pas d'entreprendre une classification qualitative des différentes manières selon lesquelles étirement et repliement peuvent être combinés et ne donnent aucune information sur les séquences de bifurcation qui peuvent survenir dans un système donné. En bref, les grandeurs moyennes qu'elles délivrent fournissent peu d'informations sur la structure du chaos, mis à part pour estimer, dans les cas où ces données peuvent être obtenues de manière fiable, le nombre de degrés de liberté du système ou l'intervalle de temps sur lequel on peut prédire son évolution future.

Ce sont les processus d'étirement et de repliement qui déterminent la manière dont les différentes trajectoires sur l'attracteur chaotique s'enchevêtrent les unes autour des autres. Inversement, on pourrait songer à mettre au point une méthode qui, en caractérisant l'enchevêtrement d'un faisceau de trajectoires, permette de remonter aux transformations géométriques de l'espace des états qui lui ont donné naissance, et de décrire ces transformations par des modèles géométriques du type « fer à cheval ». Mettre au point une telle méthode n'a cependant rien d'évident en raison de la sensibilité aux conditions initiales, qui fait que des trajectoires proches peuvent avoir rapidement des comportements tout à fait différents.

3.1.2 Un attracteur chaotique est un sac de noeuds

Mindlin, Hou, Solari, Gilmore et Tuffilaro [1] ont apporté en 1990 une contribution importante à ce problème en proposant une méthode topologique d'analyse du chaos qui faisait appel à des concepts tels que théorie des noeuds et variétés branchues[1], et reposait sur un théorème de Birman et Williams [71, 72]. Un des points clés de cette approche est de ne caractériser que des trajectoires bien particulières de l'espace des phases : les orbites périodiques instables, associées à des courbes fermées dans l'espace des états. Lorsque ce dernier est de dimension trois, les outils mathématiques de la théorie des noeuds peuvent être invoqués pour analyser la manière dont ces courbes fermées sont emmêlées et ainsi analyser comment elles ont été façonnées par l'action de l'étirement et du repliement. Les invariants topologiques des orbites périodiques constituent alors de véritables empreintes digitales.

Il peut paraître surprenant de réduire un régime chaotique à une collection, même importante, d'orbites périodiques et l'on pourrait craindre que cette simplification ne puisse s'effectuer qu'en amputant la complexité du régime chaotique. Un des nombreux paradoxes du chaos est qu'il n'en est rien : on peut montrer qu'un attracteur chaotique contient une infinité dense d'orbites périodiques instables, c'est-à-dire qu'en tout point de l'attracteur on peut trouver des orbites périodiques passant arbitrairement près [73–75]. Ces orbites ne sont pas un concept abstrait : leurs signatures sont aisément décelables dans les signaux d'un système chaotique de dimension pas trop grande (figures 3.1 et 3.2) [2, 5].

Les trajectoires périodiques d'un régime chaotique sont donc aux trajectoires apériodiques ce que les nombres rationnels sont aux nombres irrationnels : elles forment un ensemble de mesure nulle, mais qui peuvent approcher avec une précision arbitraire tout membre de l'ensemble dans lequel elles sont plongées. C'est l'ergodicité de la dynamique qui leur assure

1. Une variété branchue est une variété obtenue par le recollement à leurs extrémités de plusieurs branches.

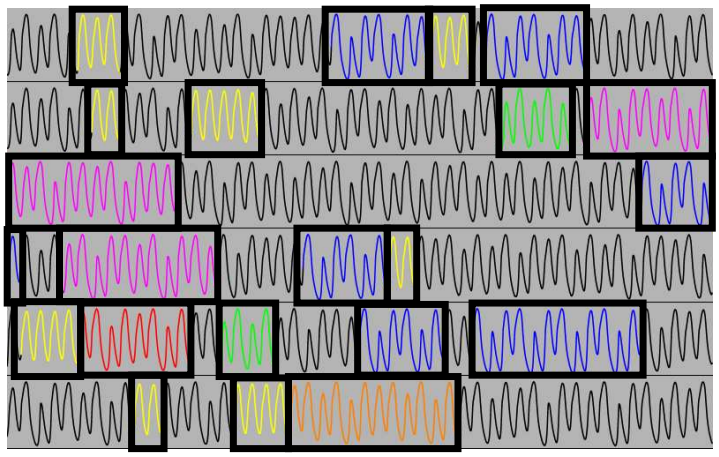

FIG. ***3.1 –*** *Bouffées de comportement quasiment périodique de période inférieure ou égale à 5 dans les signaux de la figure 2.1. Elles constituent des signatures de la rencontre d'orbites périodiques instables.*

ces propriétés : puisqu'on peut revenir arbitrairement près d'une condition initiale donnée à condition d'attendre suffisamment longtemps, il doit exister dans le voisinage de cette condition initiale des points dont la trajectoire se referme exactement. Ici aussi, le théorème mathématique a sa traduction expérimentale : les trajectoires superposées d'une bonne dizaine d'orbites périodiques instables peuvent suffir à donner une excellente approximation de la trajectoire infiniment longue qui tisse un attracteur chaotique (figure 3.3).

On voit que l'existence des orbites périodiques instables est une conséquence directe de la dynamique chaotique. Comment caractériser l'enchevêtrement de courbes fermées qu'on observe à la figure 3.3(b) ? De manière amusante, c'est en se le représentant comme un sac de noeuds que l'on arrive à appréhender l'organisation systématique des orbites périodiques. Considérons les deux orbites de périodes 1 et 4 de la figure 3.4. Le nombre de tours que la plus longue effectue autour de l'autre est un invariant topologique, le nombre d'enlacement, qui est ici égal à 2. De manière générale, la théorie mathématique des noeuds s'intéresse précisément au problème de caractériser l'entrelacement de courbes fermées dans un espace de dimension 3 par des quantités qui ne varient pas si on déforme les courbes sans les faire se croiser [76, 77].

Le point clé est que les invariants topologiques ainsi définis sont également des invariants dynamiques ! En effet, une orbite périodique ne peut jamais se croiser elle-même à cause du déterminisme, et donc son type de noeud est bien défini. De plus, elle ne peut pas non plus se croiser elle-même, ni une autre orbite, lorsqu'on fait varier un paramètre de contrôle, pour les mêmes raisons. Les invariants de noeud d'une orbite périodique sont donc constants sur tout le domaine d'existence de l'orbite, et constituent par conséquent de véritables empreintes digitales.

3.1.3 Démêler le chaos : noeuds et gabarits

Comme toute trajectoire sur l'attracteur, les orbites périodiques doivent porter la trace des processus d'étirement et de repliement qui organisent l'attracteur chaotique dans lequel

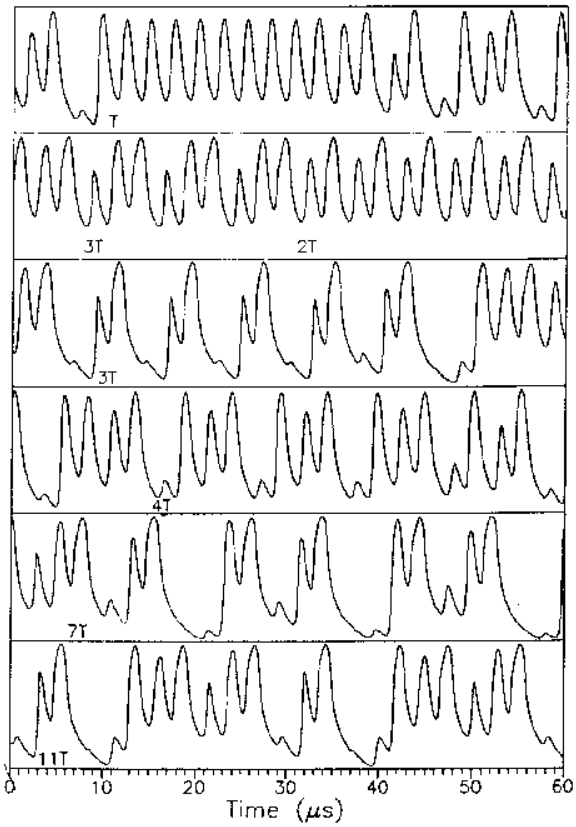

FIG. ***3.2 –*** *Quelques exemples significatifs de signatures d'orbites périodiques instables extraites des signaux d'un laser CO_2 à modulation de pertes [5].*

elles sont plongées. On s'attend donc à ce les types de noeud des orbites périodiques et leurs invariants topologiques contiennent une information relative à ces processus.

C'est précisément ce qu'énonce le théorème de Birman–Williams : tout flot chaotique tri-dimensionnel est associé à un semi-flot sur une variété bi-dimensionnelle à plusieurs branches, tel que les orbites périodiques instables du flot sont en bijection avec les orbites du semi-flot et que les ensembles d'orbites en correspondance sont isotopes [71]. En termes plus concrets, les orbites périodiques du flot peuvent être projetées de manière globale sur la surface branchue sans modifier leur enlacement et donc en préservant tous leurs invariants topologiques (figure 3.5). Ces surfaces branchues sont généralement désignées sous le nom de *gabarits* (en anglais, *templates* ou *knot-holders*).

On peut tirer parti de ce théorème pour construire une méthode d'analyse de signaux expérimentaux procédant de la manière suivante [2]. Tout d'abord, un certain nombre d'orbites périodiques sont extraites des séries temporelles en y détectant des récurrences à petit temps de premier retour. Il est bien sûr hors de question de détecter l'infinité d'orbites périodiques présentes mais, fort heureusement, on constate généralement que quelques or-

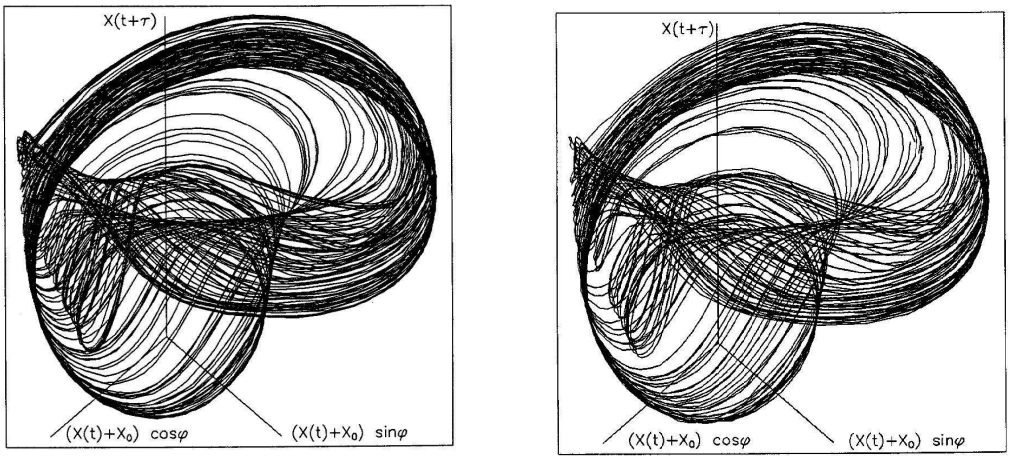

FIG. ***3.3 –*** *(a) Attracteur chaotique reconstruit à partir du signal de la figure 2.1 (b) Superposition d'une dizaine d'orbites périodiques instables contenues dans cet attracteur et détectées dans la série temporelle. On constate que leur superposition donne une excellente approximation de l'attracteur, en tout cas suffisante pour extraire des informations utiles sur la dynamique [5].*

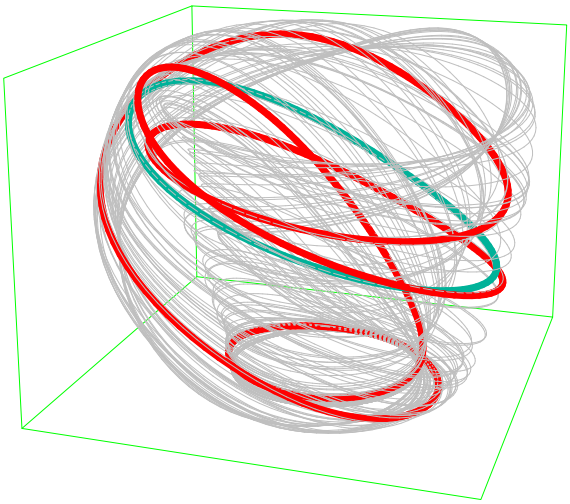

FIG. ***3.4 –*** *Deux orbites de périodes 1 et 4 plongées dans un attracteur chaotique. L'orbite de période 1 est une simple boucle tandis que celle de période 4 est isotope au noeud non trivial le plus simple, le noeud de trèfle. Le nombre d'enlacement des deux orbites est de deux.*

bites de petite période suffisent à fournir une bonne approximation de l'attracteur (voir figure 3.3). On obtient ensuite les trajectoires de ces orbites périodiques dans un espace des phases reconstruit, où on caractérise l'enlacement des trajectoires fermées correspondantes au moyen d'invariants de la théorie des noeuds. Ces invariants constituent la signature de l'organisation topologique globale de l'attracteur.

L'étape suivante est de déterminer le gabarit le plus simple compatible avec les données expérimentales, c'est-à-dire qui possède un ensemble d'orbites périodiques présentant exactement les mêmes invariants topologiques que les orbites détectées expérimentalement. Cela garantit que ces dernières peuvent être inscrites sur la surface du gabarit sans modifier leur

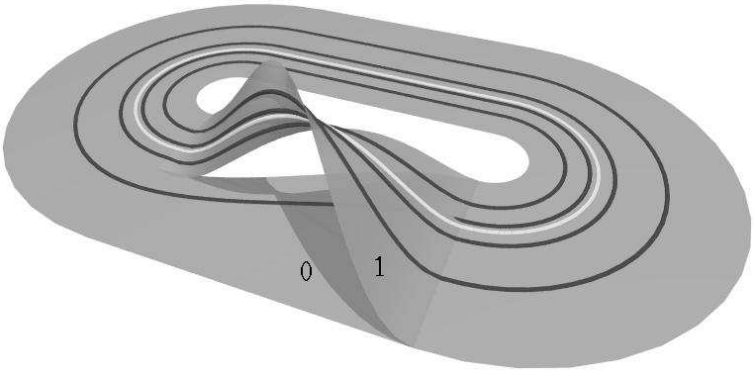

FIG. ***3.5 –*** *Un* gabarit *(ici celui du fer à cheval) caractérise l'organisation topologique globale des orbites périodiques instables plongées dans un attracteur chaotique.*

enlacement. L'organisation topologique globale de l'attracteur est alors décrite de manière concise par la structure de ce gabarit, structure qui présente l'avantage de pouvoir être caractérisée par un ensemble de quelques nombres entiers, facilement manipulables [1–4].

Cette approche se caractérise par une très grande robustesse et par sa capacité à s'adapter à des données de qualité très variable. Dans les cas les plus difficiles, il faut bien évidemment revoir ses exigences à la baisse, mais il est en général toujours possible d'extraire une information utile. Un exemple particulièrement frappant de cette robustesse est fourni par l'application de l'analyse topologique à un système non stationnaire, décrite à la section 3.5 : dans cet exemple, la série temporelle est trop courte pour reconstruire un attracteur au sens strict, mais il reste quand même possible d'extraire une orbite dont on montre qu'elle ne peut exister que dans un système chaotique, et d'obtenir par là une borne inférieure sur l'entropie topologique [15].

3.1.4 Une méthode de caractérisation robuste

La robustesse de l'analyse topologique se manifeste dès la détermination du type de noeud et des invariants associés. On ne peut en effet extraire des séries temporelles les orbites périodiques réelles, mais seulement des fragments de trajectoires visitant temporairement leur voisinage, ces fragments étant entachés d'un bruit plus ou moins important. Fort heureusement, le type de noeud d'une courbe fermée ne dépend pas de la position précise de la courbe dans l'espace, mais uniquement de la manière dont elle s'enroule sur elle-même, c'est-à-dire des positions relatives de ses différentes portions. Une trajectoire approchée qui ne se referme pas exactement suffit donc pour établir le type de noeud de l'orbite réelle lorsqu'on peut estimer que le déplacement entre les deux courbes est plus petit que la distance entre les différents brins de l'orbite. De même, le bruit n'introduit aucune erreur s'il est d'amplitude suffisamment petite pour ne pas induire de croisements entre deux tronçons différents de l'orbite. Le problème est en fait relié à celui compter le nombre de tours qu'effectue une courbe fermée du plan complexe autour de l'origine. On comprend facilement que ce problème est d'autant plus résistant aux perturbations de toutes sortes que la courbe est loin de l'origine.

Mais la méthode se montre également robuste aux étapes suivantes, et notamment lorsqu'il faut résoudre un problème d'inversion et déterminer les nombres caractéristiques du gabarit

à partir des invariants topologiques mesurés. Il s'agit en effet d'un problème surdéterminé : le nombre d'invariants est en général bien plus grand qu'il n'est nécessaire pour fixer une solution unique [2,4]. Pour fixer les idées, il suffit en général de trois orbites différentes pour identifier un gabarit à deux branches de type « fer à cheval ». En supposant que nous ayions détecté sept orbites, nous pouvons vérifier que les invariants des quatre orbites de plus grande période sont bien ceux prédits par le gabarit déterminés à partir des trois premières, et être donc confiants que ce gabarit décrit bien l'organisation topologique globale de l'attracteur. Il est suffisamment rare qu'une méthode fournisse naturellement le moyen de vérifier la cohérence des résultats qu'elle fournit pour que cela vaille la peine de le noter.

Il reste toutefois un aspect qui n'a pas encore été suffisamment élucidé. Le théorème de Birman et Williams est démontré dans le cas hyperbolique, où toutes les orbites autorisées par la structure du gabarit sont présentes [71,72]. Or, un attracteur réel se caractérise par le fait que certaines des orbites de la limite hyperbolique n'existent pas encore. Il n'est alors pas évident qu'il y ait toujours un seul gabarit hyperbolique pouvant porter l'ensemble des orbites.

Effectivement, nous avons trouvé des situations où deux gabarits différents pouvaient décrire les données observées [78]. C'est que ces deux gabarits avaient des sous-ensembles d'orbites isotopes, auxquels était également isotope le jeu d'orbites expérimentales. Cela ne remet en pas en cause le principe de l'approche, et la possiblité de classifier les régimes chaotiques, mais indique simplement qu'il faut parfois décrire la structure topologique d'un attracteur par une intersection de gabarits plutôt que par un gabarit unique.

3.1.5 Analyser la structure fine d'un attracteur : dynamique symbolique et spectres d'orbites

On pourrait craindre que malgré toutes les qualités que nous venons de rappeler, l'analyse du chaos au moyen de la théorie des noeuds et des gabarits ne fournisse qu'une information, certes intéressante, mais limitée et qu'elle ne doive sa robustesse qu'à son manque d'ambition. En supposant que l'on puisse ranger différents systèmes chaotiques dans différentes classes topologiques selon la structure du gabarit auquel ils sont associés, est-il possible d'aller plus loin une fois que l'on est en mesure de déterminer les régimes de tel système correspondent à tel gabarit ?

La réponse à cette question est fort heureusement positive. Même si on constate généralement qu'un même gabarit peut décrire l'ensemble des régimes situés dans une large région de l'espace des paramètres d'un système donné, et qu'il faut donc une description plus fine pour les distinguer entre eux, on observe que l'organisation des orbites périodiques varie sur des échelles beaucoup plus petites. Un système réel n'est en effet pas *structurellement stable* : au fur et à mesure qu'on fait varier un paramètre de contrôle, le spectre d'orbites périodiques se modifie en permanence, certaines orbites périodiques étant créées, d'autres étant au contraire détruites. Les outils développés pour l'analyse topologique sont particulièrement bien adaptés pour suivre ces évolutions car les invariants topologiques des orbites périodiques les identifient fréquemment de manière unique : ainsi, il n'existe dans la classe topologique du fer à cheval qu'une seule orbite de période 7 ayant un nombre d'auto-enlacement de 16 et une torsion impaire [11]. Les transformations du spectre d'orbites périodiques peuvent être donc tout d'abord appréhendées au travers des transformations du spectre d'invariants topologiques.

Deux propriétés fondamentales de la dynamique chaotique permettent d'organiser de manière particulièrement puissante l'information relative au spectre des orbites périodiques. Tout d'abord, il est utile, si l'on désire indiquer sans ambiguité quelles orbites périodiques sont présentes dans un régime donné, de disposer d'un schéma canonique pour étiqueter ces orbites (de la même manière qu'on peut désigner un niveau d'énergie atomique par le signe $3S_1$). Un tel schéma est fourni naturellement par la *dynamique symbolique* [4, 49, 57, 79]. On peut en effet montrer que les trajectoires d'un système chaotique peuvent être mises en bijection avec un ensemble de suites de symboles pris dans un alphabet fini, par exemple les suites de 0 et de 1. Chaque orbite périodique peut être alors repérée par un mot de longueur finie sur les lettres 0 et 1 [4,49,57]. Ainsi, l'orbite de période 7 du fer à cheval que nous avions prise comme exemple au paragraphe précédent est-elle l'orbite 0010101 si on convient que la lettre 1 désigne la branche renversant l'orientation. Comme nous le verrons à la section 3.4, nous avons mis au point une méthode efficace pour remonter des invariants topologiques d'une orbite à son nom symbolique.

Par ailleurs, la présence ou l'absence de deux orbites périodiques données dans le régime que l'on étudie ne sont en général pas indépendantes. On peut en effet montrer que la plupart des orbites forcent par leur seule présence l'existence d'une infinité d'autres orbites périodiques, ce qui introduit une relation d'ordre partiel sur les orbites périodiques [80–84]. De manière remarquable, cette relation d'ordre ne dépend que des invariants topologiques, ce qui peut s'expliquer assez simplement. En effet, les invariants topologiques décrivent la disposition relative des différentes orbites. De même qu'on ne peut assembler les pièces d'un casse-tête dans n'importe quel ordre sous peine de ne pouvoir plus ensuite placer les dernières pièces, l'ordre dans lequel les orbites périodiques apparaissent est contraint par la manière dont elles sont enchevêtrées : certaines orbites doivent impérativement être placées à un certain stade de la construction, avant que d'autres ne leur fassent obstruction [4, 80–82, 84].

L'existence de cet ordre partiel permet de décrire de manière concise le contenu en orbites périodiques d'un régime chaotique par la donnée d'une *base d'orbites*, choisies de manière à ce que toute orbite périodique présente dans l'attracteur soit forcée par l'une ou l'autre des orbites de la base [4, 80]. Cette représentation se révèle particulièrement adaptée pour étudier les différentes routes menant de l'apparition du chaos à un chaos complètement développé. Si l'ordre dans lequel les orbites apparaissent était rigide, comme on l'observe dans le cas simple de la suite logistique, la base d'orbites comporterait pour chaque valeur des paramètres une et une seule orbite : celle dernièrement apparue. Mais ce n'est pas vrai dans le cas général, et on doit alors préciser plusieurs orbites de base. L'énumération des différentes bases compatibles avec la structure topologique de l'attracteur permet alors d'établir la liste des différentes scénarios que l'on peut suivre pour faire apparaître l'ensemble des orbites périodiques qui seront présentes dans le chaos complètement développé [4, 80].

On le voit, la méthode d'analyse topologique du chaos basée sur la théorie des noeuds et sur la notion de gabarit se révèle particulièrement pertinente pour comprendre les régimes chaotiques à petit nombre de degrés de libertés. C'est qu'elle fournit une description pertinente des mécanismes d'étirement et de repliement qui sont au coeur de la dynamique chaotique. Dans les sections qui suivent, et après un bref résumé, nous décrivons de manière un peu plus détaillée les travaux dans laquelle nous l'avons mise en oeuvre.

3.1.6 Résumé des travaux

Après des premiers travaux consacrés à la démonstration de la faisabilité expérimentale de cette approche (section 3.2, [5]), nous avons exploré deux grands thèmes : d'une part l'étude des variations systématiques de la structure topologique lorsque l'on fait varier un paramètre de contrôle, qui mène à conclusion que l'organisation topologique des orbites périodiques contrôle largement la structure des diagrammes de bifurcation (section 3.3, [6–9]), d'autre part l'exploration des liens entre topologie et dynamique symbolique, à la fois numériquement ou expérimentalement (section 3.4, [8,10–12]). Ce dernier aspect permettait de faire le lien entre l'approche nouvelle à laquelle nous avons contribué, l'analyse topologique, et une approche plus ancienne et considérée comme un des outils de base de l'analyse du chaos, la dynamique symbolique. Nous avons en particulier montré expérimentalement que les informations contenues dans les invariants topologiques permettaient de construire un codage symbolique d'un attracteur chaotique, permettant de le caractériser ensuite par les méthodes de la dynamique symbolique [11]. Nous avons plus tard montré que les codages ainsi obtenus étaient parfaitement identiques à ceux fournis par les méthodes classiques, ce qui apportait au passage une confirmation supplémentaire de la validité de l'analyse topologique [12].

Si c'est la caractérisation de l'enchevêtrement des orbites périodiques permet de comprendre l'organisation globale d'un attracteur chaotique, la structure topologique d'une orbite isolée peut déjà apporter des informations essentielles. Ainsi, il a été montré que certains types de noeud ne peuvent être réalisés par une orbite périodique que dans des systèmes présentant une dynamique chaotique : la manière dont les différents brins s'enroulent les uns autour des autres implique que la dynamique dans le voisinage de l'orbite est mélangeante, en d'autres termes chaotique [85]. Cette propriété a été mise à profit pour prouver de manière rigoureuse la nature chaotique de la dynamique dans un système non stationnaire [15]. Il n'est alors pas question d'enregistrer une longue série temporelle pour reconstruire un attracteur, car un ou plusieurs paramètres dérivent dans le temps, et avec eux les lois d'évolution du système : les méthodes d'analyse traditionnelles sont alors inopérantes. Si par contre cette dérive est suffisamment petite pendant l'intervalle de temps où le système passe dans l'ombre d'une orbite périodique, et que cette orbite a un type de noeud « mélangeant », alors la preuve d'une dynamique chaotique est obtenue.

Les travaux effectués par notre équipe ou dans d'autres laboratoires pendant plus de dix ans ont permis de montrer clairement que la caractérisation du chaos déterministe par la théorie des noeuds et les gabarits était une approche extrêmement pertinente et puissante. Il était donc d'autant plus frustrant que cette approche soit limitée au systèmes à exactement trois degrés de liberté par l'un de ses ingrédients-clés : la théorie des noeuds. Ce n'est en effet qu'en dimension trois que les différentes conformations d'une courbe fermée peuvent être topologiquement inéquivalentes. A quatre dimensions et au-delà, toute courbe fermée peut se ramener sur n'importe quelle autre sans jamais se recouper elle-même, et en particulier est toujours équivalente à un simple cercle. Le concept d'enchêvetrement tombe, et plus aucune signature du chaos ne peut ainsi être extraite. La dimension quatre semble donc être une barrière infranchissable pour l'analyse topologique, au moins dans sa forme classique.

De manière étonnante, cette approche a pourtant été déjà appliquée à un système spatio-temporel à grand nombre de degrés de liberté, basé sur une valve optique à cristaux liquides : quelques orbites de petite période ont pu être détectées, et leur type de noeud était compatible

avec ce qu'on sait de la route vers le chaos par cascade de doublements de période [86]. La clé du paradoxe réside dans le fait que la dynamique de ce système est apparemment de petite dimension en un point donné de la section transverse du faisceau, mais que cette dernière se divise en domaines dont les évolutions sont indépendantes, les frontières des domaines pouvant elles-mêmes se déplacer au cours du temps.

Mais difficile ne veut pas dire impossible. Récemment une piste très prometteuse s'est ouverte pour étendre l'analyse topologique en dimension supérieure [87]. Elle est basée sur la constatation que la théorie des noeuds n'est finalement pas un ingrédient central de l'analyse topologique : les principaux fondamentaux de cette dernière sont le déterminisme (l'état actuel détermine toute l'évolution future) et la continuité. En dimension trois, la théorie des noeuds est un moyen commode de mettre en oeuvre ces principes, sans en être la seule formulation. Ainsi, nous avons montré qu'un formalisme basé sur des hypersurfaces de triangulations de points périodiques redonnait en dimension trois des résultats équivalents à ceux obtenus par l'étude des courbes fermées [87], tout en se généralisant de manière plus directe aux dimensions supérieures. La construction de la version quadridimensionnelle de ce formalisme est actuellement en cours d'étude.

Nous passons maintenant à un bref rappel des principaux résultats contenus dans les articles présentés dans ce mémoire.

3.2 ANALYSE TOPOLOGIQUE DU LASER CO_2

– "Topological analysis of chaotic signals from a CO_2 laser with modulated losses", M. Lefranc and P. Glorieux, *Int. J. Bifurcation Chaos Appl. Sci. Eng.* **3**, 643–649 (1993). [appendice D, page 293]

Il s'agit ici de la première caractérisation expérimentale de la topologie du chaos au Laboratoire [5], et l'une des toutes premières en général, suivant de près celles de la réaction de Belousov-Zhabotinskii [2], d'un laser à absorbant saturable [88] et d'un oscillateur RMN [89], les deux dernières n'ayant pas encore été publiées lorsque nos expériences durent réalisées.

Elle concerne à un système chaotique d'une stabilité et d'un rapport signal sur bruit exceptionnels : un laser CO_2 guide d'ondes à modulation de pertes construit par la Société Anonyme de Télécommunications. Ce travail n'est donc pas représentatif de ce qu'on peut attendre de l'analyse d'un système expérimental quelconque, mais il a sans doute contribué à confirmer que l'analyse topologique reposait sur des bases solides. Ainsi, les signatures d'orbites périodiques instables détectées dans les enregistrements expérimentaux sont à ma connaissance les plus spectaculaires qui aient été décrites dans la littérature consacrées au chaos, comme par exemple celle située tout en haut de la figure 3.2 où l'on voit la trajectoire du système rester sur près de 14 périodes dans l'ombre d'une orbite de période 1 avant de s'en éloigner rapidement pour visiter les autres régions de l'attracteur. De tels évènements ne sont possibles que lorsque le niveau de bruit est extrêmement faible, car la moindre perturbation éloignant le système de l'orbite est aussitôt amplifiée par le caractère instable de l'orbite. Dans le cas présent, le taux de divergence de la trajectoire par rapport à l'orbite à la fin de la bouffée périodique, et la durée de cette dernière, nous permettent d'estimer le rapport signal sur bruit à environ 3000 !

Mais au-delà de la présence d'orbites périodiques instables dans un régime chaotique, c'est le fait que l'ensemble de ces orbites fournisse une excellente approximation de l'attracteur

chaotique qui aura été illustré de manière particulièrement frappante dans cet article. Ainsi, on a pu voir à la figure 3.3 que la superposition d'une douzaine d'orbites périodiques repérées dans l'attracteur représenté à côté en fournit une excellente approximation. On peut donc se convaincre que l'on ne perd pas d'information en se limitant à l'analyse des seules orbites périodiques et l'on veut bien croire à la validité du théorème mathématique qui affirme qu'en tout point de l'attracteur, il existe des orbites périodiques instables passent arbitrairement près.

Pour ce qui est de la structure topologique de l'attracteur de la Figure 3.3(a), la conclusion de ce travail fut qu'il s'agissait d'un mécanisme de type fer à cheval, exactement comme les autres travaux réalisés à la même époque et peu après [2, 10, 65, 88–91]. Même si ce résultat était établi sans ambiguité, il était quelque peu décevant dans la mesure où entreprendre une classification topologique des régimes chaotiques n'a de sens que si l'on peut effectivement observer des structures topologiques différentes. A partir du moment où la même structure était observée dans les premières expériences réalisées ici et là, l'intérêt de l'analyse topologique était mis en doute. Ce n'est en fait qu'un peu après que les premières organisations topologiques distinctes du fer à cheval furent observées, et que le doute fut levé, comme nous le verrons dans la section suivante.

3.3 DIAGRAMME DE PHASE DES OSCILLATEURS NON LINÉAIRES FORCÉS

- G. Boulant, M. Lefranc, S. Bielawski, and D. Derozier, "Horseshoe templates with global torsion in a driven laser", *Phys. Rev.* E **55**, 5082–5091 (1997). [appendice D, page 275]
- G. Boulant, S. Bielawski, D. Derozier, and M. Lefranc, "Experimental observation of a chaotic attractor with a reverse horseshoe topological structure", *Phys. Rev.* E **55**, R3801–3804 (1997). [appendice D, page 269]
- G. Boulant, M. Lefranc, S. Bielawski, and D. Derozier, "A nonhorseshoe template in a chaotic laser model", *Int. J. Bifurcation and Chaos* **8**, 965–975 (1998). [appendice D, page 255]
- G. Boulant, J. Plumecoq, S. Bielawski, D. Derozier, and M. Lefranc, "Model validation and symbolic dynamics of modulated lasers using template analysis", proceedings of the FOURTH EXPERIMENTAL CHAOS CONFERENCE, Boca Raton, Floride, Etats-Unis (août 1997), pp. 121–126 (World Scientific, Singapore, 1998).

D'un point de vue dynamique, le laser CO_2 monomode utilisé dans les expériences décrites à la section précédente n'a rien d'original. Lorsqu'il fonctionne de manière autonome à paramètres fixes, l'intensité qu'il délivre est constante dans le temps, et l'application d'une perturbation extérieure le voit revenir vers cet état stationnaire par des oscillations amorties, de forme quasi-sinusoïdale près de l'état d'équilibre (figure 3.6) [92, 93]. Le caractère non linéaire des lois d'évolution se manifeste par des harmoniques d'autant plus présentes dans la réponse que l'amplitude initiale est importante.

Ce comportement en régime monomode est de manière générale observé dans tous les lasers dits de classe B (laser à fibre dopée au néodyme, Nd:YAG, etc.), c'est-à-dire ceux où la partie cohérente de l'interaction champ–rayonnement évolue sur des échelles de temps beaucoup plus courtes que les dynamiques des populations des niveaux haut et bas de la transition laser et du champ électromagnétique [92, 93]. En ce qui concerne leur dynamique, ces systèmes laser ne sont donc rien d'autre que des oscillateurs non linéaires amortis, et en présentent toutes les caractéristiques, dont notamment la réponse à une modulation extérieure.

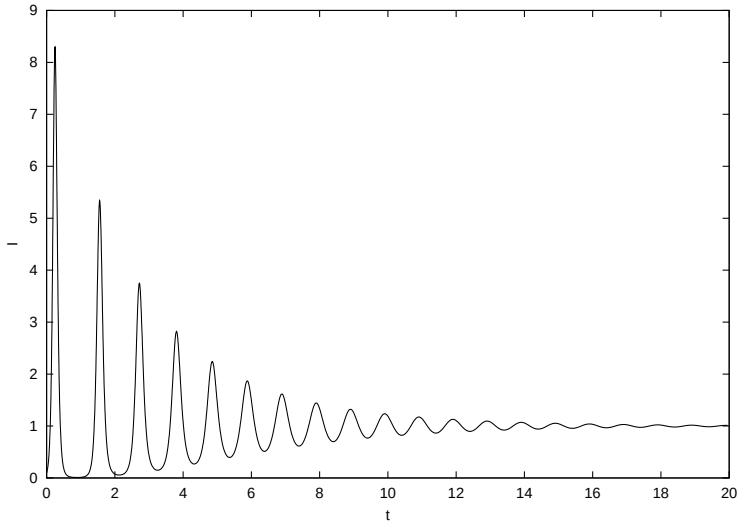

FIG. ***3.6 –*** *Oscillations de relaxation vers l'état stationnaire stable dans un modèle de laser classe B.*

On sait qu'un oscillateur amorti linéaire est caractérisé par sa fréquence de résonance, ou fréquence propre, fréquence à laquelle sa réponse à la modulation sinusoïdale est d'amplitude maximale. Cela reste valable pour un oscillateur non linéaire, à la différence qu'il peut également répondre aux sous-harmoniques de sa fréquence propre, les non linéarités engendrant une composante à la fréquence propre par somme de fréquences. Plus la réponse d'un oscillateur à une modulation est forte et l'éloigne de son état d'équilibre, et plus les non linéarités des lois d'évolution sont exacerbées. Celles-ci étant nécessaires à l'apparition d'une dynamique chaotique, c'est donc près des langues de résonance groupées autour des sous-harmoniques de la fréquence propre que l'on observe généralement des comportements chaotiques, à condition que l'amplitude du forçage extérieur soit suffisamment grande [14, 94].

On a vu qu'un régime chaotique contient une infinité d'orbites périodiques instables. Or on observe que dans la zone de comportement régulier séparant deux langues chaotiques, seule survit l'orbite périodique de période égale à celle de la modulation : l'enlacement des orbites périodiques se défait à la sortie d'une langue chaotique et se reforme lorsqu'on arrive sur la suivante. Cela suggère qu'il existe des différences qualitatives entre les différentes résonances sous-harmoniques, et en particulier que l'organisation des orbites périodiques varie d'une résonance à l'autre. Il est alors légitime de se demander si une analyse topologique peut distinguer entre régimes chaotiques appartenant à des langues différentes.

Comme le montrent l'analyse théorique de Gilmore et McCallum [14] ainsi que nos travaux expérimentaux [6–9], la réponse à cette question est positive : non seulement les régimes correspondant à des sous-harmoniques différentes sont effectivement associés à des gabarits différents, mais la séquence de gabarits décrivant la structure du chaos dans les langues successives obéit à des lois systématiques. De plus, une structure fine peut être en évidence au cours de la traversée de la langue chaotique : ce n'est pas toujours la même structure topologique qu'on observe des deux côtés de la résonance, notamment à forte amplitude [8, 14].

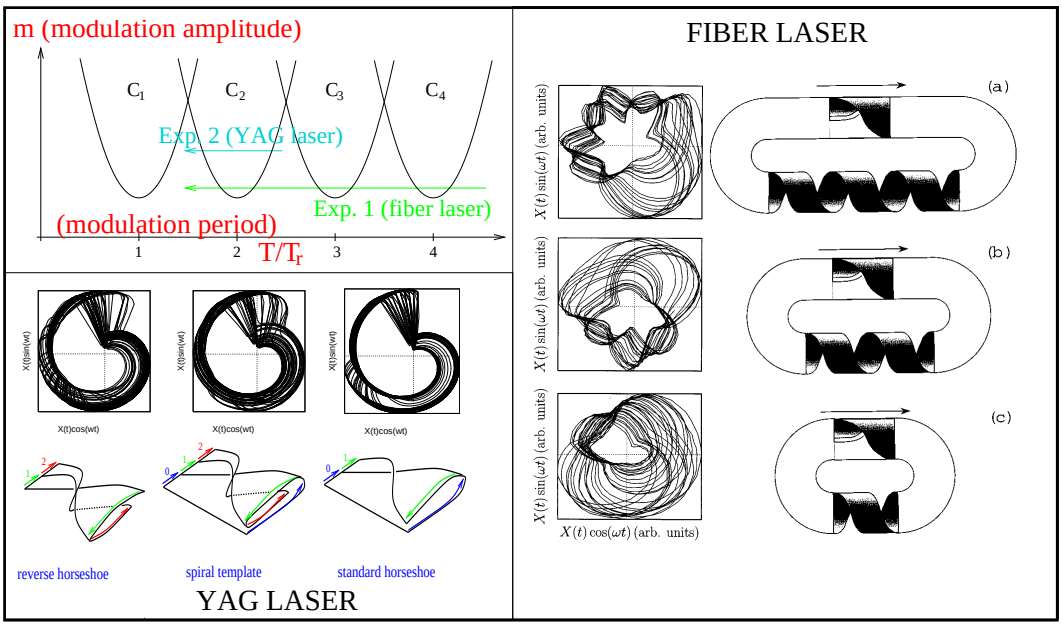

FIG. ***3.7 –*** *Structures topologiques caractérisant les attracteurs observés dans deux expériences laser. En haut à gauche : représentation schématique de l'espace des paramètres d'un oscillateur non linéaire forcé, montrant des langues chaotiques centrées autour des harmoniques de la période de modulation. A droite : gabarits observés dans l'expérience 1 (laser à fibre). La torsion globale augment d'une unité à chaque changement de langue. En bas à gauche : gabarits observés dans l'expérience du laser YAG (seule la structure des branches est indiquée) : on rencontre plusieurs structures topologiques pendant la traversée de la langue.*

Voyons plus précisément de quoi il s'agit à partir des exemples fournis par deux expériences que nous avons réalisées avec deux lasers chaotiques, un laser à fibre dopée Erbium et un laser Nd:YAG fonctionnant en régime monomode, tous deux soumis à une modulation de la pompe. Dans le premier cas, on parcourt plusieurs résonances à amplitude de modulation modérée, dans le deuxième cas, on balaye une langue unique mais à une amplitude de modulation plus élevée de manière à obtenir un chaos plus développé (Fig. 3.7). Les deux lasers ont des dynamiques tout à fait comparables et les deux expériences diffèrent donc plus par le protocole suivi que par la nature du dispositif expérimental.

Dans l'expérience du laser à fibre [7], on constate que les gabarits correspondant à des langues différentes ont leurs branches organisées de manière identique (type "fer à cheval") mais qu'ils diffèrent par la torsion du ruban recollant les deux extrémités de la partie branchue (la torsion globale) (Fig. 3.7). La torsion globale t_g est directement reliée à l'ordre de la sous-harmonique : si $T = nT_r$, où T et T_r sont la période de modulation et la période naturelle, alors on a $t_g = (n-1)$. L'analyse topologique permet donc de repérer immédiatement dans quelle langue chaotique on se trouve, ce qui n'est pas toujours un problème évident à forte modulation, la fréquence naturelle $1/T_r$ variant parfois de manière significative avec l'amplitude de modulation comme dans tous les oscillateurs non linéaires.

Dans l'expérience du laser YAG [8], on n'explore qu'une seule langue et la torsion globale est donc constante (ici égale à 1). C'est pourquoi on n'a représenté que la partie branchue du gabarit à la figure 3.7. On observe ici une variation de la structure topologique au fur et

à mesure de la traversée de la langue. En parcourant la langue à fréquence de modulation croissante (et donc à périodes décroissante sur le schéma de la figure 3.7) on observe tout d'abord un gabarit à deux branches qui serait tout à fait comparable au fer à cheval classique si les branches ne présentaient pas un demi-tour supplémentaire : on voit que les branches subissent des rotations de 1 et 2 demi-tours avant de se recoller, au lieu de 0 et 1 pour le fer à cheval classique. Ce gabarit, représenté à droite de la figure est généralement appelé "fer à cheval inversé" ("reverse horseshoe"), car il correspond à l'image dans un miroir du fer à cheval modulo une torsion globale, ou encore "fer à cheval torsadé" ("twisted horseshoe") [14]. On rencontre ensuite vers le centre de la résonance un gabarit à trois branches, ce qui indique un étirement plus vigoureux et donc un degré de chaos plus élevé. On note que ce gabarit "spirale", dont la structure est illustrée à la figure 3.8, est formé à partir du précédent par l'adjonction d'une branche de torsion 0. Enfin, les régimes observés en fin de balayage sont caractérisés par des "fers à cheval" classiques à deux branches, de torsions 0 et 1, qui sont obtenus à partir du gabarit spirale du centre de résonance par la disparition de la branche de torsion 2.

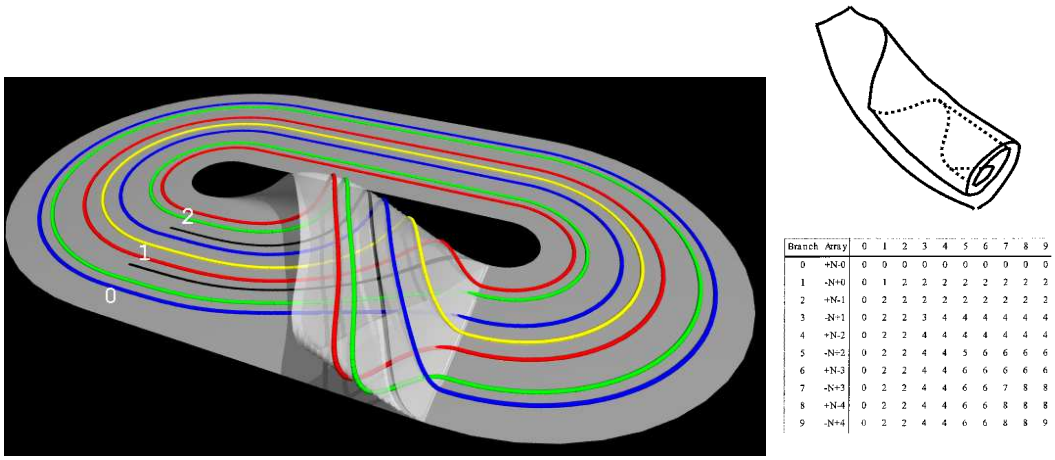

Branch	Array	0	1	2	3	4	5	6	7	8	9
0	+N-0	0	0	0	0	0	0	0	0	0	0
1	-N+0	0	1	2	2	2	2	2	2	2	2
2	+N-1	0	2	2	2	2	2	2	2	2	2
3	-N+1	0	2	2	3	4	4	4	4	4	4
4	+N-2	0	2	2	4	4	4	4	4	4	4
5	-N+2	0	2	2	4	4	5	6	6	6	6
6	+N-3	0	2	2	4	4	6	6	6	6	6
7	-N+3	0	2	2	4	4	6	6	7	8	8
8	+N-4	0	2	2	4	4	6	6	8	8	8
9	-N+4	0	2	2	4	4	6	6	8	8	9

FIG. ***3.8 –*** *Gauche : gabarit spirale à trois branches, représenté ici avec une orbite de période 1 et trois orbites de période 2. Droite : représentation schématique de l'organisation des branches du gabarit spirale infini dont le gabarit de gauche est extrait, et matrice de gabarit montrant la systématique des nombres d'enlacements des différentes branches.*

On notera en passant que l'observation d'un fer à cheval torsadé dans le laser YAG fut l'une des premières observations expérimentales d'une structure topologique différente du fer à cheval classique [6]. Cette expérience fournit d'ailleurs un exemple particulièrement frappant du fait que les propriétés d'une seule orbite peuvent donner des indices très utiles sur l'organisation topologique sous-jacentes. En effet, l'orbite de période 3 détectée dans cette expérience est nouée comme un noeud de trèfle et possède un nombre de croisements de 4, alors que celle du fer à cheval classique n'est pas nouée et ne présente que deux croisements (Fig. 3.9). Cette orbite suffit donc à montrer que ce régime présentait des caractéristiques topologiques de cequi avait été observé jusque là, la structure exacte étant bien sûr déterminée en utilisant l'ensemble des orbites périodiques détectées.

Ce qui montre clairement la pertinence de l'analyse topologique dans l'étude des diagrammes de bifurcation des oscillateurs non linéaires forcés est que la structure du gabarit

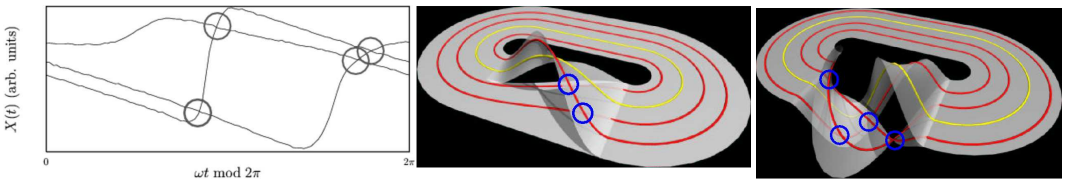

FIG. ***3.9 –*** *La tresse à quatre croisements de l'orbite de période 4 observée dans un laser YAG [6] (à gauche) est correctement prédite par le gabarit "fer à cheval torsadé" (àdroite) mais pas par celui du fer à cheval classique qui ne prévoit que deux croisements modulo six, selon la valeur de la torsion globale.*

observé en un point de fonctionnement donné indique de manière claire dans quelle partie du diagramme de bifurcation on se trouve : la torsion globale fournit l'ordre de la langue chaotique, la structure des branches détermine ensuite de manière plus ou moins précise dans quelle partie de la langue on se trouve.

Si les changements de structure topologique induits par des variations de paramètres faisant passer d'une langue à l'autre ou parcourant une langue unique sont complémentaires (dans le premier cas, la torsion globale change sans que l'organisation des branches soit modifiée, dans le deuxième cas c'est cette dernière qui évolue d'une extrémité de la langue chaotique à l'autre à torsion globale constante), ils sont également très semblables : les deux types de modifications se caractérisent en effet par une augmentation graduelle de la torsion au fur et et à mesure qu'on diminue la fréquence de modulation.

C'est en fait la signature du fait que les différents gabarits décrits ici peuvent être rassemblés dans un gabarit "générateur", dont les branches sont disposées suivant une spirale infinie (Fig. 3.8). Au fur et à mesure que la fréquence de modulation diminue, les branches de torsion de plus en plus grandes sont explorées, une oscillation le long de la spirale étant effectuée à chaque fois qu'on passe d'une sous-harmonique à la suivante, un régime s'étalant sur d'autant plus de branches que son degré de chaos est élevé. Cette structure à grande échelle du diagramme de bifurcation des oscillateurs non linéaires est une conséquence d'une propriété topologique fondamentale que chacun a probablement déjà expérimenté avec un simple tuyau d'arrosage : la convertibilité de la vrille (*writhe* en anglais) en torsion. Si on enroule le tuyau selon n boucles et qu'on tire aux deux extrémités pour l'amener dans une configuration linéaire, on constate sans difficuté qu'il présente une torsion de n tours.

3.4 DE L'ANALYSE TOPOLOGIQUE AUX CODAGES SYMBOLIQUES

- M. Lefranc, P. Glorieux, F. Papoff, F. Molesti, and E. Arimondo, "Combining topological analysis and symbolic dynamics to describe a strange attractor and its crises", *Phys. Rev. Lett.* **73**, 1364–1367 (1994). [appendice D, page 287]
- J. Plumecoq and M. Lefranc, "From template analysis to generating partitions I: Periodic orbits, knots, and symbolic encodings", *Physica D* **144**, 231–258 (2000). [appendice D, page 197]
- J. Plumecoq and M. Lefranc, "From template analysis to generating partitions II: Characterization of the symbolic encodings", *Physica* D **144**, 259–278 (2000). [appendice D, page 227]

3.4.1 Introduction

Classer les attracteurs chaotiques selon la structure du gabarit décrivant leur organisation topologique est une méthode de caractérisation extrêmement puissante et robuste, mais ce qui fait sa force peut également limiter son intérêt. Comme on l'a vu dans la section 3.3, la structure topologique d'un attracteur reste inchangée sur de larges domaines de l'espace des paramètres, même si plusieurs structures différentes peuvent être rencontrées lorsque le domaine d'exploration est suffisamment vaste.

Or, il est parfois souhaitable de passer à un niveau de description plus fin. Comment distinguer des attracteurs associés tous les deux à un gabarit de type fer à cheval? Comment détecter un désaccord entre des observations expérimentales et un modèle théorique quand les gabarits mesurés et prédits sont indentiques? La réponse à ces questions se trouve, une fois que l'organisation globale a été caractérisée au moyen du gabarit, dans l'identification individuelle des orbites au moyen de leurs invariants topologiques et dans la description du spectre d'orbites. Comme ce dernier est invariant par un changement de coordonnées (une solution périodique est périodique quelles que soient les variables d'état), on peut ainsi envisager d'analyser un attracteur indépendamment de la variable physique mesurée.

Lorsqu'on fait varier un paramètre de contrôle, des orbites périodiques sont à tout instant créées ou annihilées. Les attracteurs observés pour des valeurs différentes des paramètres d'un même système diffèrent en général par leur contenu en orbites périodiques, qui peut être caractérisé par des invariants tels que l'entropie topologique [60,95]. Cette dernière quantifie la vitesse avec laquelle le nombre $N(p)$ d'orbites périodiques de période p augmente avec la période :

$$h_T = \lim_{p\to\infty} \frac{\log N(p)}{p} \tag{3.1}$$

Deux approches différentes sont possibles pour exploiter le spectre d'orbites périodiques d'un attracteur chaotique. Dans cette section, nous utiliserons le fait qu'il existe une connexion naturelle entre les invariants topologiques des orbites périodiques et une description des trajectoires de l'attracteur en termes de séquences symboliques, par exemple des suites de 0 et de 1 [11,12].

Comme la correspondance entre trajectoire et séquence symbolique se doit d'être continue, et que les orbites périodiques sont présentes dans tous les attracteurs, on peut imaginer d'interpoler l'information contenue dans les invariants topologiques à tout point de l'attracteur dans lequel les orbites sont plongées. Cela nous permet de caractériser finement la dynamique chaotique au travers de sa "grammaire", c'est-à-dire la liste des séquences finies de symboles qui n'apparaissent dans le codage d'aucune trajectoire et de mettre en évidence des différences entre attracteurs voisins dans l'espace des paramètres.

Dans la section 3.5, nous nous intéresserons de plus près à l'ordre dans lequel apparaissent les orbites périodiques quand on va vers le chaos développé. Cet ordre n'est pas arbitraire mais est gouverné par des contraintes topologiques rigides qui peuvent être déterminées à partir des invariants topologiques : la présence de certaines orbites force l'existence d'une infinité d'autres orbites.

3.4.2 Codages symboliques et partitions génératrices

Nous avons vu en présentant l'application du fer à cheval (Sec. 2.2.2) que chacun des points de l'ensemble de l'ensemble invariant (c'est-à-dire dont l'orbite reste pour toujours

dans le carré unité) est associé de manière unique à une suite de 0 et de 1 s'étendant à l'infini vers l'arrière et vers l'avant [4, 57, 79]. A tout point x est associé une séquence unique

$$\Sigma(x) = \ldots s_{-3}s_{-2}s_{-1}.s_0s_1s_2\ldots, \quad s_i \in \{0,1,\ldots n-1\}$$

où n est le nombre de symboles. Il s'agit là d'une propriété fondamentale du chaos déterministe : de manière générale, il existe une correspondance naturelle entre trajectoires parcourant un ensemble invariant et séquences symboliques infinies. Cette correspondance est une conséquence du caractère dilatant de la dynamique. Puisque toute différence infinitésimale est amplifiée de manière exponentielle au cours du temps, une mesure grossière de l'état à un état donné (0 ou 1), suffit à extraire toute l'information que l'on peut désirer, à condition toutefois de la répéter à intervalles de temps réguliers. Ce problème est l'analogue d'une recherche du zéro d'une fonction par dichotomie, où il suffit à chaque itération de déterminer dans quelle moitié (0 ou 1) de l'intervalle courant se trouve le zéro pour le localiser avec une précision arbitraire.

De manière générale, le codage symbolique d'un ensemble chaotique est basé sur une partition de l'espace des états en plusieurs régions, chacune étant étiquetée avec un symbole différent (Fig. 3.10). Chaque orbite parcourant l'attracteur depuis un temps arbitrairement reculé dans le passé jusqu'à un temps arbitrairement avancé dans le futur peut alors être associé à la séquence bi-infinie des symboles indiquant les régions visitées successivement par l'orbite. Lorsque deux points distincts de l'espace des états ne sont jamais associés à la même séquence de symboles, comme c'est le cas pour le fer à cheval, la partition est dite *génératrice*. La dynamique dans l'espace des séquences (ou *dynamique symbolique*) reflète alors fidèlement la dynamique dans l'espace des états. Il est également exigé que le codage soit un homéomorphisme, ce qui implique que des points qui sont proches dans l'espace des états soient associées à des séquences proches l'une de l'autre.

Dans les systèmes hyperboliques, tels que l'application du fer à cheval, pour lesquels on peut distinguer en tout point entre direction stable et direction instable, il existe généralement une partition simple de l'ensemble invariant en plusieurs composantes non connexes qui se montre génératrice. Cependant, la plupart des attracteurs observés expérimentalement sont connexes et non hyperboliques et, sauf dans des cas limites tels que les systèmes très dissipatifs, il n'est en général pas facile de construire une partition génératrice, bien que des progrès importants aient été réalisés récemment [10–12, 96–100]. Une fois qu'une partition génératrice est connue, la dynamique peut être caractérisée de manière extrêmement précise en spécifiant la liste des séquences interdites (la "grammaire du chaos"), c'est-à-dire qui ne sont associées à aucune trajectoire réelle, et au moyen d'invariants divers tels que l'entropie topologique. Cette approche est d'autant plus pertinente que la structure des séquences interdites reflète directement celle de l'attracteur dans l'espace des phases [101], sous une forme combinatoire, plus facile à manipuler.

3.4.3 Invariants topologiques et dynamique symbolique

Nous avons pu montrer que les orbites périodiques, la théorie des noeuds et les gabarits sont des outils irremplaçables pour étudier la dynamique symbolique d'un attracteur chaotique [11, 12]. En effet, les gabarits décrivent par définition la structure d'un flot hyperbolique et *admettent un codage naturel lié à la décomposition de la surface en plusieurs branches* (qui est en fait identique au codage du fer à cheval). Ce codage consiste pour chaque orbite

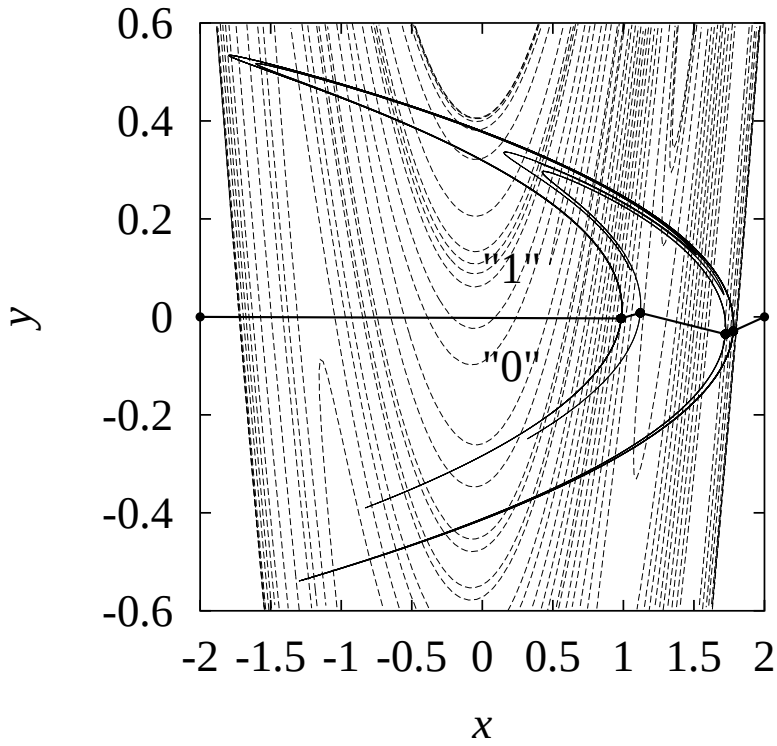

FIG. **3.10 –** *Partition de l'espace des états de l'application de Hénon. Chaque itéré est codé 0 ou 1 selon qu'il tombe en-dessous ou au-dessus de la frontière de la partition. Cette partition est obtenue avec la méthode des tangences homoclines, où la frontière de la partition relie des points où les variétés stable et instable de l'attracteur sont tangentes. Nous comparerons plus loin nos résultats à ceux obtenus par cette méthode. D'après [96].*

périodique du gabarit en la liste des branches successivement visitées. Le point clé est qu'il existe une relation directe entre ce nom symbolique et le type de noeud de l'orbite (Fig. 3.11) [4, 11]. Or, les types de noeud sont préservés lorsqu'on varie un paramètre de contrôle et forment donc une passerelle entre le cas général, non hyperbolique, et la limite hyperbolique.

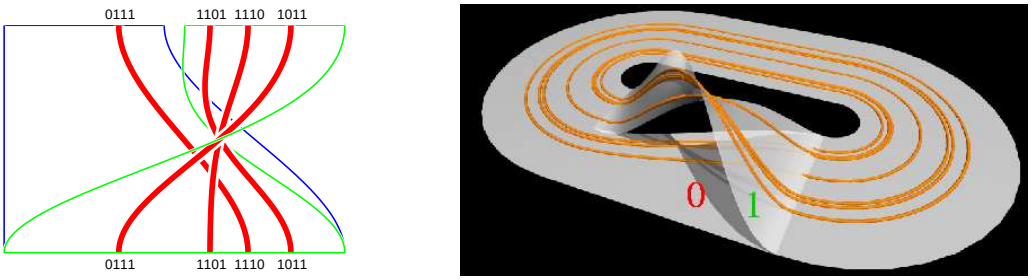

FIG. **3.11 –** *A gauche : orbite 0111 du gabarit du fer à cheval. Le code symbolique impose un itinéraire sur les branches, qui à son tour détermine le type de noeud. A droite : sur la gabarit du fer à cheval, il existe une seule orbite avec un nombre d'auto-enlacement de 16 et une torsion de 7, l'orbite 0110111. Cette orbite peut donc être identifiée sans ambiguïté au moyen de ses seuls invariants.*

En effet, supposons que le gabarit associé à un attracteur ait été déterminé et que l'on ait trouvé que les invariants d'une orbite périodique $\mathcal{P}$ n'autorisent qu'une seule projection sur le gabarit (Fig 3.11), c'est-à-dire qu'il n'existe qu'une seule orbite périodique du gabarit avec les mêmes invariants topologiques. Il est alors naturel d'associer à $\mathcal{P}$ le nom symbolique de cette projection, car c'est le nom symbolique de la seule orbite hyperbolique en laquelle $\mathcal{P}$ peut être déformée continûment en variant un paramètre de contrôle. Cela garantit que le codage non hyperbolique, que l'on cherche à construire, se raccorde de manière continue au codage hyperbolique, dont l'existence est garantie par les théorèmes. Les invariants topologiques de telles orbites constituent en effet de véritables empreintes digitales.

On constate souvent que de nombreuses orbites, et tout particulièrement celles de petite période, ont un seul nom symbolique compatible avec leurs invariants topologiques, tandis que la plupart des orbites n'ont au plus que quelques noms symboliques possibles. Une fois qu'on connaît les noms symboliques d'un certain nombre d'orbites, il est naturel d'interpoler cette information aux autres points de l'espace des phases, puisque qu'un codage symbolique se doit d'être un homéomorphisme, et donc de construire une partition de l'espace des phases prenant en compte l'information contenue dans les invariants topologiques. Quand le nom symbolique topologique d'une orbite est ambigu, on observe le plus souvent que seul l'un des noms possibles se révèle finalement compatible avec une partition réalisant un codage continu des trajectoires chaotiques, et que c'est donc celui qu'il faut retenir. Une fois identifié le seul nom possible de l'orbite, cette dernière peut alors être utilisée pour améliorer le codage symbolique.

Par itérations successives, où après avoir affiné la partition en insérant de nouvelles orbits, on identifie formellement le code symbolique de nouvelles orbites, on arrive finalement à une partition de l'espace des phases qui attribue un nom symbolique à chacune des orbites détectées expérimentalement. La propriété fondamentale de notre approche est *que si on considère l'ensemble des orbites périodiques du gabarit ayant les noms symboliques déterminés par la procédure, ces orbites abstraites forment un enlacement ayant exactement les mêmes invariants topologiques que les orbites expérimentales*. Cela permet de garantir que le codage réalisé persisterait si l'on rendait le système hyperbolique par un changement de paramètre.

Cette approche a été utilisée avec succès pour construire le codage symbolique de signaux chaotiques provenant d'un laser CO_2 à modulation de pertes [10] (Fig. 3.12). Il s'agissait de l'une des premières fois où un tel codage était construit de manière rigoureuse pour un système expérimental, l'autre méthode connue à l'époque, celle des "tangences homoclines", étant difficilement applicable à un système expérimental en raison de sa grande sensibilité au bruit.

Dans le but d'établir de manière convaincante la validité de l'approche topologique, nous avons quelques années plus tard vérifié dans le cadre de simulations numériques qu'il était possible de construire un codage symbolique d'un attracteur qui soit parfaitement compatible avec les invariants topologiques de plus de 1500 orbites périodiques de périodes allant jusqu'à 64 (Fig. 3.13) [11]. On notera au passage que ce calcul constitue l'une des meilleures preuves de la pertinence de l'analyse topologique jusqu'à des échelles extrêmement petites, puisqu'on y montra que les quatre nombres entiers décrivant la structure du gabarit permettaient de prédire de manière globale des millions d'invariants topologiques différents.

De plus, nous avons pu montrer qu'à la résolution de 10^{-4} atteinte à la fin du calcul, la partition fournie par l'approche topologique était en parfait accord avec la partition obtenue par

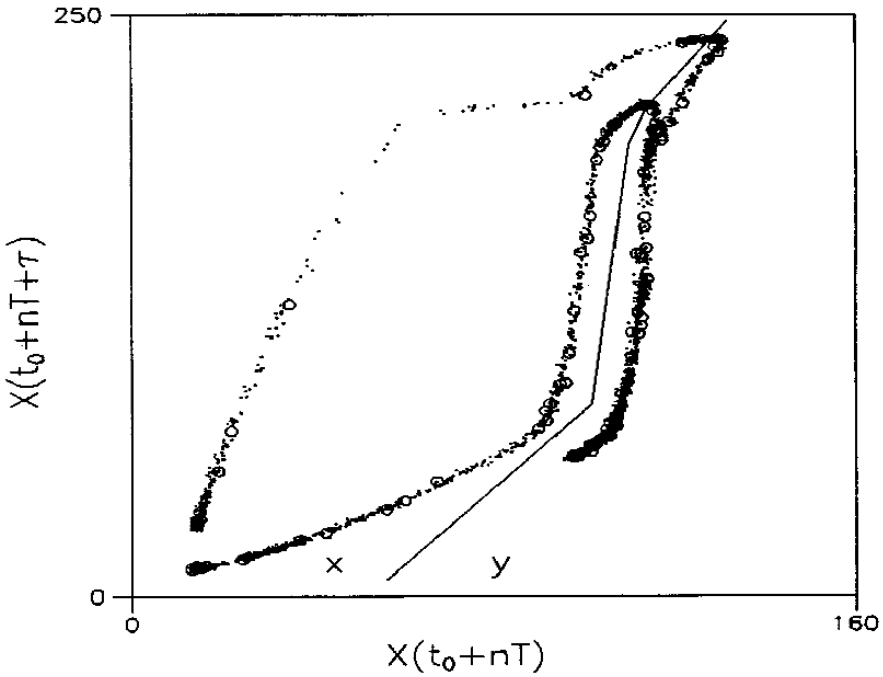

FIG. **3.12 –** *Partition d'une section de Poincaré d'un attracteur observé dans un laser CO_2 chaotique, obtenue après analyse des invariants topologiques des orbites périodiques indiquées par des cercles [10]. On remarque que la frontière ne passe pas exactement par les plis les plus visibles, comme on aurait pu le penser naïvement.*

la méthode des tangences homoclines, la méthode de référence pour construire les codages symboliques à l'époque de notre travail (Fig. 3.13, [12]). Cela est d'autant plus remarquable que cette dernière méthode, qui procède en cherchant des singularités dans les dérivées d'itérées d'ordre élevé de l'application de premier retour, est complètement orthogonale à l'approche topologique. D'autres tests ont permis par ailleurs de confirmer que la partition obtenue était génératrice, et ce avec une précision supérieure de plusieurs ordres de grandeur à celle qui peut être atteinte dans les expériences. La pertinence du codage symbolique par analyse topologique comme technique expérimentale de caractérisation du chaos était ainsi établie.

En conclusion, nous avons montré dans ces travaux que l'analyse des invariants topologiques des orbites périodiques plongées dans un attracteur chaotique permettait non seulement de caractériser de l'organisation topologique globale de cet attracteur, mais également d'analyser le détail de sa structure en en construisant un codage symbolique. Cela nous donne accès à une comparaison fine entre attracteurs grâce à l'étude des séquences interdites (la "grammaire du chaos") et à certaines grandeurs quantitatives comme l'entropie topologique. Le fait de fournir une solution nouvelle à un problème classique de l'étude du chaos déterministe montre également que l'analyse topologique n'est pas une technique exotique, mais qu'elle capture fidèlement les propriétés fondamentales d'une dynamique chaotique.

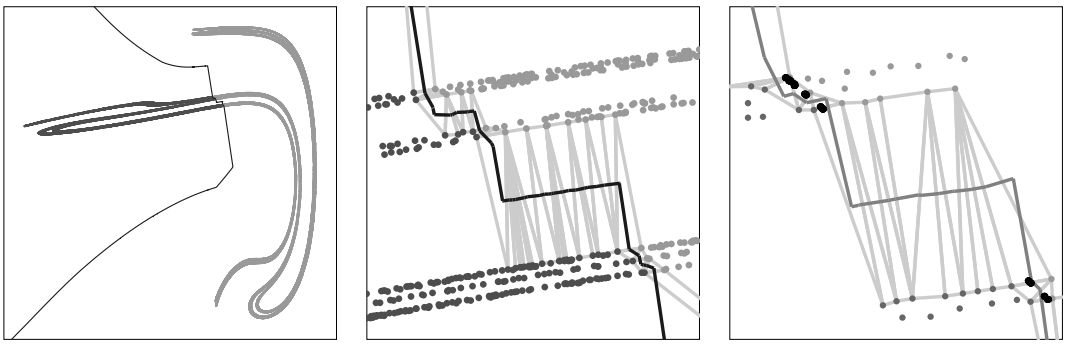

FIG. **3.13 –** *A gauche : partition d'une section d'un attracteur chaotique observé dans les simulations numériques d'un modèle de laser chaotique. Au centre : vue agrandie de la frontière de la partition. Le côté du carré est* 5×10^{-2} *relativement à la largeur du tracé de gauche. D'après [11]. A droite : le côté du carré est* 5×10^{-3}*. Les points clairs indiquent les points périodiques sélectionnés. Les points sombres indiquent les tangences homoclines (l'angle entre les deux variétés invariantes est inférieur à* 2×10^{-4} *radians). La largeur de trait est* 2.5×10^{-5}*. D'après [12].*

3.5 GÉNÉALOGIES D'ORBITES ET SIGNATURES TOPOLOGIQUES DE CHAOS

– A. Amon and M. Lefranc, "Topological signature of deterministic chaos in short nonstationary signals from an optical parametric oscillator", *Phys. Rev. Lett.* **92**, 094101 (2004). [appendice D, page 167]

Une des propriétés particulièrement intéressantes de l'analyse topologique est qu'elle permet de décomposer la complexité de l'attracteur chaotique en se focalisant sur l'étude de l'entrelacement des orbites périodiques qui y sont plongées. Bien sûr, il est préférable pour cela d'avoir détecté le plus grand nombre d'orbites possible, de manière à couvrir le plus finement possible l'attracteur, mais fort heureusement, même un petit nombre d'orbites, voire une seule orbite comme on l'a vu par exemple dans la figure 3.9, peuvent fournir des informations tout à fait pertinentes sur la dynamique. Dans cette section, nous verrons ainsi comment la présence d'orbites périodiques avec certains types de noeud implique la présence d'une infinité d'autres orbites périodiques, et indique donc l'action d'une dynamique chaotique (Sec. 3.5.1). De telles orbites peuvent être utilisées comme signatures de chaos et se révèlent des outils irremplaçables lorsque les séries temporelles ne contiennent pas assez de points pour reconstruire un attracteur complet, et tout particulièrement dans le cas de systèmes non stationnaires, dont un ou plusieurs paramètres dérivent dans le temps (Sec 3.5) [15].

3.5.1 Invariants topologiques et bifurcations

Nous sommes attachés dans les sections précédentes à analyser de manière globale l'entrelacement complexe formé par les orbites périodiques instables d'un système dynamique chaotique. Dans cette partie, nous nous concentrerons sur la manière dont cet entrelacement se tisse, lorsque de nouvelles orbites sont créées, ou se défait, lorsque des orbites sont détruites. Il s'agit là d'un problème complexe car il est soumis à deux contraintes très fortes :

1. les orbites périodiques naissent avec les invariants topologiques qu'elles garderont sur tout leur domaine d'existence dans l'espace des paramètres,

2. les orbites n'apparaissent pas isolées mais toujours confondues avec une autre orbite (orbite jumelle d'une bifurcation tangente ou orbite mère d'un doublement de période).

On rappelle en effet qu'il existe deux types principaux de *bifurcations*[2] : la *bifurcation tangente* dans laquelle un couple d'orbites jumelles, l'une stable, l'autre instable, apparaissent simultanément, et le *doublement de période* dans lequel une orbite périodique devient instable en donnant naissance à une orbite de période double [56, 57]. De manière générale, la propriété (2) ci-dessus est une conséquence du théorème des fonctions implicites, qui veut qu'une solution isolée soit structurellement stable et qu'elle existe donc pour toutes valeurs des paramètres voisines.

Ces deux contraintes ont pour conséquence qu'un gabarit ne décrit pas seulement l'organisation des orbites périodiques pour un jeu de paramètres fixes, mais détermine également quelles sont les orbites qui peuvent interagir dans une bifurcation, ainsi que l'ordre dans lequel apparaissent les orbites lorsqu'on va vers le chaos complètement développé. Par exemple, les orbites jumelles d'une bifurcation tangente doivent strictement avoir le même type de noeud, car elles forment une seule courbe au moment de la bifurcation et gardent ensuite le même type de noeud. De même, il existe une relation simple entre les types de noeud des orbites mère et fille d'un doublement de période, ce qui permet de retrouver les liens de filiation entre orbites d'après leurs enlacements.

La généalogie des orbites peut également se lire dans les nombres d'enlacement. Lorsque deux orbites interagissent dans une bifurcation, un certain nombre d'orbites ont déjà été créées dans des bifurcations antérieures. Pour ces dernières, les deux orbites bifurquant sont indiscernables et, en particulier, ne peuvent être distinguées d'un point de vue topologique. Ces deux orbites ont donc nécessairement le même nombre d'enlacement avec chacune des orbites spectatrices, et cette configuration persiste bien sûr au-delà de la bifurcation (Fig. 3.14). Inversement, cela implique que toute orbite enlaçant de manière différente deux orbites jumelles nées dans une même bifurcation est nécessairement apparue après ces dernières, à un endroit de l'espace des paramètres où les deux orbites étaient bien séparées et distinctes (Fig. 3.14) [80]. On dit alors que cette orbite *implique*, ou *force*, les deux orbites jumelles [80].

L'ensemble des relations d'implication entre orbites d'un gabarit donné peuvent être résumées dans un *diagramme d'implication* (forcing diagram). Ces relations permettent de décrire de manière concise le spectre complet d'orbites au moyens de *bases d'orbites*, ensembles d'orbites qui forcent d'autres orbites dans l'attracteur mais ne sont forcées par aucune autre [3, 4, 80]. A partir de ces orbites de base, toutes les autres orbites présentes dans l'attracteur peuvent être retrouvées à partir des relations d'implication. Cette approche permet de comparer facilement les structures fines de deux attracteurs : deux attracteurs voisins dans l'espace des paramètres auront, au moins jusqu'à une certaine période, des bases d'orbites identiques. Les bases d'orbites sont donc un outil puissant pour étudier les différentes routes qui peuvent mener d'un régime purement périodique à un chaos complètement développé.

2. De manière générale, une bifurcation est définie comme une modification quantitative d'un système dynamique, dans le cas qui nous intéresse l'apparition ou la disparition d'orbites périodiques.

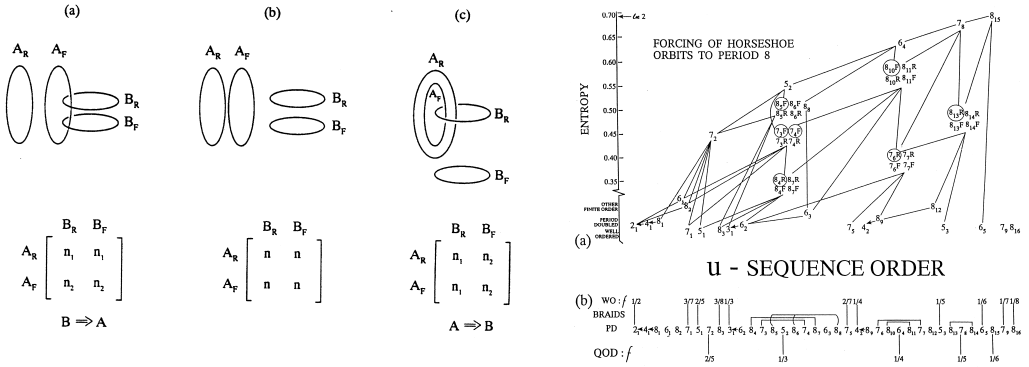

FIG. ***3.14 –*** *A gauche : dans ces trois configurations,* (A_R,A_F) *and* (B_R,B_F) *sont des paires d'orbites jumelles. En (a), les orbites* A_R *et* A_F *ne peuvent interagir avant que* B_F *et* B_R *ne s'annihilent. On en déduit que la paire* B *est apparue après la paire* A*. On aboutit à la conclusion inverse en (c). Si les membres d'une paire ne peuvent être distinguées par l'autre paire d'après leur nombres d'enlacement, c'est qu'elles sont apparues après. En (b), il n'y a pas de relation d'implication. A droite : diagramme d'implication pour les orbites du fer à cheval. Une ligne indique une relation d'implication, l'orbite forçant l'existence de l'autre étant en haut et à droite de la ligne. Tiré de [80].*

3.5.2 Tresses d'entropie positive

Mais l'étude de la topologie des bifurcations n'est pas le seul moyen de déterminer des implications entre orbites. En effet, le type de noeud d'une orbite peut forcer à lui seul l'existence d'une infinité d'autres orbites et fournir des information sur la structure globale du flot [102], à condition de faire l'hypothèse que les lois gouvernant la dynamique sont déterministes (l'état actuel fixe sans ambiguïté l'évolution future) et continues (des états proches ont des évolutions proches, au moins pendant un certain temps). L'image de gauche de la figure 3.15 nous permet de comprendre simplement de quoi il s'agit. On y a représenté deux orbites de période 3 dont les trajectoires entre les deux sections de Poincaré représentées forment deux tresses différentes. Pour chacune de ces deux tresses, on considère un disque du plan de section dont la circonférence passe par les points de l'orbite, et on suppose qu'il s'agit d'un ensemble de conditions initiales. On s'intéresse à l'évolution de cet ensemble sous l'action du flot entre la section de Poincaré initiale, en haut, et la finale en bas, où elle coïncide avec l'image du disque initial par l'application de premier retour. En d'autres termes on s'intéresse aux contraintes que l'existence de l'orbite périodique exerce sur les trajectoires des points situés dans le disque. Puisque la dynamique est déterministe et continue, cette évolution doit obéir aux contraintes suivantes : à tout instant les points de la tresse appartiennent à la circonférence de la région ; la région doit se déformer de manière continue sans jamais rentrer en intersection avec elle-même.

Après un examen rapide, on se convainc que la première tresse pourrait être compatible avec un mouvement de rotation global du plan, et l'hypothèse la plus simple est donc de supposer que l'image du disque initial est le même disque tourné d'un tiers de tour. Cette orbite, dont on pourrait d'ailleurs vérifier qu'elle est isotope au noeud trivial, ne donne donc aucune indication d'une dynamique chaotique.

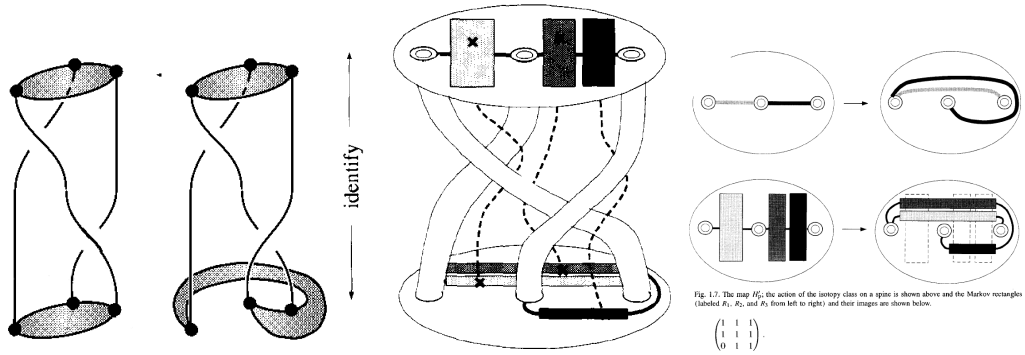

FIG. **3.15 –** *A gauche : un tresse de période 3 et l'action de l'homéomorphisme du disque qui lui est associé. A droite en haut : représentation de la tresse sous la forme d'un diagramme linéaire. A droite en bas : action de l'homéomorphisme sur un jeu de rectangles de Markov, et matrice de transition. D'après [85].*

La tresse formée par la deuxième orbite est plus complexe : on voit d'abord deux brins tourner autour l'un de l'autre dans un sens donné, puis l'un d'entre effectuer avec le troisième un mouvement de rotation dans le sens opposé. Ces deux rotations contraires créent un effet de tenaille, dont on voit qu'il ne peut qu'étirer la région grisée, sauf à considérer que cette dernière ait traversé la tresse, ce qu'on s'est interdit. Cela ne doit pas étonner celui ou celle qui a déjà utilisé un batteur de cuisine ("mixer"), car ce sont dans cet ustensile les rotations différentielles du mouvement des deux fouets qui étirent les lignes de fluide et créent l'effet de mélange recherché. De même, les brins de l'orbite agissent comme des fouets qui étirent l'espace des phases autour de l'orbite et créent du mélange dans cet espace, phénomène qui n'est rien d'autre que ce que l'on appelle du chaos déterministe.

On dit généralement que le terme « chaos »trouve son origine dans le fameux article "Period 3 implies chaos" de Li et Yorke [103][3], où il est montré que si une application d'un intervalle dans lui-même possède une orbite périodique de période 3, alors il existe des orbites de toutes les périodes, et la dynamique est chaotique. On voit sur l'exemple de la figure 3.15 que ce fameux théorème ne survit pas pour une application inversible du plan dans le plan : une orbite de période 3 peut impliquer une dynamique chaotique, comme elle peut être tout à fait compatible avec une dynamique régulière. La différence tient au fait qu'en une dimension il existe en gros une seule manière de permuter les trois points de l'orbite, alors que dans le plan, plusieurs types de tresse sont possibles.

Des outils mathématiques sophistiqués, basés sur la classification de Nielsen–Thurston des homéomorphismes d'une surface dans elle même (on prend ici comme surface le complément de l'orbite dans le plan de section, soit un disque à p trous), permettent d'estimer de manière rigoureuse le taux de mélange correspondant à un type de tresse donné [85, 104], comme l'illustrent les deux images de droite de la figure 3.15. La procédure consiste à construire parmi les applications envoyant le disque du haut sur celui du bas la plus simple qui soit compatible à la fois avec une déformation continue du disque et avec la structure de la tresse. En examinant l'action de cette application sur un jeu de rectangles, et la structure des intersections entre ces rectangles et leurs images, on détermine une matrice de transition dont

3. cependant, certains attribuent la paternité de ce terme à Ruelle.

la plus grande valeur propre, correspondant au facteur d'étirement, donne accès à l'entropie topologique de cette application minimale, et donc au le taux de mélange minimal. Pour la tresse à trois brins de la figure 3.15, on trouve que cette valeur propre est $\lambda_{\max} = \phi^2 \sim 2.618$, où ϕ est le fameux nombre d'or, et que l'entropie est $h_T = \ln \lambda_{\max} \sim 0.9624$.

Après cette introduction succincte au concept de tresse d'entropie positive, nous présentons dans la section suivante comment nous l'avons appliqué pour obtenir une signature de chaos déterministe dans un système non stationnaire.

3.5.3 Caractérisation de régimes non stationnaires

3.5.3.1 Reconstruction d'attracteurs et stationnarité Les méthodes classiques de caractérisation du chaos déterministe font toutes l'hypothèse que le système étudié est parfaitement stationnaire, c'est-à-dire que tous les paramètres de contrôle ont des valeurs parfaitement fixées. En effet, elles sont toutes basées sur la reconstruction d'un attracteur étrange dans un espace des phases à partir d'une série temporelle, et sur l'hypothèse que chaque point de l'espace des phases correspond à un état unique, à partir duquel la trajectoire future est entièrement déterminée [49, 105]. Cela revient à supposer que la dynamique est déterministe et qu'existe en tout point $\mathbf{X}$ de l'espace des états (ou du moins sur l'attracteur) un champ de vecteurs vitesses

$$\frac{\mathrm{d}\mathbf{X}}{\mathrm{d}t} = \mathbf{F}(\mathbf{X},\mu) \tag{3.2}$$

où μ est un paramètre de contrôle, même si on ne connaît pas explicitement la fonction $\mathbf{F}$, et que des points $\mathbf{X}$ proches correspondent à des vecteurs vitesse $\mathbf{F}(\mathbf{X},\mu)$ proches.

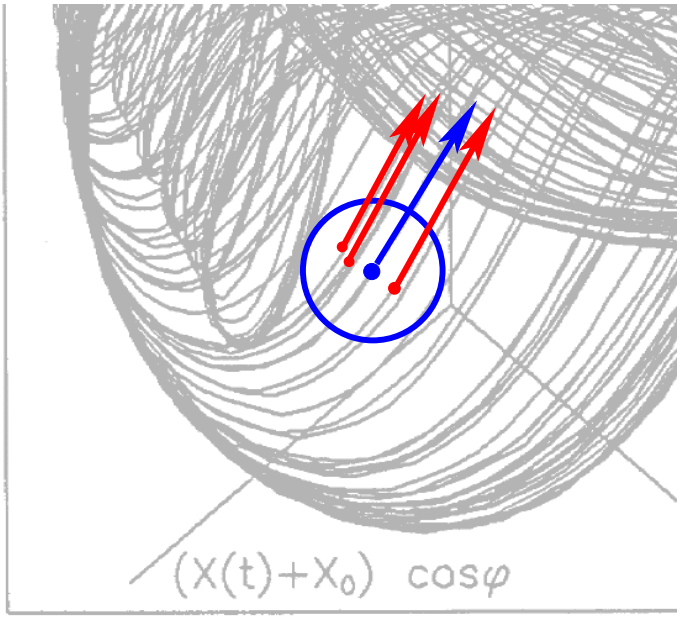

FIG. ***3.16 –*** *Lorsque le plongement d'un attracteur étrange dans un espace des phases reconstruit est correctement effectué, les points voisins de l'espace des phases correspondent à des états voisins et ont donc des trajectoires voisines. Cela est caractérisé par le fait qu'ils ont des trajectoires quasiment parallèles, et donc que la structure des trajectoires est compatible avec l'existence d'un champ de vecteurs.*

Or, des points proches dans l'attracteur sont en général éloignés dans la série temporelle car, dans une dynamique chaotique, il faut un certain temps pour revenir dans le voisinage d'une condition initiale. Supposons ainsi que les points $\mathbf{X}(t)$ et $\mathbf{X}(t+\Delta t)$, avec Δt grand, soient proches l'un de l'autres dans l'espace des phases. En supposant qu'il existe une dynamique déterministe du type (3.2), on voit en considérant que

$$\left.\begin{array}{lcl} X(t) & \sim & X(t+\Delta t) \\ F(X(t),\mu(t)) & \sim & F(X(t+\Delta t),\mu(t+\Delta t)) \end{array}\right\} \Rightarrow \mu(t) \sim \mu(t+\Delta t),$$

qu'une condition nécessaire pour que les vecteurs vitesses aux points $\mathbf{X}(t)$ et $\mathbf{X}(t+\Delta t)$ soient proches est que le paramètre μ ait approximativement la même valeur aux temps t et $t+\Delta t$, en d'autre termes que le système soit stationnaire.

Si on suppose au contraire que le système n'est pas stationnaire car le paramètre μ dérive dans le temps ($\mu(t) \neq \mu(t+\Delta t)$), alors il est clair que lorsqu'on reviendra près d'un état visité antérieurement, les lois d'évolution auront été modifiées du fait de la variation du paramètre, et le vecteur vitesse ne sera plus le même. Le déterminisme de la dynamique n'apparaîtra donc pas dans le portrait de phase car des points proches n'auront pas des trajectoires proches, et donc méthodes que calcul de dimensions fractales ou d'exposants de Lyapunov ne pourront être appliquées.

3.5.3.2 Bouffée de comportement irrégulier dans un oscillateur paramétrique optique. Les oscillateurs paramétriques optiques (OPO), dont nous décrirons la dynamique plus en détail au chapitre 4, sont comme les lasers des sources de rayonnement cohérent, qui présentent par ailleurs l'intérêt d'être largement accordables [25]. Basés comme les lasers sur une interaction non linéaire, on peut s'attendre à ce qu'ils présentent dans certaines régions de l'espace des paramètres des comportements complexes, et en particulier du chaos déterministe. Effectivement, une étude théorique du modèle le plus simple d'OPO triplement résonant, le modèle champ-moyen monomode, avait prévu il y a un plus de quinze ans que ce dispositif devait pouvoir présenter des régimes chaotiques [32]. Or, cette prédiction n'avait été confirmée par aucune observation expérimentale de chaos déterministe, que ce soit par le scénario prédit ou par un autre.

Cela peut paraître étonnant, étant donné le nombre extrêmement élevé de travaux consacrés à l'observation expérimentale de chaos déterministe, notamment pendant les années 80 et 90, mais s'explique d'une part par un intérêt relativement moindre porté à la dynamique des OPO comparativement à celles des lasers, d'autre part par le fait que les OPO triplement résonants sont des systèmes extrêmement sensibles aux moindres perturbations mécaniques, en raison de la condition de triple résonance. Or, les comportements chaotiques sont attendus à forte puissance lumineuse, où les comportements non linéaires sont exacerbés, et c'est précisément à forte puissance que des effets non désirés, et notamment des effets thermiques peuvent se manifester. Or, comme nous le verrons au chapitre 4, nous avons montré récemment que ces effets thermiques peuvent avoir des effets spectaculaires, et notamment déclencher des instabilités opto-thermiques menant à des oscillations de relaxation [33, 34] ainsi qu'à des oscillations en rafale quand des instabilités lentes se combinent à des instabilités rapides résultant de l'interaction entre modes transverses [36]. Tout cela ne contribue pas à faciliter la caractérisation de régimes chaotiques, et ce d'autant plus quand les phénomènes parasites introduisent de nouvelles échelles de temps

Ainsi, un des exemples de régimes irréguliers que nous avons pu enregistrer, et que nous analyserons dans la suite de cette section, est caractérisé par une grande instabilité des

paramètres de contrôle (Fig. 3.17). Au milieu d'une longue série temporelle constituée d'oscillations périodiques de fréquence voisine de 3 MHz, on observe soudain une bouffée de comportement irrégulier, avec une variation rapide de l'enveloppe qui suggère que le comportement n'est pas stationnaire et, en examinant plus attentivement l'épisode non périodique entre $t = 780\ \mu$s et $t = 875\ \mu$s, on note plusieurs détails qui sont font immédiatement penser à une dynamique chaotique. Tout d'abord, on observe une transition graduelle de l'oscillation de base vers un régime de période double, qui suggère une bifurcation de doublement de période. L'intervalle apériodique se termine d'ailleurs par la transition inverse. Enfin, on repère plusieurs séquences où sur un court intervalle de temps, le système suit un comportement quasiment périodique, ce qui est caractéristique du passage près d'orbites périodiques instables dans un système chaotique de petite dimension.

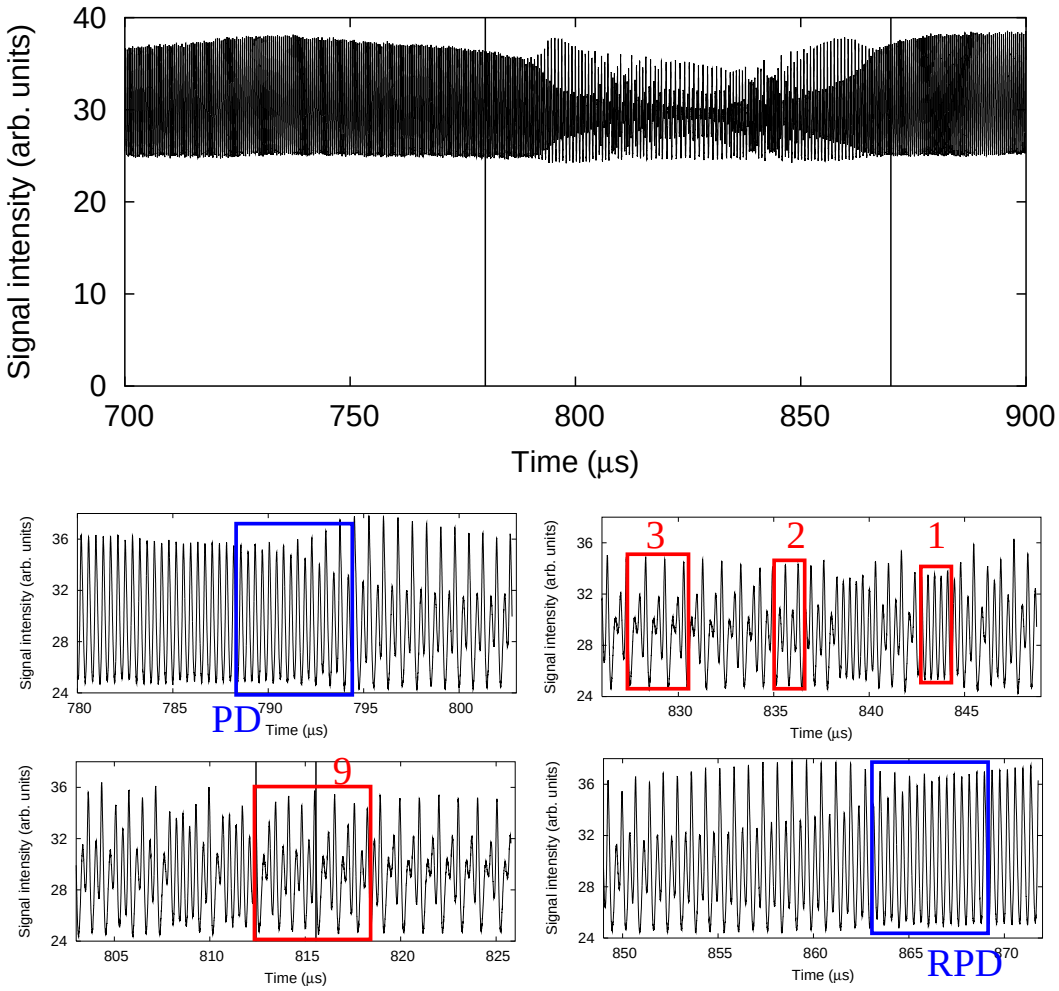

FIG. ***3.17 –*** *Haut : série temporelle de l'intensité lumineuse délivrée par un OPO, présentant une bouffée de comportement irrégulier d'environ 80 μs. Bas : détails de la série temporelle montrant un doublement de période (PD), un doublement de période inverse (RPD) ainsi que quelques épisodes de comportement périodique, dont un de période 9 qui sera utilisé plus loin comme signature du chaos.*

On peut à la fois se convaincre du caractère non stationnaire du système et renforcer la suspicion de chaos déterministe en analysant plus finement la dynamique. Pour cela, on construit à partir de la série temporelle de la figure 3.17 un portrait de phase que l'on peut voir à la figure 3.18, même si la non-stationnarité du système interdit en principe cette approche (voir Sec. 3.5.3.1). On se donne ensuite une section de Poincaré (la droite verticale de la figure 3.18), et on s'intéresse aux temps de vol entre deux traversées du plan de section qui seraient parfaitement constants pour un régime périodique. La variation de ces temps de vol au long de la série temporelle de la figure 3.18 est représentée dans la partie de droite de la figure 3.18. On y reconnaît une structure qui serait celle du diagramme de bifurcation d'un système qui passerait par une cascade de doublement de périodes menant au chaos, franchirait une zone de comportements chaotiques pour arriver finalement à une fenêtre périodique de période 3 avant de rebrousser chemin et refaire le même itinéraire en sens inverse. Cela indique que vitesse de balayage des paramètres de contrôle est non négligeable.

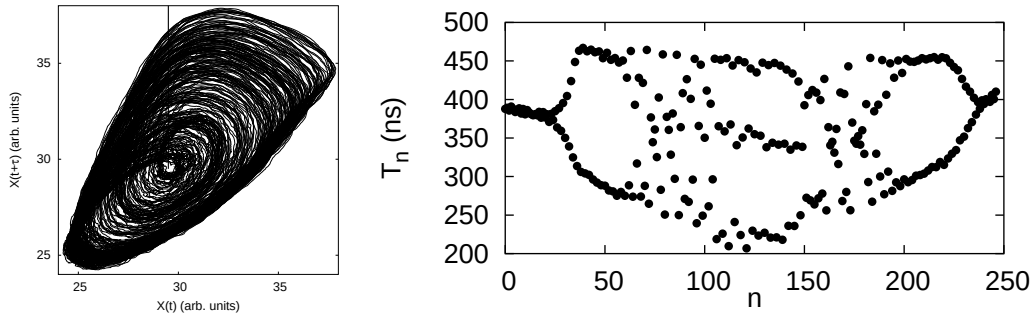

FIG. ***3.18 –*** *Gauche : portrait de phase $\{X(t), X(t+\tau)\}$ reconstruit à partir de la série temporelle de la figure 3.17. La droite horizontale marque la section de Poincaré choisie pour l'analyse des temps de vol. Droite : évolution des temps de vol entre deux passages par la section de Poincaré le long du fichier, montrant un diagramme de bifurcation caractéristique du transition vers le chaos par doublement de période.*

Tout cela devrait suffire à convaincre un esprit bienveillant que la dynamique observée est bien due à du chaos déterministe. Néanmoins, la démonstration manque un peu de solidité et n'apporte aucune information quantitative. Par ailleurs, que faire si la variation du paramètre de contrôle était plus rapide et qu'il était plus difficile de repérer une structure par une analyse standard de la série temporelle étudiée?

C'est ici que les tresses à entropie positive se révèlent être des outils clés pour montrer de façon élégante que l'on a bien affaire à du chaos déterministe et obtenir une estimation quantitative du degré de chaos. On tire pour cela parti du segment de la série temporelle situé entre les instants $t = 812$ μs et $t = 815$ μs, qui semble visiter le voisinage d'une orbite de période 9. En effet, en plongeant ce segment dans le même portrait de phase que celui de la figure 3.18, on constate que la trajectoire correspondante reboucle presque exactement après 9 oscillations, et passe donc au voisinage d'une orbite périodique (Fig. 3.19). En analysant la tresse réalisée par cette trajectoire fermée, on trouve qu'il s'agit d'une tresse à entropie positive, caractérisée par une entropie topologique $h_T \sim 0.377$. On obtient ainsi une preuve indiscutable que l'on est en présence de chaos déterministe, qui persisterait même si l'on était en mesure d'arrêter soudainement la dérive des paramètres.

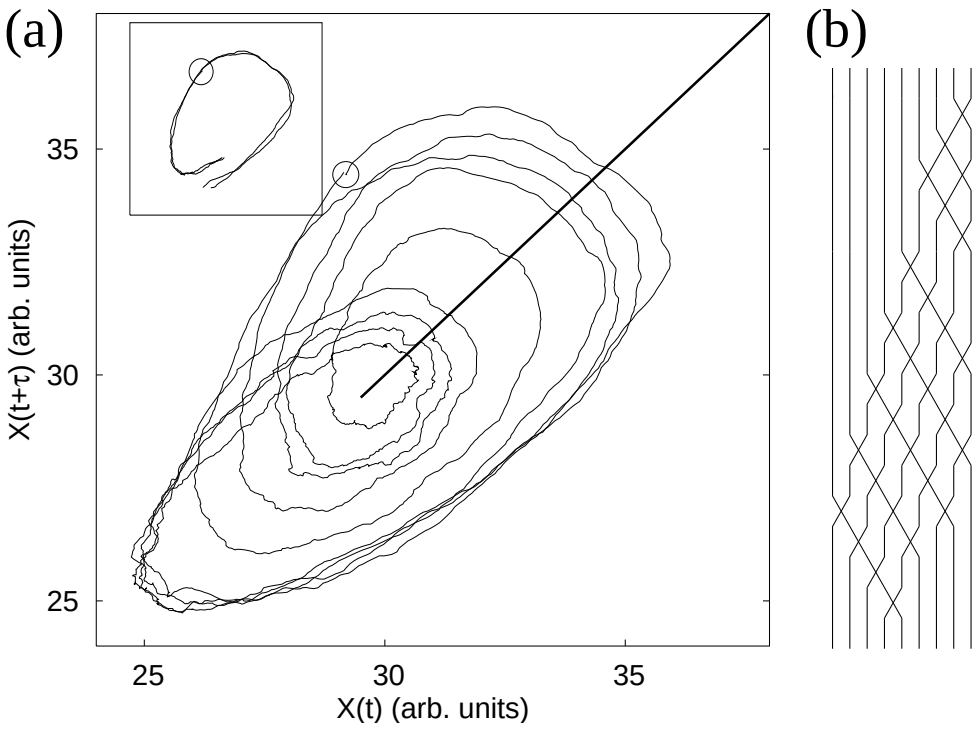

FIG. ***3.19*** – *Trajectoire quasiment fermée de période 9 reconstruite à partir d'un segment de la série temporelle 3.17. Le cercle indique les points initial et final de la trajectoire. L'insert montre la première oscillation du segment ainsi que la première oscillation suivant le segment. Les deux se superposent presque exactement, montrant que soit les paramètres n'ont pas eu le temps de varier de manière significative pendant la visite de l'orbite, soit l'orbite dépend peu des paramètres de contrôle. La tresse réalisée par l'orbite est représentée à droite de la figure.*

Deux questions viennent naturellement à l'esprit. Tout d'abord, la détection de cette orbite est-elle un hasard chanceux ou bien un événement générique que l'on est droit d'attendre dans la plupart des séries temporelles ? L'abondance d'orbites d'entropie positive dans un système chaotique (voir Fig. 3.14) nous fait plutôt pencher pour la deuxième hypothèse, et cela est d'ailleurs clairement confirmé par le fait que nous avons également détecté une orbite de période 10 d'entropie $h_T \sim 0.473$ dans le même intervalle de temps de 40 cycles (qui correspond à la première zone chaotique du diagramme de bifurcation 3.18). Le passage près d'orbites d'entropie positive semble être donc un phénomène banal.

On peut ensuite se demander si on est droit de considérer la trajectoire fermée de la figure 3.19 comme une orbite périodique, dans la mesure où les paramètres de contrôle ont en principe changé de valeur au moment où elle revient à son point de départ. Un raisonnement plus précis devrait alors commencer par démontrer que le système non dérivant doit posséder une véritable orbite périodique dans le voisinage immédiat de la trajectoire fermée observée expérimentalement. C'est certainement le cas si la variation des paramètres est faible pendant le temps nécessaire pour parcourir l'orbite ou si la trajectoire de l'orbite dépend peu des paramètres de contrôle. Dans l'exemple que nous avons présenté, on peut vérifier que l'une ou l'autre condition est remplie en traçant ensemble la première oscillation de l'orbite ainsi que la première oscillation suivant l'orbite (insert de la figure 3.19) et en

constatant qu'elles se superposent très bien. Nous sommes donc en droit d'invoquer les théorèmes mathématiques sur les orbites périodiques à entropie positive.

En conclusion, le type de noeud réalisé par les trajectoires presque fermées que l'on peut détecter dans un enregistrement expérimental constitue une signature claire de chaos déterministe lorsque l'entropie topologique associée est positive. Comme les conditions de stationnarité ne doivent être satisfaites que pendant le temps de visite de l'orbite et non plus pendant le temps nécessaire à parcourir l'attracteur chaotique, cette technique peut être utilisées dans un éventail bien plus large de situations expérimentales que les techniques classiques (calcul de dimensions fractales ou d'exposants de Lyapunov) et devient irremplaçable lorsque le système est non stationnaire ou qu'on n'a pu enregistrer qu'une série temporelle très courte.

On peut constater ici encore la puissance et la pertinence des concepts topologiques dans l'analyse du chaos déterministe. Ce qui rend d'autant plus frustrante la limitation fondamentale de l'analyse topologique basée sur la théorie des noeuds, qui ne peut être mise en oeuvre qu'en dimension trois, alors que les concepts sur lesquelles elle est basée, déterminisme et continuité, ne dépendent a priori pas de la dimension.

Dans les deux prochaines sections, nous tenterons de nous échapper vers les systèmes de grande dimension : tout d'abord dans la section 3.6, en cherchant des orbites périodiques instables dans un système à la dynamique spatio-temporelle complexe, puis ensuite dans la section 3.7.2, en essayant de jeter les bases de ce que pourrait être une analyse topologique en dimension arbitraire.

3.6 ORBITES PÉRIODIQUES DANS UN SYSTÈME SPATIO-TEMPOREL

– E. Yao, M. Lefranc, and F. Papoff, "Unstable periodic orbits in the presence of spatio-temporal chaos" *J. Opt. B: Quantum Semiclass. Opt.* **2**, 382–385 (2000).

Nous avons vu dans la section précédente que la présence d'épisodes périodiques dans une série temporelle irrégulière était souvent l'indice qu'une dynamique chaotique de petite dimension est à l'oeuvre. Dans cette section, nous nous intéressons à un système optique spatialement étendu, dont le nombre de variables est a priori infini, mais où la dynamique locale, mesurée en un point fixé, donne l'apparence de ne faire interagir que quelques degrés de liberté.

Le dispositif expérimental est construit autour d'une valve optique à cristaux liquides, un élément optique dont l'indice de réfraction varie avec la lumière incidente et se comporte donc de manière non linéaire. En transformant la modulation de phase en modulation d'amplitude au moyen de polariseurs, et en créant une boucle de rétroaction à l'aide d'un miroir, on obtient un système qui est susceptible de présenter des dynamiques complexes comme on le voit à la figure 3.20 [106–108]. Il s'agit d'un système étendu, car les intensités en différents points d'une section transverse du faisceau évoluent principalement de manière indépendante, si ce n'est que la diffraction introduit un phénomène de diffusion couplant les points voisins. Au moyen de diaphragmes et de lentilles, on peut mesurer l'intensité moyenne de domaines plus ou moins grands de la section transverse, et suivre leur évolution dans le temps.

Bien que la dynamique spatio-temporelle de ce dispositif soit globalement très complexe, on observe qu'à un instant donné, la section transverse du faisceau se décompose assez facilement en domaines chaotiques dont les points ont des évolutions fortement corrélées,

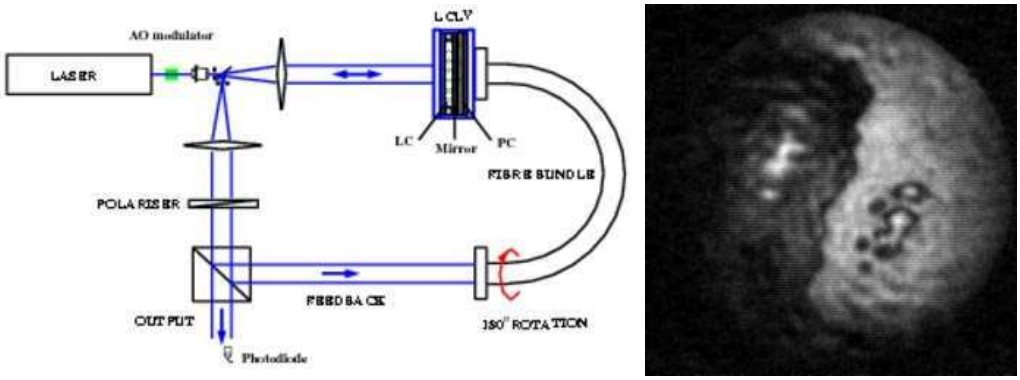

FIG. ***3.20 –*** *A gauche : dispositif expérimental. A droite : dynamique spatio-temporelle dans une section transverse du faisceau.*

les différents domaines étant largement indépendants. En fait, la dynamique locale en un point du faisceau a toutes les apparences d'une dynamique chaotique à petit nombre de degrés de liberté, la complexité globale étant due au fait que les frontières des domaines évoluent au cours du temps et se déplacent dans la section transverse.

Afin de caractériser plus précisément la dynamique locale en un point du faisceau, nous avons cherché à détecter des orbites périodiques dans les signaux enregistrés à partir d'un seul détecteur, dans le but éventuel d'en faire une analyse topologique. Comme nous cherchions à mettre en évidence sans ambiguïté la présence d'orbites périodiques, plutôt qu'à rassembler un grand nombre de trajectoires fermées différentes, les critères numériques de l'algorithme de recherche était réglés sur des valeurs extrêmement strictes.

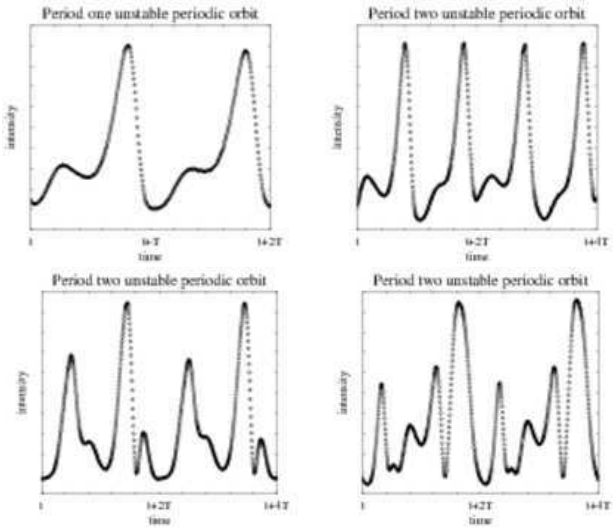

FIG. ***3.21 –*** *Orbites de période 1 et 2 détectées dans le dispositif de la figure 3.20.*

Cela ne nous a toutefois pas empêché de détecter de manière claire un certain nombre d'orbites de période 1 et 2, dont on voit quelques exemples à la figure 3.21. La structure de ces orbites est compatible avec un gabarit à deux branches de type fer à cheval avec torsion

globale de 1. Ainsi, on voit facilement que l'orbite de période 2 à droite de la figure 3.22 provient d'un doublement de période de l'orbite de période 1 de la même figure.

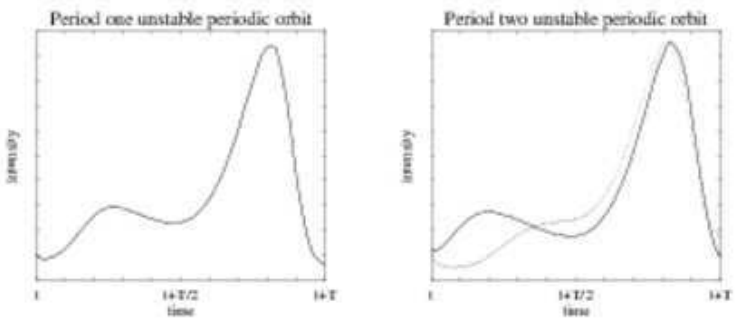

FIG. **3.22 –** *Orbites périodiques de période 1 (à gauche) et 2 (à droite).*

Au final, il n'a pas été possible de faire une analyse topologique de ces fichiers aussi poussée que celles réalisées dans d'autres systèmes en raison du déplacement des frontières de domaines au cours du temps. Il est intéressant de noter que les orbites périodiques étaient d'autant plus faciles à détecter que la taille du domaine moyenné était plus grande ce qui, à dérive spatiale constante, permettait sans doute d'observer une dynamique donnée pendant un temps plus long. Dans tous les cas, il est remarquable que dans un système à la dynamique spatio-temporelle complexe, on puisse observer des indices aussi clairs d'une dynamique de petite dimension.

3.7 ANALYSE TOPOLOGIQUE EN DIMENSION SUPÉRIEURE

3.7.1 Introduction

On a pu juger dans les précédentes sections de la puissance de l'analyse topologique, qui permet de classer les régimes chaotiques [6–8,14,68], de comprendre l'ordre d'apparition des orbites périodiques [80, 82, 83], de construire des codages symboliques [10–12], d'obtenir des indicateurs de chaos à partir d'une seule orbite périodique [2,15,102], etc. Il est d'autant plus frustrant de se voir interdire le bénéfice de cette approche dès que l'on s'intéresse à des systèmes à plus grand nombre de degrés de liberté : en effet, la théorie des noeuds ne peut être appliquée à des courbes fermées qu'en dimension trois. En dimension 4 et au delà, toute courbe fermée peut être ramenée sur une simple boucle sans induire de croisement, et toute classification basée sur le théorème de non intersection de deux trajectoire devient donc triviale.

Pourtant, si la partie du théorème de Birman–Williams [71] relative aux noeuds doit clairement être abandonnée, celle assurant l'existence d'une variété branchue semble pouvoir s'étendre en dimension supérieure. Lorsqu'il existe $n-2$ directions instables et 1 direction stable (la dernière direction étant celle du champ de vecteurs), on peut toujours imaginer contracter le flot suivant cette dernière et construire ainsi une variété branchue de dimension $n-1$ plongée en dimension n. En dimension 3, le gabarit était un hybride de cylindre et de ruban de Möbius (figure 3.5), on s'attend à rencontrer en dimension 4 des objets assemblés à partir de tores solides et de bouteilles de Klein.

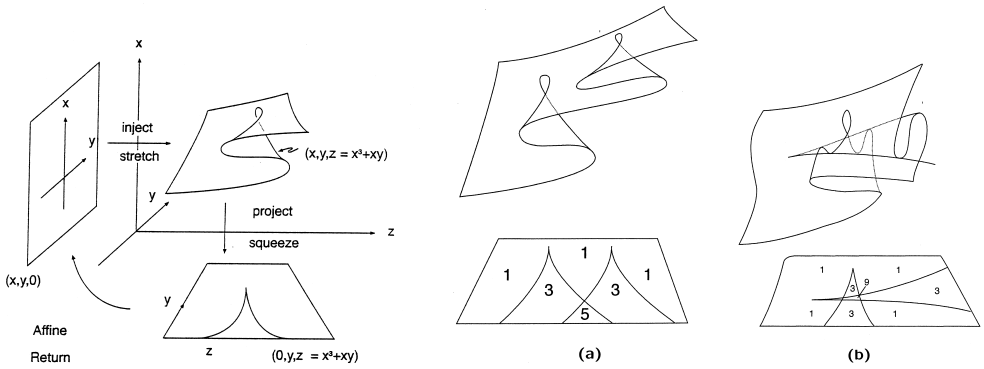

FIG. ***3.23 –*** *A gauche: en parcourant la variété branchue 3D associée à un flot 4D, une section 2D va être étirée, comprimée et repliée sur elle-même en engendrant des singularités de type fronce. A droite : on peut imaginer classer des variétés branchues d'après la manière dont leurs singularités sont organisées. D'après Gilmore et Lefranc [4].*

On soupçonne également que la théorie des singularités ait à jouer un rôle important. En effet, on peut se représenter un gabarit comme décrivant la manière dont un intervalle unidimensionnel (la ligne où les branches se recollent) se replie sur elle-même après avoir été déformé dans le plan (en faisant un tour autour de la surface, figure 3.5). Dans ce processus, les singularités apparaissant sont uniquement de type pli, les seules à être génériques en dimension 1. En dimension supérieure, c'est une surface bidimensionnelle, décrivant la dynamique de la variété instable et de ses deux directions instables, qui va être repliée sur elle-même. On sait que vont alors apparaître des singularités de type fronce. Un gabarit serait alors défini par la manière dont s'organisent ses fronces les unes par rapport aux autres (figure 3.23).

3.7.2 Un nouveau formalisme pour l'analyse topologique

– M. Lefranc, "Alternate determinism principe for topological analysis of chaos", *Phys. Rev. E* **74**, 035202(R) (2006). [appendice D, page 161]

De manière générale, les principes clés sur lesquels l'analyse topologique repose, à savoir le déterminisme et le caractère continu de la dynamique, sont valides en dimension arbitraire. Si l'on veut étendre l'analyse topologique en dimension supérieure, il faut admettre que la théorie des noeuds n'est pas un ingrédient crucial, mais simplement un auxiliaire adapté en dimension trois. En effet, imposer la non intersection des trajectoires n'est non trivial qu'en dimension trois, et il faut donc trouver un critère qui s'adapte naturellement à la dimension de l'espace des états.

Une piste extrêmement prometteuse est celle qui consiste à baser l'analyse topologique sur une formulation intégrale du théorème de non-intersection. Lorsqu'un élément de volume de l'espace des phases est transporté par un flot chaotique, l'image de sa surface se déforme au cours du temps, étant typiquement étirée et repliée. Cependant, elle ne peut en aucun cas se croiser elle-même, car sinon le théorème de non intersection serait violé aux points de croisement. Physiquement, cela revient à remarquer que si on considère une gouttelette dans un fluide, son extérieur et son intérieur restent disjoints à tout instant (figure 3.24(a)) ; mathématiquement, que l'orientation des éléments de volume est préservée. Lorsqu'on dispose d'une série de sections de Poincaré découpant l'attracteur de manière continue comme dans la figure 2.3, on peut simplifier le problème en appliquant le même principe à des éléments de volume de la section de Poincaré (figure 3.24(b)).

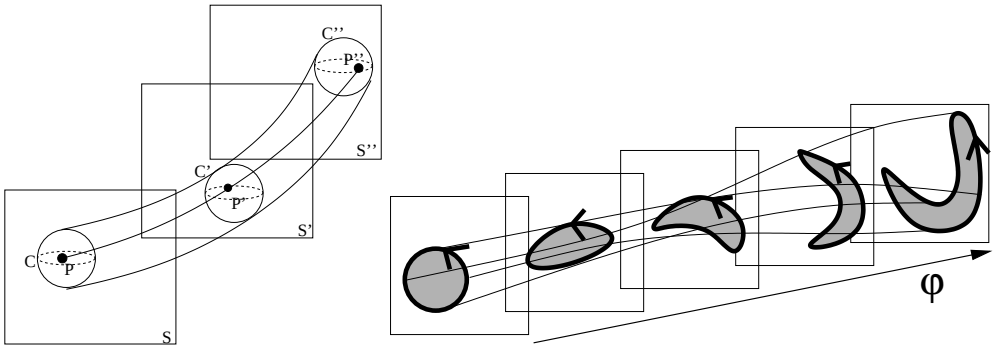

FIG. ***3.24*** – *(a) Les images successives d'un point initialement situé à l'intérieur d'une hypersurface donnée restent à tout instant dans les images de cette hypersurface car dans le cas contraire, les trajectoires du point et d'un point de l'hypersurface doivent se croiser. (b) Bien que les images d'une hypersurface dans une section de Poincaré soient typiquement étirées et repliées, elles gardent leur orientation.*

On voit que l'on déplace le critère de non intersection de trajectoires ponctuelles à celui de non intersection de trajectoires d'hypersurfaces, ce qui fait qu'il s'adapte naturellement à la dimension de l'espace des états. Il n'est cependant pas facile de reconstruire l'évolution de surfaces de grande dimension à partir de séries temporelles de longueur limitée. On souhaite donc continuer à baser notre approche sur les orbites périodiques, qui sont en effet les seules trajectoires d'un attracteur chaotique dont la dynamique asymptotique puisse être caractérisée en un temps fini. Elle ne peut donc dépendre que de la donnée des p intersections

d'une orbite avec chaque section de Poincaré, à partir desquelles nous devons déterminer l'évolution de surfaces attachées à ces p intersections.

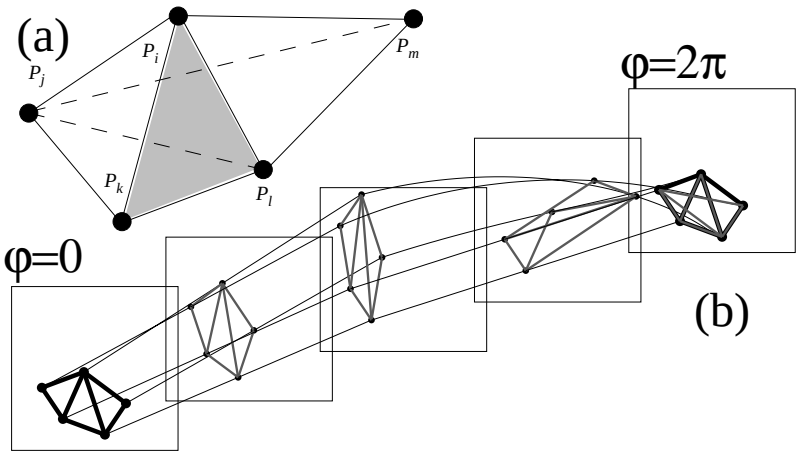

FIG. ***3.25 –*** *(a) espace triangulé basé sur des points périodiques P_i dans une section de Poincaré. (b) Le flot induit une application de cet espace dans lui-même, ici pour une orbite de période 5.*

Pour cela, on représente la dynamique dans un espace triangulé dont les noeuds sont les p points périodiques P_i dans une section de Poincaré (avec $F(P_i) = P_{i+1}$, F étant l'application de premier retour dans la section). Dans cet espace, les points sont les points périodiques P_i, les courbes sont formées de segments de droite $\langle P_i,P_j\rangle \equiv \langle ij\rangle$ reliant deux points périodiques, les surfaces bidimensionnelles sont construites à partir de triangles $\langle P_i,P_j,P_k\rangle \equiv \langle ijk\rangle$, etc (Fig. 3.25a). De manière générale, une surface m-dimensionnelle est constituée de simplexes basés sur $m+1$ des points périodiques. Lorsque l'on passe de section de Poincaré en section de Poincaré, les points périodiques P_i se déplacent dans le plan de section et donc également les simplexes qui leur sont attachés (Fig. 3.25b). On désire que la dynamique de ces simplexes reflète celle des surfaces de l'espace des phases sous l'action du flot. Chaque application F_m induite dans l'espace S_m des simplexes à m dimensions doit être continue, inversible et *préserver l'orientation*.

Un résultat préliminaire particulièrement intéressant est qu'en dimension trois, imposer la préservation de l'orientation dans un tel formalisme sélectionne de manière unique une application F_1 transformant un chemin sur une triangulation de points périodiques en un autre, et que cette application prédit les valeurs correctes d'invariants topologiques tels que l'entropie de l'orbite (que nous avons définie à la section 3.5.2).

Dans une triangulation de points périodiques à l'intérieur d'une section de Poincaré, l'élément de volume élémentaire est un triangle formé de trois points périodiques. La dynamique naturelle pourrait sembler être celle où l'image du triangle est le triangle joignant les images des trois points. Or, une telle dynamique ne préserverait pas l'orientation (Fig. 3.26). Au cours du déplacement des points dans le plan quand on va de section en section, il est en effet normal qu'à certains moments les trois points se retrouvent alignés. Si on compare les orientations des triangles situés avant et après la dégénérescence, on constate que leurs orientations sont opposées et donc que le déterminisme est apparemment violé (Fig. 3.26).

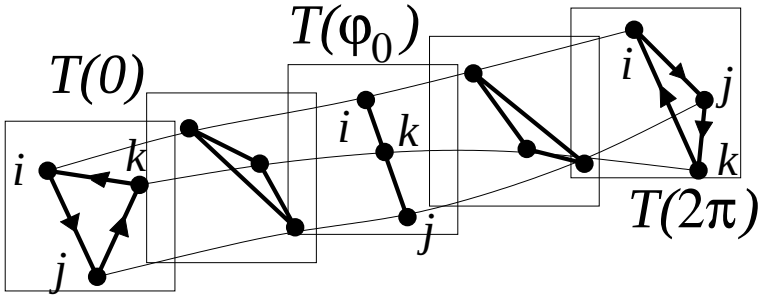

FIG. ***3.26 –*** *Lorsque des points périodiques changent de position dans des sections de Poincaré successives, le triangle qu'ils forment peut changer d'orientation.*

Il existe une solution remarquablement simple à ce problème. Il faut en effet garder à l'esprit que seul le mouvement des points est contraint par les données expérimentales, et que le mouvement des surfaces représentées par les segments entre points périodiques est reconstruit à partir de ces données. On peut donc ajouter une loi de transformation des segments au moments de l'inversion de manière à préserver l'orientation. Plus précisément, considérons les deux surfaces-chemins se faisant face à l'inversion, à savoir $\langle ik\rangle + \langle kj\rangle$ et $\langle ij\rangle$, et qui sont représentées en traits plein et pointillés sur la figure 3.27.

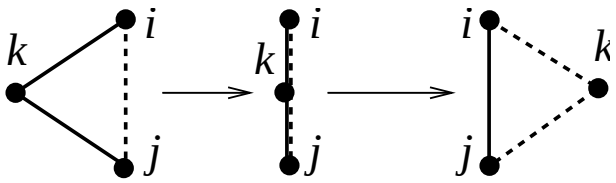

FIG. ***3.27 –*** *Le fait d'identifier les chemins en trait plein, à gauche, (resp. en trait pointillé, à droite) dans des configurations situées de part et d'autre d'une inversion de triangle induit une transformation sur les chemins.*

Le point clé est de construire la dynamique de manière à ce que la surface de gauche (trait plein) reste à gauche et la surface de droite (trait pointillé) reste à droite, ce qui est conforme au bon sens, et revient à demander que les deux surfaces ne se traversent pas, et par conséquent que l'aire située à l'intérieur du triangle ne passe pas à l'extérieur. Étant donné que la surface de gauche (resp. droite) est constituée du chemin $\langle ik\rangle + \langle kj\rangle$ (resp. $\langle ij\rangle$) avant l'inversion et du chemin $\langle ij\rangle$ (resp. $\langle ik\rangle + \langle kj\rangle$) après, leur position relative est préservée en associant l'inversion du triangle avec la règle dynamique suivante :

$$\langle ij\rangle \quad \rightarrow \quad \langle ik\rangle + \langle kj\rangle \tag{3.3a}$$

$$\langle ik\rangle + \langle kj\rangle \quad \rightarrow \quad \langle ij\rangle \tag{3.3b}$$

Les transformations (3.3) induisent une dynamique non triviale, comme on peut le voir sur la figure 3.28 où l'on a représenté le déplacement dans le plan de section des points de l'orbite de période 5 utilisée comme exemple dans la figure 3.25(b). Partant du segment $\langle 15\rangle$, on applique les règles (3.3) à chaque fois que se produit une inversion, comme par

exemple lorsque le point 4 passe entre les points 1 et 5 à la quatrième image de la première rangée. On constate qu'au fur et à mesure des itérations, le chemin s'allonge de plus en plus rapidement, suggérant que le mécanisme d'étirement à l'oeuvre dans la dynamique chaotique a été correctement capturé.

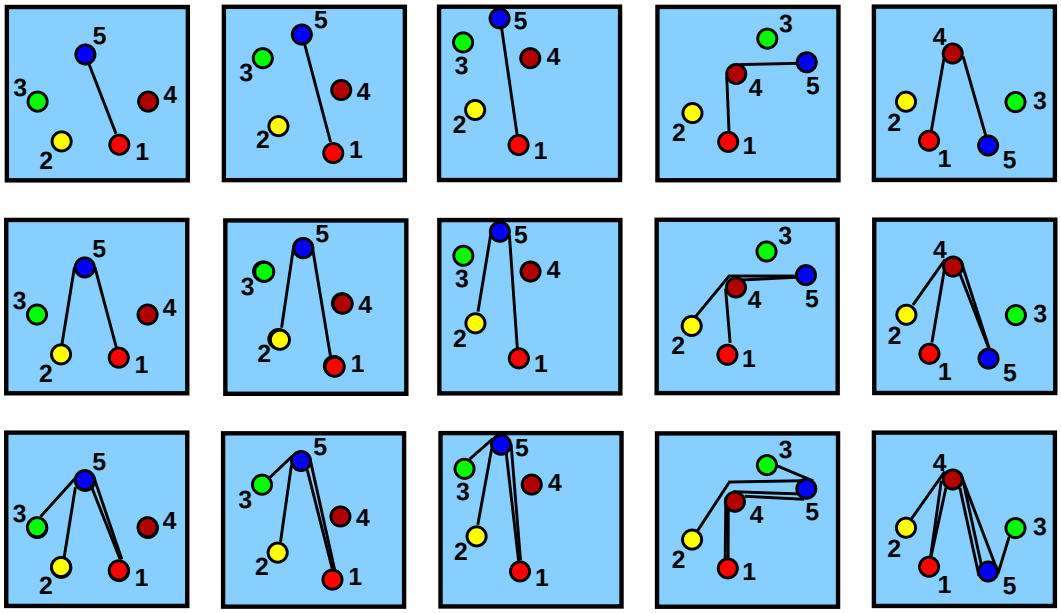

FIG. ***3.28 –*** *Dynamique induite par les règles* (3.3) *dans la triangulation des points périodiques de l'orbite de période 5 de la figure 3.25(b). Chaque rangée représente la trajectoire des points entre le départ d'une section donnée et le retour dans cette section. On a représenté le déplacement des points sur trois tours consécutifs.*

Plus précisément, on trouve que la transformation F_1 associant un chemin à son image au retour dans la section est donnée dans cet exemple par le jeu de règles de substitutions :

$$\langle 14\rangle \to \langle 25\rangle,\ \langle 15\rangle \to \langle 25\rangle + \langle 51\rangle,\ \langle 25\rangle \to \langle 35\rangle + \langle 51\rangle,\ \langle 35\rangle \to \langle 41\rangle \tag{3.4}$$

On voit facilement que quand on itère (3.4) en partant d'un chemin w, la longueur $|F_1^m(w)|$ du m-ième itéré diverge quand $m \to \infty$. Cela indique que les trajectoires dans le voisinage de l'orbite sont indéfiniment étirées par le flot. On s'attend à ce que la quantité :

$$h_(P) = \lim_{m\to\infty} \frac{\ln |F_1^m(w)|}{m} \tag{3.5}$$

soit égale à l'entropie topologique de l'orbite [85]. Pour les 746 orbites de l'application du fer à cheval [4], nous avons calculé l'entropie topologique obtenue au moyen de l'expression (3.5) et celle obtenue par l'algorithme de Bestvina-Handel, basé sur le concept de "train tracks" [85,104]. Comme l'illustre la table 3.1, *nous avons obtenu un parfait accord entre les deux approches pour toutes les orbites*. Ce résultat ne peut être le fruit du hasard et montre que le formalisme que nous proposons est équivalent aux approches précédentes. Cela nous rassure sur la pertinence d'un formalisme basé sur la préservation de l'orientation plutôt que sur la non intersection des trajectoires.

Orbite	Ce travail	TT	Orbite	Ce travail	TT
$01101\,{}^{0}_{1}1$	0.4421	0.4421	$00010\,{}^{0}_{1}1$	0.3822	0.3822
$001011\,{}^{0}_{1}1$	0.3460	0.3460	$000101\,{}^{0}_{1}1$	0.5686	0.5686
$00101\,{}^{0}_{1}1$	0.4768	0.4768	$0001\,{}^{0}_{1}1$	0.6329	0.6329
$001010\,{}^{0}_{1}1$	0.4980	0.4980	$000111\,{}^{0}_{1}1$	0.5686	0.5686
$001\,{}^{0}_{1}1$	0.5435	0.5435	$00011\,{}^{0}_{1}1$	0.3822	0.3822
$001110\,{}^{0}_{1}1$	0.4980	0.4980	$000010\,{}^{0}_{1}1$	0.4589	0.4589
$00111\,{}^{0}_{1}1$	0.4768	0.4768	$00001\,{}^{0}_{1}1$	0.6662	0.6662
$001111\,{}^{0}_{1}1$	0.3460	0.3460	$000011\,{}^{0}_{1}1$	0.4589	0.4589
$001101\,{}^{0}_{1}1$	0.4980	0.4980	$000001\,{}^{0}_{1}1$	0.6804	0.6804

TAB. ***3.1*** – *Entropies topologiques obtenues pour les orbites d'entropie positive et de période inférieure ou égale à 8 de l'application du fer à cheval de Smale, avec l'approche décrite ici (colonne 2) et avec l'algorithme "train-track" ("TT",colonne 3). [85,104].*

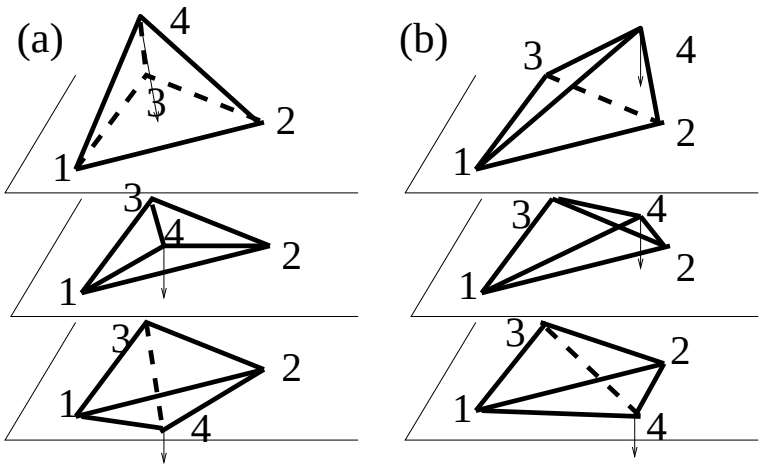

FIG. ***3.29*** – *Inversion de tétraèdres dans des sections de Poincaré de dimension 3*

Un autre résultat très prometteur concerne le chemin invariant infini obtenu en itérant indéfiniment (3.4). Il constitue un analogue discret de la variété instable de l'orbite, sur lequel la transformation (3.4) agit en le repliant sur lui-même, donnant ainsi la signature du mécanisme de repliement à l'oeuvre [16]

Reste à construire un formalisme semblable en dimension supérieure. En dimension 4, l'idée est de considérer des tétraèdres de points périodiques se déplaçant dans des sections de Poincaré à 3 dimensions, et d'appliquer les transformations nécessaires pour rétablir l'orientation lorsque des inversions se produisent. Le problème est cependant compliqué par le fait que l'on a maintenant deux types d'inversions (figure 3.29).

3.8 CONCLUSION

Le principe de déterminisme, selon lequel un état dynamique donné ne correspond qu'à un seul futur, structure les trajectoires dans l'espace des états en interdisant à deux trajectoires

de se croiser en un point, ou plus généralement à un élément de volume de changer son orientation [4, 49, 57]. Les orbites périodiques instables plongées dans l'attracteur peuvent donc exister dans des configurations topologiquement non équivalentes, qui en dimension trois sont naturellement caractérisées au moyen de la théorie des noeuds.

Les types des noeuds et entrelacements formés par les orbites périodiques, ainsi que leurs invariants, constituent des signatures des mécanismes d'étirement et de repliement à l'origine de la dynamique chaotique [3, 4]. Parce que ces derniers sont au coeur du chaos déterministe, l'analyse topologique basée sur la théorie des noeuds se montre extrêmement puissante en dimension trois et souvent irremplaçable.

Elle permet tout d'abord de répartir les régimes chaotiques en différentes classes topologiques en fonction de la structure du gabarit décrivant l'organisation de leurs orbites périodiques [1, 14, 68]. Cette classification s'est révélée utile pour mieux comprendre comment évolue la réponse chaotique d'un oscillateur non linéaire quand on fait varier amplitude et fréquence de modulation, et expliquer les régimes observés dans nos lasers modulés [6–8].

Parce qu'ils ne dépendent pas des paramètres de contrôle, les invariants topologiques des orbites périodiques jettent un pont entre les systèmes hyperboliques et les attracteurs réels que l'on observe dans les expériences. En attribuant à une orbite le nom symbolique qu'elle aurait dans la limite hyperbolique (ou d'ailleurs dans la limite infiniment dissipative), on transporte une partition génératrice d'une situation où elle est facile à construire au cas réel, où un codage symbolique est difficile à obtenir [10–12]. Outre le fait d'être compatibles avec les invariants topologiques des orbites périodiques, on peut vérifier que les partitions ainsi obtenues ont toutes les propriétés qu'on attend d'elles.

Les invariants topologiques des orbites périodiques ne renseignent pas seulement sur le régime que l'on est en train d'étudier, mais également sur les bifurcations qui peuvent survenir lorsqu'on fait varier un paramètre. C'est que l'organisation globale des orbites impose des contraintes sévères sur l'ordre dans lequel les orbites peuvent apparaître ou disparaître, ainsi que sur les interactions entre orbites dans une même bifurcation [80, 82]. Une conséquence particulièrement intéressante de cette propriété est qu'une fraction significative des orbites ne peuvent exister que dans un système chaotique, et forcent l'existence d'une infinité d'autres orbites périodiques [102]. Elles impliquent donc une entropie topologique positive et sont des indicateurs particulièrement robustes de chaos déterministe, puisqu'une seule orbite suffit alors à établir la nature chaotique de la dynamique sous-jacente [2, 15].

Cette approche est pour l'instant malheureusement limitée aux systèmes à trois degrés de liberté, mais les développements actuels basés sur la préservation de l'orientation plutôt que sur la non intersection des trajectoires permettent d'espérer disposer bientôt d'un formalisme équivalent en dimension supérieure [16].

4

Instabilités dans des Oscillateurs Paramétriques Optiques

4.1 INTRODUCTION

4.1.1 Les oscillateurs paramétriques optiques

Nous avons pu constater dans les chapitres précédents que les lasers sont des systèmes particulièrement bien adaptés à l'étude des phénomènes non linéaires, et en particulier du chaos déterministe [92, 93]. Cependant, ils ne constituent pas le seul apport de l'optique non linéaire à ces domaines, car la dynamique d'une autre source de rayonnement cohérent – l'oscillateur paramétrique optique – a récemment fait l'objet d'un nombre significatif de recherches théoriques et expérimentales. Ces travaux ont conduit à la prédiction de plusieurs instabilités [26–32] ainsi qu'à l'observation expérimentale de dynamiques oscillantes ou complexes [15, 33–36, 109], ainsi que de structures spatiales non triviales [110], sans qu'il soit toujours facile de relier les unes aux autres.

Par comparaison avec les lasers, dans lesquels on trouve une grande diversité de mécanismes de pompage, de milieux actifs, et de schémas de niveaux d'énergie, etc..., le principe de fonctionnement des OPO est très simple et repose sur l'interaction paramétrique, c'est-à-dire un mélange à trois ondes dans un cristal non linéaire [22–25, 111]. A partir d'un faisceau pompe sont engendrés deux faisceaux communément appelés signal et complémentaire (ou « idler »), dont la somme des fréquences est égale à celle de la pompe, de manière à ce que l'énergie d'un photon de pompe soit conservée lors de la conversion. De même, le processus élémentaire doit conserver l'impulsion, ce qui mène à une relation appelée communément relation d'accord de phase. Dans une approche classique, celle-ci exprime en effet que les champs pompe, signal et complémentaire se propagent dans le cristal en préservant une phase relative, ce qui permet à l'interaction de s'effectuer de manière constructive tout au long de la propagation dans le cristal. Le fait que photons signal et complémentaire soient produits conjointement dans un même processus quantique entraîne que ces deux champs sont fortement corrélés. Cela fait de l'OPO un outil de choix pour l'étude des fluctuations quantiques en optique non linéaire, et notamment pour engendrer des états comprimés de la

lumière, c'est-à-dire tels qu'une des variables présente des fluctuations réduites par rapport à la limite quantique habituelle [24, 112].

Mais l'efficacité de l'interaction paramétrique est limitée et les intensités de pompe disponibles en régime continu ne permettent pas d'atteindre des taux de conversion significatifs. Il est donc nécessaire pour produire l'intensité signal souhaitée d'insérer le cristal non linéaire dans une cavité optique, qui a le rôle habituel d'augmenter la longueur effective d'interaction. Cette cavité peut être résonante pour un des trois champs, deux d'entre eux ou pour les trois, et on parlera alors d'OPO simplement, doublement ou triplement résonant. Chaque dispositif présente ses avantages et ses inconvénients : un OPO simplement résonant est facile d'emploi mais présente des seuils d'oscillations très élevés. Un OPO triplement résonant (TROPO) se contente au contraire d'intensités pompe de quelques milliWatt, mais la triple condition de résonance est peu aisée à satisfaire et rend le dispositif extrêmement sensible aux fluctuations mécaniques ou autres.

En ce qui nous concerne, la possibilité d'explorer des zones de paramètres bien au-delà du seuil d'oscillation est un atout pour observer des phénomènes non linéaires, et plusieurs travaux consacrés aux TROPO nous avaient précédé lorsque nous nous sommes engagés dans ce thème de recherche. Ainsi, des phénomènes de bistabilité avaient été mis en évidence dans un modèle champ moyen du TROPO monomode [32] et observés expérimentalement [109], tandis que la prédiction dans ce même modèle d'une bifurcation vers un régime périodique [32, 113, 114], suivie d'une transition vers le chaos par doublement de période [32] n'a à notre connaissance toujours pas reçu de confirmation. En sens inverse, une instabilité rapide observée dans un TROPO [109] était restée inexpliquée tandis que plusieurs études montraient la richesse de la dynamique spatio-temporelle des OPO [26–32], les premiers exemples expérimentaux d'observation de structures spatiales étant récents [110].

4.1.2 Résumé des travaux

Dans ce contexte, notre groupe a contribué à l'étude de la dynamique des OPO triplement résonants, mais aussi doublement résonants, par l'observation d'instabilités expérimentales originales, ainsi que la compréhension et la modélisation des mécanismes responsables de ces instabilités. Nous avons été en cela aidés à la fois par l'acquisition d'un laser de pompe de grande puissance pour l'époque[1], ainsi que par notre expérience de la dynamique non linéaire. Essentiellement deux types d'instabilités ont été observés, qui font tous deux appel aux propriétés particulières des OPO.

Le premier est constitué d'instabilités opto-thermiques qui trouvent leur origine dans le couplage entre longueur de cavité et température du cristal [33, 34]. Leur mécanisme est toutefois original car la forte puissance de pompe injectée dans le dispositif n'y joue paradoxalement aucune rôle : c'est la boucle de rétroaction incorporant longueur de cavité, rayonnement émis et échauffement qui, lorsqu'elle s'organise autour d'un point singulier, lié à un cycle de bistabilité ou à un point d'échange de modes, en est responsable. Des variations de température de quelques milliKelvin sont alors susceptibles de déclencher des modulations à 100 % de l'intensité émise, et ce à des cadences plus rapides que l'origine thermique des instabilités ne le laisserait imaginer. Ces phénomènes seront décrits plus en détail dans la section 4.3.

1. Laser Nd:YAG doublé monomode Coherent Verdi (5W)

Le deuxième groupe d'instabilités, qui fait l'objet de la section 4.4, est lié à l'interaction de modes transverses des champs engendrés par l'oscillateur [15,35–37]. Il s'agit certes là d'un scénario bien connu en optique non linéaire [115,116], mais cette interaction présente dans les OPO des aspects surprenants et inattendus. En effet, deux modes de cavité d'un système optique ne peuvent en général interagir que dans une configuration où ils sont simultanément résonants. Cette contrainte est le plus souvent assez sévère, une coïncidence de modes n'étant observée que sur des plages de longueur de cavité très étroites autour de quelques valeurs situées dans la zone de stabilité de la cavité. Ce n'est donc que dans certaines géométries bien identifiées, comme la configuration confocale, que l'on peut voir interagir un grand nombre de modes différents. Or nos résultats semblent montrer que les instabilités à fréquence élevée que nous avons observées (typiquement entre 1 et 300 MHz), et dont nous avons montré qu'elles étaient corrélées à la coexistence de modes transverses, surviennent dans un nombre de configurations bien plus élevé que ne le prédit un calcul de coïncidences, et sur des plages plus étendues. En particulier, on observe en configuration quasi-confocale des modes qui ne peuvent pas être simultanément résonants, car de parité différente.

Les bases d'une explication de ce comportement paradoxal est sans doute à chercher dans une étude d'un modèle de TROPO dégénéré bimode décrite dans un travail conjoint avec Michel Nizette et Thomas Erneux, de l'Université Libre de Bruxelles [36] (section 4.4.4). Ce travail montre que deux modes transverses peuvent interagir même lorsqu'ils ne sont pas résonants, à condition que la fréquence d'oscillation du signal (moitié de celle de la pompe dans le cas dégénéré) soit située à mi-chemin de leurs deux fréquences de résonance, de manière à ce que l'interaction non linéaire engendre des termes résonants. C'est ce mécanisme qui explique probablement l'apparition d'oscillations à des fréquences bien supérieures à la fréquence de coupure de la cavité. Un autre résultat intéressant de ce travail est l'obtention par un calcul perturbatif d'une expression exacte pour le seuil de l'oscillation bimode.

Mais l'OPO est capable d'engendrer des signaux plus complexes que de simples régimes périodiques. Ainsi, nous avons pu décrire dans le travail mentionné ci-dessus de jolis exemples d'oscillations en rafales, résultant de la combinaison d'oscillations multimodes rapides et d'oscillations opto-thermiques [36] (section 4.4.4). Par ailleurs, nous avons également donné ce que nous pensons être la première mise en évidence indiscutable de chaos déterministe dans un OPO triplement résonant [15], observation que nous avons déjà décrite dans le chapitre consacré à l'analyse topologique, à la section 3.5.3, mais que nous reprenons ici d'un point de vue plus optique (section 4.4.5). Enfin, nous présentons un travail récent, consacré à un problème peu traité dans la littérature : les désaccords en fréquence des champs signal et complémentaire sont en général traités comme des paramètres fixes, or ils peuvent varier sous l'effet des sauts de mode, et en particulier être systématiquement ramenés vers des valeurs proches de zéro. Dans ces conditions, on est fondé à s'inquiéter de l'observabilité expérimentale des instabilités apparaissant à désaccord élevé.

4.2 DISPOSITIF EXPÉRIMENTAL

Le dispositif expérimental utilisé dans nos expériences est très classique et est schématisé dans la figure 4.1. Le cristal non linéaire de KTP, de longueur 7 ou 15 mm, est taillé de manière à ce qu'un photon de pompe à 532 nm soit converti en deux photons infrarouges aux alentours de 1064 nm, polarisés suivant des directions orthogonales (accord de phase de type II). Les photons signal and complémentaire sont donc toujours discernables, même lorsque leurs fréquences sont égales comme c'est approximativement le cas ici : on ne se trouve donc jamais dans le cas d'une situation dégénérée.

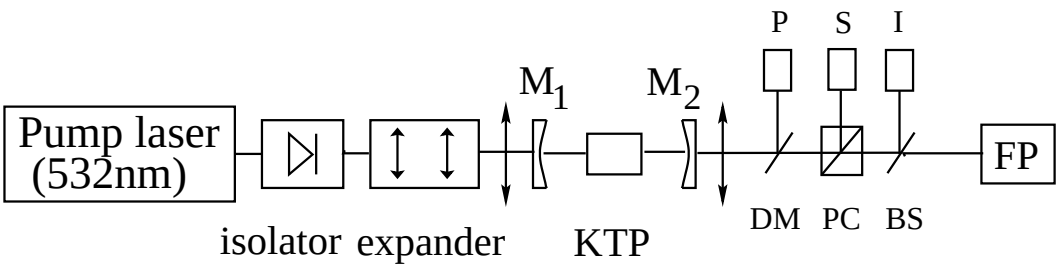

FIG. ***4.1 –*** *Dispositif expérimental utilisé dans nos expériences. Le faisceau émis par le laser de pompe Nd:YAG doublé en fréquence, est injecté après mise en forme dans la cavité contenant le cristal non linéaire où se déroule l'interaction paramétrique. En sortie de cavité, un miroir dichroïque sert à séparer la pompe à 532 nm et le rayonnement infrarouge engendré à 1064 nm, un cube polariseur à aiguiller signal et complémentaire dans des directions différentes. Le faisceau signal est envoyé à la fois sur un détecteur et sur un analyseur de spectre Fabry-Perot. Dans certaines expériences, le détecteur a été remplacé par une caméra ou une barrette de détecteur CCD afin d'étudier l'évolution du profil transverse au cours du temps.*

Notons au passage que cela n'interdit pas d'utiliser le modèle dégénéré décrivant l'interaction d'un champ signal unique avec le champ pompe car, comme nous le verrons lors de notre discussion des effets multimodes (section 4.4), on peut montrer de manière assez directe qu'en régime permanent, au moins dans le cas monomode, le modèle dégénéré décrit sans perte de généralité le cas non dégénéré [36]. Cela est dû à la gémellité des champs signal et complémentaire due à leur création, engendrés par un même processus quantique.

Ce cristal est inséré dans une cavité Fabry-Perot fortement résonante à la fréquence des champs signal et complémentaire (avec une finesse de l'ordre de 1000), le plus souvent également résonante à la fréquence de la pompe (avec une finesse d'environ 50), mais pas toujours. Ce dispositif est pompé par un laser Nd:YAG doublé de puissance maximale 5W (Coherent Verdi), les seuils d'oscillation se situant respectivement autour de 10 et 200 mW pour les configurations triplement et doublement résonante. Dans le calcul des finesses interviennent non seulement les pertes liées à la transmission des miroirs, mais également l'absorption dans le cristal, dont on notera qu'elle est relativement importante pour la pompe (environ 2 %/cm) mais très faible pour les champs infrarouges (inférieure à 0.1 %/cm). On voit donc que dans la situation triplement résonante, le laser de pompe dont nous disposions nous permettait d'atteindre des paramètres de pompe supérieurs à 400, et donc d'atteindre des régions de paramètres fortement non linéaires.

4.3 INSTABILITÉS OPTO-THERMIQUES

Lorsque nous avons entrepris l'étude de la dynamique des OPO, nous avions essentiellement deux objectifs : d'une part observer la fameuse bifurcation de Hopf prédite par le modèle d'un TROPO monomode [32] et menant à des oscillations périodiques, d'autre part explorer la dynamique spatio-temporelle des OPO continus, qui n'avait été jusque-là quasiment pas étudiée expérimentalement. Confrontés à l'expérience, nous avons rencontré des instabilités que nous n'avions pas initialement envisagées, mais auxquelles il fallait a posteriori s'attendre dans un système réel. Celles que nous présentons dans cette section, basées sur des effets opto-thermiques, sont instructives car elles illustrent combien les outils de la dynamique non linéaire peuvent être utiles pour comprendre le mécanisme déclenchant une instabilité. En particulier, les oscillations que nous décrivons maintenant s'organisent autour de singularités, dues soit à un cycle de bistabilité, soit à un point de basculement entre deux modes longitudinaux différents.

4.3.1 Oscillations monomodes

– P. Suret, D. Derozier, M. Lefranc, J. Zemmouri, and S. Bielawski, "Self-pulsing instabilities in an optical parametric oscillator: Experimental observation and modeling of the mechanism", *Phys. Rev.* A **61**, 021805(R) (2000) [appendice F, page 377].

La figure 4.2 montre un exemple typique des instabilités que nous décrivons dans cette section. Elles se caractérisent par (1) des cadences de répétition de l'ordre d'une dizaine de kHZ ; (2) une profondeur de modulation de 100 %, l'OPO s'arrêtant totalement d'émettre pendant des intervalles de temps significatifs ; (3) une alternance de commutations rapides et de phases d'évolution lente. De plus on remarque qu'étrangement, les phases d'évolution lente de la pompe se font toujours dans le sens croissant, la réinitialisation à des valeurs plus faible s'effectuant de manière brusque pendant les commutations rapides. Ces propriétés sont peu compatibles avec ce qu'on sait de la bifurcation de Hopf du modèle champ moyen du TROPO monomode. Dans nos conditions expérimentales, la fréquence du comportement périodique émergeant à la bifurcation de Hopf ne peut en effet pas être inférieure à environ 10 MHz [35], et des formes de signaux « lisses » sont attendues. Il faut donc chercher ailleurs l'origine des oscillations.

Un examen attentif des signaux de la figure 4.2, et notamment celui de l'intensité pompe fournit un indice essentiel. On constate en effet que durant les intervalles de temps où l'intensité signal est nulle, l'intensité pompe ne reste pas constante mais évolue lentement sur des échelles de temps lentes devant les temps optiques. Cela contredit formellement tout modèle basé uniquement sur l'interaction paramétrique, puisqu'à signal nul et donc en l'absence de non linéarité, le dispositif est censé se comporter comme un simple interféromètre de Fabry-Perot pour le champ de pompe. Dans ce contexte, l'intensité pompe intracavité ne peut varier que si la longueur de l'interféromètre varie puisque la puissance injectée est elle-même constante.

Il faut donc admettre que la longueur effective de cavité n'est plus un paramètre du système, mais se comporte comme une nouvelle variable dynamique, couplée aux autres variables d'état du système. Il est naturel de rechercher l'origine de couplage dans des effets thermiques, la densité de puissance intracavité induisant un échauffement du cristal, par conséquent une augmentation de son indice, et un accroissement de la longueur optique de

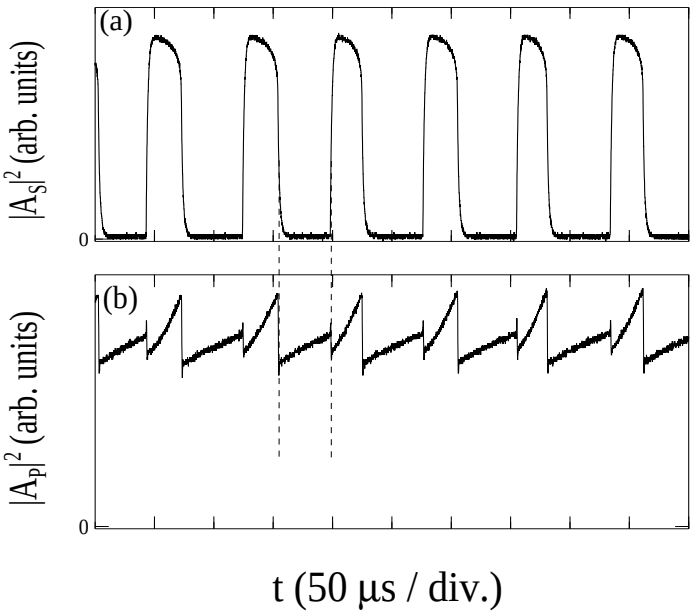

FIG. ***4.2*** – *Oscillations opto-thermiques observées dans un oscillateur paramétrique triplement résonant.*

la cavité. On serait d'ailleurs volontiers enclin à penser que lorsqu'on focalise 5 Watt de puissance lumineuse dans une cavité de finesse 50, toutes sortes de choses bizarres peuvent survenir.

Cependant, on n'observe pas de saut de mode pendant les oscillations, ce qui, compte tenu des propriétés particulières d'accord des OPO, signifie que la longueur de cavité varie en fait très peu, de quelques nanomètres au plus, et que l'amplitude thermique dans le cristal ne dépasse pas quelques milliKelvin (ce qu'on peut confirmer en notant qu'on ne parcourt qu'une petite partie du profil de raie de la pompe). On a donc affaire à un très petit effet, mais néanmoins suffisant pour entraîner une modulation complète du signal. Il est dans ces conditions difficile de considérer l'intensité pompe comme unique responsable.

Une analyse précise du mécanisme d'instabilité mène effectivement à une vision complètement différente, et montre que non seulement l'instabilité persiste en l'absence totale d'absorption, mais qu'en plus elle peut être observée pour des absorptions signal arbitrairement faibles. Le fait qu'une perturbation arbitrairement petite puisse entraîner une réponse de grande amplitude peut surprendre, mais indique en fait que la dynamique s'organise autour d'une singularité, et l'origine de cette singularité est à rechercher dans une propriété dynamique bien connue de l'OPO triplement résonant : la bistabilité [32, 109].

La figure 4.3(a) représente ainsi la variation de l'intensité signal émise en fonction de la longueur de cavité. On voit que dans les mêmes conditions, l'OPO peut être allumé ou éteint selon l'état dans lequel on l'a placé auparavant. Dès que la longueur de cavité devient une variable dynamique, ce diagramme devient un portrait de phase grâce auquel on peut comprendre facilement le mécanisme des oscillations. Imaginons que l'OPO soit éteint (intensité signal nulle), et que la longueur de cavité corresponde à un point situé à droite du point L. A partir de cette condition initiale, le cristal refroidit, et le point représentatif du

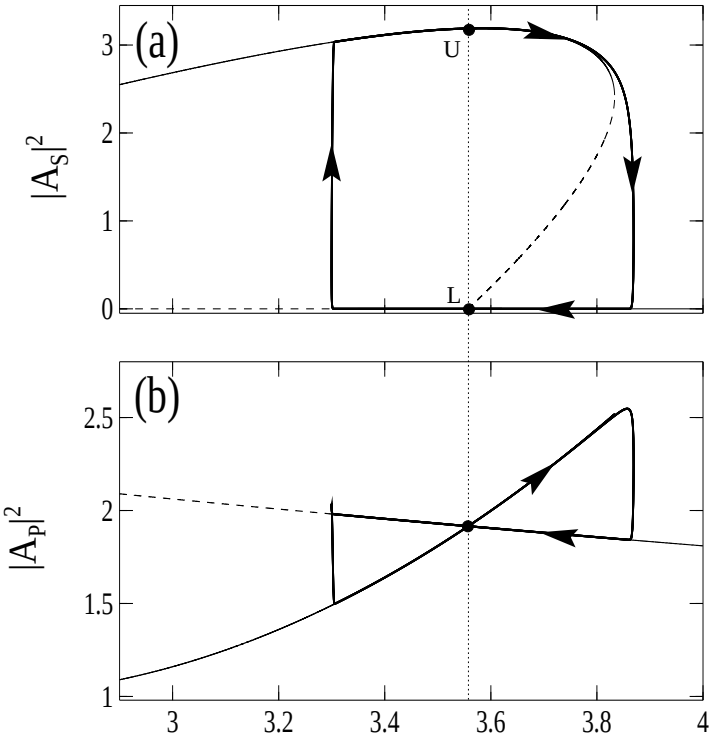

FIG. ***4.3*** – *Le mécanisme de l'instabilité est basé sur des oscillations autour d'un cycle de bistabilité.*

système se déplace vers la gauche jusqu'à franchir le point limite L au-delà duquel l'état OFF est instable. Après un petit retard du à des effets dynamiques, le système saute alors sur la branche haute et repart vers la droite car l'intensité signal non nulle réchauffe le cristal et allonge la cavité. Arrivé au point tournant du cycle de bistabilité, l'OPO s'éteint, et on repart pour un nouveau cycle.

La figure 4.3(b) montre la variation de l'intensité pompe pendant ce cycle. Elle montre que dans le cas idéal où la commutation se fait du point L au point U, il n'y a pas de discontinuité sur la pompe (c'est une propriété fondamentale du modèle monomode champ moyen du TROPO), et donc que l'absorption sur la pompe ne contribue pas à l'instabilité puisqu'elle ne peut pas inverser le sens de l'évolution de la température. Bien plus, une absorption trop forte sur la pompe aurait même tendance à stabiliser l'OPO : on voit en effet que l'intensité pompe augmente graduellement lorsque la cavité se refroidit à signal nul, et une absorption trop importante pourrait donc contrarier la tendance au refroidissement et bloquer le système sur un point de fonctionnement situé avec le point de commutation.

Inversement, on se convainc rapidement que l'instabilité périodique peut se produire pour des vitesses et des amplitudes de variation de la longueur de cavité arbitrairement petites. En effet, le mécanisme décrit plus haut dépend du fait que le cristal se refroidit en L et se réchauffe en U, mais absolument pas du temps de parcours des branches basse et haute, ni de la largeur du cycle de bistabilité. En variant les paramètres pour rendre ce dernier infiniment étroit, on maintiendrait la modulation complète de l'intensité signal, mais avec des variations

de température de plus en plus petites, et donc des fréquences de plus en plus élevées (des oscillations thermiques à 500 kHZ ont ainsi été observées dans nos OPO). De même, une absorption signal très faible rend le déclenchement de l'instabilité plus difficile à paramètres fixés, mais ne peut l'empêcher de se produire pour certaines valeurs des paramètres tant qu'il existe une discontinuité entre points L et U.

Cette sensitivité extrême à des effets infimes est la caractéristique des systèmes à *perturbation singulière* [117], dont l'oscillateur de van der Pol est le représentant le plus célèbre, et dont font également partie les oscillateurs à relaxation, que ce soit en électronique, en physique, en chimie, ou en biologie, où le mécanisme de van der Pol prend le nom de Fitzhugh-Nagumo, et sert à modéliser les propriétés électriques d'un neurone. Pour rester dans le cadre de l'optique, des mécanismes similaires ont par exemple été décrits dans un interféromètres non linéaires [118], dans une expérience de refroidissement d'atomes [119] et dans un amplificateur optique à semi-conducteur [120].

Tous ces exemples, ainsi que le travail décrit ici, montrent bien qu'à une intuition physique doit se rajouter une intuition dynamique basée sur les outils de la physique non linéaire si l'on veut être en mesure d'appréhender toutes les surprises que peut nous réserver une expérience.

4.3.2 Oscillations bimodes

– Pierre Suret, Marc Lefranc, Dominique Derozier, Jaouad Zemmouri and Serge Bielawski, "Periodic mode hopping induced by thermo-optical effects in continuous-wave optical parametric oscillators", Opt. Lett. **26**, 1415–1417 (2001). [appendice F, page 373].

Cette section est consacrée à une variation intéressante du mécanisme décrit dans la section précédente, et concerne des instabilités apparaissant au voisinage d'un point où un mode d'oscillation perd sa stabilité au profit d'un autre. Comme nous le verrons ci-dessous, ces instabilités peuvent être observées dans des OPO aussi bien triplement que doublement résonants. De manière générale, on peut s'attendre à les rencontrer dans tout système optique où un saut de mode s'accompagne d'une discontinuité dans l'intensité d'émission et sujet à des effets thermiques.

La figure 4.4 montre des signaux temporels observés dans des OPO triplement et doublement résonants [34]. Ces oscillations présentent un certain nombre de points communs avec celles de la figure 4.2, mais également des différences importantes. Ainsi, on retrouve l'alternance de phases lentes et rapides, ainsi que des cadences de quelques kHz, mais on constate par contre que l'intensité ne revient jamais à zéro, ce qui exclut que l'on soit en train de parcourir le cycle de bistabilité d'un mode unique. Ce scénario est d'ailleurs d'autant moins probable qu'il ne peut de toute façon expliquer les oscillations de l'oscillateur doublement résonant, qui, lui, ne présente pas de bistabilité.

On est donc fondé à penser que plusieurs modes sont impliqués dans les dynamiques de la figure 4.4. Mais s'agit-il de modes transverses ou longitudinaux ? Oscillent-ils simultanément ou en alternance ? Nous avons obtenu la réponse à ces questions en injectant le rayonnement signal émis par l'OPO dans un analyseur de spectre Fabry-Perot, sciemment désaligné de manière à élargir la résonance correspondant à une fréquence donnée et à rendre le temps de traversée de cette résonance grand devant la période moyenne d'oscillation. Nous avons ainsi pu montrer clairement que les signaux de la figure 4.4 sont engendrés par une alternance périodique entre deux modes longitudinaux adjacents, chacune des deux phases d'évolution lentes correspondant à un mode différent oscillant seul dans la cavité [34]. Les

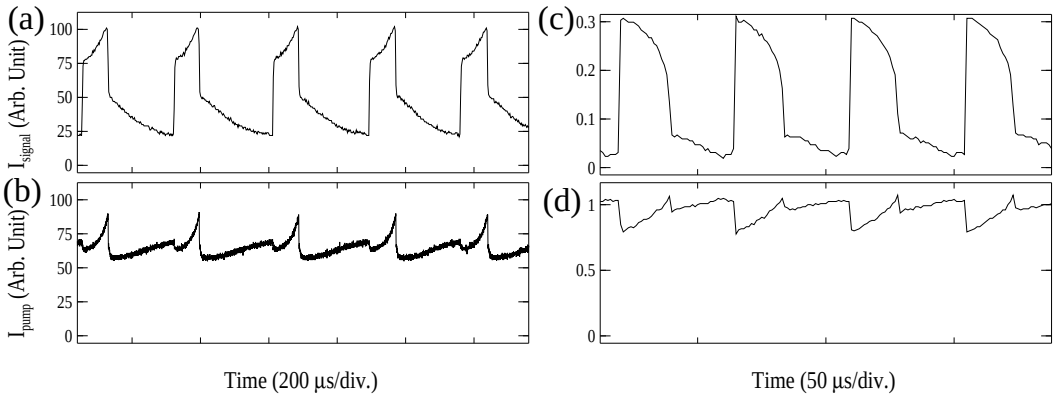

FIG. ***4.4 –*** *Oscillations périodiques observées (a) dans un OPO triplement résonant (puissance de pompe 1.5 W); (b) dans un OPO doublement résonant (puissance de pompe 3.6 W).*

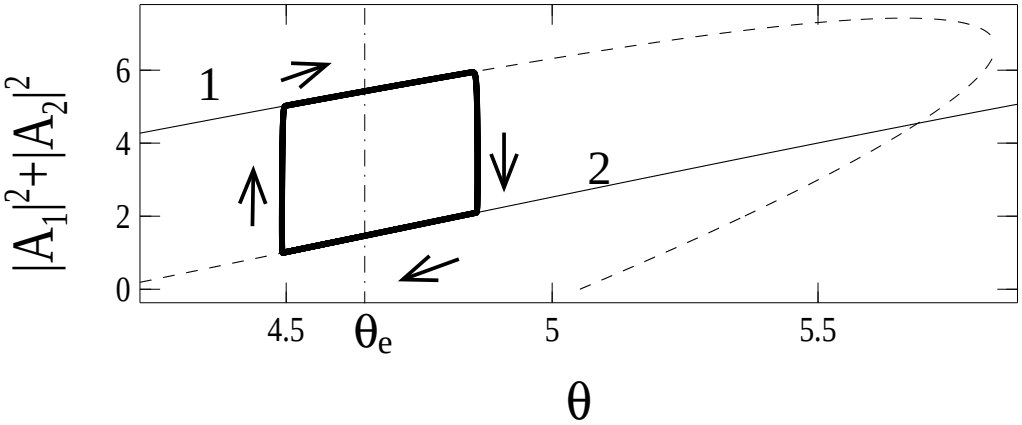

FIG. ***4.5 –*** *Portrait de phase dans le plan intensité signal–longueur de cavité associé à une alternance périodique entre deux modes longitudinaux. Chacune des deux courbes correspond à la résonance d'un mode longitudinal. L'échange de stabilité s'effectue en $\theta = \theta_e$, le mode 1 étant stable en-deçà de θ_e, le mode 2 au-delà.*

phases d'évolution rapide correspondent aux commutations entre modes, qui s'effectuent aux échelles de temps optiques.

Comme dans la section 4.3.1, ce phénomène d'alternance est provoqué par une variation de la longueur de cavité sous l'influence d'effets thermiques. Pour comprendre le mécanisme sous-jacent, nous représentons dans la figure 4.5 la dépendance de l'intensité du signal par rapport à la longueur de cavité, comme nous l'avions fait à la figure 4.3. La situation représentée est celle d'un OPO triplement résonant où les courbes de résonance de chacun des modes sont suffisamment inclinées pour présenter de la bistabilité s'il n'était pas en interaction avec un autre mode, ce fait n'étant toutefois pas essentiel pour ce qui nous intéresse.

Dans la plage de longueurs de cavités où les courbes de résonance des deux modes sont non nulles, l'OPO se comporte comme un laser à élargissement homogène : le mode de seuil le plus bas démarre et assujettit la pompe à son propre seuil, empêchant ainsi les autres

modes de démarrer (dynamique de type “winner takes all”). Dans un OPO, le seuil d’un mode longitudinal est directement fonction de son désaccord en fréquence, et c’est donc le mode de désaccord le plus petit qui est sélectionné [25, 121]. Dans la figure 4.4, le trait vertical en $\theta = \theta_e$ représente la configuration où les désaccords des deux modes sont égaux. A gauche du trait, le mode 1 est moins désaccordé et domine, à droite de ce trait c’est le mode 2 qui l’emporte. On voit que les oscillations s’organisent autour du point d’échange de stabilité. Lorsque l’on est sur la branche 1, le cristal se réchauffe et on se déplace vers la droite du portrait de phase. Une fois passé l’échange de stabilité, le mode 1 s’éteint et on passe sur le mode 2, dont l’intensité est plus petite ce qui permet au cristal de se refroidir, de repasser l’échange de stabilité, et de recommuter sur le mode 1.

On voit qu’une condition suffisante pour qu’une instabilité soit observée à certaines valeurs des paramètres est que les deux modes aient des intensités différentes à l’échange de stabilité. Or, on montre facilement que la discontinuité est proportionnelle au produit des désaccords en fréquence [32], et que c’est donc le cas dès que la pompe et le signal présentent tous les deux un désaccord en fréquence non nul par rapport à un mode de cavité. Cette condition étant nettement plus facile à satisfaire que celle contrôlant l’instabilité monomode de la section 4.3.1 (qui, elle, exige que le produit des désaccords soit supérieur à 1), on s’attend à rencontrer l’instabilité plus fréquemment et sur des plages de paramètres plus larges que l’instabilité thermique monomode[2] Dans nos expériences, nous avons ainsi constaté que dans certaines configurations, l’alternance entre modes était présente sur plus de la moitié des valeurs de la longueur de cavité donnant lieu à émission paramétrique.

D’un point de vue dynamique, cela se comprend par le fait que l’on se trouve à l’échange de modes dans une situation plus dégénérée que dans celle basée sur le cycle de bistabilité de la figure 4.3, plus précisément impliquant une singularité d’ordre supérieur. Le point d’échange de stabilité se comporte en effet comme un cycle de bistabilité infiniment fin, une situation qui génériquement nécessite d’ajuster deux paramètres simultanément, mais ne dépend ici que d’un seul. Lorsque les deux modes ont même désaccord, on peut se d’ailleurs se convaincre que n’importe quelle répartition de l’intensité totale entre les deux modes peut être observée et donc que n’importe quel point de fonctionnement situé sur le segment vertical joignant les deux résonances en $\theta = \theta_e$ est un point de fonctionnement acceptable. On est en fait dans une situation comparable à celle d’une transition de phase du premier ordre, les deux modes coexistant correspondant aux deux phases coexistant à la transition. Il est clair que dans ces conditions, le calcul de la période d’oscillation n’a rien d’évident et exige une analyse en perturbation singulière.

Une prédiction intéressante de cette analyse est que dans certaines zones de paramètres, et sur une certaine plage de longueurs, on devrait pouvoir observer une émission stationnaire multimode longitudinale, le point fixe correspondant à la coexistence étant stabilisé par les effets thermiques au lieu de donner naissance à des oscillations périodiques. Un tel fonctionnement contredit le consensus qui veut qu’un OPO ne puisse pas osciller sur deux modes longitudinaux différents. Nous avons observé des régimes qui pourraient correspondre à cette description (intensité à peu près stationnaire mis à part des fluctuations très basse fréquence, présence de deux modes longitudinaux à l’analyseur de spectre Fabry-Perot) sans

2. On ne la rencontrera certes pas dans un OPO doublement résonant au sens strict, mais il suffit que la pompe effectue un double passage ou soit, même très faiblement, résonante pour qu’elle puisse être désaccordée et donc que la condition soit satisfaite.

que nous ayons établi qu'il s'agissait de la seule explication possible. Compte tenu de la grande généralité du mécanisme, il est naturel de se demander si ce phénomène ne pourrait pas être observé dans d'autres dispositifs optiques habituellement strictement monomodes.

4.3.3 Conclusion

Les lois qui gouvernent la dynamique d'un OPO triplement résonant engendrent des points de fonctionnement singuliers – points tournants du cycle de bistabilité associé à une résonance monomode, ou échange de stabilité entre deux modes – qui peuvent transformer des variations infimes de la température du cristal en variations de grande amplitude de l'intensité du signal. Lorsqu'une boucle de rétroaction liant intensité du champ signal, longueur de cavité, et température du cristal s'organise autour de tels points singuliers, on peut observer des instabilités opto-thermiques dont les fréquences peuvent aller de quelques kHz à quelques centaines de kHz.

Ces oscillations présentent des propriétés tout à fait particulières, notamment du fait qu'elles sont associées à des passages lents par des points de bifurcation du problème statique. Par exemple, la durée d'une phase lente dépend de manière cruciale du délai après lequel on commute vers l'autre branche après avoir passé le point de bifurcation. Un sujet de recherche intéressant, que nous avons commencé à défricher mais sans le développer, serait d'utiliser les signaux expérimentaux et les délais mesurés pour remonter à des grandeurs difficilement mesurables, comme par exemple le niveau de fluorescence paramétrique dans la cavité.

Mais ces instabilités opto-thermiques n'ont pas été les seules surprises que nos oscillateurs paramétriques optiques nous ont réservées, et nous passons donc en revue dans la prochaine section des instabilités beaucoup plus rapides qui, comme nous le montrerons, trouvent leur origine dans l'interaction de modes transverses.

4.4 INSTABILITÉS MULTIMODES TRANSVERSES

Nous changeons maintenant radicalement d'échelles de temps, puisque nous nous intéressons dans cette section à des instabilités rapides dont les fréquences vont de quelques MHZ à quelques centaines de MHz. Pour autant, nous n'abandonnons pas totalement les instabilités lentes étudiées précédemment, car nous verrons dans la section 4.4.4 que ces deux types d'oscillations peuvent se combiner pour donner naissance à de très beaux exemples d'oscillations « en rafale », dont l'intérêt est en particulier justifié par leur importance dans de nombreux phénomènes biologiques [42, 122].

Comme nous le verrons plus loin, nous avons pu expliquer ces oscillations rapides par l'interaction de modes transverses, notamment en suivant l'évolution du profil transverse lorsque la longueur de cavité est balayée. C'est certes là un scénario très classique dans les systèmes optiques, et une littérature importante a ainsi été consacrée aux régimes complexes engendrés par ce phénomène dans les lasers et autres systèmes optiques [115, 116]. Dans les oscillateurs paramétriques optiques, il prend cependant des aspects tout à fait originaux, que nous n'avons certainement pas fini d'explorer. Ces aspects originaux découlent des propriétés de l'interaction paramétrique, et notamment du fait que les champs signal et complémentaire n'interagissent avec le champ de pompe que par un terme d'interaction quadratique. Les fréquences indidivuelles sont donc moins pertinentes que leur somme, et cela donne à l'oscillateur paramétrique optique une liberté dont il semble tirer parti.

En particulier, il semble résulter de nos travaux qu'il n'est pas nécessaire que deux modes transverses interagissant soient individuellement résonants avec un mode de la cavité : il suffit que leurs fréquences soient situées de part et d'autre d'une résonance, ou en d'autres termes que leurs désaccords en fréquence soient opposés. Il en résulte que les régimes multimodes sont observés dans un nombre de configurations bien plus grand que ne laisserait penser un calcul de coïncidences déterminant les géométries où deux modes donnés sont simultanément résonants.

4.4.1 Observation d'oscillations rapides

– P. Suret, M. Lefranc, D. Derozier, J. Zemmouri, and S. Bielawski, "Fast oscillations in an optical parametric oscillator", *Opt. Commun.* **200**, 369–379 (2001) [appendice F, page 357].

La figure 4.6 montre des instabilités rapides à environ 2.5 MHz, observées dans un OPO triplement résonant à des puissances de pompe d'environ 275 fois le seuil d'oscillation. Il serait évidemment tentant d'expliquer ces oscillations par la bifurcation de Hopf du modèle TROPO champ moyen monomode, mais on s'aperçoit rapidement que cela est impossible. En effet, nous avons pu obtenir une borne inférieure $\omega_L = 1/\sqrt{\tau_p\,(\tau_p + \tau_s)}$ de la pulsation des régimes périodiques émergeant de cette bifurcation (où τ_s et τ_p sont les temps de vie des photons pompe et signal, respectivement) [35], et avons montré que dans la situation expérimentale qui nous intéresse, la fréquence de Hopf ne peut être inférieure à environ 10 MHz.

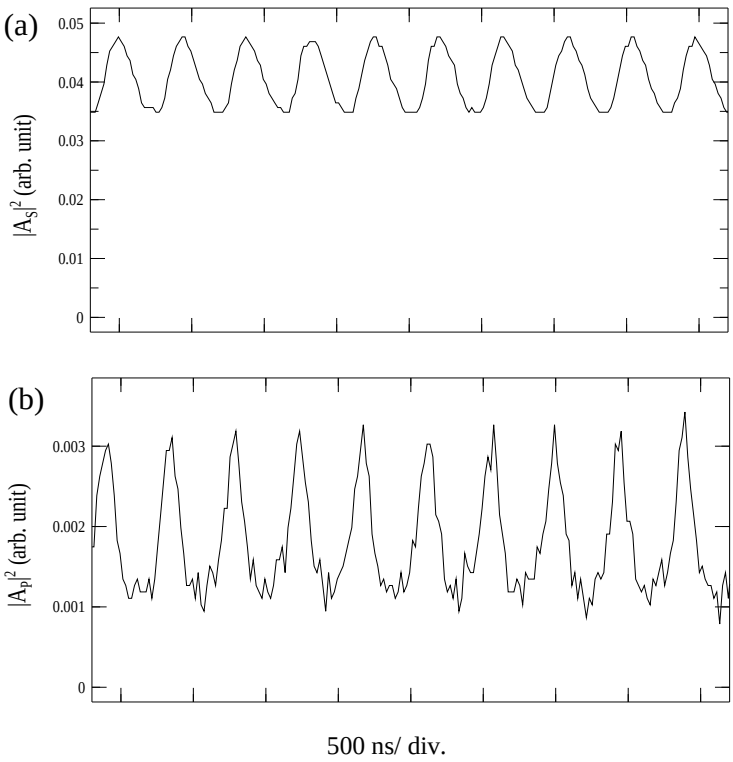

FIG. ***4.6*** – *Instabilités rapides observées dans un OPO triplement résonant à 2.5 MHz sur les intensités (a) du signal ; (b) de la pompe.*

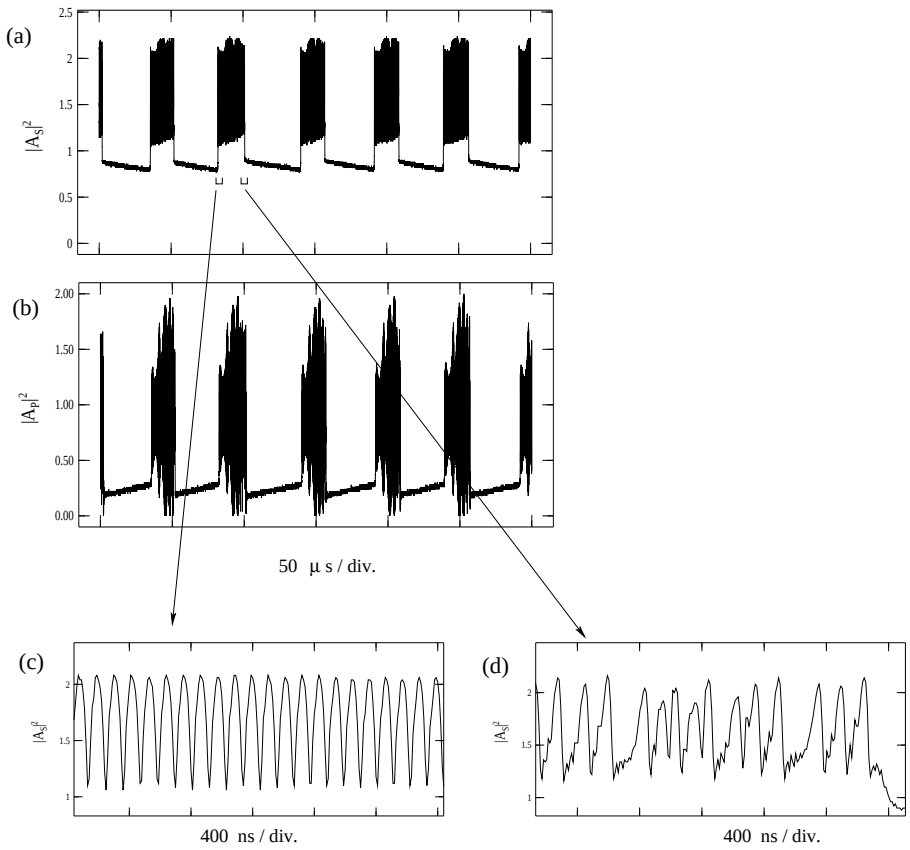

FIG. ***4.7 –*** *Instabilités rapides combinées aux instabilités lentes étudiées précédemment. Séries temporelles (a) du signal ; (b) de la pompe. On notera la variation de la forme d'onde entre (c) le début et (d) fin de la phase d'évolution rapide.*

De plus, ces instabilités rapides sont également observées en combinaison avec des instabilités lentes du type de celles de la section 4.3, comme on peut le voir à la figure 4.7. On note toutefois des différences significatives. Alors que dans la figure 4.7, on n'observe pas de retours à zéro de l'intensité, une étude à l'analyseur de spectre ne révèle qu'un seul mode longitudinal. Même si la fréquence de l'instabilité n'était pas incompatible avec celle de la bifurcation de Hopf, le régime de la figure 4.7 ne peut s'expliquer par cette dernière, car on sait qu'elle apparaît dans des zones de paramètres disjointes de celles où est observée la bistabilité nécessaire à l'apparition des oscillations thermiques monomodes [32]. Toutes ces observations nous ont naturellement conduit à émettre l'hypothèse que les instabilités rapides des figures 4.6 et 4.7 sont engendrées par l'interaction de deux modes transverses ou plus. On notera au passage la grande similitude entre les régimes de la figure 4.7 et ceux décrits par Richy *et al.* [109], qui laisse à penser qu'ils ont la même origine.

Nous avons plus récemment obtenu des indications directes de la nature multimode transverse de ces oscillations périodiques à haute fréquence, que nous décrivons ci-dessous et qui feront l'objet d'une publication actuellement en fin de rédaction.

4.4.2 Mise en évidence du caractère multimode des oscillations rapides.

– A. Amon, M. Lefranc, S. Bielawski, and D. Derozier, “Multimode behavior of optical parametric oscillators”, article en cours de rédaction.

Une première observation concerne la structure transverse du faisceau. On s’attend en effet à ce qu’en régime multimode, on puisse y lire la présence d’au moins deux modes, et en tout cas observer un profil qui soit différent du TEM_{00} habituel. C’est effectivement ce qu’on voit à la figure 4.8, qui montre des profils transverses associés à des oscillations à quelques MHz, et où on croit discerner la superposition d’un mode TEM_{00} avec un mode d’ordre supérieur. Cependant, la caméra n’est pas assez rapide pour que l’on puisse affirmer que les modes oscillent simultanément, et en particulier écarter une alternance périodique entre modes transverses du type de celle décrite à la section 4.3.2.

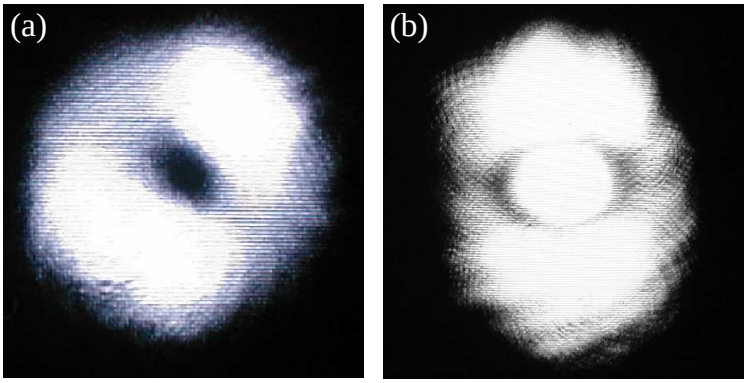

FIG. ***4.8 –*** *Profils transverses du signal lors de l’observation d’instabilités rapides, enregistrés à l’aide d’une caméra standard dans deux configurations différentes.*

Il nous faut donc observer la structure spatiale du faisceau avec une cadence plus élevée, mais l’on sait qu’un compromis doit en général être trouvé entre résolutions temporelle et spatiale lors de l’acquisition d’images. Afin de suivre la dynamique aux échelles de temps des instabilités temporelles (quelques MHz), nous nous sommes donc repliés sur la caméra la plus élémentaire que l’on puisse imaginer : celle constituée de deux détecteurs ponctuels placés à des endroits différents d’une section transverse du faisceau.

La figure 4.9 montre les signaux typiques que l’on peut obtenir dans un régime mêlant instabilités lentes et rapides, et qui nous permettent de conclure rapidement. On voit les signaux des deux détecteurs représentés séparément, ainsi qu’une superposition des deux signaux pour un court intervalle temporel situé à l’intérieur d’une phase d’oscillations rapides. On voit sur les figures 4.9(a) et 4.9(b) que les deux amplitudes sont fort dissemblables, et n’évoluent certainement pas proportionnellement l’une à l’autre comme ce serait le cas si le profil transverse était celui d’un unique mode transverse. Cela est confirmé par la figure 4.9(c) où on constate qu’elles sont approximativement en quadrature de phase. Il nous faut donc conclure que le champ émis s’appuie sur au moins deux modes transverse différents.

Afin de mieux comprendre comme apparaissent les oscillations multimodes lorsqu’on balaye la longueur de cavité, nous avons ensuite fait appel à un dispositif d’acquisition d’images de résolutions spatiale et temporelle intermédiaires, constitué d’une barrette linéaire de 256 détecteurs CCD placée dans une section transverse du faisceau. Les expositions des différents détecteurs sont simultanées, mais leur acquisition se fait de manière séquentielle,

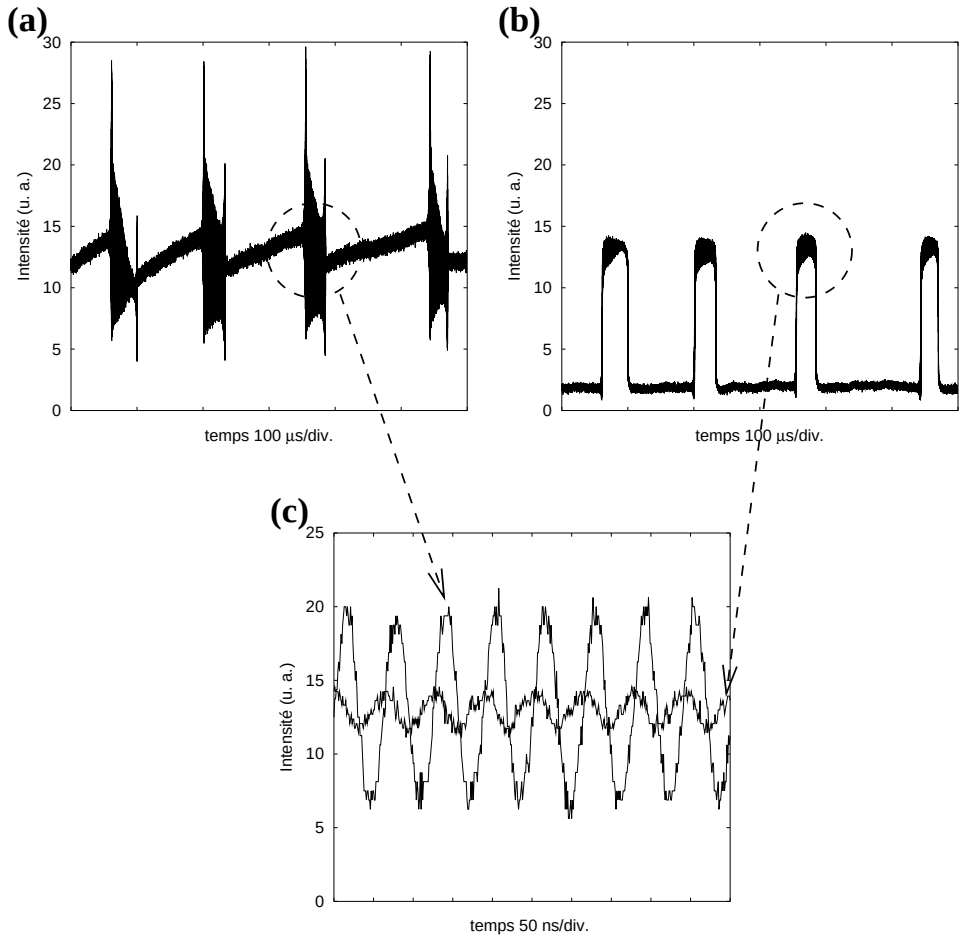

FIG. ***4.9*** – *(a) et (b) Signaux enregistrés en deux points différents de la section transverse du faisceau signal. (c) Superposition des deux signaux durant une phase d'oscillations rapides. Le fait que les deux signaux ne soient pas proportionnels et qu'ils soient déphasés montre la coexistence d'au moins deux modes transverses.*

au moyen d'un signal vidéo qui, lors d'une trame, prend successivement les valeurs de chacun des détecteurs. Pendant l'intervalle de temps correspondant à l'acquisition d'une image, on obtient donc un signal temporel donnant le profil d'intensité transverse le long de la barrette. La durée d'acquisition d'une image limite le nombre d'images par seconde à environ 67000, ce qui serait trop peu pour démontrer la coexistence de modes aux échelles de temps rapides, mais suffit pour suivre l'évolution de la structure du faisceau lors d'une variation lente de la longueur de cavité.

La figure 4.10 nous montre ainsi les signaux délivrés par un détecteur ponctuel et par la barrette CCD lors d'une expérience où la cavité dérivant lentement, l'OPO passe transitoirement par une zone d'instabilités rapides. Bien qu'il s'agisse de signaux bruts, la structure du signal vidéo nous permet de lire immédiatement sur cette figure l'évolution du profil transverse alors que se succèdent les différents régimes observés. On observe tout d'abord un saut de mode sur l'intensité accompagné d'une transition d'un profil de type gaussien à un profil à deux lobes. Ce dernier profil est à peu près constant jusqu'à ce qu'on rentre dans

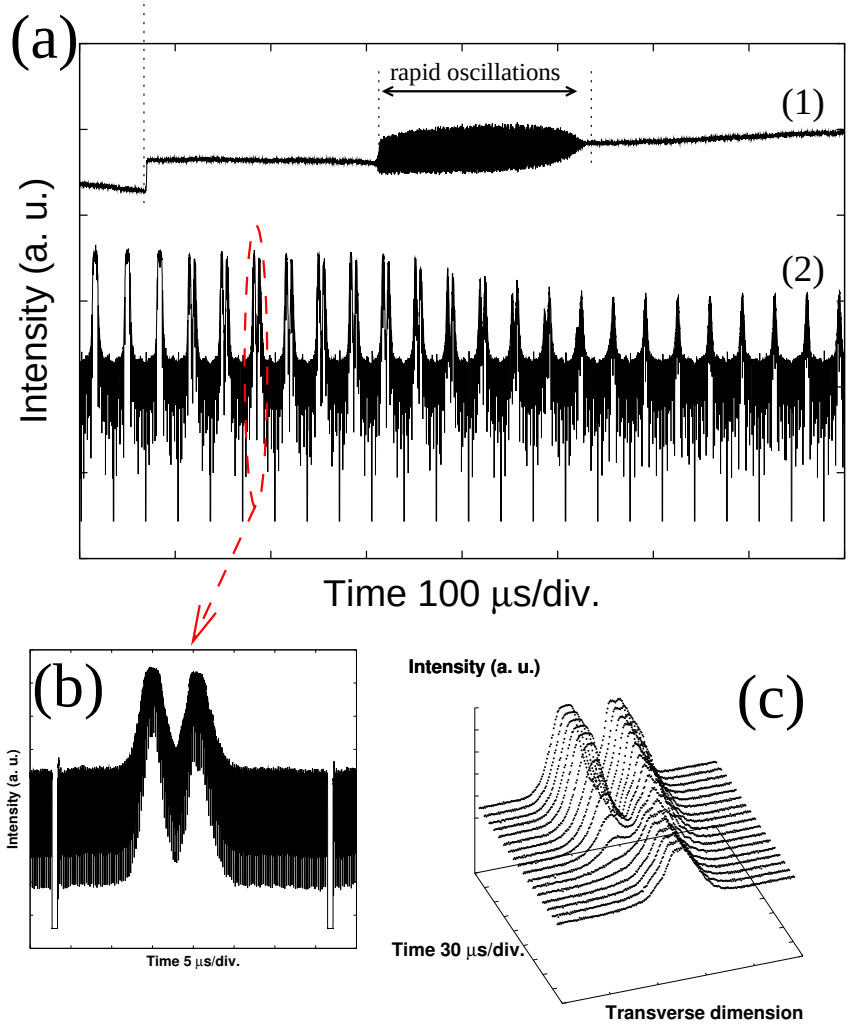

FIG. ***4.10*** – *(a) Signaux délivrés par un détecteur ponctuel (1) et par une barrette CCD (2) pendant une dérive lente de la cavité au travers d'une zone d'instabilités rapides, et permettant d'étudier la variation du profil transverse du faisceau pendant ce balayage. (b) Vue élargie du signal CCD correspondant à l'acquisition d'une image. On voit clairement les deux impulsions marquant le début et la fin de l'image. L'épaisseur du trait de la figure (b) est due aux impulsions délimitant les intervalles où le signal fournit l'intensité correspondant à un déctecteur individuel (un « pixel »). (c) Reconstitution de l'évolution du profil transverse dans la zone d'oscillations rapides.*

la zone d'instabilités rapides, et se modifie ensuite progressivement pour arriver une structure monolobe à la fin de la zone d'instabilités, et rester ensuite constant. La succession de profils rencontrés est représentée de manière plus lisible à la figure 4.10(c). Ces observations s'interprétent naturellement de la manière suivante : deux modes différents oscillent seuls de part et d'autre de la zone d'instabilité, et leur coexistence dans la région intermédiaire, avec des poids relatifs qui varient le long de la zone de recouvrement, est responsable de l'apparition des oscillations rapides. Cette interprétation est compatible avec l'hypothèse que ces dernières sont observées lorsque deux modes transverses sont simultanément résonants, en

supposant que les poids des deux modes évoluent selon leurs désaccords respectifs. Toutefois, d'autres observations montrent que le phénomène observé n'est pas aussi simple.

En effet, nous avons cherché à évaluer la fréquence d'apparition des oscillations multimodes transverses, de manière à décider si il s'agit d'un phénomène exotique ou au contraire d'un mécanisme avec lequel il faut compter dès que la puissance de pompe dépasse un certain seuil, sachant que des lasers de pompe de plus en plus puissants sont disponibles. La réponse à cette question n'était en effet pas évidente : d'une part nous avions trouvé cette instabilité sans trop la chercher (et on pouvait penser qu'il s'agissait également de l'explication de l'observation de Richy *et al.* [109]), d'autre part une condition de coïncidences imposant la résonance simultanée est extrêmement contraignante et, hormis les classiques géométries plane, confocale et concentrique, il n'existe en général que quelques configurations où deux modes donnés peuvent être simultanément résonants, et ce sur une plage de longueur de cavité très réduite, de l'ordre d'une centaine de microns [123].

4.4.3 Prévalence des oscillations multimodes

– A. Amon, M. Lefranc, S. Bielawski, and D. Derozier, "Multimode behavior of optical parametric oscillators", article en cours de rédaction.

Afin de nous faire une idée plus précise, nous avons entrepris des balayages systématiques de la longueur de cavité. Dans une expérience, nous avons ainsi modifié la longueur de cavité par pas d'environ 200 μm entre 45,3 mm et 47,6 mm, c'est-à-dire en peu deçà de la configuration confocale pour cette cavité délimitée par des miroirs de rayon de courbure 5 cm. Pour chaque longueur de cavité, nous avons effectué un balayage fin sur un intervalle spectral libre afin de localiser des éventuelles zones d'oscillations rapides. Comme le montre la figure 4.11, quatre des onze configurations explorées présentaient des oscillations à des fréquences de l'ordre de 15 MHz, auxquelles il faut rajouter des oscillations de très haute fréquence à 190 et 275 MHz (45,3 mm), et 333 MHz (46,3 mm), non représentées sur la figure. On constate sur la figure 4.11 que les oscillations observées sont à chaque fois associées à des profils transverses qui ne sont pas ceux d'un mode TEM_{00}.

Cette expérience a été répétée plusieurs fois, afin de vérifier sa reproductibilité. De manière générale, la probabilité d'apparition d'instabilités rapides pour au moins un point de l'intervalle spectral libre des configurations étudiées a été très élevée, allant même parfois jusqu'à 1. Nous avons également travaillé à des longueurs de cavité 63, 71, 77 et 89 mm, détectant à chaque fois des instabilités rapides, à des fréquences typiquement comprises entre 1 et 15 MHz.

On constate donc que les oscillations de fréquence élevée, que nous avons associées à des régimes multimodes dans la section 4.4.2, ont une fréquence d'apparition bien plus élevée que ne le prédit un calcul de coïncidence de résonances de modes transverse, et qu'à nos puissances de pompe, une cavité donnée a une probabilité élevée de laisser apparaître des oscillations rapides en un ou plusieurs points de son intervalle spectral libre. De plus, on note que les profils transverses observés sont souvent en contradiction avec la structure du peigne de modes transverses. Ainsi, l'image de la figure 4.8 suggère la coexistence de modes $\mathrm{TEM}_0 0$ et $\mathrm{TEM}_0 1$, alors que dans la configuration confocale proche, ces deux modes sont séparés d'un demi intervalle spectral libre, et ne peuvent donc certainement pas être résonants simultanément.

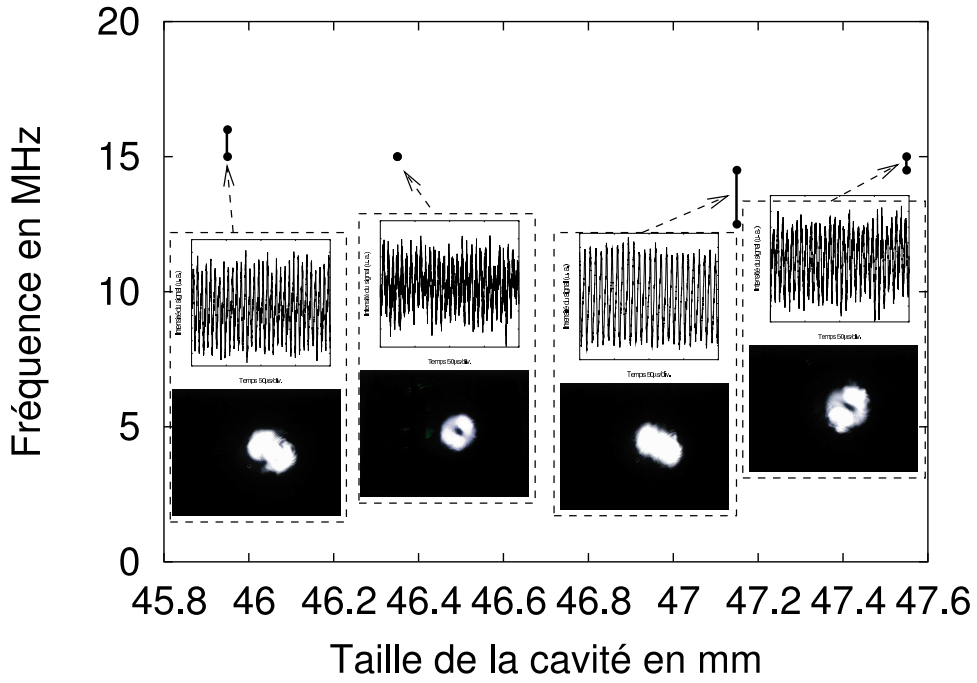

FIG. ***4.11*** – *Régimes d'oscillations de fréquences intermédiaires observés lors d'un balayage de la cavité de l'OPO sur un peu plus de 2 mm, par pas de 200 μm.*

Ces observations indiquent clairement que les régimes multimodes transverses observés dans notre OPO font intervenir des mécanismes différents de ce qu'on connaît dans les autres systèmes optiques, et qui très probablement font intervenir la dualité des faisceaux signal et complémentaire. Ces mécanismes pourraient être multiples si l'on croit les différents intervalles de fréquence relevés (entre 1 et 10 MHz, autour de 15 MHz, et au-delà de 100 MHz), et sont pour l'instant mal compris, même si certains indices laissent penser qu'une analyse complète doit s'effectuer dans le cadre du modèle non dégénéré et prendre en compte la différence entre les pas des peignes de modes du signal et du complémentaire.

Cependant, une analyse théorique d'un modèle bimode dégénéré de l'OPO triplement résonant, a d'ores et déjà pu montrer comment la nature de l'interaction paramétrique permet à l'OPO de s'affranchir de la condition de résonance simultanée des deux modes : dans un OPO, un régime bimode n'est finalement pas plus contraint qu'un régime monomode, excepté le fait que son seuil d'apparition sera en général plus haut. Cette analyse, entreprise pour comprendre les oscillations en rafales observées dans notre OPO, sera décrite dans la section suivante.

4.4.4 Oscillations en rafales

– A. Amon, M. Nizette, M. Lefranc and T. Erneux, "Bursting oscillations in optical parametric oscillators", *Phys. Rev. A* **68**, 023801 (2003) [appendice F, page 337].

Lorsqu'on s'intéresse à l'apparition d'oscillations périodiques, on est en général habitué aux formes de signal simples qui émergent d'une bifurcation de Hopf, approximativement

sinusoïdales au voisinage de la bifurcation, et enrichies en harmoniques par les non linéarités au fur et à mesure que l'on explore une région de plus en plus grande de l'espace des états.

Mais il également possible de rencontrer des signaux plus complexes, et notamment dans le cas où deux instabilités périodiques se combinent. C'est ainsi que les signaux des figures 4.7 et 4.9 sont dues à la coexistence des oscillations opto-thermiques lentes présentées dans la section 4.3 et des instabilités multimodes transverses que nous discutons actuellement. La différence des échelles de temps (les fréquences caractéristiques diffèrent de plusieurs ordres de grandeur) expliquent la phénoménologie de ces oscillations complexes : les oscillations rapides semblent être alternativement allumées et éteintes à la cadence des oscillations lentes.

Un grand nombre de travaux ont été consacrés à ces phénomènes dynamiques associant oscillations lentes et rapides, en raison non seulement de leur intérêt dynamique mais également de leur importance dans de nombreux phénomènes biologiques, principalement neuronaux mais également dans des réseaux biochimiques. Ils sont généralement connus sous le nom *d'oscillations en rafales* (en anglais, "*bursting oscillations*") et se caractérisent par une très grande diversité de mécanismes et par conséquent de types de signaux [42, 122, 124]. Leur analyse fait généralement appel à des méthodes de mathématiques appliquées assez sophistiquées.

Les oscillations en rafales observées dans l'OPO présentent également une grande richesse de comportements, comme on peut le constater dans la figure 4.12. Elles présentent également l'avantage d'une analyse mathématique relativement plus facile que dans la plupart des autres systèmes optiques. Cela est essentiellement dû au fait que la dynamique lente module un paramètre du système rapide (la longueur de cavité) et donc que la dynamique peut être visualisée dans un portrait de phase à deux variables, qui sont la longueur de cavité et l'intensité du signal émis, comme on peut le voir à la figure 4.13. Cette figure présente un type d'oscillations en rafales relativement rare dans la littérature, connu comme elliptique sous-critique de type Bautin [125], et qui correspond aux oscillations de la figure 4.12(c).

L'analyse théorique de ce travail montre comment construire des solutions approchées de ce régime, et nous intéresse tout particulièrement dans le cadre de l'étude des instabilités multimodes transverses, car il fait l'hypothèse que l'écart en fréquence des modes transverses en interaction est grand, comme c'est le cas du régime de la figure 4.12(c). Pour fixer les idées, rappelons que dans ces conditions expérimentales, la bande passante de la cavité est inférieure à 10 MHz. Comment expliquer alors que l'on observe des oscillations à plus de 100 MHz ? On comprend en effet vite que deux résonances ne peuvent être éloignées de beaucoup plus de 20 MHz s'il faut qu'elles aient un recouvrement appréciable. On remarquera au passage que la fréquence rapide observée n'est pas uniquement une fréquence de battement mais une vraie fréquence dynamique, car les oscillations ne faiblissent pas lorsqu'on focalise entièrement le faisceau sur le détecteur alors que le battement de deux modes transverses orthogonaux devrait disparaître dans ces conditions.

L'analyse perturbative d'un modèle bimode dégénéré, c'est-à-dire basé sur l'interaction de deux champs signal, fournit une réponse tout à fait éclairante à ce paradoxe apparent. En fait, les désaccords en fréquence σ_1 et σ_2 des deux modes signal influent par deux voies tout à fait indépendantes. La différence de fréquence $\Delta\sigma = |\sigma_2 - \sigma_1|$ fournit la fréquence des oscillations rapides, tandis que la valeur moyenne $\sigma_s = (\sigma_1 + \sigma_2)/2$ est celle qui contrôle l'apparition des oscillations rapides. Plus précisément, on peut, grâce à une procédure de moyennisation, reformuler le régime bimode transverse comme des oscillations rapides autour d'une valeur moyenne qui est donnée par la solution d'un problème monomode, dont

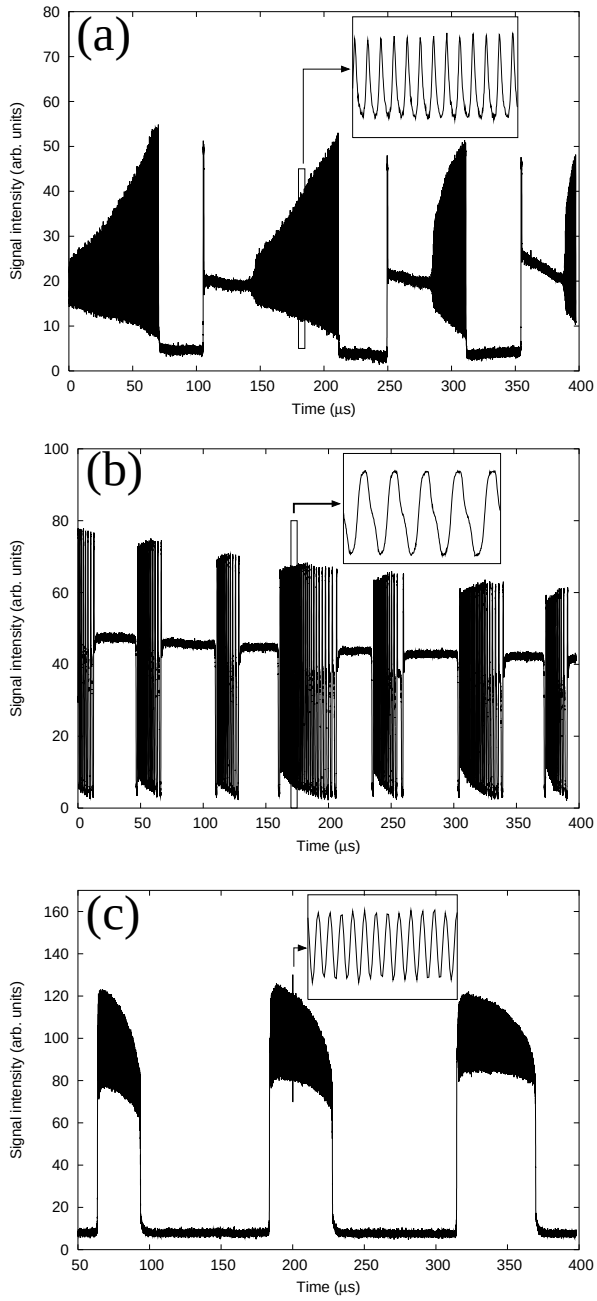

FIG. ***4.12 –*** *Différents types d'oscillations observés dans un oscillateur paramétrique optique. Les fréquences des oscillations lentes et rapides sont respectivement de (a) 8 kHz et 3 MHz ; (b) 15 kHZ et 1 MHz ; 8 kHZ et 130 MHz.*

le désaccord effectif est σ_s. Par conséquent, deux modes situés symétriquement par rapport à la fréquence d'oscillation du signal se comporteront comme s'ils étaient parfaitement à résonance, hormis l'oscillation rapide à la fréquence différence. On comprend alors qu'il soit plus facile d'observer des régimes multimodes que si les deux modes devaient être simultanément résonants.

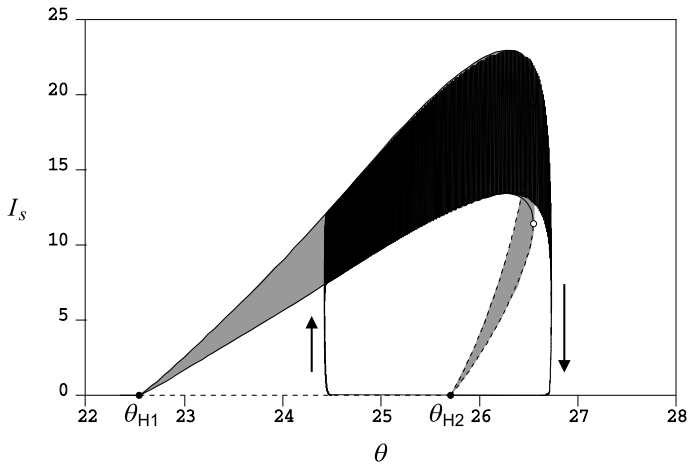

FIG. ***4.13 –*** *Portrait de phase longueur de cavité–intensité signal s'appuyant sur le diagramme de bifurcation d'un modèle bimode dégénéré en fonction de la longueur de cavité. Ce dernier comporte une bifurcation de Hopf sur-critique en θ_{H1}, une bifurcation de Hopf sous-critique en θ_{H1} et une bifurcation noeud-col à l'extrémité droite du diagramme. La figure montre un cycle qui correspond aux signaux de la figure 4.12(c). Au point gauche du cycle, le système saute sur la branche haute correspondant à la solution oscillante. Le cristal se réchauffe, et on se déplace vers la droite jusqu'à rencontrer le point tournant du cycle de bistabilité (bifurcation noeud-col), où on retombe sur la branche haute correspondant à l'OPO éteint.*

Ce résultat a des implications importantes sur le problème de la sélection du mode de fonctionnement de l'OPO, qui consiste à déterminer quel est le régime monomode qui sera choisi par l'OPO, en principe celui de désaccord le plus faible [126, 127]. Il faut en effet considérer non seulement les régimes monomodes « physiques », mais également les régimes monomodes fictifs associés à un couple de modes transverses dont les fréquences de résonance ne sont pas trop éloignées, et dont la fréquence de résonance effective sera située à mi-chemin de celles des deux modes transverses. On s'aperçoit rapidement que les modes fictifs peuvent être à puissance de pompe élevée plus nombreux que les modes réels, et donc que leur influence sur le fonctionnement de l'OPO ne peut être négligée dans certaines circonstances.

Un régime bimode sera donc sélectionné si le seuil de son régime monomode fictif est inférieur à celui de tous les autres régimes monomodes, physiques ou fictifs. L'expression de son seuil est simplement donné par l'expression classique monomode où la constante χ_{12} caractérisant l'interaction de deux modes remplace la constante χ (normalisée à 1 dans l'écriture habituelle) caractérisant l'interaction d'un mode avec lui-même lui-même :

$$E_{\mathrm{th}} = \frac{\sqrt{(1+\sigma_s^2)(1+\sigma_p^2)}}{\chi_{12}}$$

où σ_s est le désaccord moyen de la paire de modes et σ_p celui de la pompe.

De manière tout à fait remarquable, cette expression, bien qu'obtenue au premier ordre d'un calcul perturbatif, *est en fait valable à tout ordre* et généralise donc à des désaccords arbitraires les expressions obtenues par Schwob *et al.* [128] à désaccord nul. Si en toute rigueur, elle ne conditionne l'existence d'une solution bimode non nulle qu'au premier ordre

du calcul, il se trouve que les corrections aux ordres suivants sont nulles si la solution d'ordre 1 est elle-même nulle. L'expression du seuil donnée ci-dessus est donc exacte, et il est d'autant plus important de le souligner que le calcul direct est inextricable.

4.4.5 Chaos déterministe dans un OPO

– A. Amon and M. Lefranc, "Topological signature of deterministic chaos in short nonstationary signals from an optical parametric oscillator", *Phys. Rev. Lett.* **92**, 094101 (2004) [appendice F, page 167].

On a déjà décrit en détail dans la section 3.5.3 l'observation de régimes irréguliers, dont l'analyse par des méthodes topologiques a montré qu'il s'agissait du premier exemple connu de dynamique chaotique dans un oscillateur paramétrique optique. Nous ne répéterons donc pas cette description ici, excepté pour souligner que, selon toute vraisemblance, ces régimes chaotiques trouvent leur source dans les régimes multimodes transverses qui nous ont occupés tout au long de cette section. Outre le fait qu'ils apparaissent dans les mêmes conditions, il a été de plus montré que le modèle bimode dégénéré triplement résonant prédit l'existence de différents types de régimes chaotiques, dont on voit deux exemples à la figure 4.14.

Il n'existe donc toujours pas de mise en évidence expérimentale du régime chaotique monomode prédit par Lugiato *et al.* [32], mais cela n'est peut être surprenant dans la mesure où nous avons récemment souligné les difficultés liées à l'observation de la bifurcation de Hopf précédant la transition vers le chaos dans le même modèle (voir section 4.5).

Pour conclure cette section, nous présentons dans la figure 4.15 quelques exemples non publiés d'oscillations en rafales chaotiques, qui illustrent la complexité des dynamiques dont l'OPO est capable et montrent que l'observation de chaos décrite précédemment [36] n'était pas un fait isolé. L'exemple du bas est particulièrement remarquable, car les signaux sont doublement chaotiques ! On observe tout d'abord aux échelles de temps courtes que les oscillations rapides sont chaotiques (image de droite). Puis on constate qu'aux échelles de temps lentes, la succession des phases d'oscillations rapides est elle-même irrégulière (image de gauche), comme on le voit en suivant l'alternance des fronts de moyenne et grande amplitude. Il va sans dire que la caractérisation par les méthodes usuelles d'une dynamique chaotique présentant des échelles de temps aussi différentes représenterait un sérieux défi.

4.5 SAUTS DE MODE ET INSTABILITÉS DANS LES OPO

– A. Amon and M. Lefranc, "Mode hopping strongly affects observability of dynamical instability in optical parametric oscillators", soumis à Physical Review A [appendice F, page 325].

Cette dernière section sera consacrée à un bref résumé d'un travail terminé récemment, qui expose quelques réflexions sur la possibilité d'observer expérimentalement les oscillations périodiques associées à la bifurcation de Hopf prédite par le modèle monomode champ moyen de l'OPO triplement résonant, et plus généralement les instabilités survenant à désaccord en fréquence élevé dans les oscillateurs paramétriques optiques.

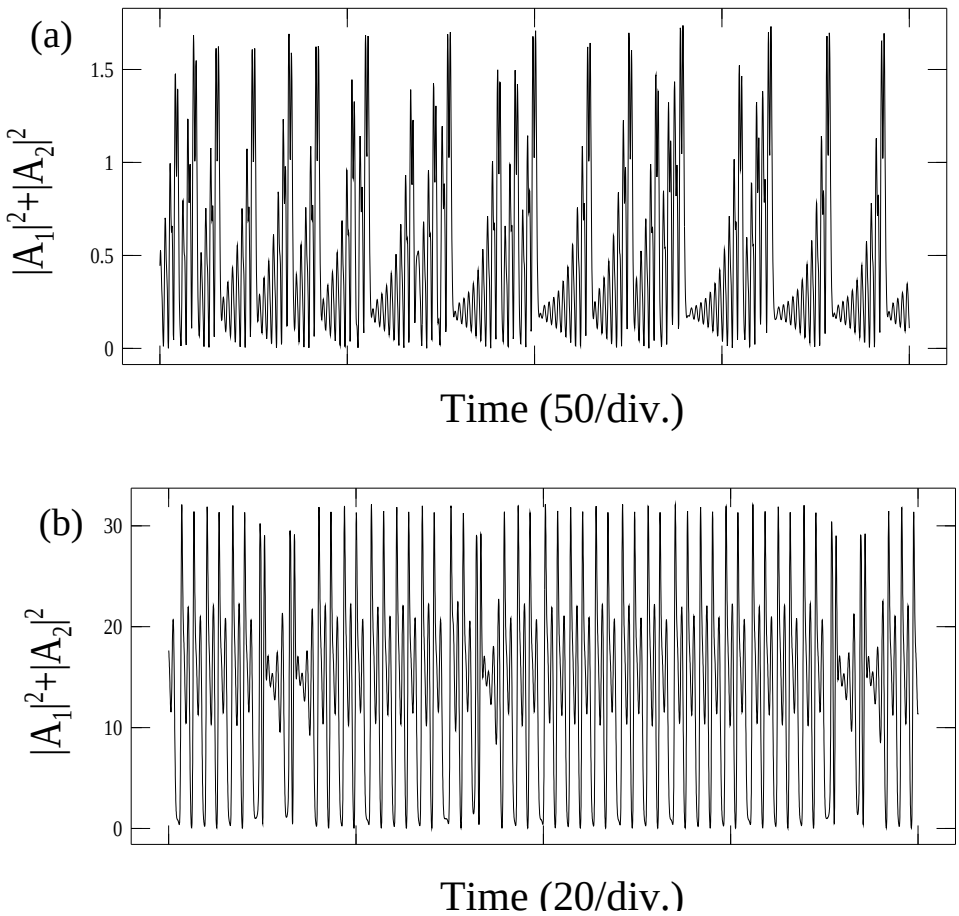

FIG. ***4.14*** – *Exemples de régimes chaotiques observés dans des simulations numériques d'un modèle d'OPO dégénéré bimode pour des jeux de paramètres différents [35]. On a représenté ici l'intensité total du signal en fonction du temps. On notera les similitudes entre le régime chaotique de la figure (a) et la dynamique observée dans l'attracteur de Lorenz.*

En supposant pour simplifier que l'on dispose d'une puissance de pompe infinie, ces oscillations apparaissent lorsque [32]

$$\Delta_p \Delta_s < -\left[1 + \frac{\gamma(1+\Delta_p^2)}{2}\right],$$

où Δ_s et Δ_p sont les désaccords en fréquence du signal et de la pompe, et γ le rapport des finesses de la cavité pour le signal et la pompe (γ est infini dans la limite où la pompe n'est plus résonante). On voit qu'à désaccord de pompe fixé, l'instabilité n'apparaît que pour des désaccords du signal suffisamment grands.

Or le désaccord du signal n'est en fait pas un paramètre fixe, mais s'ajuste par un phénomène dynamique. En supposant la largeur de la courbe d'accord de phase (qui est la courbe de gain de l'OPO) infinie, c'est le mode de désaccord le plus bas qui aura le seuil d'oscillation le plus bas, et qui sera donc sélectionné par l'OPO. Parmi le peigne de modes, il y en aura toujours un qui aura le désaccord le plus bas, pas toujours le même, et la question

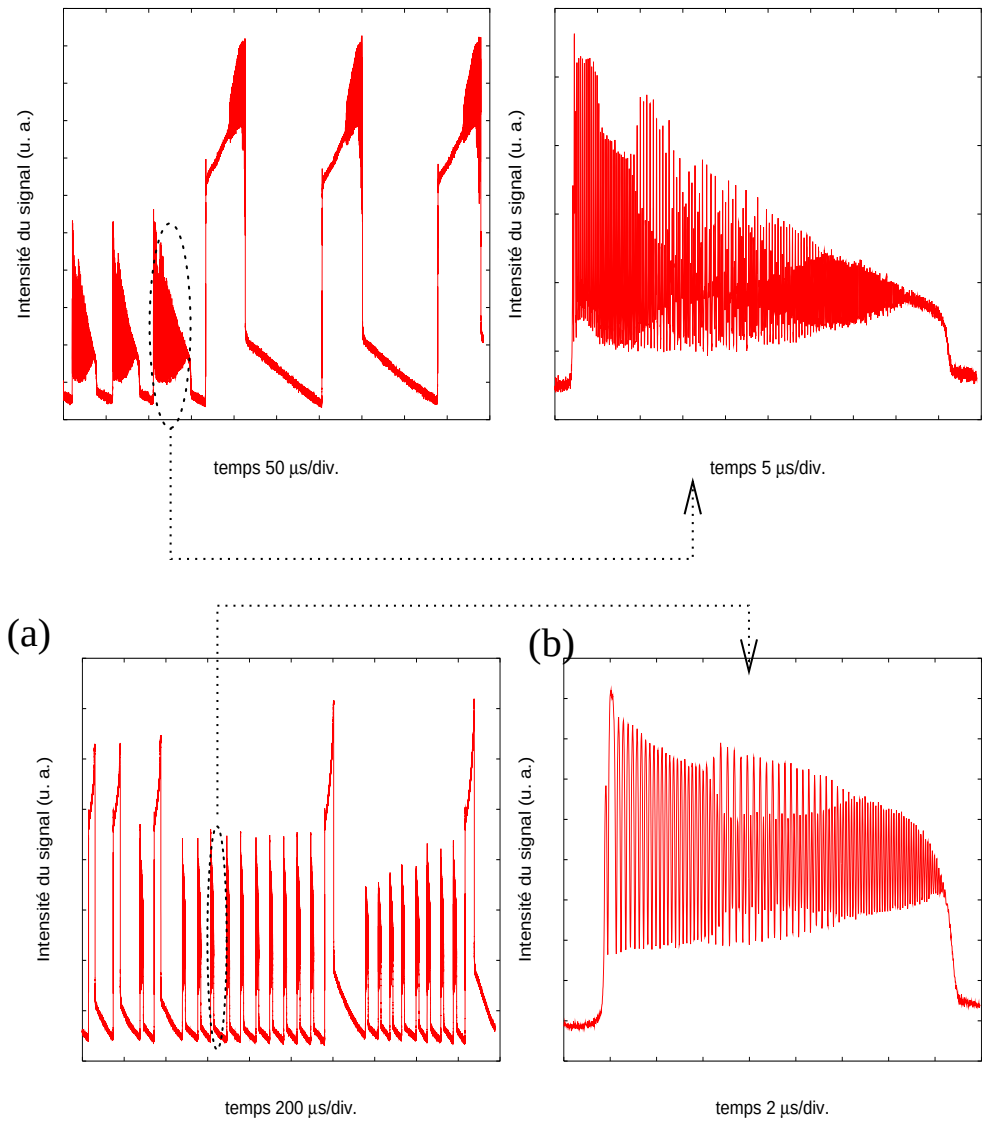

FIG. ***4.15 –*** *Exemples d'oscillations en rafales chaotiques observées expérimentalement dans un oscillateur paramétrique optique. Le chaos apparaît dans les phases d'oscillations rapides, mais on peut parfois également observer une dynamique irrégulière à l'échelle de temps lente, comme on le voit sur la figure du bas.*

est de déterminer dans quel intervalle ce désaccord minimum évolue lorsqu'on fait varier la longueur de cavité. S'il reste toujours inférieur à la valeur requise pour déclencher l'instabilité, c'est-à-dire si on saute à un autre mode avant de l'avoir atteinte, alors cette dernière ne sera pas observable.

En nous inspirant des travaux d'Eckardt *el al.* [126] et de Debuisschert *et al.* [127] relatifs à la sélection de modes dans les OPO, ainsi que de la théorie du modèle monomode [32], nous sommes parvenus à obtenir une condition simple permettant de déterminer si une configuration expérimentale donnée est susceptible de présenter la bifurcation de Hopf menant

un système monomode vers des oscillations périodiques :

$$\frac{\Delta_{\min}}{\mathcal{F}_s} = \sqrt{\frac{1}{\mathcal{F}_p}\left(\frac{1}{\mathcal{F}_p} + \frac{2}{\mathcal{F}_s}\right)} < 2\frac{|\delta n| l_c}{L_{\text{cav}}}$$

où $\mathcal{F}_s$ et $\mathcal{F}_s$ sont les finesses du signal et de la pompe, l_c et L_{cav} sont les longueurs du cristal et de la cavité, et $|\delta n|$ est la différence des indices vus par les champs signal et complémentaire. $\Delta_{\min}/\mathcal{F}_s$ représente le plus petit désaccord en fréquence auquel peut apparaître l'instabilité périodique[3]. Cette condition est obtenue à puissance de pompe infinie, mais nous avons pu montrer qu'elle est valable dans un cadre bien plus large car, de manière surprenante, la limitation sur les désaccords en fréquence est un facteur bien plus limitant que ne l'est la puissance de pompe.

La conclusion de notre étude est qu'il est extrêmement peu probable d'observer la bifurcation de Hopf dans les configurations usuelles, à moins de choisir des cavités extrêmement courtes (par exemple en configuration monolithique) et à finesse élevée pour la pompe, ce qui aurait malheureusement pour effet de rendre l'utilisation de l'OPO extrêmement difficile, et nous ferait probablement sortir du cadre de notre calcul, puisqu'il ne serait plus assuré que l'on puisse avoir simultanément pompe, signal et complémentaires résonants dans la cavité. Cela n'implique pas que la bifurcation de Hopf ne soit pas observable, mais on peut avancer que ne sera le cas que dans des configurations conçues à cet effet. Il reste maintenant à déterminer si la limitation que nous avons signalée dans le cas du modèle monomode ne s'applique pas également aux nombreuses autres instabilités spatio-temporelles qui ont été prédites dans les oscillateurs paramétriques optiques.

4.6 CONCLUSION

Relativement moins étudiée que celles des lasers, la dynamique des oscillateurs paramétriques optiques présente une grande richesse. Du fait des situations singulières liées à l'existence de cycles de bistabilité ou de points d'échange de stabilité, des instabilités opto-thermiques peuvent engendrer de fortes modulations de l'intensité émise à partir d'infimes variations de la longueur de cavité. On observe également des oscillations rapides, dont nous avons montré qu'elles étaient liées à des interactions de modes transverses. La physique de l'OPO fait que contrairement à ce qui se passe dans d'autres systèmes optiques, les modes en interaction n'ont pas à être simultanément résonants, ce qui rend ces régimes multimodes bien plus fréquents qu'on n'aurait pu le penser. Les instabilités lentes et rapides peuvent se combiner pour donner lieu à un phénomène dynamique très intéressant, les oscillations en rafale. Des dynamiques encore plus complexes, notamment du chaos déterministe et des oscillations en rafales chaotiques, ont été également observées.

3. En rapprochant l'expression que nous avons obtenue pour $\Delta_{\min}/\mathcal{F}_s$ de celle de la fréquence de Hopf que nous avions calculée précédemment [35], on note avec intérêt une relation directe entre les deux. En bref, le désaccord en fréquence non normalisé du signal ne peut être plus petit que la fréquence des oscillations apparaissant à la bifurcation, ce qui signifie que les bandes latérales de modulation ne peuvent se situer de part et d'autre de la résonance. Reste à comprendre l'origine physique de cette condition...

5

Dynamique non linéaire des réseaux de régulation génétique

5.1 INTRODUCTION

Les développements considérables que la génétique et la biologie moléculaire auront connu au cours du siècle dernier constituent sans nul doute une révolution scientifique majeure. Etape après étape, les mécanismes physiques par lesquels les organismes vivants transmettent leurs caractères héréditaires ont été explicités, et la machinerie moléculaire qui assure le fonctionnement de la cellule a été dévoilée. Il est ainsi maintenant établi qu'au sein de chaque cellule, l'information génétique est portée par la molécule d'acide desoxyribonucléique (ADN), qui constitue un mot long de milliards de lettres, écrit dans l'alphabet à quatre éléments formé par les quatre bases adénine, cytosine, guanine, thymine (Fig 5.1) [43].

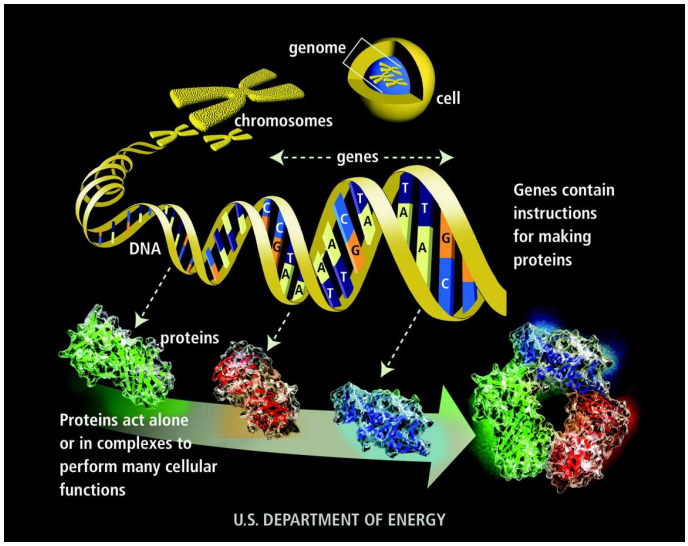

FIG. ***5.1 –*** *ADN, gènes et protéines*

Grâce à un effort expérimental de grande ampleur, le séquençage complet du génome est aujourd'hui terminé ou en voie d'achèvement pour de nombreux organismes vivants, dont l'Homme (Fig. 5.2(a)) [44]. Un des objectifs principaux de cette tâche était l'identification des gènes, sous-séquences qui contiennent l'information nécessaire à la production des protéines, acteurs essentiels de la machinerie biologique (Fig. 5.2(b)). Parmi ces dernières, certaines ont un rôle structurel, d'autres sont impliquées dans la signalisation cellulaire ou réponse immunitaire...

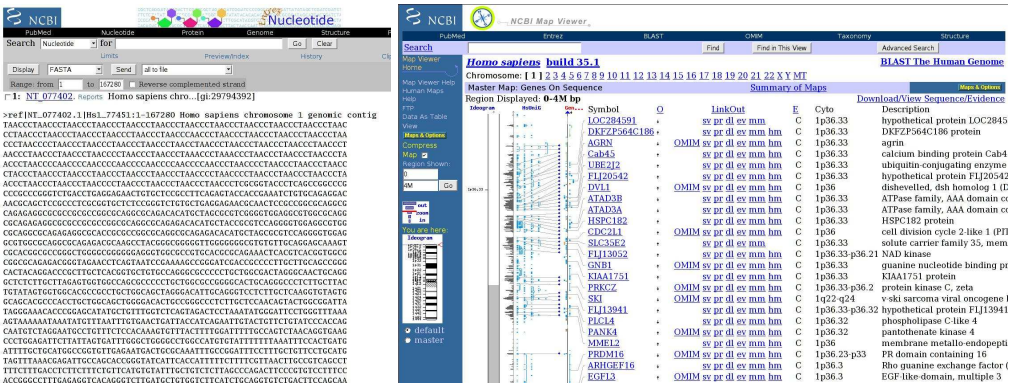

FIG. ***5.2*** – *(a) Début de la séquence génétique du chromosome 1 de l'Homme (b) annotation de cette séquence indiquant les gènes, régions de l'ADN qui codent pour les protéines.*

Selon ce qu'on appelle le « dogme central » de la biologie moléculaire, la synthèse d'une protéine s'effectue en deux étapes : la *transcription*, où l'information portée par le gène est transférée à une molécule d'*ARN messager*, puis la *traduction*, où la protéine est effectivement synthétisée sur les ribosomes à partir de l'ARN messager (Fig. 5.3) [43]. La mutation d'un gène, c'est-à-dire la modification accidentelle de la séquence codant pour la protéine, mène potentiellement à la formation d'une protéine modifiée qui ne peut remplir sa fonction, ce qui entraîne souvent une pathologie.

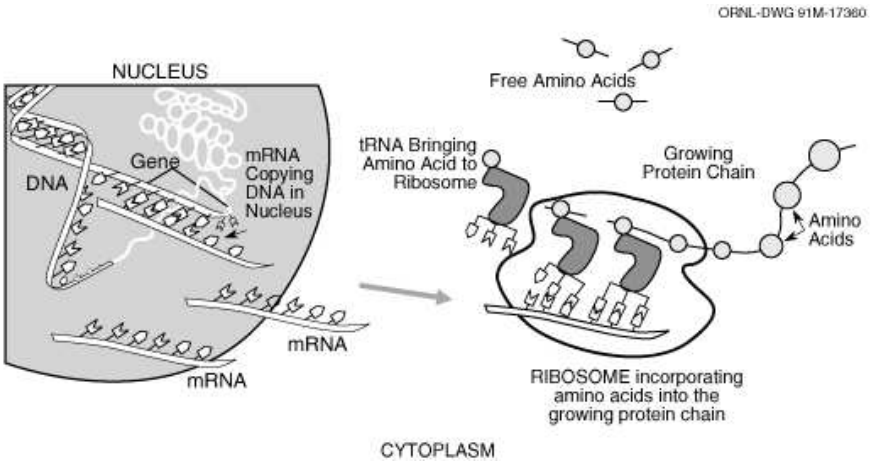

FIG. ***5.3*** – *Représentation schématique des processus de transcription et de traduction.*

Si l'information ainsi acquise est essentielle, elle est très insuffisante pour comprendre le détail des mécanismes biologiques. Ainsi, toutes les cellules d'un même organisme, qu'il s'agisse d'une neurone ou d'un lymphocyte, partagent la même information génétique. C'est que la molécule d'ADN n'est pas un objet statique. Au cours du temps, le niveau d'expression d'un gène (c'est-à-dire le taux de production de l'ARN messager) varie en fonction de nombreux facteurs, et notamment de de la concentration de certaines protéines, dites « régulatrices », qui, en se fixant sur la région en amont du gène, vont modifier la conformation de l'ADN et, soit activer, soit réprimer la transcription. Le niveau d'expression de chaque gène dépend directement de celui des gènes codant pour ses protéines régulatrices.

Gènes et protéines forment donc un gigantesque réseau d'acteurs moléculaires s'influençant réciproquement. La carte des interactions moléculaires, qui donne la structure de ce réseau, n'est donc certainement pas moins importante que la liste des nucléotides qui composent le génome (Fig. 5.4). D'ailleurs, c'est plutôt le grand nombre d'interactions protéine-protéine, et donc le grand nombre de comportements dynamiques possible, que le nombre de gènes qui distingue l'Homme d'espèces moins évoluées [43].

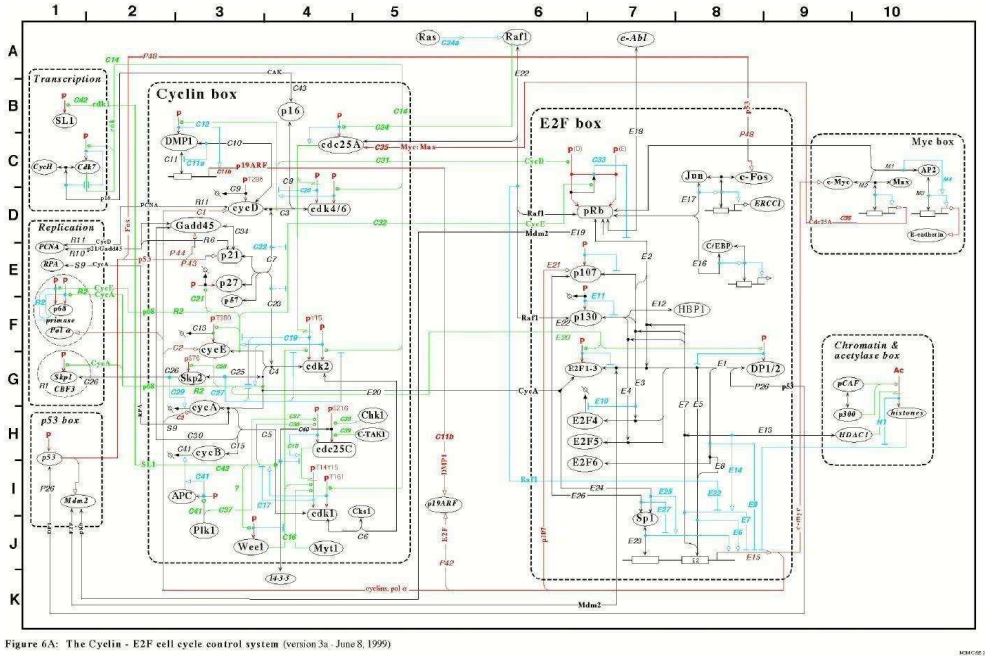

FIG. ***5.4 –*** *Réseau d'interactions moléculaires associé au contrôle du cycle cellulaire chez les mammifères (d'après [129]).*

Les cellules d'un organisme vivant sont donc le siège d'un très grand nombre de processus dynamiques qui leur permettent d'échanger des signaux entre différents modules fonctionnels, de s'adapter à des conditions environnementales ou physiologiques changeantes (lumière, température, sources d'énergie, etc...), en un mot de réguler leur fonctionnement. Le principe d'homéostasie, à savoir le maintien au voisinage d'une valeur d'équilibre des conditions générales de fonctionnement (par exemple la température interne), n'est que la conséquence la plus simple de ces processus de régulation.

Parmi les différentes approches pour modéliser un réseau de régulation génétique, une des plus naturelles est d'assimiler ce dernier à un ensemble de réactions chimiques (fixation d'un

facteur de transcription sur le promoteur d'un gène, production d'ARN messager par transcription, traduction de cet ARN en protéine, formation de complexes protéiques, processus de phoshorylation ou méthylation, etc...), dont la cinétique peut être décrite par un ensemble d'équations associées à chacun des processus élémentaires, comme pour beaucoup de processus biochimiques. Cela conduit tout naturellement à décrire le réseau de régulation par un système d'équations différentielles (ou éventuellement d'équations aux dérivées partielles lorsqu'il faut tenir compte d'effet spatiaux) [41, 130]. Si cette approche néglige un certain nombre d'effets, comme la stochasticité liée au faible nombre de molécules en présence, elle constitue un bon point de départ pour identifier les acteurs moléculaires essentiels d'une fonction biologique (voir par exemple [39, 41, 131]), et comprendre les mécanismes dynamiques à l'oeuvre.

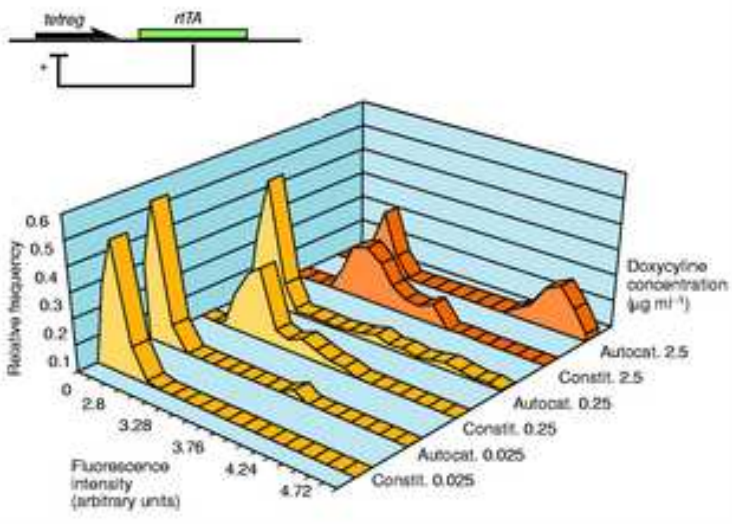

FIG. ***5.5*** – *Mise en évidence d'un phénomène de bistabilité dans le plus simple des réseaux génétiques, celui constitué par un gène qui est activé par la protéine qui produit (schéma en haut à gauche). Cette protéine est fusionnée à une protéine fluorescente afin de pouvoir suivre sa concentration en temps réel grâce à l'intensité de fluorescence. Les comportements du gène avec rétroaction (Autocat.) et sans rétroaction (Constit.), sont comparés pour différentes valeurs de la concentration en doxycyline, qui contrôle la force de la rétroaction. On voit qu'à forte concentration, la population de cellules équipées du gène autocatalytique se répartit en deux groupes correspondant aux deux points de fonctionnement du système bistable [40, 132].*

On se rend assez vite compte que les systèmes d'équations ainsi obtenus sont fortement non linéaires. Par exemple, les phénomènes de multistabilité sont extrêmement fréquents [39, 40, 133], comme l'illustre la figure 5.5. La coexistence de plusieurs états stables permet par exemple à l'organisme de choisir celui qui est le plus adapté à son environnement actuel. Elle permet également de comprendre les phénomènes de différentiation cellulaire, et le fait que des cellules ayant le même patrimoine génétique puissent avoir des fonctions extrêmement différentes [134]. La bistabilité peut enfin aider à garder la mémoire du chemin suivi par un système [39, 133] ou, grâce à la présence de séparatrices temporaires, de n'autoriser le passage à une étape ultérieure que lorsque toutes les conditions sont remplies [134]. Par ailleurs, les décisions de commutation entre différents états nécessite souvent l'amplification

de petits signaux et donc, au moins temporairement, une certaine instabilité. Il apparaît donc que l'équilibre subtil entre stabilité et instabilité qui organise une dynamique chaotique se retrouve donc, d'une autre manière, dans les systèmes dynamiques d'origine biologique.

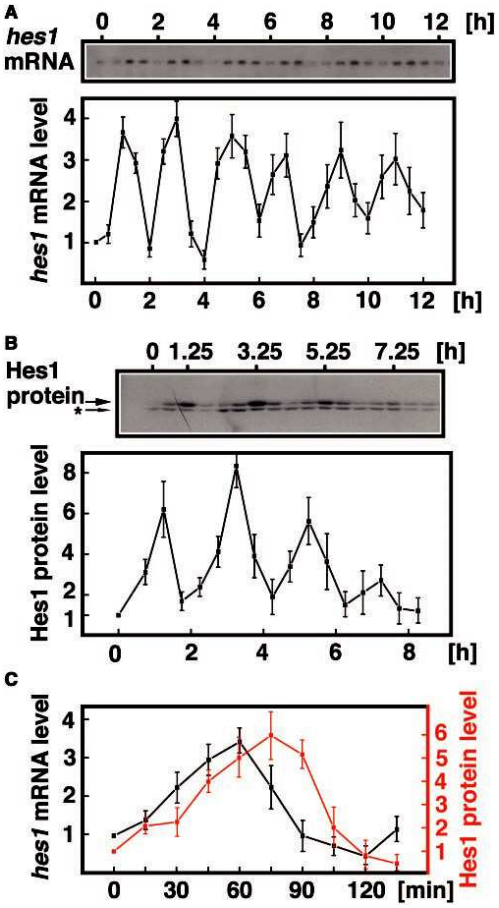

FIG. ***5.6*** – *Oscillations dans les concentrations de l'ARN messager et de la protéine du gène* hes1 *dans des cellules de souris après traitement au sérum [135].*

Un autre phénomène typiquement non linéaire est celui d'apparitions d'oscillations d'amplitudes et de fréquences bien définies, également appelés *cycles limites*, suite au passage par une bifurcation. Bien qu'il s'agisse d'un problème qui ait retenu depuis longtemps l'attention des théoriciens [136], notamment en raison de son importance dans les phénomènes circadiens que nous discuterons un peu plus loin, ce n'est que depuis peu que l'étude expérimentale des phénomènes oscillatoires dans les réseaux génétiques s'est réellement développée, en raison notamment du coût élevé du suivi en temps réel des niveaux d'expression génique. On retiendra ici deux exemples particulièrement importants. Le premier est l'observation d'oscillations dans les concentrations d'ARN et de protéine du gène *hes1* (Fig. 5.6), qui est au coeur de l'horloge moléculaire impliquée dans la segmentation des somites au cours de l'embryogénèse (liée notamment à la formation de la colonne vertébrale). Nous reviendrons sur cet exemple dans la section 5.3, car il constitue un exemple important de gène qui réprime sa propre expression. Il faut toutefois garder à l'esprit que le gène *hes1* est inséré dans un vaste réseau d'interactions : il n'est donc pas évident de décider si c'est la boucle de

rétroaction vers lui-même qui déclenche les oscillations ou si la présence du reste du réseau est essentielle.

C'est pourquoi le second exemple, le « repressilator » d'Elowitz et Leibler, est complémentaire, car il démontre qu'un tout petit réseau génétique est susceptible d'engendrer des oscillations à lui seul [137]. Dans cette expérience, un plasmide comportant trois gènes se réprimant circulairement (*a* réprime *b* qui réprime *c* qui réprime *a*) est introduit dans une bactérie. Grâce à un gène « rapporteur », activé par l'une des trois protéines du réseau circulaire et produisant une protéine fluorescente, on peut suivre les variations de concentration de cette protéine en mesurant l'intensité de fluorescence sur un domaine spatial correspondant à peu près à la taille d'une cellule. Comme on le voit sur la figure 5.7, on voit effectivement se développer des oscillations de grande amplitude, superposées à une augmentation graduelle de la fluorescence. On observe que la période des oscillations est environ trois plus longue que l'intervalle de temps entre deux divisions. De manière remarquable, on doit donc constater que l'état dynamique de l'oscillateur génétique est préservé lors d'une division cellulaire, la cellule mère et la cellule fille continuant leur route en phase.

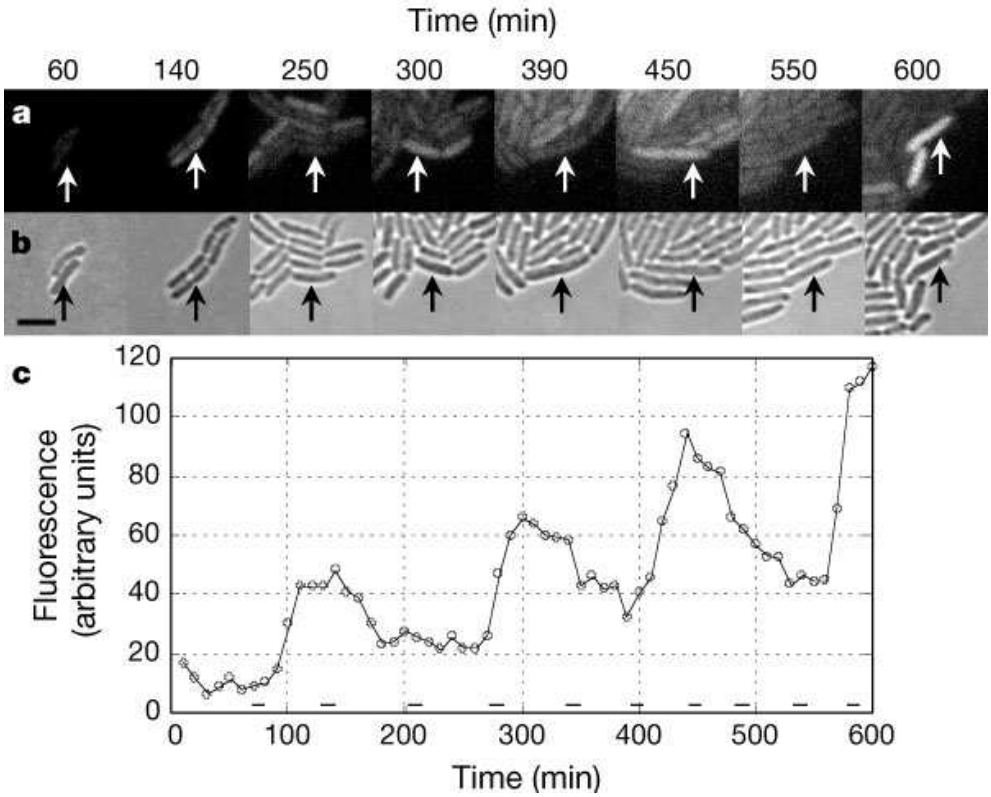

FIG. **5.7 –** *Oscillations observées lors de l'expérience du repressilator [137].*

5.2 PROJET DE RECHERCHE ET PROGRAMME DE TRAVAIL

5.2.1 Cadre général

Ces expériences, ainsi que par exemple les travaux pionniers d'Albert Goldbeter, de John Tyson et Bela Novak, et de quelques autres sur des modèles dynamiques simples de gènes et de protéines en interaction [39,41,131], nous ont convaincu que les outils classiques de la dynamique non linéaire sont tout à fait pertinents dans ce contexte. Ainsi, il est par exemple frappant de constater que l'ingrédient clé du modèle de Novak et Tyson du cycle cellulaire [134] – des oscillations de relaxation de type van der Pol autour d'un cycle de bistabilité – est précisément celui dont nous avons montré qu'il pouvait engendrer des instabilités périodiques dans un oscillateur paramétrique optique. De tels oscillateurs sont relativement fréquents dans les réseaux de régulation [39], et des chercheurs ont même avancé qu'ils pourraient être plus résistants au bruit induit par la nature stochastique des réactions chimiques qu'un oscillateur quelconque [138].

Alors que nous rentrons dans « l'ère post-génomique », le développement de méthodes pour décomposer la complexité de très grands réseaux de régulation impliquant potentiellement des centaines de gènes et de protéines représente un défi majeur, d'autant plus qu'il est maintenant possible de prendre à intervalles de temps réguliers des instantanés des niveaux d'expression de la totalité des gènes d'un organisme (techniques de « micropuces »). Nous espérons que notre expérience des systèmes non linéaires, ainsi que de la modélisation de systèmes expérimentaux, peut nous aider à contribuer utilement à cette tâche. Deux approches sont probablement à explorer simultanément : d'une part construire des modèles simplistes reproduisant grossièrement le comportement étudié, et les raffiner ensuite en incoporant d'autres acteurs ; d'autre part partir des données concernant le génome entier et essayer d'éliminer les degrés de liberté non pertinents en identifiant des groupes de gènes en interaction directe. Le pari est bien évidemment que les deux approches se rejoignent quelque part.

Parmi les problèmes auxquels nous désirons aussi nous attaquer, on peut également citer la conception et l'étude de réseaux de régulation minimaux (modules) ayant une fonction donnée, ou l'étude de l'influence du bruit due aux fluctuations à l'échelle moléculaire. L'étude systématique des bifurcations d'un modèle de mécanisme moléculaire nous semble également un problème important : elle peut en effet permettre de déterminer quelles sont les conditions expérimentales qui sont réellement indispensables à ce mécanisme, ainsi qu'inversement les plages dans lesquelles les paramètres expérimentaux peuvent varier sans conséquence notable.

Ce nouveau champ de recherches est d'autant plus stimulant que les progrès récents dans les techniques expérimentales, en rendant certaines données plus accessibles, resserrent la boucle de rétroaction entre théorie et expérience. En raison des coûts financiers et humains de certaines expériences, la modélisation et la simulation sont donc de plus en plus appelées à jouer un rôle croissant dans la préparation des expériences de biologie, en permettant de déterminer les conditions expérimentales qui apporteront le plus d'informations nouvelles par rapport à la modélisation existante, et en exploitant au mieux les expériences précédentes.

FIG. ***5.8 –*** *Image au microscope électronique d'Ostreococcus tauri. On distingue en haut à gauche le chloroplaste, siège de la photosynthèse, et le noyau en bas à droite. Le diamètre de la cellule est d'environ 1,5 μm.*

5.2.2 Étude des rythmes circadiens chez Ostreococcus tauri

Une fois défini un cadre général, il faut se donner un sujet et des objectifs précis. Nous avons donc commencé à monter un projet d'étude de l'interaction du rythme circadien avec le cycle de division cellulaire chez une algue verte unicellulaire, *Ostreococcus tauri* (Fig. 5.8). Outre l'équipe « Horloge circadienne et division cellulaire » de l'UMR 7628 (Modèles en biologie cellulaire et évolutive, observatoire océanologique de Banyuls sur mer), dirigée par François-Yves Bouget et notre équipe de dynamique non linéaire des réseaux génétiques, ce projet rassemble des informaticiens et modélisateurs de l'Université de Lille et de l'Institut de Biologie de Lille (UMR 8022 et UMR 8525).

Les rythmes circadiens se manifestent par des variations périodiques sur une durée de 24 heures de nombreuses grandeurs physiologiques, comme par exemple la température corporelle, les concentrations de certaines hormones ou encore le degré de vigilance (Fig. 5.9) [139]. Ces oscillations se justifient par un avantage adaptatif : grâce à elles, l'organisme est en mesure d'anticiper sur toute modification de l'environnement liée au cycle jour/nuit. Si leur existence est connue depuis l'antiquité, ce n'est que depuis 1729 que l'on sait qu'elles persistent en conditions d'éclairement constantes, grâce à l'expérience d'Ortous de Mairan, qui observa que les oscillations quotidiennes des feuilles de la sensitive (Mimosa pudica) continuaient dans l'obscurité pendant plusieurs jours. Cela démontra que les rythmes circadiens n'étaient pas une simple réponse à un forçage extérieur périodique, mais étaient reliées à une véritable horloge interne.

Il fallut ensuite attendre 1935 pour établir la nature génétique des oscillations circadiennes, lorsque Bünning démontra que la période des oscillations en conditions constantes était un caractère héréditaire. Le premier gène impliqué dans une horloge moléculaire, *per*, fut identifié en 1971 chez la Drosophile : une mutation de ce gène pouvait en effet soit modifier

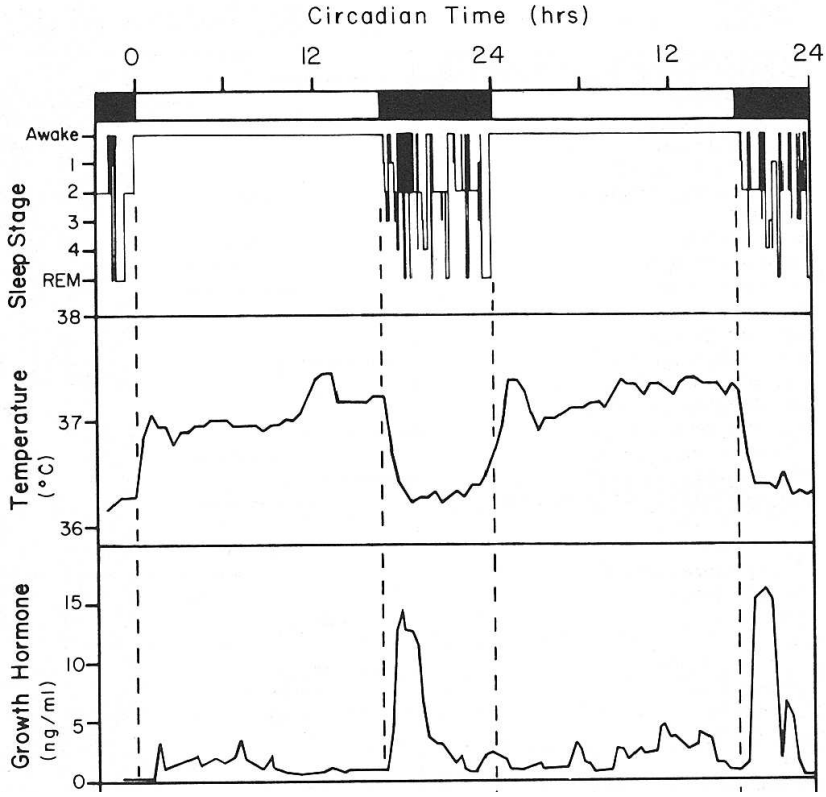

FIG. ***5.9*** *– Variations circadiennes du sommeil, de la température corporelle et de la concentration de l'hormone de croissance chez un sujet humain soumis à un rythme jour-nuit. Ces rythmes persistent en éclairement constant mais avec une période un peu plus longue. D'après [140].*

la période d'oscillation, soit provoquer une arrythmie. Chez de nombreuses espèces, on dispose maintenant d'un modèle moléculaire de ces rythmes, basés sur une horloge centrale faisant généralement intervenir une boucle de rétroaction négative, par exemple une protéine inhibant indirectement sa propre synthèse (Fig. 5.10) [41, 139].

L'algue retenue comme système modèle présente l'intérêt d'être un organisme eucaryote unicellulaire, ce qui simplifie l'étude par rapport aux modèles classiques d'étude de l'horloge circadienne (*Arabidopsis*, *Neurospora*, *Drosophila*, souris) qui sont multicellulaires. De plus, le génome d'*O. Tauri* est de taille réduite (11 Mbp pour 5000 gènes) et sa séquence est entièrement connue [141]; des micropuces à ADN couvrant l'ensemble du génome ont d'ailleurs été récemment développées et les premières données seront très prochainement disponibles.

Comme on l'a vu plus haut, les oscillations circadiennes influent sur de nombreux processus physiologiques [142], et en particulier sur le processus biologique fondamental qu'est le cycle de division cellulaire. Les voies de transduction assurant le lien entre entre l'horloge circadienne et le cycle de division cellulaire sont encore largement inconnues chez la plupart des espèces, même si il a été montré récemment qu'un des gènes impliqués dans ce cycle (Wee1) est la cible directe des composants de l'horloge circadienne au cours de la régénération du foie de souris [143]. Une des particularités d'*Ostreococcus tauri* est que dans des conditions d'éclairement normales, son cycle de division est directement asservi au

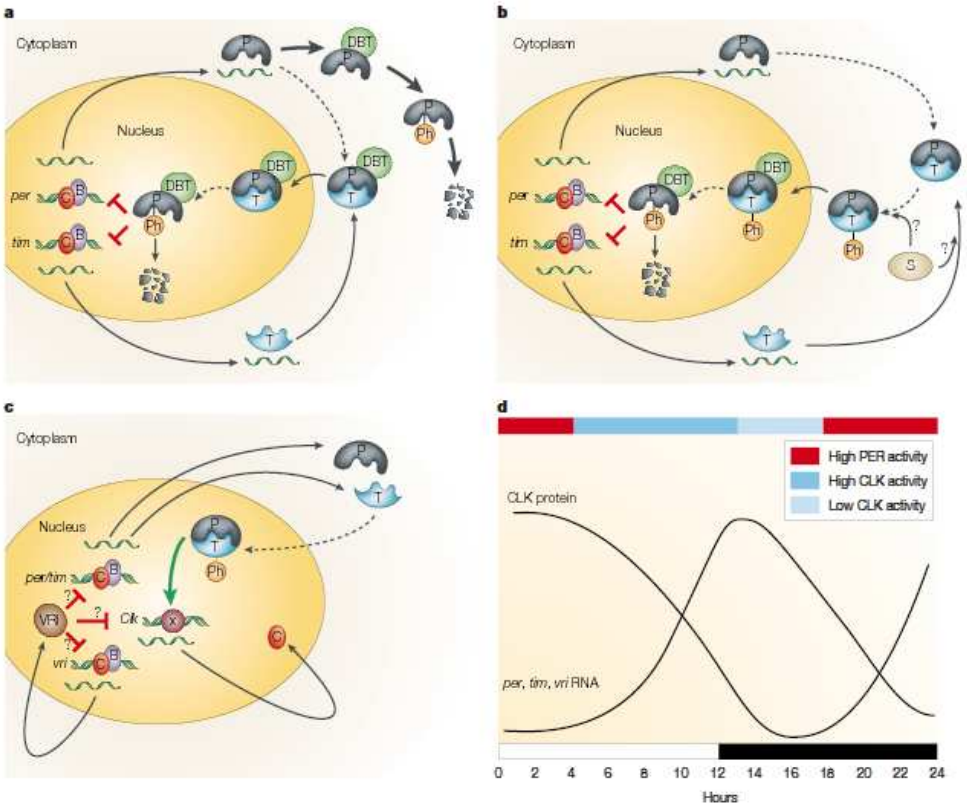

FIG. **5.10 –** *Différents modèles moléculaires de l'horloge circadienne de la Drosophile. Régulation transcriptionnelle, dimérisation, régulation de la dégradation, transport entre cytoplasme et noyau sont les mécanismes essentiels utilisés dans cette horloge pour parvenir au comportement dynamique désiré. D'après [46].*

rythme circadien, comme le montrent les courbes de croissance de population (Fig. 5.11), qui présentent une modulation de période 26 heures.

Le but de notre projet est tout d'abord de construire un modèle moléculaire de l'horloge circadienne chez *Ostreococcus tauri*, et ensuite de l'affiner pour tenir compte des interactions stabilisant l'horloge vis-à-vis des variations de température ou du métabolisme. Pour cela, nous disposons de mesures à intervalles de temps réguliers de niveaux d'expression de plusieurs gènes (Fig. 5.12). Très récemment, nos collègues sont parvenus à modifier ces algues pour fusionner les protéines des gènes clés à la luciférase (enzyme responsable de la bioluminescence chez les vers luisants). On observe donc un signal lumineux lié directement à la concentration de protéine produite, qu'on peut donc suivre en temps réel. Des données micropuce sur les niveaux d'expression des 7000 gènes d'*Ostreococcus* à intervalles de 3 heures vont également être très prochainement disponibles. Cela nous donnera un ensemble de données expérimentales très rarement disponibles dans l'étude de l'horloge circadienne d'un organisme. Nous nous attacherons ensuite à caractériser de manière détaillée les interactions entre rythme circadien, cycle de division cellulaire et métabolisme, et notamment d'identifier les acteurs moléculaires impliqués dans ces interactions.

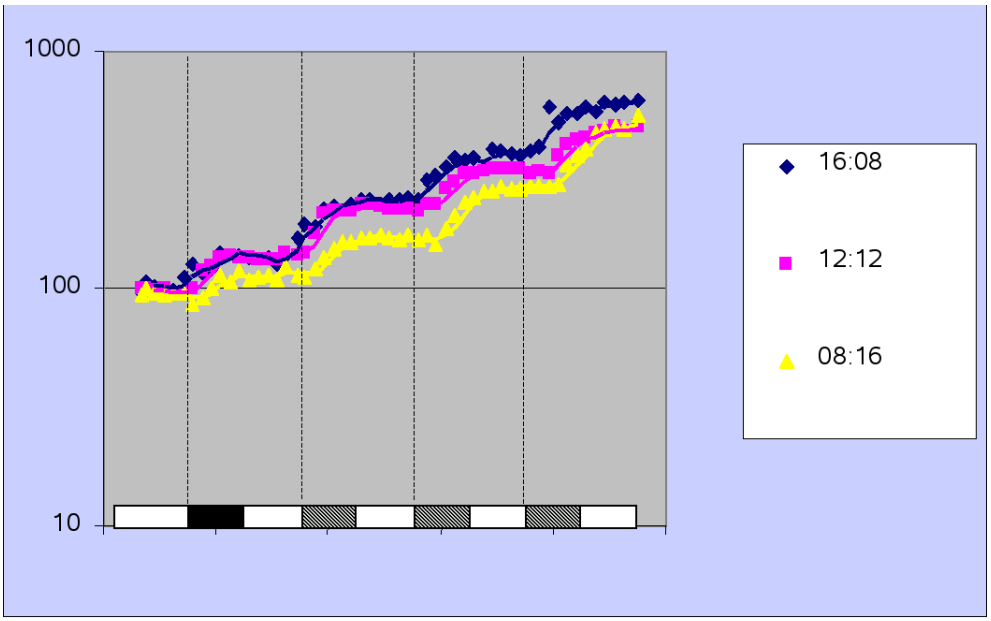

FIG. ***5.11 –*** *Variations de la population d'une colonie d'algues lors de trois expériences différentes. Les algues sont tout d'abord synchronisées par un cycle jour/nuit, puis placées en condition d'éclairement constant. On observe une alternance de plateaux et de phases de croissance, avec une période d'environ 26 heures. L'échelle en bas indique les intervalles de jour et de nuit à l'extérieur (période de 24 heures). On note qu'en régime forcé, la population recommence à croître à la tombée de la nuit. Données du groupe de F.-Y. Bouget.*

Une des difficultés auxquelles nous devons faire face est que la rythmicité de nombreux gènes laisse la place à de nombreux modèles d'horloge situés entre deux extrêmes : d'une part, celui d'une horloge centrale compacte, qui asservit les autres processus cellulaires (notamment le métabolisme de l'amidon ou le cycle de division cellulaire) ; d'autre part, une multiplicité de boucles de rétrocontrôle couplées, qui se stabilisent et se synchronisent mutuellement, assurant sans doute une grande robustesse à l'ensemble [139].

Il faudra donc probablement suivre simultanément deux approches complémentaires : d'une part la construction de modèles simples impliquant quelques acteurs moléculaires bien identifiés, qu'on étend ensuite au fur et à mesure que les comparaisons avec les expériences l'exigent; d'autre part l'analyse directe des séries temporelles décrivant l'évolution d'un grand nombre d'acteurs de la dynamique cellulaire (niveaux d'expression génique, concentration de certaines protéines, activités enzymatiques, etc.), où il s'agit d'identifier sans modèle à priori les flux d'information entre les différentes variables et d'analyser comment une perturbation externe se propage de proche en proche.

Nous espérons obtenir notre premier modèle d'ici la fin 2006, et nous terminerons donc ici cette description des phénomènes circadiens chez *Ostreococcus*. Mais cela ne clot pas ce chapitre consacré aux applications de la dynamique non linéaire à la biologie car, en travaillant sur un modèle simple de l'horloge, nous avons revisité le problème du gène regulé par sa propre protéine. Ce faisant, nous avons obtenu quelques résultats originaux, que nous décrivons dans la section suivante.

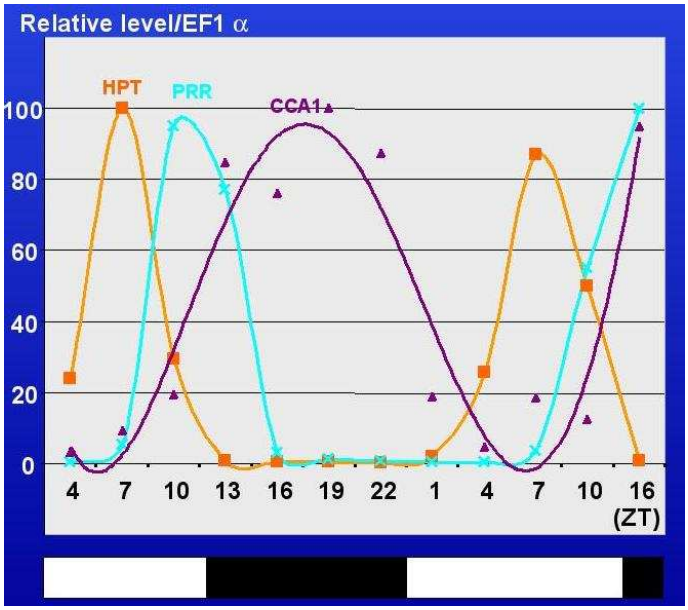

FIG. ***5.12 –*** *Variation sur 24 heures des niveaux d'expression de quelques gènes potentiellement impliqués dans l'horloge circadienne d'*Ostreococcus tauri*. Données du groupe de F.-Y. Bouget.*

5.3 OSCILLATIONS D'UN GÈNE AUTO-RÉGULÉ

– "The degradator : a single-gene oscillator", en cours de rédaction. Travail réalisé au sein d'un groupe de travail interdisciplinaire réunissant physiciens (P.-E. Morant, C. Vandermoere, Q. Thommen, S. Bielawski, M. L.), informaticiens (F. Lemaire, F. Boulier, S. Picault) et un automaticien-modélisateur moléculaire (B. Parent).

5.3.1 Introduction

Le réseau de régulation le plus simple que l'on puisse imaginer est sans nul doute constitué d'un gène unique dont l'expression est directement régulée par la protéine pour laquelle il code : ce circuit est en quelque sorte à la biologie systémique ce que l'atome d'hydrogène est à la physique atomique. Les réactions biochimiques intervenant dans ce modèle sont schématisées dans la figure 5.13, et incluent (1) la transcription du gène en ARN messager, à un taux plus ou moins élevé selon que la protéine est fixée ou non sur le promoteur, (2) la traduction de l'ARN messager en protéine, (3) la fixation de la protéine sur la zone régulatrice du gène, ainsi que les dégradations de l'ARN et de la protéine. Deux cas sont à distinguer : celui d'une rétroaction positive, c'est-à-dire qui active le gène, et celui d'une rétroaction négative, qui au contraire le réprime.

De manière générale, la rétroaction positive est plutôt susceptible d'engendrer des comportements bistables, car on peut imaginer qu'en l'absence de protéine, le gène reste peu actif, alors qu'à concentration en protéine élevée, il est fortement exprimé et aurait donc tendance à maintenir haut le niveau de protéines. Au contraire, la rétroaction négative serait intuitivement associée à des oscillations, où le gène cesse sa production lorsque la concentration en protéine est suffisamment élevée, et la reprend lorsque la dégradation a ramené cette concentration a un niveau plus bas. Mais, selon l'amplitude de la rétroaction et sa dépendance

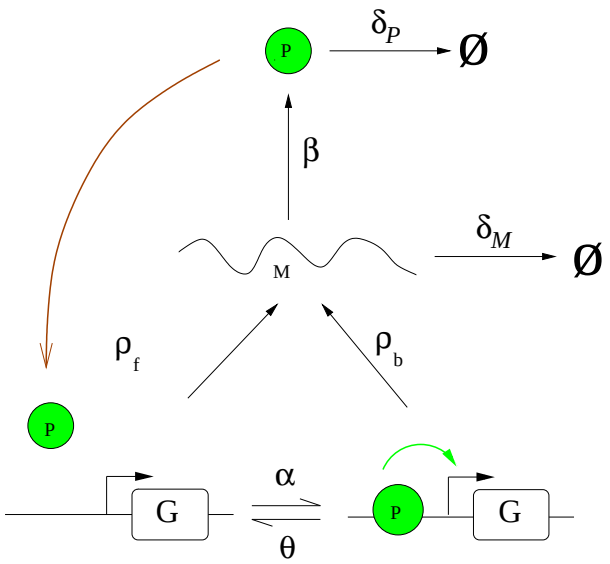

FIG. **5.13 –** *Schéma réactionnel du gène auto-regulé. Le gène est transcrit à un taux ρ_f (ρ_b) lorsqu'il est libre (lié). L'ARN est traduit en protéine à un taux β. Les constantes cinétiques contrôlant la fixation de la protéine sur l'ADN et son relargage sont α et θ. L'ARN et la protéine sont dégradées avec des taux δ_P et δ_M.*

par rapport aux variables d'état, il est, dans un cas comme dans l'autre, également possible qu'elle ait pour seul effet de stabiliser le gène sur un régime stationnaire unique, et c'est l'analyse mathématique qui nous permet de trancher en faveur de l'une ou l'autre possiblité. Dans ce qui suit, nous ne nous intéresserons qu'au problème de l'apparition d'oscillations, et nous ne considérerons donc que des rétroactions négatives.

Le problème est relativement simple et il n'est donc pas surprenant qu'il ait été abordé il y ait déjà longtemps, d'abord par Goodwin en 1965 [144], puis par Griffith en 1968 [136, 145], qui corrigea certaines erreurs du travail de Goodwin et fit une analyse mathématique détaillée du problème. Goodwin comme Griffith supposent que l'interaction entre ADN et protéine est gouvernée par des processus beaucoup plus rapides que les étapes de transcription, de traduction et de dégradation, et donc que l'état d'activation moyen du gène n'est pas une véritable variable dynamique, mais une fonction instantanée de la concentration en protéine, censée évoluer à des échelles de temps plus lentes. Cette hypothèse, dont nous testerons la validité plus loin, a été reprise par la quasi-totalité des travaux théoriques qui ont suivi, et ce jusqu'à aujourd'hui. Dans ces conditions, on décrit le schéma réactionnel de la figure 5.13 par les équations différentielles suivantes :

$$\dot{P} = \beta_0 M - \delta_P F(P) \tag{5.1a}$$

$$\dot{M} = \frac{\lambda_0}{1 + (P/P_0)^n} - \delta_M H(M) \tag{5.1b}$$

où $F(P)$ et $H(M)$ sont deux fonctions de dégradation qu'on suppose monotones, et de dérivée 1 en 0. Dans le cas d'une simple dégradation linéaire, on a $F(P) = P$ et $H(M) = M$, mais on peut aussi considérer le cas où la dégradation est catalysée par une protéase et où il faut utiliser une cinétique de type Michaelis-Menten, avec par exemple $F(P) = \kappa P/(\kappa + P)$.

Cette dernière forme exprime le fait que la dégradation atteint un plateau lorsque l'enzyme est saturée ($P \gg \kappa$). Dans (5.1a), on a supposé que l'élément régulateur pouvait être une protéine isolée, mais également un polymère comportant n copies de la protéine.

Il est facile de montrer que si F et H sont deux fonctions monotones, aucune oscillation ne peut apparaître dans le système (5.1) et donc que le gène auto-régulé est à priori inconditionnellement stable.[1] Goodwin et Griffith considèrent aussi le schéma où le répresseur n'est pas directement la protéine produite, mais une autre protéine dont la synthèse est catalysée par la protéine précédente, et montrent que, contrairement à (5.1), le système de trois équations différentielles qui lui est associé est susceptible de présenter des oscillations.

Si le gène auto-régulé ne peut présenter d'oscillations, comment expliquer alors les oscillations du niveau d'expression du gène *hes1* dans l'expérience de la figure 5.6? On peut évidemment suspecter l'influence d'autres acteurs mais, en 2003, plusieurs groupes ont indépendamment montré comment modifier de manière simple le système (5.1) afin de le faire osciller [146–148]. Ils partent du constat que toutes les étapes du schéma de la figure 5.13 ne peuvent être simultanées : une protéine ne peut influer sur l'activité du gène immédiatement après avoir été synthétisée sur le ribosome, et ce tout particulièrement chez les eucaryotes où une protéine doit pour cela repasser du cytoplasme dans le noyau. Jensen, Sneppen et Tiana tout d'abord, puis Lewis ainsi que Monk ont proposé indépendamment de rajouter un terme de délai dans les équations (5.1), c'est-à-dire de les réécrire de la manière suivante (en supposant ici les dégradations linéaires) :

$$\dot{P} = \beta_0 M(t-\tau_M) - \delta_P P(t) \tag{5.2a}$$

$$\dot{M} = \frac{\lambda_0}{1+[P(t-\tau_P)/P_0]^n} - \delta_M M(t) \tag{5.2b}$$

où τ_M et τ_P représentent respectivement le temps qu'il faut à l'ARN pour être transcrit, puis pour migrer du noyau dans le cytoplasme et à la protéine pour faire le chemin inverse. On observe effectivement que le système (5.2) peut présenter des oscillations dont la période se situe approximativement entre 2τ et 4τ, où τ est le délai total $\tau = \tau_P + \tau_M$. Comme la présence de délais à une étape ou une autre de la boucle de rétroaction est plausible, on serait enclin à penser que le modèle (5.2) fournit une explication naturelle des oscillations dans un gène auto-régulé.

Mais cette approche n'est à notre avis pas sans inconvénients. Tout d'abord, on sait qu'il est relativement facile d'engendrer des oscillations, ou même des régimes plus complexes, à l'aide d'une équation à délai, comme le montre l'exemple classique de l'équation de Mackey-Glass [149]. Réussir à reproduire des oscillations avec des équations à délai n'implique donc pas que la modélisation soit correcte. De même, les délais apparaissant dans (5.2) peuvent résulter de plusieurs effets cumulés : le modèle ne peut donc servir à identifier l'origine exacte de l'instabilité. Par ailleurs, le modèle (5.2) souffre de quelques limitations : à condition que les demi-vies de l'ARN et de la protéine soient petites devant le délai, les oscillations n'apparaissent que si $n \geq 2$, ou même $n > 4$ dans le cas contraire, plus réaliste. De plus, on sait qu'un système biologique réel présente de nombreuses régulations, l'interaction entre

1. Il suffit de noter que la trace de la matrice jacobienne est toujours strictement négative, et donc qu'il est impossible d'avoir une paire de valeurs propres $\pm i\omega$ comme c'est le cas à une bifurcation de Hopf.

deux acteurs moléculaires dépendant fréquemment d'un troisième. Or comment réguler un délai temporel τ sans introduire de formidables difficultés mathématiques?

Enfin, des modèles sans délai explicite de gènes auto-régulés oscillants existent dans la littérature, un fait parfois oublié, et ne requièrent que peu d'ingrédients supplémentaires en plus de ceux indiqués dans le schéma 5.13. Ces modèles, élaborés par Albert Goldbeter et son équipe, trouvent leur origine dans la modélisation des rythmes circadiens. Ainsi, un modèle ancien de l'horloge de la Drosophile basé sur le gène *per* oscille si on autorise la protéine PER à avoir plusieurs états de phosphorylation [150], de même qu'un modèle de l'horloge de *Neurospora* si on rajoute une équation linéaire décrivant le transport de la protéine entre cytoplasme et noyau [151].

C'est pourquoi, estimant qu'il était étonnant de considérer la réponse du gène à la concentration en protéine comme instantanée, pour ensuite s'apercevoir de la nécessité d'introduire un délai, nous avons voulu déterminer si l'approximation du « gène esclave » était toujours justifiée et si une dynamique propre du gène ne pouvait jouer un rôle dans le déclenchement d'instabilités. Nous présentons nos premiers résultats relatifs à ce problème dans la section suivante.

5.3.2 Le taux de transcription comme une variable dynamique

La transcription, par laquelle l'information portée par la région codante d'un gène est recopiée dans une molécule d'ARN, est un processus complexe comportant plusieurs étapes : l'assemblage d'un complexe protéique autour de l'ARN polymerase (facteurs sigma, etc.), fixation du complexe au promoteur du gène, ouverture de la double hélice, initiation abortive, élongation,... Il serait certainement intéressant de tenir compte de cette cascade dans la modélisation dynamique de réseaux génétiques, et des travaux récents vont dans ce sens [152]. Beaucoup plus modestement, nous nous contenterons ici, comme François et Hakim [153], de tenir compte d'une possible dynamique du taux de transcription : on suppose pour cela que le taux de transcription est une variable dynamique, que pour simplifier nous prendrons ici gouvernée par l'équation cinétique associée à la réaction inversible d'association/dissociation entre la protéine et l'ADN :

$$G + P \underset{\theta_0}{\overset{\alpha_0}{\rightleftharpoons}} G : P \tag{5.3}$$

où G représente le gène non lié, P la protéine libre et $G : P$ la protéine liée au gène. En tenant compte du fait que le nombre total de gènes, liés ou non, reste constant et égal à 1, l'équation cinétique s'écrit ainsi :

$$\dot{G} = \theta_0(1 - G) - \alpha_0 GP \tag{5.4}$$

où G et P représentent les nombres de gènes et de protéines libres. Dans le cas où c'est un complexe formé de n protéines qui se fixe, il convient de remplacer P par kP^n dans l'équation (5.4), du moins si on suppose que la polymérisation est beaucoup plus rapide que les autres réactions.

On se rend tout de suite compte d'une difficulté conceptuelle à décrire la dynamique de (5.3) par l'équation différentielle (5.4) : la variable G y est une variable qui varie continûment entre 0 et 1, alors que le gène étant lié ou ne l'étant pas, le nombre de gènes libres devrait être, soit 1, soit 0, mais rien d'autre. Cela est bien évidemment dû au fait que l'on est dans

une situation où le caractère « quantique » du nombre de molécules ne peut être ignoré, et où une description en termes d'équations différentielles n'est pas valide : il faudrait en fait passer à une description stochastique où G serait une variable aléatoire commutant de 0 à 1 et de 1 à 0 selon des lois de probabilité déterminées par la concentration en protéine.

Il est cependant possible d'interpréter comme l'équation d'évolution d'une valeur moyenne dans le temps, G représentant alors la fraction de temps passée par le gène dans l'état libre. Cela suppose toutefois que les réactions d'association/dissociation se déroulent à des échelles de temps beaucoup plus rapides que les autres réactions dans lesquelles le gène est impliqué. Comment procéder quand ce n'est pas le cas ? Nous adopterons dans la suite le point de vue pragmatique que l'équation (5.4) décrit de manière phénoménologique la relaxation exponentielle du coefficient de transcription G vers une valeur d'équilibre G_0 donnée par

$$G_0 = \frac{1}{1 + P/P_c}, \quad P_c = \frac{\theta_0}{\alpha_0} \tag{5.5}$$

et qui est l'expression habituellement utilisée pour l'activité du gène, comme on le voit dans les équations (5.1). Même dans le cas où la dynamique de relaxation est complexe, (5.4) pourra être une approximation intéressante dans le cas où les équations linéarisées autour de l'équilibre présentent une valeur propre beaucoup plus petite que les autres. Cela nous permettra d'explorer de manière simple les conséquences dynamiques des situations où la dynamique d'activation du gène n'est pas extrêmement rapide comparée aux autres processus.

5.3.3 Un oscillateur à un gène : le « degradator »

5.3.3.1 Le modèle Nous pouvons maintenant traduire en équations le schéma réactionnel de la figure 5.13, en combinant l'équation (5.4) avec les équations (5.1) discutées précédemment, ce qui nous mène au système suivant :

$$\dot{G} = \theta_0(1 - G) - \alpha_0 G P^n \tag{5.6a}$$

$$\dot{P} = n\left[\theta_0(1 - G) - \alpha_0 G P^n\right] + \beta_0 M - \delta_P F(P) \tag{5.6b}$$

$$\dot{M} = \mu_0 + \lambda_0 G - \delta_M H(M) \tag{5.6c}$$

où l'on a tenu compte de la possibilité de la régulation par un polymère de taille n. Dans la suite, nous supposerons le cas du monomère $n = 1$ pour les calculs analytiques, mais nous considérerons des valeurs plus élevées dans les simulations numériques. Le modèle (5.6) est plus général que celui donné par (5.1), car ce dernier peut être obtenu à partir de (5.6) en faisant tendre θ_0 et α_0 vers l'infini.

On voit que dans l'équation (5.6c), le taux de transcription varie continûment entre μ_0 et $\mu_0 + \lambda_0$ quand le taux d'activation G varie entre 0 et 1. Comme précédemment, nous supposons que les fonctions de dégradation $F(P)$ et $H(M)$ sont monotones, et sont nulles en 0, avec une dérivée de 1.

En utilisant les changements d'échelle suivants sur le temps et les variables dynamiques

$$t = \frac{\tau}{\delta_M}, \quad G = g, \quad P = pP_c,\ P_c = \left(\frac{\theta_0}{\alpha_0}\right)^{\frac{1}{n}}, \quad M = mM_c,\ M_c = \frac{\delta_P \theta_0}{\beta_0 \alpha_0}, \tag{5.7}$$

on peut réécrire les équations (5.6) sous la forme plus simple

$$g' = \theta\,[1 - g(1+p^n)] \tag{5.8a}$$
$$p' = n\alpha\,[1 - g(1+p^n)] + \delta[m - f(p)] \tag{5.8b}$$
$$m' = \mu + \lambda g - h(m) \tag{5.8c}$$

où $x' = dx/d\tau$ et où les paramètres et fonctions de dégradation normalisés sont donnés par

$$\theta = \frac{\theta_0}{\delta_M},\quad \alpha = \frac{\theta_0}{P_c\delta_M},\quad \delta = \frac{\delta_P}{\delta_M},\quad \lambda = \frac{M_c}{\delta_M}\lambda_0,\quad \mu = \frac{M_c}{\delta_M}\mu_0, \tag{5.9a}$$
$$f(p) = \frac{1}{P_c}F(P),\quad h(m) = \frac{1}{M_c}H(M). \tag{5.9b}$$

Le caractère monotone des fonctions de dégradation $f(p)$ and $h(m)$ implique que le modèle (5.8) a un seul état stationnaire (g_0,p_0,m_0), satisfaisant aux équations de point fixe :

$$g_0 = \frac{1}{1+p_0}, m_0 = f(p_0), g_0 = \frac{h(m_0)-\mu}{\lambda} \tag{5.10}$$

On peut noter que cet état stationnaire ne dépend que des paramètres λ et μ (à fonctions de dégradation f et h fixées), tandis que les paramètres θ, α, δ contrôlent des échelles de temps. Le cas d'une répression parfaite, c'est-à-dire d'un taux de transcription nul pour le gène lié, correspond à $\mu = 0$.

5.3.3.2 L'analyse de stabilité Nous nous intéressons maintenant à chercher si le modèle (5.8) peut osciller pour certains jeux de paramètres. Pour cela, nous limiterons à déterminer s'il présente une bifurcation de Hopf, c'est à dire si, étant données les équations originales $\dot{x} = F(x)$, les équations linéarisées $\dot{\delta x} = (\partial F/\partial x)\,\delta x = J\delta x$ décrivant l'évolution dans le temps d'une perturbation $\delta x = x - x_0$ autour du point fixe x_0 sont telles que le Jacobien J possède une paire de valeurs propres purement imaginaires $\pm i\omega$. On montre alors qu'en ce point de l'espace des paramètres, le régime stationnaire bifurque vers une solution périodique de période $2\pi/\omega$. Ce n'est pas la seule bifurcation donnant naissance à une orbite périodique, mais c'est la plus commune, surtout lorsque le système ne peut être réduit à un système dans le plan.

Pour cela, nous utiliserons le critère de Routh-Hürwitz, qui permet de détecter la présence d'une telle paire de valeurs propres sans avoir à les calculer explicitement. Plus précisément, on montre que le polynôme caractéristique

$$Q(\sigma) = \det(J - \sigma\mathrm{Id}) = \sigma^3 + a_1\sigma^2 + a_2\sigma + a_3$$

d'une matrice 3×3 possède des racines à parties réelles toutes négatives si les trois conditions suivantes sont satisfaites :

$$a_2 > 0,\quad a_3 > 0,\quad a_1a_2 - a_3 > 0. \tag{5.11}$$

Le passages par zéro des deux dernières détectent respectivement l'annulation d'une valeur propre réelle isolée et l'annulation de la partie réelle d'une paire de valeurs propres imaginaires conjuguées. C'est donc la deuxième qui nous fournit une signature d'une bifurcation de Hopf.

On trouve facilement que dans le cas $n = 1$, auquel nous nous limitons ici, le Jacobien correspondant aux équations (5.8) est

$$J = \begin{bmatrix} \theta\,(-1-p_0) & -\theta\, g_0 & 0 \\ \alpha\,(-1-p_0) & -\alpha\, g_0 - \delta\, s & \delta \\ \lambda & 0 & -u \end{bmatrix} \tag{5.12}$$

où s et u sont les dérivées des fonctions de dégradation au point fixe :

$$s = \left.\frac{df(p)}{dp}\right|_{p=p_0}, u = \left.\frac{dh(m)}{dm}\right|_{m=m_0}.$$

Il est à noter que si les fonctions de dégradation sont concaves, ce qui est le cas pour une dégradation de Michaelis-Menten, la condition de normalisation qui impose une dérivée unité en 0, ainsi que la condition de monotonicité font que $u,s \in [0,1]$. Le déterminant du Jacobien (5.12) est

$$\det J = -\theta\,\delta\,(us + up_0 s + \lambda\, g_0) \tag{5.13}$$

On voit qu'il ne passe jamais par zéro et donc que le système ne présente pas de bifurcation tangente. On note aussi l'asymétrie entre θ et α, et on pressent que le temps caractéristique de dissociation sera une grandeur plus importante que celui d'association.

Le polynôme caractéristique est

$$\begin{aligned} Q(\sigma) \;=\; & \sigma^3 + (\alpha\, g_0 + \theta + \theta\, p_0 + \delta\, s + u)\,\sigma^2 \\ & + (\alpha\, g_0 u + \theta\,\delta\, s + \theta\, u + \theta\, p_0 \delta\, s + u\delta\, s + \theta\, p_0 u)\,\sigma + \theta\, up_0 \delta\, s \\ & + \lambda\,\theta\, g_0 \delta + \theta\, u\delta\, s \end{aligned} \tag{5.14}$$

et la quantité passant par zéro à la bifurcation de Hopf est

$$\begin{aligned} \mathcal{H} \;=\; & \left(\delta^2\theta + \delta^2 u + \delta^2\theta\, p_0\right) s^2 \\ & + \left[u^2\delta + (2\,\theta\, p_0\delta + 2\,\theta\,\delta + 2\,\alpha\, g_0\delta)\, u \right. \\ & \left. + 2\,\theta^2 p_0\delta + \theta^2 {p_0}^2\delta + \alpha\, g_0\theta\,\delta + \theta^2\delta + \alpha\, g_0\theta\, p_0\delta\right] s \\ & + (\alpha\, g_0 + \theta + \theta\, p_0)\, u^2 + \left(\theta^2 {p_0}^2 + \theta^2 + 2\,\theta\,\alpha\, g_0 + \alpha^2 {g_0}^2 + 2\,\theta\, p_0\alpha\, g_0 + 2\,\theta^2 p_0\right) u \\ & - \lambda\,\theta\, g_0\delta \end{aligned} \tag{5.15}$$

De manière remarquable, on note que $\mathcal{H} = -\lambda\theta g_0\delta$ est toujours négatif quand $u = s = 0$, c'est-à-dire quand les dégradations sont complètement saturées, ce qui semble indiquer que des oscillations apparaissent systématiquement dans cette limite. Cet argument n'est cependant pas correct, car s et u sont fonctions des paramètres et il est possible pour des fonctions de dégradation données qu'il faille faire tendre certains paramètres vers 0 ou vers l'infini pour se ramener suffisamment près de cette limite, auquel cas le terme dominant n'est pas nécessairement le terme négatif de (5.15). Il suggère cependant qu'une saturation de la dégradation, qui ne peut survenir que dans le cas d'une dégradation enzymatique, est un ingrédient important pour l'apparition d'oscillations.

On peut réécrire (5.15) uniquement en fonction de u, s, et des paramètres en éliminant p_0 et g_0 entre l'expression (5.15) et les équations de point fixe (5.10). Dans le cas plus simple

où $\mu = 0$ (répression parfaite), auquel nous nous limiterons désormais, on obtient :

$$\begin{aligned}\mathcal{H} &= u{h_0}^2\,(\alpha h_0 + \delta s\lambda)\,(\delta s\lambda + u\lambda + \alpha h_0)\\ &\quad +\lambda^2 h_0\left[h_0(-\delta h_0 + 2u\alpha + \alpha\delta s) + \lambda(u+\delta s)^2\right]\theta\\ &\quad +\lambda^4\,(u+\delta s)\,\theta^2 \end{aligned} \tag{5.16}$$

où $h_0 = h(m_0)$ indique le niveau de dégradation de l'ARN au point d'équilibre. On notera que le terme négatif de (5.16) se trouve dans le coefficient de degré 1 de θ. Comme ce terme n'est dominant à autres paramètres fixés ni pour θ très grand, ni pour θ très petit, on s'attend donc, sauf conditions particulières, à ce que les oscillations ne puissent être observées dans ces deux limites.

Analysons maintenant quelques cas particuliers.

Dégradation linéaire Le cas plus simple correspond à une double dégradation linéaire pour la protéine et l'ARN, c'est-à-dire $f(p) = p$ et $h(m) = m$, et donc $s = u = 1$. On se doute que cette situation n'est pas favorable à l'apparition d'oscillations puisque u et s sont loin de zéro. On trouve effectivement que l'expression (5.16) peut être réécrite comme une somme de termes tous positifs. On en déduit que le système (5.8) est inconditionnellement stable en l'absence de dégradation enzymatique. La dynamique propre du gène n'a donc aucun effet dans ce cas.

Dégradation protéique enzymatique On prend ici $f(p) = \kappa p/(\kappa + p)$, la dégradation de l'ARN restant linéaire. En tenant compte des équations du point fixe, la condition (5.16) se réécrit en substituant $h_0 = f_0$ et $u = 1$. Une fois l'expression exacte de la fonction de dégradation connue, la dérivée s peut être exprimée en fonction de f_0, ce qui revient à écrire l'équation différentielle à laquelle obéit f. Dans le cas présent, $s = (1 - f_0/\kappa)^2$. De manière générale, on notera que c'est l'équation différentielle à laquelle obéit la fonction de dégradation, et en particulier la capacité d'avoir des pentes faibles à petit nombre de molécules, qui va conditionner l'apparition d'oscillations.

En analysant le critère (5.16) dans la limite où f_0 est maximum et s minimum, ce qui correspond à une situation de dégradation saturée, nous avons obtenu une condition nécessaire, mais non suffisante, pour l'apparition d'oscillations, qui est la suivante :

$$\delta\kappa > \lambda\,(1 + \theta\,\lambda) + \frac{(2\,\theta\,\lambda + 1)\,N_{\rm th}}{\lambda} + \frac{{N_{\rm th}}^2\theta}{\lambda^2} \tag{5.17}$$

où $N_{\rm th} = \theta/\alpha$ est le nombre de protéines qu'il faut pour activer le gène à moitié. Même si (5.17) n'est pas une condition suffisante, elle nous permet de comprendre l'influence de plusieurs paramètres.

Tout d'abord, on constate que contrairement à ce qu'on pourrait penser, il ne faut pas que κ soit trop petit, et qu'on ne donc pas saturer la dégradation en faisant tendre κ vers 0. On s'aperçoit également qu'il ne faut pas que la constante λ fixant la force de la régulation soit trop grande. En fait, on trouve qu'à $N_{\rm th}$ fixé, la valeur optimale de λ est $\lambda \sim \sqrt{N_{\rm th}}$. Le membre de droite de (5.17) devient alors égal à $2(2\theta N_{\rm th} + \sqrt{N_{\rm th}})$. Les oscillations apparaîtront donc plus facilement dans les circuits où le gène commute à très petit nombre de protéines. On constate également que l'instabilité disparaît quand $\theta \to \infty$, ce à quoi on s'attendait car on revient alors au cas classique où les réactions d'association/dissociation peuvent être éliminées adiabatiquement.

Comme on le constatera également dans le cas suivant, l'inégalité (5.17) montre que les oscillations nécessitent des valeurs de δ suffisamment grandes, et donc que la protéine soit suffisamment instable. Mais il n'est a priori pas très réaliste que la protéine soit beaucoup plus instable que l'ARN, et les zones de paramètres où δ est significativement plus grand que 1 doivent donc être considérées avec précaution.

Double dégradation de type Michaelis-Menten Les dégradations de la protéine et de l'ARN sont toutes deux sous contrôle enzymatique, et les fonctions de dégradation sont donc maintenant données par $f(p) = \kappa p/(\kappa + p)$ et $h(m) = \chi m/(\chi + m)$. Le critère de Routh-Hürwitz est plus délicat à manier, et nous n'avons pas encore de résultats généraux, mais on peut néanmoins dériver quelques critères qui semblent validés par les simulations numériques. En supposant que les pentes s et u sont suffisamment petites pour qu'on puisse ne garder que les termes d'ordre 1 en s et u, on se ramène au critère suivant :

$$\mathcal{H}' = \theta\,\lambda^2\delta\,\left(\theta\,\lambda^2 + \alpha\,h^2\right)s + \left(\theta\,\lambda^2 + \alpha\,h^2\right)^2 u - \theta\,\delta\,\lambda^2 h^3 \tag{5.18}$$

On peut alors analyser ce qui se passe dans deux cas limites. Le premier concerne la dégradation protéine saturée ($s = 0$). On trouve dans ce cas que u doit satisfaire

$$u < \frac{\delta\lambda^2 h_0^3 N_{\rm th}^2}{(\lambda^2 N_{\rm th} + h_0^2)^2\theta} \tag{5.19}$$

Dans le cas d'une dégradation ARN saturée ($u = 0$), on trouve de la même manière une condition sur la pente s de la fonction de dégradation f au point fixe :

$$s < \frac{\kappa^3 N_{\rm th}}{\theta(\lambda^2 N_{\rm th} + \kappa^2)} \tag{5.20}$$

Ces deux inégalités peuvent être exploitées en tenant compte qu'elle représentent une contrainte forte si le membre de droite est très petit, triviale s'il est plus grand que 1, puisque $u,s \in [0,1]$. De manière surprenante, étant données les approximations effectuées, on vérifie par des simulations numériques que ces deux inégalités sont très bien vérifiées dans tous les régimes oscillants que nous avons observés.

En examinant (5.19) et (5.20), on retrouve le fait que θ ne doit pas être trop grand, ce qui ne surprend pas, car on sait que l'instabilité disparaît lorsque la variable gène peut être éliminée adiabatiquement. Par contre, on note que les constantes de Michaelis-Menten κ et χ ne doivent pas être trop petites (χ intervient par l'intermédiaire de la contrainte $h_0 < \chi$), ce qui contredit apparemment la nécessité de saturer la dégradation enzymatique.

On constate effectivement que pour des fonctions de dégradation de type Michaelis-Menten, les oscillations disparaissent dans la limite de double saturation, bien que les pentes u et s tendent vers 0. La raison en est que pour approcher cette limite tout en respectant les équations de points fixes (5.10) avec f et h Michaeliennes, il faut imposer soit $\lambda \to \infty$, en faisant tendre vers l'infini le niveau de protéines à l'équilibre p^*, ou bien $\kappa,\chi \to 0$. On voit facilement que dans tous les cas, cela rend les inégalités (5.19) et (5.20) impossibles à vérifier.

On s'attend alors que les oscillations apparaissent éventuellement pour des valeurs de s et de u intermédiaires, réalisant un compromis entre les deux tendances. Il serait probablement possible de déterminer les zones d'oscillations en choisissant des lois d'échelle sur

les différents paramètres de manière à rendre dominants les termes négatifs, mais l'analyse est alors moins aisée et n'a pas encore été réalisée. Quand nous décrirons les simulations numériques dans la section 5.3.3.4, nous verrons toutefois clairement que le coeur de l'instabilité se situe à grand δ et petit θ, c'est-à-dire pour des protéines très instables et une dynamique de commutation du gène très lente, ce qui n'est pas forcément très réaliste.

5.3.3.3 Le rôle de la cinétique enzymatique de dégradation Dans la section précédente, la discussion d'une cinétique de dégradation de type Michaelis-Menten, qui est celle habituellement retenue, a pu sembler contredire la conclusion initiale, selon laquelle les oscillations apparaissent systématiquement quand la dégradation est suffisamment saturée.

Il faut en fait garder à l'esprit que le scénario d'oscillations que nous avons mis en avant demande simultanément une dégradation élevée et une saturation à petit nombre de protéines. Or, ces deux exigences ne peuvent être simultanément satisfaites par une cinétique de Michaelis-Menten à partir du moment où les fonctions $f(p)$ et $h(m)$ sont normalisées de manière à avoir une pente unité en 0 : l'expression $\kappa p/(\kappa + p)$ a un plateau d'autant plus bas qu'elle sature plus rapidement (c'est-à-dire que κ est petit).

En fait, le raisonnement qui avait été suivi suppose que l'on puisse façonner à loisir la fonction de dégradation, ou si l'on préfère, que l'évolution ait sélectionné un mécanisme de dégradation adapté à la production d'oscillations autour d'un gène auto-régulé, à partir du moment où le besoin s'en serait fait sentir. Les discussions précédentes montrent qu'il faut que la fonction de dégradation augmente rapidement jusqu'à sa valeur de saturation, et que sa pente tende ensuite très rapidement vers 0. Clairement, cela nécessite l'introduction de termes d'ordres supérieur dans la fonction de dégradation, comme par exemple :

$$f(p) = \frac{p + ap^2}{1 + bp + cp^2} \tag{5.21}$$

où les termes quadratiques mènent à une saturation beaucoup plus rapide quand p augmente.

Nous verrons dans la partie consacrée aux simulations numériques qu'une cinétique de dégradation favorise effectivement l'apparition d'oscillations pour des valeurs de paramètres réalistes. En attendant, nous présentons succinctement deux mécanismes enzymatiques menant à une cinétique du type de (5.21), afin d'illustrer nos propos.

Enzymes allostériques La cinétique de Michaelis-Menten suppose que l'enzyme possède un seul site de fixation au substrat ou, si elle en possède plusieurs, que leurs affinités aux substrats sont identiques. Or, on rencontre souvent des phénomènes de coopérativité qui font que l'association du substrat à l'enzyme se fait d'autant plus facilement que le nombre de molécules de substrat déjà fixées est grand. Dans ce cas, les constantes cinétiques caractérisant l'interaction avec l'enzyme du deuxième susbtrat diffèrent de celles relatives au premier substrat. On montre facilement que dans le cas de deux sites, on arrive à des cinétiques du type:

$$f(p) = \frac{p + p^2/aK}{1 + 2p/K + p^2/aK^2} \tag{5.22}$$

où $a = 1$ quand les deux sites sont indépendants, et $a \to 0$ quand la fixation au deuxième site est favorisée. On voit que dans cette limite, les termes quadratiques sont dominants dans

l'expression (5.22). De manière générale, une cinétique

$$f(p) \sim \frac{p^n}{K' + p^n}, \tag{5.23}$$

connue sous le nom d'équation de Hill, sera observée dans les cas de forte coopérativité à n sites. Dans la section consacrée aux simulations numériques, nous considérerons ainsi une cinétique allostérique à quatre sites associée à la fonction

$$f(p) = \frac{p + 3p^2/aK + 3p^3/a^3K^2 + p^4/a^6K^3}{1 + 4p/K + 6p^2/aK^2 + 4p^3/a^3K^3 + p^4/a^6K^4}. \tag{5.24}$$

Isoenzymes On considère maintenant le cas où la dégradation est catalysée par deux enzymes différentes, caractérisées par des constantes cinétiques également différentes. Si

$$\dot{p} = -\delta\frac{\kappa p}{\kappa + p} - \delta'\frac{\kappa' p}{\kappa' + p}, \tag{5.25}$$

on voit facilement qu'on se ramène à une expression du type (5.21) en réduisant les deux fractions au même dénominateur. De même que précédemment, on peut obtenir des expressions avec des termes d'ordres supérieurs dans le cas où n enzymes différentes catalysent la réaction.

Une cinétique comme (5.25) pourrait également se rencontrer lorsque la protéine est susceptible de modifications covalentes, par exemple lorsqu'elle existe également dans un forme phosphorylée, et lorsque les deux formes ont des propriétés de dégradation différentes.

5.3.3.4 Simulations numériques Pour conclure cette partie consacrée à nos résultats préliminaires concernant un oscillateur génétique élémentaire, nous présentons quelques simulations numériques nous permettant de vérifier si les oscillations dont l'existence semble suggérée par l'analyse du critère de Routh-Hürwitz (5.16) sont bien observées et, si c'est le cas, si elles le sont dans des régions de paramètres réalistes. Par simplicité, nous nous limitons toujours au cas de la répression parfaite ($\mu = 0$).

Pour cela, nous tirons un grand nombre de jeux de paramètres au sort, pour lesquels nous déterminons si le système a rencontré une bifurcation de Hopf en calculant les coordonnées du point fixe, ainsi que les valeurs propres du Jacobien. Les deux échelles de temps cruciales sont déterminées ici par δ et θ, qui contrôlent la stabilité de la protéine et la durée de vie du complexe régulateur sur le promoteur du gène. Nous les faisons varier entre 0.01 et 100, sachant que les situations $\delta \gg 1$ et $\theta \ll 1$ sont peu réalistes. Si on fixe la durée de vie de l'ARN à 10 minutes, on s'attend en effet peu à voir une protéine dégradée au bout de 6 secondes ou une protéine régulatrice attendre 16 heures avant de se dissocier du gène. Afin de comprendre le rôle de la saturation, nous nous intéressons également au coefficient de saturation $c_p = p^*/(p^* + \kappa)$ qui vaut 0 en régime linéaire, et 1 en dégradation complètement saturée, ainsi qu'à son analogue pour l'ARN.

Dégradation de Michaelis-Menten Les résultats des simulations numériques pour les coopérativités $n = 1$, $n = 2$, et $n = 4$ (c'est-à-dire régulation du gène par, respectivement, un monomère, dimère et un tétramère), et des cinétiques de dégradation de type Michaelis-Menten, sont donnés par la figure 5.14. Des oscillations sont observées dans tous les cas, mais on note qu'elles ne peuvent se produire que lorsque $\theta \ll 1$ ou $\delta \gg 1$, ce qui est peu réaliste. Ainsi,

les oscillations à $\theta \sim 1$ nécessitent de manière générale $\delta > 100$, et donc une extrême instabilité de la protéine. On constate également que la protéine et l'ARN se comportent de manière très différente par rapport à la dégradation. Pour $n = 1$, on trouve ainsi des régimes oscillants avec des dégradations ARN saturées ou non, alors que le coefficient de saturation de la protéine est centré autour d'une valeur bien précise.

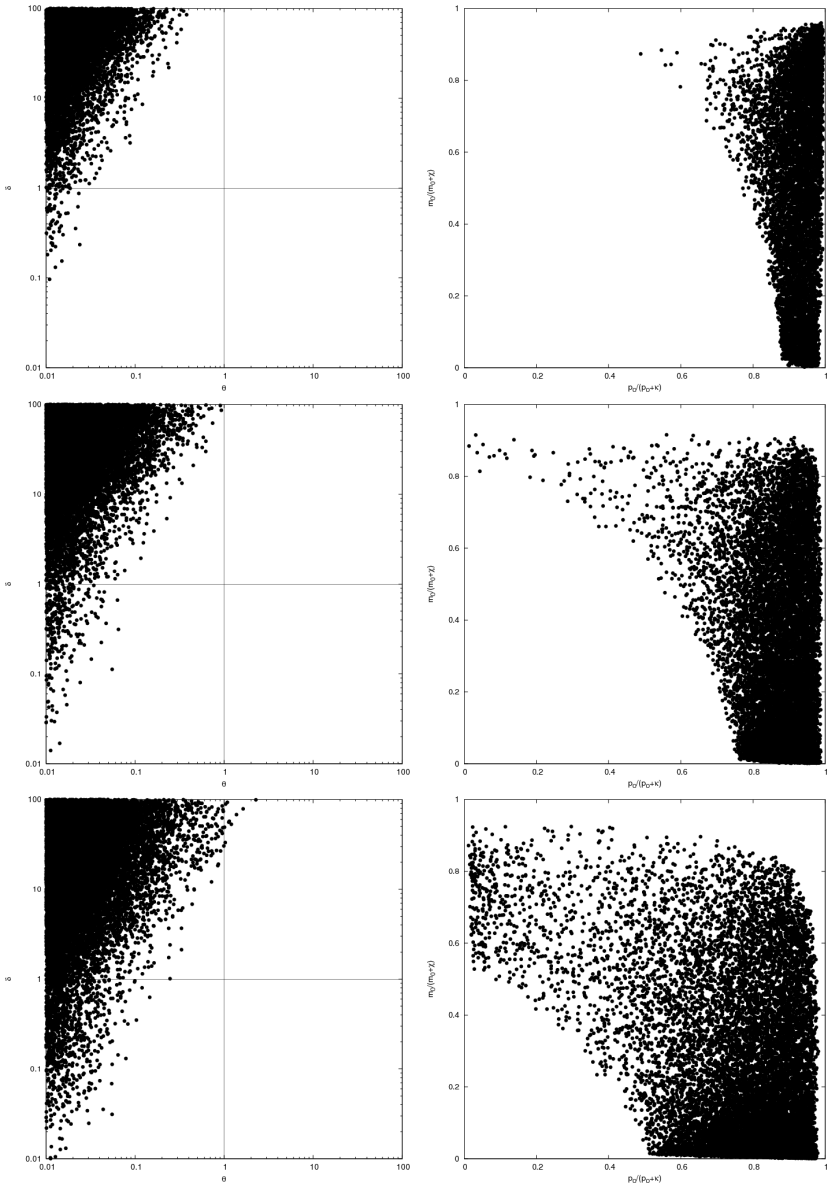

FIG. ***5.14*** – *Localisation des régimes oscillants dans l'espace des paramètres pour $n = 1$ (en haut), $n = 2$ (au centre) et $n = 4$ (en bas). Les systèmes oscillants sont représentés, à gauche dans le plan (θ,δ), à droite dans le plan $(\frac{p^*}{p^*+\kappa}, \frac{m^*}{m^*+\chi})$, ce qui permet d'estimer la saturation de la dégradation (ces deux quantités valent 0 en régime linéaire et 1 en dégradation enzymatique complètement saturée). Les lignes verticale et horizontale au centre des tracés de gauche correspondent à $\theta = 1$ et $\delta = 1$.*

Quand la coopérativité augmente, la région du plan (θ,δ) occupée par les régimes oscillants évolue très peu, par contre on observe alors également des oscillations à dégradation protéique

très peu saturée, à condition d'augmenter en conséquence la saturation de la dégradation ARN.

Dégradation coopérative Nous nous intéressons maintenant à l'effet de cinétiques de dégradation non-Michaeliennes : une fonction de dégradation judicieusement choisie permet-elle d'induire des comportements périodiques pour des valeurs réalistes des paramètres ?

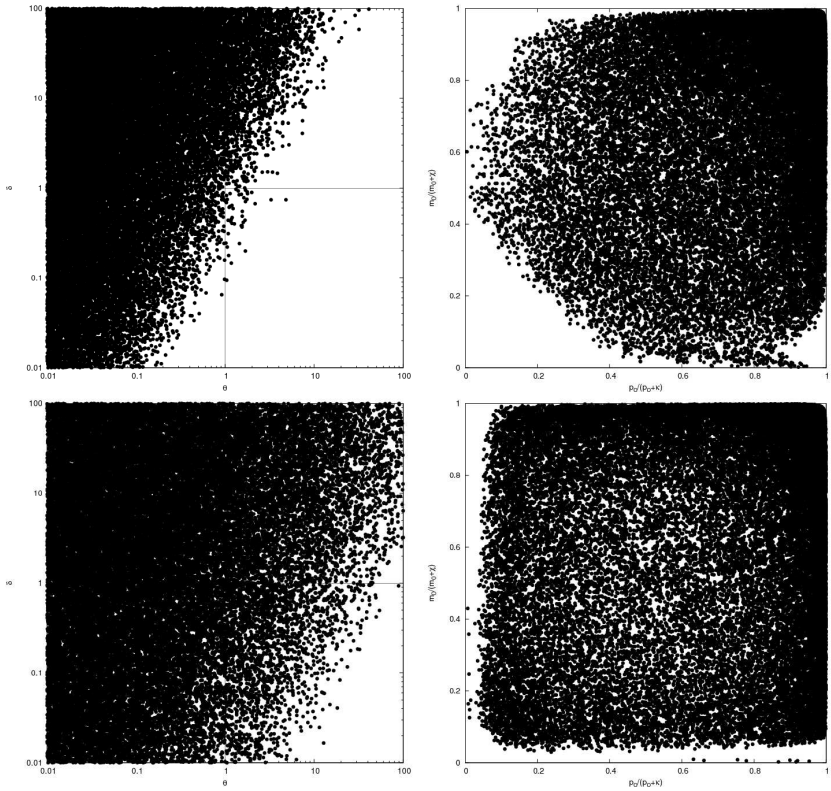

FIG. ***5.15 –*** *Localisation des régimes oscillants dans l'espace des paramètres dans le cas d'une régulation par monomère et pour des cinétiques de dégradation du type* (5.22) *(ordre 2), avec une constante de coopérativité* $a = 0.01$ *(en haut), et du type* (5.24) *(ordre 4), avec* $a = 0.1$ *(en bas). Comme dans la figure 5.14, les systèmes oscillants sont représentés, à gauche dans le plan* (θ,δ)*, à droite dans le plan* $(\frac{p^*}{p^*+\kappa}, \frac{m^*}{m^*+\chi})$*, où* κ *et* χ *sont les constantes* K *des expressions* (5.22) *et* (5.24) *relatives à la protéine et à l'ARN, respectivement. Les lignes verticale et horizontale au centre des tracés de gauche correspondent à* $\theta = 1$ *et* $\delta = 1$.

Les simulations numériques illustrées par la figure 5.15, effectuées pour des cinétiques de dégradation d'ordres 2 et 4, semblent apporter une réponse positive à cette question. On voit immédiatement que les régimes oscillants peuvent être trouvés dans une région beaucoup plus étendue du plan (θ,δ), et notamment pour des valeurs de θ beaucoup plus grandes et de δ beaucoup plus petites. Pour fixer les idées, l'instabilité périodique peut être observée lorsque $\delta = 1$ jusqu'à $\theta \sim 5$ pour une cinétique d'ordre 2 ($a = 0.01$) et $\theta \sim 100$ pour une cinétique d'ordre 4 ($a = 0.1$). La figure 5.16 présente un régime observé pour $\theta = 5$, et montre que le fait que g soit une variable rapide quasiment asservie à p ne contrarie pas les oscillations.

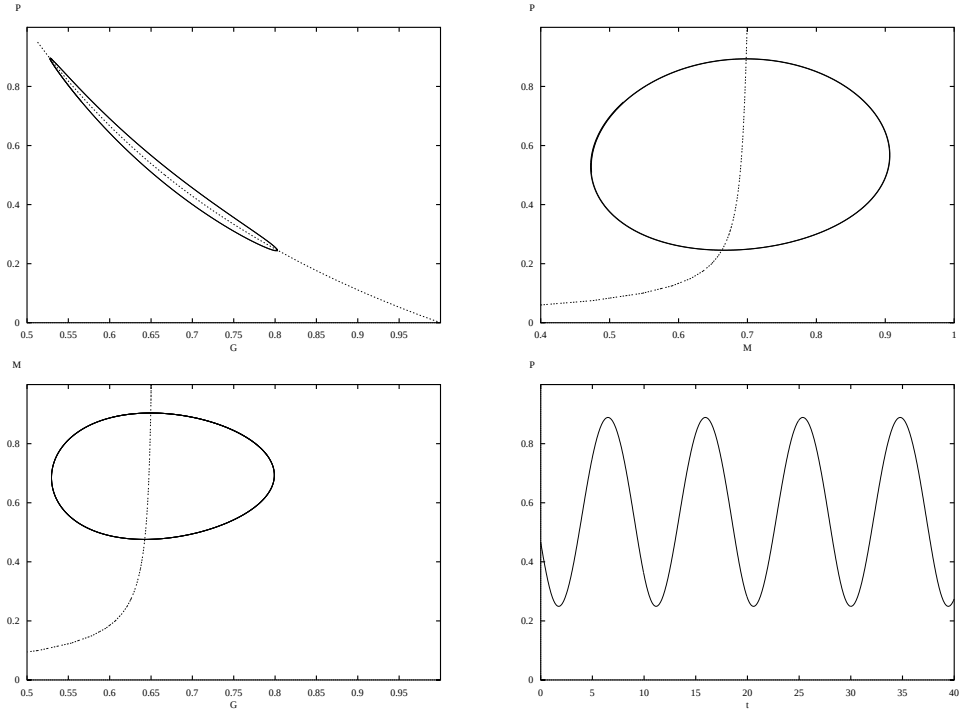

FIG. ***5.16 –*** *Oscillations observées pour* $\theta = 5$, $\alpha = 0.01$, $\delta = 1$, $\kappa = 0.703$, $\chi = 0.624$, $\mu = 0$, $\lambda = 1.075$, $a = 0.005$. *De gauche à droite, et de haut en base : portraits de phase* (g,p), (m,p), (g,m) *et variation de* p *en fonction du temps. Dans chaque portrait de phase plan est également tracée la nullcline liant les deux variables concernées, c'est-à-dire respectivement* $g = 1/(1+p)$, $m = f(p)$, *et* $\mu + \lambda G = h(m)$.

L'existence d'oscillations pour des grandes valeurs de θ est inattendue, car on pourrait penser que l'élimination adiabatique qui suppose que le taux de transcription suit instantanément les variations de concentration en protéine, et qui supprime les oscillations, est alors parfaitement justifiée. En fait, on soupçonne que des dynamiques oscillantes à des valeurs arbitrairement grandes de θ puissent être observées, à condition de choisir des fonctions de dégradation suffisamment non linéaires. En effet, si on passe à la limite où les fonctions de dégradation sont du type Heaviside ($f(p) = \mathrm{cte}$ pour $p > \kappa$), et si on peut trouver un point d'équilibre situé dans la zone de plateau, alors le critère de Routh-Hürwitz est automatiquement vérifié.

Un point où notre système diffère de manière significative d'une équation à délai du type (5.2) concerne les périodes d'oscillations. Ainsi, pour un jeu de paramètres étudié dans la simulation concernant la cinétique du deuxième ordre, nous obtenons par exemple une période $T \sim 20$ alors que $\theta \sim 8$, ce qui correspondrait à un délai $\tau = 1/\theta(p^* + 1) \sim 0.04$. On trouve que $T/\tau \sim 500$, alors que ce rapport est en général de l'ordre de 2 à 4 pour une équation à délai [147].

Ces résultats préliminaires semblent donc indiquer que si l'on admet l'existence d'une dynamique propre du taux de transcription, le niveau d'expression d'un gène auto-régulé peut présenter des oscillations dans des zones de paramètres réalistes. Cette dynamique a jusqu'ici souvent été négligée car les processus d'association/dissociation étaient considérés comme rapides, mais si on considère que l'initiation de la transcription est en fait un processus

complexe, alors notre étude montre qu'elle peut engendrer des instabilités sans avoir à prendre en compte des délais liés par exemple au transport entre cytoplasme et noyau. Le point essentiel à retenir n'est pas tant que des fonctions de dégradation ou de régulation très non linéaires facilitent les oscillations, car c'est souvent le cas dans les circuits génétiques [130], mais que les oscillations semblent persister pour des dynamiques du taux de transcription arbitrairement rapides, à condition de choisir judicieusement les mécanismes de dégradation.

Par ailleurs, nous noterons qu'alors que les auteurs ont souvent considéré l'effet d'une coopérativité élevée dans la régulation de la transcription (i.e., le gène est régulé par un complexe protéique d'ordre élevé), notre étude montre qu'une coopérativité forte dans le mécanisme de dégradation peut avoir des effets très importants, et que ce facteur d'instabilité mérite d'être étudié de manière plus approfondie.

5.4 CONCLUSION

Les réseaux de régulation constitués de gènes et protéines en interaction présentent un comportement complexe, qui ne correspond pas toujours à ce que l'intuition ou le sens commun aurait deviné. Seule une analyse mathématique précise peut établir quels sont les différents régimes dynamiques observables dans un circuit génétique donné, ainsi que sa robustesse par rapport aux changements de paramètres (à condition bien sûr de supposer que le modèle analysé incorpore correctement les principaux phénomènes à l'oeuvre dans la réalité).

L'apparition d'oscillations dans un réseau génétique est un comportement non linéaire extrêmement intéressant, et notamment en raison de son importance dans des phénomènes tels que les rythmes circadiens, la segmentation des somites ou encore les mécanismes de réparation de l'ADN. Nous sommes actuellement engagés dans un projet à long terme visant à élucider les rouages moléculaires de l'horloge circadienne d'*Ostreococcus tauri*, une algue unicellulaire qui présente l'avantage d'avoir une organisation cellulaire très simplifiée et un génome très peu redondant. Cet organisme possède en outre la particularité de présenter un fort couplage entre rythmes circadiens et cycle de division cellulaire.

Nous espérons disposer bientôt des premiers modèles de cette horloge, mais des premiers résultats ont déjà été obtenus lors d'étapes intermédiaires. Nous avons été en effet amenés à nous intéresser à considérer la dynamique du gène auto-régulé et à nous demander quelle pourrait être l'influence d'une dynamique du taux de transcription pilotée par la concentration en protéine. Nous avons montré que le simple fait que l'activité du gène devienne une variable dynamique peut suffir à induire des instabilités en conjonction avec des dégradations enzymatiques complexes. Ce résultat suggère que les différentes étapes de ce processus complexe qu'est l'initiation de la transcription devraient être mieux étudiées d'un point de vue dynamique, ainsi que les détails des mécanismes de dégradation.

6

Conclusion et perspectives

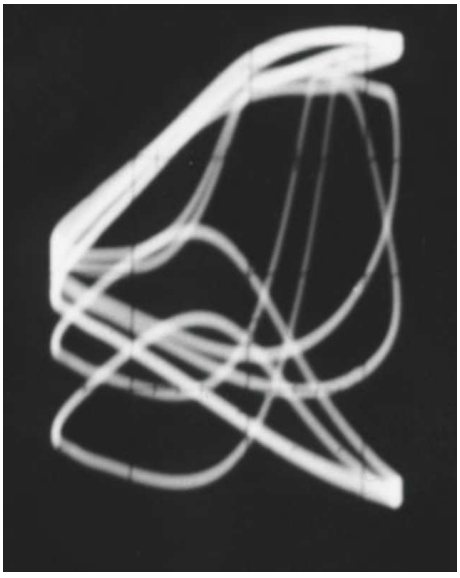

FIG. ***6.1 –*** *Visualisation sur un écran d'oscilloscope d'une orbite de période 8 observée au milieu de la cascade de doublements de période menant au chaos dans un laser à modulation de pertes. La modulation appliquée est envoyée sur la voie X, et la réponse du laser sur la voie Y.*

C'est sur une image expérimentale que j'aborderai le dernier chapitre de ce mémoire, au moment de faire un bilan sommaire et de songer à l'avenir. La photo d'écran d'oscilloscope de la figure 6.1 illustre, je l'espère, ce qui aura été une profonde motivation au cours de mes différents travaux de recherche : explorer l'interface entre le monde réel et la vision que nous en construisons, entre l'expérience et les mathématiques. Ce que nous observons au laboratoire nous suggère des images auxquelles nous n'aurions peut-être pas songé, mais

inversement nous ne mettons de l'ordre dans ce que nous percevons que grâce aux structures que nous avons déjà en tête.

Cette frontière est un monde de rencontres inattendues. La théorie des noeuds paraît à beaucoup une science abstraite, car elle ne figure pas dans les cursus de Physique. Mais, en regardant la figure 6.1, comment ne pas sentir qu'elle est un outil de laboratoire parfaitement adapté pour qui veut comprendre une dynamique où l'irrégulier et le complexe se construisent autour du simple et du répétitif, où un attracteur étrange s'organise autour d'orbites périodiques. Les séries de Fourier furent un jour un concept purement mathématique, mais elles font aujourd'hui partie du bagage de chaque ingénieur. On se prend à songer que la théorie des noeuds et des gabarits ne fait finalement pour les systèmes chaotiques que ce que l'analyse de Fourier accomplit pour les systèmes linéaires : décomposer le tout sur les parties périodiques qu'il renferme. Aux modes propres de translation répondent les « modes propres » de l'étirement et du repliement.

Les rencontres se font aussi par l'intermédiaire de ces idées qui font surface en plusieurs endroits. Ainsi, ce sont les mêmes singularités fronces qui permettront sans doute de classer le chaos en dimension quatre, et qui expliquent pourquoi un oscillateur paramétrique optique est capable de s'éteindre et de s'allumer à des fréquences élevées en réponse à des modifications infimes de sa longueur de cavité. Ailleurs, c'est le même équilibre entre instabilité et stabilité qui semble à la fois engendrer les attracteurs chaotiques et, en biologie, permettre aux organismes vivants de réagir à des signaux infimes tout en se préservant des perturbations extérieures.

Ayant un peu traîné avant de rédiger ce mémoire, je me sens obligé de m'interroger sur ce qui sépare mes recherches passées de mes projets futurs. Je crois identifier deux points tournants. En ce qui concerne l'analyse topologique, beaucoup de temps a été consacré à démontrer la pertinence de cette approche et l'aide irremplaçable qu'elle apporte pour résoudre des problèmes jugés importants et difficiles : décider de l'équivalence de deux structures chaotiques, construire des codages symboliques, extraire une signature chaotique d'un signal non stationnaire, etc. Cette voie aura suscité un certain intérêt, comme en témoignent peut-être les 1200 exemplaires de "The Topology of Chaos" diffusés un peu partout dans le monde, mais en même temps aura été peu suivie dans la pratique. L'explication est à trouver dans cette simple question, entendue presque après chaque exposé que j'aurais donné : « Et comment comptez-vous faire en dimension supérieure ? ».

Le travail que j'ai présenté sur la préservation de l'orientation dans des triangulations de points périodiques constitue peut-être, je l'espère, le premier élément de réponse à cette question. Il semble déjà qu'il permette de reformuler la théorie en dimension 3, et de simplifier considérablement certains problèmes, comme notamment celui de la construction de codages symboliques. C'est sans doute parce que ce nouveau formalisme s'attaque de manière directe au problème fondamental de la dynamique chaotique : connecter une évolution inversible aux singularités qui apparaissent à un temps infini du fait de l'action indéfiniment répétée de l'étirement et du repliement. Reste à espérer qu'il nous permette bientôt de poser le pied en dimension 4, et de mettre directement en évidence dans les séries temporelles expérimentales les fronces dont on pense qu'elles organisent la dynamique le long d'une variété instable bidimensionnelle.

Le deuxième point tournant concerne l'activité de modélisation. Ce fut hier l'analyse de comportements surprenants dans des systèmes optiques, ce sera demain la mise en équations de phénomènes biologiques. Ce qui est évidemment stimulant ici, c'est une pra-

tique expérimentale complètement différente, le fait d'être confronté à des problèmes où la capacité de l'esprit humain à isoler ce qui est immuable est poussée dans ses derniers retranchements par une complexité au premier abord déconcertante. Mais, quand on constate par exemple la grande reproductibilité d'un jour sur l'autre des profils temporels d'expression des gènes impliqués dans l'horloge circadienne, on veut bien croire qu'il y a dans ce nouveau monde, où rien ne semble sûr au physicien habitué à des systèmes dociles, des points d'ancrage qui se laisseront plus facilement manipuler. Et on se demande plus largement si le champ de la Physique ne déborde pas le cadre de l'inanimé, pour s'intéresser plus largement à tout ce qui est stationnaire et mathématisable dans une réalité changeante. Mais peut-être ce déplacement du front entraînera-t-il en retour des changements sur les méthodes mathématiques : pourra-t-on par exemple continuer à utiliser des formalismes basés sur des états ponctuels, en principe localisables avec une précision arbitraire ? Une différence essentielle subsistera cependant entre ce que nous appelons physique et la biologie : si rien ne nous permet de penser que les lois physiques que nous manipulons aient pu changer depuis le début de l'Univers, il nous faut penser devant tout système biologique que l'organisation que nous cherchons à disséquer n'est pas le fruit du hasard, mais d'une longue évolution, que si la Nature a trouvé avantageux d'osciller, elle a fini par trouvé une solution pour le faire, et sans doute pas la plus compliquée. Reste à en saisir toutes les subtilités.

Appendice A
Liste des publications, encadrement, activités diverses.

De manière générale, les références sont classées dans chaque rubrique par ordre anti-chronologique. En ce qui concerne les communications à des conférences, invitées ou non, sont mentionnées les personnes ayant participé au travail, le nom de l'orateur étant distingué par des caractères gras.

A.1 PUBLICATIONS DANS DES REVUES À COMITÉ DE LECTURE

A.1.1 Parues

1. M. Lefranc, "Alternate determinism principle for topological analysis of chaos", *Phys. Rev. E* **74**, 035202(R) (2006).
2. A. Amon and M. Lefranc, "Topological signature of deterministic chaos in short nonstationary signals from an optical parametric oscillator", *Phys. Rev. Lett.* **92**, 094101 (2004).
3. A. Amon, M. Nizette, M. Lefranc and T. Erneux, "Bursting oscillations in optical parametric oscillators", *Phys. Rev. A* **68**, 023801 (2003).
4. Pierre Suret, Dominique Derozier, Marc Lefranc, Jaouad Zemmouri, and Serge Bielawski, "Incompatibility between cavity resonances and wavevector matching: influence on threshold and beam structures of OPOs", *J. Opt. Soc. Am. B* **19** (3), 395–404 (2002).
5. P. Suret, M. Lefranc, D. Derozier, J. Zemmouri, and S. Bielawski, "Fast oscillations in an optical parametric oscillator", *Opt. Commun.* **200**, 369–379 (2001).

6. J. Plumecoq, C. Szwaj, D. Derozier, M. Lefranc, and S. Bielawski, "Eckhaus instability induced by nonuniformities in a laser", *Phys. Rev. A* **64**, 061801(R) (2001).
7. T. W. Carr, T. Erneux, C. Szwaj, M. Lefranc, D. Derozier, and S. Bielawski, "Cascade of parametric instabilities in a multimode laser", *Phys. Rev. A* **64**, 053808 (2001).
8. Pierre Suret, Marc Lefranc, Dominique Derozier, Jaouad Zemmouri and Serge Bielawski, "Periodic mode hopping induced by thermo-optical effects in continuous-wave optical parametric oscillators", Opt. Lett. **26**, 1415–1417 (2001).
9. J. Plumecoq and M. Lefranc, "From template analysis to generating partitions I: Periodic orbits, knots, and symbolic encodings", *Physica D* **144**, 231–258 (2000).
10. J. Plumecoq and M. Lefranc, "From template analysis to generating partitions II: Characterization of the symbolic encodings", *Physica* D **144**, 259–278 (2000).
11. E. Yao, M. Lefranc, and F. Papoff, "Unstable periodic orbits in the presence of spatio-temporal chaos" *J. Opt. B: Quantum Semiclass. Opt.* **2**, 382–385 (2000).
12. P. Suret, D. Derozier, M. Lefranc, J. Zemmouri, and S. Bielawski, "Self-pulsing instabilities in an optical parametric oscillator: Experimental observation and modeling of the mechanism", *Phys. Rev.* A **61**, 021805(R) (2000).
13. G. Boulant, M. Lefranc, S. Bielawski, and D. Derozier, "A nonhorseshoe template in a chaotic laser model", *Int. J. Bifurcation and Chaos* **8**, 965–975 (1998).
14. G. Boulant, M. Lefranc, S. Bielawski, and D. Derozier, "Horseshoe templates with global torsion in a driven laser", *Phys. Rev.* E **55**, 5082–5091 (1997).
15. G. Boulant, S. Bielawski, D. Derozier, and M. Lefranc, "Experimental observation of a chaotic attractor with a reverse horseshoe topological structure", *Phys. Rev.* E **55**, R3801–3804 (1997).
16. M. Lefranc, P. Glorieux, F. Papoff, F. Molesti, and E. Arimondo, "Combining topological analysis and symbolic dynamics to describe a strange attractor and its crises", *Phys. Rev. Lett.* **73**, 1364–1367 (1994).
17. M. Lefranc and P. Glorieux, "Topological analysis of chaotic signals from a CO_2 laser with modulated losses", *Int. J. Bifurc. Chaos* **3**, 643–649 (1993).
18. M. Lefranc, D. Hennequin, and P. Glorieux, "Improved correlation dimension estimates through change of variable", *Phys. Lett.* A **163**, 269–274 (1992).
19. M. Lefranc, D. Hennequin, and D. Dangoisse, "Homoclinic chaos in a laser containing a saturable absorber", *J. Opt. Soc. Am.* B **8**, 239–249 (1991).

A.1.2 Soumises

1. A. Amon and M. Lefranc, "Mode hopping strongly affects observability of dynamical instability in optical parametric oscillators", soumis à Physical Review A.
2. N. Romanazzi, M. Lefranc and R. Gilmore, "Once a horseshoe – always a horseshoe", soumis à Physical Review E.

A.1.3 En cours de rédaction

(Travaux pour lesquels l'essentiel des résultats ont déjà été obtenus et qui ont commencé à être rédigés.)

1. A. Amon, M. Lefranc, S. Bielawski, and D. Derozier, "Multimode behavior of triply resonant optical parametric oscillators at high pump power.", à soumettre à Optics Letters.
2. P.E. Morant, F. Lemaire, B. Parent, C. Vandermoere, and M. Lefranc, "The degradator: a single-gene oscillator", à soumettre à Physical Review Letters.
3. J. Used, M. Lefranc and J.C. Martin, "Topological analysis of an erbium-doped ring laser", à soumettre à Physical Review.
4. M. Lefranc, "Template structure and saddle-node bifurcations".

A.2 LIVRES ET CHAPITRES DE LIVRES

A.2.1 Livres

1. Robert Gilmore and Marc Lefranc, "The Topology of Chaos: Alice in Stretch and Squeezeland", 495 pages (Wiley, New York, 2002).

A.2.2 Chapitres de livres

1. Marc Lefranc, "The Topological Analysis of Deterministic Chaos: Stretching, Squeezing and Linking", in *Physics and Theoretical Computer Sciences: from Numbers and Languages to (quantum) Cryptography*, J.-P. Gazeau, J. Nesetril and B. Rovan eds., Lecture notes of the "Physics and Computer Science" NATO Advanced Science Institute, October 17–29 2005, Institut d'Études Scientifiques de Cargèse, Corsica, France (IOP Press, sous presse).

A.2.3 Livres édités

1. Comptes-Rendus de la 9ème RENCONTRE DU NON-LINÉAIRE, Paris, M. Lefranc, C. Letellier et L. Pastur éditeurs (Non-linéaire Publications, Orsay, 2006).

A.3 VULGARISATION ET DIFFUSION DU SAVOIR SCIENTIFIQUE

A.3.1 Articles et documents multimédia

1. M. Lefranc, S. Bielawski, D. Derozier, et P. Glorieux, « Caractérisation topologique et contrôle du chaos », *Images de la Physique 1997*, pp. 53–60 (Octobre 1997).
2. M. Lefranc et P. Glorieux, « Dénouement dans le chaos », *Pour La Science*, Dossier hors-série « La Science des Noeuds », p. 92-96 (avril 1997).
3. M. Lefranc, « L'ordre dans le chaos », animation audio-visuelle réalisée pour le livre sonore « Chaos Déterministe » de l'exposition permanente « Mathématiques » à la Cité des Sciences et de l'Industrie de la Villette, et qui est exposé depuis avril 1995.
4. M. Lefranc et P. Glorieux, « Des noeuds dans le chaos », *Pour La Science*, Dossier hors-série « Le Chaos », p. 58-63, janvier 1995.

A.3.2 Réalisations diverses

1. Réalisation d'une illustration (attracteur chaotique) pour le cycle « Hasard » des *Rendez-Vous d'Archimède*, à l'Espace Culture de l'Université de Lille I (mars-mai 2001).
2. Fourniture d'illustrations pour le numéro Hors-série de *Sciences et Avenir*, « Le futur est-il prévisible? » (Mai 1996).
3. Informations et fourniture d'illustrations pour l'article de D. Delbecq, « Démêler les noeuds du chaos », *C.N.R.S. Infos* **294**, 15 (1994), consacré à nos travaux.
4. Discussions et réalisation d'illustrations pour l'article de D. Tarnowski, « Le chaos, monstre sensible et docile », *Science & Vie* **914**, p. 38 (1993), mentionnant entre autres l'existence des orbites périodiques instables.

A.4 PUBLICATIONS DANS DES ACTES DE CONGRÈS

A.4.1 Congrès internationaux

1. A. Amon and M. Lefranc, "Topological signature of deterministic chaos in short nonstationary signals from an optical parametric oscillator", Proceedings of the 8TH EXPERIMENTAL CHAOS CONFERENCE, Florence, Italy (juin 2004), pp. 357–362, S. Bocaletti *et al.* eds., AIP Conference Proceedings Vol. 742 (American Institute of Physics, Melville, 2004).
2. G. Boulant, J. Plumecoq, S. Bielawski, D. Derozier, and M. Lefranc, "Model validation and symbolic dynamics of modulated lasers using template analysis", proceedings of the FOURTH EXPERIMENTAL CHAOS CONFERENCE, Boca Raton, Floride, Etats-Unis (août 1997), pp. 121–126 (World Scientific, Singapore, 1998).
3. C. Szwaj, D. Leroy, S. Bielawski, T. Erneux, M. Lefranc, and D. Derozier, "Faraday instability and pattern formation inside a laser spectrum", proceedings of the FOURTH EXPERIMENTAL CHAOS CONFERENCE, Boca Raton, Floride, Etats-Unis (août 1997), pp. 85–90 (World Scientific, Singapore, 1998).
4. M. Lefranc, S. Bielawski, D. Derozier, and P. Glorieux, "Characterization and control of laser chaos using unstable periodic orbits", in LEOS '95. IEEE LASERS AND ELECTRO-OPTICS SOC., 8TH ANNUAL MEETING 1995, CONF. PROC. (CAT. NO. 95CH35739), pp. 35–36 (IEEE, New York, 1995).
5. D. Dangoisse, D. Hennequin, M. Lefranc, and P. Glorieux, "The laser with a saturable absorber: a paradigm for the study of laser instabilities", in *Evolution of dynamical structures in dynamical systems*, SPRINGER PROCEEDINGS IN PHYSICS **69**, 100–113 (Springer Verlag, 1992).
6. D. Hennequin, M. Lefranc, A. Bekkali, D. Dangoisse, and P. Glorieux, "Characterization os Shil'nikov chaos in a laser containing a saturable absorber", in *Measures of Chaos and Complexity*, N.B. Abraham, A.M. Albano, A. Passamante, and P.E. Rapp Eds., NATO ASI SERIES **208**, 299–302 (Plenum Press, 1989).

A.4.2 Congrès nationaux

1. A. Amon et M. Lefranc, “Les sauts de mode tronquent la dynamique des oscillateurs paramétriques optiques”, Comptes-Rendus de la 9ème RENCONTRE DU NON-LINÉAIRE, Paris (mars 2006), pp. 13–18 (Non-linéaire Publications, Orsay, 2006).
2. P.-E. Morant, M. Nizette et M. Lefranc, “Un nouveau formalisme pour l’analyse topologique du chaos déterministe”, Comptes-Rendus de la 8ème RENCONTRE DU NON-LINÉAIRE, Paris (mars 2005), pp. 157–162 (Non-linéaire Publications, Orsay, 2005).
3. A. Amon, M. Nizette, M. Lefranc et T. Erneux, "Observation expérimentale et modélisation de bursting dans les oscillateurs paramétriques optiques", Comptes-Rendus de la 6ème RENCONTRE DU NON-LINÉAIRE, Paris (mars 2003), pp. 19–24 (Non-linéaire Publications, Orsay, 2003).
4. A. Amon et M. Lefranc, "Signature topologique de chaos déterministe dans un oscillateur paramétrique optique", Comptes-Rendus de la 6ème RENCONTRE DU NON-LINÉAIRE, Paris (mars 2003), pp. 167–172 (Non-linéaire Publications, Orsay, 2003).
5. J. Plumecoq et M. Lefranc, "Orbites périodiques, théorie des noeuds et codages symboliques", Comptes-Rendus de la 3ème RENCONTRE DU NON-LINÉAIRE, Paris (mars 2000), pp. 29–34 (Paris Onze édition - Université de Paris-Sud, 2000).
6. P. Suret, D. Derozier, M. Lefranc, J. Zemmouri, and S. Bielawski, “Oscillations spontanées dans les oscillateurs paramétriques optiques : observation expérimentale et modélisation du mécanisme”, compte-rendus du SIXIÈME COLLOQUE SUR LES LASERS ET L’OPTIQUE QUANTIQUE, Bordeaux, France (septembre 1999), Journal de Physique IV, Vol. 18, Pr 8-163 (Mai 2000).
7. J. Plumecoq, C. Szwaj, D. Derozier, M. Lefranc et S. Bielawski, “Déstabilisation d’ondes stationnaires induite par variations spatiales d’un paramètre : l’exemple d’un laser”, compte-rendus du SIXIÈME COLLOQUE SUR LES LASERS ET L’OPTIQUE QUANTIQUE, Bordeaux, France (septembre 1999), Journal de Physique IV, Vol. 18, Pr 8-239 (Mai 2000).
8. J. Plumecoq, C. Szwaj, D. Derozier, M. Lefranc, et S. Bielawski, "Instabilités induites par non uniformité dans un laser", Comptes-Rendus de la 2ème RENCONTRE DU NON-LINÉAIRE, Paris (mars 1999), pp. 170–174 (Paris Onze édition - Université de Paris-Sud, 1999).

A.5 CONFÉRENCES ET SÉMINAIRES INVITÉS

(Sont indiqués les noms de toutes les personnes ayant participé au travail présenté. Le nom de l’orateur, ou des personnes ayant présenté une affiche, est indiqué en gras.)

A.5.1 Conférences et cours invités

A.5.1.1 Internationales

1. **M. Lefranc**, “Topological analysis of deterministic chaos: stretching, squeezing and entanglements” (cours, 4 heures), NATO ADVANCED INSTITUTE “PHYSICS AND COMPUTER SCIENCE”, Institut d’études scientifiques de Cargèse (octobre 2005).

2. A. Amon, **M. Lefranc**, "Topological signature of chaos for short time traces", minisymposium "laser dynamics", FIFTH EUROMECH NONLINEAR DYNAMICS CONFERENCE (ENOC 2005), EINDHOVEN, 7–12 AOÛT 2005.
3. A. Amon, P. Suret, M. Nizette, S. Bielawski, D. Derozier, J. Zemmouri, T. Erneux and **M. Lefranc**, "Instabilities and chaos in an optical parametric oscillator", FIRST 'RIO DE LA PLATA' WORKSHOP ON NOISE, CHAOS AND COMPLEXITY IN LASERS AND NONLINEAR OPTICS, Colonia del Sacramento, Uruguay (décembre 2003).
4. A. Amon, P. Suret, S. Bielawski, D. Derozier, J. Zemmouri and **M. Lefranc**, "Dynamics of optical parametric oscillators", EUROPEAN QUANTUM ELECTRONICS CONFERENCE (EQEC) 2003, Münich, Allemagne (juin 2003).
5. J. Plumecoq, Ch. Szwaj, D. Derozier, M. Lefranc, **S. Bielawski**, and T. Erneux, "Hydrodynamics in optics: Understanding spectral waves in laser experiments using a multiple scale analysis", THE FOURTH INTERNATIONAL CONGRESS ON INDUSTRIAL AND APPLIED MATHEMATICS ICIAM99 (mini symposia: applied nonlinear dynamics of lasers), Edinburgh, Royaume-Uni (juillet 1999).
6. **J. Plumecoq**, C. Szwaj, S. Bielawski, T. Erneux, M. Lefranc and D. Derozier, "Waves and Patterns inside a laser spectrum", PATTERNS IN OPTICAL SYSTEMS (PINOS'98), Alicante, Espagne (Mai 1998).
7. M. Lefranc, S. Bielawski, D. Derozier, and **P. Glorieux**, "Characterization and control of laser chaos using unstable periodic orbits", THIRD EXPERIMENTAL CHAOS CONFERENCE, Edinburgh, Royaume-Uni (septembre 1995).
8. M. Lefranc, S. Bielawski, D. Derozier, and **P. Glorieux**, "Characterization and control of laser chaos using unstable periodic orbits", LEOS ANNUAL MEETING, San Francisco, États-Unis (octobre 1995).
9. **M. Lefranc**, "Geometric analysis of time series" (cours, 1h30). Mini-workshop on Nonlinear Time Series Analysis (N. Gershenfeld and Hao B.-L., orgs.), CONDENSED MATTER RESEARCH WORKSHOP, International Centre for Theoretical Physics, Trieste, Italie (août 1994).

A.5.1.2 Nationales

1. **M. Lefranc**, "L'analyse topologique du chaos : orbites périodiques, théorie des noeuds et dynamique symbolique", TROISIÈMES JOURNÉES DE L'ACTION SPÉCIFIQUE "SYSTÈMES DYNAMIQUES ET MODÉLISATION EN ALGORITHMIQUE", Caen (9–10 décembre 2003).
2. **M. Lefranc**, "L'analyse topologique du chaos : orbites périodiques, théorie des noeuds et dynamique symbolique", ÉCOLE JEUNES CHERCHEURS EN ALGORITHMIQUE ET CALCUL FORMEL (GdR Algorithmique, Language et Programmation), Lille (Mars 2002).

A.5.2 Séminaires

1. **M. Lefranc**, "Analyse topologique du chaos déterministe : étirement, repliement, et entrelacements", Centre de Physique Théorique de Marseille, Luminy (novembre 2006).
2. **M. Lefranc**, "The topology of deterministic chaos : stretching, squeezing and linking", Department of Engineering Mathematics, University of Bristol, Royaume-Uni (janvier 2006).

3. **M. Lefranc**, “Analyse topologique du chaos déterministe : étirement, repliement et entrelacements”, SÉMINAIRE DE GÉOMÉTRIE HAMILTONIENNE, Institut de Mathématiques de Jussieu, Paris (novembre 2005).
4. **M. Lefranc**, J. Plumecoq, G. Boulant, S. Bielawski, and D. Derozier, “Topological analysis of chaotic lasers”, DEPARTMENT OF PHYSICS AND ATMOSPHERIC SCIENCES, DREXEL UNIVERSITY, Philadelphie, Etats-Unis (mai 2001).
5. **M. Lefranc**, J. Plumecoq, G. Boulant, S. Bielawski, and D. Derozier, “Analyse topologique du chaos dans les lasers : orbites périodiques, noeuds et codages symboliques, séminaire de DEA, CORIA, UNIVERSITÉ DE ROUEN, Rouen (Mars 2000).
6. **M. Lefranc**, J. Plumecoq, G. Boulant, S. Bielawski, and D. Derozier, “Topological analysis of low-dimensional chaos: periodic orbits, knots and symbolic encodings”, CENTER FOR CHAOS AND TURBULENCE STUDIES, NIELS BOHR INSTITUTE, Copenhague, Danemark (Décembre 1999).
7. **J. Plumecoq**, C. Szwaj, S. Bielawski, D. Derozier, et M. Lefranc, “Dynamique spatiotemporelle dans un laser à fibre”, LABORATOIRE DE MÉCANIQUE, UNIVERSITÉ DU HAVRE, Le Havre (mai 1999).
8. **M. Lefranc**, J. Plumecoq, G. Boulant, S. Bielawski, and D. Derozier, “L’analyse topologique de régimes chaotiques”, LABORATOIRE DE MÉCANIQUE DE LILLE, UNIVERSITÉ DE LILLE I, Lille (Février 1999).
9. **S. Bielawski**, G. Boulant, C. Szwaj, M. Lefranc, et D. Derozier, "Dynamique nonlinéaire dans les systèmes optiques", ENSSAT, Lannion (janvier 1999).
10. **M. Lefranc**, J. Plumecoq, G. Boulant, S. Bielawski, et D. Derozier, “L’analyse topologique des attracteurs chaotiques de petite dimension: orbites périodiques, noeuds et gabarits”, LABORATOIRE D’ARITHMÉTIQUE, GÉOMÉTRIE, ANALYSE ET TOPOLOGIE, UNIVERSITÉ DE LILLE I, Lille (Décembre 1998).
11. **D. Derozier**, G. Boulant, J. Plumecoq, S. Bielawski, et M. Lefranc, “La théorie des noeuds pour démêler le chaos”, LABORATOIRE DE SPECTROMÉTRIE PHYSIQUE, UNIVERSITÉ JOSEPH FOURIER, Grenoble (Février 1998).
12. **D. Derozier**, C. Szwaj, D. Leroy, S. Bielawski, T. Erneux, et M. Lefranc, “Structures spatio-temporelles dans le spectre d’un laser”, CORIA - URA CNRS 230 - INSA DE ROUEN, Rouen (Octobre 1997).

A.6 COMMUNICATIONS ORALES ET PAR AFFICHE

Les communications orales et par affiche sont distinguées par les mentions (C) et (A).

A.6.1 Conférences internationales

1. P.-E. Morant, M. Nizette, and M. Lefranc, “Towards a knotless topological analysis of chaos”, 9TH EXPERIMENTAL CHAOS CONFERENCE, Saõ José dos Campos, Brésil (mai 2006).
2. (A) J. Used, **J. C. Martìn**, and M. Lefranc, “Topological analysis of experimental chaotic signals from an EDF ring laser”, SECOND ’RIO DE LA PLATA’ WORKSHOP ON NOISE, CHAOS AND COMPLEXITY IN LASERS AND NONLINEAR OPTICS, Colonia del Sacramento, Uruguay (décembre 2005).

3. (C) **M. Lefranc**, "Topological analysis of experimental data: knot holders and topological entropies", EIGTH SIAM CONFERENCE ON APPLICATIONS OF DYNAMICAL SYSTEMS, Snowbird, Utah, Etats-Unis (Mai 2005).
4. (A) **M. Lefranc**, **M. Nizette**, and P.-E. Morant, "Alternative determinism principle for topological analysis of chaos", EIGTH SIAM CONFERENCE ON APPLICATIONS OF DYNAMICAL SYSTEMS, Snowbird, Utah, Etats-Unis (Mai 2005).
5. (C) P.-E. Morant, M. Nizette, and **M. Lefranc**, "Topological analysis of chaos and substitution dynamical systems", NUMERATION, TILINGS, SUBSTITUTIONS, Grenoble (mars 2005).
6. (C) A. Amon and **M. Lefranc**, "Topological signature of deterministic chaos in short nonstationary signals from an optical parametric oscillator", 8TH EXPERIMENTAL CHAOS CONFERENCE, Florence, Italie (juin 2004).
7. (C) **A. Amon**, M. Lefranc, M. Nizette, T. Erneux, "Bursting in optical parametric oscillators", EUROPEAN QUANTUM ELECTRONICS CONFERENCE (EQEC) 2003, Münich, Allemagne (juin 2003).
8. (C) P. Suret, D. Derozier, M. Lefranc, J. Zemmouri and **S. Bielawski**, "Incompatibility between cavity resonances and wavevector matching: influence on threshold and beam structures of OPOs", EUROPEAN QUANTUM ELECTRONICS CONFERENCE (EQEC) 2003, Münich, Allemagne (juin 2003).
9. (C) **M. Lefranc** and R. Gilmore, "Towards topological analysis of higher-dimensional chaos", SEVENTH SIAM CONFERENCE ON APPLICATIONS OF DYNAMICAL SYSTEMS, Snowbird, Utah, Etats-Unis (Mai 2003).
10. (C) A. Amon, M. Nizette, **M. Lefranc** and T. Erneux, "Bursting oscillations in optical parametric oscillators", SEVENTH SIAM CONFERENCE ON APPLICATIONS OF DYNAMICAL SYSTEMS, Snowbird, Utah, Etats-Unis (Mai 2003).
11. (C) **S. Bielawski**, J. Plumecoq, C.Szwaj, M. Lefranc, D. Derozier and T. Erneux, "A laser with parameters that vary slowly in space: bifurcation of the Eckhaus instability", SEVENTH SIAM CONFERENCE ON APPLICATIONS OF DYNAMICAL SYSTEMS, Snowbird, Utah, Etats-Unis (Mai 2003).
12. (C) **S. Bielawski**, J. Plumecoq, C.Szwaj, M. Lefranc, and D. Derozier, "Extensive and non-extensive spatio-temporal chaos in a laser", SEVENTH SIAM CONFERENCE ON APPLICATIONS OF DYNAMICAL SYSTEMS, Snowbird, Utah, Etats-Unis (Mai 2003).
13. (C) P. Suret, M. Lefranc, D. Derozier, J. Zemmouri and **S. Bielawski**, "Periodical mode hopping induced by thermo-optical effects in the optical parametric oscillator", CLEO/EUROPE EQEC, Münich, Allemagne (Juin 2001).
14. (C) Thomas Erneux, Dominique Derozier, Jérôme Plumecoq, Marc Lefranc, **Serge Bielawski** and Christophe Szwaj, "Eckhaus Instability Induced by Nonuniformities in An Optical System", SIXTH SIAM CONFERENCE ON APPLICATIONS OF DYNAMICAL SYSTEMS, Snowbird, Utah, Etats-Unis (Mai 2001).
15. (C) Dominique Derozier, Serge Bielawski, Jérôme Plumecoq, **Marc Lefranc** and Robert Gilmore, "Symbolic Dynamics and Topological Structure of Chaotic Dynamical Systems", SIXTH SIAM CONFERENCE ON APPLICATIONS OF DYNAMICAL SYSTEMS, Snowbird, Utah, Etats-Unis (Mai 2001).

16. (C) **E. Yao**, M. Lefranc, F. Papoff, "Extracting Low Dimensional Nonlinear Dynamics From Weak Optical Turbulence Through Topological Analysis", INTERNATIONAL QUANTUM ELECTRONICS CONFERENCE (IQEC 2000)", Nice, France (septembre 2000).
17. (C) P. Suret, D. Derozier, M. Lefranc, J. Zemmouri, and **S. Bielawski**, "Eckhaus instabilities induced by nonuniformities: a laser example", INTERNATIONAL QUANTUM ELECTRONICS CONFERENCE (IQEC 2000)", Nice, France (septembre 2000).
18. (C) P. Suret, D. Derozier, M. Lefranc, J. Zemmouri, and **S. Bielawski**, "Self-pulsing instabilities in an optical parametric oscillator: experimental observation and modeling of the mechanism", CONFERENCE ON CONTROL OF COMPLEX BEHAVIOR IN OPTICAL SYSTEMS AND APPLICATIONS, Münster, Allemagne (octobre 1999).
19. (C) J. Plumecoq, C. Szwaj, M. Lefranc, D. Derozier, T. Carr, T. Erneux et **S. Bielawski**, "Eckhaus instabilities induced by nonuniformities: a laser example", CONFERENCE ON CONTROL OF COMPLEX BEHAVIOR IN OPTICAL SYSTEMS AND APPLICATIONS, Münster, Allemagne (octobre 1999).
20. (C) J. Plumecoq and **M. Lefranc**, "From template analysis to generating partitions: Periodic orbits, knots and symbolic encodings", DYNAMICS DAYS 99, Côme, Italie (Juin 1999).
21. (A) **P. Suret**, D. Derozier, **M. Lefranc**, J. Zemmouri, and S. Bielawski, "Self-pulsing instabilities in an optical parametric oscillator", DYNAMICS DAYS 99, Côme, Italie (Juin 1999).
22. (C) J. Plumecoq, **Ch. Szwaj**, D. Derozier, M. Lefranc and S. Bielawski, "Laser Spectral Waves: from Pattern Formation to Spatiotemporal Chaos", FIFTH SIAM CONFERENCE ON APPLICATIONS OF DYNAMICAL SYSTEMS, Snowbird, Utah, Etats-Unis (Mai 1999).
23. (A) **J. Plumecoq**, C. Szwaj, P. Suret, D. Derozier, M. Lefranc, and **S. Bielawski**, "Instabilities induced by nonuniformities of control parameters in a laser", PATTERNS IN OPTICAL SYSTEMS (PINOS'98), Alicante, Espagne (Mai 1998).
24. (C) C. Szwaj, D. Leroy, S. Bielawski, T. Erneux, M. Lefranc and **D. Derozier**, "Spatio-temporal structures inside a laser spectrum", PATTERNS, NON-LINEAR DYNAMICS AND STOCHASTIC BEHAVIOUR IN SPATIALLY EXTENDED, COMPLEX SYSTEMS, Budapest, Hongrie (octobre 1997).
25. (C) G. Boulant, J. Plumecoq, S. Bielawski, D. Derozier, and **M. Lefranc**, "Model validation and symbolic dynamics of modulated lasers using template analysis", FOURTH EXPERIMENTAL CHAOS CONFERENCE, Boca Raton, Floride, Etats-Unis (août 1997).
26. (C) C. Szwaj, D. Leroy, S. Bielawski, T. Erneux, **M. Lefranc**, and D. Derozier, "Faraday instability and pattern formation inside a laser spectrum", FOURTH EXPERIMENTAL CHAOS CONFERENCE, Boca Raton, Floride, Etats-Unis (août 1997).
27. (A) G. Boulant, J. Plumecoq, **S. Bielawski**, D. Derozier, and M. Lefranc, "Knot-theoretic analysis of low-dimensional attractors", FOURTH SIAM CONFERENCE ON APPLICATIONS OF DYNAMICAL SYSTEMS, Snowbird, Utah, Etats-Unis (mai 1997).
28. (C) J. Plumecoq and **M. Lefranc**, "Constructing symbolic encodings for experimental attractors using topological analysis", THIRD EUROCONFERENCE ON NONLINEAR

DYNAMICS IN PHYSICS AND RELATED SCIENCES, Montecatini Terme, Italie (mai 1997).

29. (A) **G. Boulant**, S. Bielawski, D. Derozier, and **M. Lefranc**, "Towards a classification of the chaotic attractors of modulated lasers by template analysis", THIRD EUROCONFERENCE ON NONLINEAR DYNAMICS IN PHYSICS AND RELATED SCIENCES, Montecatini Terme, Italie (mai 1997).
30. (A) **G. Boulant, M. Lefranc**, S. Bielawski, and D. Derozier, "Global torsion of templates of a driven fiber laser", DYNAMICS DAYS, Lyon, France (juillet 1996).
31. (A) **M. Lefranc** and J. Plumecoq, "Constructing symbolic encodings of low-dimensional attractors from topological analysis", DYNAMICS DAYS, Lyon, France (juillet 1996).
32. (C) G. Boulant, M. Lefranc, S. Bielawski, and **D. Derozier**, "Global torsion of the template in a subharmonically driven fiber laser", INTERNATIONAL CONFERENCE ON NONLINEAR DYNAMICS AND CHAOS, Saratov, Russie (juillet 1996).
33. (A) **M. Lefranc** and **P. Glorieux**, "Topological analysis of chaotic signals from a CO_2 laser with modulated losses", MEASURES OF COMPLEXITY AND CHAOS II, Bryn Mawr, Pennsylvanie, États-Unis (août 1992)
34. (C) M. Lefranc and **P. Glorieux**, "Characterization of chaotic signals from a CO_2 laser with modulated losses", MEASURES OF COMPLEXITY AND CHAOS II, Bryn Mawr, Pennsylvanie, États-Unis (août 1992)

A.6.2 Conférences nationales

1. **A. Amon** et M. Lefranc, "Les sauts de mode tronquent la dynamique des oscillateurs paramétriques optiques", 9ÈME RENCONTRE DU NON-LINÉAIRE, Paris (mars 2006).
2. J. Used, J.-C. Martìn et **M. Lefranc**, "Nouvelles structures topologiques dans les signaux chaotiques d'un laser à fibre dopée Erbium", 9ÈME RENCONTRE DU NON-LINÉAIRE, Paris (mars 2006).
3. (C) P.-E. Morant, M. Nizette, and **M. Lefranc**, "Analyse topologique du chaos et déterminisme", 5IÈME COLLOQUE SUR LE CHAOS TEMPOREL ET LE CHAOS SPATIO-TEMPOREL, Le Havre (décembre 2005).
4. (C) P.-E. Morant, M. Nizette, and **M. Lefranc**, "Analyse topologique du chaos et substitutions", SUBSTITUTIONS ET AUTOMORPHISMES DE GROUPES LIBRES, Centre International de Rencontres Mathématiques de Luminy (avril 2005).
5. (C) Pierre-Emmanuel Morant, Michel Nizette et Marc Lefranc, "Un nouveau formalisme pour l'analyse topologique du chaos", HUITIÈME RENCONTRE DU NON LINÉAIRE, Paris (mars 2005)
6. (A) A. Amon et **M. Lefranc**, "Signature topologique de chaos déterministe dans un oscillateur paramétrique optique", SEPTIÈME RENCONTRE DU NON LINÉAIRE, Paris (mars 2004).
7. (C) **M. Lefranc** et R. Gilmore, "Vers l'analyse topologique du chaos de grande dimension", 4ÈME COLLOQUE SUR LE CHAOS TEMPOREL ET LE CHAOS SPATIO-TEMPOREL, Rouen (décembre 2003).

8. (A) A. Amon et **M. Lefranc**, " Signature topologique de chaos déterministe dans un oscillateur paramétrique optique non stationnaire", 4ÈME COLLOQUE SUR LE CHAOS TEMPOREL ET LE CHAOS SPATIO-TEMPOREL, Rouen (décembre 2003).
9. (A) A. Amon, P. Suret, S. Bielawski, D. Derozier, J. Zemmouri et **M. Lefranc**, "Instabilités et chaos dans les oscillateurs paramétriques optiques", 8ÈME COLLOQUE SUR LES LASERS ET L'OPTIQUE QUANTIQUE, Toulouse (Septembre 2003).
10. (C) **A. Amon**, M. Nizette, M. Lefranc et T. Erneux, "Observation expérimentale et modélisation de bursting dans les oscillateurs paramétriques optiques", SIXIÈME RENCONTRE DU NON LINÉAIRE, Paris (mars 2003).
11. (A) A. Amon et **M. Lefranc**, "Signature topologique de chaos déterministe dans un oscillateur paramétrique optique", SIXIÈME RENCONTRE DU NON LINÉAIRE, Paris (mars 2003).
12. (A) J. Plumecoq, C. Szwaj, M. Lefranc, D. Derozier et T. Erneux et **S. Bielawski**, "Instabilités spatiotemporelles dans un laser", CINQUIÈME RENCONTRE DU NON LINÉAIRE, Paris (mars 2002).
13. (A) P. Suret, **M. Lefranc**, D. Derozier, J. Zemmouri et S. Bielawski, "Dynamique temporelle et effets transverses dans les oscillateurs paramétriques optiques continus", 7ÈME COLLOQUE SUR LES LASERS ET L'OPTIQUE QUANTIQUE, Rennes (Septembre 2001).
14. (A) A. Amon, S. Bielawski, D. Derozier, T. Erneux, M. Lefranc, M. Nizette, P. Suret, J. Zemmouri, "Retard à la bifurcation dans les oscillateurs paramétriques optiques", 7ÈME COLLOQUE SUR LES LASERS ET L'OPTIQUE QUANTIQUE, Rennes (Septembre 2001).
15. (A) **A. Amon**, S. Bielawski, D. Derozier, T. Erneux, M. Lefranc, M. Nizette et J. Zemmouri, "Retard à la bifurcation dans les oscillateurs paramétriques Optiques", QUATRIÈME RENCONTRE DU NON LINÉAIRE, Paris (mars 2001).
16. (A) J. Plumecoq, C. Szwaj, D. Derozier, **M. Lefranc** et S. Bielawski, "Etude de l'instabilité d'Eckhaus induite par non-uniformités dans un laser", QUATRIÈME RENCONTRE DU NON LINÉAIRE, Paris (mars 2001).
17. (A) J. Plumecoq and **M. Lefranc**, "Analyse topologique de régimes chaotiques : application au codage symbolique", QUATRIÈME RENCONTRE DU NON LINÉAIRE, Paris (mars 2001).
18. (A) J. Plumecoq and **M. Lefranc**, "Orbites périodiques, théorie des noeuds et codages symboliques, TROISIÈME RENCONTRE DU NON LINÉAIRE, Paris (mars 2000).
19. (A) **P. Suret**, **D. Derozier**, M. Lefranc, J. Zemmouri, and S. Bielawski, "Oscillations spontanées dans les oscillateurs paramétriques optiques : observation expérimentale et modélisation du mécanisme", 6eme CONFÉRENCE SUR LES LASERS ET L'OPTIQUE QUANTIQUE, Bordeaux (septembre 1999).
20. (A) J. Plumecoq, **C. Szwaj**, **D. Derozier**, M. Lefranc et S. Bielawski, "Déstabilisation d'ondes stationnaires induite par variations spatiales d'un paramètre: l'exemple du laser", 6eme CONFÉRENCE SUR LES LASERS ET L'OPTIQUE QUANTIQUE, Bordeaux (septembre 1999).
21. (A) J. Plumecoq, **C. Szwaj**, D. Derozier, M. Lefranc, S. Bielawski et T. Erneux, "Ondes et chaos spatiotemporel dans le spectre d'un laser", CONGRÉS DE LA SFP 1999

(colloque 1: Structures spatio-temporelles et turbulence en dynamique non linéaire), Clermont-Ferrand (juillet 1999).

22. (C) **Jérôme Plumecoq**, Christophe Szwaj, Dominique Derozier, Marc Lefranc, et Serge Bielawski, "Instabilités induites par non-uniformités dans un laser", DEUXIÈME RENCONTRE DU NON LINÉAIRE, Paris (mars 1999).
23. (C) J. Plumecoq, G. Boulant, S. Bielawski, D. Derozier, and **M. Lefranc**, "Analyse topologique de régimes chaotiques : validation de modèles et application au codage symbolique", DEUXIÈME COLLOQUE SUR LE CHAOS TEMPOREL ET LE CHAOS SPATIO-TEMPOREL, Rouen (Décembre 1998).
24. (C) **J. Plumecoq**, C. Szwaj, D. Derozier, M. Lefranc, and S. Bielawski, "Chaos spatio-temporel induit par nonuniformités dans un laser", DEUXIÈME COLLOQUE SUR LE CHAOS TEMPOREL ET LE CHAOS SPATIO-TEMPOREL, Rouen (Décembre 1998).

Appendice B Collaborations, encadrement, activités diverses.

B.1 COLLABORATIONS

Collaborations ayant débouché sur une publication, parue ou en cours de rédaction.

- Francesco Papoff et Ennio Arimondo, Université de Pise (Italie)
- Robert Gilmore, Drexel University, Philadelphie (Etats-Unis).
- Eric Yao et Francesco Papoff, Université de Manchester (Royaume-Uni).
- Michel Nizette et Thomas Erneux, Université libre de Bruxelles (Belgique).
- Javier Used et Juan Carlos Martìn, Université de Saragosse (Espagne).
- François-Yves Bouget, observatoire océanologique de Banyuls/mer, Université Paris 6.

B.2 ENCADREMENT DOCTORAL ET POST-DOCTORAL

Depuis 1993, j'ai encadré ou co-encadré 7 étudiants de Diplôme d'Etudes Approfondies ou Mastère 2e année, ainsi que 6 thèses, dont deux sont encore en cours. Les thèmes concernés sont ceux développés dans ce mémoire : analyse topologique, oscillateurs paramétriques optiques, dynamique des lasers multimodes, et maintenant réseaux de régulation génétique.

B.3 PARTICIPATION À DES JURYS DE THÈSE

1. Guillaume Boulant, "Caractérisation topologique de lasers chaotiques", Thèse pour le Doctorat en Physique de l'Université Lille 1, spécialité Lasers, Molécules, Rayon-

TAB. **B.1 –** *D.E.A. ET MASTÈRE 2*

Nom	Année		Thème
G. Boulant	1993-1994	50 %	analyse topologique
J. Plumecoq	1994-1995	100 % (RA)	analyse topologique
P. Suret	1996-1997	50 %	oscill. paramétriques optiques
Y. Prat	1997-1998	50 % (RA)	oscill. paramétriques optiques
C. Giuraniuc	2000-2001	50 %	analyse topologique
P.-E. Morant	2003-2004	50 % (RA)	contrôle du chaos
C. Vandermoere	2005-2006	100 % (RA)	Réseaux génétiques

TAB. **B.2 –** *THÈSES DE DOCTORAT*

Nom	Année		Thème
G. Boulant	1994-1997	50%	analyse topologique
J. Plumecoq	1996-2003	50%	analyse topologique et dynamique des lasers fortement multimodes
P. Suret	1997-2000	50%	oscillateurs paramétriques optiques
A. Amon	2000-2003	50 %	oscillateurs paramétriques optiques
P.-E. Morant	2004-	50 %	anal. topologique/réseaux génétiques
C. Vandermoere	2006-	50 %	réseaux de régulation génétique

TAB. **B.3 –** *STAGES POST-DOCTORAUX*

Nom	Année	Origine	Thème
M. Nizette	2004-2005	Bruxelles	analyse topologique

nement Atmosphérique, sous la direction de Dominique Derozier, soutenue le 24 septembre 1997 (co-directeur de thèse).

2. Céline Clément, “L’ontogenèse de contrôle temporel du comportement humain envisagé comme un système dynamique non linéaire”, Thèse pour le Doctorat en Psychologie Expérimentale et du Développement de l’Université de Lille 3, sous la direction de Jean-Claude Darcheville, soutenue le 14 décembre 1999 (examinateur).

3. Pierre Suret, “Dynamique temporelle et effets transverses dans les oscillateurs paramétriques continus : observations expérimentales et modélisation”, Thèse pour le Doctorat en Physique de l’Université de Paris XI, spécialité Champs, Particules, Matière, sous la direction de Jaouad Zemmouri, soutenue le 20 septembre 2000 (co-directeur de thèse).

4. Olivier Ménard, “Modélisation de dynamiques complexes : des systèmes chaotiques à la description de la dispersion cyclique de moteurs à allumage commandé”, Thèse pour le Doctorat en Physique, spécialité Energétique, de l’Université de Rouen, sous la direction de Gérard Gouesbet, soutenue le 13 novembre 2000 (examinateur).

5. Michel Nizette, “Temporal dynamics of driven nonlinear optical systems”, Thèse pour le Doctorat en Sciences de l’Université Libre de Bruxelles, sous la direction de Thomas Erneux, soutenue le vendredi 28 mars 2003 (examinateur).
6. Laurent Longchambon, “Effets de polarisation dans les mélanges paramétriques à trois ondes en cavité : applications au traitement classique et quantique de l’information”, Thèse pour le Doctorat de l’Université Paris VI, sous la direction de Claude Fabre, soutenue le 16 juin 2003 (examinateur).
7. Axelle Amon, “Dynamique temporelle des oscillateurs paramétriques optiques continus : oscillations multimodes, oscillations en rafales et chaos”, Thèse pour le Doctorat de l’Université de Lille 1, sous la direction de Jaouad Zemmouri, soutenue le 25 septembre 2003 (co-directeur de thèse).
8. Jérôme Plumecoq, “Caractérisation de systèmes dynamiques de petite et grande dimensions : de l’analyse topologique aux codages symboliques, et instabilités spatio-temporelles dans un laser fortement multimode”, Thèse pour le Doctorat de l’Université de Lille 1, sous la direction de Pierre Glorieux, soutenue le 6 octobre 2003 (co-directeur de thèse).
9. Alexandre Locquet, “Analyses numériques de dynamiques chaotiques dans des systèmes optiques à délai : propriétés de synchronisation et extraction du déterminisme”, Thèse pour le Doctorat de l’Université de Franche-Comté, sous la direction de Laurent Larger, soutenue le 13 décembre 2004 (examinateur).
10. Paul François, “Réseaux génétiques : conception, modélisation et dynamique”, Thèse pour le Doctorat de l’Université Paris VII, sous la direction de Vincent Hakim, soutenue le 16 septembre 2005 (examinateur).
11. Linda Achour, “Asynchronismes des interactions patient-ventilateur en ventilation non invasive”, Thèse pour le Doctorat de l’Université de Rouen, sous la direction de Christophe Letellier, soutenue le 22 novembre 2005 (examinateur).

B.4 ENSEIGNEMENT

Lors de ma thèse, j’ai bénéficié pendant trois ans (1988-90 et 1991-92) d’un poste d’Ancien normalien doctorant, puis d’un poste d’Attaché temporaire d’enseignement et de recherche (1992-93). Au cours de ces quatre années, j’ai assuré l’horaire normal d’un maître de conférences, à savoir 192 heures eq. TD par an, en première année de DEUG B et en Licence de Physique.

J’ai par ailleurs assuré, depuis la création à la rentrée 1994 du module d’Analyse Numérique de la Licence de Physique jusqu’en 1996-97, vingt heures de cours-travaux dirigés par an dans le cadre de cet enseignement. J’ai en particulier participé à sa mise en place et à la définition de son contenu avec les trois collègues y intervenant également.

B.5 COMITÉS DE LECTURE ET EXPERTISE

J’ai été ces dernières années rapporteur pour les journaux suivants (par ordre de fréquence) :

– Physical Review E
– Physical Review Letters

- Physica D
- European Physical Journal
- Physics Letters A
- Applied Physics B

Je suis par ailleurs régulièrement contacté par des agences de moyens, telles que la National Science Foundation (États-Unis) ou l'Engineering and Physical Sciences Research Council (Royaume-Uni) pour évaluer des demandes de financement [3 rapports dans 2 dernières années], ainsi que par des Universités américaines pour évaluer le dossier de candidats à des promotions [2 rapports dans les 2 dernières années].

B.6 ANIMATION SCIENTIFIQUE

- Membre depuis 2004 et Responsable depuis 2005 des comités scientifique et d'organisation de la Rencontre du Non Linéaire, manifestation qui se tient tous les ans à l'Institut Henri Poincaré, à Paris, et rassemble la communauté française du non linéaire (environ 100 participants).
- Membre du comité de direction du GDR 2489 DYCOEC, "DYnamique et COntrôle des Ensembles Complexes"
- Membre depuis 2003 du comité Scientifique du colloque sur le chaos temporel et le chaos spatio-temporel.
- Membre du comité local d'organisation du Congrès 2005 de la Société Française de Physique et de la Belgian Physical Society (Lille).

B.7 RESPONSABILITÉS ADMINISTRATIVES

Nationales

- Membre nommé, de 1996 à 2000, du Conseil National des Universités (30ième section).

Locales

- Membre nommé, à compter de 2004, de la Commission de Spécialistes de l'Université de Lille I (28ième, 30ième et 37ième sections).
- Membre nommé, à compter de 2001, de la Commission de Spécialistes de l'Université du Littoral (28ième, 30ième et 62ième sections).
- Membre nommé, de 1995 à 1997 inclus, de la Commission de Spécialistes de l'Université de Lille I (28ième, 30ième et 37ième sections).

B.8 TITRES UNIVERSITAIRES

- Docteur de l'Université des Sciences et Technologies de Lille (Décembre 1992).
- Agrégé de Sciences Physiques, option Physique (1991).
- Ancien élève de l'École normale supérieure de la rue d'Ulm (1984-88).

B.9 CURRICULUM VITAE

Né le 6 juin 1965 à Soissons, Aisne.

1982	Baccalauréat, série C.
1982-1984	Classes Préparatoires au Lycée Faidherbe à Lille. Admission à l'École normale supérieure de la rue d'Ulm, concours Physique.
1984-1985	Licence et Maîtrise de Physique (Université Paris VI).
1985-1986	Diplôme d'Études Approfondies de Physique Théorique (Université Paris VI et ENS). Stage d'un mois au Laboratoire d'Optique Quantique de l'École polytechnique (laser à colorant à impulsions ultra-courtes).
1986-1988	Travail de thèse dans le cadre de la Division de Physique Théorique de l'Institut de Physique Nucléaire d'Orsay, sous la direction de Jan Stern, Directeur de Recherche au CNRS (« Champs de jauge de spin quelconque, application aux théories de cordes et supercordes »).
1988	Nomination comme Ancien Normalien Doctorant (AND) à l'Université des Sciences et Technologies de Lille (USTL). Changement de sujet de thèse.
1988-1990	AND à l'USTL. Travail de thèse au Laboratoire de Spectroscopie Hertzienne sous la direction de Pierre Glorieux, Professeur à l'USTL (« Caractérisation du chaos dans les lasers CO_2 ») et enseignement en DEUG B 1ière année (192 h. eq. TD par an).
1990-1991	Service militaire au 43ième RI (Lille). Admission à l'Agrégation de Physique.
1991-1992	AND à l'USTL. Travail de thèse et enseignement en Licence de Physique et en DEUG B 1ière année (192 h. eq. TD).
1992-1993	Attaché Temporaire d'Enseignement et de Recherche à l'Université de Lille 1. Thèse de doctorat soutenue le 17 décembre 1992. Enseignement en Licence de Physique et en DEUG B 1ière année (192 h. eq. TD).
1993-présent	Chargé de Recherche au Laboratoire de Spectrocopie Hertzienne, devenu en 1998 le Laboratoire de Physique des Lasers, Atomes, Molécules. Passage CR1 en 1997.

Appendice C
Publications “Caractérisation du chaos”

"Homoclinic chaos in a laser containing a saturable aborber"

M. Lefranc, D. Hennequin, and D. Dangoisse

J. Opt. Soc. Am. B **8**, (1991)

a reprint from Journal of the Optical Society of America B 239

Homoclinic chaos in a laser containing a saturable absorber

M. Lefranc, D. Hennequin, and D. Dangoisse

Laboratoire de Spectroscopie Hertzienne, Associé au Centre National de la Recherche Scientifique, Université des Sciences et Techniques de Lille-Flandres-Artois, F-59655 Villeneuve d'Ascq Cedex, France

Received August 15, 1989; accepted October 11, 1990

Checks of homoclinic chaos made with nonlinear analysis techniques have been performed on the signals coming from a CO_2 laser containing CH_3I as a saturable absorber. The one-dimensional return maps of the regimes appearing inside the alternating periodic chaotic sequence are typical of homoclinic chaos. Numerical simulations give results in good agreement with the experimental observations. In the case of a fast absorber, a homoclinic tangency to a cycle created in a subcritical Hopf bifurcation is seen to be responsible for the homoclinic behavior observed in the model.

1. INTRODUCTION

A laser containing a saturable absorber (LSA) was studied extensively in connection with the requirement for easy and efficient modulation of CO_2 laser radiation, and many molecules have been used as saturable absorbers for passive Q switching (PQS). In the PQS regime, the laser is spontaneously unstable, and its output intensity exhibits periodic pulses of various shapes. In the beginning of the 1970's this PQS regime received much attention as new absorbing molecules were searched for, but only a few publications were devoted to the mechanisms from which PQS originates. To our knowledge, the first model able to reproduce the PQS shapes was a four-level model for both the laser medium and the absorber.[1–4] In the beginning of the 1980's there was renewed interest in the LSA as the field of optical instability grew.[5] New shapes of PQS pulses were discovered,[6–8] and the dual four-level model was unable to reproduce them correctly.[9] A three-plus-two-level model was then introduced by Tachikawa *et al.* to reproduce the entire experimentally observed phenomenology.[7,8,10] This model was later completed by the addition of a rotational-level bath in the gain medium.[11] Recently, chaotic pulses were observed both experimentally[12,13] and theoretically.[14] The dynamics of this chaos has been interpreted through a topological analysis of the phase space associated with the signal.[12,13,15]

The PQS regime usually corresponds to the existence of two unstable fixed points: the I_0 point has zero intensity and is a saddle point and the I_+ point has a nonzero intensity and is a saddle focus. As a control parameter is varied, the I_+ point loses its stability through a Hopf bifurcation, generating type II PQS, which destabilizes through period doubling.[12,16] Then alternating periodic and chaotic sequences appear,[12] similar to those encountered in the neighborhood of a homoclinic bifurcation,[17,18] when some conditions specified by Shil'nikov[19] are satisfied. However, the situation here is complicated by the presence of the second fixed point in the phase space and possibly by a perturbation that is due to noise.[20]

To our knowledge, no characterization of the chaotic behavior inside the alternating periodic–chaotic sequence other than in the preliminary results given by us[21] and in a related paper by Papoff *et al.*[22] has been made. Similar characterizations have been made for a CO_2 laser with feedback[23] and in the Belousov–Zhabotinskii reaction.[24] In fact, although chaos has been observed in the LSA, there has been no demonstration that this was Shil'nikov chaos and two phenomena may, in some situations, inhibit this chaotic behavior: the noise[20] and a strong attraction of I_0 along its stable manifold, which can destroy sensitivity to the initial conditions.[13,15]

Here we report on an analysis that uses methods inspired by the dynamical system theory [phase portraits, Poincaré maps, and one-dimensional (1-D) maps] of the erratic behavior inside the alternating chaotic–periodic sequence. We show that in the CO_2 + CH_3I LSA, in spite of the presence of a second fixed point in the phase space, the dynamics qualitatively follows the Shil'nikov behavior. We also study the evolution of the chaos between two periodic regimes and show that the transition from periodic behavior to chaos follows two different routes: period doubling on the one hand and the Pomeau–Manneville (type I intermittency) route on the other.

This paper is organized as follows: in Section 2 an analysis of experimental data is presented, showing that the PQS regime possesses the properties of the Shil'nikov chaos. In Section 3 the stability of the fixed points of a standard model of the LSA is discussed. The numerical solutions of this system are analyzed in Section 4 by using the same techniques as in Section 2 together with Floquet's theory.

2. EXPERIMENTS

The experimental device has already been described elsewhere.[3] It is composed of a CO_2 + CH_3I LSA, in which amplification is obtained in a mixture of CO_2, N_2, and He in the approximate proportions of 3:6.5:1 for a total pressure of 7.8 Torr; the absorber is CH_3I at a pressure of ~30 mTorr. The laser is tuned on the 10(P)32 line, in quasi-resonance with at least three absorption lines of CH_3I.[25] The general behavior exhibited by the LSA when the cavity detuning or the pump parameter is varied in this region of the parameter space[12] shows a cw regime followed by a periodic regime that becomes chaotic through

0740-3224/91/020239-11$05.00

240 J. Opt. Soc. Am. B/Vol. 8, No. 2/February 1991 Lefranc *et al.*

a period-doubling cascade; then periodic and chaotic sequences alternate, as chemical reactions have shown.[26] Beyond this sequence, the laser is off. In the particular conditions of the results discussed below, the control parameter is the cavity detuning, and the observed order of behavior is cw, T, $2T$, $4T$, chaos, $P^{(3)}$, $C^{(2)}$, $P^{(2)}$, $C^{(1)}$, $P^{(1)}$, $P^{(0)}$, off. The notation used here was introduced in Ref. 15 and may be summarized as follows:

(i) The T regime refers to type II PQS: the output of the LSA is a T periodic oscillation, emerging from the cw regime through a Hopf bifurcation. It evolves toward chaos through a period-doubling cascade (regimes 2^nT).

(ii) The $P^{(n)}$ regimes refer to type I PQS: the output of the LSA exhibits periodic pulses composed of a narrow high peak followed by a series of n undulations at period T. It has been observed[12] that the pulses also undergo a series of period doublings culminating in an erratic regime called $C^{(n)}$ when the output is located in parameter domains between the $P^{(n)}$ and $P^{(n+1)}$ regions.

We have analyzed the erratic regimes $C^{(n)}$ to find characteristic properties that support the existence of homoclinic chaos. The most remarkable one concerns the 1-D maps constructed from the Poincaré section of the attractor: the 1-D map of homoclinic chaos shows $n + 1$ branches and possibly a part of an $(n + 2)$th one; each branch is associated with p spirals in the phase space ($p \leq n$ or $p \leq n + 1$), and the distance between the branches decreases when p increases. The number of

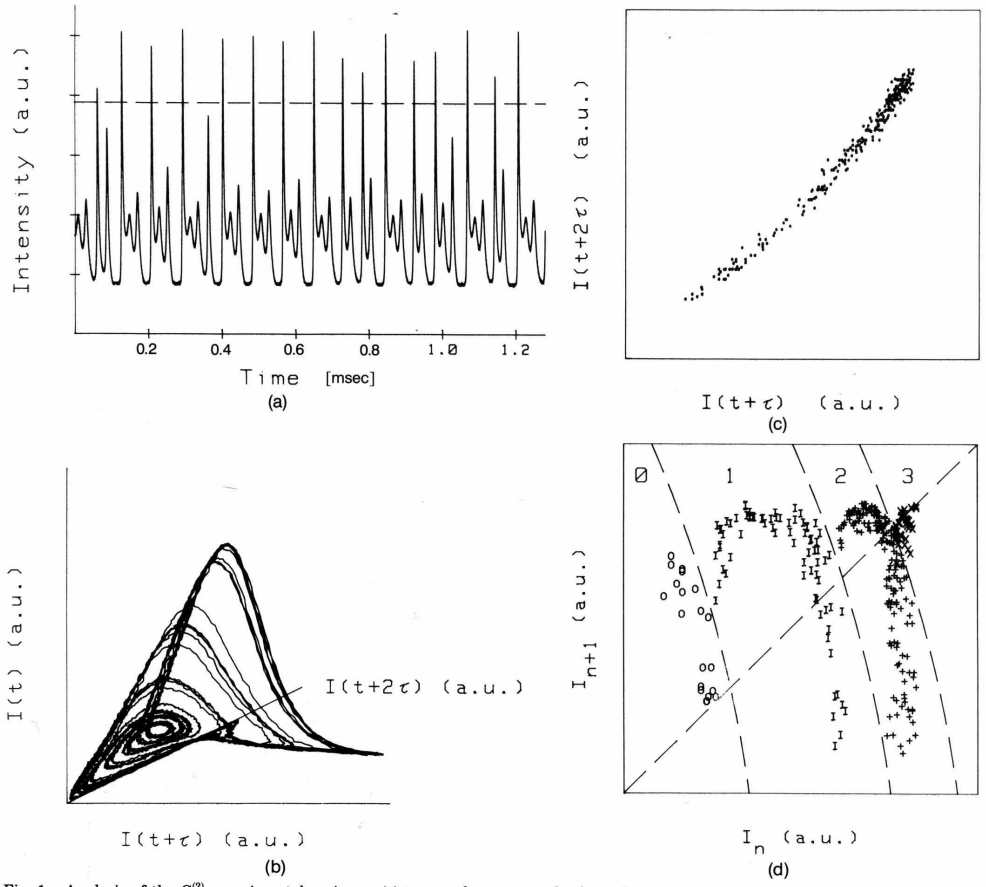

Fig. 1. Analysis of the $C^{(2)}$ experimental regime: (a) temporal sequence; (b) three-dimensional reconstruction of the attractor in the phase space $I(t)$, $I(t + \tau)$, $I(t + 2\tau)$, where $\tau = 3.2$ μsec; (c) Poincaré section performed in the reinjection loop of the attractor in a plane indicated by the dashed line in (a); (d) first return map of the Poincaré section of (c). Each point of coordinates (I_n, I_{n+1}) is represented by the number p of undulations that separate the nth and the $(n + 1)$th crossings through the Poincaré section. The symbols O, I, +, and × correspond, respectively, to $p = 0$, 1, 2, and 3. The dashed curves separate regions corresponding to a given p, which is indicated for each region at the top of each the figure. The experimental conditions are given in the text.

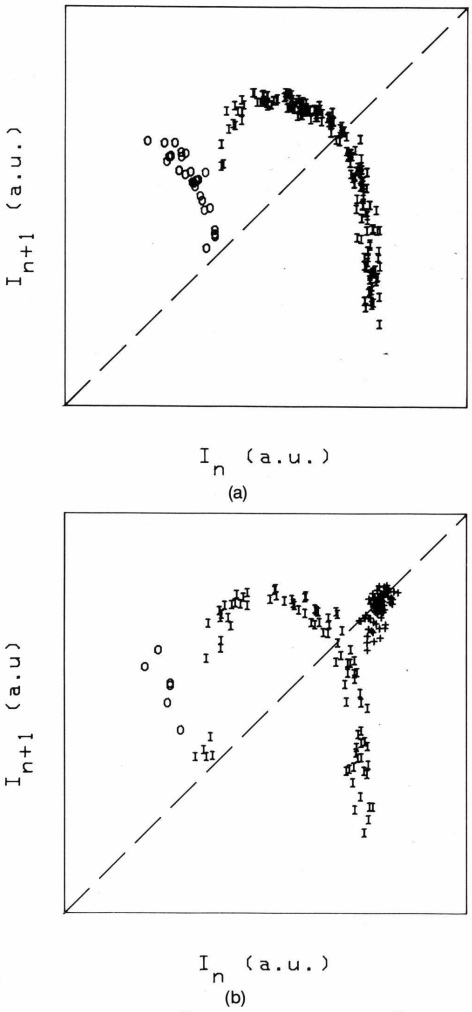

Fig. 2. 1-D maps of $C^{(1)}$ chaos: (a) close to the $P^{(1)}$ regime, (b) close to the $P^{(2)}$ regime. The symbols are the same as in Fig. 1(d).

branches becomes infinite as the system approaches the homoclinic bifurcation.[24,27]

Experimentally, the only accessible variable of the flow is the laser intensity. An example of its temporal evolution in a $C^{(n)}$ regime is shown in Fig. 1(a) for $n = 2$. The signal shows a succession of $P^{(p)}$-type pulses with $p \leq 3$. The 1-D map is obtained in three steps: (i) A reconstruction of the attractor is undertaken, using the time-delay method. A projection of this attractor in the three-dimensional space $I(t)$, $I(t + \tau)$, $I(t + 2\tau)$, with $\tau = 3.2$ μsec (i.e. $\sim T/7$, where T is the period of the small undulations), is shown in Fig. 1(b). It is composed of a spiraling part diverging from I_+ and of a reinjection loop, which, in this three-dimensional representation, passes close to I_0. (ii) A Poincaré section of this attractor is then obtained at $I(t)$ constant [Fig. 1(c)]. The value of the constant is chosen so that the Poincaré section plane cuts the trajectory in the middle of the reinjection loop, on the ascending part of the loop [dashed line of Fig. 1(a)]. (iii) Eventually the first return map associated with this section is plotted. As the Poincaré section lies almost on a straight line, this return map is equivalent to a 1-D map. The first return map $I_n(t + \tau)$, $I_{n+1}(t + \tau)$ obtained for the $C^{(2)}$ regime is shown in Fig. 1(d). Three branches appear clearly, and the beginning of a fourth one may be seen in the top right-hand corner of the figure. Additional information is provided by counting the number of small undulations separating the two crossings through the Poincaré section associated with each point. The dashed curves in Fig. 1(d) define regions where the same number of undulations are found. It is clear that each region corresponds to a branch. Note that the distance between the branches decreases when p increases. All these properties hold for other experimentally observed $C^{(n)}$ regimes. The entire behavior described above is consistent with the properties of homoclinic chaos and supports its existence in the LSA.[24]

The characterization of the behavior can be refined by studying the evolution of the chaos between the $P^{(n)}$ and $P^{(n+1)}$ regimes. The passage from $P^{(n)}$ to $C^{(n)}$ is well understood, as it occurs through a cascade of period-doubling bifurcations. On the other hand, the passage from $C^{(n)}$ to $P^{(n+1)}$ in the LSA has not been discussed. We have plotted the 1-D maps of the $C^{(1)}$ regime in a region close to $P^{(1)}$ [Fig. 2(a)] and in a region close to $P^{(2)}$ [Fig. 2(b)]. In the first case, only the two branches corresponding to $p = 0$ and $p = 1$ are visible, whereas in the second case the beginning of a third branch corresponding to $p = 2$ appears below the 45° line. This may be considered part of the third branch of the $C^{(2)}$ regime [Fig. 1(d)]. Although the control parameter noise prevents our bringing our system close to the bifurcation, the transition from $C^{(1)}$ to $P^{(2)}$ might be interpreted as follows: When the system evolves to $P^{(2)}$, a third branch appears in the first return map below the 45° line, approaching it tangentially. Finally, $P^{(2)}$ appears through a tangent bifurcation. The other experimentally observed $C^{(n)}$–$P^{(n+1)}$ transitions evolve in the same way. This behavior, completed by the fact that the transition from the $P^{(n)}$ to the $C^{(n)}$ regime occurs through a period-doubling cascade, corresponds exactly to the one exhibited by homoclinic chaos. These results confirm that the CO_2 + CH_3I LSA in our experimental conditions exhibits a dynamical behavior consistent with the properties known for Shil'nikov chaos.

3. MODEL OF THE LASER CONTAINING A SATURABLE ABSORBER

The various theoretical models of the PQS LSA differ in the number of molecular levels considered. Early models aimed at a quantitative agreement for particular experimental parameters and included a large number of variables to model the relaxation processes.[1,2] In an attempt to reach a more global description of the LSA with the

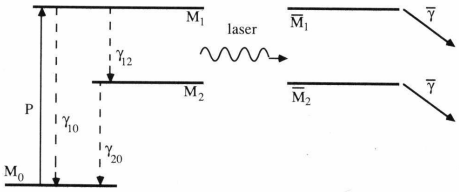

Fig. 3. Schematic representation of the energy levels used in the theoretical model of the LSA. The quantities with overbars refer to the absorber medium, those without overbars to the active medium.

simplest model, Powell *et al.* introduced a two-level description for the absorber and the active medium,[28] which displays a rich phenomenology if molecular polarization and cavity detuning are taken into account.[29] However, this model could hardly provide the range of parameters in which instabilities appear in the CO_2 LSA. For this reason, Arimondo *et al.*[3] proposed including the vibrational manifolds to which the lasing and absorbing levels are coupled, thus reproducing well the experimental domain of existence of PQS.

Nevertheless, there remained a qualitative discrepancy, since this four-level model is unable to predict the $P^{(n)}$ regimes observed experimentally. A definite step toward such prediction was made by Tachikawa and coworkers,[7,8,10] who introduced the ground state of the CO_2 molecule as a third level for the active medium. With this model other authors were able to obtain the $P^{(n)}$ periodic states and the $C^{(n)}$ erratic ones numerically.[14,15] Although Tachikawa's model neglects the influence of inhomogeneous broadening, it provides surprisingly good agreement with experimental observations.

We shall therefore use this model, which is schematically represented in Fig. 3, in numerical simulations to determine whether the different features reminiscent of homoclinic chaos observed experimentally can be reproduced.

The equations, verified by the photon density ϕ, the population densities of the upper lasing level (M_1), the lower level (M_2), and the ground state (M_0) and the population difference in the absorber $\bar{M}$, are

$$\dot{\phi} = \phi(\zeta\mathcal{A}(M_1 - M_2) - \bar{\zeta}\bar{\mathcal{A}}\bar{M} - 2\kappa), \tag{1a}$$

$$\dot{M}_1 = -\mathcal{A}(M_1 - M_2)\phi + PM_0 - (\gamma_{10} + \gamma_{12})M_1, \tag{1b}$$

$$\dot{M}_2 = \mathcal{A}(M_1 - M_2)\phi - \gamma_{20}M_2 + \gamma_{12}M_1, \tag{1c}$$

$$\dot{M}_0 = \gamma_{10}M_1 + \gamma_{20}M_2 - PM_0, \tag{1d}$$

$$\dot{\bar{M}} = -2\bar{\mathcal{A}}\phi\bar{M} - \bar{\gamma}(\bar{M} - \bar{M}^*), \tag{1e}$$

where ζ ($\bar{\zeta}$) is the relative length of the amplifying (absorbing) medium, P is the pumping rate, $2\kappa = cT/L$ is the cavity-damping rate, L is the total cavity length, T is the mirror transmittivity, $\bar{M}^*$ is the equilibrium population in the absorber, and $\mathcal{A}(M_1 - M_2)$ ($\bar{\mathcal{A}}\bar{M}$) is the saturated amplification (absorption) coefficient. γ_{ij} are the relaxation rates from level i to level j, and $\bar{\gamma}$ is the relaxation rate of the absorber's population inversion. This set of equations is just a generalization of the two-level rate-equation model of the LSA, modified to take into account the presence of the third level in the active medium and in which only the most relevant relaxation mechanisms have been included. The amplification coefficient $\mathcal{A}$ is corrected to take into account the rotational partition function and the level degeneracy factor, since emission occurs between two rotational levels not represented in this model. Note also that spontaneous emission has been neglected in the equation for the photon density.

As $M_0 + M_1 + M_2 = N$ is a constant, a change of variables can then be undertaken to express the dynamics of the LSA in terms of the evolution of the active molecule population difference $M = M_1 - M_2$ and the dimensionless intensity $I = 2\mathcal{A}\phi/\gamma_2$:

$$\dot{I} = I(\zeta\mathcal{A}M - \bar{\zeta}\bar{\mathcal{A}}\bar{M} - 2\kappa), \tag{2a}$$

$$\dot{M} = -(I + 1)\gamma_2 M + PM_0 + \gamma_1(N - M_0), \tag{2b}$$

$$\dot{M}_0 = \gamma_2 N - \gamma_1 M - (\gamma_2 + P)M_0, \tag{2c}$$

$$\dot{\bar{M}} = -2\bar{\mathcal{A}}\phi\bar{M} - \bar{\gamma}(\bar{M} - \bar{M}^*), \tag{2d}$$

where the combined relaxation rates $\gamma_2 = (\gamma_{20} - \gamma_{10} - 2\gamma_{12})/2$ and $\gamma_2 = (\gamma_{20} + \gamma_{10} + 2\gamma_{12})/2$ have been introduced as well as the total density of molecules in the amplifier $N = M_0 + M_1 + M_2$.

In Eq. (2b) the term $PM_0 + \gamma_1(N - M_0)$ may be considered a source term. When the relaxation rates are such that $\gamma_{10} + 2\gamma_{12} = \gamma_{20}$, the source term is reduced to PM_0, and the model reduces to a two-level model for both the absorber and the amplifier since Eq. (2c) is no longer coupled to the other ones.

Introducing dimensionless quantities

$$a = \frac{\bar{\mathcal{A}}}{\mathcal{A}}\frac{\gamma_2}{\bar{\gamma}}, \qquad b = \left(\frac{\gamma_1}{\gamma_2}\right)^2,$$

$$\varepsilon = \frac{\gamma_2}{2\kappa}, \qquad \bar{\varepsilon} = \frac{\bar{\gamma}}{2\kappa},$$

$$A = P(\sqrt{b} + 1)\frac{\mathcal{A}\zeta N}{2\kappa\gamma_2}, \qquad \bar{A} = \bar{M}^*\frac{\bar{\zeta}\bar{\mathcal{A}}}{2\kappa},$$

$$U = M\zeta\frac{\mathcal{A}}{2\kappa}, \qquad \bar{U} = \bar{M}\bar{\zeta}\frac{\bar{\mathcal{A}}}{2\kappa},$$

a new variable representing the source term

$$W = \frac{\mathcal{A}}{2\kappa}\frac{\zeta}{\gamma_2}[PM_0 + \gamma_1(N - M_0)],$$

and a dimensionless time $t' = 2\kappa t$, we can reformulate Eqs. (2) as follows:

$$\dot{I} = I(U - \bar{U} - 1), \tag{3a}$$

$$\dot{U} = \varepsilon[W - U(1 + I)], \tag{3b}$$

$$\dot{W} = \varepsilon(A + bU - W), \tag{3c}$$

$$\dot{\bar{U}} = \bar{\varepsilon}[\bar{A} - \bar{U}(1 + aI)]. \tag{3d}$$

In Eq. (3c) the P/γ_2 term has been considered negligible compared to unity, in good agreement with the values chosen by Tachikawa *et al.*[9] and those used in our numerical estimations ($P/\gamma_2 < 1.5 \times 10^{-3}$).

The threshold of the laser occurs at $A = A_{th} = (A + 1)(1-b)$. Above this threshold, Eqs. (3) have two

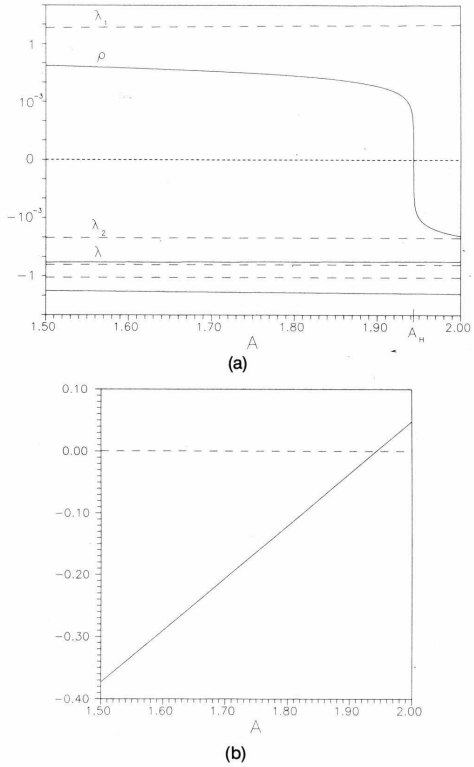

Fig. 4. (a) Evolution of the eigenvalues of the I_0 (dashed lines) and the I_+ (solid lines) eigenvalues as functions of the A parameter. $A_H = 1.943$ is the Hopf bifurcation point. (b) Values of ρ/λ (solid line) and $(\lambda_2/\lambda_1)(\rho/\lambda)$ (dashed line) versus A. Their absolute values are both smaller than 1.

stationary solutions corresponding in phase space to two fixed points I_0 and I_+ whose coordinates $(I_0, U_0, W_0, \bar{U}_0)$ and $(I_+, U_+, W_+, \bar{U}_+)$ are

$$I_0 = 0, \qquad U_0 = W_0 = A(1-b)^{-1}, \qquad \bar{U}_0 = \bar{A},$$

$$I_+ = \frac{a(A+b-1) - (\bar{A}+1) + \{[a(A+b-1) - (\bar{A}+1)]^2 + 4a(A - A_{\mathrm{th}})\}^{1/2}}{2a},$$

$$U_+ = A(1 + I_+ - b)^{-1},$$

$$W_+ = A(1 + I_+)(1 + I_+ - b)^{-1},$$

$$\bar{U}_+ = \bar{A}(1 + aI_+)^{-1}.$$

A linear stability analysis provides the eigenvalues of the linear flow in the vicinity of these two fixed points. With parameters corresponding to our experiments, the stability of I_0 is characterized by four real eigenvalues $(\lambda_1, \lambda_2, \lambda_3$, and λ_4, where λ_1 is positive and corresponds to an eigenvector collinear to the intensity vector and λ_2, λ_3, and λ_4 are negative, $|\lambda_4| \geq |\lambda_3| \geq |\lambda_2|$), and I_+ is associated with two real negative eigenvalues (λ and λ', $|\lambda'| \geq |\lambda|$) and two complex-conjugate eigenvalues ($\rho \pm i\omega$, where ρ is positive). I_0 is therefore a saddle point whose unstable manifold is along the intensity direction and I_+ is a saddle focus. These eigenvalues are plotted versus the pump parameter in Fig. 4. Note that the eigenvalues of I_+ have real parts with different orders of magnitude: for typical values of the parameters, $|\lambda'| \approx 30|\lambda| \approx 300|\rho|$. Therefore one expects that, near I_+, the eigendirection corresponding to λ' will be irrelevant and that I_+ will be equivalent to a three-dimensional saddle-focus fixed point with eigenvalues λ, $\rho \pm i\omega$. Note that the eigenvector corresponding to λ' is quasi-orthogonal to the (U, W) plane, indicating that these two variables, which describe the amplifying medium, evolve on a slow time scale.

The dynamics of the system depends strongly on the relative values of the eigenvalues of I_+ and of the global structure of the flow. Shil'nikov showed that if a homoclinic orbit is associated with a saddle focus such as I_+, and if in the neighborhood of this point the characteristic time of the flow following the focus directions is the largest one ($\rho/\lambda < 1$), the system has a chaotic behavior.[19] This is a sufficient condition but not a necessary one. In particular, if the unstable and the stable manifolds are not perfectly connected but close to form a homoclinic orbit, chaos may occur.[30] The values of ρ/λ are plotted in Fig. 4(b) for the set of parameters discussed in Section 4. It is clear that the Shil'nikov condition for chaos is fulfilled, but, as the existence of a homoclinic orbit cannot be predicted analytically, only a numerical resolution of the equations will allow the presence of chaos to be inferred.

The situation is complicated here by the presence of the second fixed point, I_0. Either of two limit configurations is possible: (i) The two points are coupled by a homoclinic cycle, which connects the unstable manifold of I_+ to the stable manifold of I_0 and the unstable manifold of I_0 to the stable manifold of I_+. In this case, the Shil'nikov condition for chaos becomes $|(\lambda_2/\lambda_1)(\rho/\lambda)| < 1$,[39] indicating that too large an attractive power of I_0 (λ_2 large) will destroy the chaos by rescaling the trajectory at each passage in the vicinity of I_0. (ii) The two points are completely decoupled, and their respective stable and unstable manifolds always remain far from the conditions of intersection. In this case, a trajectory coming from I_+ always remains out of reach from I_0, which does not interfere in the dynamics. Between these two limit cases a large number of possible intermediate configurations exists in which the influence of I_0 evolves with the strength of the coupling between the two fixed points.

Figure 4(b) shows the values of $(\lambda_2/\lambda_1)(\rho/\lambda)$ for the same set of parameters as above. It appears that the product $|(\lambda_2/\lambda_1)(\rho/\lambda)|$ is negligible compared to 1, so that, if we are in the case of strong coupling between the two fixed points, the effect of the I_0 point will be to increase the sensitivity to initial conditions of the trajectories emerging from I_+. Consequently we can conclude that, provided that the system is close to a homoclinic or heteroclinic bifurcation, chaotic behavior will be observed, since sufficient conditions for the presence of homoclinic chaos hold true in both cases.

244 J. Opt. Soc. Am. B/Vol. 8, No. 2/February 1991 Lefranc *et al.*

Table 1. Values of the Parameters Used in the Numerical Simulations

Parameter	Value
A	1.4 to 2.1
γ_{20}	2.892×10^5 sec^{-1}
γ_{10}	1.2×10^6 sec^{-1}
γ_{12}	10 sec^{-1}
$\bar{A}$	2.16
$\bar{\gamma}$	1.3×10^6 sec^{-1}
ε	0.137
$\bar{\varepsilon}$	1.2
b	0.85
a	4.17
2κ	1.1×10^6 sec^{-1}

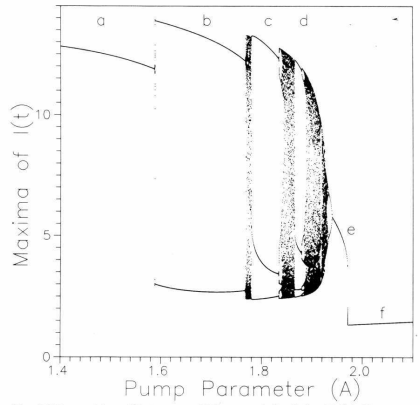

Fig. 5. Bifurcation diagram of the model of the LSA for parameters of Table 1. The letters indicate the following regimes: a, $P^{(0)}$; b, $P^{(1)}$; c, $P^{(2)}$; d, $P^{(3)}$; e, T; f, I_+.

4. NUMERICAL RESULTS

In our experiments the main control parameter is the frequency detuning. As we assume that its main effect is to change the pump parameter A,[11] this quantity has been chosen as a control parameter in the following numerical study, and all other parameters are fixed to the values given in Table 1.

In Fig. 5 we show a bifurcation diagram corresponding to the values of Table 1 in which the pump parameter A is varied from 1.4 to 2.1. For each parameter value successive maxima of the I variable are plotted. This allows us to characterize the chaotic regimes, the $P^{(n)}$ ones, and their period doublings.

The calculated bifurcation diagram is close to the experimental behavior: the $P^{(n)}$ states with $n \leq 3$ are present and are separated by chaotic regimes $C^{(n)}$, except that $P^{(0)}$ and $P^{(1)}$ experience bistability, as is often seen experimentally. The transition from $P^{(n)}$ to $C^{(n)}$ occurs through a cascade of period-doubling bifurcations. $C^{(n)}$ signals are characterized by a quasi-random sequence of $P^{(m)}$-like pulses, with $0 \leq m \leq n$ or $0 \leq m \leq n + 1$, depending on whether we are closer in parameter space to the $P^{(n)}$ or to the $P^{(n+1)}$ periodic window. The T regime (type II PQS), which appears after a subcritical Hopf bifurcation, and the successive period-doubled orbits can also be seen on the right-hand side of the Fig. 5. We shall see in the what follows that the subcritical nature of the Hopf bifurcation is a crucial point. The experimental transition from steady state to PQS appears to be subcritical or supercritical, depending on the operating conditions (e.g., see Refs. 3, 5, and 10), and it would be of interest to determine the boundary between the two kinds of behavior since supercritical bifurcations are observed numerically for smaller $\bar{\varepsilon}$.

Figures 6(a) and 7(a) show examples of the time evolution of the laser intensity inside the $C^{(1)}$ and the $C^{(2)}$ chaotic regions, respectively, of the bifurcation diagram that are quite similar to experimental signals. To compute the 1-D return maps associated with these regimes and compare them with experimental results, a Poincaré section plane must be fixed. To get the multibranched maps characteristic of the homoclinic chaos, we choose a plane of constant intensity, which is crossed once and only once between two reinjection loops corresponding to the large peaks in the temporal signal.

The Poincaré sections for $A = 1.773$ and $A = 1.86$ are shown in Figs. 6(b) and 7(b), respectively. Whereas the model is four dimensional, strong volume contraction occurs, and the projections of the sections on the (U,W) plane are seen to be quasi-1-D. Indeed, on computing the Lyapunov exponents for, e.g., $A = 1.86$, one finds the values 0.0168, 0.0, -0.191, and -7.81 inverse reduced time units, yielding from the Kaplan–Yorke formula[31] a Lyapunov dimension of 2.088, which is known to be an upper bound on the fractal dimension.[32] A projection of the corresponding attractor in the (I,U,W) subspace is displayed in Fig. 7(d). The fractal dimension is therefore close to 2, suggesting that a phenomenological model involving only three variables could in principle be found. This fact allows us to construct 1-D return maps $U_{n+1} = f(U_n)$, which are shown in Figs. 6(c) and 7(c). They are seen to have exactly the same structure as those observed experimentally, although they are computed in the $(I,U,W,\bar{U})$ phase space instead of in a reconstructed attractor.

Similar 1-D maps can be plotted for the other chaotic regimes and display the same features. In a general way, the first return map of a $C^{(n)}$ regime shows $n + 1$ or $n + 2$ branches corresponding to the $P^{(m)}$ pulses of the temporal signal. The appearance of the $(n + 2)$th branch in the $C^{(n)}$ region is linked with the proximity of the tangent bifurcation in which the $P^{(n+1)}$ periodic orbit is created. Indeed, as the $P^{(n)}$ window is approached, the $(n + 2)$th branch comes closer and closer to the $U_{n+1} = U_n$ line and eventually becomes tangent to it. Beyond the bifurcation, a stable and an unstable fixed point appear, the stable one corresponding to the $P^{(n+1)}$ state. To confirm this observation, we have computed the tranverse Floquet multipliers of the $P^{(3)}$ regime inside its domain of stability. Two are always small, owing to strong dissipation, and the evolution of the other has been plotted in Fig. 8. The value -1 for $A = 1.8780$ corresponds to the period-doubling bifurcation of $P^{(3)}$, and the value 1 for $A = 1.8647$ clearly shows that the transition from $C^{(2)}$ to $P^{(3)}$ occurs through a tangent bifurcation. This has also been verified for other bifurcations from $C^{(n)}$ to $P^{(n+1)}$. In the vicinity of the

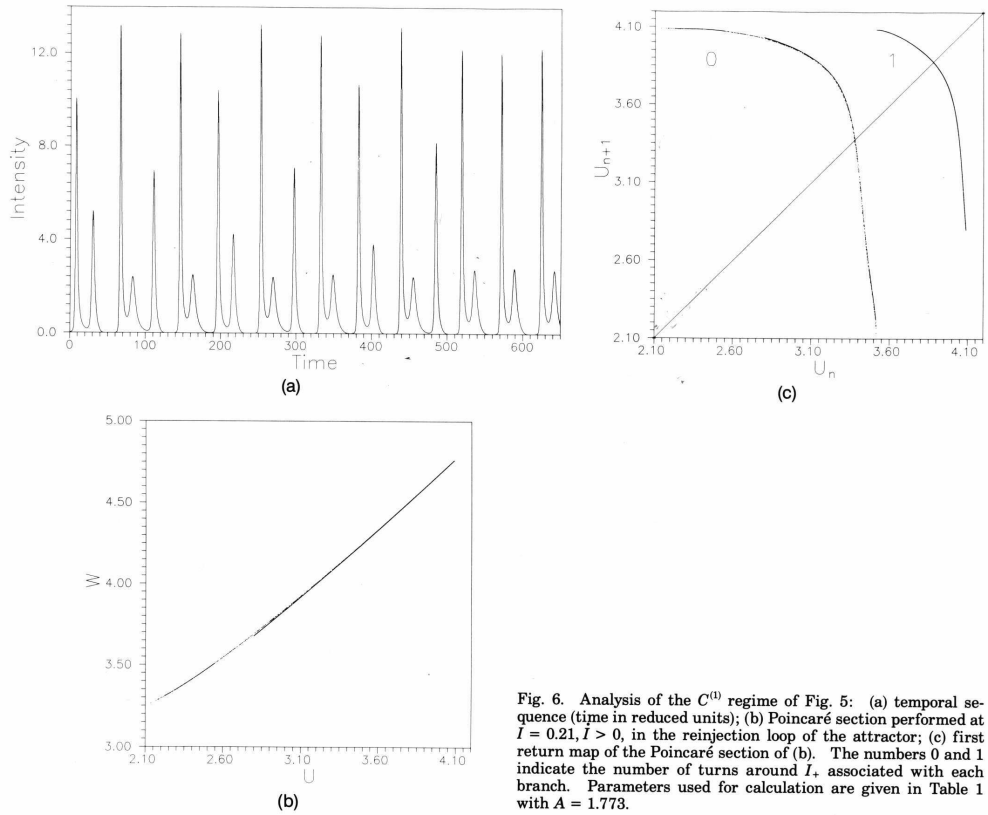

Fig. 6. Analysis of the $C^{(1)}$ regime of Fig. 5: (a) temporal sequence (time in reduced units); (b) Poincaré section performed at $I = 0.21, \dot{I} > 0$, in the reinjection loop of the attractor; (c) first return map of the Poincaré section of (b). The numbers 0 and 1 indicate the number of turns around I_+ associated with each branch. Parameters used for calculation are given in Table 1 with $A = 1.773$.

transition, there is type I intermittency, whose reinjection mechanism is deeply connected with the Shil'nikov dynamics. Recall that the creation of periodic orbits with increasing numbers of undulations by tangent bifurcations is one of the main characteristics of homoclinic chaos.[18,33]

Whereas both the scenario observed when A is varied and the 1-D maps shown strongly favor the hypothesis of homoclinic chaos in the model studied, no homoclinic bifurcation can be located for the parameters used so far. This means that our one-parameter path does not intersect the codimension-1 subset of parameter space where homoclinic bifurcations take place. We have therefore varied another parameter, $\bar{\varepsilon}$, which controls the time scale on which the absorber evolves. We stress that this does not mimic experimental operation, as increasing the absorber pressure, for example, would result in a higher $\bar{\varepsilon}$ but would also decrease the relative saturability a. Nevertheless, it corresponds to using a much more saturable absorber (for instance, SF_6) with a buffer gas. Looking at the different bifurcation diagrams obtained for increasing $\bar{\varepsilon}$, we find that the various $P^{(n)}$ regimes with increasing numbers of undulations appear successively in the bifurcation diagram in a continuous way, without changing its global structure, as can be seen from Fig. 9, indicating that we come closer to homoclinicity.

Since the numerical integration time increases rapidly with $\bar{\varepsilon}$, it was not possible to determine the value of $\bar{\varepsilon}$ above which a homoclinic bifurcation is encountered in the bifurcation diagram with control parameter A. Nevertheless, in the limit case $\bar{\varepsilon} \to \infty$, where the absorber's population inversion can be adiabatically eliminated, leading to a three-variable model, we find an homocliniclike bifurcation, in the neighborhood of which chaotic regimes with as many as 41 undulations, as in Fig. 10 for $A = 1.997$, could be located. Hence it is highly likely that the global structure of the bifurcation diagram obtained with parameters of Table 1 can be traced back to the existence of such bifurcations for higher values of $\bar{\varepsilon}$. We shall therefore concentrate in what follows on the model obtained for infinite $\bar{\varepsilon}$ and study the nature of the observed bifurcation. Figure 11 shows the corresponding bifurcation diagram.

We stress that the $P^{(n)}$ and $C^{(n)}$ solutions of this model for the lowest n are similar to those obtained in the model with four variables, as can be seen from Fig. 12 for the $C^{(2)}$ regime. The fact that the same type of dynamics is

246 J. Opt. Soc. Am. B/Vol. 8, No. 2/February 1991 Lefranc *et al.*

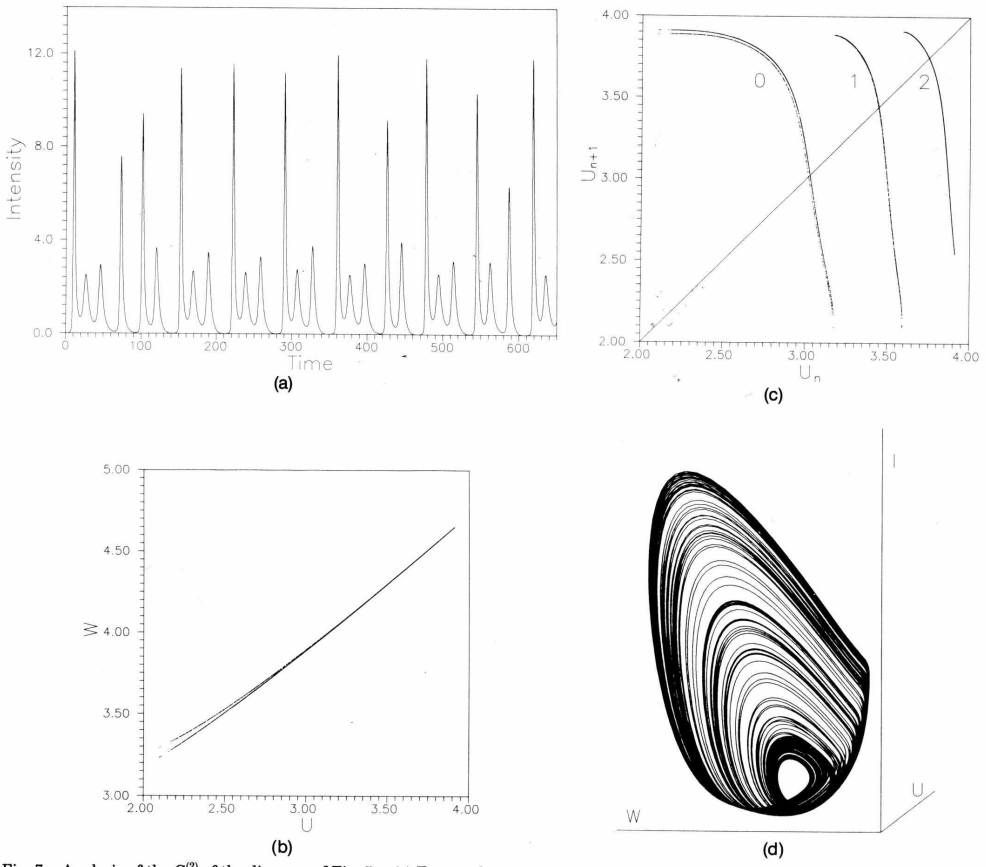

Fig. 7. Analysis of the $C^{(2)}$ of the diagram of Fig. 5: (a) Temporal sequence (time in reduced units). (b) Poincaré section performed at $I = 0.21, \dot{I} > 0$, in the reinjection loop of the attractor. (c) First return map of the Poincaré section of (b). 0–2 indicate the number of turns associated with each branch. (d) Projection of the attractor on the hyperplane (I, U, W). The parameters used for calculation are given in Table 1 with $A = 1.860$.

found indicates that the characteristic time scale of the absorber is not a crucial parameter when one is looking from homocliniclike behavior. In fact, as was already suggested,[9] the origin of the PQS behavior is the slow relaxation rate from the low level of the laser transition to the ground level.

Some facts about the behavior observed for infinite $\bar{\varepsilon}$, however, contrast with the standard Shil'nikov configuration involving a saddle-focus fixed point:

(i) The I_+ fixed point is stable at the parameter value at which the bifurcation occurs.

(ii) The amplitude of the undulations never shrinks to zero and is always greater than a minimum value.

(iii) All the $P^{(n)}$ and $C^{(n)}$ states are found on one side only of the bifurcation instead of lying symmetrically on each side.

These three facts lead to believe that we in fact observe in the reduced model a homoclinic tangency to an unstable periodic orbit with positive Floquet multipliers.[33] Using a standard method to find periodic orbits and follow them for changing parameters,[34] we were able to locate precisely the unstable cycle around which the flow spirals and determine its transverse Floquet multipliers near homoclinicity, $\lambda_u = 1.1326$ and $\lambda_s = 0.05646$. We also discovered that this cycle corresponds to the unstable cycle created at the subcritical Hopf bifurcation of I_+ for $A \approx 1.974$ and annihilated for higher A in a saddle-node bifurcation with the T periodic orbit for $A \approx 2.034$. As it corresponds to an infinite number of undulations, hereafter it will be called $P^{(\infty)}$.

For evidence that a homoclinic tangency to $P^{(\infty)}$ occurs in the model for $A \approx 1.997$, we computed the stable and unstable manifolds W_s and W_u, respectively, of $P^{(\infty)}$ for

parameter values $A = 1.997$ and $A = 1.991$. The intersection of these manifolds with a section plane transverse to $P^{(\infty)}$ is shown in Fig. 13. It is clear that, for $A = 1.997$, W_u and W_s become tangent so that a homoclinic orbit that is biasymptotic to the unstable cycle is created.[33] For $A < 1.997$ the stable manifold acts as a separatrix and prevents the trajectories that spiral around $P^{(\infty)}$ from reaching I_+. This explains the generalized bistability observed between I_+ and the $P^{(n)}$ and $C^{(n)}$ regimes for $n > 8$ ($1.974 < A < 1.997$). For $A > 1.997$, W_u intersects W_s transversally, so that the attraction basin of I_+ extends beyond $P^{(\infty)}$. This is why a sudden transition from chaos to a constant-intensity region is observed in the bifurcation diagram of Fig. 11 when $A = 1.997$ is reached. There is still bistability between the period-doubling cascade of the T regime and I_+ for $1.997 < A < 2.034$, but $P^{(\infty)}$ is no longer involved.

It is interesting to note that the 1-D maps computed in the case of a homoclinic tangency to a cycle, as in

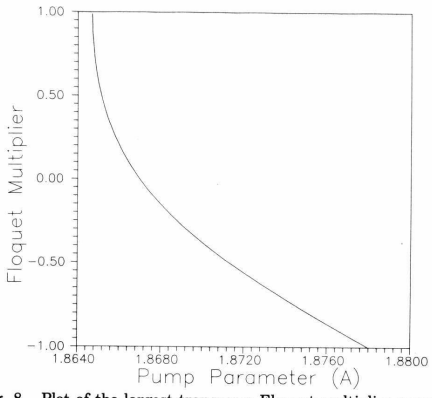

Fig. 8. Plot of the largest transverse Floquet multiplier associated with the $P^{(3)}$ periodic orbit as a function of A.

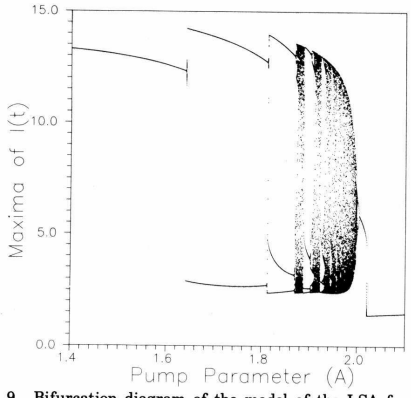

Fig. 9. Bifurcation diagram of the model of the LSA for the parameters of Table 1, except for $\bar{\varepsilon} = 6$. Periodic regimes $P^{(n)}$ with $n \leq 8$ are present.

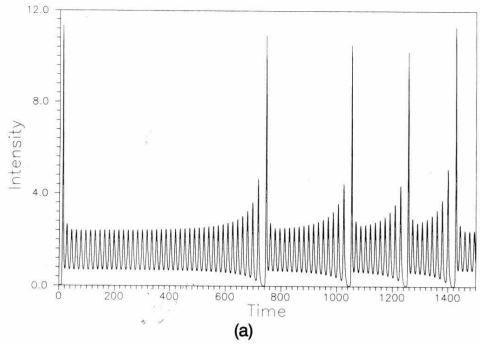

(a)

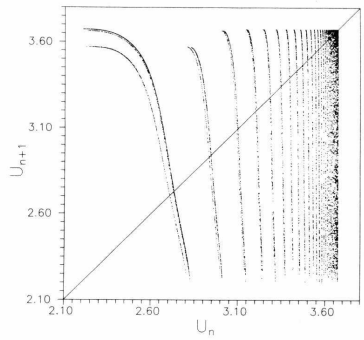

(b)

Fig. 10. (a) Temporal signal obtained for $A = 1.997$ with the reduced model ($\bar{\varepsilon}$ infinite). A pulse with 41 undulations can be seen. (b) First return map of the Poincaré section plane $I = 0.2, \dot{I} > 0$, with 42 branches. The branches converge geometrically with an asymptotic rate equal to 0.882. Except for $\bar{\varepsilon}$, the parameters may be found in Table 1, as they can for Figs. 11–13.

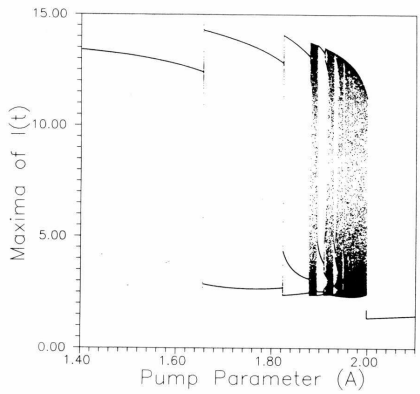

Fig. 11. Bifurcation diagram obtained with infinite $\bar{\varepsilon}$. The sudden transition from chaos to I_+, which can be seen at the right, corresponds to a homocliniclike bifurcation.

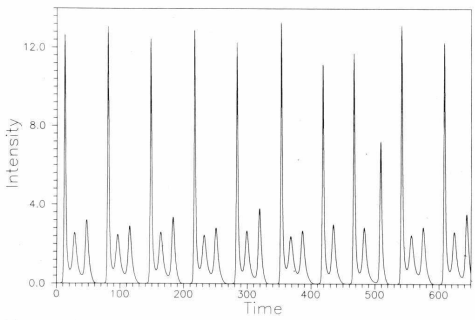

Fig. 12. Temporal signal obtained for $A = 1.888$ with the reduced model ($\bar{\varepsilon}$ infinite). It is similar to signals of the four-variable model computed for equivalent pump parameters and may be compared with Fig. 7(a).

Fig. 10, have exactly the properties that were originally established[24,27] in the case of a saddle-focus fixed point. We cannot therefore exclude the possibility that the 1-D maps observed experimentally are related to a homoclinic tangency.

The fact that the unstable cycle $P^{(\infty)}$ involved in the homoclinic tangency is created in the Hopf bifurcation of I_+ is quite important for two reasons:

(i) The $P^{(n)}$ regimes for $n \leq 8$ are created, whereas $P^{(\infty)}$ does not yet exist. This means that this part of the bifurcation diagram is controlled by the saddle focus I_+ as if we were in a standard Shil'nikov situation. As the Hopf bifurcation is encountered, there is a crossover from I_+ to $P^{(\infty)}$ as the organizing center of the dynamics, since I_+ is then isolated from the remainder of the phase space.

(ii) In experiments with CH_3I, and in numerical simulations as well, a reduction of the amplitude of the undulations of the $P^{(n)}$ regimes has not been observed; furthermore, no scenario for the type $\ldots C^{(n-1)}, P^{(n)}, C^{(n)}, P^{(n+1)} \ldots, \ldots P^{(n+1)}, C^{(n)}, P^{(n)}, C^{(n-1)} \ldots$ has been encountered. This suggests that, in the experimental situation, the mechanism leading to chaos involves homoclinicity to a periodic orbit, in the same way as in the numerical study. As the scenario described in the case of a fast absorber can occur only if the Hopf bifurcation is subcritical, working in parameter space regions where I_+ and the PQS regime experience bistability could help in locating a homoclinic tangency experimentally.

5. CONCLUSION

Experimental chaotic regimes of the LSA of the type $C^{(n)}$ have been shown to display the characteristic features of homoclinic chaos through the analysis of first return maps of the signal and the study of the transitions between chaotic and periodic regimes. A now-standard model of the Q-switching LSA has been explored numerically, reproducing the experimental behavior well. The results obtained with a fast absorber suggest that the phase diagram of a LSA is determined largely by a homoclinic tangency to an unstable cycle created in a subcritical Hopf bifurcation, which explains the homocliniclike behavior observed.

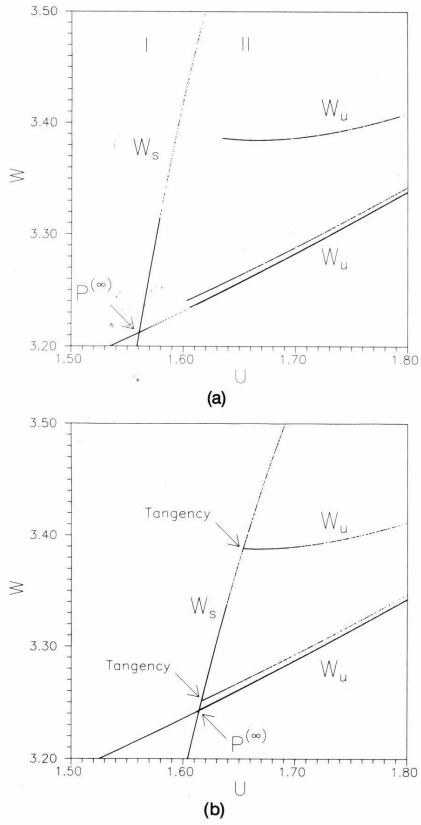

Fig. 13. Intersection with a section plane transverse to $P^{(\infty)}$ of the stable (W_s) and unstable (W_u) manifolds of $P^{(\infty)}$ in the neighborhood of the unstable cycle. The point where the two manifolds cross is the intersection of $P^{(\infty)}$ with the section plane: (a) For $A = 1.991$, W_s and W_u are disconnected. Region I is the attraction basin of I_+, and region II is the part of phase space where motion on the attractor takes place. The two regions are separated by W_s. (b) For $A = 1.997$, W_u and W_s are tangent to each other.

ACKNOWLEDGMENTS

We thank A. Bekkali for his help in the early stages of this study. We are also grateful to A. Arneodo, C. Baesens, P. Coullet, and C. Tresser for fruitful discussions of the properties of Shil'nikov chaos and to E. Arimondo and B. Zambon for stimulating exchanges and for communication to us of their papers and works before publication. We are particularly indebted to P. Glorieux for his advice and numerous suggestions.

REFERENCES

1. I. Burak, P. L. Houston, D. G. Sutton, and J. I. Steinfeld, "Mechanism of passive Q-switching in CO_2 lasers," IEEE J. Quantum Electron. **QE-7**, 73–82 (1971).

2. J. Dupré, F. Meyer, and C. Meyer, "Influence des phénomènes de relaxation sur la forme des impulsions fournies par un laser CO_2 déclenché par un absorbant saturable," Rev. Phys. Appl. **10,** 285–293 (1975).
3. E. Arimondo, F. Casagrande, L. Lugiato, and P. Glorieux, "Repetitive passive *Q*-switching and bistability in lasers with saturable absorber," Appl. Phys. B **30,** 57–77 (1983).
4. M. L. Asquini and F. Casagrande, "Passive *Q*-switching in lasers with saturable absorbers: improved treatment of a four level method," Nuovo Cimento **2D,** 917–931 (1983).
5. A. Jacques and P. Glorieux, "Observation of bistability in a CO_2 laser exhibiting passive *Q*-switching," Opt. Commun. **40,** 455–460 (1982).
6. E. Arimondo and E. Menchi, "Analysis of *Q*-switch in a CO_2 laser with saturable absorber," Appl. Phys. B **37,** 55–61 (1985).
7. M. Tachikawa, K. Tanii, M. Kajita, and T. Shimizu, "Undamped undulation superposed on the passive *Q*-switching pulse of a CO_2 laser," Appl. Phys. B **39,** 83–90 (1986).
8. K. Tanii, M. Tachikawa, M. Kajita, and T. Shimizu, "Sinusoidal self-modulation in the output of a CO_2 laser with an intracavity saturable absorber," J. Opt. Soc. Am. B **5,** 24–28 (1988).
9. E. Arimondo, P. Bootz, P. Glorieux, and E. Menchi, "Pulse shape and phase diagram in the passive *Q*-switching of CO_2 lasers," J. Opt. Soc. Am. B **2,** 193–201 (1985).
10. M. Tachikawa, K. Tanii, and T. Shimizu, "Comprehensive interpretation of passive *Q*-switching and optical bistability in a CO_2 laser with an intracavity saturable absorber," J. Opt. Soc. Am. B **4,** 387–395 (1987).
11. B. Zambon, F. de Tomasi, D. Hennequin, and E. Arimondo, "Investigations of models for the laser with a saturable absorber: theoretical and experimental studies of the stationary regimes," Phys. Rev. A **40,** 3782–3795 (1989).
12. D. Dangoisse, A. Bekkali, F. Papoff, and P. Glorieux, "Shil'nikov dynamics in a passive *Q*-switching laser," Europhys. Lett. **6,** 335–340 (1988).
13. D. Hennequin, F. de Tomasi, B. Zambon, and E. Arimondo, "Homoclinic orbits and cycles in the instabilities of a laser with saturable absorber," Phys. Rev. A **37,** 2243–2246 (1988).
14. M. Tachikawa, K. Tanii, and T. Shimizu, "Laser instability and chaotic pulsation in a CO_2 laser with intracavity saturable absorber," J. Opt. Soc. Am. B **5,** 1077–1081 (1988).
15. F. de Tomasi, D. Hennequin, B. Zambon, and E. Arimondo, "Instabilities and chaos in an infrared laser with saturable absorber: experiments and vibrorotational model," J. Opt. Soc. Am. B **6,** 45–57 (1989).
16. M. Tachikawa, F. L. Hong, K. Tanii, and T. Shimizu, "Deterministic chaos in passive *Q*-switching pulsation of a CO_2 laser with saturable absorber," Phys. Rev. Lett. **60,** 2266–2268 (1988).
17. P. Glendinning and C. Sparrow, "Local and global behavior near homoclinic orbits," J. Stat. Phys. **35,** 645–696 (1984).
18. P. Gaspard, R. Kapral, and G. Nicolis, "Bifurcation phenomena near homoclinic systems: a two-parameter analysis," J. Stat. Phys. **35,** 697–727 (1984).
19. L. P. Shil'nikov, "A case of the existence of a countable number of periodic motions," Sov. Math. Dokl. **6,** 163–166 (1965); "A contribution to the problem of the structure of an extended neighborhood of a rough equilibrium state of saddle focus type," Math. USSR Sbornik **10,** 91–102 (1970).
20. D. Hennequin, F. de Tomasi, L. Fronzoni, B. Zambon, and E. Arimondo, "Influence of noise on the quasi-homoclinic behavior of a laser with saturable absorber," Opt. Commun. **70,** 253–258 (1989).
21. D. Hennequin, M. Lefranc, A. Bekkali, D. Dangoisse, and P. Glorieux, "Characterization of Shil'nikov chaos in a CO_2 laser containing a saturable absorber" in *Measures of Complexity and Chaos,* N. B. Abraham, A. M. Albano, A. Passamente, and P. E. Rapp, eds. (Plenum, New York, 1989), pp. 299–302.
22. F. Papoff, A. Fioretti, E. Arimondo, and N. B. Abraham, "Time return maps and distributions for the laser with a saturable absorber," in *Measures of Complexity and Chaos,* N. B. Abraham, A. M. Albano, A. Passamente, and P. E Rapp, eds. (Plenum, New York, 1989), pp. 309–312.
23. F. T. Arecchi, A. Lapucci, R. Meucci, J. A. Roversi, and P. H. Coullet, "Experimental characterization of Shil'nikov chaos by statistics of return times," Europhys. Lett. **6,** 677–682 (1988); F. T. Arecchi, W. Gadomski, A. Lapucci, H. Mancini, R. Meucci, and J. A. Roversi, "Laser with feedback: an optical implementation of competing instabilities, Shil'nikov chaos, and transient fluctuation enhancement," J. Opt. Soc. Am. B **5,** 1153–1159 (1988).
24. F. Argoul, A. Arneodo, and P. Richetti, "Experimental evidence for homoclinic chaos in the Belousov–Zhabotinskii reaction," Phys. Lett. A **120,** 269–275 (1987); F. Argoul, A. Arneodo, and P. Richetti, "Dynamique symbolique dans la réaction de Belousov–Zhabotinskii: une illustration expérimentale de la théorie de Shil'nikov des orbites homoclines," J. Chim. Phys. **84,** 1367–1385 (1987).
25. E. Arimondo and P. Glorieux, "Saturated absorption experiments on a dressed molecule. Application to the spectroscopy of the ν_6 band of CH_3I," Phys. Rev. A **19,** 1067–1083 (1979).
26. See, e.g., J. S. Turner, J. C. Roux, W. D. McCormick, and H. L. Swinney, "Alternating periodic and chaotic regimes in a chemical reaction—experiments and theory," Phys. Lett. **85A,** 9–12 (1981).
27. A. Arneodo, P. Coullet, E. A. Spiegel, and C. Tresser, "Asymptotic chaos," Physica D **14,** 327–347 (1985).
28. H. T. Powell and G. J. Wolga, "Repetitive passive *Q*-switching of single-frequency lasers," IEEE J. Quantum Electron. **QE-7,** 213–219 (1971).
29. T. Erneux and P. Mandel, "Bifurcation phenomena in a laser with saturable absorber I and II," Z. Phys. B **44,** 353–363, 365–374 (1981); P. Mandel and T. Erneux, "Stationary, harmonic and pulsed operations of an optically bistable laser with saturable absorber. I and II," Phys. Rev. A **30,** 1893–1901, 1902–1909 (1984); T. Erneux, P. Mandel, and J. Magnan, "Quasi-periodicity in lasers with saturable absorbers," Phys. Rev. A **29,** 2690–2699 (1984); D. E. Chyba, N. B. Abraham, and A. M. Albano, "Semiclassical analysis of a detuned ring laser with a saturable absorber. New results for the steady states," Phys. Rev. A **35,** 2936–2950 (1987).
30. C. Tresser, "About some theorems by L. P. Shil'nikov," Ann. Inst. Henri Poincaré **40,** 441–461 (1984).
31. P. Fredrickson, J. L. Kaplan, E. D. Yorke, and J. A. Yorke, "The Lyapunov dimension of strange attractors," J. Diff. Eqs. **49,** 185–207 (1983).
32. F. Ledrappier, "Some relations between dimension and Lyapunov exponent," Commun. Math. Phys. **81,** 229–238 (1981).
33. P. Gaspard and X. J. Wang, "Homoclinic orbits and mixed-mode oscillations in far from equilibrium systems," J. Stat. Phys. **48,** 151–199 (1987).
34. C. Sparrow, *The Lorenz Equations, Bifurcations, Chaos and Strange Attractors* (Springer-Verlag, Berlin, 1982), pp. 211–220, App. E.

"Improved correlation dimension estimates through change of variable"

M. Lefranc, D. Hennequin, and P. Glorieux

Phys. Lett. A **163**, 269–274 (1992)

Physics Letters A 163 (1992) 269–274
North-Holland

PHYSICS LETTERS A

Improved correlation dimension estimates through change of variable

M. Lefranc, D. Hennequin and P. Glorieux
Laboratoire de Spectroscopie Hertzienne [1], UFR de Physique, Université de Lille I, F-59655 Villeneuve d'Ascq Cedex, France

Received 16 December 1991; accepted for publication 6 January 1992
Communicated by D.D. Holm

To evaluate the correlation dimension of chaotic regimes of a CO_2 laser with modulated losses, attractor reconstruction using the method of delays is performed using the logarithm of the intensity rather than the intensity itself. Improved convergence with respect to the embedding dimension and better reliability are observed.

1. Introduction

The measure of quantities like dimensions, entropies and Lyapunov exponents has by now become standard to analyze and characterize the chaotic dynamics which can be observed in a variety of experimental systems [1]. Most of the time, they are evaluated by reconstructing from a single time series the underlying strange attractor in $\mathbb{R}^n$ using the method of time delays proposed by Takens and Packard et al. [2]. Indeed, in the limit of an infinite, noise-free time series, the reconstructed attractor is shown to be diffeomorphic to the original one and may therefore be used to compute the above-mentioned quantities, which are left invariant by diffeomorphisms. Nevertheless the experimentalist is not only interested in the validity, but also in the robustness of the method, as he obtains from experiments finite time series corrupted by noise. He is furthermore limited by the computer time necessary to run the computational algorithms.

Among the different quantitative measures of chaotic behaviors, one of the most widely used is the evaluation of the correlation dimension of the reconstructed attractor through the Grassberger–Procaccia algorithm [3]. This procedure indicates the minimum number of degrees of freedom necessary to account for the observed dynamics and characterizes the fractal nature of the attractor by a number which may be compared to those obtained from numerical simulations of models of the system under consideration. Among the whole spectrum of generalized dimensions [4], the correlation dimension D_2 is the easiest to compute because it needs fewer data points and does not require finite sample corrections [5].

While the Grassberger–Procaccia algorithm is rather easy to implement, numerous sources of systematic errors may often prevent the result from accurately reproducing the correlation dimension of the original attractor. These include for example the effect of random and digitizing noise [6], of low-pass filtering of the signal [7], of a too strong correlation between temporal neighbours on the trajectory [8].

We will try to show in the sequel that a strong non-uniformity of the attractor can also alter the determination of the correlation dimension, and how this effect may be substantially corrected by an adequate change of variable. This will be illustrated using experimental signals and numerical simulations of a CO_2 laser with modulated losses, comparing attractors reconstructed with the output intensity of the laser and with the logarithm of this intensity.

[1] Unité de recherche associée au CNRS.

2. Experimental system

The experimental signals presented hereafter come from a CO_2 waveguide laser with an electrooptic crystal and a ZnSe Brewster angle plate inserted inside the cavity of the laser [9]. A sinusoidal voltage is applied to the crystal at a frequency of 382.5 kHz, which results in modulation of the losses for the laser. The typical scenario encountered when increasing the modulation amplitude is a sequence of period doublings culminating in chaos [9]. The output intensity of the laser is measured with a HgCdTe detector and data acquisition is done with a LeCroy 9400 transient digitizer with a maximum sampling rate of 100 MHz, a storage capacity of 32000 samples and a resolution of eight bits.

The signals which may be seen on the first rows of figs. 1a and 2a have been recorded respectively at the end of the inverse cascade and further in the chaotic region. The intensity of the laser is often close to the zero intensity, so that a large number of points (15% and 45% in the case of figs. 1a and 2a respectively) in the time series have the same digitized value. When reconstructing the attractor using the method of time delays, small regions of the attractor contain most of the data points, unless very high embedding dimensions are used. This is a problem for accurately evaluating the correlation dimension, since the fractal structure is poorly resolved in those overpopulated parts of the attractor, due to the limited resolution of the digitizer. Similar signals with long periods of almost constant intensity may also be found in other chaotic lasers such as the laser with a saturable absorber [10] and the doped fiber laser with pump modulation [11]. Heavy low-pass filtering of the signal was used in ref. [12] to circumvent this problem. However, this introduces systematic errors as discussed by Badii et al. [7].

This feature of temporal signals in lasers can easily be explained by the fact that intracavity absorption and gain through stimulated emission are proportional to the intracavity radiation intensity I. This may be illustrated for example by the evolution equations for I and the inversion population D obtained from a single-mode, homogeneously broadened, two-level model for our laser with modulated losses [13]:

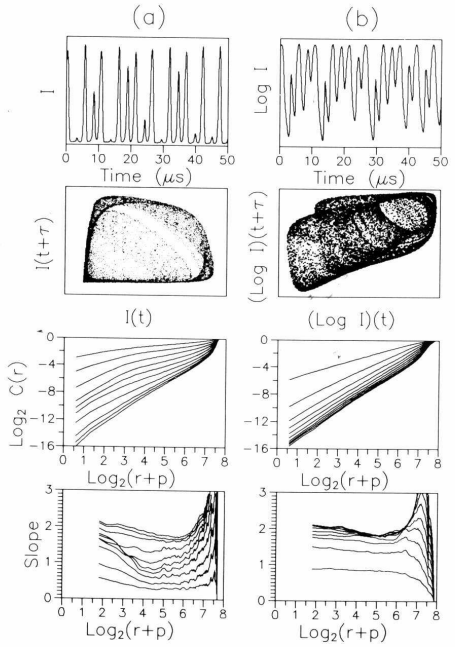

Fig. 1. Comparison of the attractors reconstructed with: (a) output of the HgCdTe detector, (b) output of the logarithmic amplifier. Row 1: simultaneous temporal sequences (625 samples). Row 2: phase portraits (20000 samples). $\tau = 7\Delta t$, where $\Delta t = 80$ ns is the sampling time. Row 3: log-log (base 2) plot of the correlation integral versus length scale $(r+p)$ for embedding dimensions 1 to 10 using τ as delay and 5000 data points. Row 4: slopes of the log-log plots of the correlation integral versus length scale for embedding dimensions 1 to 10.

$$\frac{dI}{dt} = 2\kappa I(AD - 1 - m\sin\omega t)\,,$$

$$\frac{dD}{dt} = \gamma[1 - D(1+I)]\,, \qquad (1)$$

where κ is the cavity damping rate, A the pump parameter, m and ω the modulation amplitude and frequency, γ the population inversion relaxation rate. The time derivative of I being proportional to I, the intensity seems to be frozen when it comes close to zero. It is then natural to use the logarithm of the intensity, whose time derivative is

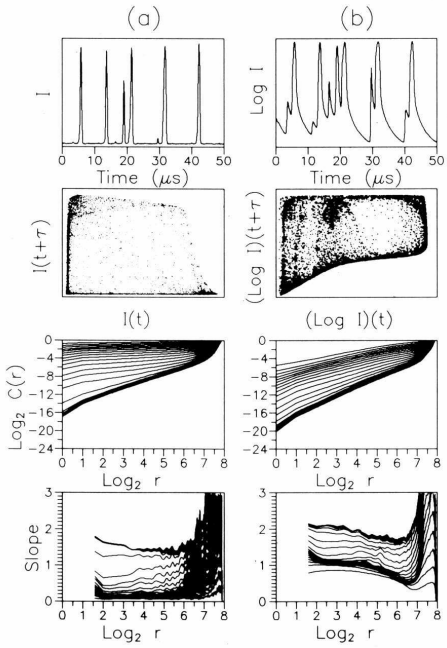

Fig. 2. Comparison of the attractors reconstructed with: (a) output of the HgCdTe detector, (b) output of the logarithmic amplifier. Row 1: simultaneous temporal sequences (625 samples). Row 2: Phase portraits (20000 samples). $\tau=8\Delta t$, where $\Delta t=80$ ns is the sampling time. Row 3: log-log (base 2) plot of the correlation integral versus length scale r for embedding dimensions 1 to 20 using τ as delay and 5000 data points. Row 4: slopes of the log-log plots of the correlation integral versus length scale for embedding dimensions 1 to 20.

$$\frac{\mathrm{d}}{\mathrm{d}t}\log I=2\kappa(AD-1-m\sin\omega t)\ ,$$

as the relevant dynamical variable. In other respects, Oppo et al. [14] remarked that the logarithm of the intensity appeared as a natural variable of their final equations in a paper in which they derived, by means of the center manifold theorem, two-dimensional equations for the CO_2 laser taking into account the coupling with rotational levels.

We have therefore inserted in our experimental setup a logarithmic amplifier between the detector and the digitizer. The output signal given by this amplifier is proportional to $\log(V_e+V_0)$, where V_e is the signal coming from the detector. The offset V_0 was chosen so that the zero intensity voltage of the detector was situated in the high slope region of the amplifier characteristics, in such a way as to discriminate the low intensity points without saturating too much the maxima. In each measurement the intensity signal coming directly from the detector and the output of the logarithmic amplifier were stored simultaneously to allow further comparison of the correlation integrals obtained in each case. The first rows of figs. 1b and 2b show the output signals of the logarithmic amplifier which were recorded simultaneously with the signals of figs. 1a and 2a respectively. These latter correspond to different modulation amplitudes and contain different amounts of low intensity periods. It is easy to see that the dynamics for the low intensity levels is well resolved. By inspecting the phase portraits on the second row of figs. 1 and 2, one can verify that the attractor reconstructed with the "logarithm" of the intensity is much more homogeneous and seems to be better reconstructed than the one obtained with the intensity.

3. Analysis of the experimental data

We present in this part the results obtained by analyzing these experimental data files with the Grassberger–Procaccia algorithm. Interpoint distances were computed using the maximum norm because, besides the fact that this speeds up significantly calculations, the systematic error induced by digitizing is more easily corrected than in the case of the Euclidean norm [6]. Indeed, because of the eight-bit resolution of the digitizer, we followed for the signal of fig. 1 a procedure suggested by Möller et al. [6], which consists in replacing r by $r+p$ in the log–log plots of the correlation integrals $C(r)$, where p is half the last significant bit of the digitizer. Such a correction was also used by Hübner et al. to compute dimensions and entropies in a NH_3 laser [15]. On the other hand, we did not use this correction in the case of the signal of fig. 2, because a noise level of the order of the last significant bit was estimated from the sudden slope increase in the log–log plots of the correlation integral. The digitizing error is substan-

tially reduced in this case [6], and using the correction would overestimate the correlation dimension. It is possible that for the first data file the correction for the digitizing error, which assumes that the data are noise free, slightly overestimates the correlation dimension. However, our primary goal is to illustrate how attractor reconstruction depends on the variable used.

The third and fourth rows of fig. 1 display the plots of $\log C(r)$ versus $\log(r+p)$ for embedding dimensions up to 10 and of the local slopes of these curves versus $\log(r+p)$ for the signals of fig. 1. The time delay τ used in the reconstruction was chosen empirically as the one which yielded the widest scaling regions, and is approximately equal to $0.21T$, where T is the period of the modulation. Whereas no clear convergence of the local slopes may yet be seen in fig. 1a, where intensity was used, saturation is observed on fig. 1b for embedding dimensions greater than 6. The plateau in this case is only approximately 1.5 octaves wide, but it is rather difficult to get wider scaling regions with eight-bit resolution, if we exclude highly homogeneous attractors such as the Lorentz attractor [16]. The good convergence with the embedding dimension allows us to estimate the correlation dimension to be close to 2.05. Fig. 3 displays the evolution of the estimation of the correlation dimension as a function of the embedding dimension for the I and $\log I$ signals of fig. 1. The fact that the curves saturate much faster with the embedding dimension improves clearly the estimation of the correlation dimension, because the systematic overestimate of the fractal dimension due to random noise increases with the embedding dimension.

The signal of fig. 2 is much more inhomogeneous than the signal of fig. 1 (the zero intensity level corresponds to more than 75% of the samples). As a consequence, we used in this case embedding dimensions up to 20 to achieve saturation of the local slopes. The optimal time delay was found to be equal in this case to $0.24T$. Saturation of the local slopes is observed in both cases for embedding dimensions greater than 16, but there is a clear-cut difference between the two correlation dimension estimates. When laser intensity is used, slopes saturate near 1.5, whereas a correlation dimension close to 2.09 may be estimated from the output of the logarithmic amplifier, as may be seen on fig. 4. It is nevertheless possible that this value is still underestimated because the inhomogeneity is only partially removed. It is indeed interesting to note that, for embedding

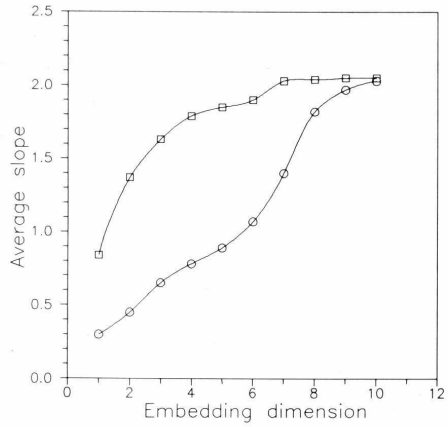

Fig. 3. Average slope in the "plateau region" versus embedding dimension for the data files of fig. 1a (circles) and fig. 1b (squares).

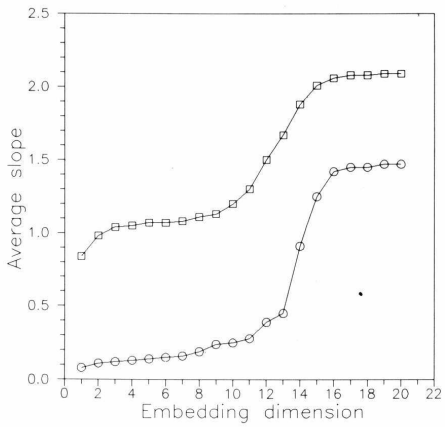

Fig. 4. Average slope in the "plateau region" versus embedding dimension for the data files of fig. 2a (circles) and fig. 2b (squares).

dimensions lower than 10, slopes of the correlation integrals are approximately equal to 0.15 in fig. 2a, indicating a very strong inhomogeneity, while in fig. 2b they cluster around 1.05. Thus, for low embedding dimensions, the reconstructed strange attractors look respectively like a point and a line.

For some other very inhomogeneous data sets, we were not able to find any clear scaling region in the log–log plots. We nevertheless systematically found that the local slopes using the logarithm were significantly higher than with the intensity and were always in the order of 2 for small distances.

4. Numerical simulations

We have also applied the same procedure to signals coming from numerical simulations, to check if similar effects could be observed even with higher precision, since in this case smaller length scales may be investigated. The set of equations (1) was numerically integrated with the Bulirsch–Stoer algorithm [17] and table 1 displays the parameters used. The signals were digitized to 32 bits. To compute the correlation integrals, we reconstructed the attractor using the method of delays, to ease the comparison with the experimental results.

To evaluate the fractal dimension with the best precision possible, since we are not limited in this case by random noise and digitizing errors, we used a maximum likelihood estimator of the correlation dimension derived by Takens [18]. The Takens estimator $D(r_0)$ of the correlation dimension for the length scales between 0 and r_0 is defined as

$$-\frac{1}{D(r_0)} = \langle \ln(r/r_0) \rangle ,$$

where the averaging is done on all the distances r between points of the attractor smaller than r_0. This

Table 1

Parameters	Value
κ	$6\times10^7\,\mathrm{s}^{-1}$
A	1.1
ω	4×10^5 Hz
m	0.0246
γ	$2.5\times10^5\,\mathrm{s}^{-1}$

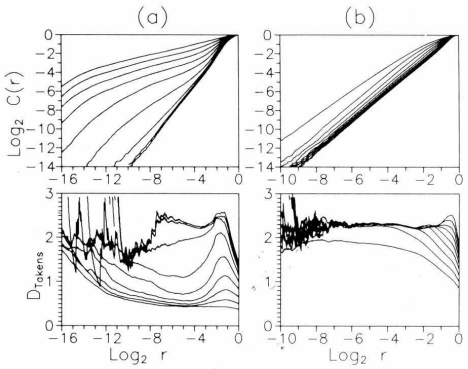

Fig. 5. Analysis of the files obtained from numerical simulations using: (a) intensity, (b) logarithm of the intensity. Row 1: log-log plot of the correlation integral versus r for embedding dimensions 2 to 10. Row 2: Takens estimator of the correlation dimension $D_{\mathrm{Takens}}(r)$ versus $\log_2 r$ for embedding dimensions 2 to 10.

method, which has the advantage of being non-parametric, is more difficult to use with digitized data of relatively low precision since there is in this case a large incertainty in the logarithms of the distances.

Correlation integrals and the Takens estimator for the numerical simulations may be seen in fig. 5. The calculations were made with 5000 points, and a delay time equal to $0.24T$. The benefit in using the logarithm of the intensity to reconstruct the attractor is even more clearly demonstrated than for the experimental data, probably because we may use here the true logarithm. For embedding dimensions higher than 3, we observe a clear convergence to a value of 2.29 over nearly three octaves for the logarithm, whereas no convergence may be seen with the curve for the intensity. To have independent information on the fractal dimension of the attractor, we computed the Lyapunov dimension of the attractor [19] which is known to be an upper bound of the correlation dimension [20]. This yielded a value of 2.304, which is very close to the correlation dimension found by the Takens estimator.

5. Conclusion

To evaluate the correlation dimension of signals

coming from a CO_2 laser with modulated losses, we have reconstructed the underlying strange attractor using the logarithm of the laser intensity instead of the intensity as is done usually. This allowed us to achieve better convergence of the slopes of the log–log plots and to remove artefacts such as false convergence to erroneous values due to inhomogeneity. We observed that, while in principle dimension is invariant under changes of variables, choosing the adequate variable to reconstruct the attractor allows one to give more reliable estimates of dimension.

Although from a mathematical point of view almost all values of the time delay give an acceptable embedding, there is in practice an optimal value of the delay for which the desired scaling law is best observed. It is interesting to note that, in the same way, while in principle reconstruction of the attractor may be done using any function of the intrinsic dynamical variables, we may conjecture from the results of this study that there should be an optimal function for the reconstruction of the attractor. In the case of our laser, the logarithm of the intensity happens to be a more natural and more efficient variable for quantitative characterization than the intensity itself. The method may obviously be used in the study of other chaotic systems with long sequences of almost constant signal [10,11].

We believe that using the logarithm of the output intensity of a laser should also prove useful for other techniques of characterizing deterministic chaos, such as symbolic dynamics [21], extraction of unstable periodic orbits [22] and template analysis [23], since it provides more details on the regions of the reconstructed phase space which are squeezed.

Acknowledgement

We are grateful to Jean Legrand and Laurent Paccou for their help in setting up the laser.

References

[1] N.B. Abraham, A.M. Albano and N.B. Tufillaro, in: Measures of complexity and chaos, eds. N.B. Abraham, A.M. Albano, A. Passamante and P.E. Rapp, NATO ASI series (Plenum, New York, 1989) p. 1.
[2] F. Takens, in: Lecture notes in mathematics, Vol. 898 (Springer, Berlin, 1981) p. 366;
N.H. Packard, J.P. Crutchfield, J.D. Farmer and R.S. Shaw, Phys. Rev. Lett. 45 (1980) 712.
[3] P. Grassberger and I. Procaccia, Phys. Rev. Lett. 50 (1983) 346; Physica D 9 (1983) 189.
[4] P. Grassberger, Phys. Lett. A 97 (1983) 227.
[5] P. Grassberger, Phys. Lett. A 128 (1988) 369; 107 (1985) 101.
[6] M. Möller, W. Lange, F. Mitschke, N.B. Abraham and U. Hübner, Phys. Lett. A 138 (1989) 176.
[7] R. Badii, G. Broggi, B. Derighetti, M. Ravani, S. Ciliberto, A. Politi and M.A. Rubio, Phys. Rev. Lett. 60 (1988) 979;
F. Mitschke, M. Möller and W. Lange, Phys. Rev. A 37 (1988) 4518.
[8] J. Theiler, Phys. Rev. A 34 (1986) 2427.
[9] C. Lepers, J. Legrand and P. Glorieux, Phys. Rev. A 43 (1991) 2573.
[10] M. Lefranc, D. Hennequin and D. Dangoisse, J. Opt. Soc. Am. B 8 (1991) 239.
[11] D. Derozier, S. Bielawski and P. Glorieux, Opt. Commun. 83 (1991) 97.
[12] G.P. Puccioni, A. Poggi, W. Gadomski, J.R. Tredicce and F.T. Arecchi, Phys. Rev. Lett. 55 (1985) 339.
[13] F.T. Arecchi, R. Meucci, G.P. Puccioni and J.R. Tredicce, Phys. Rev. Lett. 49 (1982) 1217;
T. Midavaine, D. Dangoisse and P. Glorieux, Phys. Rev. Lett. 55 (1985) 1989;
D. Dangoisse, P. Glorieux and D. Hennequin, Phys. Rev. A 36 (1987) 4775.
[14] G.L. Oppo, J.R. Tredicce and L.M. Narducci, Opt. Commun. 69 (1989) 393.
[15] U. Hübner, N.B. Abraham and C.O. Weiss, Phys. Rev. A 40 (1989) 6354.
[16] E.N. Lorentz, J. Atmos. Sci. 20 (1963) 130.
[17] W.H. Press, B.P. Flannery, S.A. Teukolsky and W.T. Wetterling, Numerical recipes (Cambridge Univ. Press, Cambridge, 1986) p. 563.
[18] F. Takens, in: Lecture notes in mathematics, Vol. 1125 (Springer, Berlin, 1985) p. 99.
[19] P. Fredrickson, J.L. Kaplan, E.D. Yorke and J.A. Yorke, J. Diff. Eqs. 49 (1983) 185.
[20] F. Ledrappier, Commun. Math. Phys. 81 (1981) 229.
[21] R. Badii, in: Measures of complexity and chaos, eds. N.B. Abraham, A.M. Albano, A. Passamante and P.E. Rapp, NATO ASI series (Plenum, New York, 1989) p. 313.
D. Hennequin and P. Glorieux, Europhys. Lett. 14 (1991) 237.
[22] D. Auerbach, P. Cvitanovic, J.P. Eckmann, G. Gunaratne and I. Procaccia, Phys. Rev. Lett. 58 (1987) 2387;
D. Lathrop and E.J. Kostelich, Phys. Rev. A 40 (1989) 4028.
[23] G.B. Mindlin, X.J. Hou, H.G. Solari, R. Gilmore and N.B. Tufillaro, Phys. Rev. Lett. 64 (1990) 2350;
F. Papoff, A. Fioretti, E. Arimondo, G.B. Mindlin, H. Solari and R. Gilmore, Phys. Rev. Lett., in press.

Appendice D Publications “Analyse topologique”

"Alternative determinism principle for topological analysis of chaos"

Marc Lefranc

Phys. Rev. E **74**, 035202(R) (2006)

RAPID COMMUNICATIONS

PHYSICAL REVIEW E **74**, 035202(R) (2006)

Alternative determinism principle for topological analysis of chaos

Marc Lefranc
Laboratoire de Physique des Lasers, Atomes, Molécules, UMR CNRS 8523, Centre d'Études et de Recherches Lasers et Applications, Université des Sciences et Technologies de Lille, F-59655 Villeneuve d'Ascq, France

(Received 7 December 2004; revised manuscript received 9 August 2006; published 13 September 2006)

The topological analysis of chaos based on a knot-theoretic characterization of unstable periodic orbits has proven to be a powerful method, however knot theory can only be applied to three-dimensional systems. Still, the core principles upon which this approach is built—determinism and continuity—apply in any dimension. We propose an alternative framework in which these principles are enforced on triangulated surfaces rather than curves, and we show that in dimension 3 our approach numerically predicts the correct topological entropies for periodic orbits of the horseshoe map.

DOI: 10.1103/PhysRevE.74.035202 PACS number(s): 05.45.Ac, 02.10.Kn, 02.40.Sf

Chaotic behavior results from the interplay of two geometrical processes in state space: *stretching* separates neighboring trajectories while *squeezing* maintains the flow within a bounded region [1,2]. A topological analysis has been developed to classify the ways in which stretching and squeezing can organize a chaotic attractor [2–4]. It relies on a theorem stating that unstable periodic orbits (UPO) of a chaotic three-dimensional (3D) flow can be projected onto a 2D branched manifold (a *template*) without modifying their knot invariants [5]. In this method, UPO extracted from an experimental time series are characterized by the simplest template compatible with their topological invariants [2–4].

However, this approach can only be applied to 3D attractors: in higher dimensions, all knots can be deformed into each other. Although other topological methods are applicable to higher dimensions [6,7], extending template analysis is still desirable because it provides a different information. A first step to overcome the 3D limitation is to recognize that knot theory is not a necessary ingredient but simply a convenient way to study how two fundamental properties, determinism and continuity, constrain trajectories in phase space. It is because two trajectories cannot intersect that the knot type of a 3D periodic orbit is well defined and is not modified as the orbit is deformed under control parameter variation.

In this paper, we note that a dimension-independent formulation of determinism is orientation preservation, and we propose an approach in which it is enforced on a representation of the dynamics in a triangulation of periodic points. In dimension 3, an explicit formalism is easily constructed, and we find that it numerically predicts the correct entropies for periodic orbits of the horsehoe map. The entropy of a periodic orbit is an invariant defined as the minimal topological entropy [8] of a flow containing this orbit [9,10]; a positive-entropy orbit is a powerful indicator of chaos [4,11,12]. This result suggests that a key ingredient for constructing a knotless template analysis has been captured, although a proof of validity and an explicit higher-dimensional extension are still lacking.

We now detail our approach. The first step is to replace the requirement of nonintersecting curves by a geometrical problem that adapts naturally to phase spaces of any dimension. It has been suggested to exploit the rigid structure of invariant manifolds of UPO [4,13]. Here, we note that when a volume element V of a d-dimensional phase space is advected by a deterministic flow Φ_t, the image $\Phi_t(\partial V)$ of its boundary cannot display self-intersections: at any time t, its interior and its exterior remain distinct, as with a droplet in a fluid flow. A technical formulation of this property is that volume orientation is preserved by the dynamics. For simplicity, we consider attractors embedded in $\mathbb{R}^n \times S^1$ (e.g., forced systems), which can be sliced into n-dimensional Poincaré sections parametrized by $\varphi \in S^1$. Determinism then imposes that boundaries of n-dimensional volume elements of Poincaré sections retain their orientation (Fig. 1).

Template analysis must be applicable to UPO extracted from experimental signals, and thus can only rely on the phase-space trajectory of a period-p orbit. Thus, we represent the dynamics in a triangulated space whose nodes are p periodic points P_i in a Poincaré section, with $P_{i+1}=F(P_i)$, F being the return map. In this space, points P_i are 0-cells, line segments $\langle P_i, P_j\rangle \equiv \langle ij\rangle$ joining two points are 1-cells, triangles $\langle P_i, P_j, P_k\rangle \equiv \langle ijk\rangle$ are 2-cells, etc. [Fig. 2(a)]. Similar concepts have been used in [14] to analyze the static structure of an attractor, but we focus here on the dynamics. We denote by S_m the set of collections of contiguous m-cells, which are the analogs of m-dimensional surfaces in the original phase space. As Poincaré sections are swept, periodic points move in the section plane and so do the m-cells attached to them [Fig. 2(b)]. The dynamics induced in S_m should reflect that of m-dimensional phase-space surfaces under action of the chaotic flow, and in particular should be organized by the same stretching and squeezing mechanisms.

A dynamics in the triangulated space is specified by maps $F_m: S_m \to S_m$ acting on collections of contiguous m-cells. Since the original return map F sends nodes to nodes but not

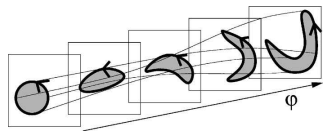

FIG. 1. Under the action of the flow, volume elements of Poincaré sections and their boundaries are stretched and squeezed but retain their orientation, as illustrated here for 2D section planes.

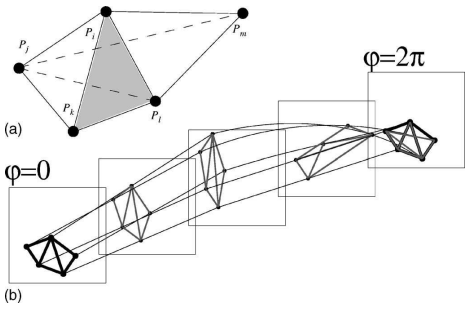

FIG. 2. (a) Triangulated space based on periodic points P_i in a 3D Poincaré section. The 2-cell $\langle ikl\rangle$ is shaded. (b) The flow induces a mapping of this triangulated space into itself, as suggested here for a period-5 orbit embedded in $\mathbb{R}^2\times S^1$.

facets to facets, the F_m are not restrictions of F for $m>0$. However, we require them to mimic F in the following way: they should be invertible, satisfy determinism, and result from a continuous deformation of facets, just as F is a continuous deformation of identity. The F_m should also satisfy $\partial F_m(\Sigma)=F_{m-1}(\partial\Sigma)$, where ∂ is the boundary operator. As we see below, facets are not necessarily trivially advected between sections because degeneracies occur, at which action must be taken to preserve orientation.

We now specialize to the 3D case. The volume element of a triangulated set of periodic points in a 2D Poincaré section is a triangle (2-cell) based on three periodic points P_i, P_j, and P_k. Let $P_i(\varphi)$ be the position of P_i in section φ, with $P_i(0)=P_i$ and $P_i(2\pi)=P_{i+1}$. The natural evolution of $T=\langle P_i,P_j,P_k\rangle$ as φ increases is

$$T(\varphi)=\langle P_i(\varphi),P_j(\varphi),P_k(\varphi)\rangle, \tag{1}$$

which would lead to a trivial induced return map $F_2(T)=T(2\pi)=\langle P_{i+1},P_{j+1},P_{k+1}\rangle$ if expression (1) were uniformly valid as a 2-cell. However, it is common that at some $\varphi=\varphi_0$, one of the three points [say $P_k(\varphi)$] passes between the two others, thereby changing the orientation of the candidate 2-cell $T(\varphi)$ given by expression (1) (Fig. 3). As emphasized above, this is strictly forbidden by determinism, and we must thus modify the representation of the dynamics. It turns out that this problem has a simple solution.

The degenerate triangle $T(\varphi_0)$ in Fig. 3 is like a flattened balloon whose boundary splits into two superimposed sides with opposing outer normals. Determinism is violated when

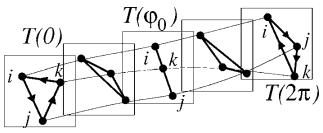

FIG. 3. As three points move in the section plane when φ is increased, the triangle they form can change its orientation.

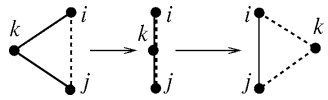

FIG. 4. A triangle is inverted as P_k passes between P_i and P_j. Identifying the solid (dashed) paths in the initial and end configurations leads to substitution (2).

these two sides cross each other so that interior and exterior, defined with respect to outer normal, seem to be exchanged. However, the experimental data only constrain node motion, from which the facet dynamics is interpolated. To preserve determinism, we force the two opposing sides not to cross by swapping them at degeneracy, thereby canceling the inversion.

This prescription is illustrated in Fig. 4, where the two opposing sides at triangle degeneracy are represented as a solid and a dashed line. The key point is that we construct the edge dynamics so that the left (solid line) and right (dashed line) sides remain at the left and right, respectively. Since the left (right) side consists of itinerary $\langle ik\rangle+\langle kj\rangle$ ($\langle ij\rangle$) before degeneracy and of itinerary $\langle ij\rangle$ ($\langle ik\rangle+\langle kj\rangle$) after degeneracy, their relative position is preserved by applying the following dynamical rule in $S_1=S_{n-1}$ at triangle inversion:

$$\langle ij\rangle\to\langle ik\rangle+\langle kj\rangle, \tag{2a}$$

$$\langle ik\rangle+\langle kj\rangle\to\langle ij\rangle. \tag{2b}$$

These rules also apply to reverse paths (e.g., $\langle ji\rangle\to\langle jk\rangle+\langle ki\rangle$). Note that $\partial T=\partial\langle ijk\rangle=\langle ij\rangle+(\langle jk\rangle+\langle ki\rangle)$ is mapped by (2) to $(\langle ik\rangle+\langle kj\rangle)+\langle ji\rangle=\partial\langle ikj\rangle$. The permutation compensates for triangle inversion so that orientation of ∂T, and hence determinism, is preserved.

Itineraries visiting edges $e_{ij}=\langle ij\rangle$ in a given order are represented by words in a language $\mathcal{A}^*$ over alphabet $\mathcal{A}=\{e_{lm}\}$, and (2) by an operator σ_{ij}^k that in each word w replaces the letter e_{ij} by the string $e_{ik}e_{kj}$ and $e_{ik}e_{kj}$ by e_{ij} [hence $(\sigma_{ij}^k)^2=1$]. For example,

$$\sigma_{ij}^k e_{kl}e_{li}\overline{e_{ij}}e_{ji}e_{li}\underline{e_{ik}e_{kj}}\overline{e_{ji}}\cdots=e_{kl}e_{li}\overline{e_{ik}e_{kj}}e_{jl}e_{li}\underline{e_{ij}}\overline{e_{jk}e_{ki}}\cdots.$$

The σ_{ij}^k generate a nontrivial dynamics, as the image of an itinerary depends on how periodic points rotate around each other. This simple dynamics faithfully reflects that of the flow around the periodic orbit, as we show by computing the entropy of the orbit.

From the motion of periodic points $P_i(\varphi)$ in the section plane as φ is swept, a list of l triangle inversions $\sigma_{i_m j_m}^{k_m}$ is obtained, from which we build an induced return map that transforms a word $w\in\mathcal{A}^*$ into another word w' as

$$F_1{:}w\to w'=N\sigma_{i_1j_1}^{k_1}\cdots\sigma_{i_2j_2}^{k_2}\sigma_{i_1j_1}^{k_1}w, \tag{3}$$

where $Ne_{ij}\cdots=e_{(i+1)(j+1)}\cdots$. Consider periodic orbit 00111 of a suspension of the standard horseshoe map equipped with the usual symbolic coding [2] [Figs. 2(b) and 5(a)]. We find that as points gradually move in the section plane from their initial location to that of their image under the return map,

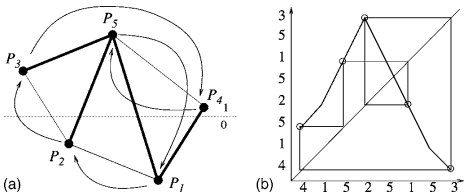

FIG. 5. (a) Periodic points of the horseshoe orbit 00111 and their schematic trajectory in section plane. Bold lines indicate edges involved in (4). (b) Path $P_4P_1P_5P_2P_5P_1P_5P_3$ folds onto itself under action of induced return map F_1. The unimodal map obtained has 00111 as a periodic orbit.

triangle inversions occur when point 4 successively crosses the four edges e_{15}, e_{13}, e_{25}, and e_{23}. Thus the induced return map for edge itineraries is $F_1 = N\sigma_{23}^4\sigma_{25}^4\sigma_{13}^4\sigma_{15}^4$. For example,

$$e_{15} \xrightarrow{\sigma_{15}^4} e_{14}e_{45} \xrightarrow{\cdots} e_{14}e_{45} \xrightarrow{N} e_{25}e_{51} = F_1(e_{15}),$$

while edges not crossed by point 4 are trivially modified (e.g., $e_{14} \xrightarrow{N} e_{25}$). This leads to the closed rule set

$$e_{14} \to e_{25},\ e_{15} \to e_{25}e_{51},\ e_{25} \to e_{35}e_{51},\ e_{35} \to e_{41} \qquad (4)$$

for edges in the invariant set of F_1. Table I displays iterates $F_1^m(e_{15})$ computed using (4). Their length $|F_1^m(w)|$ diverges exponentially as $m \to \infty$, indicating that trajectories in the neighborhood of the orbit are continuously stretched apart by the flow. The growth rate

$$h(P) = \lim_{m\to\infty} \frac{\ln |F_1^m(w)|}{m} \qquad (5)$$

is obtained as the logarithm of the leading eigenvalue of the transition matrix $(M_{ee'})$, whose entries count occurrences of edge e' or of its reverse in $F_1(e)$ given by (4). Here, $h(00111) \sim 0.5435$. Table I also shows that $F_1^{kp}(w)$ (p is the orbit period) converges to an infinite word w_∞ satisfying

TABLE I. A few iterates $F_1^m(e_{15})$ are given by their itinerary between periodic points [e.g., (35152) denotes the path $e_{35}e_{51}e_{15}e_{52}$].

m	Itinerary of $F_1^m(e_{15})$
0	(15)
1	(251)
2	(35152)
3	(41525153)
4	(5251535152514)
5	(1535152514152515351525)
6	(2514152515351525251535152514152515351)
10	(153515251415251535152525153515252515351 5⋯)
15	(153515251415251535152525153515252515351 5⋯)
100	(153515251415251535152525153515252515351 5⋯)

TABLE II. Topological entropies of positive-entropy horseshoe orbits up to period 8 obtained with the approach described here and with the train-track algorithm (TTA).

Orbit	This work	TTA	Orbit	This work	TTA
01101 $^0_1$1	0.4421	0.4421	00010 $^0_1$1	0.3822	0.3822
001011 $^0_1$1	0.3460	0.3460	000101 $^0_1$1	0.5686	0.5686
00101 $^0_1$1	0.4768	0.4768	0001 $^0_1$1	0.6329	0.6329
001010 $^0_1$1	0.4980	0.4980	000111 $^0_1$1	0.5686	0.5686
001 $^0_1$1	0.5435	0.5435	00011 $^0_1$1	0.3822	0.3822
001110 $^0_1$1	0.4980	0.4980	000010 $^0_1$1	0.4589	0.4589
00111 $^0_1$1	0.4768	0.4768	00001 $^0_1$1	0.6662	0.6662
001111 $^0_1$1	0.3460	0.3460	000011 $^0_1$1	0.4589	0.4589
001101 $^0_1$1	0.4980	0.4980	000001 $^0_1$1	0.6804	0.6804

$F_1^p(w_\infty) = w_\infty$, which is the analog of the infinitely folded unstable manifold of the periodic orbit.

The growth rate $h(P)$ is expected to be the entropy $h_T(P)$ of orbit P, defined as the minimal topological entropy [8] of a map containing P [9]. Indeed, a piecewise linear map containing P with $(M_{ee'})$ as Markov transition matrix can be constructed and has entropy $h(P)$, thus $h_T(P) \le h(P)$. Conversely, $h(P) \le h_T(P)$, as $h(P)$ is the minimal growth rate of the geometric length of curves passing through periodic points P_i and cannot be larger than the topological entropy of a map containing P, which is the supremum of stretching rates over curves in the plane [15].

For a typical orbit, unlike in (4), there are paths in the F_1-invariant set that trigger a "squeezing" rule (2b), as, for example, $e_{16}e_{67} \to e_{17}$ for horseshoe orbit 0010111. Then $F_1(e_{16}e_{67}) \ne F_1(e_{16})F_1(e_{67})$ and the transition matrix cannot be used for entropy computations, although estimates can still be obtained by direct iteration. In all the examples we considered, enlarging the alphabet by recoding contracting paths as basis edges (e.g., $e_{167} \equiv e_{16}e_{67}$) and applying other recodings required for consistency allowed us to rewrite F_1 as an ordinary substitution like (4). For example, the induced return map for horseshoe orbit 0010111 can be rewritten as ($e_{ijk} \equiv e_{ij}e_{jk}$)

$$e_{14} \to e_{25},\ e_{15} \to e_{257}e_{76},\ e_{17} \to e_{257}e_{71},\ e_{25} \to e_{37}e_{76},$$

$$e_{37} \to e_{41},\ e_{67} \to e_{71},\ e_{167} \to e_{25}e_{51},\ e_{257} \to e_{37}e_{761}.$$

Besides e_{167}, basis path e_{257} was introduced because its image overlaps e_{167}. A transition matrix can then be obtained, with entropy $h(0010111) \sim 0.4768$.

For all 746 periodic orbits of the horseshoe map up to period 12, we have compared growth rate (5) with topological entropy obtained by the train-track algorithm [9,10,16]. As illustrated in Table II, we found *agreement to machine precision in each instance*. This strongly suggests that in 3D, our approach is equivalent to the train-track approach. Qualitative properties of chaos are also reproduced: the dynamics is deterministic (by construction), invertible, and the stretching and squeezing processes are described in a symmetrical way.

Remarkably, we note that while transformations (3) are *invertible*, the asymptotic dynamics is *singular*. Consider the itinerary $w_0 = F^3(e_{15}) = (41525153)$ in Table I, which is the shortest subpath of w_∞ visiting the four edges in (4). As Fig. 5(b) shows, the image $F_1(w_0) = (5251535152514) = (525153) + (35152514)$ consists of a subpath of w_0 concatenated with a reverse copy of w_0: *this path is folded onto itself by a singular one-dimensional map*. The same property holds for all subsequent iterates $F^m(e_{15})$, hence for the infinite word w_∞. This reflects that associated to an invertible return map (e.g., Hénon map), there exists an underlying lower-dimensional noninvertible map (e.g., logistic map) describing the dynamics along the unstable manifold, a keystone of the Birman-Williams construction [2,5]. Note that the symbolic name 00111 can be recovered directly from Fig. 5(b) using the usual coding for orbits of 1D maps. This makes the new formalism promising for using topological information to construct global symbolic codings as in [17]. How segments along w_0 are folded over each other and how neighboring cells are squeezed provide us with a combinatorial description of stretching and folding that could be used to determine the simplest template carrying the periodic orbit studied.

To conclude, we have proposed that orientation preservation is a more general formulation of determinism than nonintersection of trajectories. In three dimensions we find that enforcing it on a triangulation of periodic points induces a nontrivial dynamics on paths along periodic periodic points. More precisely, a path map F_1 is constructed by (i) following triangles advected by the flow as one rotates around the attractor, (ii) restoring orientation at each triangle inversion by exchanging opposing sides via transformations (2). When paths in the F_1-invariant set do not experience contraction, entropy is obtained from a transition matrix indicating how elementary edges in the invariant set are mapped among themselves. Otherwise, new basis paths must be introduced to account for contraction. A promising result is that despite its simplicity, this formalism numerically predicts the correct entropies for periodic orbits of the horseshoe map. Preliminary calculations also suggest that it leads to a combinatorial description of the folding of the invariant unstable manifold over itself, yielding information about the symbolic dynamics of the orbit. It now remains to prove the validity of the approcach in 3D and to try to extend it to higher dimensions.

This work grew out of innumerable discussions with R. Gilmore. I thank T. Hall, J. Los, and F. Gautero for helpful explanations about train tracks, and M. Nizette, T. Tsankov, J.-C. Garreau, C. Szwaj, and S. Bielawski for a careful reading of this manuscript. CERLA is supported by the Ministère chargé de la Recherche, Région Nord-Pas de Calais and FEDER.

[1] E. Ott, *Chaos in Dynamical Systems* (Cambridge University Press, Cambridge, 1993).
[2] R. Gilmore, Rev. Mod. Phys. **70**, 1455 (1998); R. Gilmore and M. Lefranc, *The Topology of Chaos* (Wiley, New York, 2002).
[3] G. B. Mindlin, X. J. Hou, H. G. Solari, R. Gilmore, and N. B. Tufillaro, Phys. Rev. Lett. **64**, 2350 (1990).
[4] G. B. Mindlin *et al.*, J. Nonlinear Sci. **1**, 147 (1991).
[5] J. S. Birman and R. F. Williams, Topology **22**, 47 (1983).
[6] G. Froyland, O. Junge, and G. Ochs, Physica D **154**, 68 (2001).
[7] S. Day, O. Junge and K. Mischaikow, SIAM J. Appl. Dyn. Syst. **2**, 117 (2004).
[8] P. Walters, *An Introduction to Ergodic Theory* (Springer, New York, 2000).
[9] P. Boyland, Topol. Appl. **58**, 223 (1994).
[10] M. Bestvina and M. Handel, Topology **34**, 109 (1995).
[11] A. Amon and M. Lefranc, Phys. Rev. Lett. **92**, 094101 (2004).
[12] J.-L. Thiffeault, Phys. Rev. Lett. **94**, 084502 (2005).
[13] G. B. Mindlin and H. G. Solari, Physica D **102**, 177 (1997).
[14] D. Sciamarella and G. B. Mindlin, Phys. Rev. Lett. **82**, 1450 (1999).
[15] S. E. Newhouse and T. Pignataro, J. Stat. Phys. **72**, 1331 (1993).
[16] T. Hall, TRAINS, software available from http://www.liv.ac.uk/maths/PURE/MIN_SET/CONTENT/members/ T_Hall.html.
[17] J. Plumecoq and M. Lefranc, Physica D **144**, 231 (2000).

"Topological Signature of Deterministic Chaos in Short Nonstationary Signals from an Optical Parametric Oscillator"

Axelle Amon, and Marc Lefranc

Phys. Rev. Lett. **92**, 094101 (2004)

VOLUME 92, NUMBER 9 PHYSICAL REVIEW LETTERS week ending 5 MARCH 2004

Topological Signature of Deterministic Chaos in Short Nonstationary Signals from an Optical Parametric Oscillator

Axelle Amon and Marc Lefranc

Laboratoire de Physique des Lasers, Atomes, Molécules, UMR CNRS 8523, Centre d'Études et de Recherches Lasers et Applications, Université des Sciences et Technologies de Lille, F-59655 Villeneuve d'Ascq, France

(Received 24 July 2003; published 5 March 2004)

Although deterministic chaos has been predicted to occur in the triply resonant optical parametric oscillator (TROPO) 15 years ago, experimental evidence of chaotic behavior in this system has been lacking so far, in marked contrast with most nonlinear systems, where chaos has been actively tracked and found. This situation is probably linked to the high sensitivity of the TROPO to perturbations, which adversely affects stationary operation at high power. We report the experimental observation in this system of a burst of irregular behavior of duration 80 μs. Although the system is highly nonstationary over this time interval, a topological analysis allows us to extract a clear-cut signature of deterministic chaos from a time series segment of only nine base cycles (3 μs). This result suggests that nonstationarity is not necessarily an obstacle to the characterization of chaos.

DOI: 10.1103/PhysRevLett.92.094101 PACS numbers: 05.45.–a, 42.65.Yj, 42.65.Sf

It has become common knowledge that many nonlinear systems obeying deterministic equations of motion can display seemingly erratic behavior. In the last decades, deterministic chaos has been the subject of intensive experimental investigation and has been observed in a large variety of experimental systems (see, e.g., [1]). However, characterizing chaos is significantly more demanding than characterizing periodic behavior, for which measuring simple quantities such as amplitude or frequency over a short time interval is sufficient. Indeed, most quantitative measures of chaos (e.g., fractal dimensions or Lyapunov exponents) rely on constructing an approximation of the natural measure on a strange attractor, which requires observing the system for at least a few hundreds of cycles at fixed control parameters [2,3].

Thus, it is extremely difficult to assess deterministic chaos in a system that experiences parameter drifts on a time scale comparable to the mean dynamical period, so that stationarity cannot be assumed. In particular, this is the case when studying a subsystem that cannot be considered as isolated from its environment, a situation that frequently occurs in biological systems. Yet, it is often desirable to understand the behavior of a small part of a complex system before unraveling its global dynamics. A natural question then is can we infer the existence of an underlying chaotic dynamics from a very short, nonstationary, time series? In this Letter, we present a case in which this question can be answered positively: by applying topological tools [4–6] to a burst of irregular behavior recorded in a triply resonant optical parametric oscillator (TROPO) subject to thermal effects, we extract a clear-cut signature of deterministic chaos from an extremely short time series segment of only nine base cycles.

Optical parametric oscillators are sources of coherent light based on parametric down-conversion of pump photons into pairs of subharmonic photons in a nonlinear optical crystal. This effect is enhanced by enclosing the crystal inside a cavity so as to build an oscillator. When the cavity is resonant for the three waves, the threshold for infrared generation can be as low as a few mW. As lasers, TROPOs are based on a nonlinear interaction and are naturally susceptible to instabilities and chaos. Accordingly, chaotic behavior was identified in a simple TROPO model 15 years ago [7]. Surprisingly, this theoretical prediction has so far not been confirmed experimentally.

Instabilities and chaos are expected to occur in the TROPO at high power, where optical nonlinearities are emphasized. However, high energy densities in the crystal induce other effects, in particular, thermal effects. It was recently shown that the TROPO can be subject to thermo-optical instabilities where the cavity length is no longer a fixed parameter but behaves as a slow variable coupled to the optical variables [8]. This gives rise to relaxation oscillations [8,9], as well as to a variety of bursting regimes [10] when these slow oscillations combine with fast oscillations resulting from the interaction of transverse modes [11]. The coexistence of two different time scales then makes it difficult to characterize the dynamics, especially in the case of irregular regimes.

The TROPO used in the experiment is as described in Refs. [8,9,11]. It features a 15-mm-long KTP (potassium titanyl phosphate) crystal cut for type-II phase matching, enclosed inside a 63-mm-long cavity delimited by two mirrors with a radius of curvature of 50 mm. Cavity length is not actively stabilized. The cavity is resonant at 532 nm, the wavelength of the frequency-doubled Nd:YVO_4 pump laser, and at 1064 nm, near which two infrared fields are generated. Parametric threshold is reached at pump powers of the order of 10 mW. At a pump power of 3.5 W (i.e., 350 times above threshold), we

have observed in the output signal intensity waveforms more complex than the periodic instabilities reported so far [8–12]. The time series that we analyze in this paper is shown in Fig. 1. Because the raw recording had limited vertical resolution, it has been processed through an acausal low pass filter with a cutoff frequency of 7 MHz. Acausal filtering of the time series has not been shown to introduce artifacts in subsequent phase-space reconstructions [13]. Between $t = 790$ μs and $t = 870$ μs, Fig. 1(a) displays a burst of irregular behavior inside a long interval of quasisinusoidal periodic behavior of frequency approximately 3 MHz. The rapid variation of the periodic waveform with time shows clearly that the system is highly nonstationary. The drift occurs on a time scale consistent with previous reports of thermal effects in this system [8,9].

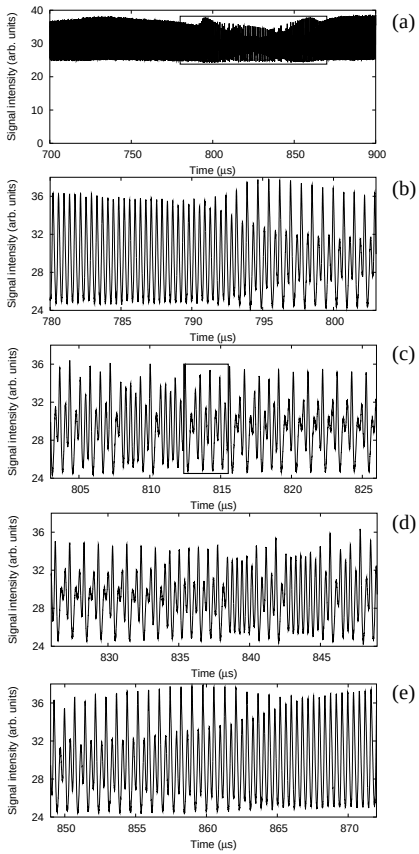

FIG. 1. (a) Signal intensity vs time; (b)–(e) consecutive excerpts from the irregular burst occurring for $t \in [780, 875]$. The segment between $t = 812.421$ and $t = 815.562$ contains a period-9 orbit used in the subsequent topological analysis.

The complex burst shown in detail in Figs. 1(b)–1(e) is highly suggestive of deterministic chaos. Between $t = 790$ μs and $t = 805$ μs, it begins by a progressive transition from the base period-1 orbit to a period-2 orbit. This is a signature of a period-doubling bifurcation, the first step of the most ubiquitous route to chaos. The reverse bifurcation can be seen in Fig. 1(e). Moreover, the time series displays a number of sequences of almost periodic behavior, a hallmark of low-dimensional chaos [4,5]. In particular, the segment between $t = 830$ μs and $t = 840$ μs contains three periodic bursts of periods 3, 2, and 1.

When chaotic behavior is suspected, a natural step is to try to reconstruct a strange attractor in a phase space using, e.g., the method of time delays [2–5]. In the present case, this procedure is questionable because the system is not stationary. Indeed, the superposition of trajectory segments corresponding to different values of control parameters is expected to yield a blurred plot. However, a phase-plane plot of the time series of Figs. 1(b)–1(e) is surprisingly similar to a Rössler-type chaotic attractor (Fig. 2). This indicates that trajectories of our system change their shape relatively slowly as a control parameter is varied.

Next, we choose a Poincaré section (Fig. 2) and construct a first return map for it. A convenient choice is the return map for the times of flight T_n between the nth and the $(n + 1)$th intersections with the section plane, which are relatively insensitive to noise. How T_n varies along the time series is shown in Fig. 3(a). This plot clearly displays the bifurcation diagram of a system that undergoes a period-doubling cascade, explores a chaotic zone followed by a period-3 periodic window, and then goes back. Note that the fraction of the diagram where complex behavior is observed is relatively small.

The plot (T_n, T_{n+1}) is shown in Fig. 3(b), where a folded structure similar to a one-dimensional map can easily be discerned. This suggests that the irregular

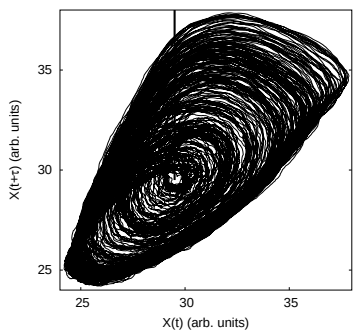

FIG. 2. Phase-plane portrait $[X(t), X(t + \tau)]$, with $X(t)$ the time series of Figs. 1(b)–1(e) and $\tau = 55$ ns. The vertical line indicates the section plane used in the subsequent analysis. Flow rotates clockwise around the hole in the middle.

VOLUME 92, NUMBER 9 PHYSICAL REVIEW LETTERS week ending 5 MARCH 2004

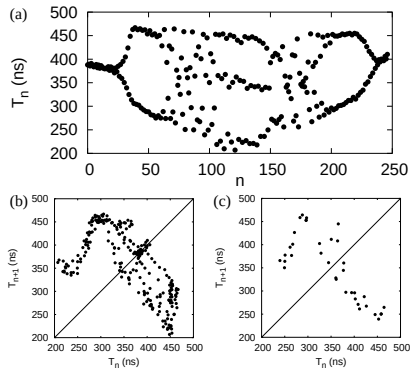

FIG. 3. (a) Poincaré section return times T_n vs intersection number n. Return maps (T_n, T_{n+1}) (b) for $n \in [1, 250]$; (c) for $n \in [70, 105]$.

dynamics observed in the experiment is deterministic. However, no quantitative information can be extracted from Fig. 3(b) which is blurred by variations in control parameters, as can be verified by plotting separately graphs corresponding to different parts of the time series. If we restrict ourselves to the first chaotic zone of Fig. 3 (i.e., for $n \in [70, 105]$, or $t \in [806.8, 819.0]$), the resulting plot is much closer to a one-dimensional map but there are now too few points to rigorously assess the presence of deterministic chaos, let alone to quantify it [Fig. 3(c)].

Indeed, most characterization methods require that the neighborhood of each point in phase space is sufficiently populated to capture the local structure of the attractor. Thus, they depend on the time series *nonlocally* in time: nearest neighbors in phase space are usually located far apart in the time series (*long-term recurrence*). This makes these methods fragile with respect to variations of control parameters along the time series. As we see below, a topological analysis circumvents this problem by extracting information from isolated time series segments, namely, those approaching a closed orbit (*short-term recurrence*): we shall not only extract a signature of an underlying chaotic dynamics in the fixed-parameter system but also obtain lower bounds on its topological entropy, a classical measure of chaos.

The time series of Fig. 1 displays many periodic events. As with the period-3 orbit, many of them correspond to stable periodic windows explored by the system as parameters are swept but some can also be found in zones of irregular behavior. They then likely correspond to a close encounter with one of the infinity of unstable periodic orbits embedded in a chaotic attractor.

The topological analysis of chaos [4,5] proceeds by characterizing the organization of periodic orbits, which are associated with closed curves in phase space. In dimension three, how these curves are intertwined can be studied using knot theory and branched manifolds (“templates”). This is because the knot invariants of periodic orbits provide topological signatures of the stretching and squeezing mechanisms organizing a strange attractor [4,5]. A major advantage of topological analysis is that each time series segment shadowing a periodic orbit, *stable or unstable*, can be analyzed independently of the others.

Although the time series of Figs. 1(b)–1(e) is very short, we have detected several closed orbits in it. The criterion was that the orbit should return to its initial condition in the (T_n, T_{n+1}) plane with 3% accuracy. These orbits are the period-1, period-2, period-4, and period-8 orbits of the period-doubling cascade, the period-3 orbit, as well as four orbits of periods 6, 7, 9, and 10.

We have found that the braids associated with these closed orbits can all be projected to a standard horseshoe template [4,5], as the structure of the return map suggests. More precisely, they have the same braid types as orbits 1, 01, 01^3, $01^3(01)^2$, 01^6, 011010111, $(011)^3 1$, 011, and 01^5 of the standard horseshoe template (ordered as in the time series). Linking numbers were not computed as this would require comparing different parts of the time series. This observation suggests that although orbits change their shape as control parameters vary along the time series, their topological organization is not modified. Such a robustness would be extremely unlikely if the irregular dynamics observed was not deterministic.

However, topological analysis can provide us with stronger evidence. Indeed, we have found that two of the closed orbits have a “positive-entropy” braid type. One is shown in Fig. 4. In a stationary system, how trajectories are stretched and folded around such an orbit forces the existence of an infinity of periodic orbits [6]. Thus, positive-entropy orbits exist only in systems that have experienced infinitely many bifurcations and are chaotic in some region of parameter space [4–6,14,15]: a “pretzel knot” (i.e., a common type of positive-entropy orbit

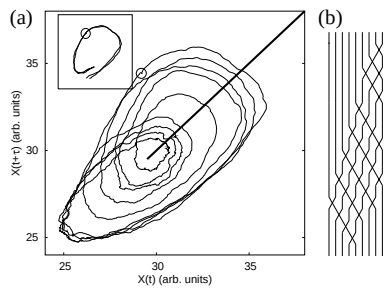

FIG. 4. (a) A period-9 closed orbit detected in the time series. The open circle indicates its starting and final points. The inset displays trajectory segments around these two points; (b) a presentation of this orbit as an open braid, using the diagonal as a Poincaré section.

having such a knot type) in a three-dimensional flow implies chaos just as a period-3 orbit in a one-dimensional map does. The presence of such an orbit in an experimental data set was first used as an indicator of chaos for the Belousov-Zhabotinskii reaction [16]. Pretzel knots have also been observed in laser experiments [17,18]. How many orbits are forced by a given braid type is quantified by its topological entropy, which is a lower bound on the topological entropy of systems containing it [6].

Using the TRAINS program by Hall [19], we have computed the topological entropy of the braid in Fig. 4(b) to be $h_T \sim 0.377\,057 > 0$. Similarly, the period-10 orbit has entropy $h_T \sim 0.473\,404 > 0$. If our system were stationary (as in Refs. [16–18]), the presence of such orbits would unambiguously imply chaos and provide a lower bound on topological entropy. However, the closed orbit in Fig. 4 is not a true periodic orbit, since control parameters have different values at its starting and final points.

Nevertheless, the following observation gives us confidence that the observed braid type is actually present in the unperturbed system. The inset of Fig. 4 shows two trajectory segments $\{X(t); t \in [t_0 - \tau_1, t_0 + \tau_2]\}$ and $\{X(t); t \in [t_0 + T - \tau_1, t_0 + T + \tau_2]\}$ centered around the starting point $X(t_0)$ and the ending point $X(t_0 + T)$ of the closed orbit, with $\tau_1 + \tau_2 = 350$ ns being approximately one orbital period. Although the two segments correspond to the extreme values of the control parameter along the closed orbit [Fig. 3(a) indicates that parameter variation is monotonic for $n \in [86, 93]$], we see that they are almost superimposed on each other. This indicates that the vector flow changes very little between $t = t_0$ and $t = t_0 + T$. The separation between the two segments can then be taken as an upper bound on the separation between the closed orbit observed and a periodic orbit of the unperturbed system. As this separation is significantly smaller than the separation between strands of the closed orbit in Fig. 4(a), the unperturbed system (i.e., the TROPO with fixed cavity length) must have a periodic orbit with the braid type shown in Fig. 4(b). We can then conclude that it exhibits deterministic chaos. Similarly, perturbations due to noise have no influence if their amplitude is small with respect to interstrand distance.

Our study shows that closed orbits with a positive-entropy braid type can be exploited when the influence of parameter variation is small over one orbit period, a modest requirement compared to other methods. However, we expect this approach to be also applicable to stronger nonstationarity. Generically, closed orbits of a system with a swept parameter connect continuously to periodic orbits of the unperturbed system as the sweeping rate goes to zero, as is easily shown using the implicit function theorem. If a positive-entropy closed orbit can be shown not to change its braid type along the homotopy path, then it provides a signature of chaos. Understanding when braid type is preserved is difficult, but a preliminary study of the logistic map with a swept parameter (where permutation of the periodic points is the counterpart of braid type) suggests that this approach is quite robust. Regarding applicability to higher-dimensional systems, where knots and braids fall apart, we are currently developing alternate methods for computing the topological entropy of a periodic orbit.

In conclusion, sophisticated topological methods have allowed us to obtain the first experimental signature of deterministic chaos in an optical parametric oscillator using only a very short segment of a nonstationary time series, which contained a positive-entropy orbit. Moreover, the fact that two such orbits were detected in less than 40 cycles indicates that these signatures of chaos are extremely robust with respect to variation in control parameters.

We thank R. Gilmore, T. Hall, S. Bielawski, D. Derozier, and J. Zemmouri for stimulating discussions. CERLA is supported by the Ministère chargé de la Recherche, Région Nord-Pas de Calais and FEDER.

[1] P. Cvitanović, *Universality in Chaos* (Adam Hilger, Bristol, 1989).
[2] E. Ott, *Chaos in Dynamical Systems* (Cambridge University Press, Cambridge, 1993).
[3] H. D. I. Abarbanel, *Analysis of Observed Chaotic Data* (Springer-Verlag, New York, 1996).
[4] R. Gilmore and M. Lefranc, *The Topology of Chaos: Alice in Stretch and Squeezeland* (Wiley, New York, 2002).
[5] R. Gilmore, Rev. Mod. Phys. **70**, 1455 (1998).
[6] P. Boyland, Topology Appl. **58**, 223 (1994).
[7] L. A. Lugiato, C. Oldano, C. Fabre, E. Giacobino, and R. J. Horowicz, Nuovo Cimento Soc. Ital. Fis. **10D**, 959 (1988).
[8] P. Suret, D. Derozier, M. Lefranc, J. Zemmouri, and S. Bielawski, Phys. Rev. A **61**, 021805(R) (2000).
[9] P. Suret, M. Lefranc, D. Derozier, J. Zemmouri, and S. Bielawski, Opt. Lett. **26**, 1415 (2001).
[10] A. Amon, M. Nizette, M. Lefranc, and T. Erneux, Phys. Rev. A **68**, 023801 (2003).
[11] P. Suret, M. Lefranc, D. Derozier, J. Zemmouri, and S. Bielawski, Opt. Commun. **200**, 369 (2001).
[12] C. Richy, K. I. Petsas, E. Giacobino, C. Fabre, and L. Lugiato, J. Opt. Soc. Am. B **12**, 456 (1995).
[13] F. Mitschke, Phys. Rev. A **41**, 1169 (1990).
[14] T. Hall, Nonlinearity **7**, 861 (1994).
[15] G. B. Mindlin, R. Lopez-Ruiz, H. G. Solari, and R. Gilmore, Phys. Rev. E **48**, 4297 (1993).
[16] G. B. Mindlin, H. G. Solari, M. A. Natiello, R. Gilmore, and X.-J. Hou, J. Nonlinear Sci. **1**, 147 (1991).
[17] F. Papoff, A. Fioretti, E. Arimondo, G. B. Mindlin, H. G. Solari, and R. Gilmore, Phys. Rev. Lett. **68**, 1128 (1992).
[18] M. Lefranc and P. Glorieux, Int. J. Bifurcation Chaos Appl. Sci. Eng. **3**, 643 (1993).
[19] T. Hall, TRAINS, software available from http://www.liv.ac.uk/maths/PURE/MIN_SET/CONTENT/members/T_Hall.html

"The Topology of Chaos: Alice in Stretch and Squeezeland"

Robert Gilmore, and Marc Lefranc

(Wiley, New York, 2002)

The Topology of Chaos

Alice in Stretch and Squeezeland

Robert Gilmore and Marc Lefranc

A Wiley-Interscience Publication
JOHN WILEY & SONS, INC.

New York / Chichester / Weinheim / Brisbane / Singapore / Toronto

Preface

Before the 1970s opportunities sometimes arose for physicists to study nonlinear systems. This was especially true in fields like fluid dynamics and plasma physics, where the fundamental equations are nonlinear and these nonlinearities masked (and still mask) the full spectrum of spectacularly rich behavior. When possible we avoided being dragged into the study of abstract nonlinear systems. For we believed, to paraphrase a beautiful generalization of Tolstoy, that

> All linear systems are the same.
> Each nonlinear system is nonlinear in its own way.

At that time we believed that one could spend a whole lifetime studying the nonlinearities of the van der Pol oscillator [Cartwright and Littlewood (1945), Levinson (1949)] and wind up knowing next to nothing about the behavior of the Duffing oscillator.

Nevertheless, other intrepid researchers had been making an assault on the complexities of nonlinear systems. Smale (1967) described a mechanism responsible for generating a great deal of the chaotic behavior which has been studied up to the present time. Lorenz, studying a drastic truncation of the Navier-Stokes equation, discovered and described 'sensitive dependence on initial conditions' (1963). The rigid order in which periodic orbits are created in the bifurcation set of the logistic map, and in fact any unimodal map of the interval to itself, was described by May (1976) and by Metropolis, Stein, and Stein (1973).

Still, $\cdots$. There was a reluctance on the part of most scientists to indulge in the study of nonlinear systems.

This all changed with Feigenbaum's discoveries (1978). He showed that scaling invariance in period doubling cascades leads to quantitative (later, qualitative) predictions. These are the scaling ratios

$$\begin{aligned} \delta &= 4.66920\,16091\,029\cdots && \text{control parameter space} \\ \alpha &= -2.50290\,78750\,959\cdots && \text{state variable space} \end{aligned}$$

which are eigenvalues of a renormalization transformation. The transformation in the attitude of scientists is summarized by the statement (Gleick, 1987)

> "It was a very happy and shocking discovery that there were structures in nonlinear systems that are always the same if you looked at them the right way."

This discovery launched an avalanche of work on nonlinear dynamical systems. Old experiments, buried and forgotten because of instabilities or unrepeatability due to incompetent graduate students (in their advisor's opinions) were resurrected and pushed as ground-breaking experiments exhibiting 'first observations' of chaotic behavior (by these same advisors). And many new experiments were carried out, at first to test Feigenbaum's scaling predictions, then to test other quantitative predictions, then just to see what would happen.

Some of the earliest experiments were done on fluids, since the fundamental equations are known and are nonlinear. However, these experiments often suffered from the long time scales (days, weeks, or months) required to record a decent data set. Oscillating chemical reactions (e.g., the Belousov-Zhabotinskii reaction) yielded a wide spectrum of periodic and chaotic behavior which was relatively easy to control and to tune. These data sets could be generated in hours or days. Nonlinear electric circuits were also extensively studied, although there was (and still is) a prejudice to regard them with a jaundiced eye as little more than analog computers. Such data sets could be generated very quickly (seconds to minutes) — almost as fast as numerical simulations. Finally, laser laboratories contributed in a substantial way to build up extensive and widely varying data banks very quickly (milleseconds to minutes) of chaotic data.

It was at this time (1988), about 10 years into the 'nonlinear science' revolution, that one of the authors (RG) was approached by his colleague (J. R. Tredicce, then at Drexel, now at the Institut Non Linéaire de Nice) with the proposition: "Bob, can you help me explain my data?" (See Chapter 1). So we swept the accumulated clutter off my desk and deposited his data. We looked, pushed, probed, discussed, studied, $\cdots$ for quite a while. Finally, I replied: "No." Tredicce left with his data. But he is very smart (he is an experimentalist!), and returned the following day with the same pile of stuff. The conversation was short and effective: "Bob," "Still my name," "I'll bet that you *can't* explain my data." (Bob sees red!) We sat down and discussed further. At the time two tools were available for studying chaotic data. These involved estimating Lyapunov exponents (dynamical stability) and estimating fractal dimension (geometry). Both required lots of very clean data and long calculations. They provided real number(s) with no convincing error bars, no underlying statistical theory, and no independent way to verify these guesses. And at the end of the day neither provided any information on "how to model the dynamics."

Even worse: before doing an analysis I would like to know what I am looking for, or at least know what the spectrum of possible results looks like. For example, when we analyze chemical elements or radionuclides, there is a Periodic Table of the Chemical Elements and another for the Atomic Nuclei which accommodate any such analyses. At that time, no classification theory existed for strange attractors.

In response to Tredicce's dare, I promised to (try to) analyze his data. But I pointed out that a serious analysis couldn't be done until we first had some handle on the classification of strange attractors. This could take a long time. Tredicce promised to be patient. And he was.

Our first step was to consider the wisdom of Poincaré. He suggested about a century earlier that one could learn a great deal about the behavior of nonlinear systems by studying their unstable periodic orbits which

> "... yield us the solutions so precious, that is to say, they are the only breach through which we can penetrate into a place which up to now has been reputed to be inaccessible."

This observation was compatible with what we learned from experimental data: the most important features that governed the behavior of a system, and especially that governed the perestroikas of such systems (i.e., changes as control parameters are changed) are the features that you can't see — the unstable periodic orbits.

Accordingly, my colleagues and I studied the invariants of periodic orbits, their (Gauss) linking numbers. We also introduced a refined topological invariant based on periodic orbits —- the relative rotation rates (Chapter 4). Finally, we used these invariants to identify topological structures (branched manifolds or templates, Chapter 5) which we used to classify strange attractors "in the large." The result was that "low dimensional" strange attractors (i.e., those that could be embedded in three-dimensional spaces) could be classified. This classification depends on the periodic orbits "in" the strange attractor, in particular, on their organization as elicited by their invariants. The classification is topological. That is, it is given by a set of integers (also by very informative pictures). Not only that, these integers can be extracted from experimental data. The data sets do not have to be particularly long or particularly clean — especially by fractal dimension calculation standards. Further, there are built in internal self-consistency checks. That is, the topological analysis algorithm (Chapter 6) comes with reject/fail to reject test criteria. This is the first — and remains the only — chaotic data analysis procedure with rejection criteria.

Ultimately we discovered, through analysis of experimental data, that there is a secondary, more refined classification for strange attractors. This depends on a "basis set of orbits" which describes the spectrum of all the unstable periodic orbits "in" a strange attractor (Chapter 9).

The ultimate result is a doubly discrete classification of strange attractors. Both parts of this doubly discrete classification depend on unstable periodic orbits. The classification depends on identifying:

Branched Manifold - which describes the stretching and squeezing mechanisms that operate repetitively on a flow in phase space to build up a (hyperbolic) strange attractor and to organize all the unstable periodic orbits in the strange

attractor in a unique way. The branched manifold is identified by the spectrum of the invariants of the periodic orbits that it supports.

Basis Set of Orbits - which describes the spectrum of unstable period orbits in a (nonhyperbolic) strange attractor.

The perestroikas of branched manifolds and of basis sets of orbits in this doubly discrete classification obey well-defined topological constraints. These constraints provide both a rigidity and a flexibility for the evolution of strange attractors as control parameters are varied.

Along the way we discovered that dynamical systems with symmetry can be related to dynamical systems without symmetry in very specific ways (Chapter 10). As usual, these relations involve both a rigidity and a flexibility which is as surprising as it is delightful.

Many of these insights are described in the paper *Topological analysis of chaotic dynamical systems*, Reviews of Modern Physics, **70**(4), 1455-1530 (1998), which forms the basis for part of this book. We thank the editors of this journal for their policy of encouraging transformation of research articles to longer book format.

The encounter (fall in love?) of the other author (M.L.) with topological analysis dates back to 1991, when he was a PhD student at the University of Lille, struggling to extract information from the very same type of chaotic laser that Tredicce was using. At that time, Marc was computing estimates of fractal dimensions for his laser. But they depended very much on the coordinate system used and gave no insight into the mechanisms responsible for chaotic behavior, even less into the succession of the different behaviors observed. This was very frustrating. There had been this very intringuing paper in Physical Review Letters about a "Characterization of strange attractors by integers", with appealing ideas and nice pictures. But as with many short papers, it had been difficult to understand how you should proceed when faced with a real experimental system. Topological analysis struck back when Pierre Glorieux, then Marc's advisor, came back to Lille from a stay in Philadephia, and handed him a preprint from the Drexel team, saying: "You should have a look at this stuff". The preprint was about topological analysis of the Belousov-Zhabotinskii reaction, a real-life system. It was the Rosetta Stone that helped put pieces together. Soon after, pictures of braids constructed from laser signals were piling up on the desk. They were absolutely identical to those extracted from the Belousov-Zhabotinskii data and described in the preprint. There was universality in chaos if you looked at it with the right tools. Eventually, the system that had motivated topological analysis in Philadephia, the CO_2 laser with modulated losses, was characterized in Lille and shown to be described by a horseshoe template. Indeed, Tredicce's laser could not be characterized by topological analysis because of long periods of zero output intensity that prevented invariants from being reliably estimated. The high signal to noise ratio of the laser in Lille allowed us to use a logarithmic amplifier and to resolve the structure of trajectories in the zero intensity region.

But a classification is only useful if there exist different classes. Thus, one of the early goals was to find experimental evidence of a topological organization that would differ from the standard Smale's horseshoe. At that time, some regimes of the

modulated CO_2 laser could not be analyzed for lack of a suitable symbolic encoding. The corresponding Poincaré sections had peculiar structures that, depending on the observer's mood, suggested a doubly iterated horsehoe or an underlying three-branch manifold. Since the complete analysis could not be carried out, much time was spent on trying to find at least one orbit that could not fit the horseshoe template. The result was extremely disappointing: For every orbit detected, there was at least one horseshoe orbit with identical invariants. One of the most important lessons of Judo is that if you experience resistance when pushing, you should pull (and vice versa). Similarly, this failed attempt to find a nonhorseshoe template turned into techniques to determine underlying templates when no symbolic coding is available and to construct such codings using the information extracted from topological invariants.

But the search for different templates was not over. Two of Marc's colleagues, Dominique Derozier and Serge Bielawski, proposed for him to study a fiber laser they had in their laboratory (that was the perfect system to study knots). This system exhibits chaotic tongues when the modulation frequency is near a subharmonic of its relaxation frequency: It was tempting to check whether the topological structures in each tongue differed. That was indeed the case: The corresponding templates were basically horseshoe templates but with a global torsion increasing systematically from one tongue to the other. A Nd:YAG laser was also investigated. It showed similar behavior, until the day where Guillaume Boulant, the PhD student working on the laser, came to Marc's office and said: "I have a weird data set". Chaotic attractors were absolutely normal, return maps resembled the logistic map very much, but the invariants were simply not what we were used to. This was the first evidence of a reverse horseshoe attractor. How topological organizations are modified as a control parameter is varied was the subject of many discussions in Lille in the following months, a rather accurate picture finally emerged and papers began to be written. In the last stages, Marc did a bibliographic search just to clear his mind and... a recent 22-page Physical Review paper, by McCallum and Gilmore, turned up. Even though it was devoted to the Duffing attractor, it described with great detail what was happening in our lasers as control parameters are modified. Every occurence of "We conjecture that" in the papers was hastily replaced by "Our experiments confirm the theoretical prediction...", and papers were sent to Physical Review. They were accepted 15 days later, with a very positive review. Soon after, the Referee contacted us and proposed a joint effort on extensions of topological analysis. The Referee was Bob, and this was the start of a collaboration that we hope will last long.

It would indeed be very nice if these techniques could be extended to the analysis of strange attractors in higher dimensions (than three). Such an extension, if it is possible, cannot rely on the most powerful tools available in three dimensions. These are the topological invariants used to tease out information on how periodic orbits are organized in a strange attractor. We cannot use these tools (linking numbers, relative rotation rates) because knots "fall apart" in higher dimensions. We explore (Chapter 11) an inviting possibility for studying an important class of strange attractors in four dimensions. If a classification procedure based on these methods is successful, the door is opened to classifying strange attractors in R^n, $n > 3$. A number of ideas that

may be useful in this effort have already proved useful in two closely-related fields (Chapter 12): Lie group theory and singularity theory.

Some of the highly technical details involved in extracting templates from data have been archived in the appendix. Other technical matter is archived at our web sites.[1]

Much of the early work in this field was done in response to the challenge by J. R. Tredicce and carried out with my colleagues and close friends: H. G. Solari, G. B. Mindlin, N. B. Tufillaro, F. Papoff, and R. Lopez-Ruiz. Work on symmetries was done with C. Letellier. Part of the work carried out in this program has been supported by the National Science Foundation under grants NSF 8843235 and NSF 9987468. Similarly, Marc would like to thank colleagues and students with whom he enjoyed working and exchanging ideas about topological analysis: Pierre Glorieux, Ennio Arimondo, Francesco Papoff, Serge Bielawski, Dominique Derozier, Guillaume Boulant, and Jérôme Plumecoq. Stays of Bob in Lille were partially funded by the University of Lille, the Centre National de la Recherche Scientifique, Drexel University under sabbatical leave, and by the NSF.

Last and most important, we thank our wives Claire and Catherine for their warm encouragement while physics danced in our heads, and our children, Marc and Keith, Clara and Martin, who competed with our research and demanded our attention, and by doing so, kept us human.

R.G. AND M.L.

Lille, France, Jan. 2002

[1] `http://einstein.drexel.edu/directory/faculty/Gilmore.html` and `http://www.phlam.univ-lille1.fr/perso/lefranc.html`

Contents

"From template analysis to generating partitions I: Periodic orbits, knots and symbolic encodings"

Jérôme Plumecoq, and Marc Lefranc

Physica D **144**, 231–258 (2000)

ELSEVIER

Physica D 144 (2000) 231–258

PHYSICA D

www.elsevier.com/locate/physd

From template analysis to generating partitions I: Periodic orbits, knots and symbolic encodings

Jérôme Plumecoq, Marc Lefranc*

Laboratoire de Physique des Lasers, Atomes, Molécules, UMR CNRS 8523, Centre d'Études et de Recherches Lasers et Applications, Université de Lille I, F-59655 Villeneuve d'Ascq Cedex, France

Received 29 April 1999; received in revised form 13 March 2000; accepted 30 March 2000
Communicated by J.D. Meiss

Abstract

We present a detailed algorithm to construct symbolic encodings for chaotic attractors of three-dimensional flows. It is based on a topological analysis of unstable periodic orbits embedded in the attractor and follows the approach proposed by Lefranc et al. [Phys. Rev. Lett. 73 (1994) 1364]. For each orbit, the symbolic names that are consistent with its knot-theoretic invariants and with the topological structure of the attractor are first obtained using template analysis. This information and the locations of the periodic orbits in the section plane are then used to construct a generating partition by means of triangulations. We provide numerical evidence of the validity of this method by applying it successfully to sets of more than 1500 periodic orbits extracted from numerical simulations, and obtain partitions whose border is localized with a precision of 0.01%. A distinctive advantage of this approach is that the solution is progressively refined using higher-period orbits, which makes it robust to noise, and suitable for analyzing experimental time series. Furthermore, the resulting encodings are by construction consistent in the corresponding limits with those rigorously known for both one-dimensional and hyperbolic maps. © 2000 Elsevier Science B.V. All rights reserved.

PACS: 05.45.+b

Keywords: Generating partitions; Symbolic dynamics; Template analysis; Knot theory

1. Introduction

Symbolic dynamics is a powerful approach to chaotic dynamics. It consists in representing trajectories in a chaotic attractor by sequences of symbols from a usually finite but possibly infinite alphabet, in a way that preserves the essential properties of the dynamics [1–4]. It is not only central to some of the most fundamental theorems of dynamical systems theory (see, e.g., [1,2]), but can also be of utmost importance with a view to practical applications, such as for transmitting numeric streams over chaotic signals [5,6].

However, we currently have a good understanding of how to construct symbolic encodings in two limiting cases only, namely for hyperbolic systems and non-invertible maps of an interval into itself [1–4]. Unfortunately, most experimental low-dimensional systems fall outside these two categories, except when they are sufficiently dissipative so that their return maps can be modeled by one-dimensional maps.

* Corresponding author.
E-mail address: marc.lefranc@univ-lille1.fr (M. Lefranc).

0167-2789/00/$ – see front matter
PII: S0167-2789(00)00082-8

To generalize one-dimensional symbolic dynamics to higher-dimensional invertible maps and to flows, the most widely used method proceeds by localizing homoclinic tangencies, i.e., points where the stable and unstable manifold of the attractor are tangent to each other [7]. Because this involves computing tangent maps and estimating their eigendirections, this method requires that the evolution equations are known, or at least that a model of the dynamics is available.

Other methods, including the topological approach [8,9] that we describe below, make use of the unstable periodic orbits (UPOs) associated with a chaotic dynamics. For example, the fact that different UPO should have different symbolic names and that UPO visit the whole phase space has been used as a criterion to select partitions that are generating [10–12]. After completion of this work, we became aware of a very recently proposed method [13] which is also based on the uniqueness criterion and utilizes an interpolation scheme similar in spirit to the one introduced in the present work. Symbolic names of periodic orbits can also be obtained by continuation from a regime where the symbolic dynamics is well understood [14].

In this paper, we present in detail an approach that is based on a topological characterization of the UPO [9,15–18], and extracts information not only in the neighborhood of the singularities, but from the geometrical structure of the whole phase space. More precisely, the way in which stretching and folding, which are intimately related to symbolic dynamics, act on the infinite number of UPOs embedded in any strange attractor is exactly reflected in the way these orbits are knotted and intertwined. Because a systematic study of the knots and links realized by periodic orbits is made possible by template theory [19,20] and template analysis [17,18], *precise information about the symbolic dynamics of the UPO can be extracted from their topological invariants*. As we show in this work, this information, combined with the knowledge of the locations of the periodic points in the section plane, allows one to determine an excellent approximation to the border of a generating partition. This method does not involve the differentiable structure of return maps at all, and uses the concept of distance only to define neighborhoods, more precisely to determine which member of a set of reference points is nearest to a given point. Moreover, the use of template theory ensures that the symbolic encodings obtained are naturally connected to the ones known in the one-dimensional and hyperbolic limits.

As this approach has already been applied to experimental time series from a modulated laser using a preliminary version of the algorithm described here [8], the primary goal of this paper is to provide numerical evidence of the validity of the method. We thus apply it to more than 1500 UPOs extracted from numerical simulations, and show that it is possible to obtain partitions which have a simple structure, yet are completely consistent with the topological organization of the UPO: the set of symbolic names assigned by the partition to the UPO corresponds to a set of orbits of the horseshoe template which have exactly the same topological invariants as the extracted ones. Direct evidence of the fact that partitions obtained in this way are generating will be presented in the second part of this work [21].

The paper is organized as follows. In the remaining part of this section, we recall the links between the geometric properties of chaos (stretching and folding) and symbolic dynamics. We then briefly review the approach based on homoclinic tangencies, and we finally illustrate the connection between symbolic dynamics and knot theory.

This connection can be precisely stated using template theory [19,20] and template analysis [17,18]. Since this approach to chaotic dynamics is not widely known, Section 2 is devoted to a review of its main concepts. We put emphasis on the relation between the symbolic name of an orbit and its topological invariants by giving examples of the analytical formulas linking them, and specify our fundamental assumptions.

In Section 3, we describe our algorithm in detail by progressively building a generating partition for a sample set of UPOs extracted from numerical simulations of a modulated laser. We finally obtain a partition that is localized with a precision of the order of 0.01% of the attractor width. Lastly, we conclude by discussing possible extensions and applications of our method.

1.1. Stretching, folding, and symbolic dynamics

A striking feature of nonlinear dynamical systems is that they can display complex behavior even when obeying simple equations of motion. This seemingly paradoxical fact can easily be understood by using a geometric description of the dynamical laws, in which they are represented as transformations of a phase space into itself. As it is by now commonly known, there are such simple transformations that generate chaotic behavior by combining stretching and folding mechanisms (as in, e.g., the Rössler system).

In the last decades, several methods have been proposed to characterize a strange attractor, and thereby the underlying dynamics [22]. Not surprisingly, some of the most popular measures of chaos are deeply linked with the existence of the stretching and folding mechanisms. For example, Lyapunov exponents quantify the efficiency of stretching by estimating the rate of divergence of infinitely close trajectories. Spectra of fractal dimensions, and especially the correlation dimension as computed with the Grassberger–Procaccia algorithm, have been widely used to analyze the fractal structure that results from the repeated action of stretching and folding.

Symbolic dynamics is another approach to chaotic dynamics that is deeply rooted in the existence of the stretching and folding mechanisms. The connection between symbolic dynamics and the geometric properties of chaos is probably best illustrated by the paradigmatic Smale's horseshoe map (Fig. 1), which is a key example to understand the link between the geometric features of chaos, symbolic dynamics and topological concepts.

One important property of the horseshoe map is that, due to stretching and squeezing, the orbits of two different points can be distinguished only by recording which of the two vertical strips depicted in Fig. 1 they successively visit. In most cases, the forward iterates of the two points will eventually fall in different strips because of stretching, which occurs along the (vertical) unstable direction. This, however, does not happen if the two points are located in the same strip and on the same segment of the stable manifold (i.e., along an horizontal line). In this case, one has

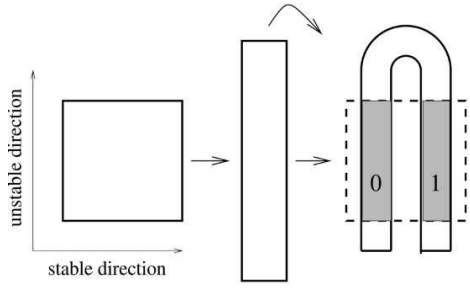

Fig. 1. Representation of the action of the Smale's horseshoe map. A unit square is first stretched along the unstable direction and squeezed along the stable direction, then folded over itself so that it intersects the original square in two disjoint strips.

to follow the backward iterates instead, as the unstable and stable directions are then reversed. Assigning distinct symbols to the two strips thus allows one to carry out a symbolic dynamical study of this map, each point of the invariant set being associated to a unique bi-infinite binary sequence. For a detailed presentation of the Smale's horseshoe map in the context of topological analysis, see Refs. [9,15,16,23,24].

In general, the symbolic encoding of a chaotic attractor is performed by dividing a Poincaré section into a few disjoint regions associated with distinct symbols (see Fig. 2). In the case of reversible equations of motion, each point of the attractor is then associated to the bi-infinite sequence made of the symbols corresponding to the regions visited by its backward and forward iterates.

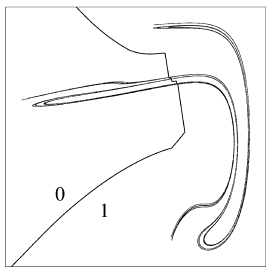

Fig. 2. Symbolic encoding of a chaotic attractor using a partition of a section plane into two disjoint regions. This Poincaré section has been obtained from the modulated laser equations (9a) and (9b) described in Section 3.1.

More precisely, consider a partition Γ of the section plane P in n disjoint regions $\Delta_i(\Gamma)$, $i = 0, \ldots, n-1$. Assume that for each point $x \in P$, $s_\Gamma(x)$ indicates the region which contains x: $s_\Gamma(x) = i$ if $x \in \Delta_i(\Gamma)$.

The point x is then represented by a bi-infinite symbolic sequence

$$\Psi(x) = \{\ldots, \Psi_{-1}(x), \Psi_0(x), \Psi_1(x), \ldots\},$$
$$\Psi_i(x) = s_\Gamma(f^i(x)),$$

where f is the Poincaré return map. Defining the shift operator σ so that the sequence $\Psi'(x) = \sigma\Psi(x)$ is made of the symbols $\Psi'_i(x) = \Psi_{i+1}(x)$, it is readily seen that σ represents the action of the return map in the space of symbolic sequences, as $\sigma\Psi(x) = \Psi(f(x))$ by definition.

Under certain conditions, such a coarse-grained measurement suffices to provide an accurate description of the dynamics: two different points, however close they may be, are associated to different symbol sequences; the partition is then said to be generating [2]. Of course, this is due to the amplifying action of stretching, which connects arbitrarily small length-scales with large ones.

Symbolic dynamics can be given a rigorous foundation in the case of hyperbolic systems, such as the Smale's horseshoe map shown in Fig. 1. Indeed, hyperbolicity allows one to define partitions (Markov partitions) that can be shown to be generating [2]. In this context, symbolic dynamics is of utmost importance to prove several fundamental theorems of dynamical system theory. For example, a symbolic dynamical analysis of the horseshoe dynamics easily shows that the invariant set contains aperiodic orbits, a dense infinity of unstable periodic orbits, and that there are infinitely many orbits which are dense in the invariant set [1,2].

For non-hyperbolic systems, rigorous results regarding the construction of a generating partition are known only in the case of non-invertible maps of an interval into itself, such as the well-known logistic map. In this case, a generating partition is obtained by dividing the one-dimensional interval into regions where the map is monotonic: the border of the partition consists of the critical points of the map, where the derivative vanishes [1,3,4].

However, most strange attractors encountered in experimental systems or numerical simulations are non-hyperbolic: orbits are created and destroyed as a control parameter is varied, which is incompatible with the structural stability implied by hyperbolicity. Moreover, one-dimensional symbolic dynamics can only be used for extremely dissipative systems, and even then only in an approximate way. Whether symbolic dynamics can be put on a sound basis in the general case thus remains an open and fascinating problem.

A guiding fact is that the parameter space of a dynamical system such as, e.g., the Hénon map $H_{a,b}(x, y) = (a - x^2 + by, x)$ contains generally both the hyperbolic and one-dimensional limits. For a sufficiently large value of the parameter a, the Hénon map has an invariant hyperbolic repellor; it becomes equivalent to the one-dimensional logistic map $L_a(x) = H_{a,0}(x) = a - x^2$ when the parameter b goes to zero. Therefore, a general procedure for constructing a symbolic encoding of a non-hyperbolic, weakly dissipative, attractor should have the one-dimensional and hyperbolic codings as limiting cases.

1.2. Symbolic encodings based on homoclinic tangencies

Accordingly, the method proposed by Grassberger et al. [7,25] is a generalization of the one-dimensional theory. For a one-dimensional map, the border of the partition naturally consists of the critical points of the map, whose existence is responsible for the non-invertibility of the map. In the case of invertible two-dimensional maps, there are no critical points, but their natural counterparts are the *homoclinic tangencies*, where the stable and unstable manifolds of the attractor are tangent to each other. Their existence stems from the non-hyperbolicity of the map: in a sense, an invertible two-dimensional map loses invertibility at homoclinic tangencies when iterated an infinite number of times. Furthermore, points of homoclinic tangency converge to backward and forward images of the critical points of the one-dimensional map when dissipation is increased to infinity.

Grassberger et al. [7,25] thus conjectured that a good symbolic encoding could be obtained by dividing

the plane with a line connecting homoclinic tangencies. Several studies have given numerical evidence that the partitions so obtained were generating to a high level of accuracy [7,25–29]. Another motivation for this rule is the fact that points located on opposite sides of a homoclinic tangency converge to each other both for positive and negative time. Thus, they can only be distinguished if they are associated to different symbols.

However, this approach has been rarely used, if ever, to characterize the symbolic dynamics of experimental chaotic time series (see, however, Ref. [30] for an application to time series generated from numerical simulations). Indeed, it heavily relies on the knowledge of the equations of motion and on the computation of the tangent map to determine the location of the homoclinic tangencies. While the direction of the invariant manifolds could in principle be estimated by fitting a model to the dynamics in the neighborhood of a point [30], the application of such a procedure to experimental time series seems hazardous. Indeed, it is a known fact that there is a dramatic noise amplification precisely at homoclinic tangencies [31]: since the stable manifold is tangent to the unstable manifold, it cannot drive perturbed trajectories back to the attractor. In this situation, extracting information from a tangent map constructed by estimating derivatives appears to be problematic.

Furthermore, it should be noted that this method is faced with the difficulty of choosing which homoclinic tangencies should be connected, because all images and preimages of a homoclinic tangency are themselves homoclinic tangencies. To address this problem, Giovannini and Politi [28] proposed to use only the so-called "primary" homoclinic tangencies, i.e., tangencies such that the sum of the curvatures of the stable and unstable manifolds is smaller than for all their images and preimages. Another approach to solving this problem was presented in Ref. [29], where the global organization of the lines of homoclinic tangencies in the phase space was studied.

This ambiguity is due to the fact that techniques based on homoclinic tangencies focus on the singularities induced by folding in the limit of infinite time. However, it is known from singularity theory (see, e.g., Ref. [32]) that singularities at a point organize the structure of an extended neighborhood of this point. Accordingly, there should be prints of the folding process in the whole phase space.

Indeed, there is another approach to the construction of symbolic encodings that focuses on the global organization of the strange attractor: it is based on a topological analysis of its unstable periodic orbits. That topological invariants of an unstable periodic orbit provide key information about the associated symbolic dynamics, to our knowledge, first noted by Solari and Gilmore [33]. A method to construct a generating partition based on this idea was then outlined by Lefranc et al. [8] and applied to experimental time series from a modulated laser.

1.3. From unstable periodic orbits and knot theory to symbolic dynamics

A strange attractor is not the only invariant set of a chaotic dynamical system, as it typically has embedded in it an infinite number of UPOs. While these UPOs, whose existence is due to ergodicity of chaotic dynamics, are known since the works of Poincaré, they have only been fully utilized to characterize and control chaos in the last decade (see, e.g., Refs. [12,18,34–36]). As we see in the following, they also prove to be invaluable for extracting symbolic dynamical information from experimental data.

As with every trajectory in the attractor, unstable periodic orbits experience stretching and folding. But, as they exactly return to their initial condition in a short amount of time, they bear the mark of these mechanisms in a very distinct way: their associated closed curves in phase space are braided in a way that precisely reflects the action of stretching and folding (see Fig. 3). Since symbolic dynamics are also intimately related to stretching and folding, the way in which periodic orbits are intertwined must carry symbolic dynamical information.

What makes this simple observation so fruitful is that this relation can be expressed in a well-defined mathematical term for strange attractors that can be embedded in a three-dimensional phase space. Indeed, characterizing the topological structure of

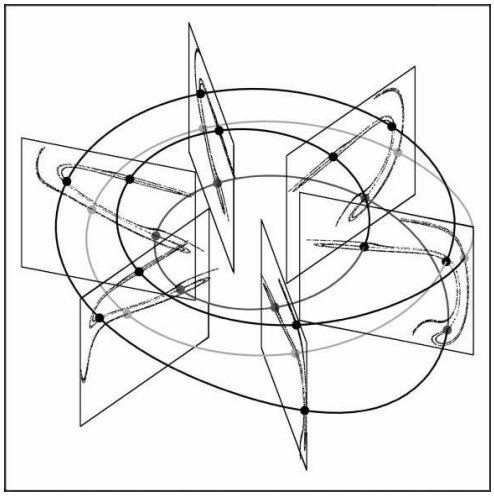

Fig. 3. Stretching and folding braid a periodic orbit in a definite way, as can be seen here with a period-4 orbit.

closed curves in such a space is nothing but the central problem of knot theory (see, e.g., [37]). Knot theory provides us with topological invariants that can be utilized to decide whether two closed curves can be continuously deformed into each other, i.e., have identical knot types or not, and thus to classify periodic orbits according to their geometrical structure.

The relevance of knot theory in the context of dynamical system theory stems from one of its fundamental theorems. Indeed, the uniqueness theorem states that one and only one trajectory passes through a non-singular point of phase space (because of determinism). In particular, this implies that a periodic orbit cannot intersect itself, or another orbit, and thus that the knots and links they form have a well-defined type. Moreover, changing a control parameter will usually change the shape of a periodic orbit but, for the same reason, will not induce intersections. Consequently, the knot type of a periodic orbit remains unchanged on the whole domain of existence of the orbit, and can be viewed as a genuine fingerprint.

It is thus obvious that topological invariants from knot theory provide us with a robust way to characterize how stretching and folding intertwine unstable periodic orbits. As an example, the simplest topological invariant, the linking number, indicates how many times one orbit winds around another. What makes these invariants relevant for experimental studies is their robustness. If two periodic orbits are sufficiently separated, knot invariants can be reliably determined even when only approximate trajectories, possibly contaminated with noise, are available (as typically extracted from a time series). Indeed, the possible perturbations then merely amount to small deformations of the orbit and do not change the invariants.

It should be noted that because the topological approach relies on knot theory, it can only be applied directly to three-dimensional flows. Orientation-preserving two-dimensional return maps can also be studied, either by constructing a suspension or by utilizing the powerful techniques presented in Refs. [38,39], where it was shown that the braid type of an orbit can be directly determined from its intersections with a surface of section, up to a global torsion (see also [40]). Orientation-reversing two-dimensional return maps, such as the Hénon map at the standard parameters ($a = 1.4$, $b = 0.3$), fall a priori outside the scope of this method. However, noting that a doubly iterated orientation-reversing map is always orientation-preserving allows us in such cases to extract topological information not from the map itself but from its square,[1] as will be illustrated in Section 2.4.

The link between topological invariants and symbolic dynamics is provided by the tools of template theory. Since the main concepts of the latter are not widely known, we review them in the next section, before presenting the details of our algorithm in Section 3.

2. Periodic orbits, knots and templates

2.1. Template theory of hyperbolic systems: the Birman–Williams theorem

As it is the case for many features of chaotic behavior, most of the rigorous results about the topological

[1] This was brought to our attention by one of the anonymous reviewers.

structure of unstable periodic orbits are known in the context of hyperbolic dynamical systems. They compose what may be called as template theory [20]. The keystone of the latter is the Birman–Williams theorem [19,41], which shows that the topological organization of the unstable periodic orbits of an hyperbolic flow can be studied in a systematic way.

Given a hyperbolic chaotic three-dimensional flow Φ_t with an invariant set Λ, let us define an equivalence relation between points of Λ in the following way:

$$x \sim y \Leftrightarrow \lim_{t\to\infty} \|\Phi_t(x) - \Phi_t(y)\| = 0 \ \ \forall x, y \in \Lambda, \quad (1)$$

which relates points having the same asymptotic future. Identifying points in the same equivalence class thus amounts to collapsing the strong stable manifold of each point of the invariant set. This operation will be hereafter referred to as the "Birman–Williams reduction". The Birman–Williams theorem [19,41] consists of two main statements:

1. In the set of equivalence classes of relation (1), the hyperbolic flow Φ_t induces a semi-flow $\bar{\Phi}_t$ on a branched manifold $\mathcal{K}$. The pair $(\bar{\Phi}_t, \mathcal{K})$ is called a *template*, or *knot-holder*, for a reason that is made obvious by the second statement.
2. Unstable periodic orbits of Φ_t in Λ are in one-to-one correspondence with unstable periodic orbits of $\bar{\Phi}_t$ in $\mathcal{K}$. Moreover, each unstable periodic orbit of (Φ_t, Λ) is isotopic to the corresponding orbit of $(\bar{\Phi}_t, \mathcal{K})$, the same property holding for any link made of a finite number of UPOs. Thus, periodic orbits in the invariant set can be continuously deformed without any crossing so as to be laid on the branched manifold.

The second statement implies that any topological invariant defined in the framework of knot theory will take identical values on a set of UPOs of the flow and on the corresponding set of periodic orbits of the template.

The proof of the Birman–Williams theorem relies on a key property: two points belonging to the same periodic orbit, or to different periodic orbits, have by definition different asymptotic futures; if initially separated, they will remain at a finite distance forever. Thus, a periodic orbit cannot intersect its own stable manifold, or the stable manifold of another orbit. As a result, *the Birman–Williams reduction does not induce crossings between periodic orbits, hence it does not modify their topological organization*.

This simple observation is central to template theory and template analysis because it clearly shows that their concepts are insensitive to the degree of dissipation, which becomes irrelevant after reduction of the strong stable manifolds. *In a given topological class, any hyperbolic flow has the same global topological organization as an infinitely dissipative flow*. This is precisely what will allow us to use template analysis as a bridge between one-dimensional and two-dimensional symbolic dynamics.

As an example, the Smale's horseshoe template,[2] i.e., the branched manifold corresponding to a flow whose return map is the Smale's horseshoe map, is shown in Fig. 4. The number of branches, the torsions and linking numbers of its branches define the structure of such a manifold, as well as the order in which branches are stacked when they rejoin. The Smale's horseshoe template presented in this form is an example of a fully expansive template: the branches are stretched to the full width of the template. This stretching and the folding of branches over each other describe geometrically the basic mechanisms of chaotic dynamics. As will be recalled in Section 2.3, the topological structure of a template can be concisely described by a small set of integers which suffice to determine topological invariants of a closed curve on the template, given its itinerary on the branched manifold (i.e., the order in which it visits the different branches).

For a more detailed exposition of the template theory of hyperbolic sets, we refer the reader to Refs. [19,23,24,41–44], and to a recent book by Ghrist et al. [20] for a comprehensive review.

2.2. Template analysis of experimental systems

The central problem of template theory is: given a hyperbolic template, what can we say about the properties of knots living on this template?

[2] By a slight abuse, the term "template" is often used to refer to the branched manifold alone, by assuming a standard structure for the semi-flow on the manifold.

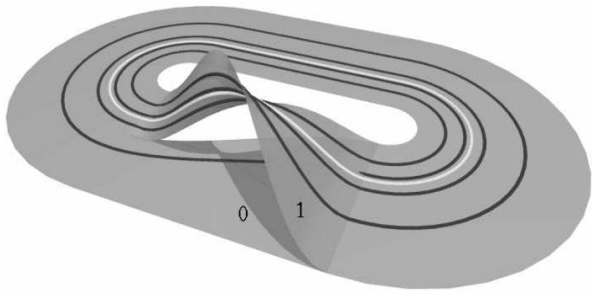

Fig. 4. The Smale's horseshoe template with period-1 and period-4 orbits. In this configuration, these orbits have exactly the same invariants they would have in a hyperbolic flow whose topological structure is described by this template. Because the branches correspond to the disjoint strips shown in Fig. 1, a symbolic description of the closed curves of the template can be given.

When we study an experimental system, however, the underlying template is not a priori known, but unstable periodic orbits can be extracted from time series, and their topological invariants and knot types determined in a reconstructed phase space. Note that while a strange attractor is generally not hyperbolic, tools from template theory are still relevant because the existing orbits should have the same organization and the same invariants as in the hyperbolic limit, provided they can be brought to this limit by a change in control parameters without experiencing a bifurcation.

In this context, the natural question then is: given a finite set of knots contained in the attractor, can we construct a simple template which holds all of them while maintaining information about quantities such as the dynamical period? If such a template is found, it can then be used to describe the global topological organization of the strange attractor.

This program was pioneered by Mindlin et al. [17], who proposed to use the concepts of template theory to characterize non-hyperbolic strange attractors by a small set of integers. They demonstrated and thoroughly discussed the relevance of this approach by showing in a beautiful work that all the topological invariants of periodic orbits detected in time series from the Belousov–Zhabotinskii chemical reaction allowed them to be globally laid on a Smale's horseshoe template [18].

In the last decade, further evidence that the topological organization of experimental chaotic systems could be described by templates has been given in a variety of systems: an NMR oscillator [45], CO_2 lasers with a saturable absorber [46,47], or with modulated losses [8,48], a glow discharge [49], a copper electro-dissolution reaction [50], a vibrating string [51], an electronic circuit [52], a fiber laser [53], or a YAG laser [54]. Similar conclusions have also been obtained in numerical simulations of the Duffing [55,56], Lorenz [57], and Rössler equations [58], and for systems modeling a bouncing ball [59], pulsating stars [60], lasers [61–63], or neural spike train bursts [64].

All these studies follow more or less the same procedure [9]. First, segments of time series shadowing unstable periodic orbits are extracted from the experimental data, and are embedded in a reconstructed phase space, where the topological invariants of the associated closed curves are computed. Then the simplest template on which the experimental orbits can be projected is determined from the measured invariants. This is made possible by the fact that the relevant information is carried by low-period orbits. Indeed, the characteristic numbers of a template are completely determined by the invariants of its spectrum of period-1 and period-2 orbits [9].

The validity of a candidate template (determined from the lowest-period orbits) can then be checked by verifying that the invariants of the higher-period orbits allow them to be also laid on the template. This is because the template characteristic numbers are over-determined by the topological invariants of the unstable periodic orbits. In the case of the Smale's

horseshoe template, e.g., four integers suffice to compute the invariants of an infinite number of periodic orbits. As we will show in the following, the seemingly redundant information carried by the topological invariants of a large set of UPOs can be used to extract information about the symbolic dynamics of the attractor.

For further information, detailed introductions to template analysis can be found in a comprehensive review paper by Gilmore [9] and in books by Tufillaro et al. [15], and by Solari et al. [16].

2.3. *Extracting symbolic dynamical information from knot invariants*

Our approach to the construction of symbolic encodings relies heavily on the mathematical link between the topological invariants of unstable periodic orbits and symbolic dynamics. To illustrate this link more precisely, we now review briefly some of the basic tools of template analysis.

As an example, we first consider the Smale's horseshoe period-4 orbit that is created in the initial period-doubling cascade. We show how its simplest invariant, namely its self-linking number,[3] is easily computed from its symbolic name, which is "0111" if we use the coding shown in Fig. 4.

In this work, we restrict ourselves to fully expansive templates, whose unique branch line (the line where the different branches are squeezed over each other) is a one-dimensional analog of a global Poincaré section: each period-n orbit intersects the branch line in exactly n points. Since template orbits cannot intersect on the two-dimensional (branched) manifold, the layout of a periodic orbit on the template is completely determined by the order in which its intersections with the branch line are visited.

Computing this order is a classic exercise in symbolic dynamics of maps of an interval into itself [1,3] (see Refs. [9,15,23] in the context of template analysis), since the return map of the branch line is one-dimensional. In the case of the Smale's horseshoe template, this return map has the same structure as the standard logistic map, with the region of positive (respectively, negative) slope corresponding to the branch with a torsion of zero (respectively, one) half-turns. In our example, it is easily found that the periodic points of the period-4 orbit are found on the branch line in the order: "0111", "1101", "1110", "1011".

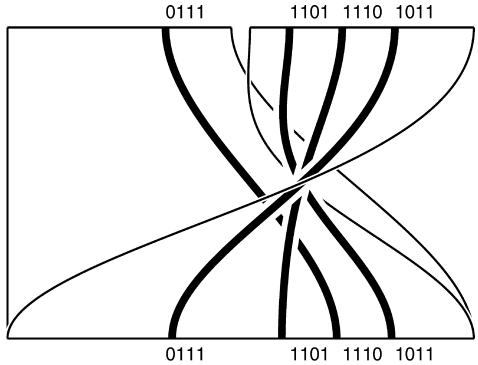

Fig. 5. Geometry of the period-4 orbit "0111" on the template. Only the non-trivial part (i.e., the branched part) of the manifold is shown, as the top line can be identified with the bottom line (the branch line). The layout of the periodic points on the branch line is completely fixed by the fact that branches "0" and "1" are orientation-preserving and orientation-reversing, respectively. Given the geometrical structure of the branches, this layout determines in turn the braid associated with the orbit, and hence all its topological invariants.

As can be seen in Fig. 5, it then suffices to connect periodic points to their images by following the semi-flow on the branched manifold to obtain the braid associated with the orbit. In this case, it is straightforward to verify that the self-linking number of the "0111" orbit of the Smale's horseshoe template is 5.

This simple example illustrates concisely the key idea that, after fixing an embedding template, *the symbolic dynamics of an unstable periodic orbit completely determines its knot invariants and that conversely, the latter can carry important information about the former*. We now want to stress that this property can be expressed by simple algebraic relations.

A template with a single branch line can be faithfully described as a framed braid (see, e.g., Ref. [65]).

[3] In the context of template analysis, the self-linking number is usually defined as the signed number of crossings of the braid representing the orbit.

Such a description allows one to compute any knot invariant (e.g., knot polynomials) of the periodic orbits carried by the template. However, as Mindlin et al. [17,18] have shown, some topological invariants, namely the (self-) linking numbers and (self-) relative rotation rates [33] (as well as the torsions), can be obtained from the information provided by an $n \times n$ matrix, the *template matrix*, and an $1 \times n$ matrix, the *layering matrix*, where n is the number of branches of the template. The template and layering matrices are related to invariants of low-period orbits in the following way.

Because the semi-flow on the branch manifold is expanding, each branch carries one and only one period-1 orbit. The template matrix t is obtained from the organization of these period-1 orbits as follows. The diagonal elements t_{ii} indicate the local torsion of the orbit on branch i, i.e., the rotation of its stable and unstable manifolds in units of π. Off-diagonal elements $t_{ij} = t_{ji}$ are equal to twice the linking number of the orbits located on branches i and j. In the case of the Smale's horseshoe with zero global torsion shown in Fig. 4, with branches labeled "0" and "1", the template matrix reads

$$t^{\mathrm{HS}} = \begin{pmatrix} 0 & 0 \\ 0 & 1 \end{pmatrix}, \tag{2}$$

where $t_{11} = 1$ describes the folding of the "1" branch.

To complete the description of the template structure, one has to specify in which order the different branches are superimposed when they are glued together. Mindlin et al. define the $1 \times n$ layering matrix l, which verifies $l_i < l_j$ iff branch j is located above branch i on the branch line. Since the twisted branch of the horseshoe template is folded over the untwisted one, its layering matrix is given by

$$l^{\mathrm{HS}} = \begin{pmatrix} 0 & 1 \end{pmatrix}. \tag{3}$$

We use a slightly different convention and introduce an $n \times n$ symmetric matrix l' such that for $i < j$, $l'_{ij} = 1$ if branch j is located above branch i and $l'_{ij} = -1$ otherwise (i.e., $l'_{ij} = -1$ indicates that the order of two branches differs from that of a standard layering graph as defined in Ref. [65]). For the horseshoe template, we thus have

$$l'^{\mathrm{HS}} = \begin{pmatrix} 0 & 1 \\ 1 & 0 \end{pmatrix}. \tag{4}$$

A key property of template analysis is that simple analytic formulas can be written to express the linking numbers, relative rotation rates, and torsions of the orbits as functions of the elements of the template and layering matrices [66], using techniques similar to those described in Appendix E of Ref. [15].

For example, the self-linking number of the "0111" orbit is given by

$$\mathrm{slk}(0111) = 3t_{01} + 3t_{11} + (3 - \pi(t_{11}))l'_{01}, \tag{5}$$

where $\pi(t) = 1(0)$ if t is odd (even). The reader may verify that the value of 5 that can be obtained from Fig. 5 is recovered by inserting in Eq. (5) the horseshoe template matrices given in Eqs. (2) and (4). Similar expressions can easily be obtained for invariants of orbits of arbitrarily high period. For example, we have

$$\begin{aligned} \mathrm{lk}(01^3 0101^2, (01^2)^3 01^4 01^3) &= \tfrac{15}{2} t_{00} + 39 t_{11} \\ &+ \tfrac{69}{2} t_{01} + (30 - \tfrac{19}{2}\pi(t_{11}) - \tfrac{1}{2}\pi(t_{00} + t_{11}))l'_{01}, \end{aligned} \tag{6}$$

where $\mathrm{lk}(\alpha, \beta)$ denotes the linking number of orbits α and β.

Another quantity that is easily expressed as a function of the template matrix is the torsion. Torsion describes the rotation of the unstable manifold of the orbit as one follows the orbit over one period, and is usually expressed in half-turns. Obviously, the torsion of an orbit cannot change on the whole domain of parameter space where the orbit is unstable and its Floquet multipliers are real (the latter condition is a consequence of the former in the Hénon map), and hence can be used as an invariant. While it is not strictly a knot invariant, it is intimately related to them: e.g., the knot type of an orbit born in a period-doubling bifurcation depends on both the knot type and the torsion of the mother orbit [23]. The torsion of a periodic orbit is obtained from its symbolic name and the template by summing the torsions of the branches visited by the orbit, i.e., the corresponding diagonal elements of the template matrix. For example,

$$t(0111) = t_{00} + 3t_{11}. \tag{7}$$

A crucial property of these expressions is that, except for the presence of the terms involving the π function, they are linear in the elements of the template matrices t and l'. This is what allows one to design a powerful algorithm to determine these elements from the topological invariants of a few orbits of low period: one considers all the possible symbolic names for these low-period orbits, and all the possible branch parities, and selects those that lead to a consistent, over-determined, set of linear equations. The solution to such a set of equations is a candidate template, whose validity has then to be checked with higher-period orbits. The general procedure will be described elsewhere [66], but some examples may be found in Refs. [53,61].

When the geometry of the branched manifold of the template has been determined in this way, we then find all sets of symbolic names such that template orbits with these names have exactly the same invariants as the experimental periodic orbits. This indicates the different possible projections of the set of UPOs on the branched manifold that preserve its topological organization.

In fact, there are only a few possible such projections for a given experimental orbit. For example, in the case of the Smale's horseshoe template, there is one and only one period-7 orbit of even torsion with a self-linking number of 16: this is the "0101011" orbit. In this case, the symbolic name of this orbit can be unambiguously extracted from its topological structure. In some other cases, there may be several possible symbolic names. For example, the horseshoe orbits "001101" and "001011" correspond to isotopic knots and thus cannot be distinguished using the self-linking number or self-relative rotation rates. However, they often can be identified using other orbits which link them differently (if these orbits are found in the attractor): in the previous example, there are four period-8 horseshoe orbits whose linking numbers with the two period-6 orbits are different (e.g., $\mathrm{lk}(00101011, 001101) = 15$ but $\mathrm{lk}(00101011, 001011) = 14$).

This important fact is illustrated in Table 1 which shows an example where the symbolic names of all orbits up to period 9 extracted from an attractor, except two of them, can be obtained using only the simplest topological invariants. This implies that there are only two sets of horseshoe orbits which reproduce the measured invariants. These sets differ by the names given to orbits 9b and 9c.

Table 1
Basic topological properties of the periodic orbits with period up to 9 extracted from numerical simulations of a modulated laser model (see Section 3.1), and that will be used as an example in Section 3[a]

Orbit	Invariants	Names
1a	1, 0, 1	"1"
2a	2, 1, 1	"01"
4a	4, 5, 3	"0111"
5a	5, 8, 3	"01011"
5b	5, 8, 4	"01111"
6a	6, 13, 5	"011111"
6b	6, 13, 4	"010111"
7a	7, 16, 5	"0110111"
7b	7, 16, 4	"0101011"
7c	7, 18, 6	"0111111"
7d	7, 18, 5	"0101111"
8a	8, 21, 6	"01101111"
8b	8, 21, 5	"01011011"
8c	8, 25, 7	"01111111"
8d	8, 25, 6	"01011111"
8e	8, 23, 5	"01010111"
9a	9, 28, 7	"011011111"
9b	9, 28, 6	"010110111", "010111011"
9c	9, 28, 6	"010110111", "010111011"
9d	9, 28, 5	"010101011"
9e	9, 30, 7	"011101111"
9f	9, 32, 8	"011111111"
9g	9, 30, 6	"010101111"
9h	9, 32, 7	"010111111"

[a]The listed invariants are: period, self-linking number, torsion. The symbolic names of horseshoe orbits with the same invariants are also displayed. Note that except for orbits 9b and 9c, there is a single possible symbolic name. The two possible symbolic names for orbits 9b and 9c are related through a time-reversal symmetry of the Smale's horseshoe template.

Although it should be noted that it is more common for higher-order orbits to have several possible symbolic names, it appears very clearly from Table 1 that topological invariants carry a large amount of information on the symbolic dynamics of a chaotic system. As we now explain in Section 2.4, this is the property which the following part of the paper will rely on.

2.4. Topological encoding as a bridge between the one-dimensional and the hyperbolic encodings

As mentioned in Section 1.3, the topological structure of a given unstable periodic orbit is not modified by a change in the control parameter. If we assume that there is a parameter that allows us to freely tune dissipation, modifying this parameter will induce isotopic deformations of the unstable periodic orbits, thus preserving their topological structure (except for orbits that are annihilated or created in saddle-node and period-doubling bifurcations).

Returning to the example of Table 1, let us appropriately vary this control parameter so as to achieve infinite dissipation. In this limit, the dynamics should be modeled by a one-dimensional return map similar to the logistic map $x_{n+1} = a - x_n^2$. Because of the deep link between template theory of the Smale's horseshoe and the symbolic dynamics of the logistic map, it is then obvious that the symbolic name given by one-dimensional symbolic dynamics theory will coincide with the one singled out by topological analysis and indicated in Table 1.

Let us now assume that by varying another parameter, we bring the system to a region of parameter space where it has an hyperbolic invariant set. Since template theory is mathematically rigorous in this case, the topological symbolic names in Table 1 must also be consistent with the ones obtained from a canonical Markov partition.

We will therefore make the fundamental hypothesis that *any relevant symbolic encoding should assign to a given periodic orbit a name that is compatible with its topological structure*, i.e., such that the orbit with the same name on the associated template has identical topological invariants. This is a strong assumption, as it implies that an orbit with a single topological name must be assigned the same name on its whole domain of existence (provided the global topological structure described by the template is not modified). However, this appears to be the only way to connect the two limiting cases in a continuous way.

Because this assumption is central to the method we describe below, it is important to discuss some observations reported in the literature regarding the well-defined symbolic codings. In particular, Hansen [67] has described the following striking phenomenon: by following a certain closed loop in the parameter space of the Hénon map starting and ending at parameters ($a = 2$, $b = 0$), where the one-dimensional canonical coding is available, the unstable periodic orbit with initial symbolic name "011111" is transformed into the orbit with symbolic name "000111". Similarly, Giovannini and Politi [68] have pointed out that at some parameter values of the Hénon map, the annihilation of primary homoclinic tangencies can induce a sudden modification of the partition line in such a way that the substring "...11000..." has to be replaced by the substring "...01001..." in all the symbolic names of the periodic orbits. Since the Hénon map is generally considered to capture the essential features of low-dimensional chaotic dynamics, these observations provide convincing evidence that a periodic orbit cannot always be assigned a single symbolic name in the whole parameter space.

A puzzling fact is that in both cases the symbolic recodings observed are in contradiction with the topological structure of a horseshoe-like flow. More precisely, these recodings connect symbolic names associated to periodic orbits of the horseshoe template having different topological invariants: e.g., the "011111" and "000111" horseshoe orbits have self-linking numbers of 13 and 7, respectively (note that their torsions, given by the number of "1" in the symbolic name, also differ). However, this does not at all contradict our main hypothesis: the examples described by Hansen and by Giovannini and Politi both involve orientation-reversing Hénon maps, which cannot be considered as return maps of a three-dimensional flow. In fact, the observed contradiction is a consequence of differences in the structures of the orientation-reversing and orientation-preserving Hénon maps, which can be analyzed using the tools provided by template analysis. Indeed, the doubly iterated Hénon map $H_{a,b}^2$ has Jacobian b^2 and is orientation-preserving regardless of the sign of the parameter b: the topological structure of its natural suspension can thus be studied in the whole parameter space (see Footnote 1). As we now show, the template associated to the $H_{a,b}^2$ map depends on

the sign of b, which explains some of the differences that exist between the orientation-reversing and orientation-preserving maps.

In the whole $b < 0$ parameter domain, the Hénon map $H_{a,b}$ is orientation-preserving and its natural suspension is associated to a standard horseshoe template. This is not surprising, given the geometrical interpretation of the action of the Hénon map [69]. Thus, the $H^2_{a,b}$ map in this parameter region is associated to a double horseshoe template, which can be obtained by concatenating two horseshoe templates.

A simple argument can then be used to determine the template describing the structure of $H^2_{a,b}$ in the $b > 0$ parameter region. Since b and y appear in the expression of the Hénon map only through their product, it is easily seen that we have $H_{a,b}(x, y) = H_{a,-b}(x, -y)$ and $H^2_{a,b}(x, y) = H^2_{a,-b}(-x, -y)$. This indicates that $H^2_{a,b}$ and $H^2_{a,-b}$ differ only by a global rotation of a half-turn around the origin. The associated templates differ in the same way, modulo a full twist (the structure of the suspension of a map is completely determined by the map itself up to a global rotation of an integer number of full turns [38–40]). Since the mirror image of the horseshoe template (a.k.a "reverse" [56], or "twisted" [20] horseshoe) differs from the horseshoe template precisely by a half-turn, the template associated to H^2 for $b > 0$ may be obtained by concatenating a horseshoe template with a reverse horseshoe template. This template, which corresponds to the $\mathcal{Z}$ template mentioned by Ghrist et al. [20], is described by the following matrices:

$$t^{\mathcal{Z}} = \begin{pmatrix} 0 & 0 & 0 & 0 \\ 0 & -1 & 0 & 0 \\ 0 & 0 & 0 & 0 \\ 0 & 0 & 0 & 1 \end{pmatrix},$$
$$l^{\mathcal{Z}} = (\,0 \quad -1 \quad -2 \quad 1\,). \tag{8}$$

We can now show that the change of symbolic name occurring in the example described by Hansen [67] is compatible with the topological structure of $H^2_{a,b}$ for $b > 0$.

Each period-6 orbit of H corresponding to a pair of period-3 orbits of H^2, the transformation between period-6 orbits occurring in the Hansen example corresponds for H^2 to two transformations between period-3 orbits. The doubly iterated logistic map at ($a = 2$, $b = 0$) has a natural partition with four symbols corresponding to two-symbol sequences of the logistic map as follows: "0"="00", "1"="01", "2"="11", and "3"="10". Thus, the 011111 $\rightarrow$ 000111 transformation corresponds to the following two transformations in H^2: 122 $\rightarrow$ 012, and 223 $\rightarrow$ 023.

It is easily checked that the "012" and "122" orbits of the template $\mathcal{Z}$ have identical invariants: they both have a self-linking number of -2 (and in fact are both trivial knots) and a torsion of -1. The same holds for the orbits "023" and "223". This was to be expected because the knot type of an orbit cannot change when this orbit is tracked along an arbitrary path in parameter space. Nevertheless, this provides a nice illustration of our core assumption that the only admissible symbolic names for an orbit are those which are compatible with its topological invariants.

As discussed above, $H^2_{a,b}$ maps with $b < 0$ are associated to a different template, whose orbits "012" and "122" are not isotopic. This indicates that no closed loop connecting the "011111" and "000111" orbits exists in this parameter region, which corresponds to the orientation-preserving Hénon map. As mentioned above, this can be deduced directly for the map iterated once, since the horseshoe orbits "011111" and "000111" are not isotopic.

In fact, knot invariants and torsion can easily be used to show that *none of the orbits with periods up to 6 of the orientation-preserving Hénon map can change its symbolic name in the domain where it is unstable*. Indeed, there are only two such orbits which have identical knot type and torsion: these are the period-6 "001011" and "001101" orbits. The former is the period-doubled orbit of the period-3 "001" orbit, while the latter belongs to the pair created in the second period-6 saddle-node bifurcation occurring in the universal sequence (see, e.g., [40,70]). This coincidence is an example of the general property that two horseshoe orbits whose symbolic names are the reverse of each other are isotopic, as noted by Holmes [44].

Because a path in parameter space is reversible, we simply have to show that no path leads from

"001101" to "001011". If we follow the "001101" orbit along a path on which it is always unstable, then its period-doubled orbit "001101001111" is also present on the whole path. It then suffices to note that the linking numbers of this period-12 orbit with "001011" and "001101" orbits are 22 and 21, respectively. Thus, the unstable "001101" orbit can always be distinguished from the "001011" orbit through the value of a simple topological invariant.

This implies that in the orientation-preserving Hénon map (whose natural suspension has a topological structure described by the horseshoe template), all the orbits with periods up to 6 can be given an unambiguous symbolic name in the domain where they are unstable, by following a path from the ($a = 2$, $b = 0$) point of parameter space: *they are uniquely identified by their invariants*. It is interesting to note that this property also holds in the "bi-unimodal" approximation to the Hénon map constructed by Hansen and Cvitanović [71]. However, the use of topological invariants allows us to obtain this result without any approximation.

Of course, this absolutely does not prove that the Hansen effect does not occur for higher-order orbits of the orientation-preserving Hénon map. We have performed a preliminary exploration of orbits of period 7, and found two coincidences (orbits with identical braid types and torsions): {"0001011", "0001101"} and {"0010111", "0011101"}. By an argument similar to that used above, the former degeneracy can be shown to be unambiguous. However, the case of the latter one is presently unclear: we were not able to find an orbit that both links differently the two ambiguous orbits and whose existence can be shown to be forced by one or the other of the two orbits, using the currently available techniques of orbit forcing theory [9,40,70,72].

In any case, we believe that the discussion above illustrates well that the topological analysis of unstable periodic orbits is a tool particularly well suited to the study of low-dimensional symbolic dynamics. The extent to which a symbolic coding can be defined in a canonical way remains an open problem, but the tools presented here appear to be currently the most promising tools to make some progress in this direction.

Therefore, we now proceed and describe a method to construct generating partitions that are compatible with the topological invariants of the UPO. We will see that while the algebraic tools of template analysis do not always select a single name for every orbit, a non-ambiguous encoding and a complete identification of the symbolic names are eventually obtained in our test case if we additionally require the symbolic encoding to be continuous, so that points which are close in a section plane are encoded by sequences that are close in sequence space. Although we cannot ascertain at the present stage that all symbolic names so assigned are independent of the procedure used, we found that the algorithm is robust in that for each orbit which could not be fully identified from its topological invariants only, one of the candidate names was clearly singled out by the requirement of continuity.

3. Description of the algorithm

3.1. Detection of the unstable periodic orbits

As we have seen in Section 2, template analysis yields for each detected periodic orbits a list of possible symbolic names. The next step is to use this information and the locations of these periodic orbits in the section plane to construct a partition, which may then be used to encode chaotic trajectories as well.

To illustrate the procedure that we discuss in detail below, we will study a chaotic attractor observed in numerical simulations of a modulated class-B laser described by the following equations [73,74]:

$$\dot{I} = I[AD - 1 - m \sin \omega t], \tag{9a}$$

$$\dot{D} = \gamma[1 - D(1 + I)], \tag{9b}$$

where the variables I and D represent the output intensity and the population inversion. In our numerical simulations, the following parameters were used: $A = 1.1$ (pump rate), $m = 0.0334$ (modulation amplitude), $T = 2\pi/\omega = 300$ (modulation period), and $\gamma = 2.5 \times 10^5/1.2 \times 10^8 \approx 2.083 \times 10^{-3}$ (ratio of the population inversion relaxation rate to the cavity damping rate). Fig. 2 shows the Poincaré section in

$(\log I, D)$ coordinates corresponding to $t = 0 \bmod T$ (as for all the Poincaré sections shown in this paper). The topological structure of this attractor is described by the Smale's horseshoe template shown in Fig. 4.

The algorithm we describe in this section will allow us to determine unambiguously the symbolic names of a set of unstable periodic orbits embedded in the strange attractor. If we want to utilize this information to perform symbolic encodings of arbitrary trajectories, we must detect a set of orbits that provides a good cover of the attractor, i.e., which is such that all trajectories on the attractor are locally shadowed with a good precision by an UPO.

Our detection code was specially designed to achieve this goal. Basically, it divides the Poincaré section in cells of size ϵ and follows a long chaotic trajectory, searching for close returns. When one is found, we check whether all the cells visited by points in the corresponding time series segment contain periodic points of period lower than or equal to the recurrence time. If this is not the case, a Newton–Raphson iteration is started from this initial condition. When the latter succeeds, the quality of the cover has been improved. The search terminates when each cell contains at least one periodic point and when no significant improvement has been obtained over a certain interval of time (the detection of a periodic point of lower period than those already contained in the cell is considered as an improvement). In this way, the computational effort is concentrated on obtaining the most uniform cover with orbits of lowest periods, rather than that finding the highest possible number of orbits.

This preliminary investigation revealed an interesting property: some parts of the strange attractor are extremely difficult to shadow with orbits of low period, especially when there are a lot of forbidden sequences in the symbolic dynamics. It turns out that these regions will be found later to be close to the partition border and to lines of homoclinic tangencies. If we view periodic and chaotic trajectories as the analog of rational and irrational numbers, respectively, this observation could be rephrased as: near principal lines of homoclinic tangencies, chaotic trajectories are more "irrational" than elsewhere in the attractor. While this may seem to be a fundamental obstacle to our approach, it should be noted that because the dynamics is weakly unstable in these regions, it is easy to detect the high-period orbits which are located in them, and that topological invariants of high-period orbits can be computed robustly. This explains why, in spite of the above-mentioned effect, we will be able to localize partition borders to within 0.01% of the attractor width in Section 3.6. Furthermore, we will show in the second part of this work [21] that because of non-hyperbolicity, obtaining a high-resolution shadowing in these regions is in fact not at all crucial for characterizing accurately the symbolic dynamics.

Following the procedure described above with $\epsilon = 0.001$ and with a maximal period of 32, we obtained a set of 1594 periodic orbits providing a uniform cover of the attractor. This set of orbits will be used throughout this section to illustrate the different stages of our algorithm. The possible symbolic names of the lowest-period orbits as determined from template analysis have been given in Table 1.

3.2. Notations

The detected set of orbits will be noted as $\mathcal{O}$, and consists of m UPO O_i. Each periodic orbit O_i has p_i intersections O_i^j, $j = 1, \ldots, p_i$, with the section plane (p_i is the topological period of the orbit). These intersections are periodic points of the first return map f, and their set will be noted as $\mathcal{P}$.

As we have seen in Section 2, knot theory and template analysis provides for each orbit O_i with one or several possible names. These "topological names", which will be noted $\mathcal{N}_k(O_i)$, are the names of the template orbits which have the same topological invariants. For definiteness, and since all cyclic permutations of a topological name represent the same orbit, we always write the topological name using the lowest permutation in the lexicographic order, enclosed inside brackets. For example, if the period-2 orbit O_2 can be named as "01" or "10", then $\mathcal{N}(O_2) = \langle 01 \rangle$.

Symbolic names are also used to label periodic points. In this case, cyclic permutations of a given string of symbols are not equivalent, since they

correspond to different periodic points. In this context, we use overlined strings. For example, the intersection of the orbit O_2 with the section plane consists of two periodic points: $\overline{01}$ and $\overline{10}$.

A partition Γ of the section plane into n disjoint regions $\Delta_i(\Gamma)$ assigns to each UPO a symbolic name $N_\Gamma(O_i)$. Because two partitions that associate a given periodic point with different cyclic permutations of the same name are to be considered different, we define $N_\Gamma(O_i)$ as being the symbolic name of its first periodic point: $N_\Gamma(O_i) = N_\Gamma(O_i^1)$. The latter is made of the symbols associated with the regions containing $O_i^1, O_i^2, \ldots, O_i^p$.

3.3. *Parameterization of partitions by periodic orbits*

Let us first consider the period-1 and period-2 orbits O_1 and O_2 whose symbolic names can be unambiguously determined as $\mathcal{N}(O_1) = \langle 1 \rangle$ and $\mathcal{N}(O_2) = \langle 01 \rangle$. The latter consists of two periodic points whose symbolic names are the cyclic permutations of $\mathcal{N}(O_2)$, namely $\overline{01}$ and $\overline{10}$.

There are thus two possibilities for assigning a symbolic sequence to the two points O_2^1 and O_2^2 of the O_2 orbit. Either $(N_\Gamma(O_2^1), N_\Gamma(O_2^2)) = (\overline{01}, \overline{10})$ or the opposite choice is made. As we will see in the second part of this work [21], these two possibilities lead to different, but dynamically equivalent solutions. For definiteness, we restrict ourselves to the first configuration in this section.

In the following, we call as *reference points* the periodic points whose symbolic sequence is assumed to be unambiguously known. We now explain how the three reference points (O_1^1, O_2^1, O_2^2), associated with sequences $(\bar{1}, \overline{01}, \overline{10})$, may be used to define a rough partition, which will be later refined by considering higher-order periodic orbits.

If we examine generating partitions such as these shown in Fig. 2 and in Refs. [7,25,27,28], we note that the regions of the section plane corresponding to different symbols are separated by a line with a simple structure, whose length is of the order of the diameter of the attractor. Consequently, there is a high probability, as higher as the points are closer, that a point and one of its close neighbors correspond to the same symbol, except if they are located in a small region around the border.

If a point is in a close neighborhood of one of the three reference points, it is natural to encode this point with the same symbol as this reference point. For points which are at comparable distances from two or more reference points, the correct symbol is uncertain. However, without using the information that will be provided by the higher-order periodic orbits, the simplest procedure that is consistent with the previous remark is to associate these points with the symbol of the closest reference point. We thus have a simple rule to encode a chaotic trajectory: at each intersection with the section plane, the closest reference point is determined and the associated symbol is inserted in the symbolic sequence.

The corresponding partition of the section plane obtained using the three initial reference points is shown in Fig. 6. In this simple case, the border line of the partition is easily constructed, since one has to merely separate points whose nearest reference point has leading symbol "0" from those whose nearest reference point has leading symbol "1". Thus, the partition border follows the mediators of the segments

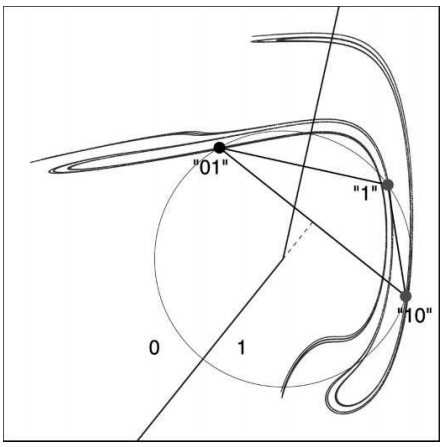

Fig. 6. The initial partition based on periodic points $\bar{1}$, $\overline{10}$, and $\overline{01}$. For points that are at the left (respectively, right) of the border, the closest reference point is the $\overline{01}$ periodic point (respectively, one of the $\bar{1}$ and $\overline{10}$ periodic points). The circumcircle of the triangle made of the three points is also shown.

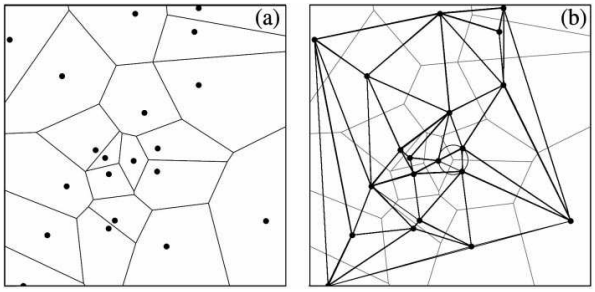

Fig. 7. (a) Voronoŝtringı diagram of a set of points; (b) the corresponding Delaunay triangulation. The circumcenter of one of the triangles is shown.

joining points with different symbols (i.e., the segments from $\overline{01}$ to $\bar{1}$ and from $\overline{01}$ to $\overline{10}$). It is a known geometrical property that these two mediators intersect at the circumcenter of the triangle made of the three initial reference points.

A nice property of the above rule is that it can be efficiently implemented for an arbitrary number of reference points, using well-known geometrical tools: Delaunay triangulations and Voronoŝtringı diagrams [75–77].

Given a reference point O_i^j, the set of points in the section plane that are closer to O_i^j than to any other reference point is nothing but the Voronoŝtringı domain of O_i^j with respect to the set of reference points. The Voronoŝtringı diagram is a graph that consists of the borders of the Voronoŝtringı domains (Fig. 7a). The dual graph of the Voronoŝtringı diagram is called the Delaunay triangulation (Fig. 7b). Among the possible triangulations of a set of points, the Delaunay triangulation is the only one such that the circumcircle of a triangle linking three sites never contains another site [75–77]. This property can be used to implement efficient algorithms for building Delaunay triangulations, from which the associated Voronoŝtringı diagrams is easily obtained. Delaunay triangulations will thus be a powerful tool to construct partitions and parameterize them in a way that is suitable for applications.

In our initial configuration based on three reference points, the Delaunay triangulation is readily obtained since it merely consists of the triangle made of the three initial reference points (Fig. 6). As explained above, the Voronoŝtringı domains of the three points are separated by the mediators of the triangle edges, which intersect at the center of the circumcircle. The "0" (respectively, "1") region consists of the Voronoŝtringı domain of $\overline{01}$ (respectively, the union of the Voronoŝtringı domains of $\bar{1}$ and $\overline{10}$).

To determine the border line for triangulations with an arbitrary number of reference points, one searches for couples of neighboring triangles whose common edge carries two different symbols. The line segments connecting the circumcenters of all such pairs of triangles constitute the border line. This allows one to compute quickly the partition corresponding to a given set of reference points. Another advantage of Delaunay triangulations is that they can be computed incrementally: adding a new reference point to an existing triangulation only requires modifying the triangles in the neighborhood of the new point [78,79]. This is a useful property, as we will now refine the initial partition by adding higher-order periodic points to it.

3.4. Refining the initial partition using orbits with a unique topological name

The three reference points and their associated symbols define an initial partition. However, this partition has a low precision and cannot be reliably used except near one of the three reference points. To refine it, we

now have to extract information from the locations of the higher-order periodic orbits. To proceed as safely as possible, we first consider the orbits which have a single topological name.

It should be noted that any cyclic permutation of the topological name of an unambiguously identified orbit can in principle be used to label its intersections with the section plane. Computing the Delaunay triangulation of these periodic points, and determining the border as explained above would yield a good partition, with different names being given to different orbits. Doing so, however, the border might be so convoluted as to be useless because most points would be close to the border. The description of such a partition would require an enormous amount of information and the encoding of a chaotic trajectory would be extremely sensitive to noise. It might also be impossible to find a continuous encoding for the remaining orbits.

For each periodic orbit with a unique symbolic name, we thus have to find the cyclic permutation of the symbolic name that keeps the current partition as simple as possible. This can be achieved by inserting periodic orbits in the partition in the following way.

Let us consider the next orbit beyond the period-1 and period-2 orbits, a period-4 orbit in our case (the attractor does not contain period-3 orbits). This orbit is associated to two, possibly different, symbolic names: (i) the topological name determined from template analysis, and (ii) the name that is obtained using the current partition. Two situations may occur, depending on whether the latter is a cyclic permutation of the former.

In the affirmative, the current partition correctly guesses the real symbolic name of the orbit (Fig. 8a): we thus add its points to the reference list, associated with the symbols indicated by the current partition. If some of the new points are closer to the border of the partition than the previous reference points, the precision of the partition is increased (Fig. 8b).

If the topological and partition names of an orbit are not consistent, we have to find the cyclic permutation of the topological name such that the insertion in the triangulation of the corresponding pairs of periodic points and symbols modifies the partition the least. To do so, we determine for each permutation

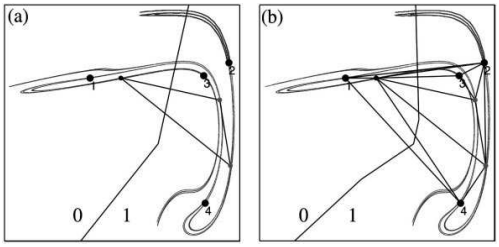

Fig. 8. Inserting an orbit into the partition: (a) comparison of the topological name and of the name indicated by the current partition. In this case, the name obtained from the partition ($N_\Gamma(O_3) = \overline{0111}$) matches the topological name; (b) the updated partition after the points of the period-4 orbit have been inserted into the list of reference points. Insertion of point 3 increases the precision of the partition.

which of the periodic points, where the topological symbol differs from the one assigned by the current partition, is most distant from the partition border, and note the corresponding distance. We then choose the cyclic permutation for which this distance is the smallest, so that the border is displaced by a small amount only.

A striking fact is that when carrying out the analysis of our sample set of orbits, there was only one orbit, the period-23 orbit $\langle(01)^2(011)^2(01011)^2(011)\rangle$, for which the second rule had to be used: the 249 other orbits with a single topological name were already correctly encoded by the partition under construction. This orbit and the partitions before and after its insertion are shown in Fig. 9. It can be seen that the discrepancy is due to a single point which is located very close to the border of the current partition.

After all orbits with a single topological name have been inserted, we obtain a partition that: (i) assigns to each of these orbits its topological name, (ii) has a simple structure, as can be seen in Fig. 10.

By using the fact that the border of this intermediate partition is localized with a very good precision, we now proceed to the orbits for which template analysis had selected several possible symbolic names, and determine which of these names is the correct one. This will allow us to further increase the resolution.

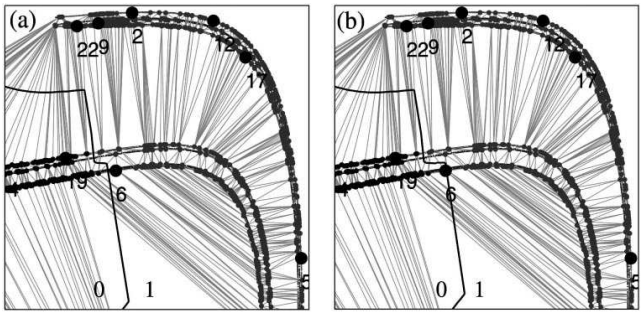

Fig. 9. Comparison of the topological and partition names of the period-23 orbit $\langle(01)^2(011)^2(01011)^2(011)\rangle$: (a) the symbolic name assigned by the current partition agrees with the topological name except at point 6; (b) the updated partition after insertion of the orbit differs only slightly from the previous one, but point 6 is now on the correct side of the border.

3.5. Final stage of the construction

Periodic orbits with several topological names were not used in the previous step, because we had then no reason of favoring one name over the others. However, once an intermediate partition has been determined from unambiguous orbits (Fig. 10), it may be used to determine the symbols of points that are far enough from the border, if we assume that it will be only slightly modified by further refinements.

More precisely, consider the periodic orbit which is displayed in Fig. 11 (this is orbit 9b of Table 1). It has two possible names, namely $\mathcal{N}_1 = \langle 010110111\rangle = \langle 0101^2 01^3\rangle$ and $\mathcal{N}_2 = \langle 010111011\rangle = \langle 0101^3 01^2\rangle$. However, it can be seen that its intersections with the section plane are far from the partition border. Therefore, there is little doubt that the name indicated by the current partition, which is $N_\Gamma = \overline{01^3 01^2 01}$, is the

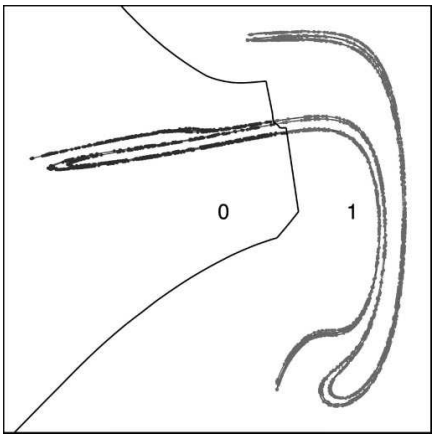

Fig. 10. The partition as obtained from orbits with a single topological name. For clarity, the triangles are not shown. The large dots represent the reference points which parameterize the partition at this stage. It can be seen that the points for which the symbolic dynamical information can be unambiguously extracted cover well the attractor. This provides a graphical illustration of the observation made about Table 1, but here with orbits of periods up to 32.

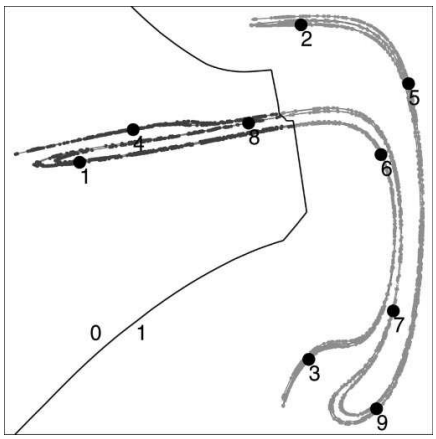

Fig. 11. The periodic points of orbit 9b of Table 1, which has two possible symbolic names, are represented with the partition obtained at the end of Section 3.4.

correct one, as is confirmed by the fact that it corresponds to a cyclic permutation of $\mathcal{N}_2$. We can therefore assign this name to the orbit and insert it in the partition. Then, by examining Table 1, one immediately sees that since $\mathcal{N}_2$ has been assigned to orbit 9b, it can no longer be a possible name for orbit 9c. Therefore, the only remaining possible name for the latter orbit is $\mathcal{N}_1$, which indeed is also the one obtained from the current partition. We thus see that a consistency check (different orbits should have different names) allows us to identify the symbolic names of two orbits at once.

A more sophisticated consistency check that has to be carried after the symbolic name of an orbit has been identified is whether all the possible names of the not yet inserted orbits remain compatible with the experimental table of topological invariants. Assume that, as in the above example, the symbolic name of the O_i orbit has just been identified as $N_i = N_\Gamma(O_i)$. If a possible name $\mathcal{N}_k(O_j)$ of another orbit O_j is such that the linking number $\mathrm{lk}(N_i, \mathcal{N}_k(O_j))$ computed from the two names does not match the measured value, $\mathcal{N}_k(O_j)$ can be discarded without hesitation, as is illustrated in Table 2. This shows how enforcing simultaneously the requirements of smoothness and of topological consistency allow one to solve the ambiguities remaining after the template analysis step.

For some orbits, one or more periodic points are located in a close neighborhood of the partition border. In this case, the name indicated by the partition is uncertain: some symbols may be erroneous due to the finite precision of the partition. Yet, this provisional name can be utilized to obtain the correct one, or at least to extract additional information. Indeed, if there are sequences of consecutive periodic points $O_n^i, O_n^{i+1}, \ldots, O_n^{i+k}$ whose symbols can be determined unambiguously, this gives us substrings $s_i s_{i+1} \cdots s_{i+k}$ of the correct symbolic name of this orbit. This information allows one to discard topological names that do not contain this substring. If only one topological name remains, the orbit can be inserted immediately in the partition. If there is still an ambiguity, we delay the insertion of the orbit until further information has been extracted from the other orbits.

Table 2
Linking numbers of some Smale's horseshoe orbits[a]

	$0101^2 01^3 = \mathcal{N}_1(\alpha)$	$0101^3 01^2 = \mathcal{N}_2(\alpha)$
$(01)^3 01^2 (01^4)^2 = \mathcal{N}_1(\beta)$	66	67
$(01)^3 (01^4)^2 01^2 = \mathcal{N}_2(\beta)$	67	66

[a] Assume that the names in the first row (respectively, first column) are the possible topological names of an experimental orbit α (respectively, β), and that the linking number of these two orbits is $\mathrm{lk}(\alpha, \beta) = 66$. If the current partition can be used to show that the correct symbolic name of α can only be $\mathcal{N}_2(\alpha)$, then it follows immediately that the correct name for β is $\mathcal{N}_2(\beta)$, since $\mathrm{lk}(\mathcal{N}_2(\alpha), \mathcal{N}_1(\beta))$ does not match the experimentally measured invariant.

The arguments presented above are very natural. Yet, to design a precise algorithm, we must specify what "far from the partition border" means. We thus need a precise rule to decide whether the symbol assigned by the current partition to a given point p in the section plane can be trusted. We have found the following procedure to be very reliable.

We first search for all the triangles of the current triangulation whose circumcircle contains the point p, i.e., the triangles which would be removed if p was to be inserted in the triangulation.[4] We then examine the symbols associated with the vertices of these triangles. If all these symbols are identical, we consider that the symbol assigned to p by the partition is certain. If some symbols differ, we conclude that the current partition is unreliable in the neighborhood of p. The rationale of this rule is that insertion of a point in the "uncertain" region defined in this way modifies the border of the partition, because it modifies the triangles whose circumcenters lie on the border.

There is, however, a small technical problem with this rule. Indeed it is known that the outer edges of the triangulation of a set of points comprise the convex hull of this set. However, the support of the strange attractor in the section plane is generally not convex because of the folding process. Consequently, there are triangles whose vertices have different symbols merely because they are located on opposite sides of the attractor (see, e.g., Fig. 9). A direct use of the rule described

[4] Because a Delaunay triangulation has the property that the circumcircle of a triangle has no point in its interior, the insertion of a new point in a triangulation is performed by removing triangles whose circumcircle contains this point, and adding new ones so as to enforce the rule.

above would then lead to conclude that the symbol of points contained in the circumcircles of these triangles cannot be reliably determined, whereas the reference points with different symbols are far away from each other on opposite sides of the attractor.

To solve this difficulty by geometrical means, we compute a polygon that tightly encloses the support of the attractor. We do so by first determining which squares of a grid with given resolution contain points of the attractor, and then computing the oriented boundary of this set of squares. This boundary consists of a set of closed curves. By starting from the leftmost point and following the boundary so as to stay on the exterior curve, an enclosing polygon is easily constructed. We have observed that the final partitions we obtain are insensitive to the size of the squares, provided that the latter is a few times smaller than that of the size of the attractor. Any method for constructing the polygon should therefore be satisfactory as long as it allows one to roughly identify regions which are inside the convex hull, but well outside the support of the attractor.

Triangles with different symbols are then classified according to whether the parts of their mediators belonging to the partition border have a non-empty intersection with the interior of the polygon or not. Only the first class of triangles is used to assess the reliability of a symbol. Thus, the modified rule states that the symbol of a point cannot be reliably determined when the insertion of this point into the triangulation would modify the partition border *inside the support of the strange attractor*, which is illustrated in Fig. 12.

To summarize, the insertion of an orbit with several possible topological names is carried out as follows. First, the symbolic encoding of this orbit by the current partition is expressed by a symbolic name N_c with "error bars". This symbolic name is made of the symbols "0", "1",. . .,"$n-1$" (for points that can be unambiguously coded) and "*" (for points located in the "uncertain" region). Then, we compare all cyclic permutations of each topological name to this symbolic name, with "*" matching any symbol. If two or more topological names are compatible with N_c, we consider that we do not have enough information at this point to insert the orbit, but nevertheless discard the incompatible topological names. On the contrary, if only one topological name has a cyclic permutation that is compatible with N_c, we consider that it is the correct symbolic name of the orbit, and insert the orbit into the description of the partition.

Alternatively, discarding names that are not compatible with the current partition and names that are no longer compatible with experimental topological invariants (as explained in Table 2) allows one to progressively insert all the orbits, so that finally each orbit is associated with a single symbolic name. The final partition, which is shown in Fig. 13, provides by construction a symbolic encoding that is both consistent with the topological structure of the set of periodic orbits and continuous (points that are close in the

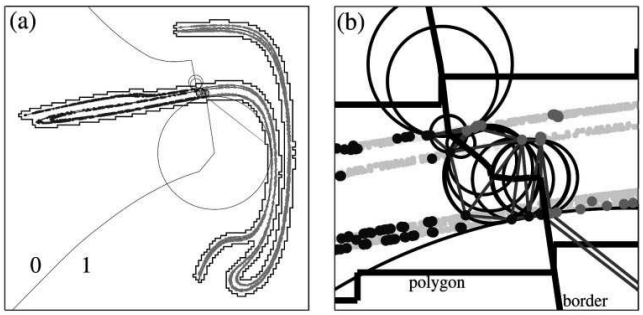

Fig. 12. Regions of certain and uncertain coding: (a) a polygon providing a good approximation of the support of the strange attractor is determined; (b) enlarged view of the border region. The uncertain region is defined to be located within the circumcircles of the triangles linking reference points with different symbols and whose mediators (which constitute the border line) lie within the shadow polygon.

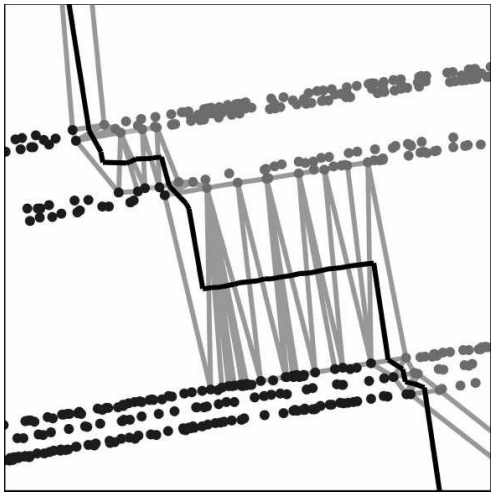

Fig. 13. Enlarged view of the border of the final partition obtained when all the periodic orbits have been inserted (the large-scale structure is virtually identical to that shown in Fig. 10). The width of the represented box is 5×10^{-2} in units of the attractor width and the linewidth used to draw the border line and the reference points is 5×10^{-4}.

section plane are associated to symbolic sequences that are close in the symbol space). Given the high number of periodic orbits in our example, it is quite remarkable that the simple rules we have followed naturally select a single name for each orbit: this supports the existence of a well-defined symbolic encoding.

Note that the rule we have defined to assess the reliability of the symbol associated to a point can be interpreted as an interpolation problem. Indeed, Delaunay triangulations are routinely used to interpolate the value of a function at an arbitrary point p from known values at the sites of the triangulation. There are essentially two methods to do so. The first averages appropriately the values at the three vertices of the triangle that contains p. The second utilizes the vertices of all the triangles whose circumcircle contains p, and is called "natural neighbor interpolation" [80].

Thus, it appears that our procedure, which we initially derived from the heuristic argument presented above, is based on the latter. When the result of the interpolation is exactly one of the n possible symbols (because all neighboring vertices have the same symbol), the result is considered as certain. When the interpolation yields a value that is intermediate between two symbols (some neighboring vertices have different symbols), the encoding is considered as uncertain. It is interesting to note that an earlier version of our algorithm based on the first interpolation method did not converge in some cases because some periodic points were incorrectly classified as certain, leading to inconsistencies when inserting the remaining orbits. This is because the reference point which is closest to p need not be a vertex of the triangle containing p, whereas it is known that it is a vertex of one of the triangles whose circumcircle contains p.

In this respect, it is interesting to note that the method described very recently in Ref. [13] is very similar to ours: in both algorithms, periodic points which have been assigned a symbol are fed to an interpolation scheme to obtain the coding of an arbitrary point in the Poincaré section. In [13], it is only required that orbits not yet identified receive a unique name, whereas we additionally require agreement with the computed topological invariants. This ensures that the symbolic names obtained are consistent with the canonical codings in the one-dimensional and hyperbolic limits, and that they are dynamically relevant, at the cost of restricting currently the applicability of the method to two-dimensional orientation-preserving maps and to flows. An interesting result of Ref. [13] is that, at least in the examples analyzed in this work, the requirements of continuity and uniqueness seem sufficient to obtain a simple generating partition.

In conclusion, it results that simple rules can be used to construct a partition of the section plane using the information provided by (i) the topological invariants of the unstable periodic orbits, and (ii) their positions in the section plane. We have seen that this algorithm yields partitions that have a very simple structure, and therefore encode points with high reliability, except in a very small region around the border of the partition.

3.6. Increasing the resolution of the partition

In describing our algorithm in the previous sections, our aim was to show that no inconsistency was found

even when shadowing all the trajectories on the attractor with a high resolution, i.e., that it was possible to assign unambiguously to every orbit a distinct symbolic name compatible with its topological invariants. To this end, we utilized a set of orbits that provided an uniform cover of the attractor. For practical applications, however, a high-resolution cover is only needed in a small neighborhood of the border of the partition. To achieve a high precision at the lowest cost, we have therefore modified our method as follows.

The procedure was split into two stages. First, an approximate partition is determined using a set of orbits of limited period providing a cover of moderate resolution. This allows one to bracket the position of the border with reasonable accuracy. Using this information, a second set of periodic orbits is selected so that it provides a cover of the attractor with high resolution in the neighborhood of the border, more precisely inside the circumcenters of the triangles enclosing it, and with moderate resolution elsewhere.

We then apply to the latter set a slightly modified version of the algorithm described in the previous sections. Indeed, we have observed that obtaining a high-resolution cover in the critical region requires using orbits of very high period, especially when there are many forbidden sequences in the symbolic dynamics. This does not induce additional difficulties in the first steps of the procedure because (i) high-period orbits localized near the border of the partition are marginally unstable, which makes their detection relatively easy, (ii) topological invariants are expressed by integer numbers and can therefore be reliably computed for orbits of very large periods, provided they are localized with the precision commonly available in numerical simulations.

In fact, the limiting step is the search for possible symbolic names using template analysis. Indeed, this search requires a considerable amount of computing time (the number of symbolic names of length p increases exponentially with p), especially when the symbolic dynamics is based on three or more symbols. For a two-symbol dynamics, the symbolic names of orbits with periods up to 32 can be determined in a reasonable amount of computing time, while in the three-symbol case, a direct search is practically limited to orbits of period lower than 20.

We thus restrict this search to the orbits up to a certain period. An intermediate partition is built from these orbits, and is utilized to list for the remaining higher-period orbits the symbolic names which (i) are compatible with this partition, as explained in Section 3.5, and (ii) correctly predict the topological invariants of these higher-period orbits.

Once a list of possible names has been so obtained for each orbit in the final set, the analysis proceeds as in Section 3. It should be stressed that this procedure is entirely equivalent to the one described in Sections 3.3–3.5, where all the topological names are determined before trying to build the partition: we simply apply the selection criteria in a different order.

With this modified algorithm, and a final set of 750 orbits of periods up to 64, we have obtained for the chaotic attractor of Fig. 2 a partition whose border is bracketed with a resolution that is almost everywhere significantly below 0.01% of the attractor width (see Fig. 14b). Note that the same precision could be obtained clearly at a lower cost by using a significantly smaller number of periodic orbits. Indeed, it can be seen in Fig. 14a that many triangles connecting two leaves of the attractor are in fact not essential for localizing precisely the border, but were nevertheless considered by our algorithm to belong to the border neighborhood. The many periodic points associated with these triangles (the detection code is in high-resolution mode in this region) could therefore be discarded from the set of orbits without modifying the result.

It should be noted that such a precision is several orders of magnitude higher than that is needed for practical purposes. In fact, as we will show in the second part of this work [21], one has to compare trajectories whose symbolic sequences have common substrings of more than 60 symbols to observe an effect due to the error in the location of the border. Nevertheless, this example has allowed us to verify the robustness of our algorithm down to very small scales. Furthermore, it provides us with a test case which we will use in the second part of this work to give evidence that our approach is consistent with methods based on homoclinic tangencies.

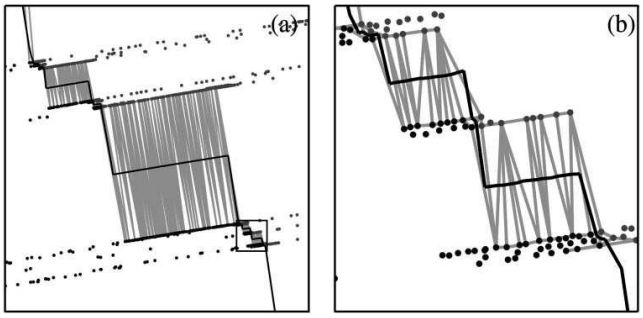

Fig. 14. (a) Enlarged view of the border of the partition obtained using a high-resolution cover of the border region by periodic points (the size of the represented box is the same as in Fig. 13, i.e., 5×10^{-2} in units of the attractor width). The triangles shown are those defining the partition border inside the shadow polygon. Note the high density of periodic points associated with these triangles due to the design of our selection algorithm. (b) Enlarged view of the small square of size 5×10^{-3} displayed in the left picture. The linewidth used to draw the border line and the periodic points is 5×10^{-5}.

4. Conclusion and perspectives

Our primary goal in showing that template analysis can be used to obtain high-resolution partitions in numerical simulations was to give strong evidence of the validity of the approach proposed in [8]. A first result is the successful outcome of an intensive check of the validity of template analysis: even when using large sets of UPO of high periods, we could always find a global projection on a simple branched manifold that preserves the topological invariants. Although the application of template theory to real, non-hyperbolic, attractors is still lacking a rigorous foundation, this work gives further evidence that it accurately describes the geometric structure of an attractor down to very small scales. Although embedded in a non-hyperbolic attractor, the UPO appears to be organized as in the hyperbolic limit, and constitutes an hyperbolic set which approximates well the strange attractor.

The foundation of this work is the fact that the knot invariants of an unstable periodic orbit carry precise information about its symbolic dynamics. Building on this idea, we have described an algorithm to construct generating partitions of a strange attractor. It combines information (i) from the topological invariants of UPO embedded in it, and (ii) from their location in a section plane, and is designed so as to yield encodings that are continuous (sequences associated to neighboring points should be close in symbol space). These basic ingredients ensure that the resulting encodings are compatible with those valid in the one-dimensional and hyperbolic limits, and that they are dynamically relevant.

In our algorithm, a partition is described by a list of reference points, whose associated symbols are given. To perform a symbolic encoding, points in the section plane are associated with the symbol carried by the closest reference point. This allows us to use simple geometrical tools such as Delaunay triangulations. Starting from an initial configuration based on the lowest-period orbits, the accuracy of the partition is progressively improved by adding periodic points of increasing period to the list of reference points in a way that preserves the simplicity of the partition and topological consistency.

Following this procedure, we have obtained partitions that have a simple structure, yet reproduce the symbolic information extracted from topological analysis: the unique symbolic name that is eventually assigned to each periodic orbit is intimately related to its topological structure, and hence to its genealogy [9,24,40,70,72]. Had we faced an inconsistency at some stage of the construction, we would have been forced to conclude that there was a fundamental flaw in our hypotheses. This was not the case neither in the example we considered in this paper (we

recall that it involved a set of 1594 periodic orbits, whose topological information was contained in about 4.4×10^6 integer numbers), nor in others that we have studied.

The present results call for further investigations in several directions. First, we have to verify more extensively the relevance of the obtained encodings, even if this should be guaranteed by the consistency checks built into our algorithm. We do so in the second part of this work [21], where in particular we show that the border of the high-resolution partition displayed in Fig. 14 follows very accurately a line of homoclinic tangencies, thus providing strong evidence of the equivalence of the two approaches. We also give in [21] additional evidence of the relevance of our algorithm by verifying (i) that encodings obtained from different initial partitions are dynamically equivalent, (ii) that accurate estimates of the metric entropy can be computed from the probabilities of symbolic sequences, and (iii) that symbolic sequences of increasing length select regions of decreasing diameter in the section plane.

The robustness of our method with respect to noise should also be more precisely studied. While template analysis behaves well in this context, it would be desirable to quantify precisely the highest noise level that is acceptable for extracting meaningful results. To achieve this, a characterization of simulated time series contaminated by various amounts of noise, and where UPO are detected from close returns, is required.

Similarly, the independence of symbolic encodings with respect to changes in parameter values should be carefully checked: in this work, we have determined generating partitions only at a given set of parameters. While it is obvious that the orbits with a unique topological name will always be assigned the same name on their whole domain of existence (provided the associated template is not modified), we have to verify under which conditions this also holds for the higher-period orbits whose identification is completed during the construction of the partition. However, determining in a systematic way which orbits have a well-defined symbolic name appears to a difficult problem at the present stage, as discussed in Section 2.4.

In the case of infinitely dissipative system, the relevant part of the triangulation essentially consists of two periodic points located on opposite sites of the border. In the mildly dissipative examples we have considered in this work, the triangles enclosing the border involve a significantly higher number of periodic points. It would be highly interesting to determine whether these borderline periodic points are directly related to the symbolic sequences defining the "pruning front" in symbol plane [26]. Another point worth investigating is whether these orbits belong to a basis set (in orbit forcing theory [9,40,70,72], a basis set is a small set of periodic orbits whose existence can be shown to force the existence of all the other orbits embedded in the attractor).

On the experimental side, we intend to apply very soon the algorithm described here to a weakly dissipative experimental system, namely a pump-modulated Nd:YAG laser. Indeed, the first experimental topological encoding was obtained for a system which was relatively dissipative (a CO_2 laser with modulated losses), even though its return map could not be described by a well-defined one-dimensional map on a wide range of parameters [8].

To conclude, we would like to comment on the links that exist between the topological approach we have discussed in this work and the classical one based on homoclinic tangencies, although they seem to have no common ground at first glance. As we will show in [21], these two methods yield results that are equivalent, and thus must correspond to different views of a single structure. In fact, both ultimately rely on the fact that a chaotic invertible return map is a diffeomorphism organized by underlying singularities.

To have these singularities appear undressed in the form of homoclinic tangencies, it is necessary to iterate the return map an infinite number of times. In doing so, however, one not only recovers the organizing singularities, but also an infinite number of copies of them. As a result, there is a fundamental ambiguity in the choice of the homoclinic tangencies defining the partition. This can only be solved by searching directly in the time-one map the singularities that are hidden in it.

The Birman–Williams construction for hyperbolic systems provides a deep answer to this problem. In the case of the horseshoe map, the one-dimensional return map of the semi-flow defined on the branched manifold features explicitly the fold singularity that is the backbone of the two-dimensional horseshoe map, as well as any three-dimensional suspension of it. It is thus tempting to conjecture that the essential features of an invertible chaotic return map are determined for the most part by the structure of the singularities of a lower-dimensional non-invertible map [81].

The initial partition based on a few low-period orbits separates their periodic point according to how they should be located on an underlying singular map, and in a sense provides a rough geometric modeling of such a map. The hierarchical refinement of the partition carried out by progressively inserting higher-order orbits can be viewed as a means to ensure that "iterates" of this singular map converge to iterates of the invertible return map. In this way, the singularities which appear in the infinitely iterated return map are eventually localized while keeping the geometrical description close to that of the time-one map. This allows one to extract information from the whole phase space without having to approach too closely the noise-perturbed singularities.

This discussion makes it easier to understand why mathematical tools that are intimately linked to the theory of one-dimensional symbolic dynamics are so perfectly suited to the study of two-dimensional dynamics. One key to this apparent paradox is that unstable periodic orbits, among all other trajectories in the attractor, have a very distinctive property: their forward symbolic sequence is uniquely determined from their backward one, and vice versa. From a symbolic dynamical point of view, periodic orbits are thus one-dimensional objects intertwined with the fully two-dimensional chaotic trajectories, which makes it possible to extend information extracted from the former to the latter.

The bridge between the non-invertible and the invertible dynamics is provided by the knot invariants of the UPO, which indicate how the latter should be laid on the domain of the underlying one-dimensional map without having to construct it explicitly. These invariants thus play a role that is not unlike the conserved quantities or symmetries that have proved so immensely useful in many fields of physics. If we want to extend topological coding to higher-dimensional chaos and understand its singularity structure, we probably have to first search for appropriate invariant quantities.

Note. The source code of the computer programs used to determine the template from the invariants of periodic orbits and to construct the partitions is available upon request to the corresponding author.

Acknowledgements

It is a pleasure to thank our colleagues Guillaume Boulant, Serge Bielawski, Dominique Derozier, and Robert Gilmore for stimulating discussions. We are also grateful to Toby Hall for clarifying some aspects of orbit forcing theory. The Laboratoire de Physique des Lasers, Atomes, Molécules is Unité de Recherche Mixte du CNRS. The Centre d'Études et Recherches Lasers et Applications is supported by the Ministére chargé de la Recherche, the Région Nord-Pas de Calais and the Fonds Européen de Développement Économique des Régions.

References

[1] J. Guckenheimer, P.J. Holmes, Nonlinear Oscillations, Dynamical Systems and Bifurcations of Vector Fields, Springer, Berlin, 1983.
[2] A. Katok, B. Hasselblatt, Introduction to the Modern Theory of Dynamical Systems, Cambridge University Press, Cambdrige, 1995.
[3] Hao Bai-Lin, Elementary Symbolic Dynamics and Chaos in Dissipative Systems, World Scientific, Singapore, 1989.
[4] R. Badii, A. Politi, Complexity: Hierarchical Structures and Scaling in Physics, Cambridge Nonlinear Science Series, Vol. 6, Cambridge University Press, Cambridge, 1997.
[5] S. Hayes, C. Grebogi, E. Ott, Communicating with chaos, Phys. Rev. Lett. 70 (1993) 3031–3034.
[6] S. Hayes, C. Grebogi, E. Ott, A. Mark, Experimental control of chaos for communication, Phys. Rev. Lett. 73 (1994) 1781–1784.
[7] P. Grassberger, H. Kantz, Generating partitions for the dissipative Hénon map, Phys. Lett. A 113 (1985) 235–238.
[8] M. Lefranc, P. Glorieux, F. Papoff, F. Molesti, E. Arimondo, Combining topological analysis and symbolic dynamics to

describe a strange attractor and its crises, Phys. Rev. Lett. 73 (1994) 1364–1367.

[9] R. Gilmore, Topological analysis of chaotic dynamical systems, Rev. Mod. Phys. 70 (1998) 1455–1530.

[10] L. Flepp, R. Holzner, E. Brun, M. Finardi, R. Badii, Model identification by periodic-orbit analysis for NMR-laser chaos, Phys. Rev. Lett. 67 (1991) 2244–2247.

[11] M. Finardi, L. Flepp, J. Parisi, R. Holzner, R. Badii, E. Brun, Topological and metric analysis of heteroclinic crisis in laser chaos, Phys. Rev. Lett. 68 (1992) 2989–2991.

[12] R. Badii, E. Brun, M. Finardi, L. Flepp, R. Holzner, J. Parisi, C. Reyl, J. Simonet, Progress in the analysis of experimental chaos through periodic orbits, Rev. Mod. Phys. 66 (1994) 1389–1415.

[13] R.L. Davidchack, Y.-C. Lai, E.M. Bollt, M. Dhamala, Estimating generating partitions of chaotic systems by unstable periodic orbits, Phys. Rev. E 61 (2000) 1353–1356.

[14] D. Sterling, H.R. Dulling, J. Meiss, Homoclinic bifurcations in the Hénon map, Physica D 134 (1999) 153–184.

[15] N.B. Tufillaro, T.A. Abbott, J.P. Reilly, An Experimental Approach to Nonlinear Dynamics and Chaos, Addison-Wesley, Reading, MA, 1992.

[16] H.G. Solari, M.A. Natiello, G.B. Mindlin, Nonlinear Dynamics: A Two-way Trip from Physics to Math, IOP Publishers, London, 1996.

[17] G.B. Mindlin, X.-J. Hou, H.G. Solari, R. Gilmore, N.B. Tufillaro, Characterization of strange attractors by integers, Phys. Rev. Lett. 64 (1990) 2350–2353.

[18] G.B. Mindlin, H.G. Solari, M.A. Natiello, R. Gilmore, X.-J. Hou, Topological analysis of chaotic time series data from Belousov–Zhabotinski reaction, J. Nonlinear Sci. 1 (1991) 147–173.

[19] J.S. Birman, R.F. Williams, Knotted periodic orbits in dynamical systems I: Lorenz's equations, Topology 22 (1983) 47–82.

[20] R.W. Ghrist, P.J. Holmes, M.C. Sullivan, Knots and Links in Three-dimensional Flows, Lecture Notes in Mathematics, Vol. 1654, Springer, Berlin, 1997.

[21] J. Plumecoq, M. Lefranc, From template analysis to generating partitions. II: Characterization of the symbolic encodings, Physica D 144 (2000) 259–278.

[22] H.D. Abarbanel, R. Brown, J.J. Sidorowich, L.S. Tsimring, The analysis of observed chaotic data in physical systems, Rev. Mod. Phys. 65 (1993) 1331–1392.

[23] P.J. Holmes, Knotted periodic orbits in suspensions of Smale's horseshoe: period multiplying and cabled knots, Physica D 21 (1986) 7–41.

[24] P.J. Holmes, in: T. Bedford, J. Swift (Eds.), New Directions in Dynamical Systems, Cambridge University Press, Cambridge, 1988, pp. 150–191.

[25] P. Grassberger, H. Kantz, U. Moenig, On the symbolic dynamics of the Hénon map, J. Phys. A 22 (1989) 5217–5230.

[26] P. Cvitanović, G.H. Gunaratne, I. Procaccia, Topological and metric properties of Hénon-type strange attractors, Phys. Rev. A 38 (1988) 1503–1520.

[27] G. D'Alessandro, P. Grassberger, S. Isola, A. Politi, On the topology of the Hénon map, J. Phys. A 23 (1990) 5285–5294.

[28] F. Giovannini, A. Politi, Homoclinic tangencies, generating partitions and curvature of invariant manifolds, J. Phys. A 24 (1991) 1837–1848.

[29] L. Jaeger, H. Kantz, Structure of generating partitions for two-dimensional maps, J. Phys. A 30 (1997) L567–L576.

[30] Z.-B. Wu, Symbolic dynamics analysis of chaotic time-series with a driven frequency, Phys. Rev. E 53 (1996) 1446–1452.

[31] L. Jaeger, H. Kantz, Homoclinic tangencies and non-normal Jacobians — effects of noise in nonhyperbolic chaotic systems, Physica D 105 (1997) 79–96.

[32] R. Gilmore, Catastrophe Theory for Scientists and Engineers, Wiley, New York, 1981 [reprinted by Dover, New York, 1993].

[33] H.G. Solari, R. Gilmore, Relative rotation rates for driven dynamical systems, Phys. Rev. A 37 (1988) 3096–3109.

[34] D. Auerbach, P. Cvitanović, J.-P. Eckmann, G. Gunaratne, I. Procaccia, Exploring chaotic motion through periodic orbits, Phys. Rev. Lett. 58 (1987) 2387–2389.

[35] D. Lathrop, E.J. Kostelich, Characterization of a strange attractor by periodic orbits, Phys. Rev. A 40 (1989) 4028–4031.

[36] E. Ott, C. Grebogi, J. Yorke, Controlling chaos, Phys. Rev. Lett. 64 (1990) 1196–1199.

[37] L.H. Kaufmann, Knots and Physics, World Scientific, Singapore, 1991.

[38] M.A. Natiello, H.G. Solari, Remarks on braid theory and the characterisation of periodic orbits, J. Knot Theory Ramifications 3 (1994) 511.

[39] H.G. Solari, M.A. Natiello, M. Vázquez, Braids on the Poincaré section: a laser example, Phys. Rev. E 54 (1996) 3185–3195.

[40] T. Hall, The creation of horseshoes, Nonlinearity 7 (1994) 861–924.

[41] J. Birman, R. Williams, Knotted periodic orbits in dynamical systems II: knot holders for fibered knots, Cont. Math. 20 (1983) 1–60.

[42] P.J. Holmes, R.F. Williams, Knotted periodic orbits in suspensions of Smale's horseshoe: torus knots and bifurcation sequences, Arch. Rational Mech. Anal. 90 (1985) 15–194.

[43] P.J. Holmes, Knotted periodic orbits in suspensions of annulus maps, Proc. R. Soc. London A 411 (1987) 351–378.

[44] P.J. Holmes, Knotted period orbits in suspensions of Smale's horseshoe: extended families and bifurcation sequences, Physica D 40 (1989) 42–64.

[45] N.B. Tufillaro, R. Holzner, L. Flepp, R. Brun, M. Finardi, R. Badii, Template analysis for a chaotic NMR laser, Phys. Rev. A 44 (1991) R4786–R4788.

[46] F. Papoff, A. Fioretti, E. Arimondo, G.B. Mindlin, H.G. Solari, R. Gilmore, Structure of chaos in the laser with a saturable absorber, Phys. Rev. Lett. 68 (1992) 1128–1131.

[47] A. Fioretti, F. Molesti, B. Zambon, E. Arimondo, F. Papoff, Topological analysis of laser with saturable absorber in experiments and models, Int. J. Bifurc. Chaos, Appl. Sci. Eng. 3 (1993) 559–564.

[48] M. Lefranc, P. Glorieux, Topological analysis of chaotic signals from a CO_2 laser with modulated losses, Int. J. Bifurc. Chaos, Appl. Sci. Eng. 3 (1993) 643–649.

[49] T. Braun, R.R.B. Correira, N. Altmann, Topological model of homoclinic chaos in a glow discharge, Phys. Rev. E 51 (1995) 4165–4168.

[50] C. Letellier, L.L. Sceller, P. Dutertre, G. Gouesbet, Z. Fei, J.L. Hudson, Topological characterization and global vector field reconstruction of an experimental electrochemical system, J. Phys. Chem. 99 (1995) 7016–7027.

[51] N.B. Tufillaro, P. Wyckoff, R. Brown, T. Schreiber, T. Molteno, Topological time series analysis of a string experiment and its synchronized model, Phys. Rev. E 51 (1995) 164–174.

[52] C. Letellier, G. Gouesbet, N.F. Rulkov, Topological analysis of chaos in equivariant electronic circuits, Int. J. Bifurc. Chaos, Appl. Sci. Eng. 6 (1996) 2531–2555.

[53] G. Boulant, M. Lefranc, S. Bielawski, D. Derozier, Horseshoe templates with global torsion in a driven laser, Phys. Rev. E 55 (1997) 5082–5091.

[54] G. Boulant, S. Bielawski, D. Derozier, M. Lefranc, Experimental observation of a chaotic attractor with a reverse horseshoe topological structure, Phys. Rev. E 55 (1997) R3801–R3804.

[55] J.W.L. McCallum, R. Gilmore, A geometric model for the Duffing oscillator, Int. J. Bifurc. Chaos, Appl. Sci. Eng. 3 (1993) 685–691.

[56] R. Gilmore, J.W.L. McCallum, Structure in the bifurcation diagram of the Duffing oscillator, Phys. Rev. E 51 (1995) 935–956.

[57] C. Letellier, P. Dutertre, G. Gouesbet, Characterization of the Lorenz system, taking into account the equivariance of the vector field, Phys. Rev. E 49 (1994) 3492–3495.

[58] C. Letellier, P. Dutertre, B. Maheu, Unstable periodic orbits and templates of the Rössler system: toward a systematic topological characterization, Chaos 5 (1995) 271–282.

[59] N.B. Tufillaro, Braid analysis of a bouncing ball, Phys. Rev. E 50 (1994) 4509–4522.

[60] C. Letellier, G. Gouesbet, F. Soufi, J.R. Buchler, Z. Kolláth, Chaos in variable stars: topological analysis of W Vir model pulsations, Chaos 6 (1996) 466–476.

[61] G. Boulant, M. Lefranc, S. Bielawski, D. Derozier, A non-horseshoe template in a chaotic laser model, Int. J. Birfurc. Chaos, Appl. Sci. Eng. 8 (1998) 965–975.

[62] R. Gilmore, R. Vilaseca, R. Corbalan, E. Roldan, Topological analysis of chaos in the optically pumped laser, Phys. Rev. E 55 (1997) 2479–2487.

[63] E. Roldan, G.J. de Valcárcel, R. Vilaseca, V.J. Martínez, R. Gilmore, The dynamics of optically pumped molecular lasers. On its relation with the Lorenz–Haken laser model, Quant. Semiclassical Opt. 9 (1997) 1–35.

[64] R. Gilmore, X. Pei, F. Moss, Topological analysis of chaos in neural spike train bursts, Chaos 9 (1999) 812–8817.

[65] P. Melvin, N.B. Tufillaro, Templates and framed braids, Phys. Rev. A 44 (1991) 3419–3422.

[66] M. Lefranc, unpublished.

[67] K. Hansen, Remarks on the symbolic dynamics for the Hénon map, Phys. Lett. A 165 (1992) 100–104.

[68] F. Giovannini, A. Politi, Generating partitions in Hénon-type maps, Phys. Lett. A 161 (1992) 332–336.

[69] M. Hénon, A two-dimensional mapping with a strange attractor, Commun. Math. Phys. 50 (1976) 69–77.

[70] G.B. Mindlin, R. Lopez-Ruiz, H.G. Solari, R. Gilmore, Horseshoe implications, Phys. Rev. E 48 (1993) 4297–4304.

[71] K.T. Hansen, P. Cvitanović, Bifurcation structures in maps of Hénon type, Nonlinearity 11 (1998) 1233–1261.

[72] T. Hall, Weak universality in two-dimensional transitions to chaos, Phys. Rev. Lett. 71 (1993) 58–61.

[73] J.R. Tredicce, F.T. Arecchi, G.P. Puccioni, A. Poggi, W. Gadomski, Dynamics behavior and onset of low-dimensional chaos in a modulated homogeneously broadened single-mode laser: experiments and theory, Phys. Rev. A 3 (1986) 2073–2081.

[74] D. Dangoisse, P. Glorieux, D. Hennequin, Chaos in a CO_2 laser with modulated parameters: experiments and numerical simulations, Phys. Rev. A 36 (1987) 4775–4791.

[75] F. Aurenhammer, Voronoi diagrams — a survey of a fundamental geometric data structure, ACM Comput. Surveys 23 (1991) 345–405.

[76] F.P. Preparata, M.I. Shamos, Computational Geometry: An Introduction, Springer, Berlin, 1985.

[77] A. Okabe, B. Boots, K. Sugihara, Spatial Tessellations: Concepts and Applications of Voronoi Diagrams, Wiley, Chichester, UK, 1992.

[78] D.F. Watson, Computing the n-dimensional Delaunay tesselation with application to Voronoi polytopes, Comput. J. 24 (1981) 167–172.

[79] J.-D. Boissonat, M. Teillaud, in: Proceedings of the Second Annual ACM Symposium on Computing Geometry, ACM, New York, 1986, pp. 260–268.

[80] D.F. Watson, Natural neighboring sorting, Austral. Comput. J. 17 (1985) 189–193.

[81] R. Gilmore, in: B. Bosacchi, J.C. Bezdek, D.B. Fogel (Eds.), Applications of Soft Computing, Proceedings of SPIE, Vol. 3165, SPIE, Bellingham, 1997, pp. 243–257.

"From template analysis to generating partitions II: Characterization of the symbolic encodings"

Jérôme Plumecoq, and Marc Lefranc

Physica D **144**, 259–278 (2000)

ELSEVIER

Physica D 144 (2000) 259–278

PHYSICA D

www.elsevier.com/locate/physd

From template analysis to generating partitions II: Characterization of the symbolic encodings

Jérôme Plumecoq, Marc Lefranc*

Laboratoire de Physique des Lasers, Atomes, Molécules, UMR CNRS 8523, Centre d'Études et de Recherches Lasers et Applications, Université de Lille I, F-59655 Villeneuve d'Ascq Cedex, France

Received 29 April 1999; received in revised form 13 March 2000; accepted 30 March 2000
Communicated by J.D. Meiss

Abstract

We give numerical evidence of the validity of a previously described algorithm for constructing symbolic encodings of chaotic attractors from a template analysis. We verify that the different solutions that can be found are dynamically equivalent, and that our approach yields results that are consistent with those obtained from methods based on homoclinic tangencies. This is further confirmed by verifying directly that the computed partitions are generating to a high degree of accuracy, and that they can be used to estimate precisely the metric entropy. It is also shown that the correct number of symbols needed to describe the dynamics is naturally provided, and that a compact parameterization of a partition can easily be determined, which makes our algorithm suitable for applications such as real-time encoding. © 2000 Elsevier Science B.V. All rights reserved.

PACS: 05.45.+b

Keywords: Generating partitions; Symbolic dynamics; Template analysis; Knot theory

1. Introduction

In the first part of this work [1], we have presented an algorithm to construct symbolic encodings of a chaotic attractor, which follows the approach proposed in Ref. [2]. This algorithm utilizes template analysis [3–7] to extract symbolic dynamical information from the topological invariants of a set of unstable periodic orbits (UPOs) embedded in the attractor.

Template analysis has its roots in the observation that the topological organization of UPOs of a three-dimensional hyperbolic flow can be studied in a systematic way [8,9]. More precisely, there exists a branched two-dimensional manifold, a *template*, on which all the unstable periodic orbits of such a flow can be laid without modifying their knot-theoretic invariants. The structure of the template thus describes concisely the global organization of the flow.

Because periodic orbits cannot intersect themselves when a control parameter is varied, a set of UPOs embedded in a three-dimensional chaotic attractor can be tracked to a regime where the system is hyperbolic without modifying their invariants. In the hyperbolic case, there is a natural coding for periodic orbits: their symbolic names are obtained by listing whose branches are successively visited by their projections on the template. It is thus only natural to extend this

* Corresponding author.
E-mail address: marc.lefranc@univ-lille1.fr (M. Lefranc).

PII: S0167-2789(00)00083-X

coding to experimental orbits by requiring that each UPO is assigned the symbolic name of one of the template orbits that has the same topological invariants. This correspondence is one-to-one for a large number of low-period orbits.

Once the possible symbolic names for each detected UPO have been identified in this way, this information must be combined with the knowledge of the position of periodic points in a section plane to construct a generating partition of the latter. In our algorithm, partitions are parameterized by a set of periodic points associated with given symbols, called *reference points*. To represent an arbitrary trajectory by a symbolic sequence, each intersection with the section plane is encoded by the symbol attached to the closest reference point. Starting from an initial partition based on a small set of low-period orbits (e.g., a period-1 and a period-2 orbits), our method progressively refines this partition by inserting higher period orbits in it while preserving the simplicity of its structure.

The main result of [1] is that this method allows one to obtain high-resolution partitions that have a simple structure, yet which are such that the topological invariants of each detected periodic orbit can be directly read from the symbolic name it has been assigned. That this can be achieved is by itself a strong indication of the validity of the approach. Indeed, we had successfully analyzed a set of more than 1500 orbits, whose intertwining was described by several millions of integers. Preserving the topological consistency of the partition in such a case is by no means trivial. As a matter of fact, we have observed that our algorithm quickly concludes that no consistent solution can be obtained when fed with some arbitrarily chosen initial partitions, or when the input value of a single invariant is purposely modified. This can be because no simple template can be found or because it becomes at some point impossible to make the encoding continuous (such that neighboring points are associated with close symbolic sequences). To be fully convinced of the validity of this approach, however, additional verifications have to be carried out. The aim of this paper is to provide such evidence.

A first test is related to the internal consistency of the algorithm. As different initial partitions lead to different final partitions, we must verify that the latter describe the same dynamics. Returning to the test partition we had obtained in Ref. [1], we show in Section 3 that this is indeed the case: the partitions that are obtained from the simplest initial partitions that can be built with orbits of periods 1, 2, and 4 are images or preimages of each other.

If partitions obtained by a topological approach are relevant, they should easily identify cases where more than two symbols are needed to describe faithfully the dynamics. We show that this is so in Section 4, by considering attractors of the modulated laser equations and of the Duffing equations which display a three-symbol dynamics. The latter example is particularly interesting because a generating partition had been previously obtained for it in Ref. [10], using a method based on homoclinic tangencies [11].

Because the latter method, which is supported by strong numerical evidence [10,12–14], is completely orthogonal to ours, a direct comparison of the outputs of both methods is probably the most stringent test one can consider for assessing the validity of the topological approach. As will be seen in Section 5, the agreement is excellent: a line of principal homoclinic tangencies is entirely located in the triangles enclosing the border of the partition that was obtained in Ref. [1] with a precision of 10^{-4}. This is a strong indication that not only the two approaches are equivalent, but also that our algorithm provides reliable error bounds.

This result suggests that the partitions we obtain are generating, as this is generally believed to be true for methods based on homoclinic tangencies. Nevertheless, we carry out in Section 6 a direct test of this property. It allows us to verify that, with an appropriate balance between the numbers of forward and backward symbols, the largest distance between points whose symbolic sequences coincide on a large number of symbols is of the order of the precision with which the partition has been determined. The dependence of this distance with respect to the number of coinciding symbols also indicates that even partitions determined with a relatively low precision suffice to characterize precisely the symbolic dynamics of a chaotic attractor.

In Section 7, we compare estimates of the metric entropy obtained (i) from a Lyapunov exponent calcu-

lation and (ii) from probabilities of symbol sequences computed from a partition. Again, we find an excellent agreement. For reference, we also characterize the symbolic dynamics of the attractors which we have considered in this work by giving for each of them the list of irreducible forbidden words (IFWs).

Finally, we discuss in Section 8 how to provide a compact description of a partition by reducing as much as possible the number of periodic points parameterizing it. Last, we conclude by discussing possible extensions and applications of our work.

2. Notations

We first briefly recall the notations that have been defined in Ref. [1]. The input data fed to the algorithm is a set $\mathcal{O}$ of m periodic orbits O_i, whose intersections with a section plane are noted O_i^j, $j = 1, \ldots, p_i$. From the topological invariants of these orbits, a set of possible symbolic names $\mathcal{N}_k(O_i)$ is first determined. These names are written inside brackets (e.g., $\mathcal{N}(O_2) = \langle 01 \rangle$), to distinguish them from symbolic names of periodic points, which are written using overlined strings (e.g., $N(O_2^1) = \overline{01}$). Indeed, different cyclic permutations of a given name represent the same periodic orbit, but different periodic points.

A partition Γ of a section plane divides it into disjoint regions $\Delta_i(\Gamma)$, $i = 1, \ldots, n$. The symbolic name $N_\Gamma(O_i)$ assigned by a partition Γ to a periodic orbit O_i is defined as being the one assigned to its first periodic point: $N_\Gamma(O_i) = N_\Gamma(O_i^1) = \overline{s_1 \ldots s_{p_i}}$, which is such that $O_i^k \in \Delta_{s_k}(\Gamma)$.

In [1], we had obtained two partitions of an attractor of the modulated laser equations. The first was computed from a set of periodic orbits providing a uniform cover of a Poincaré section of the attractor with a resolution of 10^{-3} (in units of the attractor width), and will be hereafter noted Γ_a^f. This partition and the corresponding set of orbits will be used in Section 3 to study the relation between partitions computed from different initial partitions, and in Section 8 to describe how a compact parameterization of a partition may be obtained.

Using an improved algorithm, and a set of orbits such that the region of the partition border was covered with a high-resolution, we had also obtained a second partition whose border line was localized with a precision of 10^{-4}. This partition will be noted Γ_{h}^f in the following. It will be used to carry out precise tests related to the equivalence with methods based on homoclinic tangencies (Section 5), the closeness to a generating partition (Section 6), and estimation of the metric entropy (Section 7).

3. Influence of the choice of the initial partition

We have reproduced in Fig. 1 the partition Γ_a^f, with the initial partition Γ_a that had been used as input. As explained in Ref. [1], there is some arbitrariness in the choice of this initial partition. For instance, we know

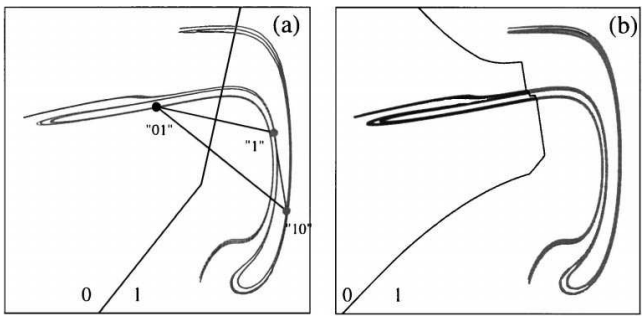

Fig. 1. Symbolic encoding of the attractor used as an example in the description of the algorithm in Ref. [1]. (a) Initial partition; (b) final partition.

that one point of the period-2 orbit $\langle 01 \rangle$ must be assigned the name $\overline{01}$ and the other $\overline{10}$, but this gives two possible choices, which are in principle equivalent: $(N_\Gamma(O_2^1), N_\Gamma(O_2^1)) = (\overline{01}, \overline{10})$ (as in Fig. 1), or $(N_\Gamma(O_2^1), N_\Gamma(O_2^1)) = (\overline{10}, \overline{01})$. Different initial partitions will obviously lead to different final partitions, since the algorithm does not modify the symbols of the reference points after they are inserted in the partition.

We must therefore verify that the solutions obtained using different initial partitions model equivalently the symbolic dynamics of the chaotic attractor, i.e., that the quantities which can be computed using the partition do not depend on the choice of the initial partition, provided the latter is reasonably chosen.

Orbits with a unique topological name are not a problem in this respect. If they were the only orbits to consider, they could in principle be named using any cyclic permutation of their topological name. The first step of the algorithm described in Ref. [1] merely ensures that the permutation we choose for each orbit preserves the simplicity of the partition. However, the names of the remaining orbits are determined using not only the topological invariants, but also an intermediate partition. These names might thus vary depending on which initial configuration is chosen, and we must verify that this is not the case.

An initial partition is based on l periodic orbits $O_{i_1}, O_{i_2}, \ldots, O_{i_l}$ of periods p_{i_j}, each having a unique topological name $\mathcal{N}(O_{i_j})$. Such a partition is completely defined if one specifies for each orbit O_{i_j} the symbolic name $N_\Gamma(O_{i_j}) = N_\Gamma(O_{i_j}^1) = \sigma^{l_j}\mathcal{N}(O_{i_j})$ $(0 \le l_j < p_{i_j} - 1)$ assigned to its first periodic point. The initial triangulation then consists of the reference points $O_{i_j}^k$, associated with the symbols corresponding to the chosen cyclic permutations.

In the following, we denote by $\Gamma_{i_1,\ldots,i_l}^{N_1,\ldots,N_l}$ an initial partition specified in this way, where $N_j = N_\Gamma(O_{i_j}^1)$. With this notation, $\Gamma_a = \Gamma_{1,2}^{\overline{1},\overline{01}}$ represents the initial partition shown in Fig. 1a (with O_2^1 being the leftmost periodic point of the $\langle 01 \rangle$ orbit).

Since our algorithm is deterministic, the final partition $\Gamma^f = \Gamma_{1,\ldots,m}^{N_1,\ldots,N_m}$ that contains all the m periodic orbits detected in the attractor is a functional of the initial partition, which we will denote by

$$\Gamma^f = A[\Gamma_{i_1,\ldots,i_l}^{N_1,\ldots,N_l}]. \tag{1}$$

Consider now the second possible initial partition based on the period-1 and period-2 orbits, which is $\Gamma_b = \Gamma_{1,2}^{\overline{1},\overline{10}}$ (shown in Fig. 2a). The difference with Γ_a in Fig. 1a is that the symbols associated with the points of the period-2 orbit have been exchanged. Using this new initial partition, we obtain a final partition $\Gamma_b^f = A[\Gamma_b]$ (Fig. 2b), that markedly differs from $\Gamma_a^f = A[\Gamma_a]$ (Fig. 1b).

In fact, Γ_a^f and Γ_b^f are related in a very simple way, and describe the same dynamics. Indeed, if we compare for each orbit O_i the symbolic names $N_{\Gamma_a^f}(O_i)$ and $N_{\Gamma_a^f}(O_i)$ assigned by these two partitions, we find that in each case the latter is recovered by shifting the

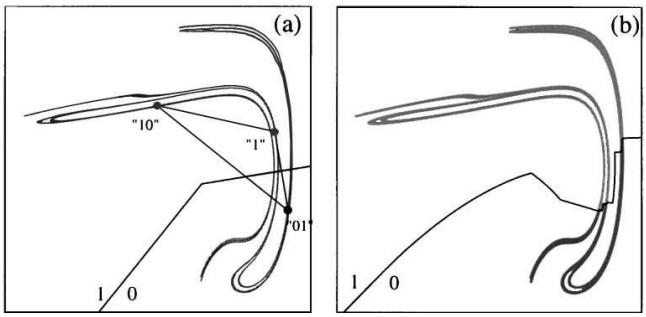

Fig. 2. (a) Another possible initial partition using the first two orbits; (b) the resulting partition.

former by one symbol

$$N_{\Gamma_b^f}(O_i) = \sigma N_{\Gamma_a^f}(O_i) \quad \forall\, O_i \in \mathcal{O}. \tag{2}$$

For example, $N_{\Gamma_a^f}(O_3) = \overline{0111}$ and $N_{\Gamma_a^f}(O_3) = \overline{1110}$. As a first result, we note that the orbits that had several compatible topological names are identified in the same way by the two final partitions (i.e., up to a cyclic permutation). This seems to indicate that the symbolic names which are singled out in the final partition do not result from an arbitrary choice, but are dynamically relevant.

If we define the action of the shift operator σ on a partition as follows (the symbolic names of the orbits parameterizing the partition are all shifted by one symbol)

$$\sigma\Gamma_{i_1,\dots,i_n}^{N_1,\dots,N_n} = \Gamma_{i_1,\dots,i_n}^{\sigma N_1,\dots,\sigma N_n}, \tag{3}$$

and since relation (2) is verified for every periodic orbit involved in the final partitions, we can write

$$\Gamma_b^f = \sigma\Gamma_a^f. \tag{4}$$

It is trivial to remark that a similar relation holds for the initial partitions

$$\Gamma_b = \Gamma_{1,2}^{\overline{1},\overline{10}} = \sigma\Gamma_{1,2}^{\overline{1},\overline{01}} = \sigma\Gamma_a \tag{5}$$

and thus we have a kind of commutative relation

$$\Gamma_b^f = A[\sigma\Gamma_a] = \sigma A[\Gamma_a] = \sigma\Gamma_a^f. \tag{6}$$

While relation (6) is formally correct in our particular example, it should not be extrapolated to higher powers of the shift operator, because $\sigma^2\Gamma_a = \Gamma_a$, but $\sigma^2\Gamma_a^f \neq \Gamma_a^f$. Indeed, for any partition defined with orbits of periods p_i, we have $\sigma^l\Gamma = \Gamma$, where l is the least common multiple of the p_i. What Eq. (6) essentially indicates is that our algorithm preserves the dynamical relation that exists between initial partitions Γ_a and Γ_b. This seems to indicate that it converges to the simplest partition that is consistent with the information contained in the initial partition.

The two solutions obtained from two different initial conditions are thus dynamically equivalent, as is best seen by translating Eq. (4) into a relation involving the first return map f. Since the shift operator is conjugate to f, we have for any detected periodic point $O_i^k \in \mathcal{P}$

$$N_{\Gamma_b^f}(O_i^k) = \sigma N_{\Gamma_a^f}(O_i^k) = N_{\Gamma_a^f}(f(O_i^k)). \tag{7}$$

Consider the set $\Delta_i^{\mathcal{P}}(\Gamma) = \Delta_i(\Gamma) \cap \mathcal{P}$ of all the detected periodic points lying in region $\Delta_i(\Gamma)$ of the partition Γ. Eq. (7) implies that

$$x \in \Delta_i^{\mathcal{P}}(\Gamma_b^f) \Leftrightarrow f(x) \in \Delta_i^{\mathcal{P}}(\Gamma_a^f) \quad \forall i \tag{8}$$

and therefore

$$\Delta_i^{\mathcal{P}}(\Gamma_b^f) = f^{-1}(\Delta_i^{\mathcal{P}}(\Gamma_a^f)) \quad \forall i. \tag{9}$$

Because $\Delta_i^{\mathcal{P}}(\Gamma_a^f)$ approximates $\Delta_i(\Gamma_a^f)$ (the periodic points were chosen so as to provide a uniform cover of the attractor), we have

$$\Delta_i(\Gamma_b^f) \approx f^{-1}(\Delta_i(\Gamma_a^f)) \quad \forall i, \tag{10}$$

where $\Delta_i(\Gamma)$ should be understood as the intersection of region i with the support of the strange attractor.

Since the image of a partition $\Gamma = \{\Delta_0(\Gamma), \Delta_1(\Gamma), \dots\}$ can be defined naturally as $f(\Gamma) = \{f(\Delta_0(\Gamma)), f(\Delta_1(\Gamma)), \dots\}$, the relation between partitions Γ_a^f and Γ_b^f can be concisely written as

$$\Gamma_b^f \approx f^{-1}(\Gamma_a^f). \tag{11}$$

The reason why the border of Γ_b^f shown in Fig. 2b is not exactly the preimage of the border of Γ_a^f shown in Fig. 1b is that the mediators of the triangles in the latter partition need not be exactly mapped to those of the former. Therefore, if we consider a long chaotic trajectory, and encode it using the two partitions, the obtained symbolic sequences will not be entirely shift-equivalent (whereas this is rigorously true for the periodic orbits used in the partition): there might be discrepancies for points located very close to the border. The degree of equivalence will therefore depend on the precision with which the partition has been determined, i.e., on the size of the triangles enclosing the border of the partition.

To assess the degree of equivalence in our example, we have analyzed a chaotic trajectory of 10^7 iterations, and compared the symbolic sequences obtained with the two partitions (taking into account the shift by one

symbol): we found that less than 0.02% of the symbols differed. These observations clearly show that the final partitions obtained using the two initial partitions describe essentially the same dynamics. Note also that to localize the border with a higher precision, it should be possible to use a more sophisticated interpolation scheme where these discrepancies would be taken into account to obtain a solution, i.e., consistent with its images and preimages.

We have examined all initial partitions based on the period-1 and period-2 orbits. To test further the robustness of our method, we now consider initial partitions based on the four periodic points of the period-4 orbit, which will allow us to explore different configurations.

We have four possible initial partitions, each corresponding to a different cyclic permutation of the topological name $\mathcal{N}(O_3) = \langle 0111 \rangle$. In the first two of these partitions, namely $\Gamma_3^{\overline{0111}}$ and $\Gamma_3^{\overline{1110}}$, the period-4 orbit is assigned the same name as in the final partitions Γ_a^f and Γ_b^f, respectively. Not surprisingly, we obtain from these two initial configurations the two final partitions that have previously been computed: $A[\Gamma_3^{\overline{0111}}] = \Gamma_a^f = A[\Gamma_{1,2}^{\overline{1},\overline{01}}]$ and $A[\Gamma_3^{\overline{1110}}] = \Gamma_b^f = A[\Gamma_{1,2}^{\overline{1},\overline{10}}]$.

The two other initial partitions, $\Gamma_3^{\overline{1101}}$ and $\Gamma_3^{\overline{1011}}$, shown in Figs. 3a and 4a, yield different partitions which are displayed in Figs. 3b and 4b, respectively. Again, these partitions are equivalent to the partition Γ_a^f shown in Fig. 1b, since we have $A[\Gamma_3^{\overline{1101}}] = \sigma^2 \Gamma_a^f$, and $A[\Gamma_3^{\overline{1011}}] = \sigma^{-1} \Gamma_a^f$.

The four partitions based on the period-4 orbit are therefore related by

$$\sigma^{-2} A[\Gamma_3^{\overline{1101}}] = \sigma^{-1} A[\Gamma_3^{\overline{1110}}] = A[\Gamma_3^{\overline{0111}}] = \sigma A[\Gamma_3^{\overline{1011}}] \tag{12}$$

which translates to

$$f^{-1}(A[\Gamma_3^{\overline{1011}}]) \approx A[\Gamma_3^{\overline{0111}}] \approx f(A[\Gamma_3^{\overline{1110}}]) \approx f^2(A[\Gamma_3^{\overline{1101}}]) \tag{13}$$

which clearly shows that the six simplest initial configurations (two based on $\{O_1, O_2\}$ and four on O_3) lead to four dynamically equivalent final partitions.

However, it should be noted that our algorithm does not converge for every possible initial partition. For example, we have tried the eight initial partitions based on the seven periodic points of the set of orbits $\{O_1, O_2, O_3\}$. Four or them lead to the four final partitions that have already been obtained: these are the initial partitions of the form $\sigma^k \Gamma_{1,2,3}^{\overline{1},\overline{01},\overline{0111}}$. The four other initial partitions are of the form $\sigma^k \Gamma_{1,2,3}^{\overline{1},\overline{01},\overline{1110}}$: in this case, the algorithm terminates after finding an inconsistency, or yields a partition which has a complicated structure. Note that the latter four initial partitions do not belong to the σ-orbit of the $\Gamma_{1,2,3}^{\overline{1},\overline{01},\overline{0111}}$ initial partition which leads to the simple solution Γ_a^f as shown in Fig. 1b.

This observation and other tests we carried out lead us to conclude that our algorithm is successful whenever the input names defining the initial partition are those assigned by a partition, i.e., one of the first few (pre-) images of the Γ_a^f partition. This supports the

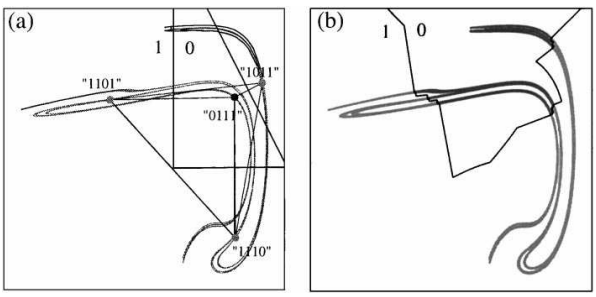

Fig. 3. (a) Initial partition $\Gamma_3^{\overline{1101}}$; (b) the corresponding final partition $A[\Gamma_3^{\overline{1101}}]$.

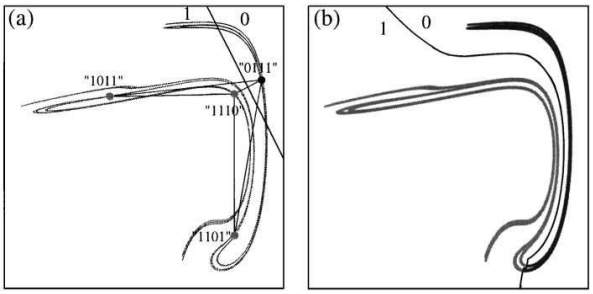

Fig. 4. (a) Initial partition $\Gamma_3^{\overline{1011}}$; (b) the corresponding final partition $A[\Gamma_3^{\overline{1011}}]$.

idea that there is a natural solution of lowest complexity, and that our algorithm successfully approximates it.

To conclude this section, we note an interesting consequence of the fact that our partitions are parameterized by periodic orbits: forward and backward images of partitions can easily be computed without being faced with the exponential divergence of nearby orbits. To do this, it suffices to shift all the symbolic names given by the final partition by the same amount, and to recompute the border. This property could be useful in chaos-based digital communications by using the $\sigma^n \Gamma_a^f$ partition, one can predict the n iterations in advance the symbol corresponding to the standard partition Γ_a^f, allowing for early error recovery.

4. Examples of three-symbol partitions

A difficult problem when trying to construct a symbolic encoding of a given attractor is to determine how many different symbols are needed to describe faithfully the dynamics. If topological entropy cannot be easily computed, metric entropy, which is a lower bound of topological entropy, could be estimated from the greatest Lyapunov exponent. For example, at least n symbols should be used when $\lambda_1 T > \ln n$, where T is the modulation period. However, there can be situations where the right number of symbols is larger than indicated by the topological entropy because there are many forbidden symbolic sequences.

Besides their robustness, methods based on template analysis have the advantage that the correct number of symbols is automatically obtained from the preliminary template analysis: this is just the number of branches of the simplest template that describes the topological organization of the data.

To illustrate this, we now apply our algorithm to two strange attractors whose symbolic dynamics involve three symbols: an attractor of the modulated laser equations used in Ref. [1], but at different parameter values, and an attractor of the Duffing system at the parameters studied in Ref. [10], where a generating partition was determined from the locations of the homoclinic tangencies.

4.1. Symbolic encoding of a spiral modulated laser attractor

Depending on the parameters, the regimes displayed by a chaotic system can have different degrees of complexity: some may correspond to a two-symbol dynamics while the description of other, more chaotic, regimes requires a larger number of symbols.

This is the case of the modulated laser equations whose parameter space is divided into several regions corresponding to different topological organizations, as is common for nonlinear oscillators [15]. To test our algorithm in a more complicated case than the one considered in Ref. [1], we have studied an attractor close to the three-branch spiral attractor described in Ref. [16], and whose parameters are the same as in Ref. [1], except that $m = 0.08125$, $\gamma = 1.5 \times 10^{-3}$, and $\omega \approx 0.923077\omega_r$, where $\omega_r = \sqrt{\gamma(A-1)}$ is the relaxation frequency of the laser.

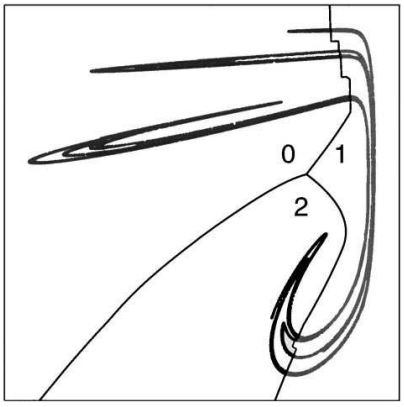

Fig. 5. Generating partition for a three-branch spiral attractor of the modulated laser equations.

That an analysis of this attractor requires at least three symbols is readily indicated by the fact that it contains four period-3 orbits, whereas at most two exist in a two-symbol dynamics. This is confirmed by a template analysis, which indicates that the topological structure of this attractor is described by a spiral three-branch template (a.k.a. "Gâteau Roulé"), described by the following template and layering matrices:

$$t^{\mathrm{S}} = \begin{pmatrix} 0 & 0 & 0 \\ 0 & 1 & 2 \\ 0 & 2 & 2 \end{pmatrix}, \qquad l^{\mathrm{S}} = (\,0 \quad 2 \quad 1\,). \tag{14}$$

An illustration of the corresponding three-branch manifold can be found in Fig. 6 of Ref. [16]. The partition shown in Fig. 5 has been obtained using the improved procedure outlined at the end of Ref. [1], and is based on a set of 1250 orbits of periods up to 32 which provides a resolution better than 10^{-3} in the region of the border. It should be noted that in this case, there is only one initial partition based on the period-1 and period-2 orbits $\langle 1 \rangle$ and $\langle 01 \rangle$ that leads to a simple solution, the one which assigns the symbol "0" to the leftmost period-2 point. Indeed, the algorithm does not converge if we exchange the symbols of the period-2 points. This is due to the template having three branches: exchanging these two periodic points would amount to placing branch "0" between branches "1" and "2" and would violate the requirement of continuity.

4.2. Symbolic encoding of a Duffing attractor

The Duffing system

$$\dot{x} = y, \qquad \dot{y} = -\delta y + x - x^3 + \gamma \cos ft \tag{15}$$

is one of the few three-dimensional flows for which a generating partition has been determined by methods based on homoclinic tangencies [10]. To verify that our approach yields results that agree with these methods, we have applied our procedure to the regime studied in Ref. [10], which corresponds to parameters $\delta = 0.25$, $\gamma = 0.4$, and $f = 1$.

A direct template analysis indicates that the topological structure can be described by the following six-branch matrices:

$$t^{\mathrm{D}} = \begin{pmatrix} 2 & 2 & 0 & 0 & 0 & 2 \\ 2 & 1 & 0 & 0 & 0 & 2 \\ 0 & 0 & 0 & 0 & 0 & 2 \\ 0 & 0 & 0 & 2 & 2 & 2 \\ 0 & 0 & 0 & 2 & 1 & 2 \\ 2 & 2 & 2 & 2 & 2 & 2 \end{pmatrix},$$

$$l^{\mathrm{D}} = (\,0 \quad -1 \quad 1 \quad 3 \quad 2 \quad -2\,). \tag{16}$$

It can be seen that the template matrix in Eq. (16) does not describe a continuous branched manifold because the torsions of two adjacent branches differ by two units. Presumably, these matrices correspond to a part of a larger template. This is however not important, as it turns out that the dynamics of this regime can be studied with only three symbols.

Indeed, as noted in Refs. [10,15], we can take advantage of a symmetry of the Duffing equations (15) to simplify the analysis, namely the invariance under the transformation $x \to -x, y \to -y, \phi \to \phi + \pi$. This symmetry indicates that the dynamics during the first half-period and during the second half-period are equivalent. As a consequence, the Poincaré sections at $\phi = 0$ and $\phi = \pi$ are identical modulo an inversion around the origin. We will thus consider the reduced dynamical system, where the integration of Eq. (15) over half a period is followed by a twist of a half-turn.

If we discard two solutions where torsions of adjacent branches differ by more than one half-turn and which are algebraically equivalent to the solutions presented below [16], we find two possible templates for this reduced system. The first one is described by the matrices

$$t^{D_1} = \begin{pmatrix} 1 & 2 & 2 \\ 2 & 2 & 2 \\ 2 & 2 & 3 \end{pmatrix}, \quad l^{D_1} = (\,0 \quad -2 \quad -1\,) \tag{17}$$

which correspond to the spiral template described by Eqs. (14) with an additional half-twist and which was identified as a building block for the Duffing template by Gilmore and McCallum [15]. The other one is an S-shaped template, whose matrices are

$$t^{D_2} = \begin{pmatrix} 2 & 2 & 2 \\ 2 & 1 & 2 \\ 2 & 2 & 2 \end{pmatrix}, \quad l^{D_2} = (\,0 \quad -1 \quad -2\,). \tag{18}$$

These two solutions are algebraically compatible with the topological invariants of the UPO: for each of the two templates, it is possible to find a set of periodic orbits lying on it that has exactly the same invariants as the experimental ones. This means that the spectra of periodic orbits of the two templates have subsets that are isotopic, and that the set of detected orbits in the Duffing attractor belongs to this intersection. Yet, this indeterminacy is intriguing, as the above two solutions have quite different topological structures.

However, there is a clear-cut difference between these two solutions which is unveiled when trying to construct a symbolic encoding. Whereas a partition is easily found using the first template (described by Eq. (17)), our algorithm quickly stops when the second one is used as input: at some point the current partition is such that some orbits no longer have at least one topological name compatible with it. This means that one cannot find a symbolic encoding that is simultaneously continuous in the section plane and reproduces the symbolic dynamics associated with the template (18). We believe that this indicates that only the first solution is dynamically relevant. Thus, although we focus here on the application of template analysis to the construction of symbolic encodings, we see that our algorithm can also be helpful to discriminate algebraic solutions of the template finding problem.

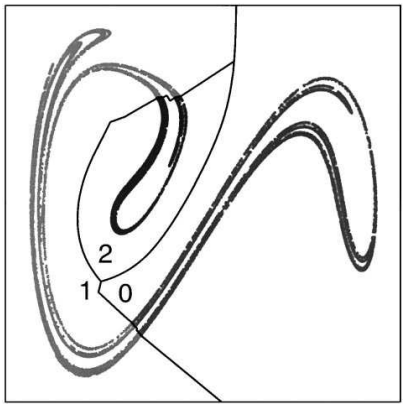

Fig. 6. Generating partition obtained for the Duffing attractor.

The partition obtained with template (17) is shown in Fig. 6. It is based on a set of 1326 periodic orbits of periods up to 36, providing a cover with a resolution better than 10^{-3} in the neighborhood of the border. It is seen to reproduce Fig. 4 of Ref. [10], where the partition had been computed by following lines of homoclinic tangencies. It should be stressed that in our case, this partition is the simplest and most natural solution (obtained from an initial configuration based on the period-1 and period-2 orbits). In contrast to this, it was noted in Ref. [10] that some homoclinic tangencies involved in this partition are not primary, and that heuristic considerations had to be used to select these particular tangencies. This shows that the topological approach provides us with additional information that cannot be obtained from the study of homoclinic tangencies, and is thus a powerful tool for selecting the correct lines of tangencies.

Although the partition shown in Fig. 6 does not differ to the eye from the partition computed in Ref. [10], we still have to verify precisely that the two approaches still agree at the smallest scales. In particular, we must check whether the error bounds naturally provided by our algorithm are correct: if so, the partition border determined using homoclinic tangencies should be entirely located inside the region where the

coding is considered uncertain (i.e., in the circumcircles of the triangles with different symbols, see [1]). We carry out this verification in Section 5.

5. Comparison with methods based on homoclinic tangencies

A difficult problem associated with using homoclinic tangencies to construct partitions is that there is a countable infinity of homoclinic tangencies: all the forward and backward images of a homoclinic tangency are themselves homoclinic tangencies. As a consequence, there are homoclinic tangencies everywhere in the attractor (just as the critical point of the logistic map has preimages in every part of the interval).

However, there are homoclinic tangencies that are more relevant for a large-scale characterization of an attractor, because their influence is felt over a wider region: they should be preferably selected to build a partition line. A possible selection criterion proposed in Ref. [10] is that the sum of the curvatures of the stable and unstable manifolds at the tangency should be minimal, because the curvature of the stable (unstable) manifold diverges when following the backward (forward) orbit of a given tangency.

To illustrate the existence of "principal" homoclinic tangencies in the case of the modulated laser equations (at the same parameters as in Ref. [1]), we have plotted in Fig. 7 the points (extracted from a sequence of 10^8 iterations) where the angle between the invariant manifolds, computed using the method described in Appendix B of Ref. [17], is smaller than a prescribed value. It is readily seen that there are regions where this angle remains small over a significantly large region of the section plane, whereas no point with a small angle is detected elsewhere (although there are regions with such points everywhere, there are too small to be visited in a reasonable amount of time by a typical trajectory).

A first interesting result is that the wider small-angle regions in Fig. 7 are seen to correspond to some of the partitions that have been obtained in Section 3 for different initial configurations. This is obviously related to the fact that these borders have been shown to be images or preimages of each other.

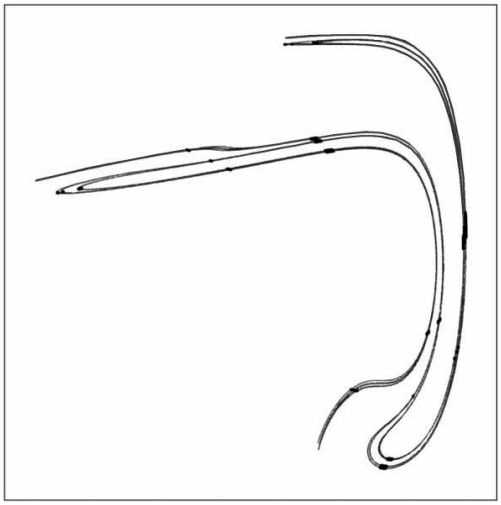

Fig. 7. Poincaré section of an attractor of the modulated laser equations. The points where the angle between the stable and the unstable manifolds is smaller than 0.1 rad are plotted in black.

To make the comparison more precise, we show in Fig. 8 enlarged views of neighborhoods of the border of the high-resolution partition Γ_{h}^{f} (see Section 2), in which we have indicated the approximate locations of homoclinic tangencies. The agreement is seen to be excellent: all the homoclinic tangencies are located inside the triangles that enclose the border of the partition. This not only shows that the partition line is well approximated by our method but also that the error bounds it provides strictly hold.

We have also verified this to be true in the case of the spiral laser attractor and of the Duffing attractor which were considered in Section 4. Because the latter example is important in that it is one of the few three-dimensional flows for which a generating partition has been obtained from homoclinic tangencies [10], Fig. 9 illustrates the excellent agreement that is also obtained in that case.

The reason why the locations of homoclinic tangencies are better resolved in Fig. 9a than in Fig. 9b is that the same limit angle (5×10^{-4} rad) was used in both cases. As the line of homoclinic tangencies shown in Fig. 9b is a principal line, but not the one of Fig. 9a, the region in Fig. 9b where the angle

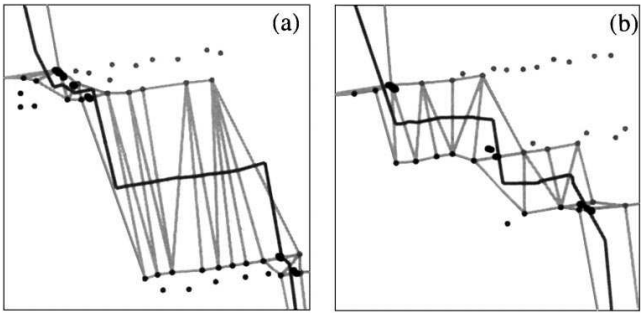

Fig. 8. Enlarged views of two neighborhoods of the border line of the high-resolution partition Γ_h^f. The size of the two represented squares is 2.5×10^{-3}, in units of the attractor width. Light dots represent periodic points parameterizing the partition. Heavy dots indicate homoclinic tangencies (the angle between the two invariant manifolds at these points is below 2×10^{-4} rad). The border line and the triangles enclosing it are also represented. The linewidth used to draw the border line is 2.5×10^{-5}.

between invariant manifolds is smaller than this value is markedly wider than in Fig. 9a. However, the relatively lower precision in Fig. 9b still allows one to verify that homoclinic tangencies are located inside the triangles enclosing the border of the partition.

As can be seen in Figs. 8 and 9, the results of this section give strong evidence that algorithms based on template analysis and on the structure of the homoclinic tangencies converge to the same answer. The theoretical tools which these two methods rely on are so utterly different that this agreement is quite fascinating and suggests that chaotic dynamics can be studied from multiple points of view. Because of the (at least superficially) complete independence of the two approaches, we believe that this result not only supports the validity of the topological approach but also provides an additional confirmation of the correctness of methods based on homoclinic tangencies.

Since partitions based on homoclinic tangencies are believed to be generating, this should also be true for the partitions obtained with our algorithm. Nevertheless, in order to make our study complete and to obtain an estimate of the resolutions that would actually be required for practical applications, we carry out in Section 6 a direct test of this property.

6. Are topological partitions generating?

The defining property of a generating partition is that the trajectories of two different points are encoded

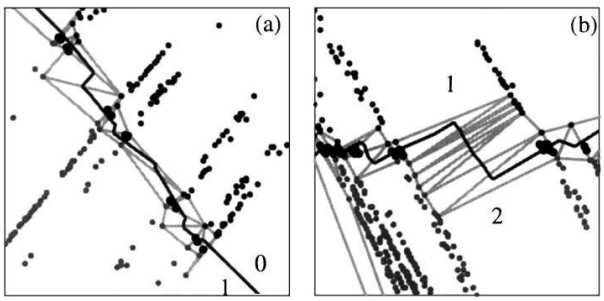

Fig. 9. Enlarged views of two neighborhoods of the border line of the partition of the Duffing attractor shown in Fig. 6. Black heavy dots represent points of homoclinic tangency. The widths of the represented squares and of the border line are 10^{-2} and 10^{-4}, respectively. (a) Part of the border between Δ_0 and Δ_1; (b) part of the border between Δ_1 and Δ_2.

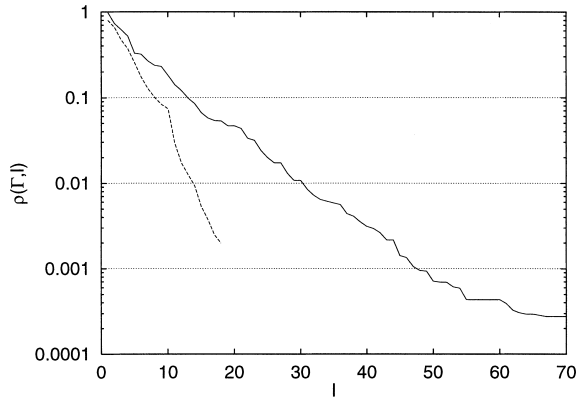

Fig. 10. Convergence of $\rho(\Gamma, l)$ vs. the total number of symbols l. Diameters are expressed in units of the attractor width. For comparison purposes, the dashed line represents the evolution of the geometric average of all cylinder diameters for a given number of symbols (only values for which all cylinder sizes could be reliably estimated are shown). The latter curve is seen to converge to 0 much more rapidly. We have verified that it is almost insensitive to the precision with which the border is located.

with different symbol sequences. In our algorithm, this is by construction enforced for the periodic orbits detected in the strange attractor and utilized in the topological analysis. Nevertheless, it is important to quantify the deviation of the obtained partitions from the ideal case where the mapping from bi-infinite symbolic sequences to chaotic trajectories is well defined and continuous.

More precisely, let us consider "cylinders"

$$C(s_{-m} \dots s_{-1}.s_0 s_1 \dots s_{n-1}) = \{x;\ s_\Gamma(f^i(x)) = s_i,\ i = -m, \dots, n-1\} \quad (19)$$

which are regions of the Poincaré section of the attractor containing points whose m backward and n forward symbols are identical. A partition Γ is generating if and only if

$$\lim_{n,m\to\infty} \delta_M(\Gamma, m, n) = 0 \quad \text{with} \quad \delta_M(\Gamma, m, n) = \max_{C \in \mathcal{C}_\Gamma[m,n]} \delta(C), \quad (20)$$

where $\mathcal{C}_\Gamma[m, n]$ is the set of all cylinders with m backward and n forward symbols and $\delta(C)$ is the diameter of a cylinder.

For a given sequence of length $l = m + n$, there is a number n of forward symbols that will minimize $\delta_M(\Gamma, l - n, n)$. Because backward (resp. forward) symbols specify the position of a point along a segment of the local stable (resp. unstable) manifold, the optimal n and m verify $n\lambda_1 \approx m\lambda_2$, with λ_1 and λ_2 being the positive and negative Lyapunov exponents of the return map, respectively.

We can thus characterize how close a partition Γ is to a generating partition by the quantities

$$\rho(\Gamma, l) = \min_n \delta_M(\Gamma, l - n, n), \qquad \rho(\Gamma) = \lim_{l\to\infty} \rho(\Gamma, l). \quad (21)$$

For a generating partition, $\rho(\Gamma)$ should be zero. If a finite value is obtained, it quantifies the deviation of the partition Γ from a generating one.

We have studied the convergence of $\rho(\Gamma, l)$ with increasing l for the high-resolution partition Γ_{h}^f (see Section 2), as shown in Fig. 10. After an approximately logarithmic decrease, $\rho(\Gamma, l)$ is seen to saturate slightly below 3×10^{-4} of the attractor width. It should be noted however that because $\rho(\Gamma, l)$ can be reliably estimated only if there is a sufficient number of points in the largest cylinder, we did not carry out the computations for $l > 70$. Thus, we cannot guarantee that $\rho(\Gamma, 70)$ represents the final plateau. Nevertheless, it is consistent with the fact that the border of this partition is localized almost everywhere with a precision better than 10^{-4}.

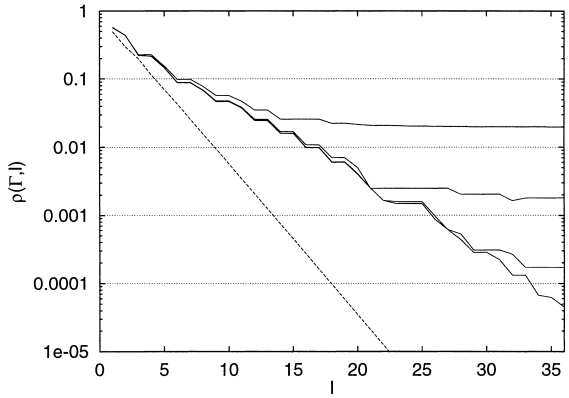

Fig. 11. Equivalent of Fig. 10 for the logistic map. The solid curves represent the evolution of the largest cylinder diameter vs. the number of symbols for the correct partition and for partitions where the border is displaced by a fraction 10^{-4}, 10^{-3}, and 10^{-2} of the attractor width. These curves can be seen to saturate at a value which is roughly twice the error on the location of the partition border. The dashed line corresponds to the geometric average of cylinder diameters.

To illustrate the fact that the saturation value of the quantity (21) provides an estimate of the quality of the partition, we have performed the same test for the logistic map $x_{n+1} = 4ax_n(1 - x_n)$ at $a = 0.955$, where it has roughly the same symbolic dynamics as our sample system (up to length 12, there is only one forbidden sequence, which is "00"). Besides the correct partition, whose border is located at the critical point, we characterized different partitions with borders displaced by a small amount (Fig. 11). As a rule of thumb, $\rho(\Gamma, l)$ appears to saturate at roughly twice the error on the location of the partition border. As this ratio is likely to be larger in the case of a two-dimensional system, the curve in Fig. 10 seems to be consistent with an error on the partition border of the order of 10^{-4} of the attractor width.

A comparison of Figs. 10 and 11 also indicate that to reach a given maximal diameter, the two-dimensional case requires roughly twice as many symbols as the one-dimensional one. We attribute this to the fact that two directions are needed to locate a point in the former case. As a result, the convergence of the curve in Fig. 10 is very slow: it takes 31 symbols for the maximal diameter to fall below 0.01. Since saturation is reached at much smaller scales, this should be a genuine property of the system and not an artifact of our algorithm.

This slow convergence can be traced back to the nonhyperbolicity of the attractor. Near the border, hence near homoclinic tangencies, the stretching rate is very close to 1, and very little information is gained at each iteration of the return map. This has important consequences, as this indicates that it would be pointless to require that the border be localized with a high precision.

Whether we want to characterize the grammar of chaos, i.e., determine the list of forbidden sequences, or use the chaotic system to transmit a digital signal [18,19], 10–12 symbols should represent a reasonable amount of information. From the curve in Fig. 10, we see that the maximal diameter for 12 symbols is around 0.12. If error estimates obtained from saturation values can be trusted (Fig. 11), a precision of a few percent should therefore be sufficient.

In regions of parameter space where the topological entropy is sufficiently large (the number of forbidden symbolic sequences, hence of pruned periodic orbits, should not be too large), such a precision can be easily obtained from a topological analysis of unstable periodic orbits embedded in an experimental chaotic attractor. In fact, a precision of about one percent has already been achieved for a partition of an attractor observed in a modulated laser [2]. Topological methods for constructing symbolic encodings thus appear

to be perfectly suited to the symbolic dynamical characterization of experimental systems, especially given their robustness to noise.

To conclude this section, we note that the above remarks are consistent with the observations reported by Bollt et al. [20] in their work on noise resistance in chaos-based communication schemes. To prevent noise-induced "bit-flipping", the trajectory of a chaotic communication device should be kept at a finite distance of the partition border. Enforcing a forbidden zone inside the attractor discards some symbolic sequences and in principle reduces the channel capacity (measured by the topological entropy). Bollt et al. [20] noted that in fact the latter decreases very slowly when the gap is increased. This is of course due to the near-border cylinders having a large diameter. In contrast with this, the diameters of cylinders in the remaining of the attractor decrease very rapidly with the number of symbols, as is shown by the evolution of the geometric average of the cylinder diameters in Figs. 10 and 11. This ensures that a system can be forced to follow a prescribed symbolic sequence using only tiny perturbations.

A key property of a generating partition is that it can be utilized to estimate various invariant quantities such as metric entropy. In Section 7 we characterize our partitions by measuring the latter and by giving for each of our sample attractors the list of forbidden sequences.

7. Estimates of metric entropy

There are quantitative measures of chaos that can be recovered both from a study of symbolic dynamics and from a direct analysis of trajectories in phase space. The most important is probably the metric entropy h_1 which can be defined in symbolic dynamical terms as

$$h_1 = \lim_{l\to\infty} h_1(l), \quad h_1(l) = H(l) - H(l-1),$$
$$H(l) = -\sum_{S_l} p(S_l) \ln p(S_l), \tag{22}$$

where S_l are the allowed symbolic sequences of length l, and $p(S_l)$ are their probabilities of occurrence in the sequence associated with a typical chaotic orbit. In phase space, a good estimate of h_1 can be obtained by a standard Lyapunov exponent calculation, since it is conjectured that the metric entropy is equal to the sum of the positive Lyapunov exponents (see, e.g., [21]).

To verify that a partition constructed from a topological analysis of unstable periodic orbits allows one to compute an accurate estimate of the metric entropy, we have thus compared estimates obtained by these two approaches for the regime of the modulated laser system which was studied in Ref. [1], using the partition Γ_{h}^{f} (see Section 2).

First, an estimate of the positive Lyapunov exponent was obtained in the standard way by integrating the linearized equations of motion around a numerical solution over a time interval of 10^7 periods of modulation. This yielded the value $\lambda_1 \approx 0.3730$.

Then we computed the probabilities $p(S_l)$ for symbol strings of length up to $l_M = 30$ from a sequence of 10^8 symbols obtained by encoding a chaotic orbit with the partition Γ_{h}^{f}. To minimize systematic errors due to low-probability strings, we applied to Eq. (22) the finite sample corrections derived by Grassberger [22]. The corresponding estimates of $h_1(l)$ are shown in Fig. 12.

The best estimate is $h_1 \approx h_1(30) = 0.374$ which closely agrees with λ_1 as they differ by only 0.3%. Furthermore, estimates within 1% of the correct value are obtained for $l > 20$. It is however difficult to give precise error bars. Indeed, Eq. (22) systematically overestimates the metric entropy because it does not take into account the forbidden strings of length greater than l_M. Conversely, the fact that some low-probability sequences may have not been observed can lead to underestimate the entropy.

Furthermore, it should be noted that this test is probably not very sensitive to the quality of the partition: the metric entropy estimate is maximal for a generating partition and thus should remain almost constant when the border of the partition is slightly displaced. Nevertheless, we see it as another check of the validity of our algorithm.

A perhaps more robust characterization of a chaotic regime is to give the list of IFWs [23], which define the "grammar" of this regime. They are the shortest

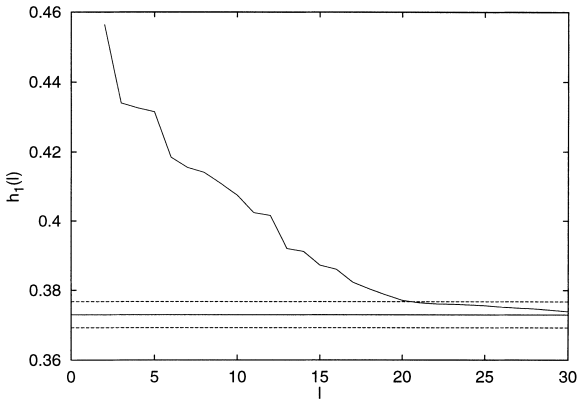

Fig. 12. Estimates of the metric entropy using finite sample corrections of Eq. (22) vs. string length l. The horizontal line indicates the value obtained from Lyapunov exponent calculations and the dashed lines correspond to ±1% deviations from this value.

forbidden symbolic sequences such that every forbidden sequence contains at least one of them, and can be used to compute topological entropy. If we do so for the regime under study, this reveals that it is very close to the crisis where the attractor collides with a period-3 orbit [2]: the only forbidden sequence up to period 12 is the "00" string. For reference, we give in Table 1 the list of irreducible forbidden words up to length 17. Because the list of IFWs is an important characterization of the dynamics, and to allow future comparisons of our results with those obtained from other methods, we also provide in Tables 2 and 3 the list of IFWs for the spiral laser and Duffing attractors studied in Sections 4.1 and 4.2. In the latter example, note that symbols "0" and "1" should be exchanged to compare the list of IFWs to that of Ref. [10].

It can be seen that one of our seven period-6 IFWs is not listed in Ref. [10]: it is "211100", which seems to be paired with "211101". We do not presently have an explanation for this discrepancy, as we have showed in Section 5 that the partition border we obtain with our approach follows exactly lines of homoclinic tangencies. We can however note that there is a line of homoclinic tangencies located slightly below the lower

Table 1
List of IFWs up to length 17 for the partition Γ_h^f

Length	IFWs
2	0^2
13	$(01)^2(011)^3$, $0111(011)^3$
15	$(01)^2(011)^2(01)^20$, $0111(011)^2(01)^20$, $(011)^5$
17	$(01)^2(011)^20101110$, $0111(011)^20101110$, $(011)^4(01)^20$, $1^301(011)^4$, $1^5(011)^4$

Table 2
List of IFWs up to length 7 for the partition of the spiral laser attractor shown in Fig. 5

Length	IFWs
2	21, 22
3	202
4	0000, 0001
5	10201, 11000, 11201, 12000
6	1010^3, 1020^3, 102002, 11011, 110012, 112002, 120011, 120012, 2010^3
7	0^320^3, 1002010, 1002011, 1012010, 1012011, 1100102, 1200102, 2002010, 2010011, 2010012, 2012010

Table 3
List of IFWs up to length 7 for the partition of the Duffing attractor shown in Fig. 6[a]

Length	IFWs
2	12, 22
4	2020
5	11111, 21111
6	101111, 102111, 111100, 111101, <u>211100</u>, 211101, 202102
7	1011100, 1021100, 2021011

[a]The underlined IFW of length 6 is not listed in Ref. [10].

one of Fig. 6, and which has perhaps been used in Ref. [10].

8. Compact parameterization of partitions

In the algorithm described in the previous sections, all the detected periodic points were eventually inserted in the triangulation. While this ensures that all the available information is utilized, it makes the description of the final partition complex. Consequently, encoding is computationally intensive, since one has to find at each iteration the nearest neighbor of the current state among thousands of reference points. However, as seen in Ref. [1], only those points that are in a small neighborhood of the border line are relevant to specify the partition. In this section, we accordingly show that the high-resolution partitions we have obtained in the previous sections can in fact be parameterized by a small number of reference points.

The border line is built with the mediators of triangles having vertices with different symbols. Since only the part of the border line which is located inside the polygon enclosing the strange attractor is relevant to perform the encoding, the essential information is actually carried by triangles whose mediators are located inside this polygon. Therefore, we can discard reference points which do not belong to such triangles without modifying the border of the partition inside the shadow polygon, hence inside the support of the attractor. In the case of the partition Γ_a^f computed in Ref. [1] and displayed in Fig. 1b, this allows one to parameterize the final partition using only 46 reference points among the 34 090 detected periodic points, as shown in Fig. 13a. The reason why the number of reference points remains relatively high is that triangles that connect different leaves of the attractor, but are entirely located inside the polygon, cannot be removed by the above rule whereas they in fact do not carry information about the location of the border. This limitation is of course due to the naive way in which the procedure used to decide whether the encoding of a point is uncertain has been implemented: it was suited to determining the partition but not to find its smallest parameterization.

Going back to the core ideas of the algorithm, we can achieve a much more compact description if we allow the border to be slightly displaced, but without modifying the encoding of any periodic point. Consider periodic points located in the Voronoï domain V_p of a given reference point p. If the second nearest neighbors of all these points have the same symbol as p, p can be safely removed without modifying the symbols that the partition assigns to any periodic point. To simplify the partition, one can therefore search for such reference points until further removals would change the encoding of some periodic points.

To achieve a compact parameterization, we have proceeded as follows. Given a periodic point O_i^j located in region $\Delta_s(\Gamma)$, we define $n_{\mathrm{r}}(O_i^j)$ as being the number of reference points with symbol s which are closer than the closest reference point with symbol $s' \neq s$. Then, the redundancy of each reference point p is estimated by $r(p) = \min_{O \in V_p} n_{\mathrm{r}}(O)$.

We then remove the reference points with the highest $r(p)$ until the number of removed points is equal to the highest $r(p)$ for the remaining points, so as to ensure that for each periodic point there is still a nearest neighbor with the correct symbol. Indeed, a high value of $r(p)$ indicates that p carries little information, as at least $r(p)$ reference points, including p, can be removed before the symbols associated to periodic points $O \in V_p$ are modified. This step is repeated until no reference point can be removed.

We have applied this procedure to the partition shown in Fig. 13a, and obtained a simplified partition (displayed in Fig. 13b) which is parameterized by only eight reference points, yet has the same precision (of the order of 0.1% of the attractor width) as the original partition Γ_a^f (Fig. 1b).

It can be seen from Fig. 13b that a compromise has to be found between compactness and robustness to noise. Indeed, with a small number of reference points, the partition line tends to wiggle and to pass close to a large number of periodic points, which increases the probability of encoding errors due to noise. A satisfying balance between these two requirements can be tuned, e.g., by allowing the removal of a reference point p only if $r(p) > r_{\min}$, where $r_{\min}$ is appropriately chosen. Our current selection algorithm

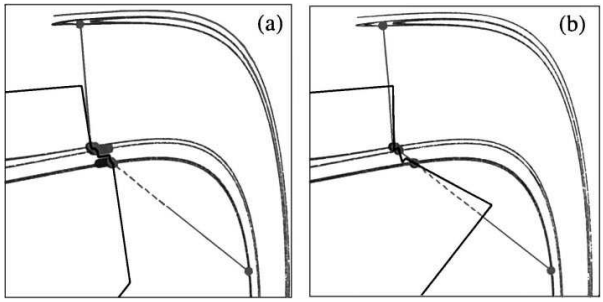

Fig. 13. (a) Parameterizing a partition with reference points belonging to triangles bearing different symbols and whose mediators are located inside the shadow polygon yields a partition that cannot be distinguished from the original, yet has a much more compact description. (b) The number of reference points can be further reduced by keeping only those whose removal would change the encoding of one of the detected points.

can probably be much improved. However, the partitions of Fig. 13 shows clearly that a high-resolution can be achieved at a minimal cost. Furthermore, it should be recalled that in practical applications, such as chaos-based communication, the system trajectory is usually forced to stay at a finite distance of the partition border, which should allow one to simplify the description even more.

To conclude this section, we would like to show with a simple example that the method we have presented here has modest computational requirements when we limit ourselves to resolutions relevant to practical applications, and that it is well suited to perform a real-time encoding of a chaotic system.

To this end, we computed a cover of the attractor of Fig. 1b with UPO of period up to 15, and with a resolution of 3%, obtained with 75 periodic orbits. We applied to this set of UPO the standard algorithm described in Ref. [1]. The resulting partition was then simplified as described above to obtain the partition of Fig. 14 whose description utilizes only seven reference points. The computational costs of the different stages of the algorithm are given in Table 4 and can be seen to be very small.[1] Yet, in spite of its much lower precision, the partition shown in Fig. 14b is characterized by exactly the same IFWs as the high-resolution partition Γ_{h}^{f} (see Section 2), at least up to length 19 included. Remarkably, we observed the same agreement for a similar partition based on 43 orbits of periods up to 12 which displayed a much wider gap around the border.

This example clearly shows that experimental systems can be precisely characterized using the

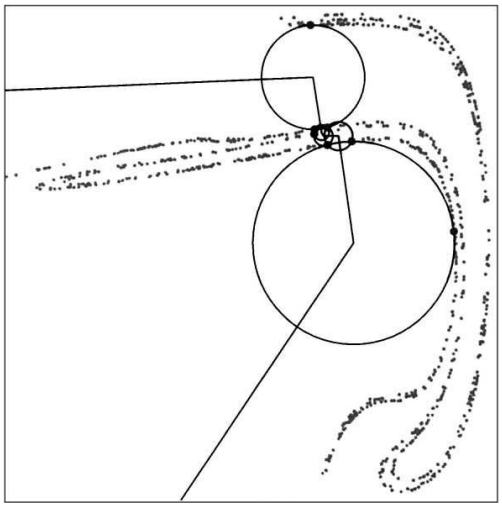

Fig. 14. Partition obtained with a small set of periodic orbits (shown in grey), parameterized with only seven points. The circumcenters delimiting the uncertain region are also displayed.

[1] It should however be noted that, because of the exponential complexity of the problem, the determination of the high-resolution partitions presented in the previous sections required CPU times of the order of 100 h, essentially for the detection of UPO.

Table 4
Computational cost of the different stages of this algorithm for the partition of Fig. 14[a]

Task	CPU time (s)
UPO detection	287.5
Computation of topological invariants	47.9
Template determination	0.9
Determination of topological names	2.0
Construction of the partition	5.4

[a]CPU times are given for a Pentium 133 computer running under the Linux operating system.

topological approach. It should be noted that for regimes that have a higher topological entropy, such as these found after the period-3T crisis as in Ref. [2], a higher precision can be obtained using lower-period orbits. Also, the partition shown in Ref. [2] shows that even if most of the periodic orbits of period larger than 10 are very difficult to detect, this is in general not the case for those located just near the border line, as they are weakly unstable.

9. Conclusion

In this work, we have carried out precise tests of the validity of the algorithm presented in Ref. [1]. A first indication that the resulting encodings faithfully describe the dynamics is that partitions determined from different initial configurations are equivalent: they encode a given trajectory in the same way, up to a shift of the symbolic sequences (Section 3). Furthermore, we have also directly verified that these partitions closely meet the criteria for being a generating partition by (i) observing that symbolic sequences of increasing length were associated to regions of decreasing diameters (Section 6), and (ii) by obtaining good estimates for the metric entropy from a long chaotic sequence (Section 7).

However, the most convincing evidence of the relevance of our method is provided by the perfect agreement between our results and those obtained by the classical method based on homoclinic tangencies. Indeed, we have found that important lines of homoclinic tangencies are entirely located inside the triangles enclosing the border of the partition (Section 5). This not only indicates that the partitions we obtain are very close to what is conjectured to be the correct solution, but also that our method naturally provides reliable error bounds, which are determined from the circumcircles of the triangles enclosing the partition border.

Even if the ultimate precision we can reach is probably lower than with homoclinic tangencies, the topological approach to constructing symbolic encodings has several distinctive advantages.

First, the problem of how to choose the tangency lines that will define a good partition is naturally solved. This was illustrated by the study of the Duffing attractor (Section 4.2). In this example, our algorithm naturally selects the lines of homoclinic tangencies that were found in Ref. [10] to yield the correct partition although some of them do not correspond to lines of primary homoclinic tangencies. That the solutions so obtained are the most natural ones is confirmed by the results of Section 3, where it was found that the different solutions were images or preimages of each other.

Second, the determination of the underlying template automatically indicates the correct number of symbols on which the dynamics is based. This is because this number is nothing but the number of branches of the template. This is also a key property since we have seen that for a given system, the number of symbols may depend on the parameter values as is the case, e.g., for the modulated laser system (compare the partitions shown in Figs. 1b and 5).

Last but not least, the topological approach should be extremely robust to noise. Indeed, it makes use of trajectories located in the whole phase space, and only gradually converges to the lines of homoclinic tangencies, where it is known that a dramatic noise amplification takes place [17]. The latter phenomenon is likely to adversely affect the determination of the directions of the invariant manifolds in the neighborhood of the tangencies from the time series, especially as the most expanding direction is orthogonal to the unstable manifold [17] there.

In contrast with this, the very fact that at homoclinic tangencies noise perturbs trajectories orthogonally to the unstable manifold implies that the locations of periodic points as estimated from close returns will be

in first approximation displaced in a direction that is parallel to the border of the partition. The latter should thus be minimally affected, unless noise is so strong as to make the periodic point appear to be in different leaf of the attractor than the one it belongs to. Furthermore, it should be noted that the determination of topological invariants is relatively insensitive to noise level as the knot type of an orbit generally can still be exactly determined from a noisy, approximate trajectory shadowing this orbit.

All these properties clearly show that the topological approach should be a method of choice to construct generating partitions from experimental time series. As a matter of fact, we recall that a preliminary version of our algorithm has already been successfully applied to obtain with a very good accuracy a generating partition for a chaotic attractor of a modulated laser [2]. The relevance of template analysis to study the symbolic dynamics of experimental systems is further confirmed by the observation in Sections 6 and 8 that a precision of only a few percent is sufficient to characterize very precisely the grammar of a chaotic regime.

We believe that our algorithm, and the way in which partitions are parameterized, could also prove useful in practical applications, and especially for transmitting information over chaotic signals, as proposed by Hayes et al. [18,19]. In this approach, the message to be transmitted is first encoded into a sequence of symbols, which is compatible with the symbolic dynamics of the transmitting device. Then, tiny perturbations are applied to this device so that among all possible chaotic trajectories, it follows the one whose associated symbolic sequence is the given sequence. Indeed, we showed in Section 8 that once the partition has been determined, it is possible to simplify very much its description, so that encoding a signal merely amounts to finding among a few reference points which is closest to the point in phase space representing the current state of the system. This computation could easily be implemented in a digital signal processor, to achieve real-time encoding at the receiving side of the transmission line and recover thereby the digital message.

The fact that the images of a given partition can be easily and exactly computed (reference points are periodic) would also be beneficial at the sending side because it makes it easier to predict the next symbols that the device would emit if it was free-running, and thus to compute the tiny perturbation needed to synchronize the symbolic stream with the prescribed sequence. Finally, we note that our algorithm naturally selects a region where the encoding is to be considered uncertain, and which the transmitting device should not visit in order to avoid any ambiguity at the receiving side.

In conclusion, we believe that the present work shows that topological analysis, in the present form or in future extensions, is a promising tool to master the symbolic dynamics of experimental chaotic systems, especially given its robustness to noise and its ability to select the appropriate tangency lines and the correct number of symbols.

Acknowledgements

It is a pleasure to thank our colleagues Guillaume Boulant, Serge Bielawski, Dominique Derozier, and Robert Gilmore for stimulating discussions. The Laboratoire de Physique des Lasers, Atomes, Molécules is Unité de Recherche Mixte du CNRS. The Centre d'Études et Recherches Lasers et Applications is supported by the Ministère chargé de la Recherche, the Région Nord-Pas de Calais and the Fonds Européen de Développement Économique des Régions.

References

[1] J. Plumecoq, M. Lefranc, From template analysis to generating partitions I: Periodic orbits, knots and symbolic encodings, Physica D 144 (2000) 231–258.
[2] M. Lefranc, P. Glorieux, F. Papoff, F. Molesti, E. Arimondo, Combining topological analysis and symbolic dynamics to describe a strange attractor and its crises, Phys. Rev. Lett. 73 (1994) 1364–1367.
[3] G.B. Mindlin, X.-J. Hou, H.G. Solari, R. Gilmore, N.B. Tufillaro, Characterization of strange attractors by integers, Phys. Rev. Lett. 64 (1990) 2350–2353.
[4] G.B. Mindlin, H.G. Solari, M.A. Natiello, R. Gilmore, X.-J. Hou, Topological analysis of chaotic time series data from Belousov–Zhabotinski reaction, J. Nonlinear Sci. 1 (1991) 147–173.
[5] R. Gilmore, Topological analysis of chaotic dynamical systems, Rev. Mod. Phys. 70 (1998) 1455–1530.

[6] N.B. Tufillaro, T.A. Abbott, J.P. Reilly, An Experimental Approach to Nonlinear Dynamics and Chaos, Addison-Wesley, Reading, MA, 1992.

[7] H.G. Solari, M.A. Natiello, G.B. Mindlin, Nonlinear Dynamics: a Two-Way Trip from Physics to Math, IOP, London, 1996.

[8] J.S. Birman, R.F. Williams, Knotted periodic orbits in dynamical systems I: Lorenz's equations, Topology 22 (1983) 47–82.

[9] R.W. Ghrist, P.J. Holmes, M.C. Sullivan, Knots and Links in Three-Dimensional Flows, Lecture Notes in Mathematics, Vol. 1654, Springer, Berlin, 1997.

[10] F. Giovannini, A. Politi, Homoclinic tangencies, generating partitions and curvature of invariant manifolds, J. Phys. A 24 (1991) 1837–1848.

[11] P. Grassberger, H. Kantz, Generating partitions for the dissipative Hénon map, Phys. Lett. A 113 (1985) 235–238.

[12] P. Grassberger, H. Kantz, U. Moenig, On the symbolic dynamics of the Hénon map, J. Phys. A 22 (1989) 5217–5230.

[13] P. Cvitanović, G.H. Gunaratne, I. Procaccia, Topological and metric properties of Hénon-type strange attractors, Phys. Rev. A 38 (1988) 1503–1520.

[14] G. D'Alessandro, P. Grassberger, S. Isola, A. Politi, On the topology of the Hénon map, J. Phys. A 23 (1990) 5285–5294.

[15] R. Gilmore, J.W.L. McCallum, Structure in the bifurcation diagram of the Duffing oscillator, Phys. Rev. E 51 (1995) 935–956.

[16] G. Boulant, M. Lefranc, S. Bielawski, D. Derozier, A non-horseshoe template in a chaotic laser model, Int. J. Bifurc. Chaos 8 (1998) 965–975.

[17] L. Jaeger, H. Kantz, Homoclinic tangencies and non-normal Jacobians — effects of noise in non-hyperbolic chaotic systems, Physica D 105 (1997) 79–96.

[18] S. Hayes, C. Grebogi, E. Ott, Communicating with chaos, Phys. Rev. Lett. 70 (1993) 3031–3034.

[19] S. Hayes, C. Grebogi, E. Ott, A. Mark, Experimental control of chaos for communication, Phys. Rev. Lett. 73 (1994) 1781–1784.

[20] E. Bollt, Y.-C. Lai, C. Grebogi, Coding, channel capacity and noise resistance in communicating with chaos, Phys. Rev. Lett. 79 (1997) 3787–3790.

[21] J.-P. Eckmann, D. Ruelle, Ergodic theory of chaos and strange attractors, Rev. Mod. Phys. 57 (1985) 617–656.

[22] P. Grassberger, Finite sample corrections to entropy and dimension estimates, Phys. Lett. A 128 (1988) 369–373.

[23] R. Badii, A. Politi, Complexity: Hierarchical Structures and Scaling in Physics, Cambridge Nonlinear Science Series, Vol. 6, Cambridge University Press, Cambridge, 1997.

"Unstable periodic orbits in the presence of spatio-temporal chaos"

E. Yao, M. Lefranc, and F. Papoff

J. Opt. B: Quantum Semiclass. Opt. **2**, 382–385 (2000)

J. Opt. B: Quantum Semiclass. Opt. **2** (2000) 382–385. Printed in the UK PII: S1464-4266(00)09644-0

Unstable periodic orbits in the presence of spatio-temporal chaos

E Yao†, M Lefranc‡ and F Papoff†

† Department of Physics, University of Manchester, Manchester M13 9PL, UK
‡ Laboratoire de Physique des Lasers, Atomes, Molécules, Bat P5, UFR de Physique, Université des Sciences et Technologies de Lille, France

E-mail: eric.yao@man.ac.uk

Received 17 November 1999, in final form 27 January 2000

Abstract. In this paper we investigate spatio-temporal disorder in a liquid crystal light valve with two-dimensional feedback and modulated input. We focus on the specific case of an optical feedback with a 180° rotation. By modulating the input field with appropriate amplitude and frequency, chaotic domains are formed in different locations of the transverse space [1, 2]. Because of diffusion, a global description of the spatio-temporal dynamics requires a partial differential equation. However, the local dynamics of the chaotic domains can be embedded in low-dimensional manifolds. The detection of a variety of different unstable periodic orbits (UPOs) at different spatial locations and the presence of UPOs for different detector sizes are strong indications that the dimensionality of the model of spatio-temporal chaos in our system can be drastically reduced.

Keywords: Weak turbulance, topological analysis, spatio-temporal chaos, unstable periodic orbits, liquid crystal light valve

1. Introduction

There is now a great effort in developing data analysis techniques for nonlinear systems in which different spatial domains are chaotic in time as well as spatially decorrelated. In systems where the spatial derivatives are linear and the nonlinear operator is uniform in space, it is possible to use topological analysis as a tool to access the properties of the nonlinear operator and hence separate it from the spatial derivative. By extending techniques developed for low-dimensional dynamical systems [3], the topology of the local attractors of different spatial domains can be studied. These can be checked for compatibility with low-dimensional systems. These kinds of dynamical systems, such as those described by reaction–diffusion type equations, are common in the field of pattern formation in optics as well as in other branches of science. Therefore, our approach can yet prove to have a general application. Moreover, for strongly dissipative systems a great advance could be achieved by drastically reducing the dimension of the problem by modelling the systems with ordinary differential equations instead of partial differential equations (PDEs). While standard techniques are not yet available to perform this reduction, the stable and unstable manifolds of any global attractors and their topology are generally believed to be paramount to this program. As the first step in this process, we have detected unstable periodic orbits (UPOs) within high-resolution time series data of chaotic domains in a liquid crystal light value (LCLV) experiment with modulated input and a feedback rotated by 180°.

2. Dynamical system

The experimental setup (figure 1) used is similar to other LCLV systems used in the study of nonlinear dynamics and pattern formation in optics [4] reviewed in [5]. The LCLV consists of a liquid crystal layer, a mirror and a photoconducting layer, all sandwiched between two transparent electrodes. The molecules of the liquid crystal reorientate under the influence of an applied electric field, lowering its refractive index. The photoconducting layer changes its impedance depending on the intensity of light illuminating it. Therefore, when a voltage is applied across the two electrodes, to the first approximation, the refractive index of the liquid crystal layer changes linearly with the intensity of light falling onto the photoconductor side of the LCLV. Therefore, the LCLV acts as a nonlinear medium, with a defocusing Kerr-type nonlinearity, in this optical system. The input beam is phase modulated after travelling through the liquid crystal layer and being reflected back from the mirror in the LCLV. The photoconducting side of the LCLV is only sensitive to intensity variations in the beam. Hence, the polarizer converts the phase modulation into intensity modulation completing the feedback loop. Here the feedback fibre bundle is rotated by 180° so that the feedback loop closes upon itself after two round trips of the system. A sinusoidal modulation of the input light intensity is achieved by means of an acousto-optic modulator. Photodiode detectors are used to monitor the temporal evolution of the dynamics of the intensity at a local spot in the transverse plane. By using a variable iris in conjunction with a lens, the effective size of the detector can be changed.

1464-4266/00/030382+04$30.00

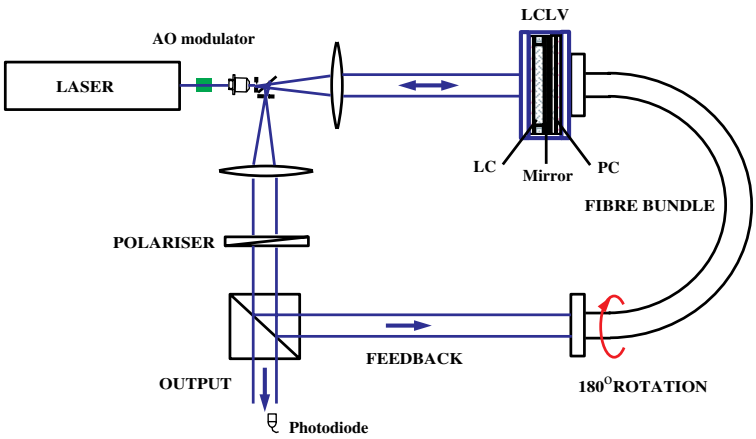

Figure 1. Schematic diagram of the experiment.

This type of system is normally modelled by a PDE with one transverse variable ϕ, which is the phase shift in the cross section of the laser beam due to the LCLV. However, because of the 180° rotation of the feedback we can split this into two, ϕ_1 and ϕ_2, where $\phi_1(r,\theta,t) = \phi_2(r,\theta+\pi,t)$ [2,6]. The two split variables appear one in the source term of the other. Hence, our system is modelled with the following PDEs of reaction–diffusion type:

$$\tau\frac{\mathrm{d}\phi_1(\vec{r},t)}{\mathrm{d}t} + \phi_1(\vec{r},t) = D^2\nabla^2\phi_1(\vec{r},t) + \kappa[1-\varepsilon\cos(ft)][1+\gamma\cos(\phi_2(\vec{r},t)+\phi_0)],$$
$$\tau\frac{\mathrm{d}\phi_2(\vec{r},t)}{\mathrm{d}t} + \phi_2(\vec{r},t) = D^2\nabla^2\phi_2(\vec{r},t) + \kappa[1-\varepsilon\cos(ft)][1+\gamma\cos(\phi_1(\vec{r},t)+\phi_0)]. \quad (1)$$

Here κ and γ are the strength of nonlinearity and the feedback coefficient respectively. κ is directly proportional to the intensity of the input (driving) beam and γ is a function of the orientation of the polarizer. τ is the relaxation time constant, D is the effective diffusion coefficient, and ϕ_0 is the constant phase shift. f and ε are the frequency and depth of the modulation applied to the input beam respectively.

In our experiment we monitor the time evolution of the intensity, which is related to the phase by a noninvertible relation:

$$I = B\left[\cos^2(\psi_1-\psi_2)\cos^2\left(\frac{\phi+\phi_0}{2}\right) + \cos^2(\psi_1+\psi_2)\sin^2\left(\frac{\phi+\phi_0}{2}\right)\right]I_{in}, \quad (2)$$

where B is the total loss of the system. The liquid crystal director (the general preferred orientation of the molecules) makes angles of ψ_1 and ψ_2 with the polarization axis of the input beam and the axis of the polarizer. There may be several values of the phase which correspond to the same value of the intensity. This has no effect on the detection of the UPO and the topological analysis can still be performed as will be shown in future papers.

When the system parameters are set at the appropriate values, this system shows complex spatio-temporal dynamics and the formation of chaotic domains both in the experiment and in numerical simulations [1, 2]. Figure 2 shows a snapshot of the intensity profile of the beam in the experiment. The spatial domains have chaotic dynamics of fractal dimension lower than three.

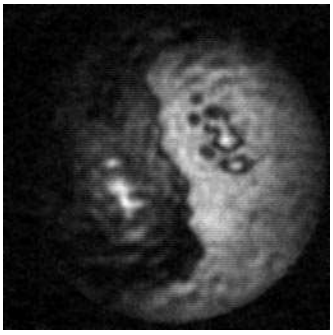

Figure 2. A snapshot of the beam profile in the experiment.

3. Extracting UPOs from time series

A chaotic attractor has a infinite set of UPOs embedded in it, which provide a powerful tool to study its organization. A low-dimensional dynamical system frequently visits the neighbourhoods of low-period UPO, closely tracking them for a while before escaping along the unstable direction. A clear signature of such an event is a ‘close return’ [7]: in a short amount of time, the trajectory passes twice near the same state. This property can be used to extract UPOs from time series by searching for time intervals where the signal is almost periodic. In modulated systems, this simply amounts to locating time series segments $\{X(t), t \in [t_0, t_0+\Delta t]\}$ which verify $|X(t)-X(t+pT)| < \epsilon$ for a large Δt, where p is an integer, T the modulation period (typically a few 100 ms in the experiment), and ϵ a fixed fraction of the signal amplitude.

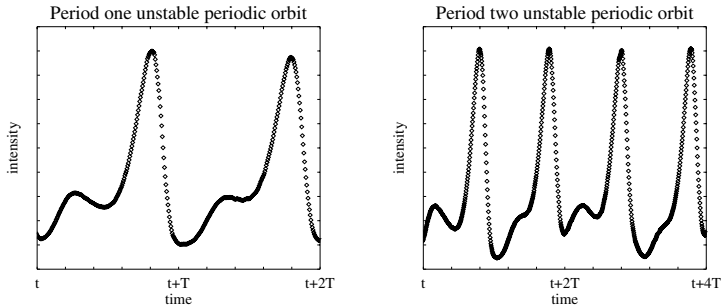

Figure 3. Unstable periodic orbits (experiment).

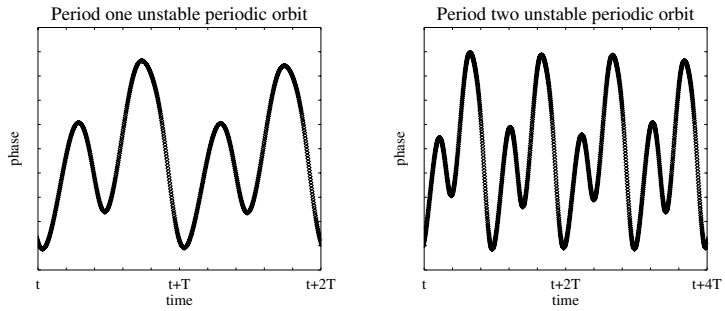

Figure 4. Unstable periodic orbits (numerical).

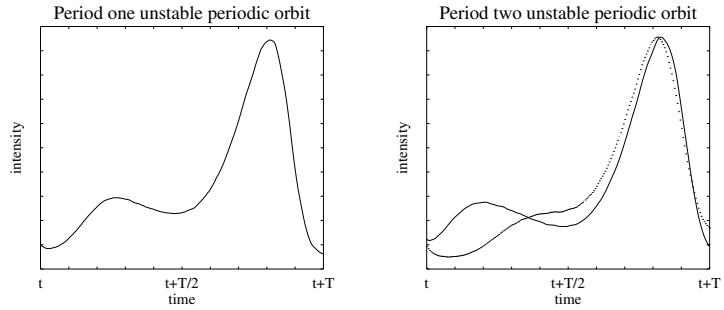

Figure 5. Linking of the period-doubled UPOs (experiment).

We have found that in this particular spatio-temporal system, such signatures appear distinctly in the local dynamics.

Long sequences of high-resolution time series data have been obtained and processed using this technique by computer programs previously used for a topological characterization of chaotic laser attractors [8]. A typical time series data set analysed consists of 200 samples per modulation period over 100 modulation cycles. To ensure that a detected close return faithfully reflects the shadowing of a low-period UPO by the system, search parameters were fixed at the conservative values $\Delta t = pT$ and $\epsilon = 0.05$.

We present here examples of the UPOs detected from experimental as well as numerical time series data monitoring a small fraction of the total cross section of the light valve with small area detectors.

These UPOs can be embedded in a three-dimensional space and their linking is compatible with a local low-dimensional dynamics whose topological template has at least two branches, one of which is orientation reversing. This is usually known as a horseshoe template. The orientation reversing branch is associated with a period-doubling bifurcation and, indeed, the topological analysis shows that the period-two orbit on the right of figure 3 arises from a period-doubling bifurcation of the period-one orbit shown on the left of the same figure. This is also the case in the numerical data (figure 4). Figure 5 shows the linking of the period-doubled UPO and its relation to the corresponding period-one orbit.

Other UPOs of period two and higher can also be detected (figure 6).

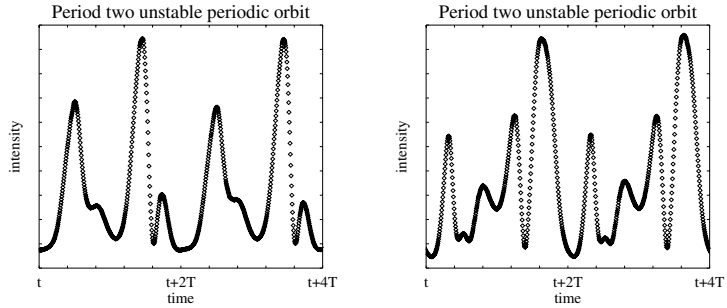

Figure 6. Unstable periodic orbits (experiment).

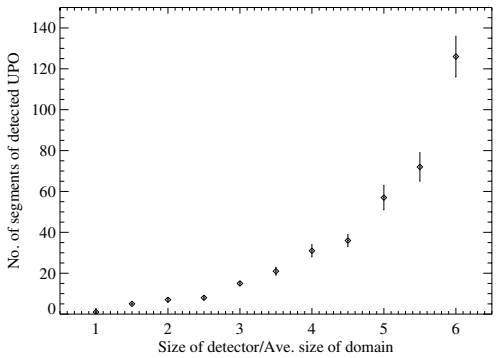

Figure 7. Number of detected UPOs versus detector size.

The entire time series cannot be embedded in the same way because, despite the low metric dimension of the time series, there are self-intersections of the trajectory in the embedding space which correspond to the passage of domains across the detector.

4. Spatial variation and subsystem size

Since the detection of UPOs originates from time-series data of local dynamics while the dynamical system is chaotic and spatially extended, the sizes of the detectors as well as their spatial locations are expected to be important parameters.

It is found that the number of segments of UPOs detected increases as the area of detector used increases (figure 7). This is accompanied by a decrease of the largest positive Lyapunov exponent. When the detector size is much smaller than the average size of the chaotic domains no UPO can be detected unless the length of the time series data is increased. The system becomes less chaotic when averaged over a bigger area in the transverse plane. Hence the trajectories are less spread out and more likely to shadow the UPO, making them easier to detect.

When an array of detectors is used to record time-series data from different locations, the types as well as the number of segments of UPOs detected are found to differ from each other. In general, however, time-series data from adjacent detectors tend to be similar to one another. Due to small spatial inhomogeneities in the experiment, chaotic domains are on average more likely to form in some locations than others. Differences between spatial locations are not observed in numerical data.

5. Conclusions

We have shown that UPOs can also be detected in systems with weak spatio-temporal chaos. The topology of these orbits is compatible with templates associated with low-dimensional dynamics. We believe that our results suggest the use of topological analysis of UPOs as a way to assess the properties of the nonlinearity, at least in systems where the nonlinear coupling between the variables is uniform in space and the operators containing spatial derivatives are linear.

Acknowledgment

We acknowledge financial support from EPSRC (grant GR/M 17983).

References

[1] Yao E, Papoff F and Oppo G-L 1998 Characterization of spatio-temporal complexity in optical experiments *Opt. Commun.* **155** 73
[2] Yao E, Papoff F and Oppo G-L 1999 Statistics and scaling behaviour of chaotic domains in liquid crystal light valves experiment *Phys. Rev.* E **59** 2918–26
[3] Sciamarella D and Mindlin G B 1999 Topological structure of chaotic flows from human speech data *Phys. Rev. Lett.* **82** 147
[4] Akhmanov S A, Vorontsov M A and Ivanov V Y 1988 *JETP Lett.* **47** 707–11
Akhmanov S A, Vorontsov M A, Ivanov V Y, Larichev A V and Zheleznykh N I 1992 *J. Opt. Soc. Am.* B **9** 78–90
Arecchi F T, Larichev A V and Vorontsov M A 1994 *Opt. Commun.* **105** 197–301
Neubecker R, Thuring B and Tschudi T 1994 *Chaos, Solitons Fractals* **4** 1307–22
[5] Vorontsov M A and Miller W B (ed) 1995 *Self-Organization in Optical Systems and Applications in Information Technology* (Berlin: Springer)
[6] D'Alessandro G, Pampaloni E, Ramazza P-L, Residori S and Arecchi F T 1995 Amplitude equations and pattern formation in a liquid crystal light valve experiment *Phys. Rev.* A **52** 4176
[7] Mindlin G B *et al* 1991 *J. Nonlinear Sci.* **1** 147
[8] Boulant G, Lefranc M, Bielawski S and Derozier D 1997 Horseshoe templates with global torsion in a driven laser *Phys. Rev.* E **55** 5082

"A non-horseshoe template in a chaotic laser model"

G. Boulant, M. Lefranc, S. Bielawski, and D. Derozier

Int. J. Birfurcation Chaos Appl. Sci. Eng. **8**, 965–975 (1998)

International Journal of Bifurcation and Chaos, Vol. 8, No. 5 (1998) 965–975

A NONHORSESHOE TEMPLATE IN A CHAOTIC LASER MODEL

G. BOULANT*, M. LEFRANC†, S. BIELAWSKI‡ and D. DEROZIER§
Laboratoire de Spectroscopie Hertzienne, URA CNRS 249,
Centre d'Études et de Recherches Lasers et Applications,
Université des Sciences et Technologies de Lille,
F-59655 Villeneuve d'Ascq Cedex, France

Received October 1, 1996

We have performed a topological analysis of a chaotic regime of a modulated single-mode class-B laser model, at realistic parameter values. In contrast with previous numerical and experimental studies of this type of laser, we observe a topological structure which differs from the one described by the paradigmatic horseshoe template. In view of this result, class-B lasers appear to be good candidates for the first clear characterization of a nonhorseshoe template in an experimental system.

1. Introduction

In the last years, unstable periodic orbits (UPO) have been recognized as a major tool to extract invariant quantities from the apparently erratic regimes of chaotic systems [Auerbach *et al.*, 1987] In particular, the template analysis proposed by Mindlin *et al.* [1990, 1991, 1992] is a powerful method to compare and classify chaotic attractors (see also [Tufillaro *et al.*, 1992]). It proceeds by characterizing the topological organization of the UPO embedded in a strange attractor through their invariant linking properties. In the phase space of the system, UPO are represented by intertwined closed curves which can be analyzed using concepts from knot theory, provided the system is three-dimensional (3D) [Kaufmann, 1991]. Key to this approach is the existence of a 2D branched manifold, the so-called "template", or knot-holder, such that for any set of UPO of the attractor, one can find a set of closed curves on the template with identical topological invariants. This allows a systematic study of the structure of chaotic attractors, which is all the more relevant as the topology of the UPO has a major influence on the bifurcation sequences of a chaotic system, as illustrated by Mindlin *et al.* [1993] and Gilmore and McCallum [1995]. In particular, template analysis can dramatically highlight the difference between two attractors if they are found to be associated to different templates.

The dynamics of several chaotic lasers has been studied by a topological analysis of their attractors: The CO_2 laser with a saturable absorber [Papoff *et al.*, 1992] or with modulated losses [Lefranc & Glorieux, 1993; Lefranc *et al.*, 1994], the nuclear magnetic resonance laser-type oscillator [Tufillaro

*E-mail: boulant@lsh.univ-lille1.fr
†E-mail: lefranc@lsh.univ-lille1.fr
‡E-mail: serge@lsh.univ-lille1.fr
§E-mail: domi@lsh.univ-lille1.fr

et al., 1991], and the Nd^{3+}-doped fiber laser [Boulant *et al.*, 1996]. Except for the laser with a saturable absorber which displays autonomous chaotic oscillations, these are modulated systems. The topological organizations of all these attractors have been shown to be described by a Smale's horseshoe template, including nonzero global torsions in the case of the fiber laser. Similar results have been reported for other experimental systems such as the Belouzov–Zhabotinskii chemical reaction [Mindlin *et al.*, 1991], an electrochemical reaction [Letellier *et al.*, 1995a], a glow discharge [Braun *et al.*, 1995] and a vibrating string [Tufillaro *et al.*, 1995].

Contrary to what these results may seem to imply, the horseshoe template is not universal, as shown by numerical studies of the Rössler system [Letellier *et al.*, 1995b] and of the Duffing oscillator [Gilmore & McCallum, 1995]. On the experimental side, the existence of a nonhorseshoe topological organization has been evidenced in only one system, a catalysis experiment, whose data were however not of sufficient quality to resolve the exact form of the associated template [Firle *et al.*, 1996].

In this paper, we report the observation of a nonhorseshoe template for chaotic regimes of a realistic dynamical model, the modulated single-mode class-B laser equations, at physically relevant parameter values. The three-branch structure of the corresponding template clearly differs from the one of the horseshoe template. This result is particularly interesting because previous template analyses of a modulated CO_2 laser [Lefranc & Glorieux, 1993; Lefranc *et al.*, 1994], which is well described by this model, had found a horseshoe template with zero global torsion, as had been predicted by previous numerical studies of this model [Solari & Gilmore, 1988]. Furthermore, the template we have found corresponds to one of those described by Gilmore and McCallum [1995] for a generic nonlinear driven oscillator. Thus, our result gives some confidence that a nonhorseshoe template may be soon evidenced in a modulated class-B laser.

The paper is organized as follows. In Sec. 2, we describe the single-mode class-B laser equations and give relevant derived quantities such as the relaxation frequency and damping rate. We then detail in Sec. 3 the procedure leading from the equations to the determination of the template via the computation of unstable periodic solutions and their topological invariants in phase space. Finally, we discuss how this work could be validated by an experimental study.

2. The Modulated Single-Mode Class-B Laser Equations

In "two-level" schemes, semi-classical theory model laser dynamics using three variables, the radiation field, the population inversion of the two-level gain medium and the atomic polarization coupling the two former variables [Narducci & Abraham, 1988; Khanin, 1995]. A laser is said to be class B when the polarization evolves much faster than the two other ones, and thus can be adiabatically eliminated [Tredicce *et al.*, 1985; Narducci & Abraham, 1988; Khanin, 1995]. In this case, when operated in single-mode regime, the laser dynamics is described, under the mean field approximation and neglecting any transverse spatial dependence, by the following dimensionless ordinary differential equations (ODE) for the light intensity $I(t)$ and the population inversion $D(t)$ [Narducci & Abraham, 1988; Khanin, 1995; Dangoisse *et al.*, 1987]:

$$\frac{\mathrm{d}I}{\mathrm{d}t} = I(D-1) \tag{1a}$$

$$\frac{\mathrm{d}D}{\mathrm{d}t} = \gamma[A - D(1+I)] \tag{1b}$$

These rate equations (or equivalent versions) have been extensively used in numerous numerical [Tredicce *et al.*, 1986; Dangoisse *et al.*, 1987; Solari *et al.*, 1987; Solari & Gilmore, 1988; Schwartz, 1988] and analytical [Erneux *et al.*, 1987, 1995; Schwartz & Erneux, 1994] studies of the modulated CO_2 and Nd:YAG lasers. Time t is measured in units of the photon lifetime in the cavity. A is the pump parameter normalized so that $A = 1$ at lasing threshold. The parameter γ is the population inversion relaxation rate in inverse reduced time units, and is usually small in class-B lasers (of the order of 10^{-3} for a CO_2 laser and 10^{-4} for a Nd:YAG laser).

A linear stability analysis of Eqs. (1) shows that for $A > 1$ the steady state $I = A - 1$, $D = 1$ is unconditionally stable and that transients consist of relaxation oscillations with relaxation frequency ω_r and damping rate Γ_r given by:

$$\omega_r = \sqrt{\gamma(A-1)} + O(\gamma^{3/2}) \tag{2a}$$

$$\Gamma_r = -\gamma A/2 \tag{2b}$$

At least one more degree of freedom is thus necessary to observe chaotic behavior. This may be achieved by modulating a parameter of the system, for example the intracavity losses. In this case,

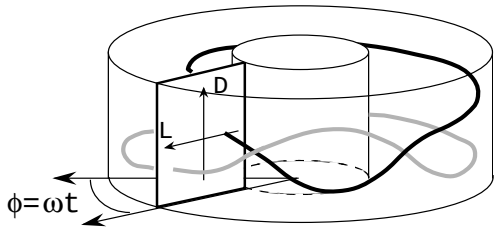

Fig. 1. Phase space of the modulated system (4). The plane of constant phase shown can be used to perform a Poincaré section. Two periodic orbits of period T are schematically drawn. Their linking number is equal to 1.

Eq. (1a) becomes:

$$\frac{\mathrm{d}I}{\mathrm{d}t} = I(D - 1 - m\cos\omega t) \tag{3}$$

where m ($|m| < 1$) and ω are respectively the amplitude and the frequency of the periodic modulation.

The parameter values we have used in our numerical experiment are $\gamma = 10^{-3}$, $A = 1.1$, and $m = 2.5 \times 10^{-2}$. The modulation frequency is $\omega = \omega_r = 10^{-2}$. Numerical integration has been performed using an adaptative step-size Runge–Kutta algorithm of order 8 [Hairer *et al.*, 1987]. When integrating Eqs. (3) and (1b), the I variable displays an alternation of almost constant sequences near $I = 0$ and of abrupt variations, which adversely affects the efficiency of the algorithm. We thus perform the change of variable $L = \ln I$ (see e.g. [Schwartz, 1988; Lefranc *et al.*, 1992]) and integrate the following ODE for L and D:

$$\frac{\mathrm{d}L}{\mathrm{d}t} = D - 1 - m\cos\omega t \tag{4a}$$

$$\frac{\mathrm{d}D}{\mathrm{d}t} = \gamma[A - D(1 + e^L)]\,. \tag{4b}$$

The natural phase space of this dynamical system, schematically displayed in Fig. 1, is three-dimensional and reads $\{L(t), D(t), \phi(t)\}$, where $\phi(t) = (t/T)(\mathrm{mod}\ 1)$ is the phase of the period-T modulation. It has the same topology as a solid torus $D^2 \times S^1$, D^2 being the unit disk and S^1 the unit circle.

In this phase space, a Poincaré section of the attractor can be readily obtained by means of a stroboscopic sampling, i.e. by choosing a section plane of constant phase. Figure 2 shows the Poincaré section of the attractor corresponding to $\phi = 0$ in the given operating conditions.

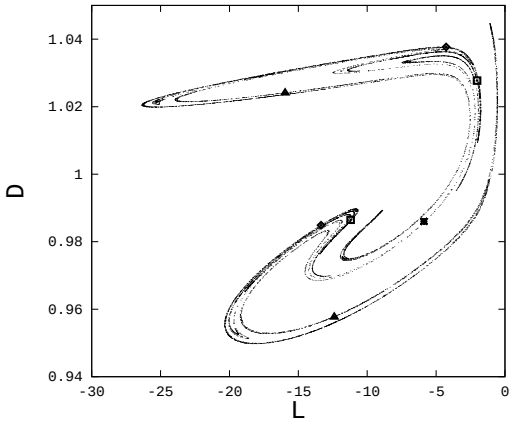

Fig. 2. Poincaré section of the attractor (10^4 points). The section plane is defined by $\phi = 0$ where ϕ is the modulation phase. The period-T orbit α (star), the period-$2T$ orbits β (diamond), γ (square) and δ (triangle) are plotted.

It should be pointed out that the knot invariants of the unstable periodic orbits have identical values in the $\{L(t) = \ln I(t), D(t), \phi(t)\}$ and $\{I(t), D(t), \phi(t)\}$ phase spaces. This can easily be seen by considering the one-parameter family of embeddings $\{\xi_\alpha(t), D(t), \phi(t)\}$, where $\xi_\alpha(t) = \alpha \ln I(t) + (1-\alpha)I(t)$ depends continuously on α. Since $\ln I$ is a monotonic function of I, the map $(I, D, \phi) \to (\xi_\alpha, D, \phi)$ is a diffeomorphism for each α. Therefore, going from the $\alpha = 0$ to the $\alpha = 1$ phase space amounts to performing an isotopy move and does not affect the topological invariants of the UPO. The results of the template analysis we will now carry out on system (4) are therefore transposable to the original system (1).

3. Template Analysis

As complex as it may appear, a strange attractor is a highly organized geometrical object. In particular, it contains an infinite number of unstable periodic orbits (UPO), densely embedded in it (see e.g. [Auerbach *et al.*, 1987]): Arbitrary close to any point of the attractor passes a periodic orbit. As it evolves on a strange attractor, a typical chaotic trajectory visits the neighborhood of these UPO, approaching them along their stable direction and, after an interval of time whose duration depends on

how closely the periodic orbit has been approached, leaving them along the local unstable direction.

Periodic orbits are closed curves in phase space which cannot intersect themselves or another orbit without violating determinism at the point of intersection [Guckenheimer & Holmes, 1983]. Consequently, in a three-dimensional phase space, the way an UPO is knotted and linked with other ones does not change in its whole domain of existence in parameter space. These properties thus constitute a robust tool for characterizing strange attractors.

The intertwining of the UPO can be described in the mathematical framework of knot theory by quantities which are invariant with respect to isotopy moves, i.e. which are not modified when the curves are continuously deformed without intersection [Kaufmann, 1991]. For example, the relative placement of a pair (α, β) of UPO can be characterized by their linking number $lk(\alpha, \beta)$, which indicates how many times α winds around β, as illustrated in Fig. 1.

In the hyperbolic limit, i.e. when all the UPO are present, the UPO of a three-dimensional chaotic flow are in one-to-one correspondence with those of a semi-flow defined on a two-dimensional branched manifold. The existence of such a manifold, termed a "template", is the keystone of this topological approach [Birman & Williams, 1983; Holmes, 1988; Mindlin *et al.*, 1990; Mindlin & Gilmore, 1992; Tufillaro *et al.*, 1992].

Strange attractors are usually not hyperbolic. In particular, periodic orbits can be created or destroyed as a control parameter is varied. However, existing periodic orbits are organized as in the hyperbolic limit, since their topological invariants do not depend on control parameters. As a result, even if not in the hyperbolic limit, the template keeps a physical relevance as a "knot-holder", a two-dimensional surface on which all the UPO of the attractor can be projected by continuous deformation without modifying their topological invariants.

It should be noted that if two attractors are associated to the same template, one cannot conclude to their complete topological equivalence because they may not have the same set of UPO. However, two attractors are most likely not topologically equivalent if they are found to be associated to different templates while topologically equivalent embeddings are used.

The derivation of the template from the topological invariants will be discussed in Sec. 3.3. We now locate the UPO in phase space and characterize their linking properties.

3.1. *Detection of the unstable periodic orbits*

The periodic solutions of the system (4) are computed by means of an iterative Newton–Raphson method (see e.g. [Hao, 1988]). The Poincaré section is first divided with a 64×64 grid. Then, for each period pT ($p = 1, 2, \ldots, p_{\max}$), we perform the following procedure.

In each visited cell of the grid where no periodic orbit of lower period has been detected, we choose a point of the attractor as the initial condition of a Newton–Raphson step applied to the time-pT return map. If the output of this initial step is located in the same cell or one of its neighbors, the Newton–Raphson method is iterated until convergence to a periodic solution is obtained.

With $p_{\max} = 10$, we detect 27 periodic orbits in the chosen operating conditions. Figure 2 indicates the location of the period-T and of the period-$2T$ UPO in the Poincaré plane.

3.2. *Computation of topological invariants*

Once the UPO have been extracted from the attractor, one can proceed to compute their topological invariants. Since template identification can be achieved using only a few of them, we have limited ourselves to the computation of (i) the self-linking number and the local torsion of each periodic orbit, and (ii) the linking number of pairs of orbits. We now briefly recall how they can be computed in numerical simulations and refer the reader to [Solari & Gilmore, 1988; Mindlin *et al.*, 1991; Mindlin & Gilmore, 1992; Gilmore & McCallum, 1995; Tufillaro *et al.*, 1992] for further details.

The linking number $lk(\alpha, \beta)$ of two orbits α and β indicates how many times α winds around β. Obviously, $lk(\alpha, \beta) = lk(\beta, \alpha)$. If $\mathbf{x}_\alpha(t)$ and $\mathbf{x}_\beta(t)$ denote their trajectories in phase space, and $p_\alpha T$ and $p_\beta T$ their periods, then the linking number of α and β is the Gauss integral:

$$lk(\alpha, \beta) = \frac{\varepsilon}{4\pi} \int_0^{p_\alpha T} \int_0^{p_\beta T} \frac{(\mathbf{x}_\beta - \mathbf{x}_\alpha) \cdot (\dot{\mathbf{x}}_\alpha \wedge \dot{\mathbf{x}}_\beta)}{\|\mathbf{x}_\beta - \mathbf{x}_\alpha\|^3} \mathrm{d}t_\alpha \mathrm{d}t_\beta \tag{5}$$

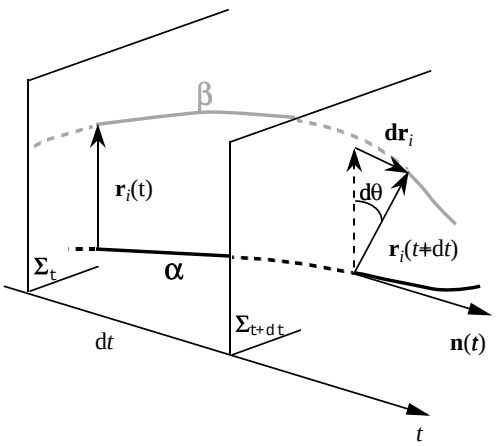

Fig. 3. Illustration of the computation of $R_i(\alpha, \beta)$ [Eq. (7)].

where $\varepsilon = \pm 1$ depending on the sign convention. In this formula and the following ones, we set $\varepsilon = -1$ so that topological invariants have positive values.

In the case of modulated systems, this double integral may be rewritten as a sum of simple integrals:

$$lk(\alpha, \beta) = \sum_{i=0}^{g-1} R_i(\alpha, \beta) \tag{6}$$

where g is the greatest common divisor of p_α and p_β and

$$R_i(\alpha, \beta) = \frac{\varepsilon}{2\pi} \int_0^{lT} \mathbf{n} \cdot \left(\frac{\mathbf{r}_i \wedge \dot{\mathbf{r}}_i}{\|\mathbf{r}_i\|^2} \right) \mathrm{d}t = \frac{\varepsilon}{2\pi} \int \mathrm{d}\theta \tag{7}$$

In Eq. (7), l is the least common multiple of p_α and p_β, $\mathbf{r}_i(t) = \mathbf{x}_\beta(t + iT) - \mathbf{x}_\alpha(t)$, and $\mathbf{n}(t)$ is a unitary vector normal to the plane Σ_t defined by $\phi = (t/T)(\mathrm{mod}\ 1)$ (see Fig. 3). Note that $\mathbf{r}_i(t)$ and $\dot{\mathbf{r}}_i(t)$ belong to the plane Σ_t and are therefore orthogonal to $\mathbf{n}(t)$.

$R_i(\alpha, \beta)$ is an integer giving the number of revolutions that $\mathbf{r}_i(t)$ operates around α before coming back to its initial position after a time lT.

The self-linking number $slk(\alpha)$ is given by:

$$slk(\alpha) = \sum_{i=1}^{p_\alpha - 1} R_i(\alpha, \alpha)\,. \tag{8}$$

Obviously, period-T orbits have a self-linking number of zero. It should be noted that while linking numbers are well-defined in any three-dimensional phase space, self-linking numbers are topological invariants only when the phase space has the topology of $D^2 \times S^1$, as is the case for modulated systems, or for attractors where trajectories rotate in a fixed sense around a central point. Table 1 gives the self-linking (diagonal terms) and

Table 1. Linking numbers and self-linking numbers of the lowest-order periodic orbits ($p \leq 7$).

	T	$2T$			$4T$		$6T$						$7T$				
	α	β	γ	δ	ϵ	ζ	η	ι	κ	λ	μ	ν	ξ	υ	ρ	σ	χ
α	0																
β	1	1															
γ	1	2	1														
δ	1	2	2	1													
ϵ	2	4	4	3	5												
ζ	2	4	5	4	8	7											
η	3	6	6	5	10	12	13										
ι	3	6	6	5	10	12	15	13									
κ	3	6	6	5	10	12	15	16	13								
λ	3	6	7	6	12	14	18	18	18	17							
μ	3	6	6	5	10	12	15	16	16	18	13						
ν	3	6	7	6	12	14	18	18	18	21	18	17					
ξ	3	7	7	6	12	14	18	18	18	21	18	21	18				
υ	3	7	7	6	12	14	18	18	18	21	18	21	21	18			
ρ	3	7	7	6	12	14	18	19	18	21	19	21	21	21	18		
σ	3	7	7	6	12	14	18	18	18	21	18	21	21	21	21	18	
χ	3	7	7	6	12	14	18	18	18	21	18	21	21	21	21	21	18

Table 2. Local torsion θ_l of the lowest-order periodic orbits ($p \leq 7$).

	T	$2T$			$4T$		$6T$						$7T$				
	α	β	γ	δ	ϵ	ζ	η	ι	κ	λ	μ	ν	ξ	υ	ρ	σ	χ
θ_l	1	2	3	1	3	5	4	6	5	7	5	8	6	6	7	5	7

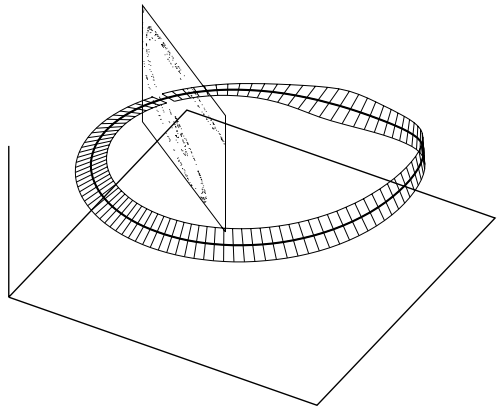

Fig. 4. The local stable manifold of the T-periodic orbit α rotates clockwise by a half-turn along the orbit. Thus, the local torsion of α is 1 if the sign convention $\varepsilon = -1$ is used. The Poincaré section defined by $\phi = 0$ is also indicated.

linking numbers (off-diagonal terms) measured for the detected periodic orbits of period lower or equal to $7T$.

Finally, the local torsion, that we will note $\theta_l(\alpha)$, characterizes in which way trajectories infinitely close to a periodic orbit wind around it. More precisely, as one follows the UPO over one period $p_\alpha T$, the direction of the local stable (unstable) manifold $W_l^s(\alpha)$ ($W_l^u(\alpha)$) rotates by an integer number of half turns, as is illustrated in Fig. 4. This number is defined to be the local torsion.

In numerical simulations, θ_l can be computed by using a linearization of the equations of motion around the periodic orbit. Given a set of ODE:

$$\frac{\mathrm{d}\mathbf{x}}{\mathrm{d}t} = \mathbf{f}(\mathbf{x},\, t)\,, \tag{9}$$

the linearized equations govern the time evolution of infinitesimal perturbations $\delta\mathbf{x}$ of the trajectory $\mathbf{x}$:

$$\frac{\mathrm{d}(\delta\mathbf{x}(t))}{\mathrm{d}t} = \mathbf{J}(\mathbf{x},\, t) \times \delta\mathbf{x}(t)\,, \tag{10}$$

where the Jacobian matrix $\mathbf{J}(\mathbf{x},\, t)$ is given by:

$$J_{ij}(\mathbf{x},\, t) = \frac{\partial f_i(\mathbf{x},\, t)}{\partial \mathbf{x}_j}\,. \tag{11}$$

Given a periodic orbit $\mathbf{x}_\alpha(t)$ of period $p_\alpha T$, its Floquet matrix $\mathbf{M}_\alpha(t)$, which expresses the linear relation between $\mathbf{x}(t + p_\alpha T)$ and $\mathbf{x}(t)$:

$$\delta\mathbf{x}(t + p_\alpha T) = \mathbf{M}_\alpha(t) \times \delta\mathbf{x}(t) \tag{12}$$

can be computed by integrating Eq. (10) over one period of the orbit for a basis of initial conditions.

The eigenvector $\boldsymbol{\xi}_s(t)$ ($\boldsymbol{\xi}_u(t)$) of $\mathbf{M}_\alpha(t)$ with eigenvalue smaller (greater) than one indicates the direction of the local stable (unstable) manifold at time t. Integrating Eq. (10) from the initial condition $\delta\mathbf{x}(0) = \boldsymbol{\xi}_u(0)$, the local torsion is then given by a formula similar to Eq. (7):

$$\theta_l(\alpha) = \frac{\varepsilon}{\pi} \int_0^{p_\alpha T} \mathbf{n} \cdot \left(\frac{\delta\mathbf{x} \wedge \dot{\delta}\mathbf{x}}{\|\delta\mathbf{x}\|^2} \right) \mathrm{d}t \tag{13}$$

where we choose $\varepsilon = -1$ as previously. Table 2 lists the torsions of orbits with periods lower or equal to $7T$. Note that the local torsion is sometimes defined as the mean number of full turns per period [Gilmore & McCallum, 1995]. In this case, the expression (13) should be divided by twice the period of the orbit.

3.3. *Determination of the underlying template*

The spectrum of detected periodic orbits gives a first indication about the complexity of the template corresponding to Tables 1 and 2: It must have three or more branches, since two-branch templates can only hold one period-2 orbit. Hence, the simple procedure which consists of checking that the computed topological invariants are those predicted by a horseshoe template cannot be applied. To determine the exact form of this new template from the data of Tables 1 and 2, we proceed as follows.

As proposed by Mindlin *et al.* [1990, 1991], the basic topological structure of a n-branch template

can be described by a $n \times n$ matrix $\mathbf{\Theta}$, the *template matrix* and a $1 \times n$ matrix $\mathbf{l}$, the *layering matrix* whose indices are labeled from 0 to $n-1$, as are the branches of the template. The template matrix $\mathbf{\Theta}$ describes the geometry of the period-1 orbits of the template (one per branch):

$$\Theta_{ii} = \theta_l(\bar{i}) \tag{14a}$$

$$\Theta_{ij} = 2lk(\bar{i}, \bar{j}), \quad i \neq j \tag{14b}$$

where the symbolic name $\overline{s_1 s_2 \ldots s_p}$ ($s_i \in \{0, 1, \ldots, n-1\}$) represents the only period-p orbit of the template visiting successively branches $s_1, s_2, \ldots, s_p$.

As for the layering matrix $\mathbf{l}$, its elements are integer numbers chosen so that $l_0 = 0$ and $l_i < l_j$ if branch i lies under branch j when branches are joined after being stretched and folded.

Given the symbolic name of a periodic orbit of the template, its (self-)linking numbers and torsion can be computed as a function of the template and layering matrices. For example, we have:

$$lk(\overline{1}, \overline{0121}) = 1 + \Theta_{11} + \frac{1}{2}(\Theta_{01} + \Theta_{12} - (l_{01} + l_{12})\Pi(\Theta_{11})) \tag{15}$$

where $\Pi(m) = 0(1)$ if $m \in N$ is even (odd), and $l_{ij} = 1$ (resp. -1) when $(i-j) \times (l_i - l_j) > 0$ (resp. < 0).

Template identification is most easily performed when a symbolic encoding of the attractor is available. When the first return map in a Poincaré section is well approximated by a map of an interval onto itself, such an encoding is usually performed by using the well-known symbolic dynamics of one-dimensional (1D) maps [Hao, 1989] (see e.g. [Mindlin *et al.*, 1991, Tufillaro *et al.*, 1991, Papoff *et al.*, 1992; Lefranc & Glorieux, 1993]). The template is then determined so that any periodic orbit of the attractor has the same invariants as the periodic orbit of the template with identical symbolic name, using formulas similar to Eq. (15).

In our case however, no well-defined 1D map can be found, as is shown in Fig. 5. We thus must find sets of symbolic names for which the equations expressing the measured (self-)linking numbers and torsions of the periodic orbits as a function of the template and layering matrices, such as Eq. (15), are consistent and have a valid solution (see e.g. [Solari & Gilmore, 1988; Lefranc *et al.*, 1994]). If

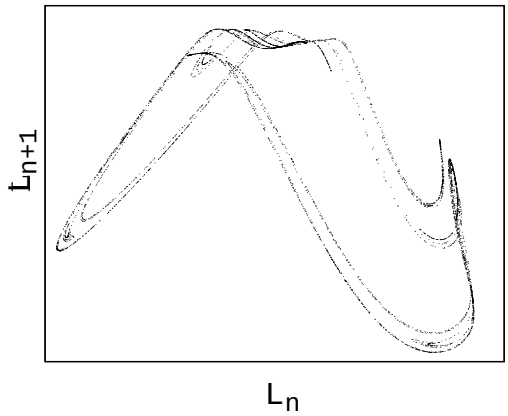

Fig. 5. First return map: $L_{n+1} = P(L_n)$ with $L_n = L(t_0 + nT)$. The time t_0 corresponds to the Poincaré plane (f) in Fig. 7, defined by $\phi_0 = t_0/T(\text{mod } 1) = 5/12$, where the $L_{n+1} = P(L_n)$ graph is the closest to a 1D map.

such sets exist, each of the corresponding solutions yields a template that is compatible with the given data.

The simplest hypothesis is that the unknown template has three branches. In this case, the period-T orbit and each of the period-$2T$ orbits have three possible symbolic names (resp. $\overline{0}$, $\overline{1}$, $\overline{2}$ and $\overline{01}$, $\overline{02}$, $\overline{12}$). We first consider the $9 = 3 \times 3$ possible sets of symbolic names for the first two orbits.

For each set, we may get three different results when trying to solve the above-mentioned equations: Either (i) the equations are inconsistent, or they are consistent and the solution is (ii) underdetermined, or (iii) fully determined. In the first case, the current set of symbolic names is discarded. In the second case, all sets made of the current set for the first two orbits and of one possible name for the next orbit are considered. The process described above is recursively applied to these sets until all combinations have either no solution or a fully determined solution.

Applying this method to the data given in Tables 1 and 2, we get the two following solutions:

$$\mathbf{\Theta}_a = \begin{pmatrix} 0 & 0 & 0 \\ 0 & 1 & 2 \\ 0 & 2 & 2 \end{pmatrix}, \tag{16a}$$

$$\mathbf{l}_a = \begin{pmatrix} 0 & 2 & 1 \end{pmatrix}, \tag{16b}$$

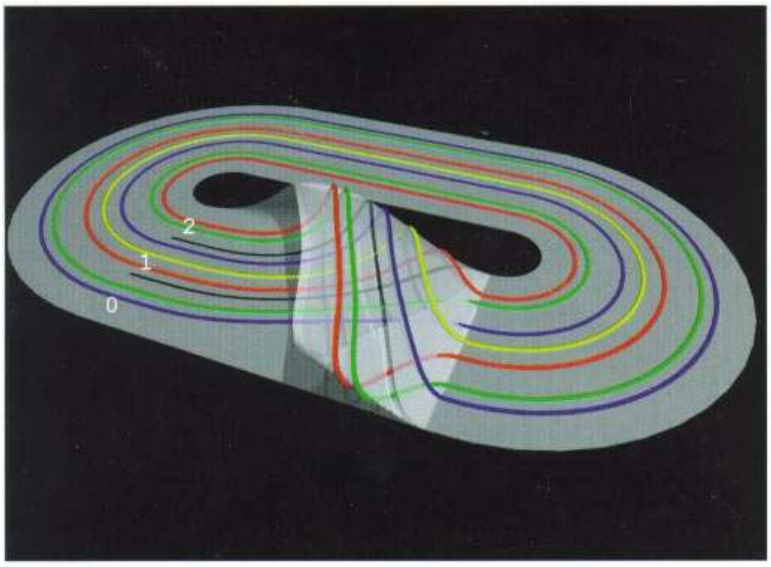

Fig. 6. This template describes the topological organization of the chaotic regime studied in this paper. It displays three branches, which are rolled-up by the stretching and folding mechanisms. The projections of the four lowest-order orbits of the attractor have been represented with the following colors: (i) yellow: period-T orbit α ($\overline{1}$), (ii) green: period-$2T$ orbit β ($\overline{02}$), (iii) red: period-$2T$ orbit γ ($\overline{12}$) and (iv) blue: period-$2T$ orbit δ ($\overline{01}$).

and

$$\mathbf{\Theta}_b = \begin{pmatrix} 0 & 0 & 0 \\ 0 & 2 & 2 \\ 0 & 2 & 1 \end{pmatrix}, \tag{17a}$$

$$\mathbf{l}_b = \begin{pmatrix} 0 & 2 & 1 \end{pmatrix}, \tag{17b}$$

with two other solutions which can be obtained from Eqs. (16a) and (17a) by the transformations $\Theta'_{ij} = \Theta_{2-i,2-j}$ and $l'_i = l_2 - l_{2-i}$ and correspond to the same templates viewed from the rear side. We have checked that these templates correctly predict the topological invariants of all the detected UPO (up to period $10T$).

In solution (17a), the torsions of branches 0 and 1 differ by more than one half-turn: This template cannot describe continuous stretching and folding mechanisms and must be discarded. Solution (16a) thus remains as the simplest template that can describe the topological organization of the chaotic attractor we have analyzed, and is represented in Fig. 6. The reader may check that this solution is nothing but the $(0, 1, 2)$ spiral template that has been predicted to occur in some regions of the parameter space of a generic driven nonlinear oscillator by Gilmore and McCallum [1995].

To get further confidence in the validity of this result, we may examine the evolution of the Poincaré section of the attractor as the modulation phase ϕ is swept from 0 to 1, as is shown in Fig. 7. In principle, this could have allowed us to guess the template structure by studying how the folding and stretching mechanisms act on trajectories. For templates with more than two branches, however, this is a difficult exercise and the method we have presented has the distinct advantage that it can be fully automated. In any case, we can verify that the template given by Eqs. (16a) correctly models the evolution of the Poincaré sections in Fig. 7.

4. Conclusion

We have carried out a template analysis of a chaotic attractor of the modulated class-B laser model, at parameter values corresponding to realistic experimental conditions. This study has revealed that the topological structure of this attractor is described by a three-branch template, the $(0, 1, 2)$ spiral

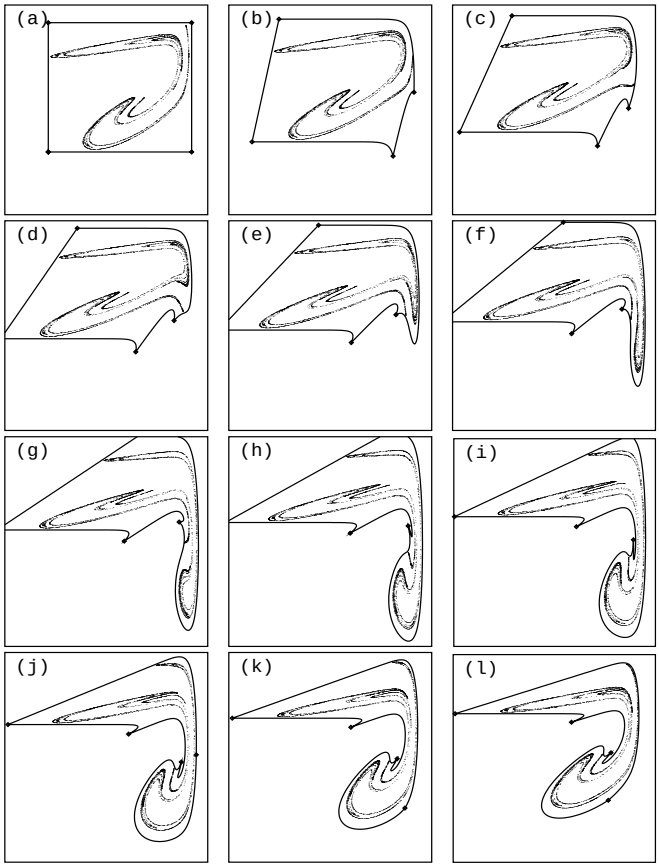

Fig. 7. Evolution of the Poincaré section from (a) $\phi = 0$ to (l) $\phi = 11/12$ by steps of 1/12. This sequence shows the rolling process demonstrated by the template analysis. The solid line corresponds to a set of points initially disposed along a rectangle and illustrates the action of the return map on the section plane. Two folding mechanisms may be seen. The first becomes visible in the right-hand section in Fig. (d) and the second is initiated in the bottom section in Fig. (g).

template described by Gilmore and McCallum [1995], and thus differs from the horseshoe structure reported by previous numerical [Solari & Gilmore, 1988] and experimental [Lefranc & Glorieux, 1993; Lefranc *et al.*, 1994] investigations of this type of laser.

This not only shows that the modulated class-B laser model can exhibit more complex behaviors than was generally believed, but also gives reasonable confidence that a nonhorseshoe template may be soon clearly evidenced in an experimental system. Indeed, most experimental investigations so far, in optics, chemistry, or mechanics, have reported the observation of a horseshoe template [Mindlin *et al.*, 1991; Papoff *et al.*, 1992; Lefranc & Glorieux, 1993; Lefranc *et al.*, 1994; Tufillaro *et al.*, 1991; Boulant *et al.*, 1996; Letellier *et al.*, 1995a; Braun *et al.*, 1995; Tufillaro *et al.*, 1995], except for a catalysis reaction for which the exact topological structure has however not been resolved [Firle *et al.*, 1996]. Class-B lasers are all the more good candidates for the observation of a nonhorseshoe template as they comprise several widely-used lasers such as the modulated CO_2, Nd:YAG, or optical fiber lasers. Furthermore, their fast time scales and high signal to noise ratios considerably ease the experimental detection of unstable periodic orbits by close-return techniques.

We believe that the experimental observation of a three-branch template in a class-B laser, as we predict in this paper, would certainly emphasize the usefulness of template analysis to validate theoretical models of experimental systems.

Acknowledgments

The Laboratoire de Spectroscopie Hertzienne is Unité de Recherche Associée au CNRS. The Centre d'Études et Recherches Lasers et Applications is supported by the Ministère chargé de la Recherche, the Région Nord-Pas de Calais and the Fonds de Développement Économique des Régions.

References

Auerbach, D., Cvitanovic, P., Eckmann, J.-P., Gunaratne, G. & Procaccia, I. [1987] "Exploring chaotic motion through periodic orbits," *Phys. Rev. Lett.* **58**, 2387–2389.

Birman, J. S. & Williams, R. F. [1983] "Knotted periodic orbits in dynamical systems I: Lorenz's equations," *Topology* **22**, 47–82.

Boulant, G., Lefranc, M., Bielawski, S. & Derozier, D. [1997] "Horseshoe templates with global torsion in a driven laser," *Phys. Rev. E.* **55**, 5082–5091.

Braun, T., Correira, R. R. B. & Altmann, N. [1995] "Topological model of homoclinic chaos in a glow discharge," *Phys. Rev.* **E51**, 4165–4168.

Dangoisse, D., Glorieux, P. & Hennequin, D. [1987] "Chaos in a CO2 laser with modulated parameters: Experiments and numerical calculations," *Phys. Rev.* **A35**, 4775–4791.

Erneux, T., Baer, S. M. & Mandel, P. [1987] "Subharmonic bifurcation and bistability of solutions of periodic solutions in a periodically modulated laser," *Phys. Rev.* **A35**, 1165–1171.

Erneux, T., Bielawski, S., Derozier, D. & Glorieux, P. [1995] "Stabilizing or destabilizing lasers by continuous delayed feedback," *Quantum Semiclass. Opt.* **7**, 951–963.

Firle, S. O., Natiello, M. A. & Eiswirth, M. [1996] "Topological dynamics in a catalysis experiment — a non-horseshoe template," *Phys. Rev.* **E53**, 1257–1260.

Gilmore, R. & McCallum, J. W. L. [1995] "Structure in the bifurcation diagram of the Duffing oscillator," *Phys. Rev.* **E51**, 935–956.

Guckenheimer, J. & Holmes, P. J. [1983] *Nonlinear Oscillations, Dynamical Systems, and Bifurcations of Vector Fields* (Springer, Berlin).

Hairer, E., Norsett, S. P. & Wanner, G. [1987] *Solving Ordinary Differential Equations: I. Non Stiff Problems* (Springer, Berlin).

Hao, B.-L. [1988] "Numerical methods to study chaos in ordinary differential equations," in *Directions in Chaos*, Vol. 2., ed. Hao, B.-L. (World Scientific, Singapore), pp. 294–309.

Hao, B.-L. [1989] *Elementary Symbolic Dynamics and Chaos in Dissipative Systems* (World Scientific, Singapore).

Holmes, P. J. [1988] "Knots and orbit genealogies in nonlinear oscillators," in *New Directions in Dynamical Systems*, eds. Bedford, T. & Swift, J. (University Press, Cambridge), pp. 150–191.

Kaufmann, L. H. [1991] *Knots and Physics* (World Scientific, Singapore).

Khanin, Y. I. [1995] *Principles of Laser Dynamics* (Elsevier, Amsterdam).

Lefranc, M., Hennequin, D. & Glorieux, P. [1992] "Improved correlation dimension estimates through change of variable," *Phys. Lett.* **A163**, 269–274.

Lefranc, M. & Glorieux, P. [1993] "Topological analysis of chaotic signals from a CO_2 laser with modulated losses," *Int. J. Bifurcation and Chaos* **3**, 643–649.

Lefranc, M., Glorieux, P., Papoff, F., Molesti, F. & Arimondo, E. [1994] "Combining topological analysis and symbolic dynamics to describe a strange attractor and its crises," *Phys. Rev. Lett.* **73**, 1364–1367.

Letellier, C., Le Sceller, L., Dutertre, P., Gouesbet, G., Fei, Z. & Hudson, J. L. [1995a] "Topological characterization and global vector field reconstruction of an experimental electrochemical system," *J. Phys. Chem.* **99**, 7016–7027.

Letellier, C., Dutertre, P. & Maheu, B. [1995b] "Unstable periodic orbits and templates of the Rossler system: Toward a systematic topological characterization," *Chaos* **5**, 271–282.

Mindlin, G. B., Hou, X.-J., Solari, H. G., Gilmore, R. & Tufillaro, N. B. [1990] "Classification of strange attractors by integers," *Phys. Rev. Lett.* **64**(20), 2350–2353.

Mindlin, G. B., Solari, H. G., Natiello, M. A., Gilmore, R. & Hou, X.-J. [1991] "Topological analysis of chaotic time series data from Belousov–Zhabotinski reactions," *J. Nonlin. Sci.* **1**, 147–173.

Mindlin, G. B. & Gilmore, R. [1992] "Topological analysis and synthesis of time series," *Physica* **D58**, 229–242.

Mindlin, G. B., Lopez-Ruiz, R., Solari, H. G. & Gilmore, R. [1993] "Horseshoe implications," *Phys. Rev.* **E48**, 4297–4304.

Narducci, L. M. & Abraham, N. B. [1988] *Laser Physics and Laser Instabilities* (World Scientific, Singapore).

Papoff, F., Fioretti, A., Arimondo, E., Mindlin, G. B., Solari, H. G. & Gilmore, R. [1992] "Structure of chaos in the laser with saturable absorber," *Phys. Rev. Lett.* **68**, 1128-1131.

Schwartz, I. B. [1988] "Sequential horseshoe formation in the birth and death of chaotic attractors," *Phys. Rev. Lett.* **60**, 1359–1362.

Schwartz, I. B. & Erneux, T. [1994] "Subharmonic hysteresis and period doubling bifurcations for a periodically driven laser," *SIAM J. Appl. Math.* **54**, 1083–1100.

Solari, H. G., Eschenazi, E., Gilmore, R. & Tredicce, J. R. [1987] "Influence of coexisting attractors on the dynamics of a laser system," *Opt. Commun.* **64**, 49–53.

Solari, H. G. & Gilmore, R. [1988] "Relative rotation rates for driven dynamical systems," *Phys. Rev.* **A37**, 3096–3109.

Tredicce, J. R., Arecchi, F. T., Lippi, G. L. & Puccioni, G. P. [1985] "Instabilities in lasers with an injected signal," *J. Opt. Soc. Am.* **B2**, 173–183.

Tredicce, J. R., Arecchi, F. T., Puccioni, G. P., Poggi, A. & Gadomski, W. [1986] "Dynamic behavior and onset of low-dimensional chaos in a modulated homogeneously broadened single-mode laser: Experiment and theory," *Phys. Rev.* **A34**, 2073–2081.

Tufillaro, N. B., Holzner, R., Flepp, L., Brun, R., Finardi, M. & Badii, R. [1991] "Template analysis for a chaotic NMR laser," *Phys. Rev.* **A44**, 4786–4788.

Tufillaro, N. B., Abbott, T. A. & Reilly, J. P. [1992] *An Experimental Approach to Nonlinear Dynamics and Chaos* (Addison-Wesley, Reading).

Tufillaro, N. B., Wyckoff, P., Brown, R., Schreiber, T. & Molteno, T. [1995] "Topological time series analysis of a string experiment and its synchronized model," *Phys. Rev.* **E51**, 164–174.

"Experimental observation of ... a reverse horsehoe topological structure"

G. Boulant, S. Bielawski, D. Derozier, and M. Lefranc

Phys. Rev. E **55**, 3801–3804(R) (1997)

PHYSICAL REVIEW E

STATISTICAL PHYSICS, PLASMAS, FLUIDS, AND RELATED INTERDISCIPLINARY TOPICS

THIRD SERIES, VOLUME 55, NUMBER 4 APRIL 1997

RAPID COMMUNICATIONS

The Rapid Communications section is intended for the accelerated publication of important new results. Since manuscripts submitted to this section are given priority treatment both in the editorial office and in production, authors should explain in their submittal letter why the work justifies this special handling. A Rapid Communication should be no longer than 4 printed pages and must be accompanied by an abstract. Page proofs are sent to authors.

Experimental observation of a chaotic attractor with a reverse horseshoe topological structure

G. Boulant, S. Bielawski, D. Derozier, and M. Lefranc
Laboratoire de Spectroscopie Hertzienne, URA CNRS 249, Centre d'Études et de Recherches Lasers et Applications, Université de Lille I, F-59655 Villeneuve d'Ascq Cedex, France
(Received 31 December 1996)

We have characterized the topological organization of chaotic regimes of a modulated Nd:YAG (yttrium aluminum garnet) laser using template analysis. This investigation revealed a topological structure not previously observed in an experimental system nor in numerical simulations of models of this laser to our knowledge. This structure corresponds to the so-called reverse horseshoe theoretically described by Gilmore and McCallum [Phys. Rev. E **51**, 935 (1995)]. [S1063-651X(97)50104-8]

PACS number(s): 05.45.+b, 42.65.Sf, 42.55.Rz

The experimental study of a system displaying chaotic behavior requires characterization methods which can extract in a robust way the invariant properties of a chaotic regime from apparently erratic signals. This is usually done by reconstructing a strange attractor, an invariant set of the phase space which the asymptotic dynamics is confined to, and analyzing this highly complex geometrical object (see, e.g., [1]). Traditionally, quantitative measures of chaos have focused on global statistical properties of the attractor, such as fractal dimensions or Lyapunov exponents [1].

However, attractors are not the only invariant sets of chaotic dynamics. In recent years, there has been an increased interest in using unstable periodic orbits (UPO) to characterize chaotic attractors. Indeed, a typical chaotic attractor has embedded in it a dense set of UPO, and one may reasonably hope to use these to approximate the attractor in a hierarchical way: low-period orbits model the overall structure of the attractor, while finer details can be resolved using higher-period ones (see, e.g., [2]). Of particular importance is the fact that UPO can be extracted from experimental time series.

In the phase space of the system, unstable periodic orbits are represented by closed curves. While these are relatively simple objects, they are intertwined in a very complex way due to the chaotic dynamics. For three-dimensional systems with at most one positive Lyapunov exponent, the template analysis proposed by Mindlin *et al.* [3,4] allows one to unfold this complexity by analyzing UPO using concepts from knot theory [5,6]. For example, a pair of periodic orbits can be characterized by their linking number, which measures how many times one orbit winds around the other. The relevance of knot invariants to chaotic dynamics owes much to the fact that determinism precludes that different trajectories intersect. As a consequence, linking numbers and other topological invariants remain constant as a control parameter is varied. Additionally, their invariance with respect to small deformations makes their experimental determination quite insensitive to noise, provided periodic orbits are well separated.

Moreover, a systematic study of the topological organization of the UPO embedded in a chaotic attractor is allowed by the existence of a two-dimensional branched manifold, the *template* (or ''knot-holder'') [7,8], such that all the periodic orbits can be laid on it without modifying any of their topological invariants. The template, whose structure can be concisely described by small integer matrices [3], thus describes the global topological organization of the chaotic attractor. Experimentally, measuring the invariants of a few periodic orbits suffices to determine the associated template, the remaining orbits being used to check the validity of the results [4].

As advocated by their authors [3,4,9], one distinct advantage of this approach is its ability to give a clear-cut

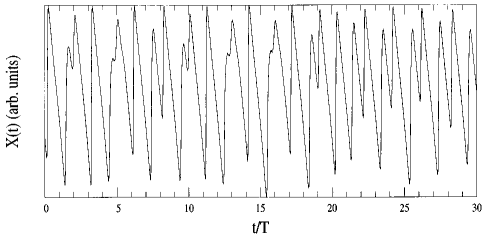

FIG. 1. Time series of $X(t)=\log(I+I_0)$ where I is the laser output intensity and I_0 is a small constant which can be adjusted in the logarithmic amplifier used for signal processing. T is the modulation period.

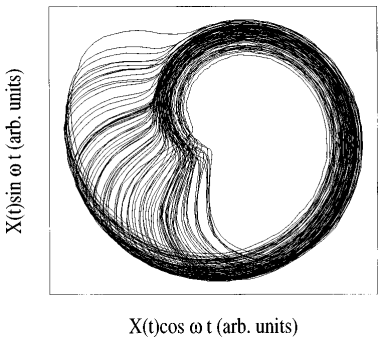

FIG. 2. Phase portrait of the attractor in the plane $[X(t)\cos\phi, X(t)\sin\phi]$, where $\phi=\omega t$ is the modulation phase.

answer as to whether a theoretical model is incompatible with given experimental data. If the analysis of experimental time series and of time series generated from numerical simulations of a model, embedded in the same phase space, yields different templates, then this model, at least for the values of the parameters used in the simulations, has to be rejected.

However, except for a catalytic reaction whose template has unfortunately not been exactly determined [10], most experimental investigations so far, in optics [9,11–13], in chemistry [4,14] or mechanics [15], have revealed the same topological structure, namely the one described by the so-called Smale's horseshoe with zero global torsion. Horseshoe templates with global torsions have been observed in an optical fiber laser [16]. One may then wonder whether the horseshoe class is so ubiquitous as to make template analysis helpless for testing the relevance of a model.

In this Communication we show that this is not the case, by reporting the observation of regimes of a Nd:YAG (yttrium aluminum garnet) laser with pump modulation that are associated with a different type of template. The corresponding topological organization has been theoretically predicted to be observable in nonlinear driven oscillators by Gilmore and McCallum [17] (they termed it ''reverse horseshoe''), but to our knowledge has not yet been encountered in other experiments, nor in numerical studies of models of this type of laser. While this template has a two-branch structure as is the case of the above-mentioned templates, the difference is readily shown by analyzing the lowest-period orbits: the period-$2T$ orbit (T is the modulation period) is unknotted, but the knot type of the period-$3T$ orbits is that of a trefoil knot, the simplest knot beyond a trivial loop. In contrast to this, the period-$2T$ and $3T$ orbits of experimental chaotic attractors characterized by topological analysis were either all unknotted [4,9,11–15] or all knotted [16].

The experimental system consists of a Fabry-Perot laser cavity, end-pumped by a cw laser diode operating at 812 nm. The Nd:YAG rod is 10 mm long, 7 mm in diameter, and contains a nominal Nd^{3+} concentration of 1.1%. One of the two plane ends is highly reflective at the laser wavelength (1064 nm), and the other is antireflection coated. The output coupler is concave, with a radius of curvature of 40 mm, and has a reflectivity of 97%. A Fabry-Perot etalon and a Brewster plate are inserted inside the cavity to select single-mode oscillation on a linear polarization. In these conditions, the pump parameter A (the ratio of pump power to its value at threshold) can range up to 3. In our experiment, the pump power is sinusoidally modulated, $A=A_0(1+m\cos\omega t)$, and the laser undergoes a classical period-doubling cascade leading to chaos when the frequency modulation is of the order of the relaxation frequency ω_r of the laser, which is about 100 kHz here. In this paper, the topological organization of a chaotic regime for parameters $A_0=1.2$, $m=0.5$, and $\omega=54$ kHz, is analyzed. It should be noted that as the resonance frequency markedly decreases when the modulation amplitude is increased, these parameters in fact belong to the resonance tongue originating at $\omega=\omega_r$. The laser output intensity was monitored with a $In_xGa_{1-x}As$ detector, and processed using a logarithmic amplifier in order to obtain a signal suitable for topological analysis (see, e.g., [12]). The present analysis has been carried out on a time series corresponding to 5×10^3 periods of modulation, recorded at a rate of 100 samples per modulation period. A typical signal is shown in Fig. 1.

Let us now briefly describe the procedure of the analysis. First, unstable periodic orbits are extracted from the time series using close return techniques similar to those described in Refs. [4,9,12,13]: a time series segment $\{X(t); t_0<t<t_0+nT\}$ is considered to shadow an unstable period-nT orbit if $|X(t)-X(t+nT)|<\epsilon$ for each $X(t)$ belonging to that segment, where ϵ is in the order of a few percent. Doing so, we detected eight orbits, with periods up to $9T$.

These periodic segments then have to be embedded in a phase space, so that the topological invariants of the corresponding trajectories can be computed. As in previous investigations [12,13], we embedded the time series in a phase space with cylindrical coordinates $[X(t),\dot{X}(t),\phi(t)]$, where $\phi(t)=\omega t \bmod 2\pi$ is the modulation phase. A plane phase portrait of the embedded attractor is displayed in Fig. 2, and a first return map in a section plane of constant phase is plotted in Fig. 3. We recall that the analysis does not require the actual computation of the time derivative of $X(t)$. Rather, given a time series segment corresponding to a period-nT orbit, a simple plot of $X(\phi(t))$ versus $\phi(t)$ displays the orbit as a braid on n strands (see, e.g., [12,13]), as can be seen in Fig. 4. Listing the crossings which occur as ϕ is increased from 0 to 2π gives an algebraic description of the braid, the braid word [6], from which the various topological invariants

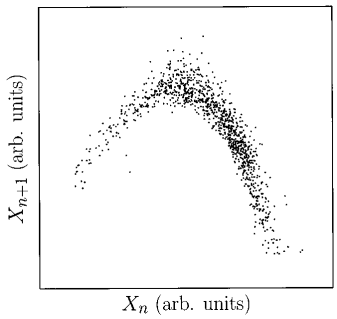

FIG. 3. First return diagram X_{n+1} vs X_n, where $X_n = X(t_0 + nT)$ is a stroboscopic sampling of the signal, and T is the modulation period. This map corresponds to a section plane of constant modulation phase. It can be seen to be highly similar to those observed in systems whose topological organization is described by the standard Smale's horseshoe template.

can be computed. One distinct feature of the embedding we have used is that periodic orbits are naturally presented as positive braids, i.e., all their crossings have the same sign, which can be chosen to be positive. This implies that the entries of the template matrix, which are directly related to the torsions and linking numbers of period-T orbits [3,4], are positive. This property will be of particular importance in the foregoing discussion.

Table I displays the (self-) linking numbers of the lowest-period orbits detected in our experiment. Given this information about the relative placement of the UPO, we may now seek a template that holds a set of periodic orbits with identical periods and topological invariants. As usual, the template branches are labeled ''0,'' ''1,'' . . . , starting from the leftmost branch. We find that two two-branch templates are compatible with the experimental data. They correspond to two equivalent representations of the same topological structure, and can be distinguished according to whether the orbit corresponding to the experimental period-T orbit is located on the ''0'' or the ''1'' branch of the template. For definiteness, and to ease comparison with other works, let this orbit be held by the ''1'' branch. The template matrix of the corresponding solution reads

$$\mathcal{T} = \begin{pmatrix} 2 & 2 \\ 2 & 1 \end{pmatrix}, \tag{1a}$$

with the insertion matrix being

$$\mathcal{I} = (0 \quad -1). \tag{1b}$$

This result is to be contrasted with the standard horseshoe template, whose template and insertion matrices are given by

$$\mathcal{T}_\theta^{\mathrm{HS}} = \begin{pmatrix} 2\theta & 2\theta \\ 2\theta & 1+2\theta \end{pmatrix} = \begin{pmatrix} 0 & 0 \\ 0 & 1 \end{pmatrix} + \theta \begin{pmatrix} 2 & 2 \\ 2 & 2 \end{pmatrix} \tag{2a}$$

$$\mathcal{I}_\theta^{\mathrm{HS}} = (0 \quad 1), \tag{2b}$$

where the integer θ stands for the global torsion.

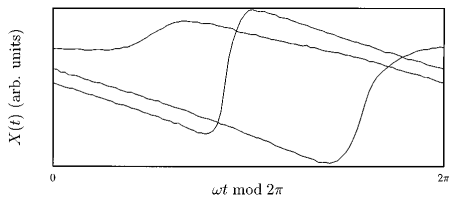

FIG. 4. A time series segment shadowing one of the period-$3T$ orbits is plotted as a function of $\phi(t) = \omega t \bmod 2\pi$. This presents this orbit as a braid on three strands. The number of crossings in this plot gives the self-linking number of the orbit which here is 4. This value is to be contrasted with that obtained for standard horseshoe templates, i.e., $2+6\theta$, where the integer θ is the global torsion.

It should be recalled that, depending on the sign conventions, the same system can be described by two templates differing only by their handedness. However, when using, as here, an embedding which forbids negative topological invariants, only one of them may be a solution. To compare our result to those of previous investigations, we thus choose in each case the sign convention leading to positive invariants. With this point in mind, the $\theta = 0$ case corresponds to the experiments reported in Refs. [4,9,11–15], while horseshoe templates with $\theta = 1$, 2, or 3 have been observed in an optical fiber laser [16].

Rewriting Eq. (1a) as

$$\mathcal{T} = \begin{pmatrix} 0 & 0 \\ 0 & -1 \end{pmatrix} + \begin{pmatrix} 2 & 2 \\ 2 & 2 \end{pmatrix}, \tag{3}$$

it is easily seen that the template we have observed is in fact the mirror image of the standard horseshoe template with zero global torsion [as described by Eqs. (2)], plus a global torsion of one turn. From the discussion above, it should be clear that this discrepancy with previous reports does not stem from an unfortunate choice of sign convention nor of phase-space orientation. Moreover, we do not think that the phenomenon recently described by Mindlin and Solari— under certain conditions the topology of an attractor may dramatically depend on the chosen embedding [18]—can ex-

TABLE I. Self-linking numbers and linking numbers of the lowest-period orbits detected in the experimental time series. The entries left blank correspond to invariants whose value could not be ascertained, because different estimates were obtained when using two different time series segments corresponding to the same orbit.

	$1T$	$2T$	$3T_a$	$3T_b$	$4T$	$5T$	$7T$	$9T$
$1T$	0							
$2T$	1	1						
$3T_a$	2	4	4					
$3T_b$	2	4	6	4				
$4T$	2	5	8		7			
$5T$	3	6	10	10		12		
$7T$		8	14	14			24	
$9T$	5		18					

plain our observations, since the attractors we studied are not split into several disjoint pieces. We can therefore conclude that our results are the signature of a different type of topological organization, and are not due to artifacts of the analysis.

What makes this result highly interesting is that previous template analyses of a modulated CO_2 laser [12,13], using the same embedding as here, found a horseshoe template with zero global torsion. Indeed, the Nd:YAG laser and the CO_2 laser are generally both considered to be class-B lasers, i.e., lasers where the polarization of the gain medium evolves much faster than the inversion population or the radiation intensity [19–21]. As a result, the single-mode behaviors of these two lasers can in principle be modeled by the very same set of equations, the so-called ''two-level rate equations'' [20,21], and correspond to parameters of the same order of magnitude. Furthermore, numerical studies of this model with parameters corresponding to the CO_2 experiments seemed to indicate that the topological organization of its chaotic regimes was globally described by the horseshoe template with zero global torsion [22], until a three-branch spiral template was discovered very recently for slightly different values of the control parameters [23]. As for the reverse horseshoe template that corresponds to our experiment, it remains to be observed in numerical simulations of the modulated class-B laser model.

To summarize, we are in a situation where (i) standard and reverse horseshoes have been observed in laser experiments, and (ii) standard horseshoes and a spiral three-branch template have been identified in numerical studies of these lasers. In view of the complex structure of the bifurcation diagram of nonlinear driven oscillators described by Gilmore and McCallum [17], this gives us some confidence that a systematic exploration of the parameter space of these systems using template analysis may provide an accurate test of the validity of the class-B laser model.

In conclusion, we performed a template analysis of chaotic regimes from a Nd:YAG laser. This characterization showed a topological organization of the reverse horseshoe type, which to our knowledge has not yet been observed experimentally. Topological analysis thus allowed us to unveil clear-cut differences from previous laser experiments which would likely have remained otherwise unnoticed, given the high similarity of the signals corresponding to standard and reverse horseshoes.

We believe that the present work certainly motivates further experiments and numerical investigations of the model describing both these lasers, and illustrates the relevance of template analysis in the study of the dynamical properties of low-dimensional chaotic systems.

The Laboratoire de Spectroscopie Hertzienne is Unité de Recherche Associée au CNRS. The Centre d'Études et Recherches Lasers et Applications is supported by the Ministère chargé de la Recherche, the Région Nord-Pas de Calais, and the Fonds de Développement Économique des Régions.

[1] E. Ott, *Chaos in Dynamical Systems* (Cambridge University Press, Cambridge, 1993).
[2] D. Auerbach *et al.*, Phys. Rev. Lett. **58**, 2387 (1987).
[3] G. B. Mindlin *et al.*, Phys. Rev. Lett. **64**, 2350 (1990).
[4] G. B. Mindlin *et al.*, J. Nonlinear Sci. **1**, 147 (1991).
[5] N. B. Tufillaro, T. A. Abbott, and J. P. Reilly, *An Experimental Approach to Nonlinear Dynamics and Chaos* (Addison-Wesley, Reading, MA, 1992).
[6] L. H. Kaufmann, *Knots and Physics* (World Scientific, Singapore, 1991).
[7] J. S. Birman and R. F. Williams, Topology **22**, 47 (1983).
[8] P. J. Holmes, in *New Directions in Dynamical Systems*, edited by T. Bedford and J. Swift (Cambridge University Press, Cambridge, 1988), pp. 150–191.
[9] F. Papoff *et al.*, Phys. Rev. Lett. **68**, 1128 (1992).
[10] S. O. Firle, M. A. Natiello, and M. Eiswirth, Phys. Rev. E **53**, 1257 (1995).
[11] N. B. Tufillaro *et al.*, Phys. Rev. A **44**, 4786 (1991).
[12] M. Lefranc and P. Glorieux, Int. J. Bifurcation Chaos Appl. Sci. Eng. **3**, 643 (1993).
[13] M. Lefranc *et al.*, Phys. Rev. Lett. **73**, 1364 (1994).
[14] C. Letellier, L. L. Sceller, and J. L. Hudson, J. Phys. C **99**, 7016 (1995).
[15] N. B. Tufillaro *et al.*, Phys. Rev. E **51**, 164 (1995).
[16] G. Boulant, M. Lefranc, S. Bielawski, and D. Derozier, Phys. Rev. E (to be published).
[17] R. Gilmore and J. W. L. McCallum, Phys. Rev. E **51**, 935 (1995).
[18] G. B. Mindlin and H. G. Solari, Phys. Rev. E **52**, 1497 (1995).
[19] F. T. Arecchi, in *Instabilities and Chaos in Quantum Optics*, edited by F. T. Arecchi and R. G. Harrison (Springer, Berlin, 1987), p. 9.
[20] L. M. Narducci and N. B. Abraham, *Laser Physics and Laser Instabilities* (World Scientific, Singapore, 1988).
[21] Y. I. Khanin, *Principles of Laser Dynamics* (Elsevier, Amsterdam, 1995).
[22] H. G. Solari and R. Gilmore, Phys. Rev. A **37**, 3096 (1988).
[23] G. Boulant, M. Lefranc, S. Bielawski, and D. Derozier, Int. J. Bifurcation Chaos Appl. Sci. Eng. (to be published).

"Horseshoe templates with global torsion in a driven laser"

G. Boulant, M. Lefranc, S. Bielawski, and D. Derozier

Phys. Rev. E **55**, 5082–5091 (1997)

PHYSICAL REVIEW E VOLUME 55, NUMBER 5 MAY 1997

Horseshoe templates with global torsion in a driven laser

G. Boulant,* M. Lefranc,† S. Bielawski,‡ and D. Derozier§
Laboratoire de Spectroscopie Hertzienne, URA CNRS 249, Centre d'Etudes et de Recherches Lasers et Applications, Université de Lille I, F-59655 Villeneuve d'Ascq Cedex, France
(Received 26 December 1996)

We perform a topological analysis of chaotic signals from a Nd-doped fiber laser with pump modulation at different values of the modulation frequency. In this experiment, the system displays chaotic behavior in three regions $C_{1/4}$, $C_{1/3}$, and $C_{1/2}$ of parameter space, located around the subharmonics $\omega_r/4$, $\omega_r/3$, and $\omega_r/2$ of the relaxation frequency ω_r. We observe that the topological structures of the chaotic regimes inside a given region $C_{1/n}$ are described by the same template. However, templates corresponding to different regions display different global torsions θ_g, which we find to be related to the order of the subharmonics by $\theta_g(C_{1/n})=n-1$. [S1063-651X(97)09804-8]

PACS number(s): 05.45.+b, 42.65.Sf, 42.55.Wd

I. INTRODUCTION

Template analysis allows a relevant classification and comparison of chaotic attractors according to their topological properties and provides a clear-cut characterization thereof by a set of integer topological indices [1] which are robust with respect to variations in control parameters. In particular, attractors observed experimentally in various fields such as chemistry [2,3], mechanics [4], nuclear magnetic resonance [5], and optics [6–8], have been shown to belong to the same class, namely, that of the Smale's horseshoe with zero global torsion. Let us note, however, that nonhorseshoe dynamics has been reported by Firle, Natiello, and Eiswirth [9] and that other structures have been predicted to be observable in experiments [10,11].

In this paper, our aim is to use topological analysis in order to study and compare the attractors of a single system (a modulated Nd-doped fiber laser), at different values of a control parameter (the modulation frequency ω). We do this in an experimental situation where chaotic behavior is observed when ω lies near the subharmonics 1/2, 1/3, and 1/4 of the natural relaxation frequency ω_r, the highest linear resonance frequency (see, e.g., [12,13]) of the system.

Let us briefly recall the principle of the method. A chaotic attractor has typically embedded in it a dense set of unstable periodic orbits (see, e.g., [14]) which cannot intersect because of the deterministic nature of the evolution laws. Thus the way the unstable periodic orbits (UPO) are linked together can be characterized using concepts from knot theory, provided the attractor is confined to a three-dimensional (3D) manifold. The existence of a two-dimensional manifold, the *template*, such that all UPO can be placed on it while preserving their invariant linking properties, allows one then to describe concisely the global topological organization of the attractor under study.

The fiber laser (FL) is known to be a possibly high-dimensional system with many longitudinal modes oscillating simultaneously. Hence, in Sec. II we describe the experimental system and check that topological analysis is applicable by estimating the Lyapunov dimension of the attractors. Then, Sec. III is devoted to the extraction of UPO from experimental data and the computation of their topological invariants. We show there how careful signal processing can greatly help in extracting topological information from noisy time series of finite length and precision. Finally, in Sec. IV, we determine the templates of the different attractors, compare them, and relate them to the values of the modulation frequency. In particular, we show that these templates have a nonzero global torsion, and that this torsion increases by one full turn when the period of modulation increases by $2\pi/\omega_r$. This observation is in close agreement with the theoretical studies of modulated nonlinear oscillators by Gilmore and McCallum [10].

II. THE EXPERIMENTAL SYSTEM

The experimental setup is a Fabry-Pérot laser cavity. The active medium, a 4 m long silica fiber doped with 300 ppm Nd^{3+}, is pumped by a laser diode emitting a single polarized mode at 810 nm. The optogeometrical properties of the fiber make the laser transversally monomode at the operating wavelength $\lambda=1.08$ μm. However, the large cavity length and the broad inhomogeneous gain profile (100 cm^{-1}) allow some 10 000 longitudinal modes to oscillate simultaneously. In addition, in the absence of polarization selective elements in the cavity, each mode is split into two eigenstates of polarization depending on the birefringence of the fiber [15]. On output, the two polarization eigenstates of the cavity are separated by a polarizing beam splitter combined with an half-wave plate to select the direction of analysis. In typical operating conditions, the low laser threshold allows us to reach pump parameters (i.e., the ratio of the pump power to its value at threshold) up to 5 and to explore a wide range of parameters.

Under modulation of a control parameter, this laser exhibits chaotic oscillations [16], reached via period doubling cascade or quasiperiodicity. In our experiment, we modulate sinusoidally the pump parameter $A(t)=A_0(1+m\cos\omega t)$

*Electronic address: Guillaume.Boulant@univ-lille1.fr
†Electronic address: Marc.Lefranc@univ-lille1.fr
‡Electronic address: Serge.Bielawski@univ-lille1.fr
§Electronic address: Dominique.Derozier@univ-lille1.fr

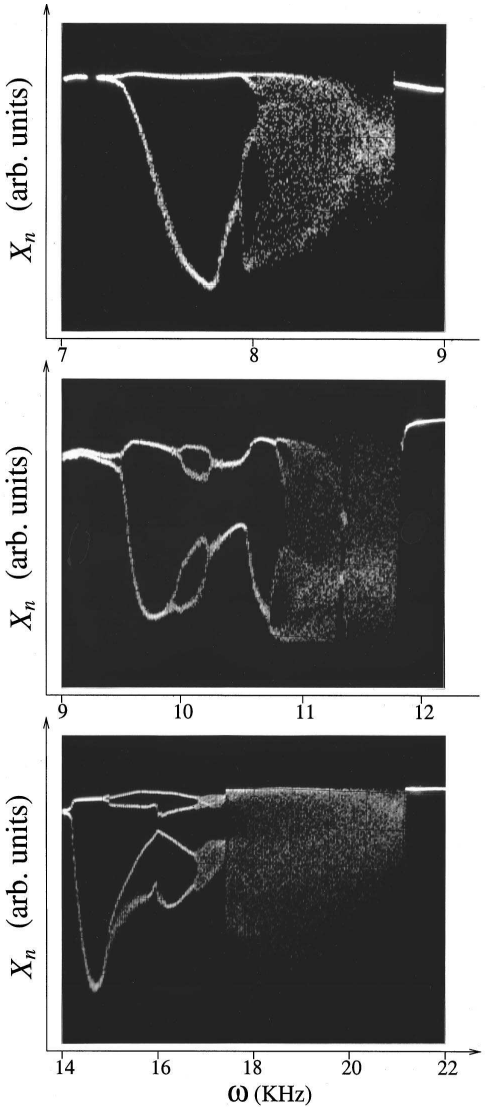

FIG. 1. Experimental bifurcation diagram for increasing modulation frequency. Note the localization of the three chaotic regimes around $\omega_r/4$, $\omega_r/3$, and $\omega_r/2$.

around an average value $A_0=2.7$ with a rate $m=0.6$. The frequency is chosen as a control parameter and swept from 0 to the relaxation frequency ω_r, which, under these conditions, is about 36 kHz. The bifurcation diagram, shown in Fig. 1, displays a sequence of three chaotic windows $C_{1/4}$, $C_{1/3}$, and $C_{1/2}$ located around $\omega_{1/4}\approx 9$ kHz, $\omega_{1/3}\approx 12$ kHz, and $\omega_{1/2}\approx\approx 18$ kHz, respectively. The notations have been chosen to emphasize the harmonic relation between the chaotic frequencies and ω_r

$$\omega_r\approx 2\omega_{1/2}\approx 3\omega_{1/3}\approx 4\omega_{1/4}. \tag{1}$$

TABLE I. Estimated Lyapunov exponents of sample regimes in $C_{1/4}$, $C_{1/3}$, and $C_{1/2}$ regions, given in modulation frequency units. d_L is the Lyapunov dimension defined as $d_L=2+|\lambda_1/\lambda_3|$ according to the Kaplan-Yorke conjecture [29] and is believed to estimate the dimension of the attractor.

Regime	λ_1	λ_2	λ_3	d_L
$C_{1/4}$	0.37	−0.06	−0.57	2.6
$C_{1/3}$	0.34	−0.00	−0.92	2.3
$C_{1/2}$	0.52	−0.03	−0.66	2.7

This bifurcation structure is common in nonlinear oscillators (see, e.g., [10]) except that, in the present case, we do not observe chaotic behavior around the relaxation frequency ω_r.

To verify that, in spite of the great number of degrees of freedom, the dynamics is sufficiently low dimensional so that template analysis can be applied, we have performed Lyapunov exponent estimates for regimes in the three regions using the program DLIA by Briggs [17]. Table I displays the results obtained for three sample regimes. While the numerical values should be taken with caution, especially for the negative exponent (the regimes appear to be much more dissipative than indicated by this analysis), they definitely show that there is only one unstable direction and that three-dimensional volumes are contracted under the action of the flow. This means that most of the dynamical variables relax so quickly that they are enslaved by a few number of collective variables which are confined to a three-dimensional manifold. This motivates the topological analysis carried out in the sequel of this paper, whose relevance will, furthermore, be confirmed by the consistency of the measured topological invariants [18].

III. TOPOLOGICAL ANALYSIS

As complex as it may appear, a strange attractor is a highly organized geometrical object. In particular, it contains an infinite number of unstable periodic orbits (UPO), densely embedded in it (see, e.g., [14]): the neighborhood of any point of the attractor, however small it is, is visited by periodic orbits. As it evolves on a strange attractor, a typical chaotic trajectory visits the neighborhood of a number of these UPO, approaching them along their stable direction and leaving them along the local unstable direction, after an interval of time whose duration depends on how closely the periodic orbit has been approached.

In low-dimensional attractors, the crossing of the neighborhood of an UPO of relatively low period by a chaotic trajectory shows itself clearly in the temporal signal as a burst of almost periodic behavior. This allows one to extract approximations of periodic orbits from experimental time series. Some examples of such sequences, with a high signal to noise ratio, can be found, for instance, in Ref. [7].

Unstable periodic orbits have been recognized as a major tool to analyze chaotic systems. Indeed, they provide a hierarchical approximation of a strange attractor: low-period orbits model the global structure of the attractor, while finer details can be resolved using high-period orbits. One promising and powerful method based on this approach is the

topological analysis proposed by Mindlin *et al.* [1], which proceeds as follows.

Periodic orbits are associated with closed curves in the phase space of the system. When this phase space is three dimensional, these curves can be characterized using the mathematical framework of knot theory (see, e.g., Ref. [19]). The latter associates with a three-dimensional closed curve (or a set of such curves) topological numbers which are invariants with respect to isotopy, i.e., which remain unchanged when the curve is continuously deformed without intersecting itself.

The relevance of these invariants stems from the deterministic nature of chaotic behavior. Indeed the uniqueness theorem (see, e.g., Ref. [20]) implies that a periodic orbit cannot intersect itself or another orbit without violating determinism at the point of intersection. As a result, invariants from knot theory are well defined and are insensitive to deformations induced by modifying a control parameter. For example, the relative placement of a pair (α,β) of unstable periodic orbits can be characterized on its whole domain of existence in parameter space by several topological quantities such as the linking number $lk(\alpha,\beta)$, which indicates how many times α winds around β.

The keystone of topological analysis is that any set of periodic orbits embedded in the attractor is associated to a set of orbits with identical topological invariants on a two-dimensional manifold, called the *template* [21–23,1]. This surface can be viewed as a *knot holder* on which all the periodic orbits extracted from the attractor can be laid down via a continuous deformation without crossing. Thus the template provides a simple and complete description of the global topological organization of the flow.

In this section, we describe the steps we have followed to extract UPO from experimental signals of the FL and to compute their topological invariants. The determination of the corresponding templates will be presented in Sec. IV.

To perform a topological analysis, a time series $X(t)$ has to be embedded in a three-dimensional phase space, so that knot theory can be applied. In Sec. III A, we first describe the particular phase space we have used. Due to the relatively complex nature of the signals coming from the FL, it has been necessary to process them using analog techniques — which we present in Sec. III B — in order to obtain a time series suitable for topological analysis. Indeed, computing the topological invariants of the UPO detected in the time series requires an embedding phase space where orbits are well separated. If two orbits are too close to each other in some region of the attractor, the experimental noise and the slight uncertainty in their precise localization (we use orbits approximating the true UPO) may result in unreliable measurements of their relative positions and, thus, of their linking invariants. In Sec. III C, we briefly review the close-return technique used to extract the unstable periodic orbits from the time series. Last, we classify the detected orbits using symbolic dynamics and compute their topological invariants for chaotic regimes inside the $C_{1/4}$, $C_{1/3}$, and $C_{1/2}$ chaotic regions in Sec. III D.

A. Embedding phase space

As mentioned above, topological analysis requires that the time series $X(t)$ under study be embedded in a 3D phase space. In our experiments, we have used a phase space with coordinates $[X(t),\dot{X}(t),\phi(t)]$, where $\phi(t)=\omega t(\mathrm{mod}\ 2\pi)$ is the phase of the period-T modulation. This phase space, which is schematically displayed in Fig. 2, is topologically equivalent to a solid torus $D^2\times S^1$ (D^2 being the unit disk and S^1 the unit circle). This is a natural geometry for a modulated system, as a Poincaré section of the attractor can be readily obtained by means of a stroboscopic sampling. Moreover, this topology restricts isotopy moves to a smaller class, namely, regular isotopy, and allows one to make use of more powerful invariants, such as the relative rotation rates introduced by Solari and Gilmore [24,25], which provide a finer description of the relative rotation of the UPO than the linking number.

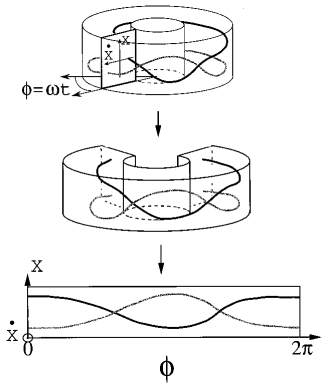

FIG. 2. 3D differential embedding phase space. $X(t)$ is a dynamical variable and ϕ the modulation phase. The topological information (contained in overcrossings and undercrossings) is completely preserved in a plot of X vs ϕ. For example, the two crossings in the latter reflect the fact that each orbit winds one time around the other, which corresponds to a linking number of 1.

$X(t)$ and its time derivatives are natural variables to describe a dynamical system. There is, however, one more reason for choosing the time derivative $\dot{X}(t)$ as the second coordinate. Indeed, the topological structure of a periodic orbit α of period T_α can then be completely analyzed by plotting its representative time series segment $X_\alpha(t)$, $t\in[t_0,t_0+T_\alpha]$ as a function of $\phi=\omega t(\mathrm{mod}\ 2\pi)$ [7]. As illustrated in Fig. 2, this plot can be seen as a projection of the orbit onto the $\dot{X}=0$ cylinder along the $\dot{X}$ direction, and presents the orbit as a braid on n strands. Topological information is preserved provided that we know at each crossing which of the two strands passes over the other in the 3D space. This is, in fact, trivial since the strand with the greater slope corresponds to the higher value of $\dot{X}$.

As a result, listing the successive crossings as ϕ increases from 0 to 1 provides an algebraic description of the topological structure of the orbit, from which any topological invariant can be readily computed. As a simple example, computing the linking number of two orbits amounts to counting the number of crossings between the strands of these two orbits in a $X(\phi)$ plot (see the example of Fig. 2).

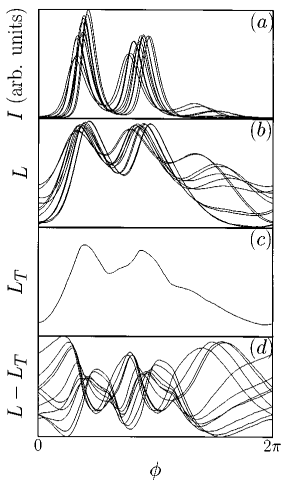

FIG. 3. Enhancement of the topological information of the signal by analog processing. (a) A polarization eigenstate intensity: I. (b) Logarithmic amplification of this signal: $L=\ln(I)$. (c) The unwanted period-T oscillation L_T. (d) The final signal $X=L-L_T$.

Clearly, evaluating this number requires that different strands be well separated, particularly because of the limited resolution of the eight-bit transient digitizer used in the experiments. This is not necessarily so when directly recording a natural variable of the system, for example, the laser intensity. In this case, the signal has to be processed using analog techniques before the topological analysis of digitized data can be carried out.

B. Signal processing

As Fig. 3(a) shows, the intensity I of a polarization eigenstate is not a suitable variable, because it almost completely vanishes during long periods of time. In these regions of low intensity, the different orbits are indiscernible and we cannot determine whether some crossings occur. As advocated in Ref. [26], this problem can be overcome by using a logarithmic amplifier which delivers an output signal $L(t)=\ln(I(t)+I_0)$. Let us note that this procedure, successfully followed in previous topological investigations of the modulated CO_2 laser [7,8], preserves the topological information since $L(t)$ is a monotonic function of $I(t)$.

As can be seen in Fig. 3(b), this first step improves the quality of the signal to some extent but yet does not suffice. Indeed, the resulting signal $L(t)$ displays a strong periodic component at frequency $1/T$ which masks the rest of the dynamics: the signal remains confined to a narrow band around this period-T oscillation. Fortunately, any T-periodic transformation of the form $L(t)\rightarrow L(t)+f(\phi(t))$ does not modify the relative positions of crossings and, hence, leaves isotopy invariants unchanged.

Experimentally, one simple way to proceed is thus to subtract a T-periodic signal $L_T(t)=L_T(\phi(t))$ from $L(t)$, where $L_T(t)$ approximates the unwanted period-T oscillation. In our experiments, we have chosen $L_T(t)$ to be

$$L_T(t)=\frac{\xi_+(\phi(t))+\xi_-(\phi(t))}{2}, \tag{2}$$

where $\xi_+(\phi(t))$ and $\xi_-(\phi(t))$ are, respectively, the high and low envelopes of $L(t)$ computed from a record of about 1000 modulation periods

$$\xi_+(\phi_0)[\text{resp. } \xi_-(\phi_0)]=\max(\text{resp. min})\{L(t);\phi(t)=\phi_0\}.$$

Figure 3(c) displays the L_T correction corresponding to the signal of Fig. 3(b).

This periodic signal is then generated with a programmable synthesizer phase locked on the modulation, and subtracted from the output of the logarithmic amplifier. The final signal, shown in Fig. 3(d), clearly displays the topological information and provides a suitable dynamical variable. In the following, the time series $X(t)$ will, thus, always designate the dynamical variable

$$X(t)=L(t)-L_T(\phi(t)) \tag{3}$$

and the embedding 3D phase space will be the $D^2\times S^1$ torus $[X(t),\dot{X}(t),\phi(t)]$.

C. Detection of the unstable periodic orbits

The extraction of periodic orbits embedded in the attractor is carried out by applying to time series of $X(t)$ the close-return technique proposed in Ref. [2]. The latter proceeds by looking for time series segments $\{X(t);t\in[t_0,t_0+pT]\}$ satisfying

$$|X(t+pT)-X(t)|<\varepsilon \qquad \text{for } t_0<t<t_0+pT. \tag{4}$$

Such a sequence indicates that the trajectory in phase space is shadowing a period-pT orbit and can be used as an approximation of this orbit, as better as ε is smaller.

In our experiments, with a signal to noise ratio in the order of 1%, we have chosen ε to be 5% of the maximum amplitude of $X(t)$ and have narrowed the search to orbits of period pT up to $p=10$.

Due to ergodicity, an infinitely long chaotic trajectory passes arbitrary close to any UPO. On the contrary, a finite experimental time series can only approach a finite number of periodic orbits. Furthermore, the presence of noise will prevent higher-period orbits to be shadowed over a sufficient interval of time. Therefore, only a relatively small number of orbits can, in practice, be extracted, except when the signal to noise ratio is high. For each attractor we have recorded signals over 10 000 modulation periods, which typically contained some hundred almost periodic sequences, corresponding to about ten distinct UPO for the $C_{1/4}$ and $C_{1/3}$ regions. In the $C_{1/2}$ region, we have observed the chaotic regimes to be much less dissipative than in the two former ones. This adversely affects the detection of the UPO for two reasons: the time needed before entering the neighborhood of a given UPO is significantly increased, and the influence of noise is strengthened. This explains why the results we present for this part of the parameter space are obtained from a smaller number of periodic orbits than for the $C_{1/4}$ and $C_{1/3}$ regimes. We are currently trying to design an alternate detection method to overcome this limitation.

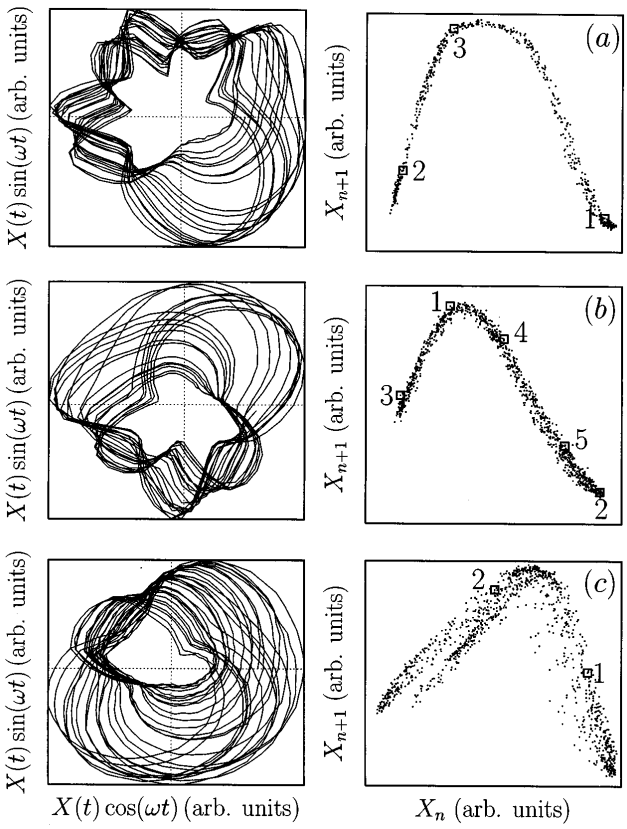

FIG. 4. Two-dimensional projections of attractors (on the left) and their corresponding first return diagram (X_{n+1},X_n), where X_n is the stroboscopically sampled variable $X_n=X(\phi_0+2n\pi)$. (a) Regime $C_{1/4}$. (b) Regime $C_{1/3}$. (c) Regime $C_{1/2}$. Note that these return diagrams are well approximated by a unimodal map, and can be used to perform a symbolic encoding of the orbits. On diagram (a) is plotted the $xxy=x^2y$ period-$3T$ orbit, on (b) the x^2y^3 period-$5T$ orbit, and on (c) the xy period-$2T$ orbit.

D. Spectrum of periodic orbits and computation of the topological invariants

Template analysis is significantly easier when the extracted periodic orbits can be classified using symbolic dynamics. Symbolic dynamics is a powerful approach of chaotic behavior and proceeds by representing a chaotic trajectory as a sequence of symbols while retaining most of the dynamical information. Most topological investigations, so far, have been carried out in cases where symbolic coding could be obtained by means of 1D first return maps [2,5–7], with the exception of Ref. [8].

For each regime of the FL, the 1D first return diagram (X_n,X_{n+1}), where the $X_n=X(t_0+nT)$ are obtained by a stroboscopic sampling, is well approximated by a unimodal map of an interval onto itself: $X_{n+1}=P(X_n)$, as can be seen in Fig. 4. The theory of symbolic dynamics for such maps is well established (see, e.g., Ref. [27]) and thus can be used here to encode periodic orbits.

A unimodal map has a single critical point X_c which separates the regions with positive and negative slope. A pT orbit, identified by p samples $X_1=X(t_1)$, $X_2=X(t_1+T),\ldots,X_p=X(t_1+(p-1)T)$, is encoded by a binary string $\overline{s_1s_2\ldots s_p}$, where $s_i=x$ (respectively, y) when $X_i<X_c$ (respectively, $X_i>X_c$). As an example, the period-$3T$ orbit $\overline{yxx}=\overline{yx^2}$ of a $C_{1/4}$ regime, the period-$5T$ $\overline{yxxyy}=\overline{yx^2y^2}=\overline{x^2y^3}$ of a $C_{1/3}$ regime, and the period-$2T$ $\overline{xy}$ of the $C_{1/2}$ regime are displayed in Figs. 4(a)–4(c). The relevance of this symbolic encoding will fully appear in Sec. IV.

Once the periodic orbits have been extracted and classified according to symbolic dynamics, one can proceed to compute their topological invariants. For each periodic orbit, we have computed its self-linking number and self-relative rotation rates, while pairs of orbits have been characterized by their linking number and relative rotation rates. Note that, with the exception of the linking number, these invariants are available thanks to the toroidal topology of the phase space.

(Self-)linking numbers are determined by counting crossings in $X(\phi)$ plots as described in Sec. III A: the self-linking (respectively, linking) number is simply the sum (respectively, half-sum) of the number of crossings of the orbit with itself (respectively, the other orbit).

As for the relative rotation rates, let us briefly recall that a period-pT orbit α and a period-qT orbit β can be characterized by $p\times q$ relative rotation rates $\{Rij(\alpha,\beta);\ i=1,\ldots,p \text{ and } j=1,\ldots,q\}$. If the intersections of α and β with a Poincaré section are labeled $X_1^\alpha,\ldots,X_p^\alpha$ and $X_1^\beta,\ldots,X_q^\beta$, the R_{ij} relative rotation rate is defined as the

TABLE II. Relative rotation rates of UPO extracted from the $C_{1/4}$ regime. The exponents indicate the relative weight of the given values. For example, the pair $(5T_b,5T_c)$ is characterized by $5\times5=25$ rotation rates, of which $15=3\times5$ (respectively, $10=2\times5$) take the value 17/5 (respectively, 16/5). Blank entries correspond to measurements whose exact value could not be ascertained.

Orbits	T	$2T$	$3T_a$	$3T_b$	$4T$	$5T_a$	$5T_b$	$5T_c$
$T=y$	0							
$2T=xy$	$\frac{7}{2}$	$0,\frac{7}{2}$						
$3T_a=xy^2$	$\frac{10}{3}$	$\frac{10}{3}$	$0,(\frac{10}{3})^2$					
$3T_b=x^2y$	$\frac{10}{3}$	$\frac{10}{3}$	$\frac{10}{3}$	$0,(\frac{10}{3})^2$				
$4T=xy^3$	$\frac{7}{2}$	$\frac{13}{4},\frac{7}{2}$	$\frac{10}{3}$	$\frac{10}{3}$	$0,\frac{13}{4},(\frac{7}{2})^2$			
$5T_a=x^2y^3$	$\frac{17}{5}$	$\frac{33}{10}$	$\frac{49}{15}$	$\frac{10}{3}$	$\frac{67}{20}$	$0,(\frac{16}{5})^2,(\frac{17}{5})^2$		
$5T_b=x^2yxy$	$\frac{17}{5}$			$\frac{10}{3}$	$\frac{67}{20}$		$0,(\frac{16}{5})^2,(\frac{17}{5})^2$	
$5T_c=xyxy^2$	$\frac{17}{5}$	$\frac{17}{5}$	$\frac{10}{3}$			$(\frac{16}{5})^2,(\frac{17}{5})^3$	$(\frac{16}{5})^2,(\frac{17}{5})^3$	$0,(\frac{17}{5})^4$
$6T_a=x^2y^2xy$	$\frac{10}{3}$	$\frac{10}{3}$	$\frac{19}{6},(\frac{10}{3})^2$	$\frac{10}{3}$	$\frac{10}{3}$	$\frac{33}{10}$	$\frac{33}{10}$	$\frac{10}{3}$
$6T_b=x^2y^4$	$\frac{10}{3}$	$\frac{10}{3}$	$\frac{19}{6},(\frac{10}{3})^2$	$\frac{10}{3}$	$\frac{10}{3}$	$\frac{33}{10}$	$\frac{33}{10}$	$\frac{10}{3}$
$6T_c=x^2yxy^2$	$\frac{10}{3}$	$\frac{10}{3}$		$\frac{10}{3}$	$\frac{10}{3}$	$\frac{33}{10}$		
$8T=x^2y^3x^2y$	$\frac{27}{8}$	$\frac{13}{4},\frac{27}{8}$						

	$6T_a$	$6T_b$	$6T_c$	$8T$
$6T_a=x^2y^2xy$	$0,\frac{19}{6},(\frac{10}{3})^4$			
$6T_b=x^2y^4$		$0,\frac{19}{6},(\frac{10}{3})^4$		
$6T_c=x^2yxy^2$	$\frac{19}{6},(\frac{10}{3})^5$		$0,\frac{19}{6},(\frac{10}{3})^4$	
$8T=x^2y^3x^2y$				$0,(\frac{27}{8})^3,(\frac{13}{4})^4$

number of times trajectories starting from X_i^α and X_j^β wind around each other until both return simultaneously to their initial condition, divided by the number of elapsed periods. Self-relative rotation rates are similarly defined for single orbits with the convention that $R_{ii}(\alpha,\alpha)=0$. The reader may find a more detailed exposition in Refs. [24,25,5,28]. In practice their determination amounts to evaluating partial sums of crossings.

Inside each of the $C_{1/4}$, $C_{1/3}$, and $C_{1/2}$ regions of parameter space, we have analyzed several chaotic regimes, and we present below the spectra of orbits and the measured invariants for three sample regimes. Table II collects the symbolic sequences and (self-)relative rotation rates for the one located in the $C_{1/4}$ region. Table III displays the corresponding linking numbers, which are computed from the relation [24,25,28]

$$lk(\alpha,\beta)=\sum_{i=1}^{p}\sum_{j=1}^{q}R_{ij}(\alpha,\beta). \tag{5}$$

The self-linking number of an orbit α is simply given by $slk(\alpha)=lk(\alpha,\alpha)$. Tables IV and V contain the linking numbers for the regimes located inside the $C_{1/3}$ and $C_{1/2}$ regions.

A variation of a control parameter modifies the spectrum of orbits. This explains why no period $3T$ orbit appears in Table IV: the corresponding chaotic regime is located before the $3T$ periodic window, in contrast with the two other

TABLE III. Linking and self-linking numbers of the UPO extracted from the $C_{1/4}$ regime. For example, $lk(2T,4T)=4\times\frac{13}{4}+4\times\frac{7}{2}=27$.

Orbits	T	$2T$	$3T_a$	$3T_b$	$4T$	$5T_a$	$5T_b$	$5T_c$	$6T_a$	$6T_b$	$6T_c$	$8T$
$T=y$	0											
$2T=yx$	7	7										
$3T_a=x^2y$	10	20	20									
$3T_b=xy^2$	10	20	30	20								
$4T=xy^3$	14	27	40	40	41							
$5T_a=x^2y^3$	17	33	49	50	67	66						
$5T_b=x^2yxy$	17			50	67		66					
$5T_c=y^2xyx$	17	34	50			83	83	68				
$6T_a=x^2y^2xy$	20	40	59	60	80	99	99	100	99			
$6T_b=x^2y^4$	20	40	59	60	80	99	99	100		99		
$6T_c=x^2yxy^2$	20	40		60	80	99			119		99	
$8T=x^2y^3x^2y$	27	53										185

TABLE IV. Linking and self-linking numbers of the UPO extracted from the $C_{1/3}$ regime.

Orbits	T	$2T$	$4T$	$5T_a$	$5T_b$	$6T_a$	$6T_b$	$7T_a$	$7T_b$	$7T_c$	$9Ta$	$9Tb$
$T=y$	0											
$2T=xy$	5	5										
$4T=xy^3$	10	19	29									
$5T_a=xy^4$	12	24	48	48								
$5T_b=xyxy^2$	12	24	48	60	48							
$6T_a=xy^5$	15	29		72	72	73						
$6T_b=xyxy^3$	15	29	58	72	72		73					
$7T_a=xyxyxy^2$	17	33	67	84	83	101	100	100				
$7T_b=xy^6$	17	34	68	84	84		102	118	102			
$7T_c=xyxy^4$	17	34	68	84	84	102				102		
$9T_a=xy^2xyxy^3$	22	43	86	108		130				151	172	
$9T_b=xyxyxy^4$	22	43	87									174

sample regimes. We have observed that inside a single region $C_{1/n}$, topological invariants depend on symbolic sequences only. For example, we have found $lk(y,xy)=7$ for any $C_{1/4}$-type regime. Since the linking number of two orbits does not depend on control parameters in their whole domain of existence, this gives strong evidence that a given periodic orbit is associated to one and only one symbolic sequence throughout a chaotic region $C_{1/n}$.

On the contrary, two orbits with the same symbolic sequence, but which belong to two different $C_{1/n}$ regions, appear to be different, as shown by their topological properties. For example, we have found that $lk(y,xy)=7$ in the $C_{1/4}$ region but $lk(y,xy)=5$ (respectively, 3) in the $C_{1/3}$ (respectively, $C_{1/2}$) one. As we will see in Sec. IV, this discrepancy is explained by the fact that these regions correspond to three different templates, and thus to three different types of topological organization.

IV. DETERMINATION OF THE TEMPLATES

As we have seen in the preceding section, the first stage of topological analysis yields tables collecting the invariants of orbits and pairs of orbits, from which the global structure of the flow is hard to discern.

To gain more insight into this structure, the organization of the knotted orbits can be modeled by means of a branched 2D manifold, the *template*. The mathematical definition of a template (a.k.a. ''knot holder'') has been introduced by Birman and Williams [21]. They have proved that the periodic orbits of a three-dimensional hyperbolic flow exhibiting chaos are in one-to-one correspondence with those of a semiflow defined on the template. The latter is obtained by collapsing the invariant set of the 3D flow along its stable manifold, i.e., by identifying points whose images converge to each other as time goes to infinity. As, for obvious reasons, a periodic orbit intersects neither its stable manifold nor those of other periodic orbits, the topological organization is preserved in the process.

TABLE V. Linking and self-linking numbers of UPO extracted from the $C_{1/2}$ regime.

Orbits	T	$2T$	$3T$	$4T$	$10T$
$T=x$	0				
$2T=xy$	3	3			
$3T=x^2y$	4	8	8		
$4T=x^2y^2$	5	10	15	15	
$10T=xy^2x^2y^2x^2y$	13				

Strange attractors are generally not hyperbolic. In particular, periodic orbits can be created or destroyed as a control parameter is varied. However, existing periodic orbits are linked as in the hyperbolic limit, since their topological invariants do not depend on control parameters, and can be put in correspondence with some periodic orbits of the hyperbolic template. Thus, for experimental systems, the template is still a relevant concept but differ from the mathematical definition by the fact that not all its periodic orbits do have a counterpart in the attractor.

One of the most simple chaotic topological structures is the one described by the horseshoe template, named after the Smale's horseshoe, a celebrated paradigm of a chaotic dynamical system (see, e.g., Ref. [28]). Figure 5 shows the horseshoe template holding a $3T$ orbit. It is essentially divided into two parts. The most important one models the folding and stretching processes organizing the strange attractor. At its beginning, the surface splits into several branches (two in the present case). Each branch may be twisted by an integer number of half turns and/or wind around the other branches. All branches then rejoin each other along a common line (the *branch line*) where they are

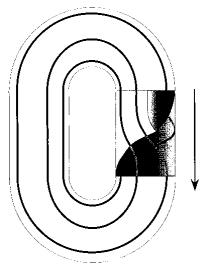

FIG. 5. The horseshoe template holding the x^2y period-$3T$ orbit. Its algebraic representation is given by the matrices in Eqs. (8).

superimposed in a certain order. The remaining part merely connects the branch line with the one where branches split off. It may display one or more full twists, whose number is called the global torsion of the template.

The horseshoe template is of particular interest not only because of its simplicity but also because it is the only one that has been, so far, clearly observed in experimental systems. It has been identified in optical systems, such as CO_2 lasers with modulated losses [7,8] or with a saturable absorber [6], a NMR laserlike oscillator [5], and other dynamical systems such as the Belousov-Zhabotinskii chemical reaction [2], an electrochemical reaction [3], or a vibrating string [4].

To relate experimentally measured invariants to the structure of the template, an algebraic description of the latter is needed. As proposed by Mindlin *et al.* [1,2], this can be achieved by defining two matrices, the $n\times n$ template matrix $\mathcal{T}$ and the $1\times n$ insertion matrix $\mathcal{I}$, where n is the number of branches of the template.

As we will see below, the topological organization of the chaotic regimes described in previous sections, corresponds to templates with two branches, and we therefore limit ourselves in the sequel to the $n=2$ case. Let us label the two branches x and y. We recall that each periodic orbit on the template can be given a unique symbolic name (which we write overlined) by listing the symbols of the branches that it successively visits. For example, the $\overline{x^2y^3}$ orbits visits branch x twice, then branch y thrice before returning to its starting point. In particular, there are two period-1 orbits $\overline{x}$ and $\overline{y}$ associated to the two branches of the template.

The template matrix is written out as

$$\mathcal{T}=\begin{pmatrix} t_x & 2l \\ 2l & t_y \end{pmatrix}, \tag{6}$$

where t_x (respectively, t_y) is the local torsion, in units of π, of the $\overline{x}$ (respectively, $\overline{y}$) orbit, and thus the number of half-twists of the associated branch, and $l=lk(\overline{x},\overline{y})$ is the linking number of the $\overline{x}$ and $\overline{y}$ orbits.

The insertion matrix $\mathcal{I}$ reads

$$\mathcal{I}=(0 \quad m), \tag{7}$$

where $m=1$ (respectively, -1) if the y branch is above (respectively, below) the x branch on the branch line.

For example, the horseshoe structure with zero global torsion of Fig. 5 is described by the two following matrices:

$$\mathcal{T}_{hs}=\begin{pmatrix} 0 & 0 \\ 0 & 1 \end{pmatrix}, \tag{8a}$$

$$\mathcal{I}_{hs}=(0 \quad 1). \tag{8b}$$

The four numbers t_x, t_y, l, and m completely describe the structure of a two-branch template. As a result, the linking number of two periodic orbits with given symbolic sequences, as well as their self-linking numbers, can be expressed as functions of these numbers using techniques similar to those presented in Ref. [28]. In fact, these formulas are almost nearly linear, except for the presence of terms involving $o(t_{x,y})$, where $o(t)$ indicates the parity of $t\in Z$: $o(t)=1$ (respectively, 0) if t is odd (respectively, even).

Determining the template structure from the experimentally measured invariants thus amounts to equating the formulas yielding the invariants of some extracted orbits with the measured values, and then solving for the four unknowns t_x, t_y, l, and m. Four equations should, in principle, suffice. However, due to the presence of the $o(t_{x,y})$ terms, the computation is usually simpler when using a few more equations. As an example, we now determine the topological structure of the $C_{1/4}$ sample regime from the following five equations:

$$slk(\overline{xy})=2l+m=7, \tag{9a}$$

$$lk(\overline{y},\overline{xy})=l+\tfrac{1}{2}[t_y+o(t_y)m]=7, \tag{9b}$$

$$lk(\overline{y},\overline{xyy})=l+t_y=10, \tag{9c}$$

$$lk(\overline{y},\overline{xyyy})=l+\tfrac{1}{2}[3t_y+o(t_y)m]=14, \tag{9d}$$

$$lk(\overline{xy},\overline{xxy})=3l+m+t_x+\tfrac{1}{2}[t_y+o(t_y)m]=20. \tag{9e}$$

Combining Eqs. (9b) and (9d) yields

$$t_y=lk(\overline{y},\overline{xyyy})-lk(\overline{y},\overline{xy})=7. \tag{10}$$

Substituting this value of t_y in Eq. (9c) readily gives

$$l=10-t_y=3. \tag{11}$$

Equation (9a) then indicates that

$$m=7-2l=1, \tag{12}$$

and, finally, Eq. (9e) yields the last unknown

$$t_x=20-3l-m-\tfrac{1}{2}[t_y+o(t_y)m]=6. \tag{13}$$

The template and insertion matrices are thus equal to

$$\mathcal{T}=\begin{pmatrix} 6 & 6 \\ 6 & 7 \end{pmatrix}=\underbrace{\begin{pmatrix} 0 & 0 \\ 0 & 1 \end{pmatrix}}_{\text{horseshoe}}+\underbrace{3\times\begin{pmatrix} 2 & 2 \\ 2 & 2 \end{pmatrix}}_{\text{global torsion}} \tag{14a}$$

$$\mathcal{I}=(0 \quad 1), \tag{14b}$$

In Eq. (14a), the decomposition of $\mathcal{T}$ shows that the corresponding template has a horseshoelike structure with a global torsion of 3. Indeed, as illustrated by Fig. 6, each element of a template matrix is increased by two when one full turn is added to the global torsion.

Note that we have found t_x and t_y to be even and odd, respectively. This could have been expected, as x and y, respectively, correspond to the branches of positive and negative slope of the 1D first return map. Hence, we could have slightly simplified the calculation by assuming from the beginning that $o(t_x)=0$ and $o(t_y)=1$. However, we wanted to stress that this piece of information is not strictly required.

As the reader may have noticed, we have used fewer topological invariants than have been measured. The remain-

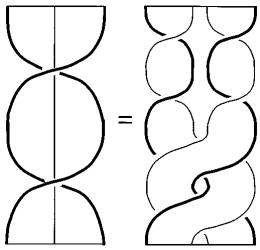

FIG. 6. Illustration of global torsion. Cutting the left ribbon in the middle yields the two ribbons on the right. It is easily seen that the contribution of the latter to the template matrix elements t_x, t_y, and $2l$ is equal to two.

ing ones can, thus, be used to validate the template by verifying that they are correctly predicted by the solution displayed in Eqs. (14). As an example,

$$lk(\overline{xyxy^2},\overline{x^2y^2xy}) = 15l + 3t_x + \tfrac{9}{2}t_y + m\{\,6 - o(t_y)[\tfrac{1}{2} + o(t_x)]\,\}. \quad (15)$$

It can be easily checked that the experimentally measured value of 100 is obtained by substituting in Eq. (15) the values of t_x, t_y, l, and m given by Eqs. (14). In the same way, we have verified that all the unambiguous invariants listed in Tables II and III were correctly predicted by the template given in Eqs. (14).

The same procedure has been carried out for the chaotic attractors of the $C_{1/3}$ and $C_{1/2}$ windows and reveals horseshoe templates with global torsions of 2 and 1, respectively, [see Figs. 7(b) and 7(c)]

$$\mathcal{T}_{1/3} = \begin{pmatrix} 4 & 4 \\ 4 & 5 \end{pmatrix} = \begin{pmatrix} 0 & 0 \\ 0 & 1 \end{pmatrix} + 2 \times \begin{pmatrix} 2 & 2 \\ 2 & 2 \end{pmatrix}, \quad (16a)$$

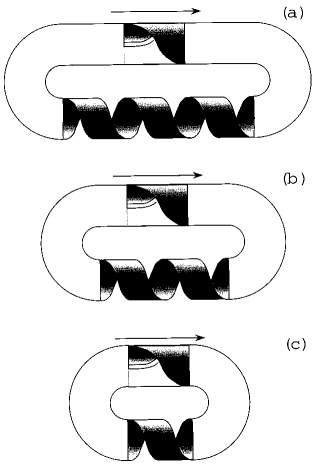

FIG. 7. Evolution of the template with the control parameter. (a) $C_{1/4}$ (b) $C_{1/3}$ (c) $C_{1/2}$.

$$\mathcal{I}_{1/3} = (0 \quad 1) \quad (16b)$$

and

$$\mathcal{T}_{1/2} = \begin{pmatrix} 2 & 2 \\ 2 & 3 \end{pmatrix} = \begin{pmatrix} 0 & 0 \\ 0 & 1 \end{pmatrix} + 1 \times \begin{pmatrix} 2 & 2 \\ 2 & 2 \end{pmatrix}, \quad (17a)$$

$$\mathcal{I}_{1/2} = (0 \quad 1). \quad (17b)$$

It should be noted that for $\mathcal{T}_{1/2}$, due to the limited number of invariants, another template, with $t_y = 4$ instead of 3, is compatible with the measured topological invariants. We have, however, discarded this solution as (i) it does not reproduce the known parities of the two branches, (ii) a difference of two between the torsions of the two branches seems incompatible with the existence of a continuous flow.

It thus appears that chaotic regimes located inside the three chaotic regions $C_{1/2}$, $C_{1/3}$, and $C_{1/4}$ experience the same stretching and folding mechanisms as those described by Smale's horseshoe, but that they can be distinguished according to the global torsion of the template. The latter is closely connected to the ratio of the control parameter ω to the linear resonance frequency ω_r, as expected from the theoretical studies on nonlinear oscillators by Gilmore and McCallum [10]. The reader may verify that the existence of this global torsion is visible in Fig. 4 where global twists of, respectively, three, two, and one full turns can easily be seen.

V. CONCLUSION

We have analyzed the topological structure of chaotic attractors of a pump-modulated Nd-doped fiber laser for various values of the modulation frequency. Under the experimental conditions investigated, these chaotic regimes are found in islands $C_{1/n}$ located around the subharmonics ω_r/n $(n=2,3,4)$ of the relaxation frequency ω_r.

Our main result is that the topological organization of the regimes found inside the $C_{1/n}$ region is not described by a simple horseshoe template, but by a horseshoe with a global torsion θ_g of $n-1$ in 2π units. This relation agrees with the theoretical study of the topology of nonlinear driven oscillators carried out by Gilmore and McCallum [10], and should accordingly hold in other experimental driven systems exhibiting chaos at subharmonic resonances. However, the present work provides, to our best knowledge, the first experimental illustration of this phenomenon, as well as the first experimental characterization of a system yielding different templates for different regions of the parameter space, in particular, templates with a nonzero global torsion.

Let us conclude by noting that more complex templates than those reported here should be found in other regions of parameter space. In the present study, indeed, the successive resonance tongues $C_{1/n}$ are separated by stable period-T behavior. When leaving the $C_{1/n}$ domain, all periodic orbits embedded in the strange attractor must be annihilated before the $C_{1/(n+1)}$ region is reached, because their invariants are

incompatible with the new topological organization. However, it is well known that resonance tongues may overlap when the modulation amplitude is sufficiently increased (see, e.g., [10]). In this case, some UPO of the $C_{1/n}$ domain can coexist in the same attractor with UPO of the $C_{1/(n+1)}$ region. As none of the above-mentioned templates can support simultaneously both types of orbits, this calls for the existence of more complex templates with more than two branches. The hope of observing such a template certainly motivates further experimental investigations of the fiber laser and of other modulated class-*B* lasers.

ACKNOWLEDGMENTS

The Laboratoire de Spectroscopie Hertzienne is Unité de Recherche Associee au CNRS. The Centre d'Etudes et Recherches Lasers et Applications is supported by the Ministère Chargé de la Recherche, the Région Nord-Pas de Calais and the Fonds de Développement Economique des Régions.

[1] G. B. Mindlin *et al.*, Phys. Rev. Lett. **64**, 2350 (1990).
[2] G. B. Mindlin *et al.*, J. Nonlinear Sci. **1**, 147 (1991).
[3] C. Letellier, L. L. Sceller, and J. L. Hudson, J. Phys. Chem. **99**, 7016 (1995).
[4] N. B. Tufillaro *et al.*, Phys. Rev. E **51**, 164 (1995).
[5] N. B. Tufillaro *et al.*, Phys. Rev. A **44**, 4786 (1991).
[6] F. Papoff *et al.*, Phys. Rev. Lett. **68**, 1128 (1992).
[7] M. Lefranc and P. Glorieux, Int. J. Bifurcation Chaos Appl. Sci. Eng. **3**, 643 (1993).
[8] M. Lefranc *et al.*, Phys. Rev. Lett. **73**, 1364 (1994).
[9] S. O. Firle, M. A. Natiello, and M. Eiswirth, Phys. Rev. E **53**, 1257 (1995).
[10] R. Gilmore and J. W. L. McCallum, Phys. Rev. E **51**, 935 (1995).
[11] G. Boulant, M. Lefranc, S. Bielawski, and D. Derozier, Int. J. Bifurcation Chaos Appl. Sci. Eng. (to be published).
[12] D. Pieroux and P. Mandel, Opt. Commun. **107**, 245 (1994).
[13] Y. I. Khanin, *Principles of Laser Dynamics* (Elsevier, Amsterdam, 1995).
[14] D. Auerbach *et al.*, Phys. Rev. Lett. **58**, 2387 (1987).
[15] S. Bielawski, D. Derozier, and P. Glorieux, Phys. Rev. A **46**, 2811 (1992).
[16] D. Derozier, S. Bielawski, and P. Glorieux, Opt. Commun. **83**, 97 (1991).
[17] K. Briggs, Phys. Lett. A **151**, 27 (1990).
[18] G. B. Mindlin and R. Gilmore, Physica D **58**, 229 (1992), special issue on Interpretation of Time Series from Nonlinear Dynamics.
[19] L. H. Kaufmann, *Knots and Physics* (World Scientific, Singapore, 1991).
[20] J. Guckenheimer and P. J. Holmes, *Nonlinear Oscillations, Dynamical Systems, and Bifurcations of Vector Fields* (Springer, Berlin, 1983).
[21] J. S. Birman and R. F. Williams, Topology **22**, 47 (1983).
[22] P. J. Holmes, in *New Directions in Dynamical Systems*, edited by T. Bedford and J. Swift (Cambridge University Press, Cambridge, 1988), pp. 150–191.
[23] P. J. Holmes, Physica D **40**, 42 (1989).
[24] H. G. Solari and R. Gilmore, Phys. Rev. A **37**, 3096 (1988).
[25] N. B. Tufillaro, H. G. Solari, and R. Gilmore, Phys. Rev. A **41**, 5717 (1990).
[26] M. Lefranc, D. Hennequin, and P. Glorieux, Phys. Lett. A **163**, 269 (1992).
[27] B.-L. Hao, *Elementary Symbolic Dynamics and Chaos in Dissipative Systems* (World Scientific, Singapore, 1989).
[28] N. B. Tufillaro, T. A. Abbott, and J. P. Reilly, *An Experimental Approach to Nonlinear Dynamics and Chaos* (Addison-Wesley, Reading, 1992).
[29] J. L. Kaplan and J. A. Yorke, in *Functional Differential Equations and Approximation of Fixed Points*, edited by H. O. Walter and H.-O. Peitgen (Springer, Berlin, 1979), Vol. 730, pp. 204–227.

"Combining topological analysis and symbolic dynamics to describe a strange attractor and its crises"

M. Lefranc, P. Glorieux, F. Papoff, F. Molesti, and E. Arimondo

Phys. Rev. Lett. **73**, 1364–1367 (1994)

VOLUME 73, NUMBER 10 PHYSICAL REVIEW LETTERS 5 SEPTEMBER 1994

Combining Topological Analysis and Symbolic Dynamics to Describe a Strange Attractor and Its Crises

M. Lefranc,[1] P. Glorieux,[1] F. Papoff,[2] F. Molesti,[3] and E. Arimondo[3]

[1]*Laboratoire de Spectroscopie Hertzienne, URA CNRS 249, Université de Lille I, F-59655 Villeneuve d'Ascq, France*

[2]*Physics Department, University of Strathclyde, 107 Rottenrow, Glasgow, G4 ONG, United Kingdom*

[3]*Dipartimento di Fisica, Piazza Torricelli 2, 56126 Pisa, Italy*

(Received 27 July 1993)

We show how to use topological analysis to construct from experimental data a symbolic coding of a chaotic attractor. Time series data from a chaotic CO_2 laser with modulated losses operating within parameter regions corresponding to attractor crises have been analyzed. A procedure for determining a generating partition from the data is presented, and the connection between crises and a symbolic description of the dynamics is determined.

PACS numbers: 05.45.+b, 42.50.Lc, 42.55.Lt

Unstable periodic orbits have been recognized as a major tool in characterizing low-dimensional chaotic behavior, particularly because they can be extracted from experimental time series [1]. An analysis of strange attractors proposed by Mindlin *et al.* [2] proceeds by determining the topological organization of these orbits, and has been successfully applied to a few experimental systems [3–5], including the laser with modulated losses (LML) used in the experiments reported below [6].

Key to this approach is the fact that, for an attractor embedded in a three-dimensional (3D) phase space, topological invariants, such as linking numbers or knot polynomials [7], may be used to determine in which way its periodic orbits are knotted and linked with each other. Moreover, there is a one-to-one correspondence between unstable periodic orbits of a 3D hyperbolic chaotic flow and periodic orbits carried by a 2D branched manifold, the "template" (or "knot holder") [8], each periodic orbit of the flow having the same invariants as the associated template orbit. Experimental strange attractors are generally not hyperbolic, but the existing orbits are organized as in the hyperbolic limit as they cannot intersect on their whole domain of existence.

Coding trajectories as sequences of symbols (symbolic dynamics) is another powerful approach used to classify chaotic evolution and is intimately connected to topological analysis [8]. Methods to construct symbolic codings for 2D maps, including Poincaré maps of 3D flows, have been proposed [9], but their application to experimental systems seems difficult. This explains why topological analysis has been applied so far only to experimental investigations where symbolic coding could be obtained by means of 1D first return maps [3–6].

In this Letter, we apply the topological and symbolic dynamics approaches to cases where methods based on a 1D first return map method cannot be used. As the modulation amplitude is increased, the LML exhibits a series of crises [10–12] which widen or destroy the attractor [13]. Beyond the first crisis, no well-defined 1D map can be found, and thus there is no simple symbolic coding. However, this does not preclude the existence of a well-defined symbolic coding: one objective of this Letter is to present a method of constructing such a coding from the experimental data. We also want to show that, with or without a symbolic coding, important information can be extracted from the topological invariants of the unstable periodic orbits.

To check if the topological structure of the attractor is preserved in the crises, we have followed a self-consistent approach first used by Solari and Gilmore in their analysis of a theoretical model [14]. We have matched invariants of experimental periodic orbits to those of orbits with the same period belonging to the previously determined precrisis template [6], the Smale's horseshoe (SH) template with zero global torsion [8].

Identification of topologically allowed symbolic names for the detected periodic orbits has revealed that the observed crises are associated with the appearance of particular symbol sequences in the symbolic dynamics. If periodic orbits are classified on the basis of these sequences, we find that a crisis occurs when all orbits in a given class have been created. Furthermore, the topological identification of periodic orbits, with only a small part needed to determine the template, has allowed us to construct a symbolic coding for the experimental data by determining an approximate generating partition. This allowed us to study the order of appearance of periodic orbits with specified names when parameters change, and to compare this order with the "kneading order" [8] (the latter classifies periodic orbits of unimodal maps of the interval with respect to their symbolic name, and predicts in which order they are generically created in such maps).

This approach, combining topology and symbolic dynamical concepts, represents a general and very powerful method to analyze experimental data without the restriction of the 1D first return map, and to define a more precise generating partition than that found empirically in Refs. [15,16].

0031-9007/94/73(10)/1364(4)$06.00

The experimental setup consists of a waveguide CO_2 laser with intracavity losses modulated at a frequency of 382.5 kHz. This system is well known to display chaotic behavior [10–12,17]. Rather than the output intensity I of the laser, we have recorded $X = \ln I$ which was recently shown to be a more efficient variable to characterize chaotic regimes [18]. Figure 1 displays a segment of a typical time series. For various values of modulation amplitude and laser frequency detuning, we have recorded from 25 to 100 files, each containing 32 000 8-bit samples, at a sampling rate of approximatively 65 samples per period.

Periods of unstable orbits are integer multiples of the modulation period T. A segment of the time series $X(t)$ where $|X(t + nT) - X(t)| < \epsilon$ for $t_0 < t < t_0 + nT$ indicates that the system trajectory in phase space shadows a period nT orbit, and may be used as an approximation of this orbit. Figure 1 shows such a burst of periodic behavior. We have only kept segments for which ϵ was smaller than 4% of the maximum amplitude of $X(t)$, but for most extracted orbits, representative segments with ϵ of the order of the digitizing noise (i.e., 1%) have been detected, thanks to the very low internal noise of the laser used in the experiments. For each set of parameters, we have typically extracted from 20 to 38 orbits with a period lower than or equal to $13T$, with up to 304 periodic points in a Poincaré section.

If periodic orbits are embedded in a phase space with coordinates $(X(t), dX(t)/dt, \phi)$, where $\phi = t/T(\text{mod } 1)$ is the phase of the forcing term, their regular isotropy invariants can easily be obtained by plotting the corresponding time series segment versus ϕ (Fig. 2) [6], which gives a representation of the orbit as a braid on n strands [7]. For each periodic orbit, the following invariants were determined: self-relative rotation rates and torsion (the latter characterizing the rotation of nearby trajectories around the orbit), as well as relative rotation rates and linking numbers with other orbits [3,14].

Template determination is most easily performed when a symbolic coding of trajectories on the attractor is already available: The template is constructed so that attractor and

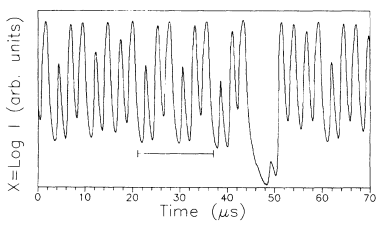

FIG. 1. Plot of the logarithm of the output intensity vs time. The underlined segment shadows a period $3T$ orbit.

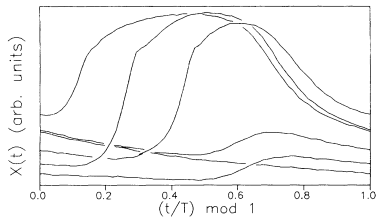

FIG. 2. Plot of a period $6T$ orbit vs time modulo T. Undercrossings and overcrossings are determined as explained in Ref. 6.

template orbits with the same name have identical invariants. Let us recall that if a different symbol is assigned to each branch of a template, this provides for each periodic orbit on it a symbolic name listing successively visited branches. We will hereafter call x (y) the orientation-preserving (-reversing) branch of the SH template.

Once a coding can be obtained from a partition of a Poincaré section, with a different symbol for each of its members, each trajectory may be coded with the symbols associated to successive intersections with the section plane. A partition is generating (i.e., associates to each bi-infinite sequence a unique point in the section plane), only if each periodic orbit is given a unique symbolic name. While the existence of generating partitions for nonhyperbolic systems is not rigorously ascertained, there is numerical evidence that partitions can be constructed which are generating down to scales well below realistic experimental resolutions [9].

Determining experimentally such a partition is not straightforward, except when an almost 1D first return map can be constructed, with a symbol assigned to each monotonic part of the map. For low modulation amplitudes, we could always find such a map and Fig. 3(a) shows a Poincaré section obtained in this case. For these parameters, the template is the SH template [6].

At higher amplitudes, after an interior crisis [13,10–12] in which the attractor suddenly widens after colliding with the xyy ($\equiv xy^2$) $3T$ unstable orbit, the first return diagram of $X(t + T)$ versus $X(t)$ associated to any Poincaré section, such as the one in Fig. 3(b), is multivalued and thus not the graph of a 1D map. In this case, it is not even clear whether new symbols should be used, though the method of sweeping Poincaré sections (see, e.g., Ref. [6]) apparently indicates that the stretching and folding mechanisms remain unchanged. Thus we have only the topological invariants from which to extract the symbolic information.

Invariants of single orbits show remarkable robustness with respect to experimental uncertainties. When the signal to noise ratio is high, as here, very few (typically 2%–3%) measured linking numbers of close orbits may

VOLUME 73, NUMBER 10 PHYSICAL REVIEW LETTERS 5 SEPTEMBER 1994

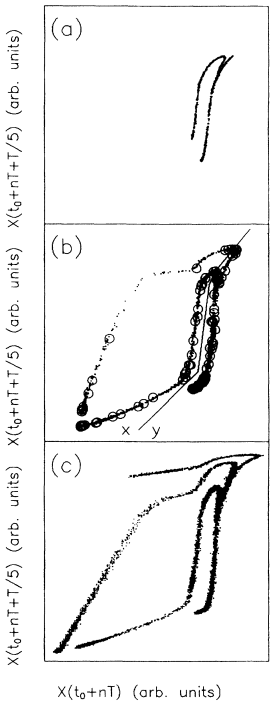

FIG. 3. Poincaré sections of attractors recorded (a) at low modulation amplitudes (contains only C_2 orbits), (b) after collision with the $3T$ orbit xy^2 (contains C_2 and C_3 orbits; circles are intersections of periodic orbits with the section plane; the solid line is the boundary of an approximate generating partition), and (c) after collision with the $4T$ x^2y^2 orbit (contains C_2, C_3, and C_4 orbits).

differ from their actual value due to spurious crossings [6]. These discrepancies are, however, easily detected, being inconsistent with other measured invariants; unless discarded, they prevent any template from fitting the data. We found that the SH template is the simplest template compatible with data recorded beyond the crisis.

For a certain number of periodic orbits, including most of low period ones, invariants are genuine fingerprints: They correspond to a unique SH orbit, and only one symbolic name may be assigned to these orbits. More generally, determining all sets of SH orbits with invariants identical to experimental ones left us with only a few possible symbolic names for each periodic orbit.

Although symbolic names of all orbits are not fully determined in this way, a remarkable feature nevertheless emerges: Defining a C_n orbit as having a name containing the sequence x^{n-1}, but not the x^n one (e.g., the name of a C_2 orbit only contains isolated x's), every orbit visiting the precrisis (postcrisis) part of the attractor can only be a C_2 (C_3) orbit. The crisis thus coincides with the appearance of the previously forbidden sequence x^2 in the symbolic dynamics. This simple rule has also been reported for a NMR oscillator [16], but it should be stressed that it is obtained here from merely computing topological invariants, without relying on any partition. Furthermore, we have found this rule to be part of a pattern, as shown by the following scenario observed as the modulation amplitude was increased.

The attractor of Fig. 3(b) first collides with the unstable $4T$ orbit x^2y^2 (identified by its invariants), and the system switches to the stable $4T$ orbit x^3y, which gives birth through period doublings to a four-piece chaotic attractor. This attractor experiences then an interior crisis involving the x^2y^2 orbit again, after which the Poincaré section in Fig. 3(c) has been recorded. The corresponding attractor next collides with the x^3y^2 orbit, and motion settles down on the stable orbit x^4y.

All these crises are thus due to collisions with the $x^{n-1}y^2$ orbits, and the sequences x^n appear just after such collisions, at least, as observed here, for $n = 2$, 3, and 4. Note that the $x^{n-1}y^2$ and x^ny orbits ($n \geq 2$) are the only period $n + 1$ unknotted SH orbits. Moreover, just before the collision with the xy^2 orbit, we have unambiguously detected the $13T$ orbit $(xy^2)^4y$, which is "quasi-one-dimensional" (QOD): Its presence implies the existence of all periodic orbits preceding it in the kneading order [19]. This proves the presence of all C_2 orbits up to period $13T$, and of almost all higher order C_2 orbits: The collision with the xy^2 orbit very likely occurs just after all C_2 orbits have been created. Similarly, the collision with the x^2y^2 orbit should occur when all C_3 orbits have been created, as shown by the presence of the $(x^2y^2)^3y$ QOD orbit in files recorded just before this collision. Thus, there appears to be a deep connection between the observed crises and the spectrum of periodic orbits.

Selecting periodic orbits with an unambiguous name, we have constructed a partition of the section plane in Fig. 3(b), so that it gives to each periodic orbit its topological symbolic name. This partition is defined by a list of reference points, each associated to a symbol; intersections of trajectories with the section plane are coded with the symbol assigned to the closest reference point. To get a partition as simple as possible, we proceeded through successive refinements. First, $1T$ and $2T$ periodic points y and xy were the only reference points. Then, for each periodic orbit from low-period to high-period ones, the following steps were carried out: (i) The cyclic permutation of the topological symbolic name least differing from the name given by the partition was first determined, and (ii) periodic points for which a discrepancy remained were then added to the reference list to update the

partition. In this way, large-scale features are determined from low-period orbits, while small-scale details of the partition are extracted from high-period ones.

The boundary of the approximate partition so obtained usually can be localized within a region small enough to code points not in its vicinity without ambiguity. We have thus used this partition to identify substrings of symbolic names of not yet identified periodic orbits, and discarded symbolic names not containing these substrings. Alternatively checking topological consistency and refining the accuracy of the partition with newly identified orbits, we finally determined for each orbit a unique symbolic name; the resulting partition is shown in Fig. 3(b). Note that whereas detected orbits do not uniformly cover the attractor, they are found in abundance near the boundary of the partition, which makes the precision of the latter of the order of the experimental resolution. Furthermore, the partition is seen to pass near but not exactly through the most apparent folds of the Poincaré section, showing that naively connecting these latter would not yield a correct solution.

Data files recorded as the modulation amplitude was increased contain an increasing number of unstable periodic orbits. Before the first crisis, we have observed that periodic orbits appear in an order corresponding to the kneading order for C_2 orbits, at least up to period $8T$. Similarly, between the collisions with the xy^2 and x^2y^2 orbits, kneading order governs the order of appearance of lowest periodic orbits. Note that, in this case, some symbolic names have been obtained by means of partitions as described above: The agreement with the kneading order seems to indicate that these partitions yield sensible symbolic codings.

In unimodal maps of the interval such as the logistic map, C_n orbits appear only when all C_{n-1} orbits have been created. This is not true in the LML, which is known to exhibit multistability [17,10–12,14]: C_3 or C_4 orbits may coexist with a C_2 attractor, and thus the kneading order governs the order of appearance of periodic orbits only within each class C_n of orbits. As noted in Ref. [13], multistability and the subsequent crises can occur even in highly dissipative systems, such as the LML in our case, for which correlation dimension estimates near 2.1 have been obtained [18], while the relation between multistability and dissipativity has been addressed by Arecchi and coworkers [11] in the context of the LML. From the above symbolic dynamical analysis, we see that these phenomena are very much controlled by the topological organization of the unstable periodic orbits, and certainly deserve further study through topological methods.

In conclusion, we have determined the template for the LML in parameter regions where there was no simple symbolic coding. The topological information extracted from unstable periodic orbits allowed us to very simply characterize the observed crises in terms of symbolic dynamics. The fact that their organization can be analyzed entirely by symbolic dynamics implies that the features reported here should hold for many horseshoelike chaotic systems. We have also constructed an approximate symbolic coding for the experimental data from the topological information. The methods presented here may be improved, yet we believe they already clearly illustrate how powerful topology methods can unfold chaotic complexity in experimental systems.

We are very much indebted to R. Gilmore for useful discussions and a careful reading of the manuscript. We also thank N. B. Tufillaro and T. D. Hall for useful advice and communicating their work before publication.

[1] D. Auerbach, P. Cvitanović, J.-P. Eckmann, G. H. Gunaratne, and I. Procaccia, Phys. Rev. Lett. **58**, 2387 (1987).
[2] G. B. Mindlin, X.-J. Hou, H. G. Solari, R. Gilmore, and N. B. Tufillaro, Phys. Rev. Lett. **64**, 2350 (1990).
[3] G. B. Mindlin, H. G. Solari, M. A. Natiello, R. Gilmore, and X.-J. Hou, J. Nonlinear Sci. **1**, 147 (1991).
[4] N. B. Tufillaro, R. Holzner, L. Flepp, M. F. E. Brun, and R. Badii, Phys. Rev. A **44**, R4786 (1991).
[5] F. Papoff, A. Fioretti, E. Arimondo, G. B. Mindlin, H. G. Solari, and R. Gilmore, Phys. Rev. Lett. **68**, 1128 (1992).
[6] M. Lefranc and P. Glorieux, Int. J. Bifurcation Chaos **3**, 643 (1993).
[7] L. H. Kaufmann, *Knots and Physics* (World Scientific, Singapore, 1991).
[8] P. Holmes, in *New Directions in Dynamical Systems*, edited by T. Bedford and J. Swift (Cambridge University Press, Cambridge, 1988), p. 150.
[9] P. Grassberger, H. Kantz, and U. Moenig, J. Phys. A **22**, 5217 (1989); P. Cvitanović, G. H. Gunaratne, and I. Procaccia, Phys. Rev. A **38**, 1503 (1988); F. Giovannini and A. Politi, J. Phys. A **24**, 1837 (1991).
[10] D. Dangoisse, D. Hennequin, and P. Glorieux, Phys. Rev. Lett. **57**, 2657 (1986).
[11] R. Meucci, A. Poggi, F. T. Arecchi, and J. R. Tredicce, Opt. Commun. **65**, 151 (1987).
[12] H. G. Solari, E. Eschenazi, R. Gilmore, and J. R. Tredicce, Opt. Commun. **64**, 49 (1987).
[13] C. Grebogi, E. Ott, and J. A. Yorke, Physica (Amsterdam) **7D**, 181 (1983).
[14] H. G. Solari and R. Gilmore, Phys. Rev. A **37**, 3096 (1988).
[15] L. Flepp, R. Holzner, E. Brun, M. Finardi, and R. Badii, Phys. Rev. Lett. **67**, 2244 (1991).
[16] M. Finardi, L. Flepp, J. Parisi, R. Holzner, R. Badii, and E. Brun, Phys. Rev. Lett. **68**, 1989 (1992).
[17] F. T. Arecchi, R. Meucci, G. P. Puccioni, and J. R. Tredicce, Phys. Rev. Lett. **49**, 1217 (1982); T. Midavaine, D. Dangoisse, and P. Glorieux, *ibid.* **55**, 1989 (1985); J. R. Tredicce, F. T. Arecchi, G. P. Puccioni, A. Poggi, and W. Gadomski, Phys. Rev. A **34**, 2073 (1986); D. Hennequin, D. Dangoisse, and P. Glorieux, *ibid.* **36**, 4775 (1987).
[18] M. Lefranc, D. Hennequin, and P. Glorieux, Phys. Lett. A **163**, 269 (1992).
[19] T. D. Hall, Phys. Rev. Lett. **71**, 58 (1993).

"Topological analysis of chaotic signals from a CO_2 laser with modulated losses"

M. Lefranc, and P. Glorieux

Int. J. Bifurcation Chaos Appl. Sci. Eng. **3**, 643–649 (1993)

International Journal of Bifurcation and Chaos, Vol. 3, No. 3 (1993) 643–650

TOPOLOGICAL ANALYSIS OF CHAOTIC SIGNALS FROM A CO_2 LASER WITH MODULATED LOSSES

MARC LEFRANC and PIERRE GLORIEUX
Laboratoire de Spectroscopie Hertzienne (Unité de Recherche associée au CNRS), UFR de Physique, Université de Lille I, F-59655 Villeneuve d'Ascq, France.

Received September 20, 1992; Revised October 30, 1992

Unstable periodic orbits have been extracted from chaotic time series coming from a CO_2 laser with modulated losses. Topological analysis of their organization reveals that chaos in this laser occurs through the formation of a Smale's horseshoe.

A topological method has recently been proposed to analyse experimental time series from low-dimensional chaotic systems [Mindlin *et al.*, 1990]. It relies on the identification of unstable periodic orbits embedded in the strange attractor associated with chaotic behavior, and on the analysis of their topological organization. Indeed, periodic orbits of dynamical systems are closed curves in phase space, and the uniqueness theorem [Guckenheimer & Holmes, 1983] precludes that they intersect each other as a control parameter is varied. When a strange attractor can be embedded in a three-dimensional phase space, topological invariants from knot theory [Kauffman, 1987] may thus be used to determine in which way its unstable periodic orbits are knotted and linked together. The global organization of periodic orbits can then be characterized by a two-dimensional branched manifold, the template (or "knot holder") [Birman & Williams, 1983] (see also [Holmes, 1988; Tufillaro *et al.*, 1992]) in which they can be embedded while preserving their topological invariants. The structure of the template is described with a small set of integers which depend only on the properties of orbits of lowest period, and can be used to classify attractors.

This analysis has been successfully applied to experimental time-series data from the Belousov-Zhabotinskii reaction [Mindlin *et al.*, 1991], from a laser containing a saturable absorber [Papoff *et al.*, 1992] and from an NMR oscillator [Tufillaro *et al.*, 1991]. We report here the result of such an analysis in the case of the CO_2 laser with sinusoidally modulated losses.

This laser is known to reach chaos through a cascade of period-doubling bifurcations and has been the subject of intense investigations [Arecchi *et al.*, 1982; Midavaine *et al.*, 1985; Dangoisse *et al.*, 1987]. The various control parameters include cavity frequency detuning and the amplitude of the external driving, the frequency of which being equal to 382.5 kHz in our experiments. Experimental data analysed here have been obtained from the laser as described by Lepers *et al.* [1991]. Because of the high stability of the laser, files may be successively stored and sets of 25 to 100 files of 32000 samples have been analysed for each setting of the control parameters.

Correlation dimension analyses using the Grassberger-Procaccia algorithm [Grassberger & Procaccia, 1983] have been made on signals coming from this laser operated in the chaotic regime. They have shown that the reliability of dimension estimates is greatly improved when time series of the logarithm of the laser output intensity, rather than of the intensity $I(t)$ itself as in previous analyses, is used

PACS numbers: 05.45.+b, 42.50.Lc, 42.55.-f

to reconstruct an experimental strange attractor through the time delay method [Lefranc *et al.*, 1992]. This occurs because typical time series display long sequences of very weak intensity, resulting in a very large inhomogeneity of reconstructed strange attractors. It must be noted that because of the particular nature of the laser equations, Log I appears as a natural variable of the dynamical system [Oppo *et al.*, 1989]. Similarly, topological analysis using intensity is made meaningless by the uncertainties of the relative positions of trajectories in the near zero intensity region. The results reported here have therefore been obtained from time series of $\mathrm{Log}(I + I_0)$, where I_0 is a very small constant which can be adjusted in the logarithmic amplifier used for signal processing. This procedure was allowed by the high signal-to-noise ratio achieved in this laser, limited practically by the resolution (8 bits) of the transient digitizer used in these experiments.

Let us now describe the procedure of the analysis. First, unstable periodic orbits are extracted from time-series data by searching for close returns [Mindlin *et al.*, 1991]. The fact that our system is periodically driven simplifies this step, since periodic orbits have periods which are multiples of the modulation period $T = 2\pi/\omega$. A segment of the time series $X(t)$ where $|X(t) - X(t + nT)| < \varepsilon$ for $t_0 < t < t_0 + nT$ indicates the shadowing of a period nT orbit by the trajectory of the system on the attractor, and can be used as an approximation to this orbit. In our analysis, ε was chosen to be equal to $0.04 \times (X_{\max} - X_{\min})$. Examples of such segments are shown in Fig. 1. The fact that the period T orbit on first row is shadowed very closely during several periods of modulation is an indication that the internal dynamics of our laser is very little perturbed by noise (similar sequences lasting up to 14 periods have been extracted). This allowed us to extract high order periodic orbits up to period $17T$. Note the peculiar case of the second row, where after a few cycles near a period $3T$ orbit the system enters directly the vicinity of a period $2T$ orbit. It should be stressed that a time series with strong recurrence properties has almost certainly a low-dimensional deterministic origin, as such bursts of almost periodic behavior are extremely unlikely in stochastic or high-dimensional systems.

Second, periodic orbits must be embedded in a three-dimensional phase space. Taking advantage of the particular nature of periodically driven systems, we used $\{X(t),\ X(t + \tau),\ \phi\}$ or $\{X(t),$

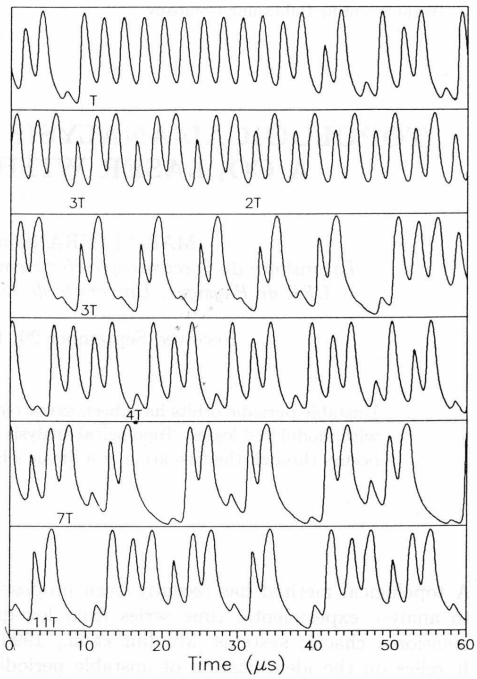

Fig. 1. Examples of time-series segments which closely follow unstable periodic orbits. Periods of these orbits are indicated at the beginning of segments.

$dX(t)/dt,\ \phi\}$ embeddings, where τ is a time delay and $\phi = \omega t \bmod 2\pi$ is the phase of the external modulation. We found that these two phase spaces led to consistent results, provided that τ be small enough (i.e., smaller than $T/4$ in the worst case). An experimental strange attractor and the extracted unstable periodic orbits are displayed in Figs. 2(a) and 2(b) respectively, using the first kind of embedding. These two figures illustrate well the fact that the essential features of the dynamics can be obtained from the study of unstable periodic orbits. Note that $\{X(t),\ dX(t)/dt,\ \phi\}$ is the natural phase space of the system, as the free CO_2 laser is well described by two first-order ordinary differential equations (see, for example, Dangoisse *et al.*, [1987] or Oppo *et al.* [1989]).

More conveniently than in 3D phase space, the topological structure of periodic orbits can be analyzed by plotting the corresponding time-series seg-

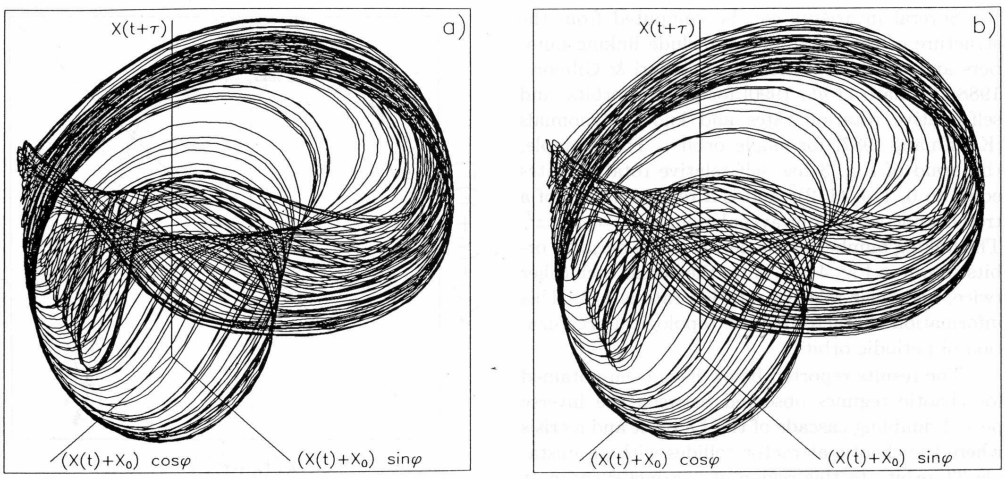

Fig. 2. (a) Experimental strange attractor reconstructed using an $\{X(t), X(t+\tau), \phi\}$ phase space with $\tau = T/4$. (b) Some unstable periodic orbits embedded in this attractor and extracted from the time series.

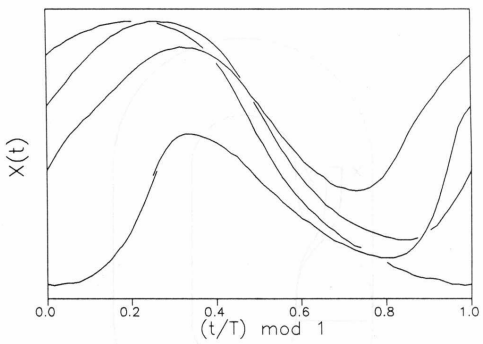

Fig. 3. Plot of a time-series segment corresponding to a period $4T$ orbit versus time modulo T.

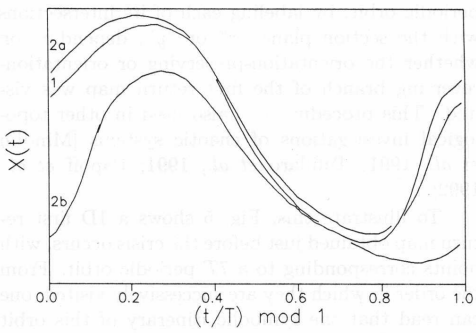

Fig. 4. Plot of time series segments to period T (strand 1) and $2T$ (strands 2a and 2b) orbits versus time modulo T.

ments versus time modulo T. Periodic orbits are represented in this way as braids on n strands [Birman, 1975], provided we determine for each crossing of two strands which one crosses over the other. This is straightforward if a $\{X(t), dX(t)/dt, \phi\}$ phase space is implicitly used. Indeed, whenever two strands cross, the one with a lower value of $X(t)$ before the crossing corresponds to a higher value of $dX(t)/dt$ (which is the coordinate perpendicular to the plot) and therefore passes over the other. This implies that only positive braids can be obtained. A braid on four strands representing a $4T$ orbit is shown in Fig. 3, where over- and undercrossings have been indicated for clarity, following this convention. Plotting together a period nT orbit and a period mT orbit gives in the same way a braid on $n+m$ strands, as in Fig. 4, where $1T$ and $2T$ orbits have been plotted.

Several invariants can be computed from the structure of the braid. They include linking numbers and relative rotation rates [Solari & Gilmore, 1988; Tufillaro *et al.*, 1990] for pairs of orbits, and self-relative rotation rates and knot polynomials [Kauffman, 1987] for single orbits. For example, the braid of Fig. 3 has self relative rotation rates equal to 0, 1/4, $(1/2)^2$ and is a representation of a trefoil knot with Conway polynomial $\nabla = 1 + z^2$. The linking number of the period 1 and period 2 orbits shown in Fig. 4 is 1, since they cross each other twice, and their relative rotation rate is 1/2. This information characterizes the topological organization of periodic orbits.

The results reported below have been obtained for chaotic regimes observed between the inverse period-doubling cascade of the $1T$ orbit and a crisis where the chaotic attractor collides with an unstable $3T$ orbit. In this region of parameter space, it has always been possible to find a Poincaré section of constant phase with a return map well approximated by a unimodal 1D map $X(t_0 + (n+1)T) = f(X(t_0+nT))$. The existence of such a map allowed us to assign a symbolic itinerary to each extracted periodic orbit, by labeling each of its intersections with the section plane "x" or "y", depending on whether the orientation-preserving or orientation-reversing branch of the first return map was visited. This procedure was also used in other topological investigations of chaotic systems [Mindlin *et al.*, 1991; Tufillaro *et al.*, 1991; Papoff *et al.*, 1992].

To illustrate this, Fig. 5 shows a 1D first return map obtained just before the crisis occurs, with points corresponding to a $7T$ periodic orbit. From the order in which they are successively visited, one can read that the symbolic itinerary of this orbit is $xyxyxy^2$. The fact that two different extracted periodic orbits receive in this way different names indicates that this binary symbolic encoding is a good approximation to a generating partition.

It can then be checked that a template can be constructed, so that each experimental periodic orbit is associated with a unique orbit of the template, with the same symbolic name and identical topological invariants.

The topological properties of the three lowest order periodic orbits suffice to determine the structure of any two-branch template [Mindlin *et al.*, 1991]. For most of the files analysed in the parameter space region under study, these orbits were the y, xy, and xy^3, orbits, whereas $3T$ orbit xy^2 could be extracted from signals recorded in the vicinity of the crisis. Indeed, this orbit is located on the boundary of the basin of attraction of the chaotic attractor, and the collision of this orbit with the attractor is responsible for the occurrence of a crisis.

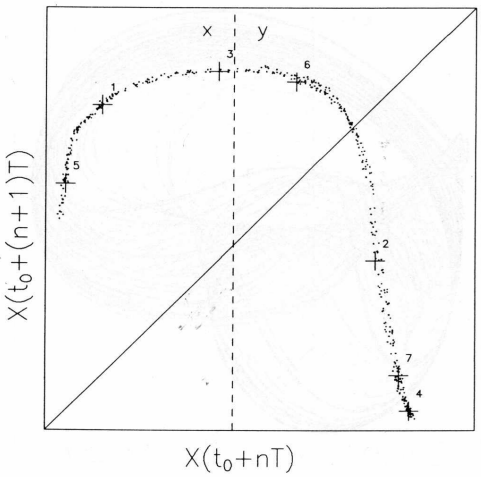

Fig. 5. 1D first return map on a Poincaré section of constant phase. Orientation-preserving and -reversing branches are labeled "x" and "y" respectively. Points corresponding to a $7T$ orbit have been plotted, from which the symbolic itinerary "$xyxyxy^2$" can be read.

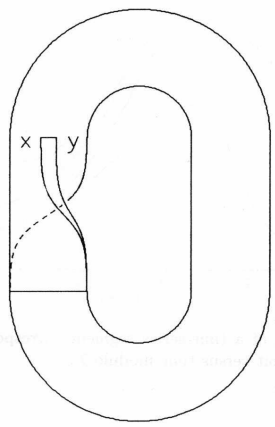

Fig. 6. The horseshoe template with zero global torsion. The "x" (respectively "y") branch is orientation-preserving (respectively-reversing).

Table 1. Relative rotation rates of extracted periodic orbits up to period $8T$. Values in square brackets have been obtained using the correction described in the text. Values in braces differ from those predicted by the horseshoe template.

Orbits		1	2	3	4	5a	5b	6a	6b
y	1	0							
xy	2	$\frac{1}{2}$	0, $\frac{1}{2}$						
xy^2	3	$\frac{1}{3}$	$\frac{1}{3}$	0, $(\frac{1}{3})^2$					
xy^3	4	$\frac{1}{2}$	$\frac{1}{2}$, $\frac{1}{4}$	$\frac{1}{3}$	0, $\frac{1}{4}$, $(\frac{1}{2})^2$				
xy^4	5a	$\frac{2}{5}$	$\frac{2}{5}$	$\frac{1}{3}$	$\frac{2}{5}$	0, $(\frac{2}{5})^4$			
$xyxy^2$	5b	$\frac{2}{5}$	$\frac{2}{5}$	$\frac{1}{3}$	$\frac{2}{5}$	$\frac{2}{5}$	0, $(\frac{2}{5})^4$		
$xyxy^3$	6a	$\frac{1}{2}$	$\frac{1}{2}$, $\frac{1}{3}$	$\frac{1}{3}$	$\frac{1}{2}$, $\frac{1}{3}$	$\frac{2}{5}$	$[\frac{2}{5}]$	0, $(\frac{1}{3})^2$, $(\frac{1}{2})^3$	
xy^5	6b	$\frac{1}{2}$	$\frac{1}{2}$, $\frac{1}{3}$	$\frac{1}{3}$	$\frac{1}{2}$, $\frac{1}{3}$	$[\frac{2}{5}]$	$\frac{2}{5}$	$\frac{1}{2}$, $\frac{1}{3}$	0, $(\frac{1}{3})^2$, $(\frac{1}{2})^3$
$xyxy^4$	7a	$\frac{3}{7}$	$\frac{3}{7}$	$\frac{1}{3}$	$\frac{3}{7}$	$\frac{2}{5}$	$[\frac{2}{5}]$	$[\frac{3}{7}]$	$[\frac{3}{7}]$
xy^6	7b	$\frac{3}{7}$	$\frac{3}{7}$	$\frac{1}{3}$	$\frac{3}{7}$	$\frac{2}{5}$	$[\frac{2}{5}]$	$\frac{3}{7}$	$[\frac{3}{7}]$
$(xy)^2xy^2$	7c	$\frac{3}{7}$	$\frac{5}{14}$	$\frac{1}{3}$	$[\frac{11}{28}]$	$\frac{2}{5}$	$\frac{13}{35}$	$\frac{8}{21}$	$\frac{17}{42}$
$(xy)^2xy^3$	8a	$\frac{1}{2}$	$\frac{1}{2}$, $\frac{1}{4}$	$\frac{1}{3}$	$\frac{1}{4}$, $[\frac{3}{8}]$, $(\frac{1}{2})^2$	$\frac{2}{5}$	$[\frac{2}{5}]$	$\frac{1}{3}$, $\frac{1}{2}$	$\frac{1}{2}$, $\frac{1}{3}$
xy^7	8b	$[\frac{1}{2}]$	$\frac{3}{8}$, $\frac{1}{2}$	$\frac{1}{3}$	$\frac{3}{8}$, $\frac{1}{2}$	$\frac{2}{5}$	$\frac{2}{5}$	$\frac{3}{8}$, $\frac{1}{2}$	$\{\frac{5}{12}\}$, $\frac{1}{2}$
$xyxy^5$	8c	$\frac{1}{2}$	$\frac{3}{8}$, $\frac{1}{2}$	$\frac{1}{3}$	$[\frac{3}{8}]$, $\frac{1}{2}$	$\frac{2}{5}$	$[\frac{2}{5}]$	$\{\frac{5}{12}\}$, $\frac{1}{2}$	$[\frac{3}{8}]$, $\frac{1}{2}$
xy^2xy^4	8d	$\frac{3}{8}$	$\frac{3}{8}$	$\frac{1}{3}$	$\frac{3}{8}$	$\frac{3}{8}$	$[\frac{3}{8}]$	$\frac{3}{8}$	$\frac{3}{8}$

Orbits		7a	7b	7c	8a	8b	8c	8d
$xyxy^4$	7a	0, $(\frac{3}{7})^6$						
xy^6	7b	$[\frac{3}{7}]$	0, $(\frac{3}{7})^6$					
$(xy)^2xy^2$	7c	$(\frac{3}{7})^5$, $(\frac{2}{7})^2$	$(\frac{3}{7})^6$, $(\frac{2}{7})$	0, $(\frac{2}{7})^2$, $(\frac{3}{7})^4$				
$(xy)^2xy^3$	8a	$[\frac{3}{7}]$	$\frac{3}{7}$	$\frac{3}{8}$	0, $\frac{3}{8}$, $(\frac{1}{4})^2$, $(\frac{1}{2})^4$			
xy^7	8b	$[\frac{3}{7}]$	$[\frac{3}{7}]$	$\frac{23}{56}$	$\frac{3}{8}$, $\frac{1}{2}$	0, $(\frac{3}{8})^3$, $(\frac{1}{2})^4$		
$xyxy^5$	8c	$\{\frac{23}{56}\}$	$\frac{3}{7}$	$[\frac{11}{28}]$	$\frac{3}{8}$, $\frac{1}{2}$	$\frac{3}{8}$, $\frac{1}{2}$	0, $(\frac{3}{8})^3$, $(\frac{1}{2})^4$	
xy^2xy^4	8d	$\frac{3}{8}$	$\frac{3}{8}$	$[\frac{3}{8}]$	$\frac{3}{8}$	$\frac{3}{8}$	$\frac{3}{8}$	0, $(\frac{3}{8})^7$

At each parameter value, the lowest order periodic orbits have been found to be knotted and linked as in the Smale's horseshoe template with zero global torsion [Holmes & Williams, 1985], which is shown in Fig. 6. Furthermore, it has been checked that invariants of higher order orbits were correctly predicted by this template, as is required to give definite evidence that its structure determines the global topological organization of the attractor.

As an example, we present results for a chaotic attractor about to collide the xy^2 orbit, as many periodic orbits could be extracted from the corresponding signals. The associated first return map is shown in Fig. 5.

The corresponding relative rotation rates of orbits up to period $8T$ are shown in Table 1. To compute them, the number of crossings of two strands of the braids was determined by looking for time intervals where the distance between them was smaller than some constant η. If the relative positions of the two strands at the beginning and at the end of such an interval were different, one crossing was counted. Choosing $\eta = 3\,b_0$, where b_0 is the least

Table 2. Self relative rotation rates of extracted periodic orbits from period $9T$ up to period $12T$.

Orbits		Self Relative Rotation Rates
$(xy)^3xy^2$	9a	$0, (\frac{1}{3})^4, (\frac{4}{9})^4$
xy^2xy^5	9b	$0, (\frac{1}{3})^4, (\frac{4}{9})^4$
$(xy)^2xy^4$	9c	$0, (\frac{1}{3})^2, (\frac{4}{9})^6$
xy^3xy^4	9d	$0, (\frac{1}{3})^2, (\frac{4}{9})^6$
$xyxy^2xy^4$	10a	$0, \frac{3}{10}, (\frac{2}{5})^8$
$xyxy^4xy^2$	10b	$0, \frac{3}{10}, (\frac{2}{5})^8$
$(xy)^4xy^2$	11a	$0, (\frac{3}{11})^2, (\frac{4}{11})^4, (\frac{5}{11})^4$
$xyxy^3xy^4$	11b	$0, (\frac{4}{11})^4, (\frac{5}{11})^6$
$xyxy^2xy^5$	11c	$0, (\frac{5}{11})^4, (\frac{4}{11})^6$
$xy(xy^2)^3$	11d	$0, (\frac{4}{11})^{10}$
$(xy)^2xy^4xy^2$	12a	$0, (\frac{1}{3})^4, (\frac{5}{12})^7$
xy^2xy^8	12b	$0, (\frac{1}{3})^2, (\frac{5}{12})^9$

significant bit of the digitizer (i.e., η is 1.2% of the maximum amplitude of the signal), prevents counting spurious crossings caused by digitizing noise or by imperfect shadowing of orbits.

However, there remained a few discrepancies, especially when dealing with orbits very close to each other. We observed that these errors occurred when two orbits were closer than η over more than a full period of modulation. It was possible in these cases to find long time intervals where no crossing was detected by the procedure described above whereas at least one crossing should have occurred, as indicated by the fact that the two trajectories had passed through the orientation-reversing part of the Poincaré section. We have therefore modified our algorithm so that two crossings are counted when such intervals were detected. This simple correction yielded the expected results in almost any case. Values of Table 1 for which this has been applied are displayed in square brackets. It should be noted that in many cases, the correct results could also be recovered by decreasing η to $2b_0$, which gives some confidence about the validity of this procedure. However, decreasing η induces spurious crossings for some other pairs of orbits, and a sensible comparison between theoretical and experimental values requires that these latter be obtained from a unique algorithm with fixed parameter η.

Three values in Table 1 are not those predicted by the horseshoe template and are displayed in braces. We have observed that these errors were removed by increasing η to $4b_0$ or $5b_0$, and should therefore be due to spurious crossings.

Self relative rotation rates of orbits up to period $12T$ can be found in Tables 1 and 2, and Table 3 displays knot polynomials of orbits up to period $8T$. Invariants of single orbits seem to be less sensitive to experimental uncertainties than those characterizing pairs of orbits, as self relative rotation rates and knot polynomials computed from the experimental data are in perfect agreement with those predicted from the horseshoe template.

These results strongly support the hypothesis that chaos in the CO_2 laser with modulated losses occurs through the formation of a Smale's horseshoe, one of the simplest mechanisms responsible for chaotic behavior. This result is consistent with previous theoretical investigations [Solari & Gilmore, 1988].

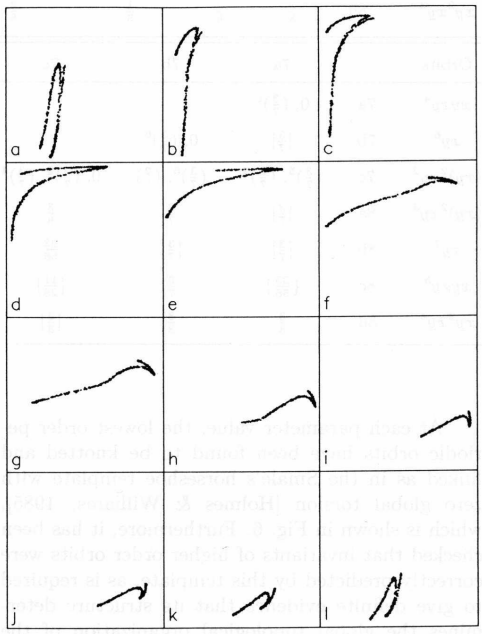

Fig. 7. Poincaré sections of a chaotic attractor in a $\{X(t), X(t+\tau), \phi\}$ phase space with $\tau = T/4$. ϕ increases by $\pi/6$ between consecutive figures.

Table 3. Conway polynomials and knot types of extracted periodic orbits up to period $8T$. $(a_0, a_1, \ldots, a_n)_{2n}$ stands for the polynomial $a_0 + a_1 z^2 + a_2 z^4 + \cdots + a_n z^{2n}$.

Orbits		Conway Polynomial	Knot Type
y	1	1	trivial
xy	2	1	trivial
xy^2	3	1	trivial
xy^3	4	$1+z^2$	$(2,3)$ torus
xy^4	5a	$1+3z^2+z^4$	$(2,5)$ torus
$xyxy^2$	5b	$1+3z^2+z^4$	$(2,5)$ torus
$xyxy^3$	6a	$1+8z^2+14z^4+7z^6+z^8$	$(3,5)$ torus
xy^5	6b	$1+8z^2+14z^4+7z^6+z^8$	$(3,5)$ torus
$xyxy^4$	7a	$1+16z^2+60z^4+78z^6+44z^8+11z^{10}+z^{12}$	$(3,7)$ torus
xy^6	7b	$1+16z^2+60z^4+78z^6+44z^8+11z^{10}+z^{12}$	$(3,7)$ torus
$(xy)^2xy^2$	7c	$1+12z^2+31z^4+27z^6+9z^8+z^{10}$	$(7, 3, -2)$ pretzel
$(xy)^2xy^3$	8a	$(1, 25, 155, 385, 451, 275, 90, 15, 1)_{16}$	$\{(2, 13); (2, 3)\}$ iterated torus
xy^7	8b	$(1, 30, 235, 741, 1131, 936, 442, 119, 17, 1)_{18}$	$(4,7)$ torus
$xyxy^5$	8c	$(1, 30, 235, 741, 1131, 936, 442, 119, 17, 1)_{18}$	$(4,7)$ torus
xy^2xy^4	8d	$(1, 21, 105, 189, 157, 65, 13, 1)_{14}$	$(3,8)$ torus

The template of a flow describes schematically in which way trajectories on the attractor experience the folding and stretching mechanisms which are responsible for chaotic behavior. When the attractor has a fractal dimension sufficiently close to 2, the template is also easily determined by inspecting the evolution of Poincaré sections at $\phi = \phi_0$ when ϕ_0 is varied from 0 to 2π. This is illustrated in Fig. 7, which shows successive Poincaré sections as ϕ_0 is increased in steps of $\pi/6$. Folding occurs from Fig. 7(f) to Fig. 7(l), where the Poincaré section has the characteristic form of a horseshoe. It can be checked that the left branch of the section in Fig. 7(l) contains trajectories which do not experience rotation between 0 and 2π, indicating that the global torsion of the flow is zero, whereas the right branch corresponds to a torsion of half a turn.

It should be emphasized that topological analysis is complementary to dimension or entropy calculations since it assigns the mechanisms from which chaos originates (e.g., formation of a Smale's horseshoe) in addition to simply proving that the data set is chaotic. It is yet not disconnected from metric measures of chaos, as the first return map of an attractor with an n-branch template has a topological entropy bounded by Log n. This means that the positive Lyapunov exponent λ of our system verifies $\lambda T <$ Log 2.

In conclusion, unstable periodic orbits have been extracted from time series from a CO_2 laser with modulated losses for various values of the control parameters. While knots and links are defined in three-dimensional space only, the topological invariants of periodic orbits could be determined directly from the time series, using only implicitly a three-dimensional embedding. Knowledge of the topological organization of the observed chaotic regimes allowed us to identify, in the range of parameters studied, the template for our system with the Smale's horseshoe template with zero global torsion.

Acknowledgments

We are very much indebted to Francesco Papoff, Ennio Arimondo and Robert Gilmore for enlightening discussions.

References

Arecchi, F. T., Meucci, R., Puccioni, G. P. & Tredicce, J. R. [1982] "Experimental evidence of subharmonic bifurcations, multistability, and turbulence in a *Q*-switched gas laser," *Phys. Rev. Lett.* **49**, 1217.

Birman, J. S. & Williams, R. F. [1983] "Knotted periodic orbits in dynamical systems I: Lorenz's equations," *Topology* **22**, 47.

Birman, J. S. [1975] *Braids, Links and Mapping Class Groups* (Princeton University Press, Princeton).

Dangoisse, D., Glorieux, P. & Hennequin, D. [1987] "Chaos in a CO_2 laser with modulated parameters: Experiments and numerical simulations," *Phys. Rev.* **A36**, 4775.

Grassberger, P. & Procaccia, I. [1983] "Characterization of strange attractors," *Phys. Rev. Lett.* **50**, 346.

Guckenheimer, J. & Holmes, P. [1983] *Nonlinear Oscillations, Dynamical Systems, and Bifurcations of Vector Fields* (Springer-Verlag).

Holmes, P. & Williams, R. F. [1985] "Knotted periodic orbits in suspensions of Smale's horseshoe: Torus knots and bifurcation sequences," *Arch. Rat. Mech. Anal.* **90**, 115.

Holmes, P. [1988] "Knots and orbit genealogies in nonlinear oscillators" in *New Directions in Dynamical Systems*, eds. Bedford, T. & Swift, J. (Cambridge University Press, Cambridge), p. 150.

Kauffman, L. H. [1987] *On Knots* (Princeton University Press, Princeton).

Lefranc, M., Hennequin, D. & Glorieux, P. [1992] "Improved correlation dimension estimates through change of variable," *Phys. Lett.* **A163**, 269.

Lepers, C., Legrand, J. & Glorieux, P. [1991] "Experimental investigation of the collision of Feigenbaum cascades in lasers," *Phys. Rev.* **A43**, 2573.

Midavaine, T., Dangoisse, D. & Glorieux, P. [1985] "Observation of chaos in a frequency-modulated CO_2 laser," *Phys. Rev. Lett.* **55**, 1989.

Mindlin, G. B., Hou, X.-J., Solari, H. G., Gilmore, R. & Tufillaro, N. B. [1990] "Classification of strange attractors by integers," *Phys. Rev. Lett.* **64**, 2350.

Mindlin, G. B., Solari, H. G., Natiello, M. A., Gilmore, R. & Hou, X.-J [1991] "Topological analysis of chaotic time series data from the Belousov–Zhabotinskii reaction," *J. Nonlinear Sci.* **1**, 147.

Oppo, G.-L., Tredicce, J. R. & Narducci, L. M. [1989] "Dynamics of vibro-rotational CO_2 laser transitions in a two-dimensional phase space," *Opt. Commun.* **69**, 393.

Papoff, F., Fioretti, A., Arimondo, E., Mindlin, G. B., Solari, H. & Gilmore, R. [1992] "Structure of chaos in the laser with saturable absorber," *Phys. Rev. Lett.* **68**, 1128.

Solari, H. G. & Gilmore, R. [1988] "Relative rotation rates for driven dynamical systems," *Phys. Rev.* **A37**, 3096.

Tufillaro, N. B., Solari, H. G. & Gilmore, R. [1990] "Relative rotation rates: Fingerprints for strange attractors," *Phys. Rev.* **A41**, 5717.

Tufillaro, N. B., Abbott, T. & Reilly, J. [1992] *An Experimental Approach To Nonlinear Dynamics And Chaos* (Addison-Wesley).

Tufillaro, N. B., Holzner, R., Flepp, L., Brun, E., Finardi, M. & Badii, R. [1991] "Template analysis for a chaotic NMR laser," *Phys. Rev.* **A44**, 4786.

Appendice E
Publications “Dynamique spectro-temporelle”

"Eckhaus instability induced by nonuniformities in a laser"

J. Plumecoq, C. Szwaj, D. Derozier, M. Lefranc, and S. Bielawski

Phys. Rev. A **64**, 061801(R) (2001)

RAPID COMMUNICATIONS

PHYSICAL REVIEW A, VOLUME 64, 061801(R)

Eckhaus instability induced by nonuniformities in a laser

Jérôme Plumecoq, Christophe Szwaj, Dominique Derozier, Marc Lefranc, and Serge Bielawski
Laboratoire de Physique des Lasers, Atomes et Molécules, UMR CNRS 8523, Centre d'Études et de Recherches Lasers et Applications, Université des Sciences et Technologies de Lille, F-59655 Villeneuve d'Ascq Cedex, France

(Received 17 April 2000; revised manuscript received 13 April 2001; published 16 November 2001)

We show that the Eckhaus instability induced by spatial nonuniformities, observed in hydrodynamics, can also destabilize optical systems. On the example of a one-dimensional parametric system (a modulated multimode laser), we show numerically that the nonuniformities select a wave number outside the Eckhaus-stable band, leading to periodic or irregular phase slips. The instability is confirmed experimentally by using a modulated fiber laser.

DOI: 10.1103/PhysRevA.64.061801 PACS number(s): 42.65.Sf, 05.45.Jn, 47.54.+r

In hydrodynamics, *slow spatial dependences of control parameters* are known to induce instabilities in systems that would otherwise display stationary patterns (the Riecke and Paap instability [1]). Since the mechanism is conjectured to be general, the possible occurrence of this instability in the context of optical pattern formation appears as an important question. Indeed, real-life optics experiments necessarily involve such slow nonuniformities, in particular through the use of Gaussian pumps, mirrors with finite curvature radii, or spectroscopic line shapes.

The possibility of this instability is generally overlooked in numerical and theoretical works, that usually concentrate on the basic mechanisms of pattern formation [2], or other consequences of nonuniformities [3]. The question is also surprisingly overlooked experimentally mainly because of the lack of a suitable theoretical framework for these optical systems. Indeed, the complexity of the secondary instabilities together with the two-dimensional character of the patterns hide a clear identification of possible nonuniformity-induced instabilities [4], directly from experiments. More importantly—and in opposition to hydrodynamics [1]—it is generally not possible to remove the nonuniformities in order to compare the system with and without nonuniformities.

In this paper, we show how the Riecke and Paap instability appears in the model of an optical system when the slow spatial variations of the control parameters are taken into account. We consider the physical model of a one-dimensional parametric system (a modulated fiber laser) displaying stationary waves after a primary instability [5]. In a first step we show numerically, using this model, that the predictions made under uniform assumption are in qualitative contradiction with the real situation including nonuniformities. Then, we identify numerically the signature of the instability. Finally, we will see that this instability explains the regimes observed experimentally in a large range of parameters in a modulated fiber laser.

Let us recall that the Riecke and Paap instability is closely related to the problem of wave-number selection considered in particular by Kramer *et al.* [6] and Pomeau and Zaleski [7]. In a uniform and infinite medium developing stationary periodic patterns, the wave number can be located anywhere inside a finite band (see, e.g., [8]). However, if a control parameter slowly varies in space from a subcritical value to a supercritical one (i.e., from below to above the threshold for pattern formation), the allowed band of wave numbers collapses to a single value [7] that depends on the details of the ramp. As a spectacular consequence, Riecke and Paap found that the wave number selected by the nonuniformities can fall outside the Eckhaus-stable domain [1]. The resulting instability leads to recurrent "phase-slips," i.e., the destruction or creation of cells in the stationary wave structure, that can occur either periodically or chaotically [9,10].

Before considering wave-number selection in our system, we will first describe the physical model and its main properties. We show that an instability occurs in the realistic model (with nonuniformities), that has no counterpart in an "ideal" uniform system. Then, we give quantitative evidence that the mechanism is the *Eckhaus instability induced by nonuniformities* [1] by comparing the wave number selected in the realistic system with the Eckhaus limit of the uniform model. We will see in particular that very small variations of the wave number—too small to be measured experimentally in our system—are responsible for the occurrence of the phase slips. Finally, we describe the regimes observed experimentally in a fiber laser. We show that the instability occurs in a large parameter domain, and is consistent with numerical predictions concerning the regimes' nature and parameter thresholds.

We consider an inhomogeneously broadened class B laser [11] with many longitudinal modes. Although the present system seems *a priori* unusual [12], it is formally similar to other very classical propagation media displaying parametric waves. It is known to behave as a chain of locally coupled oscillators, each associated with one longitudinal mode [12]. The relevant "space" is thus the mode index j (or, equivalently, the wavelength), and the information that propagates from mode to mode is the deviation of the mode intensities from their steady-state values. Patterns are obtained by modulating the pump power. At a threshold modulation amplitude, the trivial solution destabilizes through a parametric instability similar to the Faraday instability in hydrodynamics [13]. This is predicted to lead to a stationary wave inside the laser spectrum [5].

The following model is known to reproduce quantitatively all experimentally observed regimes, as well as the bifurcation points. The laser is described by a set of mode intensities $s_j(t)$ and a continuous set of population inversions $d(\xi,t)$ [11,5]:

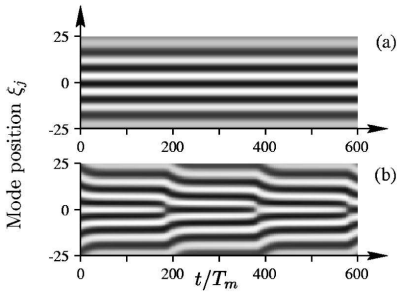

FIG. 1. Transition observed with the physical model (1) including nonuniformities. (a) $\omega_m = 0.97\sqrt{\gamma(A-1)}$: stationary wave, (b) $\omega_m = 0.887\sqrt{\gamma(A-1)}$: periodic phase slips. Note that integration of the model (1) without nonuniformities and with periodic boundary conditions leads to a stationary wave solution in all cases. The subharmonic component is represented (see text) with a gray scale, white corresponding to high intensities. T_m is the modulation period.

$$\dot{s}_j = -s_j + (s_j + a)\int_{-\infty}^{+\infty} \beta(\xi_j - \xi) d(\xi) d\xi, \tag{1a}$$

$$\dot{d} = \gamma\left[g(\xi)A(t) - \left\{1 + \sum_l \beta(\xi - \xi_l) s_l\right\} d\right]. \tag{1b}$$

The relevant spatial variable ξ is the optical wavelength (relative to the line center), expressed in units of the homogeneous width Δ. The ξ_j are the mode wavelengths. The time t is expressed in units of the cavity lifetime τ_c. The parameters used below are motivated by the typical experimental values. $\gamma = 1.24\times 10^{-3}$ is the population relaxation rate in units of $1/\tau_c$. $\beta(\xi) = (1/\pi)/[1+\xi^2]$ is a Lorentzian of half-width 1 (i.e., the homogeneous width). Thanks to the finite-range coupling provided by β, this system appears as a chain of *locally* coupled oscillators [12]. $A(t)$ is the instantaneous pumping rate; under pump modulation, it reads $A(t) = A(1 + m\cos\omega_m t)$. We use the experimental values $A = 2.45$ and $m = 0.18$. The modulation frequency ω_m is chosen near the resonance frequency of the system ω_r that is approximately equal to $\sqrt{\gamma(A-1)}$ [here $\omega_r \approx 0.95\sqrt{\gamma(A-1)}$]; $a = 2\times 10^{-3}$ is the spontaneous emission coefficient. The nonuniformity is built into the selective pumping $g(\xi)$, that we choose Gaussian in the first part of the numerical study:

$$g(\xi) = \exp\left(-\frac{1}{2}\rho^2\xi^2\right). \tag{2}$$

The width $1/\rho$ is typically of the order of 40, and is estimated from a fit of the emission spectrum [approximatively equal to $Ag(\xi) - 1$] on experimental data (an example will be illustrated in Fig. 4).

Equations (1) are integrated with periodic boundary conditions, using a pseudospectral method, and because the mode spacing is small compared to the homogeneous width ($\xi_{j+1} - \xi_j \approx 5\times 10^{-4} \ll 1$), we approximate the discrete sum by an integral [5].

The visualization of the regimes is obtained after the following processing. The data typically consist of a periodic component at half the modulation frequency ω_m, modulated by a slower temporal evolution, namely, $X(\xi,t)\cos\omega_m t/2$. We therefore extract the relevant slow amplitude $X(\xi,t)$ using a classical demodulation (multiplication by $\cos\omega_m t/2$ and low-pass filtering).

In a first step, we perform the numerical integration with nonuniformities fixed at a realistic level ($1/\rho = 40$). The stationary wave predicted by the uniform theory [5] [Fig. 1(a)] is observed at frequencies near or much greater than ω_r, *but never at lower frequencies* (for ω_m smaller than a threshold value of the order of ω_r). When we decrease the modulation frequency from $\omega_m \approx \omega_r$, the initially stationary wave structure [Fig. 1(a)] undergoes an instability characterized by annihilations of cells near the center (phase slips), and recurrent creations near the edges. This appears in a space-time diagram [Fig. 1(b)] as spatiotemporal dislocations.

At this point, one should, however, not conclude on the instability type on the basis of the regimes appearance, because different mechanisms can be *a priori* involved. Similar defects are observed in nonuniformity-induced instabilities such as in Taylor-Couette experiments [14,15]. However, pictorially similar behaviors are also observed for topological defects of wave patterns that do not require spatial nonuniformities [16], and are based on bistability between counterpropagating waves. Therefore, additional tests are needed to conclude whether we are in the presence of the Eckhaus instability induced by nonuniformities.

First we have gradually decreased ρ toward zero, transforming continuously the realistic system into a uniform one with periodic boundary conditions. The phase-slips regimes are found to systematically disappear, and become simple stationary waves. We, therefore, conclude that the phase slips, and the defectlike structures are induced by the spatial variations of the control parameters.

Then, in order to quantitatively test whether the underlying scenario is the Eckhaus instability induced by nonuniformities, we will proceed as in the works on Taylor vortex flows [14]. We will verify that, at the transition to the phase-slips regime, the wave number selected at the center of the pattern reaches the Eckhaus boundary of the associated uniform system. The marginal and Eckhaus curves of the uniform model are obtained straightforwardly since the amplitude equations for the involved waves can be extracted from the initial model (1) with $g = 1$. At first order the solution is of the form $s(\xi,t)/(A-1) = 1 + 4i\epsilon[L\exp[i(\omega_m/2 + k_0\xi)] + R\exp[i(\omega_m/2 - k_0\xi)] + Ue^{i\omega_m t}]$ (see [5] for details), with $\omega_m/2 = \sqrt{\gamma(A-1)}e^{-|k_0(\omega_m)|}$. The amplitude equations read

$$R_\theta - \frac{1}{2}R_\zeta = -R + UL^*, \tag{3a}$$

$$L_\theta + \frac{1}{2}L_\zeta = -L + UR^*, \tag{3b}$$

$$U_\theta + iHU_\zeta = -(1+i\sigma_1)U - 2RL - \delta_2. \qquad (3c)$$

R, L, and U depend on the slow time and space variables $\theta=\epsilon t$ and $\zeta=\epsilon\xi$, where $\epsilon=\Gamma_r/\omega_r \ll 1$ and Γ_r is the damping associated with ω_r [17]; $\sigma_1=(\omega_m/\omega_r-1)/\epsilon$ and $m=16\epsilon^2(A-1)/A\delta_2$. This is similar to Ref. [5], except that we do not neglect here the first-order term of the expansion of the integral coupling for U. H denotes the Hilbert transform: $HU_\zeta(\zeta)=(1/\pi)\int_{-\infty}^{+\infty}(\zeta-\zeta')^{-1}U_\zeta(\zeta')d\zeta'$.

The main results are summarized in Fig. 2. For each modulation frequency ω_m, we have plotted the selected wave number k_s [computed from the physical model with nonuniformities (1)], and compared it to the stability curves of the associated uniform system [obtained from Eq. (3)]. When ω_m is decreased from high values, we first reach the threshold for stationary wave formation, where only one wave number $k_s \approx k_0$ is selected. When ω_m is further decreased, $k_s(\omega_m)$ clearly deviates from the most unstable wave number $k_0(\omega_m)$ of the uniform system, and eventually reaches the upper Eckhaus boundary curve. Beyond this point, the stationary wave no longer exists and is replaced by the time-dependent regimes described before [Fig. 1(b)]. This scenario is a clear signature of the *nonuniformity-induced Eckhaus instability* [1]. Note that the relative variation of k_s and k_0 are very small (of the order of ϵ). Though crucial for the system stability, they are not experimentally measurable.

It is known from the hydrodynamical context [9] that this instability can lead to chaos, depending on the precise shape of the nonuniformities (although no general rules are known). In consequence we have examined different shapes for $g(\xi)$. With the present values of the parameters, the instability always led to periodic phase slips when a Gaussian shape was used. However, we observed chaos with flatter profiles as well as with asymmetric ones. For instance, with

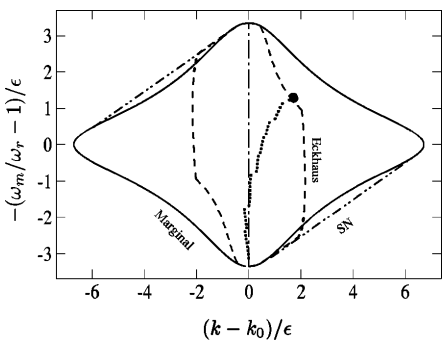

FIG. 2. Wave-number selection vs modulation frequency ω_m (high frequencies are at bottom). Dots: wave number k_s selected at center in the physical model (1) with nonuniformities ($1/\rho=40$). The marginal (solid line), saddle-node (SN, dash-dot-dot line) and Eckhaus curves (small dashes) of the associated uniform system are directly computed from the amplitude equations (3). $k_0(\omega_m)$ (dash-doted line) is the most unstable wave number of the associated uniform system.

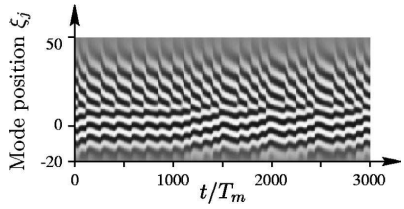

FIG. 3. Spatiotemporal chaos obtained from the model (1) with an asymmetric profile [Eq. (4a)]. $\omega_m=0.85\sqrt{\gamma(A-1)}$.

$$g(\xi)=\exp\left(-\frac{1}{2}\rho_-^2\xi^2\right) \quad \text{for} \quad \xi<0, \qquad (4a)$$

$$g(\xi)=\exp\left(-\frac{1}{2}\rho_+^2\xi^2\right) \quad \text{for} \quad \xi>0, \qquad (4b)$$

and $1/\rho_-=50/3$, $1/\rho_+=50$ we observe chaos at low frequencies (Fig. 3). This regime is characterized by one clearly positive Lyapunov exponent $\lambda_1=4.2\times10^{-3}$, a signature of chaos. Besides one trivially null exponent λ_2, we find one exponent near zero ($|\lambda_3|<10^{-5}$). The other exponents are strongly negative ($\leqslant -9.3\times10^{-2}$).

In order to verify if this instability occurs experimentally in a similarly wide range of parameters, we have recorded the evolutions of the set of modes in a Nd-doped fiber laser. The experimental setup is similar to the one previously de-

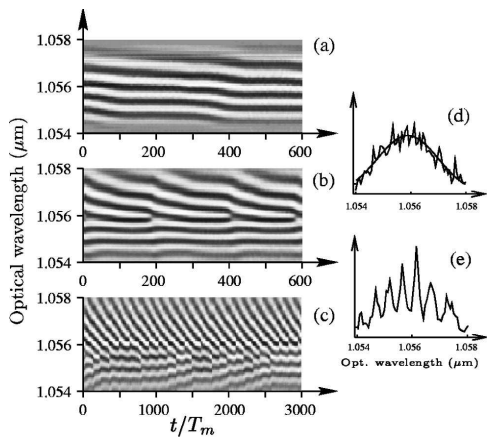

FIG. 4. Experimental evolution of the mode intensities for decreasing modulation frequencies (the amplitude of modulation is $m=0.18$). (a) Expected stationary wave ($\omega_m=1.05\omega_r$, the slow drift is due to spectrum asymmetry); (b) beyond threshold of the nonuniformity-induced Eckhaus instability ($\omega_m=0.98\omega_r$); (c) spatiotemporal chaos ($\omega_m=0.92\omega_r$); (d) experimental average lasing line shape and fit of the slowly varying Gaussian function $Ag(\xi)-1$ used for estimation of the nonuniformity parameter ρ in the numerical study; (e) snapshot of the mode intensities profile for the regime of Fig. 4(b).

scribed in Ref. [5]. The amplifying medium consists of a Nd-doped fiber emitting around 1.056 μm, cooled to 77 K, and pumped by a 810-nm diode laser. The only difference concerns the mirrors' reflection coefficients (4% and 100% for the input and end mirrors, respectively). The average pump power is 2.45 times the laser threshold.

The characteristic time scale, determined by the *relaxation frequency* ω_r [11], is very slow compared to optical time scales, as usual in class-B lasers ($\omega_r/2\pi=75$ kHz here), and thus allows real-time recording of the pattern evolutions. The pump power can be modulated sinusoidally in the 0–100 kHz range. The mode intensities are monitored by acquiring one optical spectrum at each modulation period, integrated over the period, and the visualization of the regimes is obtained by the same signal processing as for the numerical results.

Experimentally, when we decrease the modulation frequency ω_m from ω_r, we observe the same transition from stationary wave [Fig. 4(a)] to periodic phase slips [Fig. 4(b)] as predicted numerically. At the transition, the phase slips can occur either periodically or chaotically depending on the operating conditions. For ω_m/ω_r between 1 and 0.9, we observe an alternation of windows of periodic phase-slips regimes and irregular regimes [Fig. 4(c)], similar to numerical ones (Fig. 3). At much lower modulation frequencies ($\omega_m/\omega_r \approx 0.8$–$0.7$), we ultimately observe a stable set of two counterpropagating traveling waves. Note that the considered bifurcation points (transition values for ω_m) are in good agreement with numerical predictions.

In conclusion, spatial nonuniformities are shown to prevent pattern stability in one optical system (a multimode laser), following the Riecke and Paap mechanism. Since the main ingredient (slowly-varying nonuniformity) is almost omnipresent in optics, we expect a range of other optical pattern-forming systems to be affected in a similar way. The next step consists in reconsidering the problem of optical pattern formation, case by case, taking into account real nonuniformities. However, in numerous optical systems (and possibly other ones [18]), a deep study of these effects will require an attempt to extend the work of Riecke and Paap to two-dimensional systems.

We would like to thank H. Riecke for stimulating discussions. The doped fiber has been provided by the CNET Lannion. The Laboratoire Physique des lasers, Atomes et Molécules is Unité Mixte de Recherche du CNRS. The Centre de Recherches Lasers et Applications is supported by the Ministère chargé de la Recherche, the Région Nord-Pas de Calais and the FEDER.

[1] H. Riecke and H.-G. Paap, Phys. Rev. Lett. **59**, 2570 (1987).
[2] G.-L. Oppo, M. Brambilla, and L.A. Lugiato, Phys. Rev. A **49**, 2028 (1994).
[3] M.N. Ouarzazi, P.A. Bois, and M. Taki, Phys. Rev. A **53**, 4408 (1996); L.A. Lugiato *et al.*, Opt. Express **3**, 71 (1998).
[4] F. Castaldo, D. Paparo, and E. Santamato, Opt. Commun. **143**, 57 (1997).
[5] C. Szwaj, S. Bielawski, D. Derozier, and T. Erneux, Phys. Rev. Lett. **80**, 3968 (1998).
[6] L. Kramer, E. Ben-Jacob, H. Brand, and M.C. Cross, Phys. Rev. Lett. **49**, 1891 (1982).
[7] Y. Pomeau and S. Zaleski, J. Phys. (France) Lett. **44**, 135 (1983).
[8] M. Cross and P. Hohenberg, Rev. Mod. Phys. **65**, 851 (1993).
[9] H. Riecke and H.-G. Paap, Europhys. Lett. **14**, 433 (1991).
[10] H. Riecke and H.-G. Paap, in *Ordered and Turbulent Patterns in Taylor-Couette Flows*, edited by C. Andereck and F. Hayot (Plenum Press, New York, 1992).
[11] Y. Khanin, *Principles of Laser Dynamics* (Elsevier, Amsterdam, 1995).
[12] C. Szwaj, S. Bielawski, and D. Derozier, Phys. Rev. Lett. **77**, 4540 (1996).
[13] P. Coullet, T. Frisch, and G. Sonnino, Phys. Rev. E **49**, 2087 (1994).
[14] L. Ning, G. Ahlers, and D.S. Cannell, Phys. Rev. Lett. **64**, 1235 (1990).
[15] R. Wiener *et al.*, Phys. Rev. E **55**, 5489 (1997).
[16] P. Coullet, C. Elphick, L. Gil, and J. Lega, Phys. Rev. Lett. **59**, 884 (1987).
[17] The accurate values of ω_r, Γ_r, $\epsilon=\Gamma_r/\omega_r$, and σ_1 are obtained from the computation of the eigenvalue associated to the steady state of Eq. (1), with largest imaginary part $(-\Gamma_r + i\omega_r)$.
[18] K.M.S. Bajaj, N. Mukolobwiez, N. Currier, and G. Ahlers, Phys. Rev. Lett. **83**, 5282 (1999).

"Cascade of parametric instabilities in a multimode laser"

T. W. Carr, T. Erneux, C. Szwaj, M. Lefranc, D. Derozier, and S. Bielawski

Phys. Rev. A **64**, 053808 (2001)

PHYSICAL REVIEW A, VOLUME 64, 053808

Cascade of parametric instabilities in a multimode laser

T. W. Carr* and T. Erneux
Université Libre de Bruxelles, Optique Nonlinéaire Théorique, Campus Plaine, C. P. 231, 1050 Bruxelles, Belgium

C. Szwaj, M. Lefranc, D. Derozier, and S. Bielawski
Laboratoire de Physique des Lasers, Atomes et Molécules, Université des Sciences et Techniques de Lille, F-59655 Villeneuve d'Ascq Cedex, France

(Received 3 April 2001; published 4 October 2001)

We analyze analytically and experimentally a cascade of parametric instabilities in an inhomogeneously broadened multimode laser under pump modulation. From the physical model we use a multiple-scale analysis to derive slow time and slow space amplitude equations, taking nonlocal coupling into account. Each of the two waves appearing at the primary instability acts as a pump for the parametric excitation of two new traveling waves with higher wave numbers. These predictions compare well with numerical simulations of the original laser equations and experimental results obtained with a modulated Yb-doped fiber laser.

DOI: 10.1103/PhysRevA.64.053808 PACS number(s): 42.65.Sf, 47.54.+r

INTRODUCTION

Multimode laser instabilities have been the subject of many numerical investigations during the past decade [1,2]. However, combined analytical and experimental studies of their possible origins remain rare. In this paper, we concentrate on one of the simplest mechanisms, namely, a cascade of parametric instabilities that occurs in inhomogeneously broadened class-B lasers.

An inhomogeneously broadened class-B laser, such as a fiber laser, can behave as a chain of coupled oscillators, each associated with one longitudinal mode [3]. It is therefore dynamically equivalent to a one-dimensional spatio-temporal system for which the mode index j (or equivalently the optical wavelength) plays the role of the spatial variable [3,4]. Damped waves (called "spectral waves") may propagate in this set of modes (and thus in the optical spectrum) [3] and can be parametrically excited by modulating the pump [4]. They admit the typical bifurcation properties of parametrically excited systems, such as the Faraday experiment in hydrodynamics [5] and plasmas [6].

The laser system exhibits two unusual features that make it particularly interesting for analytical, numerical, and experimental studies. First, each laser mode is coupled to a large number of other modes (called finite range coupling or nonlocal coupling) [1,7,3]. Second, the laser admits a decreasing dispersion curve for the spectral traveling waves. There is currently a large interest for dynamical systems showing finite range coupling [8,9] as well as devices with unusual dispersion properties [10]. General conclusions or their effects are, however, harder to determine. For instance, we may be tempted to artificially add a term modeling finite range coupling to an already existing amplitude equation (such as a Ginzburg-Landau equation [8]). But extracting amplitude equations from the original equations exhibiting finite range coupling remains a difficult project when the coupling is not diffusive. Indeed, if the coupling between modes depends on the original space scale, we intuitively expect that its effect on the long space scale will be local. As we shall demonstrate, this idea is correct for all periodic traveling wave modes but not for the uniform time-periodic mode.

In this paper we propose an analysis of laser rate equations modeling an inhomogeneously broadened laser subject to a modulated pump. We show that a cascade of bifurcations results from the particular dispersion curve as well as from the finite range coupling. Each bifurcation corresponds to a particular combination of spectral modes and we determine slow time and long space amplitude equations for their respective evolution. In contrast to our earlier work on the problem [4], the objectives of this paper are twofold. First, we resolve a multiple scale difficulty which was ignored in [4] and properly derive the amplitude equations. Second, we consider a higher number of resonant modes leading to higher order bifurcations. This bifurcation analysis is motivated by our recent experiments which clearly show a gradual increase of the number of spectral modes as we progressively increase the modulation amplitude from zero.

The plan of the paper is as follows. In Sec. I we formulate the laser rate equations and take advantage of the laser natural range of parameters. In Sec. II we construct small amplitude traveling wave solutions and derive their amplitude equations. In Sec. III we analyze the first two bifurcations. They provide a guide for our numerical simulations of the laser original equations, summarized in Sec. IV. Finally, we discuss in Sec. V experimental results obtained by using a Yb-doped fiber laser.

I. FORMULATION

We consider an inhomogeneously broadened class-B laser without phase-sensitive interactions. The state of such a laser can be described by a set of mode intensities $s_j(t)$ and a continuous set of population inversion $d(x,t)$ [4,1,7]. In dimensionless form and considering the continuous limit of a large number of modes [i.e., $s_j(t)$ is replaced by $s(x,t)$],

*Permanent address: Department of Mathematics, Southern Methodist University, Dallas, Texas 75275.

these equations take a simple form given by [4]

$$\partial_t s(x,t) = -s(x,t) + [s(x,t)+a]\int_{-\infty}^{\infty}\beta(y-x)d(y,t)dy, \tag{1a}$$

$$\partial_t d(x,t) = \gamma\left[g(x)A(t) - d(x,t)\left(1+\int_{-\infty}^{\infty}\beta(y-x)\times s(y,t)dy\right)\right]. \tag{1b}$$

In these equations, $\beta(x)$ is a cross-saturation coupling coefficient defined by

$$\beta(x) \equiv \frac{1}{\pi}\frac{1}{1+x^2} \tag{2}$$

and its Lorentzian shape ensures the coupling between the modes. The spatial coordinate x refers to an emission optical frequency of a specific mode. Note that the intensities and populations evolve according to much slower time scale than the optical ones. Time t is measured in units of the cavity lifetime τ_c which is typically in the microsecond range. The parameter a is the spontaneous-emission coefficient; it will be neglected in the analytical calculation, but not in the numerical simulation. The parameter γ is the population inversion rate normalized by the photon decay rate τ_c^{-1} and is typically small. $A(t)=A[1+m\cos(\omega_m t)]$ denotes the modulated pumping rate where A, m, and ω_m represent its average, amplitude, and frequency, respectively. ω_m and m are our two control parameters and ω_m is chosen close to the relaxation oscillation frequency of the single mode laser defined by $\omega_r \equiv \sqrt{\gamma(A-1)}$. Nonuniformities of the laser spectrum are modeled by the selective pumping coefficient $g(x)$. In our analytical work, we shall consider an infinitely large medium with $g(x)=1$. In our numerical simulations, we use a Gaussian function for $g(x)$.

We may rewrite Eqs. (1a) and (1b) in a more elegant form for analysis by introducing deviations from the uniform steady state, $(s,d)=(A-1,1)$, and by rescaling time with the relaxation oscillations frequency ω_r. Specifically, we introduce the variables u, v, and τ defined by

$$u = -1 + \frac{s}{A-1}, \quad v = \frac{d-1}{\omega_r}, \quad \text{and} \quad \tau = \omega_r t \tag{3}$$

into Eqs. (1a) and (1b) and obtain

$$\partial_\tau u = (1+u)\int_{-\infty}^{\infty}\beta(y-x)v(y)dy, \tag{4a}$$

$$\partial_\tau v = -(1+2\varepsilon F^{-1}v)\int_{-\infty}^{\infty}\beta(y-x)u(y)dy - 2\varepsilon v + \delta\cos(\sigma\tau), \tag{4b}$$

where new parameters ε, δ, σ are

$$\varepsilon \equiv \frac{\gamma A}{2\omega_r}, \quad \delta \equiv \frac{Am}{A-1}, \quad F \equiv \frac{A}{A-1}, \quad \text{and} \quad \sigma \equiv \frac{\omega_m}{\omega_r}. \tag{5}$$

In Eq. (4b), all parameters are $O(1)$ except the dissipation parameter ε and the forcing amplitude δ. The small parameter ε measures the natural damping of the laser relaxation oscillations in units of the relaxation frequency ω_r. Since ω_r is $O(\sqrt{\gamma})$ small, ε is an $O(\sqrt{\gamma})$ small quantity. δ is proportional to the modulation amplitude m, and σ is the modulation frequency normalized by the relaxation oscillation frequency ω_r.

It is worthwhile to briefly describe the results of the linear stability analysis in the case of no pump modulations ($\delta=0$) [3]. Introducing $u=c_1\exp(ikx)\exp(\lambda\tau)$ and $v=c_2\exp(ikx)\exp(\lambda\tau)$ into the linearized equations leads to the characteristic equation $\lambda^2+2\varepsilon\lambda+B^2=0$, where $B(k)=\exp(-|k|)$ is the Fourier transform of $\beta(x)$. For small ε, λ admits the following approximation:

$$\lambda = \pm i\omega - \varepsilon + O(\varepsilon^2), \tag{6}$$

where ω is given by

$$\omega = B(k) = \exp(-|k|). \tag{7}$$

Equation (7) is the leading expression of the dispersion relation $\omega=\omega(k)$ for the periodic traveling waves of the form $u=c_1\exp(i\omega\tau\pm ikx)$ and $v=c_2\exp(i\omega\tau\pm ikx)$. It will reappear in our bifurcation analysis.

We wish to determine the solution generated by near resonance modulations ($\sigma\sim 1$). A fundamental parametric instability similar to Faraday instability in hydrodynamics may then occur if $\omega\sim 1/2$. This instability leads to a period doubling bifurcation to a stationary wave which we have studied numerically and experimentally in [4]. The wave number k_1 of this stationary wave verifies the dispersion relation (7). But other traveling wave solutions exhibiting other frequencies and wave numbers have been observed experimentally. Our goal is to show that these waves do not appear by chance but sequentially appear through higher order bifurcations. To this end, we develop a multiple scale analysis of the laser equations (4a) and (4b) and reduce the original laser equations to amplitude equations which are easier to investigate.

II. MULTIPLE-SCALE ANALYSIS

We wish to determine the solution, Eqs. (4a) and (4b), for σ close to 1 and δ small. To this end, we first expand these parameters as

$$\sigma = 1 + \varepsilon\sigma_1 + \cdots, \quad \delta = \varepsilon^2\delta_2 + \cdots, \tag{8}$$

where ε is defined in Eq. (5). The scaling for δ is imposed by the solvability conditions. We then seek a solution of the form

$$u = \varepsilon u_1(T,\theta,x,\zeta) + \varepsilon^2 u_2(T,\theta,x,\zeta) + \cdots, \tag{9a}$$

$$v = \varepsilon v_1(T,\theta,x,\zeta) + \varepsilon^2 v_2(T,\theta,x,\zeta) + \cdots, \tag{9b}$$

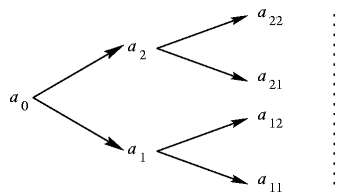

FIG. 1. Diagram showing the cascade process.

where $T \equiv \sigma\tau$ is our new basic time, $\theta \equiv \varepsilon\tau$ is a slow time variable, and $\zeta \equiv \varepsilon x$ is a long space variable. The two independent time scales require the chain rule $u_\tau = \sigma u_T + \varepsilon u_\theta$. The assumption of two distinct space variables needs, however, a careful treatment because the spatial coupling between the modes is realized through an integral operator rather than a differential operator. All mathematical details are relegated to the Appendixes and we summarize the main results. The leading order problem for u_1 and v_1 is linear and admits a multimode solution of the form

$$u_1 = \sum_n a_n(\theta,\zeta)\exp(i\Omega_n T + ik_n x) + \text{c.c.}, \tag{10}$$

$$v_1 = \sum_n i a_n(\theta,\zeta)\exp(i\Omega_n T + ik_n x) + \text{c.c.}, \tag{11}$$

provided that all frequencies $\omega = \Omega_n$ and wave numbers $k = k_n$ satisfy the dispersion relation (7). c.c. means complex conjugate. We shall consider the interaction of seven modes which appear through a cascade of parametric instabilities illustrated in Fig. 1. Specifically, the uniform mode of amplitude a_0 excites a stationary wave made of two counterpropagating traveling waves of amplitudes a_1 and a_2, respectively. Next, the traveling wave of amplitude a_l excites the pair of traveling waves of amplitudes a_{ll} and a_{lm} (with l and $m = 1,2$). For example, the amplitude a_1 excites the pair of traveling waves of amplitude a_{11} and a_{12}. This notation allows us to identify the origin of a_n ($n = 0,1,2,11,12,21,22$), and will be useful as we examine the symmetries in the amplitude equations.

The first parametric instability is realized by the resonance condition

$$k_1 + k_2 = 0 \quad \text{and} \quad \Omega_1 = \Omega_2 = 1/2. \tag{12}$$

The second parametric instability is possible if

$$k_{11} + k_{12} = k_1, \quad \Omega_{11} + \Omega_{12} = \Omega_1 = 1/2, \tag{13}$$

$$k_{21} + k_{22} = -k_1 \quad \text{and} \quad \Omega_{21} + \Omega_{22} = \Omega_2 = 1/2. \tag{14}$$

Because the amplitudes a_n in Eqs. (10) and (11) are unknown, we need to investigate the next problem for u_2 and v_2 and apply solvability conditions. These conditions lead to equations for the amplitudes a_n which are given by Eqs. (A13)–(A19) in Appendix A. They exhibit both sum-frequency terms $S_n = a_i a_j$ as well as parametric gain terms $P_n = a_i a_j^*$ thanks to the resonance conditions (12)–(14). Before we analyze these equations, we evaluate all wave numbers and frequencies using the conditions (7) and (12)–(14). They are listed in Table I for clarity. We have verified that the linear terms appearing in the amplitude equations (A13)–(A19) reproduce the informations from the linear stability analysis, i.e., the growth rate in powers of ε given by Eq. (6) (see Appendix C). These linear terms provide the $O(\varepsilon)$ changes of each resonant wave number and each resonant frequency resulting from the detuning σ_1. It will be physically and mathematically useful to take into account these changes and reformulate the leading approximation of the solution. Specifically, we introduce the new amplitude

TABLE I. Parametric resonances. The primary resonance involves the first three modes and verifies the conditions (12). The second resonance is realized with the four remaining modes and verifies the conditions (12)–(14).

n	Ω_n	k_n
0	1	0
1	1/2	$-\ln(2)$
2	1/2	$\ln(2)$
11	1/6	$-\ln(6)$
12	1/3	$\ln(3)$
21	1/3	$-\ln(3)$
22	1/6	$\ln(6)$

$$b_n = a_n \exp(-i\mu_n\theta - i\kappa_n\zeta) \quad (n \neq 0) \tag{15}$$

into Eqs. (10) and (11) and require that μ_n and κ_n satisfy the $O(\varepsilon)$ contribution of the dispersion relation (7). Noting that the $O(\varepsilon)$ correction of the frequency measured in units of time τ is $\mu_n + \Omega_n\sigma_1$, this relation is given by

$$\mu_n + \Omega_n\sigma_1 = v_{gn}\kappa_n \quad \text{for} \quad n \neq 0, \tag{16}$$

where v_{gn} is the group velocity defined by Eq. (A20). We may then rewrite the solutions (10) and (11) as

$$u_1 = \sum_n b_n(\theta,\zeta)\exp(i\hat{\omega}_n\tau + i\hat{k}_n x) + \text{c.c.}, \tag{17}$$

$$v_1 = \sum_n i b_n(\theta,\zeta)\exp(i\hat{\omega}_n\tau + i\hat{k}_n x) + \text{c.c.}, \tag{18}$$

where $\hat{\omega}_n(\varepsilon) \equiv \Omega_n + \varepsilon(\mu_n + \Omega_n\sigma_1)$ and $\hat{k}_n(\varepsilon) \equiv k_n + \varepsilon\kappa_n$ represent the effective frequencies and wave number associated with each traveling wave mode and $b_0 = a_0$, $\mu_0 = \kappa_0 = 0$. The main benefit of Eqs. (17) and (18) is the fact that a constant b_n now corresponds to a traveling wave mode amplitude at the effective frequencies and wave number. Moreover, the evolution equations for the b_n are simpler than the equations for the a_n. Of course, we also wish that the effective frequencies and wave numbers satisfy the parametric resonance conditions. From Eqs. (12)–(14) with $\hat{\Omega}_n = \sigma^{-1}\hat{\omega}_n$ replacing Ω_n and $\hat{k}_n$ replacing k_n, respectively, we obtain the following conditions for μ_n and κ_n:

$$\kappa_1+\kappa_2=0, \quad \mu_1=\mu_2=0, \tag{19}$$

$$\kappa_{11}+\kappa_{12}=\kappa_1, \quad \mu_{11}+\mu_{12}=0, \tag{20}$$

$$\kappa_{21}+\kappa_{22}=-\kappa_1, \quad \mu_{21}+\mu_{22}=0. \tag{21}$$

Together with Eq. (16), we easily determine κ_n and μ_n as

$$\mu_1=\mu_2=0, \tag{22}$$

$$\kappa_1=-\kappa_2=\sigma_1, \tag{23}$$

$$\mu_{11}=\mu_{22}=-\mu_{12}=-\mu_{21}=\frac{\sigma_1}{9}, \tag{24}$$

$$\kappa_{11}=-\kappa_{22}=\frac{5\sigma_1}{3}, \quad \kappa_{12}=-\kappa_{21}=-\frac{2\sigma_1}{3}. \tag{25}$$

Using Eq. (15) with Eqs. (22)–(25), our amplitude equations (A13)–(A19) simplify as

$$\dot{b}_0-iH(b_0')=-b_0-i\sigma_1 b_0-\frac{i\delta_2}{4}+\frac{i}{2}b_1b_2, \tag{26}$$

$$\dot{b}_1-v_{g1}b_1'=-b_1+\frac{i}{4}(b_0b_2^*+b_{11}b_{12}), \tag{27}$$

$$\dot{b}_2-v_{g2}b_2'=-b_2+\frac{i}{4}(b_0b_1^*+b_{21}b_{22}), \tag{28}$$

$$\dot{b}_{11}-v_{g11}b_{11}'=-b_{11}+\frac{i}{12}b_1b_{12}^*, \tag{29}$$

$$\dot{b}_{12}-v_{g12}b_{12}'=-b_{12}+\frac{i}{6}b_1b_{11}^*, \tag{30}$$

$$\dot{b}_{21}-v_{g21}b_{21}'=-b_{21}+\frac{i}{6}b_2b_{22}^*, \tag{31}$$

$$\dot{b}_{22}-v_{g22}b_{22}'=-b_{22}+\frac{i}{12}b_2b_{21}^*, \tag{32}$$

where the σ_1 term do not appear in the equation for b_n ($n\neq 0$). In these equations, dot and prime mean partial derivatives with respect to time θ and space ζ, respectively. v_{gn} is the group velocity defined by Eq. (A20) and $H(b_0')$ represent the Hilbert transform of b_0' defined by Eq. (A6).

III. CASCADING BIFURCATIONS

In this section we determine the bifurcation diagram of the steady and uniform solutions of Eqs. (26)–(32). The analysis is long and tedious but leads to simple analytical results which we summarize.

The basic solution verifies the condition $b_n=0$ ($n\neq 0$) and admits the amplitude

$$|b_0|=\frac{\delta_2}{4\sqrt{1+\sigma_1^2}}. \tag{33}$$

It represents a uniform $2\pi/\omega_m$ time-periodic solution of the original laser equations (1a) and (1b). We next determine a primary bifurcation from this spatially uniform solution to a stationary wave solution.

The stationary wave solution satisfies the condition $b_n=0$ ($n=11,12,21,22$). We first solve the equations for b_1 and b_2 and then the equation for b_0 and obtain

$$|b_0|=4, \quad |b_1|=|b_2|. \tag{34}$$

$|b_1(\delta_2^2)|$ is given by the implicit solution

$$\delta_2^2-\delta_P^2=64|b_1|^2(1+\tfrac{1}{16}|b_1|^2), \tag{35}$$

where δ_P is a primary bifurcation point defined by

$$\delta_P\equiv 4\sqrt{1+\sigma_1^2}. \tag{36}$$

The bifurcation is clearly supercritical (i.e., $\delta_2>\delta_P$ if $|b_1|\neq 0$) and leads to a $4\pi/\omega_m$ time-periodic stationary wave solution of the original laser equations which we analyzed in [4]. But this solution may itself exhibit a secondary bifurcation to a more complex solution with now all the $b_n\neq 0$.

We determine this new solution by solving first the equations for b_{11}, b_{12}, b_{21}, b_{22}, then the equations for b_1 and b_2, and finally the equation for b_0. We find

$$|b_1|=|b_2|=6\sqrt{2}, \tag{37}$$

$$|b_{12}|=|b_{21}|=2|b_{11}|=2|b_{22}|, \tag{38}$$

where $|b_{11}|$ is related to $|b_0|$ by

$$|b_{11}|=2\sqrt{6}\left(\frac{|b_0|}{4}-1\right). \tag{39}$$

Finally $|b_0(\delta_2^2)|\geqslant 4$ is given by the implicit solution

$$\delta_2^2-\delta_S^2=16(|b_0|-4)[(|b_0|+4)(1+\sigma_1^2)+72], \tag{40}$$

where δ_S is a secondary bifurcation point defined by

$$\delta_S=16\sqrt{100+\sigma_1^2}. \tag{41}$$

The bifurcation is clearly supercritical since $|b_0|\geqslant 4$. It leads to a multifrequency traveling wave solution of the original laser equations. Computing the frequencies $\hat{\omega}_n(\varepsilon)$ shows that this solution is not periodic if $\sigma_1\neq 0$.

IV. NUMERICAL STUDY

Our previous analysis of the laser equations (1a) and (1b) with $g(x)=1$ and $a=0$ led to simple analytical expressions for the primary and secondary bifurcations. They will be useful as we integrate Eqs. (1b) and (1b) numerically with a spatial variation of the pump and nonzero values of the spontaneous emission coefficient. Specifically, we consider $g(x)$

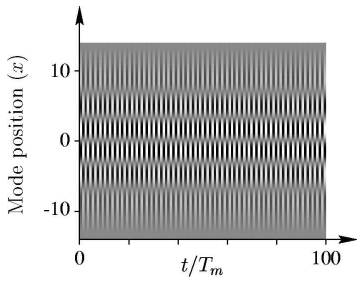

FIG. 2. Numerical solution of the laser equations (1a) and (1b) after the primary bifurcation ($\omega_m = 0.80\omega_r$ and $m = 0.16$).

$=\exp(-x^2/2\rho^2)$ where the width of the Gaussian ρ is changed from 70 to 10, and the values of a from 10^{-3} to 10^{-5}. We also investigated the change of the bifurcation diagram as the laser fixed parameter A and γ are changed [A (several unities) and γ (10^{-3} to 10^{-5})].

The values of the laser fixed parameters that best correspond to our experiments are given by $A=3$, $\gamma=1.34\times10^{-4}$, $a=8.3\times10^{-4}$, $\rho=75/7$, and $\omega_m=0.8\omega_r$. The

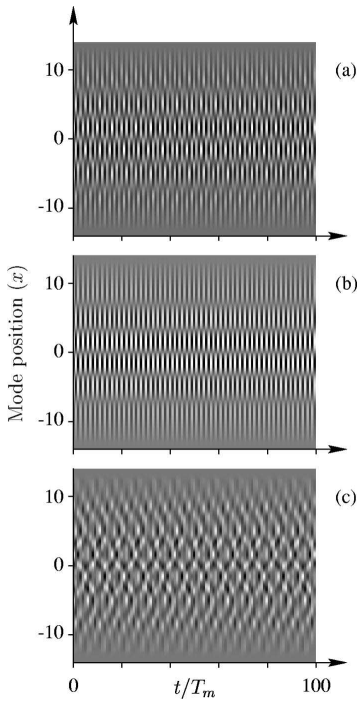

FIG. 3. (a) Numerical solution of the laser equations (1a) and (1b) after the secondary bifurcation ($\omega_m = 0.8\omega_r$ and $m = 0.195$); (b) high temporal frequency part showing the basic stationary wave; (c) low temporal frequency part showing the new waves emerging at the secondary bifurcation.

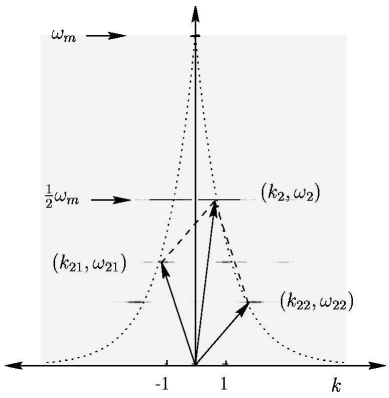

FIG. 4. Temporal and spatial Fourier transform of the solution shown in Fig. 3(a). The dispersion curve, given by Eq. (7), is shown in the figure by a dashed line.

modulation amplitude m is the bifurcation parameter. As we progressively increase m from zero, we typically observe the Faraday instability as the primary instability. This bifurcation leads to a subharmonic stationary wave (Fig. 2), as previously reported in Ref. [4]. As we further increase m, this solution changes stability through a secondary bifurcation. The new solution exhibits additional modulations in space and time (Fig. 3).

In order to clearly identify the new components of the secondary bifurcating solution and verify that they appear through the mechanism predicted in Sec. III, it is worth examining the Fourier transforms both in space and time of the spectrochronogram of Fig. 3(a) (Fig. 4). As can be seen in Fig. 4, we observe six main spectral components in addition to the fundamental component (located at $\omega_m=\omega_r, k=0$). The two first are localized at the subharmonics of the modulation and correspond to the usual Faraday waves ($\omega_1=\omega_2=\omega_m/2, k_1=-k_2$). The four other components appear at the secondary bifurcation and correspond to four traveling waves. Furthermore, one pair of traveling waves $\{(\omega_{21},k_{21}),(\omega_{22},k_{22})\}$ satisfies the resonance conditions

$$k_2 = k_{21} + k_{22}, \tag{42a}$$

$$\omega_2 = \omega_{21} + \omega_{22}, \tag{42b}$$

and a similar relation is verified for the other pair of traveling waves $\{(\omega_{11},k_{11}),(\omega_{12},k_{12})\}$. Graphically (see Fig. 4), this relation means that we may draw a parallelogram in the (ω,k) diagram which connects the origin, one point associated to the Faraday mode, and two points associated to the new modes appearing at the secondary instability. This parallelogram clearly indicates that we are in presence of the secondary bifurcating solution predicted by our analysis.

High-frequency temporal filtering ($\omega > 0.4\omega_m$) allows us to extract and visualize the high-frequency part [i.e., the basic Faraday stationary wave, Fig. 3(b)]. Low-frequency filtering ($\omega < 0.4\omega_m$) allows us to keep only the four traveling

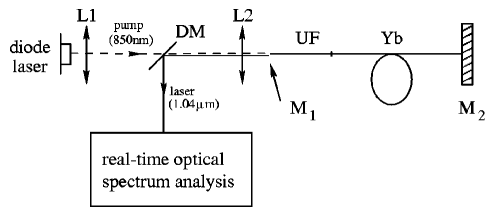

FIG. 5. Experimental setup. The laser cavity is delimited by the R_{max} mirror (M_2), and the air/glass interface (M_1) at the extremity of the undoped fiber (UF). Yb is the Yb^{3+}-doped fiber; ($L1$) and ($L2$) are, respectively, a collimating lens, and a microscope objective ($\times 10$); the dichroic mirror (DM) is R_{max} at the laser wavelength.

waves which exhibit the lowest frequencies and which appear at the secondary bifurcation. Their superposition leads to the pattern shown in [Fig. 3(c)].

V. EXPERIMENTAL STUDY

A. Experimental setup

The system under investigation is a Yb-doped fiber laser operating at 1.04 μm. The fiber is cooled at 77 K in order to obtain a small homogeneous width. Thus we obtain a large aspect ratio, as is supposed in the theoretical study [11]. The experimental setup is represented in Fig. 5. The active Yb^{3+} silica fiber (CNET FPGA461Yb) is fusion spliced to 2 m of an undoped one. Both fibers are single mode at pump and laser wavelengths and the overall length is 19 m. The pump is provided by a single mode 852 nm diode laser (SDL5411). The input mirror is constituted by the glass/air interface ($R = 4\%$) at the input, and the output mirror is a R_{max} around 1.04 μm. Under typical conditions, the output power can typically reach 15 mW. The optical spectrum is analyzed by means of a monochromator followed by a Silicium charge-coupled device (CCD) array (EGG RL0256D). One spectrum is recorded at each period of modulation by a Datel PCI416H acquisition board, and we perform a real-time visualization of the spectrochronograms during the experiment. In the following, the pump rate is $A=3$, and the modulation frequency $\omega_m = 0.8\omega_r$, with ω_r the relaxation frequency of the laser $\omega_r = 40$ kHz.

B. Results

Experimentally, when we increase the modulation amplitude from zero, we observe the same bifurcations scenario as noted numerically. First, a supercritical bifurcation occurs leading to a stationary wave inside the spectrum (Fig. 6). This corresponds to the primary bifurcation (or Faraday instability). When the modulation amplitude is further increased, we observe a secondary bifurcation leading to a multifrequency regime [Fig. 7(a)].

We have verified that the Fourier transform in space and time of this regime displays the six spectral components that characterizes the secondary bifurcation (Fig. 8). As in our numerical study, high frequency temporal filtering [Fig. 7(b)]

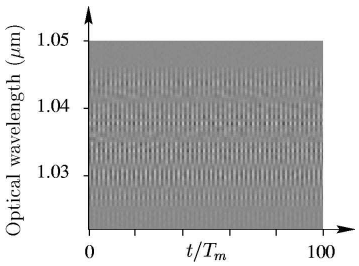

FIG. 6. Experimental regime observed after the primary bifurcation ($m = 0.18$).

allows us to visualize the Faraday stationary wave while the low temporal filtering reveals the secondary bifurcating traveling wave modes [Fig. 7(c)]. At much higher modulation amplitudes, the quasiperiodic regime becomes unstable and we observe more complex (chaotic) regimes which we do not analyze.

VI. SUMMARY

In this paper we proposed a combined analytical, numerical, and experimental study of an inhomogeneously broad-

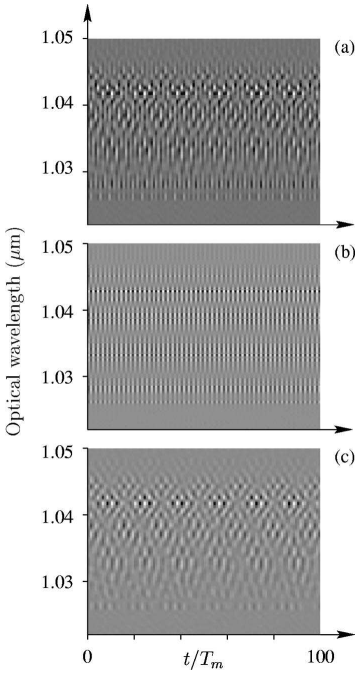

FIG. 7. (a) Experimental regime observed after the secondary bifurcation ($m = 0.20$). (b) High temporal frequency part showing the basic stationary wave. (c) Low temporal frequency part showing the new waves appearing after the secondary bifurcation.

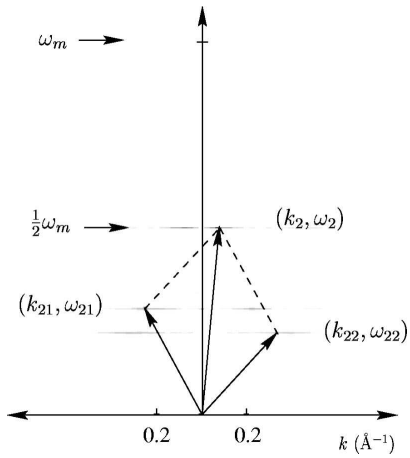

FIG. 8. Temporal and spatial Fourier transform of the pattern shown in Fig. 7(a).

ened multimode fiber laser. We concentrated on the first two bifurcations because they are immediately followed by more complex (chaotic) regimes as the modulation amplitude is further increased.

The analysis of the laser equations considers the simple case of a uniform pump $[g(x)=1]$. We derived amplitude equations for the resonant traveling wave modes that appear at the primary and secondary bifurcation points. Of particular interest is the nonlocal coupling term (the Hilbert transform) that appears for the uniform periodic mode. It models the effect of finite range coupling now on the long space scale $\zeta=\varepsilon x$. It is interesting to note that the same Hilbert transform appears in a single partial differential equation describing a planar flame front subject to Darrieus-Landau instability [12,13]. The main advantage of our amplitude equations is the fact that steady states solutions of these equations correspond to traveling wave solutions of the original laser equations. Consequently, we obtained useful expressions of the bifurcation points in term of the laser parameters. Other spatio-temporal solutions of these equations may be possible but were not suggested by our numerical study of the laser equations. If we consider $g(x)$ as a slowly varying function of ζ [i.e., we consider ρ in $g(x)=\exp(-x^2/2\rho^2)$ as an $O(\varepsilon^{-1})$ large parameter and reformulate $g(x)$ as $g=g(\zeta)$], amplitude equations similar to Eqs. (26)–(32) can still be derived but exhibit coefficients which are functions of ζ. Consequently, constant solutions for the a_n are no longer possible and their equations need to be studied numerically. This problem is currently investigated.

The numerical study of the original laser equations considers the realistic case of $g(x)$ given by a Gaussian function of x. We have found that the first two bifurcations correspond to the bifurcations documented analytically for $g(x)=1$. In particular, we identified the main features of the primary and secondary bifurcating solutions by examining their spectral properties in detail. Finally, we found experimentally the laser two first bifurcations leading to two distinct patterns that compare well with the solutions obtained numerically.

ACKNOWLEDGMENTS

We would like to thank Dominique Razafimahatratra and Philippe Verkerk for their contributions in the experiment. The Laboratoire de Physique des Lasers, Atomes et Molecules is Unité de Recherche Mixte du CNRS. The Center d'Études et de Recherches Lasers et Applications is supported by the Ministère chargé de la Recherche, the Région Nord-Pas de Calais, and the Fonds Européen de Développement Économique des Régions. T.W.C. was supported by the National Science Foundation Grant No. DMS-9803207. The research by T.E. was supported by the U.S. Air Force Office of Scientific Research Grant No. AFOSR F49620-98-1-0400, the National Science Foundation Grant No. DMS-9973203, the Fonds National de la Recherche Scientifique (Belgium), and the InterUniversity Attraction Pole program of the Belgian government.

APPENDIX A

The integral operator

$$F(u,\varepsilon)=\frac{1}{\pi}\int_{-\infty}^{\infty}\frac{1}{1+(y-x)^2}u(y,\varepsilon y)dy \tag{A1}$$

depends on ε because we assume that u is a function of two independent spatial variables x and $\zeta=\varepsilon x$. A naive two terms expansion of the integral (A1) gives

$$F(u,\varepsilon)=\frac{1}{\pi}\int_{-\infty}^{\infty}\frac{1}{1+(y-x)^2}u(y,\varepsilon x+\varepsilon(y-x))dy \tag{A2}$$

$$=F_0(u)+\varepsilon F_1(u)+\cdots, \tag{A3}$$

where

$$F_0(u)=\frac{1}{\pi}\int_{-\infty}^{\infty}\frac{1}{1+(y-x)^2}u(y,\zeta)dy, \tag{A4}$$

$$F_1(u)=\frac{1}{\pi}\int_{-\infty}^{\infty}\frac{(y-x)}{1+(y-x)^2}u_\zeta(y,\zeta)dy. \tag{A5}$$

Equation (A4) is the original operator evaluated at $\varepsilon y=\varepsilon x$ while Eq. (A5) is a new integral acting on u_ζ. If $u(y,\zeta)$ is only a function of ζ and if u_ζ is assumed constant as we integrate with respect to the fast spatial variable y, the integral (A5) is clearly unbounded. A more careful treatment is needed for this case and leads to a Hilbert transform given by (see Appendix B)

$$F_1(u)=H(u_\zeta)=\frac{1}{\pi}\int_{-\infty}^{\infty}\frac{1}{\xi-\zeta}u_\xi(\xi)d\xi. \tag{A6}$$

In our perturbation analysis, we apply the integral operator (A1) when u is a sum of periodic functions of the form

$$u=\sum_m a_m(\zeta)\exp(ik_m x). \tag{A7}$$

Using Eq. (A7), we may evaluate F_0 and F_1 and obtain the useful formula

$$F_0(u)=\sum_m a_m(\zeta)\exp(-|k_m|)\exp(ik_m x), \tag{A8}$$

$$F_1(u)=\sum_{m\neq 0}\operatorname{sgn}(k_m)ia_m'(\zeta)\exp(-|k_m|)\exp(ik_m x) + H(a_0'(\zeta)), \tag{A9}$$

where $H(a_0')$ is the Hilbert transform of a_0', and the prime means derivation with respect to ζ.

We are now ready to start our perturbation analysis. Introducing Eqs. (8)–(9b) into Eqs. (4a) and (4b) leads to the following sequence of problems for (u_1,v_1) and (u_2,v_2): for $O(\varepsilon)$

$$u_{1T}=F_0(v_1) \quad \text{and} \quad v_{1T}=-F_0(u_1). \tag{A10}$$

For $O(\varepsilon^2)$

$$u_{2T}-F_0(v_2)=R_1\equiv u_1F_0(v_1)-\sigma_1u_{1T}-u_{1\theta}+F_1(v_1), \tag{A11}$$

$$v_{2T}+F_0(u_2)=R_2 \equiv -2v_1+\delta_2\cos(T)-\sigma_1v_{1T}-v_{1\theta}-F_1(u_1).$$

The solution of Eq. (A10) is a sum of periodic plane wave solutions given by (10) and (11). Because the amplitude $a_n(\theta,\zeta)$ in (10) and (11) are unknown, we consider the higher order problem given by Eq. (A11) and apply solvability conditions with respect to each critical mode. Taking the T derivative of Eq. (A11) and using the equation for u_2, we obtain an equation for v_2 only. The solvability conditions are then the following orthogonality conditions:

$$0=\int_0^{2\pi/\Omega_m}\int_0^{2\pi/k_m}\exp(-i\Omega_nT-ik_nx)[R_{2T}-F_0(R_1)] \times dTdx. \tag{A12}$$

These conditions lead to seven coupled partial differential equations for the amplitudes a_n given by

$$\dot{a}_0-iH(a_0')=-a_0-i\sigma_1a_0-\frac{i\delta_2}{4}+\frac{i}{2}a_1a_2, \tag{A13}$$

$$\dot{a}_1-v_{g1}a_1'=-a_1-\frac{i}{2}\sigma_1a_1+\frac{i}{4}(a_0a_2^*+a_{11}a_{12}), \tag{A14}$$

$$\dot{a}_2-v_{g2}a_2'=-a_2-\frac{i}{2}\sigma_1a_2+\frac{i}{4}(a_0a_1^*+a_{21}a_{22}), \tag{A15}$$

$$\dot{a}_{11}-v_{g11}a_{11}'=-a_{11}-\frac{i}{6}\sigma_1a_{11}+\frac{i}{12}a_1a_{12}^*, \tag{A16}$$

$$\dot{a}_{12}-v_{g12}a_{12}'=-a_{12}-\frac{i}{3}\sigma_1a_{12}+\frac{i}{6}a_1a_{11}^*, \tag{A17}$$

$$\dot{a}_{21}-v_{g21}a_{21}'=-a_{21}-\frac{i}{3}\sigma_1a_{21}+\frac{i}{6}a_2a_{22}^*, \tag{A18}$$

$$\dot{a}_{22}-v_{g22}a_{22}'=-a_{22}-\frac{i}{6}\sigma_1a_{22}+\frac{i}{12}a_2a_{21}^*. \tag{A19}$$

In these equations, the dots and primes mean partial derivatives with respect to time θ and space ζ, respectively. The coefficient v_{gn} is the group velocity defined as

$$v_{gn}\equiv\left[\frac{dB(k)}{dk}\right]_{k=k_n}=-\Omega_n\operatorname{sgn}(k_n) \tag{A20}$$

and $H(a_0')$ represents the Hilbert transform of $a_0'(\zeta)$.

APPENDIX B

We wish to find the limit of the integral

$$I(x)=\frac{1}{\pi}\int_{-\infty}^{\infty}\frac{1}{1+(y-x)^2}u(\varepsilon y)dy \tag{B1}$$

as $\varepsilon\to 0$. In order to find the correct limit, we shall consider the Fourier transform of Eq. (B1) and expand its expression in power series of ε. To this end, we introduce the coordinates $X\equiv\varepsilon x$ and $Y\equiv\varepsilon y$ and rewrite Eq. (B1) as

$$I(x)=\frac{\varepsilon}{\pi}\int_{-\infty}^{\infty}\frac{1}{\varepsilon^2+(Y-X)^2}u(Y)dY \tag{B2}$$

so that ε appears explicitly in the integral. The Fourier transform is defined by the integral [14]

$$F(\xi)=\frac{1}{\sqrt{2\pi}}\int_{-\infty}^{\infty}f(x)\exp(i\xi x)dx \tag{B3}$$

and the inversion integral is

$$f(x)=\frac{1}{\sqrt{2\pi}}\int_{-\infty}^{\infty}F(\xi)\exp(-i\xi x)d\xi. \tag{B4}$$

The expression (B2) is proportional to the Fourier convolution of the two functions $f(X)=(\varepsilon^2+X^2)^{-1}$ and $g(X)=u(X)$,

$$I(X)=\frac{\varepsilon}{\pi}\sqrt{2\pi}f\bigcirc g(X). \tag{B5}$$

The convolution operation then gives (using the table in [14])

$$\begin{aligned}\mathrm{Im}[I(X);\xi] &= \frac{\varepsilon}{\pi}\sqrt{2\pi}F(\xi)G(\xi)\\ &= \frac{\varepsilon}{\pi}\sqrt{2\pi}\varepsilon^{-1}\sqrt{\frac{\pi}{2}}\exp(-\varepsilon|\xi|)U(\xi)\\ &= \exp(-\varepsilon|\xi|)U(\xi) = (1-\varepsilon|\xi|+\cdots)U(\xi).\end{aligned} \tag{B6}$$

Consider now the Hilbert transform of the function $u'(X)$ [15]

$$H(u'(X)) = \frac{1}{\pi}\int_{-\infty}^{\infty}\frac{1}{T-X}u'(T)dT. \tag{B7}$$

Equation (B7) is proportional to the Fourier convolution of the two functions $f(X)=X^{-1}$ and $g(X)=u'(X)$, i.e.,

$$H(u'(X)) = \frac{1}{\pi}\sqrt{2\pi}f\bigcirc g(X). \tag{B8}$$

The convolution operation now gives (using the table in [14])

$$\begin{aligned}\mathrm{Im}[H(u'(X));\xi] &= \frac{1}{\pi}\sqrt{2\pi}F(\xi)G(\xi)\\ &= \frac{1}{\pi}\sqrt{2\pi}\sqrt{\frac{\pi}{2}}i\,\mathrm{sgn}(\xi)(-i\xi)U(\xi)\\ &= \mathrm{sgn}(\xi)\xi U(\xi) = |\xi|U(\xi).\end{aligned} \tag{B9}$$

Comparing Eq. (B9) and the $O(\varepsilon)$ correction term in Eq. (B6), we conclude that

$$I(X) = u(X) - \varepsilon H(u'(X)) + \cdots, \tag{B10}$$

where the Hilbert transform $H(u'(X))$ is defined by Eq. (B7).

APPENDIX C

It is interesting to note that the linear terms in Eqs. (A13)–(A19) could be anticipated from the linear stability analysis. If $n\neq 0$, the linearized problem for a_n is

$$\dot{a}_n - v_{gn}a_n' = -a_n - i\Omega_n\sigma_1 a_n. \tag{C1}$$

Inserting $a_n = c\exp(\mu_1\theta + ik_{n,1}\zeta)$ into Eq. (C1) leads to

$$\mu_1 = -1 + iv_{gn}k_{n,1} - i\Omega_n\sigma_1. \tag{C2}$$

Using now $u = a_n(\theta,\zeta)\exp(i\Omega_n T + ik_n x)$ with $T=\sigma\tau$, the growth rate in units of time τ is given by (the terms multiplying σ_1 simplify)

$$\lambda = i\Omega_n + iv_{gn}\varepsilon k_{n,1} - \varepsilon. \tag{C3}$$

Now, expanding Eq. (6) with $k = k_n + \varepsilon k_{n,1}$, we obtain the same expression as Eq. (C3). If $n=0$, the linearized equation for a_0 is

$$\dot{a}_0 - iH(a_0') = -a_0 - i\sigma_1 a_0. \tag{C4}$$

Inserting $a_0 = c\exp(\mu_1\theta + ik_{0,1}\zeta)$ into Eq. (C4) and evaluating $H(a_0')$, we find

$$\mu_1 = -1 - i|k_{0,1}| - i\sigma_1. \tag{C5}$$

With $u = a_0(\theta,\zeta)\exp(iT)$ and $T=\sigma\tau$, Eq. (C5) implies the growth rate

$$\lambda = i - i\varepsilon|k_{0,1}| - \varepsilon, \tag{C6}$$

which is matching Eq. (6) after inserting $k=\varepsilon k_{0,1}$.

[1] Y. Khanin, *Principles of Laser Dynamics* (Elsevier, Amsterdam, 1995).
[2] P. Mandel, *Theoretical Problems in Cavity Nonlinear Optics* (Cambridge University Press, Cambridge, 1997).
[3] C. Szwaj, S. Bielawski, and D. Derozier, Phys. Rev. Lett. **77**, 4540 (1996).
[4] C. Szwaj, S. Bielawski, T. Erneux, and D. Derozier, Phys. Rev. Lett. **80**, 3968 (1998).
[5] J. Miles and D. Henderson, Annu. Rev. Fluid Mech. **22**, 143 (1990).
[6] A. Dinklage, C. Wilke, G. Bonhomme, and A. Atipo, Phys. Rev. E **62**, 7219 (2000).
[7] M. Le Flohic *et al.*, IEEE J. Quantum Electron. **27**, 1910 (1991).
[8] Y. Kuramoto and H. Nakao, Phys. Rev. Lett. **76**, 4352 (1996).
[9] G.F.N. Mazouz, G. Flätgen, and K. Krischer, Phys. Rev. E **55**, 2260 (1997).
[10] A. Gorshkov, G. Lyakhov, K. Voliak, and L. Yarovoi, Physica D **122**, 161 (1998).
[11] In a fiber laser, the homogeneous width decreases with temperature. At room temperature, the homogeneous and the inhomogeneous width have the same order of magnitude (≈ 100 Å), thus the system is globally coupled. At liquid nitrogen temperature, the homogeneous width is much smaller (≈ 8 Å) than the inhomogeneous width, thus providing a local coupling.
[12] G.I. Sivashinsky, Acta Astron. **4**, 1177 (1977).
[13] D. Vaynblat and M. Matalon, SIAM (Soc. Ind. Appl. Math.) J. Appl. Math. **60**, 679 (2000).
[14] I. Gradshteyn and I. Ryzhik, in *Table of Integrals, Series and Products* (Academic, New York, 1980), p. 1147.
[15] D. Zwillinger, in *Handbook of Differential Equations* (Academic, New York, 1989), p. 254.

Appendice F
Publications “Oscillateurs paramétriques optiques”

"Mode hopping strongly affects observability of dynamical instability in optical parametric oscillators"

Axelle Amon and Marc Lefranc

soumis à Physical Review A

Mode hopping strongly affects observability of dynamical instability in optical parametric oscillators

Axelle Amon[1,*] and Marc Lefranc[2]

[1]*Laboratoire PALMS, UMR CNRS 6627, Université de Rennes I, Campus de Beaulieu, F-35042 Rennes Cedex, France*

[2]*Laboratoire PhLAM, UMR CNRS 8523, CERLA, Université des Sciences et Technologies de Lille, F-59655 Villeneuve d'Ascq Cedex, France*

(Dated: May 22, 2006)

Theoretical investigations of dynamical behavior in optical parametric oscillators (OPO) have generally assumed that the cavity detunings of the interacting fields are controllable parameters. However, OPOs are known to experience mode hops, where the system jumps to the mode of lowest cavity detuning. We note that this phenomenon significantly limits the range of accessible detunings and thus may prevent instabilities predicted to occur above a minimum detuning from being evidenced experimentally. As a simple example among a number of instability mechanisms possibly affected by this limitation, we discuss the monomode Hopf bifurcation and show that it probably can be observed only in very specific setups.

PACS numbers: 42.65.-k, 42.65.Sf, 42.65.Yj

I. INTRODUCTION

Continuous-wave optical parametric oscillators (OPOs) are tunable sources of coherent light that have proved extremely useful in quantum optics or high resolution spectroscopy [1]. They also have attracted great interest as model systems in nonlinear dynamics because they are based on the simplest optical nonlinearity, three-wave mixing, and are expected to exhibit complex dynamical behavior in some regions of parameter space. Indeed, many theoretical studies have predicted a variety of complex temporal and spatio-temporal dynamics (see, e.g., [2–10]). In particular, the simplest model of a triply resonant OPO (TROPO), the degenerate monomode mean-field model, was shown twenty-five years ago to display a Hopf bifurcation leading to periodic behavior [2, 3], and later to exhibit deterministic chaos [4]. Quite surprisingly, this instability has to our knowledge not yet been observed experimentally. Although oscillatory behaviors have been reported in several experiments [11–14], they have been shown to stem either from thermal effects [12, 13] or from the interaction of transverse modes [14]. Very recently, chaotic behavior has been evidenced in a TROPO [15] but is believed to be also linked to multimode operation.

Most of the instabilities that have been investigated theoretically require large values of the cavity detunings and of the pumping rate. As the latter is obviously limited by the power of the pump laser, it would only be natural to identify it as the limiting factor when searching for the instability [10]. As for detunings, they are generally considered as parameters that can be easily tuned so as to pull the system away from equilibrium and observe complex behaviors. However, there are two limitations on the values cavity detunings can take. The first is simply that the OPO threshold increases quadratically with detuning, and thus that operation is restricted to detuning values for which threshold power remains below available pump power. The second arises because of a phenomenon known as mode hopping: OPOs spontaneously choose their operation frequency so as to operate on the cavity mode with smallest detuning. As the OPO is pulled away from a cavity resonance in order to increase detuning, a more favorable operating point appears near another cavity resonance and the system jumps to it. Because mode hops in OPOs occur for variations of cavity length as small as a few nanometers, they make it difficult to stabilize doubly or triply resonant OPO and to achieve smooth tuning [16–18]. Here, our concern is that mode hops prevent the OPO from achieving high values of the detunings and thus restraint the parameter range that can be explored. Such a limitation might very well preclude the experimental observation of dynamical behaviors predicted theoretically.

In this paper, we discuss this problem in a simple example, the Hopf bifurcation that leads to periodic behavior in the monomode mean-field model of a TROPO. We show that mode selection in OPOs indeed prevents experimental observation of this instability in most practicable configurations. We first recall the basic properties of the monomode mean-field TROPO model and the conditions under which the Hopf bifurcation occurs. In the limit of infinite pump power, a simple lower bound for signal detunings at which the Hopf bifurcation can occur is easily obtained, which confirms that this bifurcation requires high values of the signal detuning. In a second part we derive the expression of the maximal value that signal detuning can reach before a mode hop occurs, which depends on the length and finesse of the cavity as well as on crystal birefringence. By comparing the two bounds and searching for parameter regions where they are compatible, we find that mode hops generally keep the TROPO

*Electronic address: axelle.amon@univ-rennes1.fr

away from parameter ranges where the Hopf bifurcation can be observed, unless very high-finesse and very short cavities are used, which would make operation extremely difficult. This is confirmed by a numerical exploration at finite pump power of the parameter space of this model for various values of the cavity finesses. It shows that mode hopping rather than pump power is the limiting factor in order to reach instability. This result provides a plausible explanation of the fact that the Hopf bifurcation of the monomode TROPO has not yet been observed experimentally. It also calls for further investigations in order to determine whether mode hopping also interferes with other predicted instabilities.

II. TROPO MONOMODE MEAN-FIELD DEGENERATE MODEL: HOPF INSTABILITY

We now recall the main features of the simplest TROPO model, the degenerate longitudinally and transversely monomode mean-field model [2–4]. Light generation in an optical parametric oscillator is based on parametric down-conversion in a nonlinear crystal of a pump photon into two lower-frequency photons called signal and idler. In a TROPO, the optical cavity enclosing the crystal is resonant for all three fields so as to minimize operation threshold. In the mean-field (a.k.a. uniform-field) approximation, the time evolution of the normalized amplitudes A_s, A_i and A_p of the signal, idler and pump fields inside the cavity can be described by the following differential equations [4]:

$$\dot{A}_s = -(1+i\Delta_s)A_s + A_i^* A_p, \quad (1a)$$
$$\dot{A}_i = -(1+i\Delta_i)A_i + A_s^* A_p, \quad (1b)$$
$$\dot{A}_p = \gamma\left[-(1+i\Delta_p)A_p - A_s A_i + E\right], \quad (1c)$$

where Δ_s, Δ_i and Δ_p are the detunings between the optical frequency and the frequency of the closest cavity resonance for the signal, idler and pump fields, respectively, and E is the pumping rate. The time unit is the cavity decay time of the signal field and γ is the cavity decay rate for the pump. In this paper we focus on the stationary regimes of Eqs (1), and are interested in determining when they become unstable to give birth to periodic oscillations depending on values of control parameters.

A little known property of Eqs. (1) is that although the signal and idler fields are in principle distinct, their time evolution can be described by a single amplitude after transients have died out. First it should be noted that stationary solutions of Eqs. (1) exist only for $\Delta_s = \Delta_i$, a relation that can be shown to follow from photon number conservation [19]. Replicating a similar calculation carried out in the analysis of a bimode model [20], it is then easy to show that Eqs. (1a) and (1b) imply that after a sufficiently long time, the amplitudes A_s and A_i are equal up to a constant phase difference that can always be removed by a redefinition of the amplitudes. This is obviously linked to the fact that signal and idler photons are twin photons created in the same quantum process. Without loss of generality, the asymptotic dynamics of the TROPO can then be modeled by the following normalized equations (degenerate model) describing the time evolution of the complex amplitude of the signal field A_s and of the pump field A_p [4]:

$$\dot{A}_s = -(1+i\Delta_s)A_s + A_s^* A_p, \quad (2a)$$
$$\dot{A}_p = \gamma\left[-(1+i\Delta_p)A_p - A_s^2 + E\right], \quad (2b)$$

For pumping rates above the parametric emission threshold given by

$$E_{th}^2 = (1+\Delta_p^2)(1+\Delta_s^2), \quad (3)$$

equations (2) have non-zero stationary solutions which have been shown to fit accurately experimental observations in the vicinity of threshold [11]. When pump rate is increased, these stationary solutions can become unstable through a Hopf bifurcation giving rise to oscillatory behavior [2–4]. A necessary condition for this bifurcation is [4]

$$\Delta_p\Delta_s < -\left[1+\frac{\gamma(1+\Delta_p^2)}{2}\right], \quad (4)$$

which ensures that there is a finite pump rate $E_H > E_{th}$ at which the stationary nonzero solution bifurcates to a periodic solution, which is is given by [4]

$$E_H^2 = \left[\frac{\gamma^2(1+\Delta_p^2)+4(1+\gamma)}{-2(1+\gamma)^2[1+\frac{2(1+\Delta_p\Delta_s)}{\gamma(1+\Delta_p^2)}]} - (\Delta_p\Delta_s - 1)\right]^2 + (\Delta_p+\Delta_s)^2, \quad (5)$$

At higher pump rates, the limit cycle born in the Hopf bifurcation undergoes a period-doubling cascade leading to chaos [4].

As inequality (4) is closer and closer to equality, the Hopf threshold E_H given by (5) becomes larger and larger and is eventually rejected to infinity. For a given maximal pump rate available, $E_{\max}$, whether the instability can be observed at fixed detunings inside the parameter domain delimited by (4) is determined by the inequality $E_{\max} > E_H(\Delta_p, \Delta_s)$. Since we are interested here in specifying the unstable region by simple bounds on the detunings, we first assume that we have infinite pump power available. Under this approximation, whose validity will be checked in numerical simulations in Sec. IV, the Hopf instability domain is solely determined by inequality (4).

The instability domains in the (Δ_p, Δ_s) plane have been plotted in Fig. 1 for different values of γ, and are seen to be bounded away from the origin. Along their boundaries, (4) is an equality and defines the signal detuning as a function of pump detuning. It is easily found

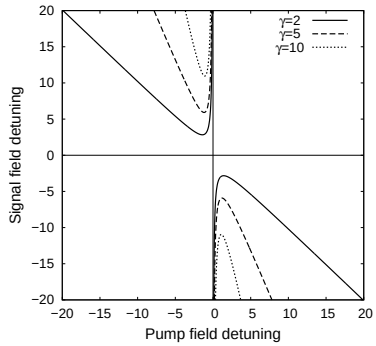

FIG. 1: Map (Δ_p, Δ_s) for different values of the parameter γ. The curves delimits the areas for which condition (4) is fulfilled.

that the minimum absolute value that the signal detuning can take on the boundary, and hence in the instability domain, is:

$$\Delta^H_{\min} = \min\{|\Delta_s|\} = \sqrt{\gamma(\gamma+2)}, \tag{6}$$

and is obtained for $|\Delta_p| = \sqrt{(2+\gamma)/\gamma}$. Note that $\Delta^H_{\min}$ is roughly proportional to γ and thus increases with it.

Since (4) still holds at finite pump power, the lower bound provided by (6) is always valid. This clearly shows that the Hopf bifurcation of the monomode degenerate mean-field model can only occur for sufficiently high signal detunings. In the next Section, we describe the process of mode hopping and how it limits the values that signal detunings can take leading to a maximal absolute value for the detunings. Whether the two constraints can be satisfied simultaneously will eventually determine whether the Hopf bifurcation can be observed experimentally.

III. LIMITATION OF SIGNAL DETUNING DUE TO MODE HOPPING

A. Theory

In the theoretical analysis of Sec II, it was assumed that the frequency detuning of the signal field is a fixed parameter. This is however not entirely true, because the operating frequency of an OPO is not actually chosen by the experimentalist but results from a complex mode selection process. While small variations of the cavity length most often modify frequency and hence detuning gradually, sudden jumps will occur when a remote operating point becomes more favorable. As we discuss below, this process tends to minimize frequency detuning and consequently to limit its maximum value, which can be derived analytically.

As with any optical oscillator where an amplifying medium is enclosed inside an optical cavity, there are two main constraints that determine the operating conditions of an OPO: the first one is that the gain in the amplifying medium must be sufficient to overcome cavity losses over each round trip in the cavity, the second one is that the generated field must be nearly resonant with one of the cavity modes so that amplification by the gain medium is cumulative over successive round trips.

In optical parametric oscillators, the nonlinear interaction is optimal when the relative phases of the three interacting waves remain fixed during propagation. The phase-matching condition is easily formulated in a corpuscular point of view: the conversion of one pump photon into signal and idler photons must satisfy energy and momentum conservation:

$$\omega_p = \omega_s + \omega_i \tag{7a}$$
$$\vec{k}_p = \vec{k}_s + \vec{k}_i \tag{7b}$$

where $\omega_{p,s,i}$ and $k_{p,s,i}$ denote the frequencies and the wavevectors of the pump, signal and idler fields.

The pump properties being fixed, relations (7) generally single out unique values for the signal and idler frequencies and much of OPO design consists in ensuring that these values fall in the desired frequency range. However, while energy conservation (7a) strictly holds for continuous-wave OPOs, momentum conservation may be satisfied only approximately because of the finite size of the nonlinear crystal. Thus there is a small but finite frequency domain around the exact phase-matching frequency where the nonlinear gain is adequate for OPO operation. It is usually the case that many cavity resonances fall inside this domain, and an important problem is to determine the resonances near which oscillation will actually occur.

Monomode optical parametric oscillators behave as homogenously broadened lasers in that when there are several frequencies for which gain overcome losses in the empty cavity, the one with the lowest threshold takes over by saturating the gain in such a way that competing modes remain below threshold. Mode selection thus amounts to determining which operating modes have lowest threshold. If variation of raw gain in the domain around perfect phase-matching is neglected, and considering pump detuning as a fixed parameter, this is equivalent to finding the allowed operating frequencies for signal and idler fields that have lowest frequency detuning, as expression (3) for parametric threshold shows.

In doubly and triply resonant OPOs, this problem is made difficult by the fact that the signal and idler fields must be simultaneously resonant. Thus operation can only take place at coincidences between two frequency combs. In general the two combs have different periods, either because the signal and idler fields have very different frequencies or because they are polarized along different axes of a birefringent crystal (the so-called type-II phase-matching [21]). A singular configuration that we

will not consider here is when signal and idler have identical polarizations and frequencies (type-I phase matching at degeneracy). As a result, frequency tuning in OPOs is a complicated problem that has been studied very carefully both in the type-I and type-II cases [16, 17].

The detunings of the signal and the idler fields are given respectively by $\Delta\omega_s = \omega_s - \omega_s^R$ and $\Delta\omega_i = \omega_i - \omega_i^R$, where ω_s and ω_i are the optical frequencies of the signal and idler fields and ω_s^R and ω_i^R are the closest resonance frequencies of the cavity. For the sake of simplicity, we assume in the following that ω_s and ω_i are close to a 1:1 ratio but the argument can be generalized easily to any rational number.

Taking energy conservation (7a) into account, the total frequency mismatch $\Delta\omega = \Delta\omega_s + \Delta\omega_i$ for the signal-idler mode pair is given by :

$$\Delta\omega = \omega_p - \omega_s^R - \omega_i^R, \tag{8}$$

which does not depend of the specific oscillation frequencies ω_s and ω_i chosen by the system, but only of the pump frequency and the resonance frequencies of the cavity for the signal and the idler modes. For our purposes, $\Delta\omega$ is the relevant quantity to consider as the individual detunings $\Delta\omega_s$ and $\Delta\omega_i$ are proportional to it in a stationary state, as a consequence of energy and photon number conservation [19]. The mode pair selected by the OPO will be the one that minimizes the total frequency mismatch $\Delta\omega$ so as to minimize threshold.

Taking into account that ω_s^R and ω_i^R belong to two frequency combs specified by the free spectral ranges $\delta\omega_s$ and $\delta\omega_i$:

$$\omega_s^R = N_s\delta\omega_s, \quad \omega_i^R = N_i\delta\omega_i \tag{9}$$

where N_s and N_i are the mode indices, and having in mind that $|\delta\omega_s - \delta\omega_i| \ll \delta\omega_s, \delta\omega_i$, we rewrite (8) as

$$\Delta\omega = \omega_p - \bar{N}(\delta\omega_s + \delta\omega_i) - \Delta N(\delta\omega_s - \delta\omega_i) \tag{10}$$

with $\bar{N} = (N_s + N_i)/2$ and $\Delta N = (N_s - N_i)/2$. Under our hypotheses, we have $\Delta N \ll \bar{N}$. Hence the last term in (10) is in first approximation negligible compared to the second term, and the integer value of $\bar{N}$ that minimizes $\Delta\omega$ is determined independently of ΔN. Then the optimization problem can be refined by searching for the integer value of ΔN that minimizes (10) at fixed $\bar{N}$. Studies of tuning properties of double or triply resonant OPO have shown that the operating modes are grouped into clusters, each cluster consisting of a sequence of adjacent modes [16, 17]. In (10), $\bar{N}$ indicates the cluster and ΔN distinguishes between adjacent modes inside the cluster.

An important consequence of (10) is that $\Delta\omega$ can at best be adjusted in steps of $|\delta\omega_s - \delta\omega_i|$. With such steps, the frequency mismatch $\Delta\omega$ can always be made to belong to the interval $[-\frac{|\delta\omega_s-\delta\omega_i|}{2}, \frac{|\delta\omega_s-\delta\omega_i|}{2}]$ but cannot be brought closer to zero. This minimal $\Delta\omega$ corresponds to the mode pair chosen by the OPO. By considering the worst case, the maximal frequency mismatch that can be reached is

$$\Delta\omega_{\max} = \frac{|\delta\omega_s - \delta\omega_i|}{2}, \tag{11}$$

which agrees with the general expression of the detuning given in [16]. As the OPO is pulled away from an exact cavity resonance by increasing the cavity length, the frequency mismatch will increase up to the maximal value given by (11), at which point there will be an operating mode with a lower mismatch to which the OPO will switch. This phenomenon is well known as mode hopping [16, 17].

Before (11) can be compared with the bound found for the Hopf bifurcation in Sec. II, it has to be expressed in the same units. The detunings used in equations (2) are normalized so that half-height width of the cavity resonance is 2. Since the cavity finesse $\mathcal{F}$ is defined so that the half-height width is $\delta\omega/\mathcal{F}$, we have

$$\Delta_s = 2\mathcal{F}_s\frac{\Delta\omega_s}{\delta\omega_s}, \tag{12a}$$

$$\Delta_i = 2\mathcal{F}_i\frac{\Delta\omega_i}{\delta\omega_i}. \tag{12b}$$

As mentioned before, Δ_s and Δ_i are not independent in the stationary regime but obey the simple relation $\Delta_s = \Delta_i$ as a consequence of energy and photon number conservation [19]. Taking into account that $\Delta\omega = \Delta\omega_s + \Delta\omega_i$, one obtains from (12):

$$\Delta_s = \Delta_i = \frac{2\mathcal{F}_s\mathcal{F}_i\Delta\omega}{\mathcal{F}_i\delta\omega_s + \mathcal{F}_s\delta\omega_i}. \tag{13}$$

This expression was derived assuming $\omega_s \simeq \omega_i$, so that we should fix $\mathcal{F}_s \simeq \mathcal{F}_i$ for consistency. The maximal value of the frequency mismatch authorized by mode selection, as given by equation (11), can thus be rewritten as

$$\Delta_{\max}^M = \mathcal{F}_s\frac{|\delta\omega_s - \delta\omega_i|}{\delta\omega_s + \delta\omega_i}, \tag{14}$$

Before we can discuss whether the Hopf bifurcation can be observed in typical experiments, we have to reformulate (14) in terms of the experimental configuration.

Given that

$$\delta\omega_{s,i} = \frac{2\pi c}{2(L_{cav} + (n_{s,i} - 1)l_c)} \tag{15}$$

where L_{cav} is the geometric length of the cavity, l_c is the length of the nonlinear crystal, $n_{s,i}$ the indices of the signal (resp. idler) fields and c is the celerity of light in the vacuum, (14) can be rewritten as

$$\Delta_{\max}^M = 2\mathcal{F}_s\frac{|\delta n|l_c}{[L]}, \tag{16}$$

where

$$[L] = 2(L_{cav} + (\frac{n_s + n_i}{2} - 1)l_c)$$

is the average optical path for the signal and the idler fields over one round trip in the cavity and

$$\delta n = \frac{|n_s - n_i|}{2}.$$

In the limit case of a monolithic OPO ($L_{cav} = l_c$), expression (16) leads to the remarkably simple expression

$$\Delta^M_{\max}/\mathcal{F}_s = \frac{2|\delta n|}{n_s + n_i} \tag{17}$$

showing the key role played by cristal birefringence. Expression (17) yields an absolute upper bound for (16) since cavity length obviously cannot be smaller than crystal length.

Note that since $\delta n \ll n_{s,i}$ for a standard crystal, expressions (16) and (17) ensure that the small-detuning hypothesis of the mean-field approximation is fulfilled for the signal and idler fields.

We are now in a position to obtain a simple criterion to determine whether the Hopf bifurcation can be observed in a given configuration at infinite pump power. Obviously, we must have

$$\Delta^H_{\min} < \Delta^M_{\max} \tag{18}$$

which, using (6) and (16), and expressing the pump cavity decay rate as

$$\gamma = \frac{\mathcal{F}_s}{\mathcal{F}_p},$$

translates into

$$\sqrt{\frac{1}{\mathcal{F}_p}\left(\frac{1}{\mathcal{F}_p} + \frac{2}{\mathcal{F}_s}\right)} < 2\frac{|\delta n| l_c}{[L]} \tag{19}$$

which is the main result of our paper. Again, (19) simplifies in the monolithic case. A noteworthy feature of inequality (19) is the asymmetry in the dependences with respect to the pump and signal finesses. It is easily seen that increasing pump finesse is much more effective to have (19) satisfied. Assuming $\mathcal{F}_p = 50$ and $\mathcal{F}_s = 500$, doubling the pump finesse decreases the left hand side of (19) by 46% while doubling the signal finesse only does so by 4%.

B. Numerical estimates

To get a better understanding of whether the criterion obtained in Sec III A is easily satisfied or not, we now compute numerical estimates for typical experimental configurations. In previous experiments [12–15, 20], we used a KTP crystal of length $l_c = 15$ mm cut for type-II phase-matching, with an extraordinary index $n_e = 1.75$ and an ordinary index $n_o = 1.83$. The crystal is enclosed in a Fabry-Perot cavity delimited by two spherical mirrors with a radius of curvature of 5 cm. The cavity finesses for the signal and pump fields are around 500 and 50, respectively.

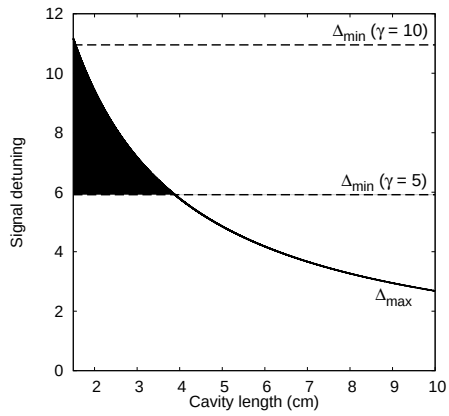

FIG. 2: Solid lines : values of maximal detuning authorized by mode selection when cavity length is varied between 1.5 cm and 10 cm. Dashed lines : minimal detuning permitted by the conditions of the Hopf bifurcation for two different values of γ : 5 and 10.

The most easily adjustable parameter is the geometrical cavity length, which is bounded from below by the crystal length (1.5 cm) and from above by the concentric condition (∼10 cm). Figure 2 shows the evolution of the maximal detuning $\Delta^M_{\max}$ with cavity length. The main feature is that $\Delta^M_{\max}$ decreases monotonically with cavity length, as is easily seen in expression (16). Thus the most favorable situation will always be obtained in the "monolithic" configuration where cavity length equals crystal length. In practice, this configuration cannot be reached when spherical mirrors are used because of the size of the crystal mount, but the shortest feasible cavity length (3 cm in our experiments) should be sought.

In our experiment, $\gamma = \mathcal{F}_s/\mathcal{F}_p = 10$, from which we can compute the value $\Delta^H_{\min} = \sqrt{\gamma(\gamma+2)}$ of the minimal detuning necessary to obtain the Hopf bifurcation. This value does not depend on cavity length and is represented in Fig. 2 by the upper dashed horizontal line. We see that there is hardly a configuration where $\Delta^H_{\min} < \Delta^M_{\max}$. In this configuration, the Hopf bifurcation cannot be observed regardless of pump power because mode hopping prevents to reach sufficiently high detunings.

In order to lower $\Delta^H_{\min}$, assume now that pump finesse is increased to 100 so that γ decreases to 5. This corresponds to the lower horizontal dashed line in Fig. 2. There is now a range of cavity lengths where $\Delta^H_{\min} <$

$\Delta^M_{\max}$ as shown by the black area between the two curves.

If $\mathcal{F}_s$ and $\mathcal{F}_p$ are increased simultaneously keeping γ constant, $\Delta^M_{\max}$ will increase while $\Delta^H_{\min}$ remains unchanged, and the instability region will also widen.

C. Conclusion

In this section we have taken into account the fact that the signal frequency detuning is not a fixed parameter but is determined by the operating frequency chosen by the OPO so as to minimize this detuning. As a result the signal frequency detuning is bounded from above by the mode hopping phenomenon. Since signal detunings at which periodic behaviors appear are bounded from below, the Hopf bifurcation can only be observed if $\Delta^H_{\min} < \Delta^M_{\max}$. Our analysis has shown that even in the ideal case where infinite pump power is available, mode hopping can prevent from reaching detunings sufficiently large to observe the Hopf bifurcation of the monomode model.

The numerical estimates obtained for the configuration used in our previous experiments explain why we could not observe the Hopf bifurcation in this setup. In order to obtain instabilities, one should take into account that $\Delta^H_{\min}$ depends on the ratio of signal and pump finesses while $\Delta^M_{\max}$ is proportional to signal finesse. More generally, the finesses should satisfy inequality (19). As will be discussed in Sec. V, the theoretically most favorable configurations are extremely difficult to build experimentally. In all cases, cavity should be made as short as possible.

It remains to be checked that in cases where the instability can be observed, it persists when pump power is limited. We do so in Section IV.

IV. NUMERICAL INVESTIGATIONS AT FINITE PUMP POWER

So far, our analysis has assumed infinite pump power, which has allowed us to obtain simple analytical formulas such as (19) to decide whether the Hopf bifurcation is screened by mode hopping or not. We now have to determine how good this approximation is in the real-life situation where only finite pump power is available and if conclusions drawn from our theoretical analysis remain relevant.

At finite pump power, whether the Hopf bifurcation can be observed no longer depends only on inequality (4) but also on whether the Hopf threshold (5) can be reached given available pump power. Because expression (5) is much more complicated than inequality (4), we restrict ourselves here to a numerical exploration of the detuning ranges where periodic behavior is found and compare our results with predictions from the infinite pump power analysis. This exploration is carried out for several values of the cavity finesses, other parameters being chosen so as to match our previous experiments [12–15, 20]. As we shall see, it will allow us to conclude that pump power is not a limiting factor with commonly available pump lasers and that the criteria derived in the infinite pump power analysis remain relevant.

A few general observations are in order before we present our numerical results. The relevant criterion is whether the minimum detuning $\Delta^H_{\min}$ at which Hopf bifurcation occurs is smaller than the larger detuning $\Delta^M_{\max}$ allowed by mode hopping. Thus it is interesting to comment on how these bounds evolve when pump power is limited.

Regarding onset of periodic behavior, it should be recalled that inequality (4) holds regardless of pump power, that equality can be achieved only for infinite pump power and that otherwise the Hopf threshold (5) yields a more stringent condition than (4) on the detunings. As a result, the instability regions are systematically shifted towards higher values of the detunings, leading to an increase of $\Delta^H_{\min}$ compared to expression (6).

As for the maximal value $\Delta^M_{\max}$ of the detuning allowed by mode hopping [Expr. (14)], it does not depend on pump power as it is obtained by considering the frequency combs of the cavity resonances. However a limitation that has to be taken into account at finite pump power is that if the OPO is below parametric emission threshold at $\Delta_s = \Delta^M_{\max}$, then the latter bound certainly cannot be achieved and the actual bound will be lower (the stationary ON state must exist for the bifurcation to occur). Using the expression for parametric threshold (3), the expression for the maximal signal detuning value becomes

$$\Delta^{MT}_{\max} = \min\left(\Delta^M_{\max}, \sqrt{\frac{E^2}{1+\Delta_p^2} - 1}\right) \qquad (20)$$

where E is the pump parameter and Δ_p is the pump detuning. The compatibility between the values of the minimal detuning at which periodic behavior occurs and of the maximal detuning at which stationary parametric emission occurs is now more difficult to analyze because both depend on pump detuning. However, it is easy to see that as pump power is decreased, the former can only increase and the latter only decrease so that the Hopf bifurcation is necessarily harder to observe in the finite pump power case. We now assess by how much by carrying out numerical simulations.

The phase diagrams in Fig. 3 shows in black the regions in the (Δ_p, Δ_s) parameter plane where periodic behavior is found for different values of the cavity finesses, the values of the remaining parameters being fixed so as to match our experiments [12–15, 20]. For each parameter set, the dynamical regime is classified as periodic when

- Inequality (4) is satisfied, and
- $E_H(\Delta_p, \Delta_s) < E_{max}(\mathcal{F}_p, \mathcal{F}_s)$

where $E_{\max}(\mathcal{F}_p, \mathcal{F}_s)$ is the maximum pump parameter corresponding to the pump power available in our experimental conditions (4 W) [23]. Since the unstable zones are enclosed inside the regions where parametric emission occur and the instability regions at infinite pump power, the boundaries of these regions, which can be computed analytically, are also shown in Fig. 3 so that we can estimate how well they approximate the numerical results. In order to make meaningful comparisons between setups corresponding to different values of the finesses, the domains of variations of the pump and signal detunings are chosen so that $\Delta_{s,p} \in [-\mathcal{F}_{s,p}/(10\pi), \mathcal{F}_{s,p}/(10\pi)]$. This corresponds in each case to the same variation of the physical cavity length ($\Delta L = \lambda/40\pi$) and thus there is no difference in the scans from an experimental point of view. Since $|\Delta_{s,p}| \ll 2\mathcal{F}_{s,p}$, this also ensures that the small-detuning hypothesis of the mean-field model is satisfied.

Fig. 3(a) shows that for parameter values corresponding to our experimental setup, periodic behavior does not occur, explaining why we do not observe the Hopf bifurcation in this setup. It also shows that the boundaries of the unstable region at infinite pump power are located outside the central band where $\Delta_s \in [-\Delta^M_{\max}, \Delta^M_{\max}]$ and thus that mode hopping prevents the bifurcation from being observed in this configuration even if infinite pump power was available. The proximity of the two curves corresponding to parametric threshold and bifurcation at infinite pump power probably explains why no instability can be observed.

In contrast with Fig. 3(a), Figs. 3(b) to 3(d) display larger and larger instability zones as cavity finesses are increased. While in Fig. 3(b) the intersection of the unstable region with the central band of allowed signal detunings is very small, it becomes sizable in Fig. 3(d). More precisely, the fraction of the central band occupied by unstable regions is 1.6% in Fig. 3(b), 3.5% in Fig. 3(c) and 17% in Fig. 3(d). These numbers are meaningful as probability estimates if we assume that there is no correlation between the signal and pump detunings on average, i.e., that the entire allowed band may be explored over several experiments. It should be noted that during a scan of cavity length through a single resonance of the pump, pump and signal detuning will vary jointly as illustrated in Fig. 3(a) and that this may affect the probability of hitting the unstable zone. However, it is expected that there is no relation between paths followed in the (Δ_p, Δ_s) plane for different pump resonances so that no part of the allowed band should remain inaccessible.

Examination of Figs. 3(a)-(d) shows that although increasing finesses globally makes it easier to observe the Hopf bifurcation, finesses for the pump and signal fields have different influences. The twofold increase in $\mathcal{F}_p$ between Figs. 3(a) and (b) clearly modifies the phase diagram much more than the twofold increase in $\mathcal{F}_s$ between Figs. 3(b) and (c). Similarly, increasing $\mathcal{F}_p$ from 100 to 500 is critical to have a significant probability of observing the Hopf bifurcation. This is consistent with the

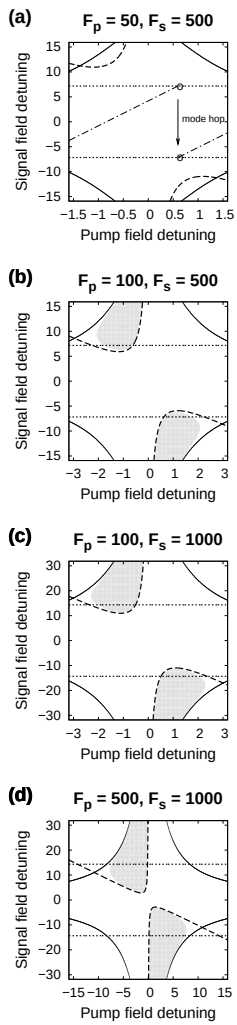

FIG. 3: Phase diagrams in the (Δ_p, Δ_s) plane showing the instability regions as black areas for different values of the finesses of the pump ($\mathcal{F}_p$) and of the signal ($\mathcal{F}_s$) field: (a) $\mathcal{F}_p = 50, \mathcal{F}_s = 500$, (b) $\mathcal{F}_p = 100, \mathcal{F}_s = 500$, (c) $\mathcal{F}_p = 100, \mathcal{F}_s = 1000$, (d) $\mathcal{F}_p = 500, \mathcal{F}_s = 1000$. Solid curves delimit areas above parametric emission threshold. Dashed lines indicate where (4) is an equality and delimit unstable areas in the infinite pump power approximation. Dotted horizontal lines indicate the maximal detuning value allowed by mode hops. In (a), the dotted and dashed line shows a possible path followed by detunings as cavity length is scanned. The discontinuity occurring as the path reaches the horizontal dotted line corresponds to a mode hop.

discussion of criterion (19) in Sec. III which showed that increasing pump finesse was much more effective than increasing signal finesse. However increasing pump finesse is extremely difficult from a practical point of view, as we discuss in Sec. V. Interestingly, it was similarly noted in Ref. [10] that increasing pump finesse while keeping signal finesse allowed one to observe an hexagonal transverse pattern at lower signal detunings.

An important conclusion that can be drawn from the numerical exploration summarized in Figs. 3(a)-(d) is that except in Fig. 3(a), the theoretical analysis at infinite pump power provides a very good approximation of the finite pump power case, all the better as finesses are higher and as observing the Hopf bifurcation becomes more plausible. Indeed the instability zones are tightly delimited by the boundaries obtained at infinite pump power and by the parametric threshold line except for larger pump detunings. In particular, the agreement is excellent at the tip of the unstable zones, near the point of minimal signal detuning. This makes us confident that for pump lasers currently available, the criterion obtained in (19) is effective in assessing the probability of occurrence of the Hopf bifurcation. It also shows that pump power is not a limiting factor as when there is a nonempty intersection between the unstable zone and the central band of allowed detunings, its area only marginally increases from the finite to the infinite pump case, mostly in regions far from the minimum detuning value.

To conclude, numerical calculations at finite pump power show that while the Hopf bifurcation becomes harder to observe than in the infinite pump power case, the mode hopping phenomenon remains the main limiting factor by limiting the range of values signal detuning can take. In order to obtain experimental evidence of the bifurcation, building a dedicated setup would be much more effective than increasing pump power. However, there are some experimental difficulties in doing so, which we discuss in Section V.

V. EXPERIMENTAL CONSIDERATIONS

The theoretical analysis at infinite pump power of Sec. III and the numerical computations at finite pump power of Sec. IV have suggested that the Hopf bifurcations of the monomode mean-field model might be observable in some configurations. In this Section, we discuss the feasibility of an experimental setup specially designed for evidencing the bifurcation.

Some parameters are easily optimized using the findings of Sec. III and IV. As discussed in Sec. III B, cavity should be as short as possible and in this respect a monolithic configuration would be optimal. Then, crystal birefringence should be chosen as large as possible [see Eq. (17)]. However this may not be an option as brifrigence is primarily used to achieve phase-matching in the desired operating range. Of course, pump power should be as large as possible, but our analysis has shown that there were modest returns in increasing it much beyond that offered by currently available pump lasers. The two parameters left for setup optimization are then the signal and pump cavity finesses. Criterion (19) indicates that those finesses, and especially the pump finesse, should be taken as large as possible.

However, cavities of very high finesse are critical to align and are very sensitive to fluctuations. For example, a change of δL of the cavity length will induce a variation of $\delta\Delta = 4\mathcal{F}\delta L/\lambda$ of the detuning, where λ is the optical wavelength. For $\lambda = 1064$ nm and $\mathcal{F} = 1000$, a fluctuation $\delta L = 5$ Å of the cavity length will induce a variation of the detuning $\delta\Delta = 2$, corresponding to full-width of the resonance. The length of the cavity must thus be adjusted carefully and maintained constant to within less than a few angströms.

This stability problem is all the more critical when thermal effects are taken into account. In our configuration, it has been shown that thermal effects can induced complex dynamical behaviors [12, 13] during which cavity length can be spontaneously swept by a few nanometers. Such instabilities were observed even at incident pump powers around 500 mW [12], which for a pump finesse of 45 corresponds to an intracavity pump power of about 6.5 W. For 4 W of incident pump power and a finesse of 500, intracavity pump power would reach ∼640 W at resonance and thermal effects would then be a hundred times as strong. For illustration purposes, let us recall that the only chaotic regime reported so far in an TROPO was observed in a situation where cavity length could not be made stationary [15], although the configuration was standard.

Another adverse influence of pump absorption in the crystal is that it puts a limit on the highest finesse achievable. In our setup, for example, pump absorbtion in the 1.5cm-long crystal is 2% cm^{-1} which implies that pump finesse cannot be higher than about 100 even if perfectly reflecting mirrors were used. Except for crystals with exceptional low absorption, high values of the pump cavity finesses such as 500 appear to be completely unrealistic.

Apart from the previous remarks which hold for all systems featuring an absorbing material enclosed in a resonant cavity, specific restrictions on the finesses are to be considered for a TROPO, inside which several fields must be simultaneously resonant. Generally cavity finesses in an experimental TROPO setup are chosen so that $\mathcal{F}_p \ll \mathcal{F}_s$. It ensures that numerous resonances of the signal field are found inside the wider resonance of the pump field, in other terms that several mode hops occur before OPO falls below threshold. This allows one to only consider coincidences of signal and idler cavity modes. For very high cavity finesses of the pump, the mode with smallest signal detuning might very well be below threshold because of a large pump detuning. In fact, the analysis of part III should then be reworked and reformulated in terms of coincidences of three resonances instead of two. It is not certain that this more complicated problem admits solutions.

To conclude, an OPO designed in order to observe the Hopf bifurcation should have a short cavity (e.g., monolithic setup), high birefringence and pumping rate. The pump cavity finesse should be as high as possible. Under these conditions, however, an OPO would be very difficult to operate and to stabilize on an operating point. Even then, the numerical analysis of Sec. IV indicates that unstable zones would remain small compared to the range of operating parameters. This casts serious doubts on the experimental observability of the Hopf bifurcation of the monomode mean-field model.

VI. CONCLUSION

In this paper we have raised the issue that contrary to what is commonly assumed in theoretical studies of the dynamics of optical parametric oscillators, signal detuning is not a fixed parameter but a dynamical variable whose value results from a complex selection process. Thus, detuning limitation due to mode hopping may affect the occurrence of dynamical instabilities occurring at high values of the detuning. As a simple example, we analyzed under which conditions the Hopf bifurcation leading to periodic behavior in the monomode mean-field model of a triply resonant OPO can be observed.

We first showed that signal detuning must reach a minimal value for the bifurcation to occur, even at infinite pump power. We then described how the mechanism of mode hopping restraints the values signal detuning can take and we gave an analytical expression of the maximal detuning allowed by mode hopping. By comparing the two bounds so obtained, we showed that they are incompatible in many configurations, showing that finite pump power is not necessarily the limiting factor for observing this instability. This was confirmed in numerical computations of instability domains carried out at a finite pump power corresponding to our experimental configuration, in which we observed that most of the unstable domains are inaccessible because of mode hopping. We found that pump finesse is a critical parameter that should be made as large as possible in order to observe the Hopf bifurcation. However experimental setups designed for this purpose should most certainly be extremely difficult to operate.

For the sake of simplicity, our derivation of the maximal detuning allowed by mode hopping relied on two main hypotheses. One was that signal and idler have frequencies close to 1:1 ratio but experience different indices, as in our type-II experiments. Generalization to other frequency ratios in the type-II configuration should be straightforward and is not expected to modify the conclusions of the present work. Type-I OPOs near frequency degeneracy have more complex tuning properties and should be analyzed separately. The other hypothesis was that parametric gain can be considered constant along a frequency domain containing many longitudinal modes so that the lowest possible detuning is always selected. If that is not the case, then values of signal detuning higher than predicted may be obtained and our analysis would have to be adapted. However, it does not seem likely that our conclusions would be modified a lot.

An open question is whether conclusions drawn for the Hopf bifurcation of the monomode mean-field model also hold for other theoretical predictions of temporal or pattern-forming instabilities in doubly or triply optical parametric oscillators. Indeed, such instabilities have usually been predicted for relatively high values of the signal detuning and/or of the pumping rate (see, e.g., Refs. [4, 6–10]). Thus, their observability may very well be also affected by detuning limitation due to mode hopping rather than by finiteness of the pump power. A detailed comparison of instability thresholds in detuning space with the maximum values allowed by mode hopping is in order for these theoretical predictions so that their relevance for experimental systems can be assessed. To conclude, mode hops are not only a nuisance for stabilizing and tuning OPOs but also for using them as tools to study complex dynamical behavior.

ACKNOWLEDGMENTS

We are most grateful to S. Bielawski, D. Derozier, P. Suret, and J. Zemmouri for stimulating discussions. The Centre d'Études et de Recherches Lasers et Applications is supported by the Ministère chargé de la Recherche, the Région Nord-Pas de Calais and the Fonds Européen de Développement Économique des Régions.

[1] *Special issue on $\chi^{(2)}$ second order nonlinear optics*, Quantum and semiclassical Optics **9**(2) (1997).
[2] K. McNeil, P. Drummond, and D. Walls, Opt. Commun. **27**, 292 (1978).
[3] P. Drummond, K. McNeil, and D. Walls, Opt. Acta **27**, 321 (1980).
[4] L. A. Lugiato, C. Oldano, C. Fabre, E. Giacobino, and R. J. Horowicz, Nuovo Cimento **10 D**, 959 (1988).
[5] G. Oppo, M. Brambilla, and L. Lugiato, Phys. Rev. A **49**, 2028 (1994).
[6] K. Staliunas, J. Mod. Opt. **42**, 1261 (1995).
[7] M. Marte, H. Ritsch, K. Petsas, A. Gatti, L. Lugiato, C. Fabre, and D. Leduc, Opt. Express **3**, 71 (1998).
[8] C. Schwob, P. Cohadon, C. Fabre, M. Marte, H. Ritsch, A. Gatti, and L. Lugiato, Appl. Phys. B **66**, 685 (1998).
[9] M. Tlidi, M. L. Berre, E. Ressayre, A. Tallet, and L. D. Menza, Phys. Rev. A **61**, 043806 (2000).
[10] G. Oppo, A. Scroggie, D. Sinclair, and M. Brambilla, J. Mod. Opt. **47**, 2005 (2000).
[11] C. Richy, K. I. Petsas, E. Giacobino, C. Fabre, and L. Lu-

giato, J. Opt. Soc. Am. B **12**, 456 (1995).
[12] P. Suret, D. Derozier, M. Lefranc, J. Zemmouri, and S. Bielawski, Phys. Rev. A **61**, 021805(R) (2000).
[13] P. Suret, M. Lefranc, D. Derozier, J. Zemmouri, and S. Bielawski, Opt. Lett. **26**, 1415 (2001).
[14] P. Suret, M. Lefranc, D. Derozier, J. Zemmouri, and S. Bielawski, Opt. Commun. **200**, 369 (2001).
[15] A. Amon and M. Lefranc, Phys. Rev. Lett. **92**, 094101 (2004).
[16] R. Eckardt, C. Nabors, W. Koslovsky, and R. Byer, J. Opt. Soc. Am. B **8**, 646 (1991).
[17] T. Debuisschert, A. Sizmann, E. Giacobino, and C. Fabre, J. Opt. Soc. Am. B **10**, 1668 (1993).
[18] A. Henderson, M. Padgett, F. Colville, J. Zhang, and M. Dunn, Opt. Commun. **119**, 256 (1995).
[19] C. Fabre, P. F. Cohadon, and C. Schwob, Quantum and Semiclassical Optics **9**, 165 (1997).
[20] A. Amon, M. Nizette, M. Lefranc, and T. Erneux, Phys. Rev. A **68**, 023801 (2003).
[21] R. W. Boyd, *Nonlinear Optics* (Academic Press, 2003), 2nd ed.
[22] A. Yariv and W. Louisell, IEEE J. Quantum Electron. **QE-2**, 418 (1966).
[23] $E_{max}(\mathcal{F}_p, \mathcal{F}_s) = \sqrt{\mathcal{P}_{max}/\mathcal{P}_{th}(\mathcal{F}_p, \mathcal{F}_s)}$ with $\mathcal{P}_{max}$ the maximum pump power available and $\mathcal{P}_{th}(\mathcal{F}_p, \mathcal{F}_s)$ the pump power at threshold. It is known that $\gamma_p \mathcal{P}_{th}(\mathcal{F}_p, \mathcal{F}_s) \propto \gamma_s^2 \gamma_p^2$ [17, 22] and consequently $\frac{E^2_{max}(\mathcal{F}_p, \mathcal{F}_s)}{\mathcal{F}_p \mathcal{F}_s^2} = cst$. In our experimental setup, $\mathcal{F}_{p0} = 45$, $\mathcal{F}_{s0} = 550$, $\mathcal{P}_{max} \simeq 4$ W and $\mathcal{P}_{th}(\mathcal{F}_{p0}, \mathcal{F}_{s0}) \simeq 10$ mW, which leads to $\frac{E^2_{max}(\mathcal{F}_p, \mathcal{F}_s)}{\mathcal{F}_p \mathcal{F}_s^2} \simeq 400$.

"Bursting oscillations in optical parametric oscillators"

A. Amon, M. Nizette, M. Lefranc, and T. Erneux

Phys. Rev. A **68**, 023801 (2003)

PHYSICAL REVIEW A **68**, 023801 (2003)

Bursting oscillations in optical parametric oscillators

A. Amon,[1] M. Nizette,[2] M. Lefranc,[1] and T. Erneux[2]
[1]*Laboratoire de Physique des Lasers, Atomes et Molécules, UMR CNRS 8523, Centre d'Études et de Recherches Lasers et Applications, Université des Sciences et Technologies de Lille, 59655 Villeneuve d'Ascq, France*
[2]*Université Libre de Bruxelles, Optique Nonlinéaire Théorique, Campus Plaine, C.P. 231, 1050 Bruxelles, Belgium*
(Received 13 February 2003; published 6 August 2003)

Different forms of bursting oscillations with frequencies from a few MHz to hundreds of MHz separated by intervals of no activity have been observed experimentally for an optical parametric oscillator (OPO) system subject to thermal effects. These oscillations have been simulated numerically using previously derived equations for two interacting transverse modes. In this paper, we investigate one particular case in detail and show that a simple phase-plane analysis explains the bursting cycle. Furthermore, by taking advantage of the values of the parameters, we determine an approximation for the solution of the OPO equations, leading to estimates of the oscillation frequency and of the threshold of the bimode regime.

DOI: 10.1103/PhysRevA.68.023801 PACS number(s): 42.65.Yj, 42.65.Sf

I. INTRODUCTION

Neurons as well as many other cell types communicate by brief bursts of oscillations separated by quiescent periods during which changes are slow [1–3]. Although specific models describing these bursting oscillations can be complex, they are generally based on the assumption that the phenomenon is caused by a slow variable modulating a rapid oscillatory system. Phase-plane studies where the response of a fast variable is studied as a function of this slow variable have been particularly useful to explain the periodic switching between oscillatory and steady responses [4,5].

In optics, lasers experiencing passive Q switch can display a similar alternation of pulse trains and periods of slow activity [6–8], but their dynamics cannot easily be decomposed in terms of slow and fast variables, which is a prequisite for the occurrence of bursting. Recently, autonomous bursting has been investigated in a CO_2 laser subject to two feedback loops operating on wildly different time scales [9], however the corresponding oscillations are too complex to be described in terms of a simple two-variable phase plane.

In this paper, we show that such a simple analysis is possible for continuous-wave optical parametric oscillators (OPOs) subject to thermal effects. OPOs are optical devices based on parametric frequency down-conversion in a nonlinear crystal and are promising sources of coherent light, with interesting applications such as tunable optical frequency generation for high-precision spectroscopy [10]. As many practical lasers, OPOs exhibit a variety of dynamical instabilities, but their dynamics has so far been much less studied. Although periodic and chaotic behaviors have been predicted to occur in cw OPO long ago [11,12], self-pulsing regimes in experimental systems have been described only recently [13–16].

In particular, instabilities observed in an OPO at frequencies of a few kHz have been traced back to slow variations of the crystal temperature and successfully described in terms of a simple thermo-optic model [14,15]. Observation of fast oscillations at frequencies in the MHz range has also been reported [13,16] and a mechanism based on the interaction of two transverse modes [17] has been proposed [16]. When both effects are combined, these fast oscillations appear in bursts separated by periods of no activity. The main objective of this paper is to propose a simple description of these bursting oscillations.

Our analysis unveils a surprising property of our OPO system. The regime where two cavity modes with well-separated optical wavelengths jointly oscillate is to a first approximation equivalent to a weakly detuned monomode oscillation. This indicates that, contrary to naive intuition, two-mode operation does not necessarily rely on the near coincidence of two cavity resonances. Thus, these new regimes cannot be neglected when studying frequency selection in OPOs, especially at the high pump powers presently available.

In Sec. II, we describe recent experimental results on these bursting oscillations. Section III introduces the model equations used in Ref. [16] and describes the numerical simulations in a slow-fast phase plane. The bursting cycle is then explained by studying the bifurcation properties of a reduced system of equations. We note that the bursting oscillations are the result of a slow passage through a subcritical Hopf bifurcation followed by a rapid jump to fast oscillations. The analysis of the bursting cycle in the phase plane encourages further analysis of the reduced problem which we propose in Sec. IV.

II. EXPERIMENTS

The experimental setup is a type-II triply resonant optical parametric oscillator. It consists of a 15-mm-long KTP crystal enclosed in a 47-mm-long cavity delimited by two spherical mirrors with a radius of curvature of 50 mm. The cavity is resonant at 532 nm, the wavelength of the pump laser (Coherent Verdi, maximum power 5W), and highly resonant at the first subharmonic at 1064 nm, near which two infrared fields ("signal" and "idler") are generated in the crystal. At these two wavelengths, the cavity finesses estimated from mirror reflectivities and crystal absorption coefficients are of 50 and 540, respectively. When observing the regimes described below, the threshold for parametric oscillation was reached at pump powers of the order of 30 mW, and pump

power injected in the cavity was at its maximum value of 3.5 W (i.e., about a hundred times the threshold power).

Different regimes are obtained as the cavity length is scanned with a piezoelectric transducer over one wavelength of the infrared field: no parametric emission stable parametric emission and thermo-optical instabilities [14,15], as well as fast oscillations with frequencies from a few MHz [16] to hundreds of MHz [18]. While fast oscillations do not appear for every cavity geometry, we have observed them at a high pump power for widely different cavity lengths. The instability mechanism was conjectured in Ref. [16] to be based on the interaction of two transverse modes as described by Schwob *et al.* [17]. This interpretation has been recently confirmed by experiments monitoring simultaneously the spatial structure of the output beam and its total intensity [18].

In many situations, fast oscillations interact with the slow thermal oscillations, giving rise to bursting oscillations. A large variety of bursting regimes can be observed, both with respect to wave form and to oscillation frequency. We present here three examples recorded under the operating conditions described above. Figure 1(a) shows a regime where the slow dynamics alternates between two branches, with fast oscillations appearing on the upper branch through a supercritical Hopf bifurcation and stopping suddenly to return to the lower branch. The low and high frequencies are around 8 kHz and 3 MHz, respectively. In Fig. 1(b), fast oscillations at 1 MHz are periodically switched on and off, with a characteristic frequency in the 15–20 kHz range. Finally, the wave form in Fig. 1(c) features fast oscillations that start with a nonzero amplitude and occupy the entire time interval where the signal intensity is above zero. The parabolic envelope at the end of the burst suggests that the oscillations are approaching an inverse saddle-node bifurcation. While the low frequency is comparable to the low frequencies observed in Figs. 1(a) and 1(b), the high frequency, with a value of 130 MHz, is much larger than the high frequency displayed in the two other examples.

In this paper, we concentrate on the last case and take advantage of the large value of the high frequency in order to simplify the OPO evolution equations. We generate solutions that are qualitatively similar to the regime of Fig. 1(c) and show how a bursting cycle is possible.

III. THEORY

In Ref. [16], the fast oscillations of an OPO were successfully simulated using the following equations, which describe the interaction of the pump field with two degenerate signal fields oscillating in two different transverse modes [17]:

$$A_p' = \gamma[-(1+i\sigma_p)A_p - A_1^2 - \chi A_2^2 - 2\chi_{12}A_1A_2 + E], \tag{1a}$$

$$A_1' = -(1+i\sigma_1)A_1 + A_pA_1^* + \chi_{12}A_pA_2^*, \tag{1b}$$

$$A_2' = -(1+i\sigma_2) + \chi A_pA_2^* + \chi_{12}A_pA_1^*. \tag{1c}$$

In these equations, A_p and the A_i are defined as the slowly varying field envelopes of the pump field $E_p = A_p(t)\exp(i\omega_p t - ik_p z)$ and of the two signal fields $E_j = A_j(t)\exp(i\omega_p t/2 - ik_p z/2)$. The parameters $\sigma_p = (\omega_p - \omega_p^*)/\gamma_p$, $\sigma_1 = (\omega_p/2 - \omega_1^*)/\gamma_s$, and $\sigma_2 = (\omega_p/2 - \omega_2^*)/\gamma_s$ are the normalized cavity detunings of the three fields. Here, ω_p^* and ω_j^* denote the frequencies of the closest mode resonances and γ_p and γ_s are the cavity damping rates at pump

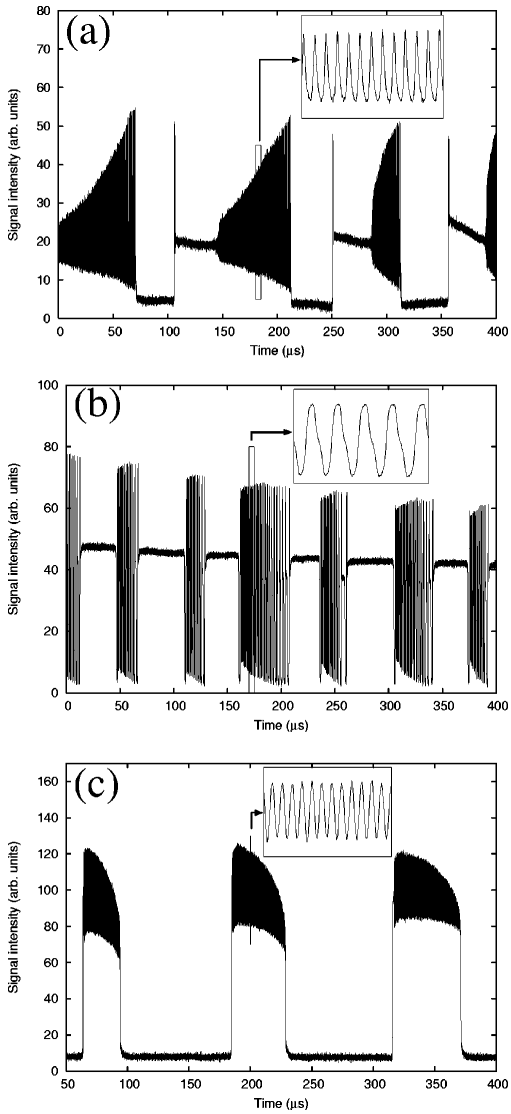

FIG. 1. Signal intensity versus time for three different bursting regimes observed in the experiments. In each plot, the inset shows the fast oscillations inside the narrow box for time intervals (a) of 5 μs following $t=180$ μs, (b) of 5 μs following $t=170$ μs, and (c) of 100 ns following $t=200$ μs.

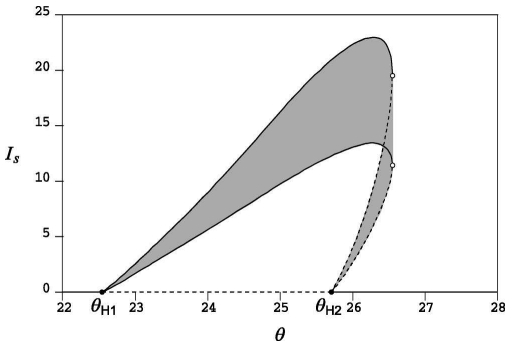

FIG. 2. Bifurcation diagram of Eqs. (1) where θ is treated as a parameter. The intensity $I_s \equiv |A_1|^2 + |A_2|^2$ is represented as a function of θ for the interval $22 < \theta < 28$. The gray region is bounded by the lines of maxima and minima of a branch of periodic solutions connecting two Hopf bifurcation points appearing on the zero solution. Black and white circles denote Hopf and saddle node of limit cycle bifurcation points, respectively. The values of the fixed parameters are $E = 17.5$, $\chi_1 = 1$, $\chi_2 = 0.7$, $\chi_{12} = 0.4$, $\Delta_p = 1.5$, $\Delta_1 = 12.5$, $\Delta_2 = 35.5$, and $\gamma = 10$. The lines of maxima and minima connecting the two Hopf bifurcation points have been obtained by using a continuation method (AUTO).

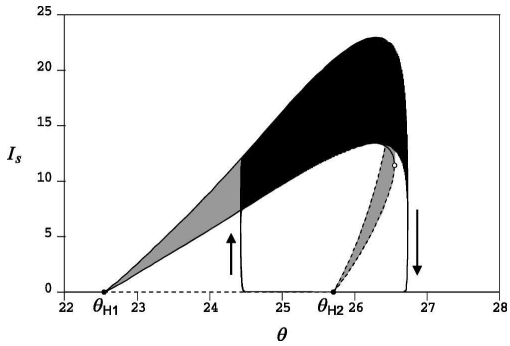

FIG. 3. Bursting cycle. The solution of Eqs. (1) and (3) is shown in the phase plane I_s versus θ. Parameter values are the same as in Fig. 2. In addition, $\varepsilon = 10^{-3}$, $\alpha = 0$, and $\beta = 4$.

and signal wavelength, respectively. Time is expressed in units of $\tau_s = 1/\gamma_s$ and $\gamma = \gamma_p / \gamma_s$ is the pump damping rate in reduced time units. The parameter $\chi = \chi_2^{(2)}/\chi_1^{(2)}$ is the ratio of the nonlinear coefficients characterizing parametric generation for modes 1 and 2. The cross-coupling coefficient χ_{12} is associated to the process in which a pump photon is converted into one photon in mode 1 and one photon in mode 2, and is proportional to an overlap integral between the three fields [17].

An important assumption supported by the experiments in Refs. [14–16] is that the optical length of the crystal slowly changes due to thermal effects. These effects can be taken into account by assuming linear dependences of the detunings with respect to temperature θ of the form

$$\sigma_p = \Delta_p - 2\theta/\gamma \quad \text{and} \sigma_j = \Delta_j - \theta, \tag{2}$$

where Δ_p and Δ_j are detunings at room temperature ($\theta = 0$). The temperature slowly changes due to field absorption in the crystal and its evolution can be described phenomenologically by the following equation for θ [14]:

$$\theta' = \varepsilon[-\theta + \alpha|A_p|^2 + \beta(|A_1|^2 + |A_2|^2)]. \tag{3}$$

Here, $\varepsilon \ll 1$ describes the slow rate of change of the temperature and α and β are proportional to the absorption coefficients of the crystal at the wavelength of the pump and of the signal, respectively. If $\varepsilon = 0$, then $\theta' = 0$, meaning that θ is a constant. This motivates a study of the reduced problem (1), where θ is treated as a parameter.

Figure 2 shows the bifurcation diagram of the solutions of Eqs. (1) for a given set of parameters. The figure represents the intensity of the signal $I_s \equiv |A_1|^2 + |A_2|^2$ as a function of θ and shows a closed branch of periodic solutions. The lines of maxima and minima are the boundaries of the gray region. The branch emerges from a first Hopf bifurcation at $\theta_{H1} \simeq 22.5$, reaches a limit point (saddle-node bifurcation of limit cycles) at $\theta \simeq 26.5$, and then connects a second (subcritical) Hopf bifurcation at $\theta_{H2} \simeq 25.7$.

We next consider $\varepsilon \neq 0$ and note that the long-time solution of the OPO equations (1) and (3) exhibits bursting oscillations that follow the bifurcation diagram of Fig. 2 (see Fig. 3). The bursting oscillations for $I_s(t)$ and $I_p(t)$ are shown in Fig. 4. In Fig. 3, the system periodically switches between the branch of zero-intensity steady states and the stable branch of rapid oscillations. Key to the bursting cycle are the subcritical Hopf bifurcation at $\theta_{H2} \simeq 25.7$ and the inverse saddle-node bifurcation at the right of the bifurcation diagram, which force the jumps from the lower branch to the upper branch and vice versa. This bursting scenario is relatively rare in the biological or biochemical literature and has been called subcritical elliptic bursting of Bautin type in Ref. [19]. Note that the actual amplitude of θ is larger than the distance between these two bifurcations because the system changes its state only after a delay.

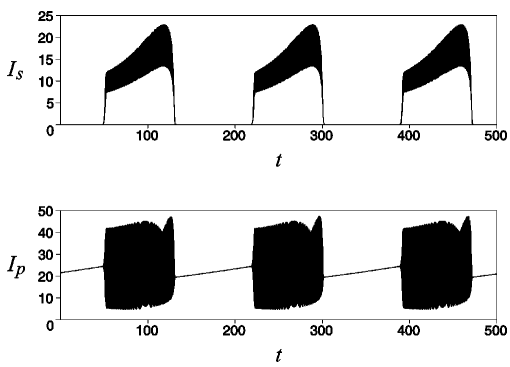

FIG. 4. Bursting oscillations for $I_s \equiv |A_1|^2 + |A_2|^2$ and $I_p \equiv |A_p|^2$ as functions of time t.

IV. ANALYSIS

The phase-plane analysis in Sec. III showed that the bursting oscillations can be understood as a periodic switching between two branches of solutions of a reduced system of equations where temperature is the bifurcation parameter. Its simplicity encourages further analytical studies. As a first step, we consider regimes with a very high fast frequency, such as the one shown in Fig. 1(c), so that the slow and fast frequencies are well separated. We assume that these regimes are associated with a large value of the beat frequency

$$\Delta\sigma_s = |\sigma_2 - \sigma_1|, \tag{4}$$

which, by definition, is the distance between the resonance frequencies of the two modes [16]. Under this condition, a bursting dynamics is observed when the mean signal detuning

$$\sigma_s = \tfrac{1}{2}(\sigma_1 + \sigma_2) \tag{5}$$

and the pump detuning σ_p are both small with respect to $\Delta\sigma_s$. Physically, this corresponds to the case where the signal carrier frequency $\omega_p/2$ is approximately half-way between the two resonance frequencies (see Fig. 4 of Ref. [16]), as is the case in the numerical simulation of Figs. 3 and 4.

This leads us to carry out an asymptotic analysis of Eqs. (1) based on the assumption $|\sigma_j| \gg |\sigma_p|, |\sigma_s|$. This analysis is described in detail in the Appendix. The main idea is as follows. Because $|\sigma_j|$ are large, we note from Eqs. (1b) and (1c) that

$$A_j \sim \exp(-i\sigma_j t) \tag{6}$$

are rapidly oscillating functions of t. This then suggests to average the OPO evolution equations with respect to these fast oscillations. The averaging is done in the Appendix by using a two-time perturbation analysis.

We find that the long-time solution of the system can be described in terms of a monomode OPO model coupling an amplitude a_p for the pump field and a common amplitude a_s for the two modes:

$$a_s' = -(1 + i\sigma_s)a_s + \chi_{12} a_p a_s^*, \tag{7a}$$

$$a_p' = \gamma[-(1 + i\sigma_p)a_p - 2\chi_{12} a_s^2 + E], \tag{7b}$$

where $\sigma_s = \frac{1}{2}(\sigma_1 + \sigma_2)$ is the mean signal detuning, and where the amplitudes A_p, A_j are approximately related to the new variables a_p and a_s as follows:

$$A_1(t) \simeq a_s(t)\exp\left(i\frac{(\sigma_2 - \sigma_1)}{2}t\right), \tag{8a}$$

$$A_2(t) \simeq a_s(t)\exp\left(i\frac{(\sigma_1 - \sigma_2)}{2}t\right), \tag{8b}$$

$$A_p(t) \simeq a_p(t). \tag{8c}$$

Remarkably, Eqs. (7) do not depend on the separation $\Delta\sigma_s$ between the two-mode resonances. We then show that the total signal intensity I_s exhibits limit-cycle oscillations of the form

$$I_s = F_0(t) + \{F_1(t)\exp[i(\sigma_2 - \sigma_1)t] + \text{c.c.}\}, \tag{9}$$

where $F_i(t)$ are varying on a slow time scale so that the fast frequency is the beat frequency $\Delta\sigma_s/2\pi = |\sigma_2 - \sigma_1|/2\pi$, which thus provides a good estimate of the frequency of the bursting oscillations when the two resonance frequencies are well separated. This confirms that our analysis applies to regimes with a high fast frequency such as in Fig. 1(c).

V. DISCUSSION

Figure 1 shows that different forms of bursting oscillations are possible in the OPO. We have examined the simplest case where the rapid bursting oscillations exhibit a large frequency [Fig. 1(c)]. This frequency can be estimated analytically by an asymptotic analysis of the OPO equations. Numerically, a simple phase-plane description in terms of one fast variable (the intensity of the signal I_s) and one slow variable (the temperature θ) is sufficient for a description of the bursting cycle. To our knowledge, this is the first attempt for such an analysis for a problem documented experimentally.

Our perturbation analysis also gives some insight into OPO operation. An important result is the fact that the averaged solution is determined by a monomode problem. Since each solution of the complete model (1) is associated with a solution of this monomode model, many properties of the latter can be extended to the former. In particular, the off state of the monomode model corresponds to the off state of the complete model, and thus the condition of existence of the bimode regime for large $\Delta\sigma_s$ involves the threshold of the monomode averaged model [12]:

$$E > E_{\text{th}} = \frac{\sqrt{(1+\sigma_p^2)(1+\sigma_s^2)}}{\chi_{12}}. \tag{10}$$

A remarkable property of Eq. (10) [and of the averaged problem (7)] is that it depends on the mean signal detuning $\sigma_s = \frac{1}{2}(\sigma_1 + \sigma_2)$, but not on the difference $\Delta\sigma_s = |\sigma_2 - \sigma_1|$ between the two resonance frequencies. This indicates that contrary to naive intuition the two resonance curves need not overlap for the two modes to interact, as long as they are approximately symmetrical with respect to the signal carrier frequency $\omega_p/2$ so that the effective detuning σ_s is small. This was illustrated in the numerical simulation of Fig. 3, carried out for $\Delta\sigma_s = 23$ in units of the resonance half-width. Thus, bimode regimes featuring fast oscillations are expected to be much more common than if near coincidence of the resonances was required, especially at high power. This is consistent with our experiments where such oscillations have been observed relatively easily in a number of different configurations [16,18].

ACKNOWLEDGMENTS

We acknowledge stimulating discussions with our colleagues S. Bielawski, D. Derozier, P. Suret, and J. Zemmouri. The research was supported by the US Air Force Office of Scientific Research, Grant No. AFOSR F49620-98-1-0400, the National Science Foundation, Grant No. DMS-9973203, the Fonds National de la Recherche Scientifique (Belgium), and the Interuniversity Attraction Pole program of the Belgian government. The Center d'Études et de Recherches Lasers et Applications was supported by the Ministère chargé de la Recherche, the Région Nord–Pas de Calais and the Fonds Européen de Développement Économique des Régions.

APPENDIX

In this appendix, we construct a solution of the OPO equations (1) by taking advantage of the relatively large values of $|\sigma_j|$ compared to $|\sigma_p|$ and $|\sigma_s|=\frac{1}{2}|\sigma_1+\sigma_2|$. We scale σ_j as

$$\sigma_j=\eta^{-1}\omega_j, \tag{A1}$$

where η is a small positive parameter and ω_j are $O(1)$ functions of θ. An important point in our analysis is the observation that

$$\sigma_s=\tfrac{1}{2}(\sigma_1+\sigma_2) \tag{A2}$$

is an $O(1)$ quantity for the range of θ of interest. We now seek a solution of the form

$$A_j=A_{j0}(s,t)+\eta A_{j1}(s,t)+\cdots, \tag{A3a}$$

$$A_p=A_{p0}(s,t)+\eta A_p(s,t)+\cdots, \tag{A3b}$$

where $s\equiv\eta^{-1}t$ and t are fast and slow time variables, respectively. The assumption of two independent times implies the chain rule $A_j'=\eta^{-1}A_{js}+A_{jt}$ and $A_p'=\eta^{-1}A_{ps}+A_{pt}$, where the subscripts s and t mean partial derivatives with respect to s and t. Inserting Eqs. (A1)–(A3) into Eqs. (1) and equating to zero each power of η lead to a sequence of problems for the functions in (A3a) and (A3b). The leading-order problem is $O(\eta^{-1})$ and is given by

$$A_{j0s}=-i\omega_jA_{j0} \quad\text{and}\quad A_{p0s}=0. \tag{A4}$$

The solution of Eq. (A4) is of the form

$$A_{j0}=B_j(t)\exp(-i\omega_js) \quad\text{and}\quad A_{p0}=B_p(t), \tag{A5}$$

where $B_j(t)$ and $B_p(t)$ are unknown functions of t. The next problem is $O(1)$ and is given by

$$A_{p1s}=-A_{p0t}+\gamma[-(1+i\sigma_p)A_{p0}-A_{10}^2-\chi A_{20}^2 -2\chi_{12}A_{10}A_{20}+E], \tag{A6a}$$

$$A_{11s}+i\omega_1A_{11}=-A_{10t}-A_{10}+A_{p0}A_{10}^*+\chi_{12}A_{p0}A_{20}^*, \tag{A6b}$$

$$A_{21s}+i\omega_2A_{21}=-A_{20t}-A_{20}+\chi A_{p0}A_{20}^*+\chi_{12}A_{p0}A_{10}^*. \tag{A6c}$$

Solvability with respect to the fast time s requires the three conditions

$$B_1'=-B_1+\chi_{12}B_pB_2^*\exp(2i\sigma_st), \tag{A7a}$$

$$B_2'=-B_2+\chi_{12}B_pB_1^*\exp(2i\sigma_st), \tag{A7b}$$

$$B_p'=\gamma[-(1+i\sigma_p)B_p-2\chi_{12}B_1B_2\exp(-2i\sigma_st)+E], \tag{A7c}$$

where primes mean differentiation with respect to time t. Note that the terms proportional to $\exp(2i\sigma_st)$ are present in the slow time equations only because we assumed $\sigma_s=O(1)$. The exponential can be removed by substituting

$$B_1=a_1\exp(i\sigma_st),\ B_2=a_2\exp(i\sigma_st),\ B_p=a_p \tag{A8}$$

into Eqs. (A7). We obtain

$$a_1'=-(1+i\sigma_s)a_1+\chi_{12}a_pa_2^*, \tag{A9a}$$

$$a_2'=-(1+i\sigma_s)a_2+\chi_{12}a_pa_1^*, \tag{A9b}$$

$$a_p'=\gamma[-(1+i\sigma_p)a_p-2\chi_{12}a_1a_2+E]. \tag{A9c}$$

From Eqs. (A9a) and (A9b), we may determine equations for $|a_1|$, $|a_2|$ and a_2/a_1, and find that $|a_1|=|a_2|$ and $a_2/a_1=e^{i\varphi}$ as $t\to\infty$, with φ a constant. With a suitable phase redefinition, we may set $a_1=a_2=a_s$. We then find from Eqs. (A9) two equations for a_s and a_p, given by

$$a_s'=-(1+i\sigma_s)a_s+\chi_{12}a_pa_s^*, \tag{A10a}$$

$$a_p'=\gamma[-(1+i\sigma_p)a_p-2\chi_{12}a_s^2+E]. \tag{A10b}$$

These equations describe a degenerate monomode OPO with signal detuning σ_s equal to the average of the two mode detunings σ_1 and σ_2. The steady-state solutions of Eqs. (A10) can be determined analytically [12]. The solution $|a_s|\neq 0$ emerges from the $|a_s|=0$ solution at two bifurcation points satisfying the condition

$$(1+\sigma_p^2)(1+\sigma_s^2)-\chi_{12}^2|E|^2=0. \tag{A11}$$

Equation (A11) is equivalent to a quadratic equation in θ which can be analyzed. These bifurcation points correspond to Hopf bifurcation points of the complete model (1), leading to a close branch of solutions (see Fig. 2). Of particular physical interest is the total signal intensity defined by I_s

$=|A_1|^2+|A_2|^2$. To determine I_s, we need to write the first-order correction of the solution. From (A6b) and (A6c), we find that

$$A_{j1}=B_{j1}(t)\exp(-i\omega_j s)+\frac{A_{p0}B_j^*\exp(i\omega_j s)}{2i\omega_j}, \quad \text{(A12)}$$

where $B_{j1}(t)$ is a new unknown amplitude. Then computing $|A_j|^2=|A_{j0}+\eta A_{j1}|^2$ and using (A1) to simplify the ω_j, we obtain

$$I_s=|a_1|^2+|a_2|^2+\eta[B_1B_{11}^*+B_2B_{21}^*+\text{c.c.}]+\left[\left(\frac{a_2^{*2}A_{p0}}{2i\sigma_2}-\frac{a_1^2A_{p0}^*}{2i\sigma_1}\right)\exp(i(\sigma_2-\sigma_1)t)+\text{c.c.}\right]+O(\eta^2). \quad \text{(A13)}$$

The terms in the third line of Eq. (A13) indicate that the intensity is rapidly oscillating with period $T=2\pi/|\sigma_2-\sigma_1|$.

[1] A. Goldbeter, *Biochemical Oscillations and Cellular Rhythms* (Cambridge University Press, Cambridge, 1996).
[2] J. Keener and J. Sneyd, *Mathematical Physiology, Interdisciplinary Applied Mathematics* (Springer, Berlin, 1998), Vol. 8.
[3] F. C. Hoppensteadt and E. M. Izhikevich, *Weakly Connected Neural Networks*, Applied Mathematical Sciences Vol. 126 (Springer, Berlin, 1997).
[4] A. Sherman and J. Rinzel, Proc. Natl. Acad. Sci. U.S.A. **89**, 2471 (1992).
[5] R. Bertram, M.J. Butte, T. Kiemel, and A. Sherman, Bull. Math. Biol. **57**, 413 (1995).
[6] E. Arimondo, F. Casagrande, L. Lugiato, and P. Glorieux, Appl. Phys. B: Photophys. Laser Chem. **30**, 57 (1983).
[7] M. Tachikawa, K. Tanii, and T. Shimizu, J. Opt. Soc. Am. B **4**, 387 (1987).
[8] M. Tachikawa, F.L. Hong, K. Tanii, and T. Shimizu, Phys. Rev. Lett. **60**, 2266 (1988); M. Tachikawa, K. Tanii, and T. Shimizu, J. Opt. Soc. Am. B **5**, 1077 (1988).
[9] R. Meucci, A. Di Garbo, E. Allaria, and F.T. Arecchi, Phys. Rev. Lett. **88**, 144101 (2002).
[10] M. Ebrahimzadeh, R.C. Eckardt, and M.H. Dunn, J. Opt. Soc. Am. B **16**, 1477 (1999).
[11] K. McNeil, P. Drummond, and D. Walls, Opt. Commun. **27**, 29 (1978).
[12] L.A. Lugiato, C. Oldano, C. Fabre, E. Giacobino, and R.J. Horowicz, Nuovo Cimento Soc. Ital. Fis., D **10D**, 959 (1988).
[13] C. Richy, K.I. Petsas, E. Giacobino, C. Fabre, and L. Lugiato, J. Opt. Soc. Am. B **12**, 456 (1995).
[14] P. Suret, D. Derozier, M. Lefranc, J. Zemmouri, and S. Bielawski, Phys. Rev. A **61**, 021805(R) (2000)
[15] P. Suret, M. Lefranc, D. Derozier, J. Zemmouri, and S. Bielawski, Opt. Lett. **15**, 1415 (2001).
[16] P. Suret, M. Lefranc, D. Derozier, J. Zemmouri, and S. Bielawski, Opt. Commun. **200**, 369 (2001).
[17] C. Schwob, P.F. Cohadon, C. Fabre, M.A.M. Marte, H. Ritsch, A. Gatti, and L. Lugiato, Appl. Phys. B: Photophys. Laser Chem. **66**, 685 (1998).
[18] A. Amon, S. Bielawski, D. Derozier, and M. Lefranc (unpublished).
[19] E. Izhikevitch, SIAM (Soc. Ind. Appl. Math.) J. Appl. Math. **60**, 503 (2000).

"Incompatibilities of cavity resonances with wave-vector matching: influence on threshold and beam structures of optical parametric oscillators"

P. Suret, D. Derozier, M. Lefranc, J. Zemmouri, and S. Bielawski

J. Opt. Soc. Am. B **19**, 395–404 (2002)

Incompatibility of cavity resonances with wave-vector matching: influence on threshold and beam structures of optical parametric oscillators

Pierre Suret, Dominique Derozier, Marc Lefranc, Jaouad Zemmouri, and Serge Bielawski

Laboratoire de Physique des Lasers, Atomes et Molécules, Unité Mixte de Recherche 8523, Centre National de la Recherche Scientifique, Centre d'Études et de Recherches Lasers et Applications, Université des Sciences et Technologies de Lille, F-59655 Villeneuve d'Ascq Cedex, France

Received April 9, 2001

We investigate theoretically and experimentally the interplay between cavity and double refraction in continuous-wave optical parametric oscillators. We show that basic *geometrical effects* can prevent transverse wave-vector matching for TEM_{00} modes and thus increase the threshold and dramatically change the beam structures when a resonant (or double-pass) pump is used. We extend the results of Boyd and Kleinman [J. Appl. Phys. **39**, 3597 (1968)] to take these cavity-induced mismatches into account and test the theoretical results experimentally, using a continuous-wave type II KTP optical parametric oscillator. The transverse wave-vector mismatch leads to the appearance of transverse modes with increasing order (up to $TEM_{40\ 0}$). The theory is able to predict quantitatively all selected transverse modes and admits of a simple interpretation in transverse Fourier space. © 2002 Optical Society of America

OCIS codes: 190.4970, 190.4410, 190.4420.

1. INTRODUCTION

Continuous-wave optical parametric oscillators (OPOs) are tunable sources with many applications.[1] Hence a number of studies have been made with the goal of understanding the physical processes involved in OPO operation. With respect to OPO efficiency, a powerful framework is the one used by Boyd and Kleinman[2] in their study of parametric interaction of Gaussian beams (see also subsequent papers)[3–5] whose results are commonly used today in the design of OPO cavities.

However, we shall see that, for OPO cavities with critical phase matching, the available results[2] are not always sufficient to permit prediction of the OPO threshold and beam structures. Indeed, an extension of the Boyd–Kleinman theory to OPO cavities with critical phase matching requires one to take into account an additional ingredient. In such a cavity, the three beam directions are uniquely imposed by the coexistence of the crystal and the cavity resonances. This geometric effect, which was not considered in previous studies,[2] can lead to new effects that do not appear in the case of noncritical phase matching[2,5] or in critical phase matching in free space.[2–4]

In this paper we show that this simple geometric effect can have far-reaching consequences in configurations based on a cavity that is triply resonant or doubly resonant with a double-pass pump. We shall see that, in these conditions, double refraction can, in addition to exhibiting the well-known imperfect overlap of beams,[2] prevent the TEM_{00} modes from satisfying wave-vector matching in the transverse direction. We shall see that this transverse wave-vector mismatch can lead to a loss of efficiency for TEM_{00} modes and lead ultimately to the selection of transverse structures that can be different for signal and idler, for instance, in type II KTP OPOs. All these phenomena are explained here in the framework of an extension of the Boyd–Kleinman theory. This extension to cavities includes consideration of wave-vector mismatch and of transverse modes for the signal and idler fields.

In Section 2 we consider the example of a triply resonant type II KTP OPO. Using elementary geometric optics, we first show that the coexistence of cavity resonance conditions and birefringence determines angles among pump, signal, and idler beams that are distinct from the usual walk-off angle[6] (for instance, these angles can reach arbitrarily large values).

We conclude that these angles can often be inconsistent with wave-vector conservation: If $\mathbf{k}_p$, $\mathbf{k}_o$, and $\mathbf{k}_e$ are the average wave vectors of pump, signal, and idler, a nonvanishing transverse wave-vector mismatch $\mathbf{k}_p - \mathbf{k}_o - \mathbf{k}_e \neq 0$ can appear. The first experiment is naturally devoted to measuring these tilt angles and to their comparison with predictions. Then we observe that large angle values (and hence important wave-vector mismatches) are systematically associated with the appearance of transverse structures that are different for signal and idler (Subsection 2.B).

In Section 3 we show that, in triply resonant OPOs with double refraction, a realistic prediction of threshold power and transverse modes requires one to take into account the transverse wave-vector mismatch. Hence we first derive the OPO threshold by extending the theory of Boyd and Kleinman to OPO cavities with double refraction. Using this model, we find that the transverse wave-vector mismatch dramatically changes the OPO threshold

0740-3224/2002/030395-10$15.00

for TEM_{00} operation and also favors high-order mode operation instead of TEM_{00} operation for certain cavity designs. The theoretical results of transverse mode selection are quantitatively compared with the observations performed on a triply resonant type II KTP-based OPO. Then, in Section 4, we interpret the pattern selection process as a consequence of the wave-vector mismatch discussed in Section 2.

Finally, we evaluate numerically the consequence of the wave-vector mismatch for the OPO threshold (Section 5) and briefly address the problem of the doubly resonant OPO (Section 6).

2. BEAM TILTS AND TRANSVERSE WAVE-VECTOR MISMATCH

A. Theory

For three-wave interaction in a $\chi^{(2)}$ medium, the effect of double refraction occurs at a more basic level in a cavity than in free space. In most practical free-space cases (e.g., sum-frequency generation or frequency doubling[2–4]), there is no geometric constraint on the direction of the generated beam(s). Generally the interaction process generates a nonlinear polarization that can radiate in all field modes. In consequence, it is generally found that maximum emission occurs when the three main wave vectors are matched in a vectorial relation of the type $\mathbf{k}_1 + \mathbf{k}_2 = \mathbf{k}_3$. This relation holds exactly for plane waves and approximately for Gaussian beams, independently of the existence of double refraction. In fact, in free space, double refraction limits only the overlap of the field envelopes by tilts of the beam axes but does not strongly affect the phase-matching conditions.

In a cavity, double refraction still induces imperfect beam overlap, but a more important consequence can appear: a transverse wave-vector mismatch, which stems from a purely geometric constraint. Figure 1 illustrates a situation for which the effect is typically important: a triply resonant OPO with an extraordinary pump, which corresponds, for instance, to KTP-based OPOs operating near degeneracy (signal and idler near 1.06 μm; pump at 532 nm).

At this point it is important to note that in our problem it will be crucial always to distinguish the polarization states of the beams. Hence, in what follows, we shall not use the usual signal and idler designation but rather name the two generated beams: ordinary and extraordinary signals.

Before any nonlinear interaction is even considered the cavity resonance conditions require normal incidence of each beam axis on the mirrors and satisfaction of refraction laws at the crystal interfaces [Figs. 1(a) and 1(b)]. Each beam-axis direction is thus perfectly determined by the cavity geometry, and we can therefore expect that it will not in general be compatible with wave-vector matching. Indeed, let us denote by α_e^c and α_o^c the angles inside the crystal of extraordinary and ordinary signals, respectively, with respect to the pump axis (the pump angle is hence $\alpha_p^c = 0$). Before any calculation, the problem appears qualitatively in the example of Fig. 1(c) because angles α_e^c and α_o^c have the same sign.

Evaluating the wave-vector mismatch effect quantitatively requires, first, knowledge of the angles of the beam axes inside the crystal, which we obtain by finding the ray paths that are orthogonal to both mirrors, using Snell's laws at the crystal interfaces (Fig. 1) and first-order paraxial approximation. For a given cavity, we find that the result is unique and is independent[7] of the pump's angle of incidence upon the crystal. For the example of the KTP-based triply resonant OPO displayed in Fig. 1, this result leads to the following expression for the angles inside the crystal of the pump the ordinary and the extraordinary parametric signals:

$$\alpha_p^c = 0 \quad \text{(by definition)}, \tag{1}$$

$$\alpha_o^c = -\frac{\rho_p}{n_o}\frac{l_c}{L_o^{\max} - L}, \tag{2}$$

$$\alpha_e^c = \frac{-\rho_p + \rho_e}{n_e}\frac{l_c}{L_e^{\max} - L'}, \tag{3}$$

where l_c is the crystal thickness and $\rho_e = 3.5 \times 10^{-3}$ rad and $\rho_p = 4.5 \times 10^{-3}$ rad are the double-refraction angles. $L_o^{\max} = 2R + l_c(n_o - 1)/n_o$ and $L_e^{\max} = 2R + l_c(n_e - 1)/n_e$ are the cavity lengths for which

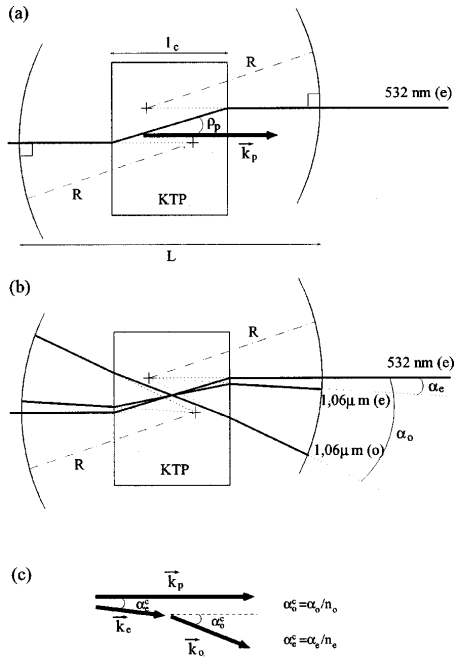

Fig. 1. Beam-direction selection and wave-vector mismatch. In a triply resonant cavity containing a birefringent crystal, the cavity geometry determines a unique set of beam paths. (a) Pump beam direction and wave vector for a type II KTP crystal with an extraordinary pump. (b) Beam directions for the pump, ordinary, and extraordinary signals. (c) Inside the crystal, the resulting average wave vector directions do not satisfy the phase-matching relations $\mathbf{k}_p = \mathbf{k}_o + \mathbf{k}_e$. The angles are exaggerated for clarity, but note that their relative signs suffice to prevent wave-vector matching.

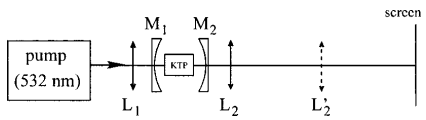

Fig. 2. Experimental setup. The injection lens has a focal length $f_1 = 20$ cm. L_2 and L_2' symbolize the two positions of the imaging lens ($f_2 = 10$ cm) that permit observation of the near field (L_2) and the far-field (L_2') on the screen. The measures of the beam angles are made without this imaging lens.

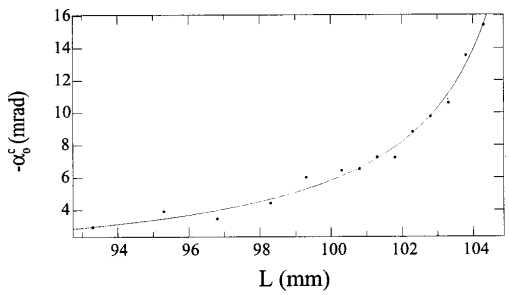

Fig. 3. Angle between signal and pump beams inside the crystal versus various cavity length. Filled circles, experimental measures; solid curve, fit of Eq. (2) to the experimental data.

the cavity becomes unstable (concentric) for the ordinary and the extraordinary signals, respectively.

From Eqs. (1)–(3), we see immediately that the angles prevent the wave vectors from satisfying $\Delta\mathbf{k} = \mathbf{k}_p + \mathbf{k}_o - \mathbf{k}_e = \mathbf{0}$ in the crystal at a given operating wavelength $(\omega_o, \omega_e, \omega_p)$. Requiring the transverse part of $\Delta\mathbf{k}$ to vanish:

$$|\Delta\mathbf{k}_\perp| = (1/c)|n_p\omega_p\alpha_p^c - n_o\omega_o\alpha_o^c - n_e\omega_e\alpha_e^c| = 0, \quad (4)$$

would not in general be compatible with Eqs. (1)–(3). Furthermore, we note that this mismatch is expected to become important when one of the denominators of Eqs. (1)–(3) tends to zero, i.e., when the cavity length is increased toward the concentric limit for one of the beams.

B. Experimental Verification: Beam Angles

The experimental setup is represented in Fig. 2. The pump is provided by a frequency-doubled YVO_4 laser (Coherent Verdi; 5 W at 532 nm) and the nonlinear crystal (KTP) is cut for type II operation at 1.064 μm for signal and idler ($\theta = 0°$, $\phi = 24°$). The refractive indices are $n_p = 1.79$ for the pump and $n_o = 1.83$ and $n_e = 1.75$ for the ordinary and the extraordinary generated signals, respectively.[8] The cavity is composed of two spherical mirrors with radius $R = 5$ cm. The reflection coefficients of the input mirror (M_1) are $R_{\max}$ at 1.064 μm and 90% at 532 nm. The reflection coefficients of the output mirror (M_2) are 99% at 1.064 μm and $R_{\max}$ at 532 nm.

The threshold power is typically 5–20 mW for a cavity length $L < 90$ mm and increases with L (as is discussed below). It is known that triply resonant continuous-wave OPOs are highly sensitive to fluctuations of cavity length,[9–11] and this sensitivity is of course enhanced close to the edge of the stability region (concentric geometry). To decrease sensitivity to mechanical vibrations, and because the phenomena are not strongly power dependent, we made the following measurements at a high pump power (3.5 W) at which the OPO can be self-stabilized by thermal effects.[12]

The angles were measured as follows: At two locations outside the cavity, we measured the axis positions of the ordinary and the extraordinary signals relative to the pump beam's axis. Then we deduced the resulting angles (α_o^c, α_e^c) inside the crystal, taking into account the transverse of the divergent lens formed by the output mirror. The cavity length relative to a reference length was measured with high precision (with a micrometric translation stage), and the reference length was measured with a precision of 1 mm.

The measured angles agreed with the predictions of Section 2. As expected, the larger angle was observed in the ordinary beam. Thus it could be more precisely measured, and we used it to check the theory quantitatively by fitting expression (2) of $\alpha_o^c(L)$ to experimental data, with $L_o^{\max}$ and ρ as free parameters (Fig. 3). The agreement is quantitatively correct because we found fitted values of $\rho_p = 4.9$ mrad and $L_o^{\max} = 107.2$ mm, which are close to the results obtained by classical methods.[8,13–15] The measure of ρ_p in Ref. 8 gives a value of 4.5 mrad, and we found a theoretical value $L_o^{\max} = 106.8$ mm from Eq. (2).

C. Experimental Consequences: Beam Structures

In situations when the wave-vector mismatch becomes noticeable (typically for cavity lengths of 90–106 mm), we observed that the OPO threshold increases and that the emitted beams present systematically a nontrivial transverse structure (the pump mode was maintained at TEM_{00}).

The structures of signal and idler were found to be different: The ordinary signal beam is a high-order

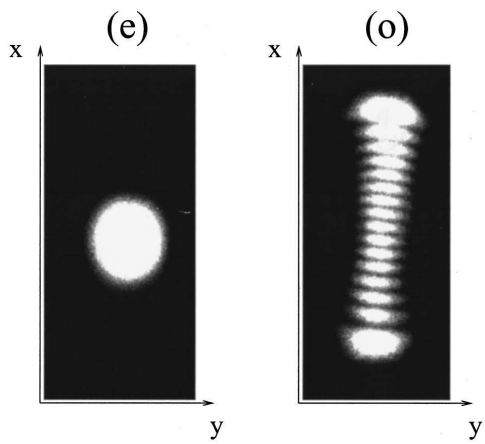

Fig. 4. Example of transverse structures observed simultaneously at the cavity output on signal and idler for a cavity length $L = 101.8$ mm; (*o*), (*e*) ordinary and extraordinary polarized beams, respectively (the relative positions in x have been rescaled). The pump remains TEM_{00}.

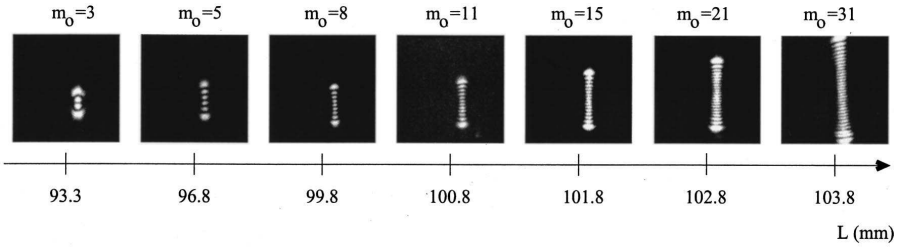

Fig. 5. Structures observed on the ordinary signal versus cavity length. Note that the extraordinary signal and the pump remain TEM_{00}.

Gaussian mode, $TEM_{m_o 0}$, with m_o odd or even, whereas the extraordinary beam always remains TEM_{00} (Fig. 4). The precise value of m_o (the order of the selected ordinary signal mode) increased with cavity length, up to high values (more than 40) near the concentric limit (Fig. 5). Furthermore, we note that this observation is highly reproducible: For a given cavity length we always observed the same mode order, with variations of 1 or 2. However, in spite of the apparent simplicity and reproducibility, no simple explanation of the phenomenon is available at this point.

Finally, it is worth noting that these drawbacks (increase of threshold and appearance of transverse modes) appeared precisely where small waists (tens of micrometers) were present. Then one could have been *a priori* tempted to use Boyd–Kleinman results on parametric interaction optimization to (incorrectly) conjecture low-threshold operation. The problem is that these theoretical results were obtained in a different situation[2] and need to be extended before being applicable to resonant cavities with type II critical phase matching, even for obtaining orders of magnitudes of the threshold.

3. EXTENSION OF THE BOYD–KLEINMAN THEORY

In this section we shall see that all the experimental results can be explained in the framework of an extension of the Boyd–Kleinman theory[2] to birefringent cavities. First we write the cavity modes and analyze their parametric interactions. This approach is guided by the observation that all phenomena (large-angle mismatches and high-order transverse patterns) already appear far from transverse-mode degeneracy (several millimeters from the concentric limit). Thus there is no need to consider subtle effects of pattern formation in the sense considered for nonlinear dynamics,[16–19] because predicted transverse instabilities are supposed to occur near the limit of transverse degeneracy for all beams.

Technically, we shall determine the threshold associated with a given set of transverse cavity modes for pump and signals, using its expression in the form of an overlap integral as in Refs. 2, 5, and 20. In this formulation, two physical effects (which must not be confused with each other) are taken into account: imperfect field envelope overlap as in the classic Boyd–Kleinman work, and wave-vector mismatch (which is linked to the angles between the normals of the plane-wave carriers).

A. Cavity-Mode Expressions and Formalization of the Transverse Wave-Vector Mismatch

We denote by ψ^p_{mn}, ψ^o_{mn}, and ψ^e_{mn} the normalized cavity field modes of the pump, ordinary signal, and extraordinary signal, respectively. Given the symmetry properties of the cavity, it is appropriate to express the mode functions in terms of $g_{mn}(x, y, z)$, the usual Hermite–Gauss functions of order (m, n) (Ref. 21):

$$g_{mn}(x, y, z) = \frac{\sqrt{2}}{w(\tau)} C_m H_m\left[\frac{\sqrt{2}x}{w(\tau)}\right] C_n H_n\left[\frac{\sqrt{2}y}{w(\tau)}\right] \times \exp\left[-\frac{(x^2 + y^2)}{w_0^2(1 + i\tau)} - i(m + n + 1)\arctan(\tau)\right], \tag{5}$$

with

$$\tau = \frac{\lambda(z - z_0)}{\pi w_0^2}, \tag{6}$$

$$w(\tau) = w_0\sqrt{1 + \tau^2}, \tag{7}$$

$$C_q = \frac{1}{\sqrt{\pi^{1/2} 2^q q!}}, \tag{8}$$

where w_0, z_0, and λ_0 are, respectively, the beam waist size, the beam waist position, and the wavelength inside the crystal of the considered cavity mode. For pump, ordinary, and extraordinary signals we denote by g^p_{mn}, g^e_{mn}, and g^o_{mn} the corresponding slowly varying functions with adequate waists and wavelengths. If we define (x, z) as the plane inside which double refraction occurs, the mode functions in the OPO, ψ^p_{mn}, ψ^e_{mn}, and ψ^o_{mn}, can be expressed as

$$\psi^p_{mn}(x, y, z, t) = g^p_{mn}(x - \rho_p z, y, z)\exp[i(\mathbf{k}_p \mathbf{r} - \omega_p t)], \tag{9}$$

$$\psi^e_{mn}(x, y, z, t) = g^e_{mn}(x - (\rho_e + \alpha^c_e)z, y, z + \alpha^c_e x) \times \exp[i(\mathbf{k}_e \mathbf{r} - \omega_e t)], \tag{10}$$

$$\psi^{a}_{mn}(x,y,z,t) = g^{o}_{mn}(x - \alpha^{c}_{o}z, y, z + \alpha^{c}_{o}x) \times \exp[i(\mathbf{k}_o\mathbf{r} - \omega_o t)], \tag{11}$$

where $\mathbf{r}(x,y,z)$ and $\omega_p = \omega_o + \omega_e$. α^c_o and α^c_e are the beam tilt angles [Eqs. (1) and (3)] that appear in the geometric optics approach of Section 2. Assuming small tilt angles, the associated wave vectors can be expanded as

$$\mathbf{k}_p = \begin{pmatrix} 0 \\ 0 \\ k_p \end{pmatrix}, \qquad \mathbf{k}_o = \begin{pmatrix} \alpha^c_o k_o \\ 0 \\ k_o \end{pmatrix}, \qquad \mathbf{k}_e = \begin{pmatrix} \alpha^c_e k_e \\ 0 \\ k_e \end{pmatrix} \tag{12}$$

to first order in α^c_o and α^c_e.

At this point it is worthwhile to examine how appear the two different physical effects of imperfect envelope overlap and transverse wave-vector mismatch. The first effect (the classic imperfect envelope overlap) appears in the arguments of g^p, g^o, g^e in Eqs. (9)–(11) and reflects the z dependence of the relative beams positions (as in Boyd–Kleinman theory) and the relative angle between beam axes. The second effect, which is the main subject of this paper, is due mostly to the differences in the directions of the normals of plane-wave carriers [the wave vectors involved in Eqs. (9)–(11)]. We define the wave-vector mismatch as

$$\Delta\mathbf{k} = \mathbf{k}_p - \mathbf{k}_o - \mathbf{k}_e = \begin{bmatrix} -(\alpha^c_o k_o + \alpha^c_e k_e) \\ 0 \\ \Delta k_z \end{bmatrix}, \tag{13}$$

where $\Delta k_z = k_p - k_o - k_e$. $\Delta\mathbf{k}$ contains two different types of component that have distinctly different consequences. The longitudinal component, Δk_z, is only a free (optimizable) parameter: this reflects mainly the choice of the wavelength that gives the minimum threshold as in the Boyd–Kleinman treatment.[2] The transverse component, $\Delta\mathbf{k}_\perp = (-\alpha^c_o k_o - \alpha^c_e k_e, 0, 0)$, however, is fixed by the cavity geometry (Section 2) and is therefore not an optimizable parameter.[22] We shall see that this property of $\Delta\mathbf{k}_\perp$ has a crucial role in the coupling between the transverse modes.

B. Selection of Transverse Modes

1. *Principle of the Boyd–Kleinman Extension*

We consider now a TEM_{00} pump and seek the signal–idler pair (ordinary–extraordinary signals pair) of transverse modes that gives the lowest threshold. This will provide the modes that are typically selected experimentally. To compute the threshold for the appearance of a given ordinary–extraordinary pair $\{\psi^o_{m_o n_o}, \psi^e_{m_e n_e}\}$ associated with a given pump mode $\psi^p_{m_p n_p}$ requires two steps. First, we use the known expression for the threshold pump power, in terms of the nonlinear coupling between the involved fields. The pump power at threshold is proportional to $1/|\Gamma_{m_p n_p m_o n_o m_e n_e}(\Delta k_z)|^2$, where $\Gamma_{m_p n_p m_o n_o m_e n_e}(\Delta k_z)$ is an integral that describes the overlap of pump, ordinary, and extraordinary signals[2,20]:

$$\Gamma_{m_p n_p m_o n_o m_e n_e}(\Delta k_z) = \int_{-\infty}^{+\infty}\int_{-\infty}^{+\infty}\int_{-l_c}^{+l_c} \psi^p_{m_p n_p}\psi^{o*}_{m_o n_o}, \psi^{e*}_{m_e n_e}\,\mathrm{d}x\,\mathrm{d}y\,\mathrm{d}z \tag{14}$$

$$= \int_{-\infty}^{+\infty}\int_{-\infty}^{+\infty}\int_{-l_c}^{+l_c} g^p_{mn}(x - \rho_p z, y, z) \times g^{e*}_{mn}(x - (\rho_e + \alpha^c_e)z, y, z + \alpha^c_e x) \times g^{o*}_{mn}(x - \alpha^c_o z, y, z + \alpha^c_o x) \times \exp[i(\Delta\mathbf{k}_\perp\mathbf{r} + \Delta k_z z)]\,\mathrm{d}x\,\mathrm{d}y\,\mathrm{d}z. \tag{15}$$

Then, as in Ref. 2, we use the fact that Δk_z is an optimizable parameter that is experimentally chosen by spontaneous adjustment of the wavelengths that correspond to the minimum threshold.

We therefore need to evaluate the maximal value $|\Gamma^{\max}_{m_p n_p m_o n_o m_e n_e}|^2$ of $|\Gamma_{m_p n_p m_o n_o m_e n_e}(\Delta k_z)|^2$. Generally, the corresponding optimal value of longitudinal mismatch parameter Δk_z is different from zero,[2] in contrast to the plane-wave situation, and must be calculated for each case. The computation details are given Appendix A, and we concentrate here on the numerical results obtained by use of the experimental parameter values of Section 2.

2. *Results: Comparison with Experiment*

For a large set of experimentally relevant cavity lengths, and assuming a TEM_{00} pump, we have computed the coefficient thresholds for the appearance of signal–idler pairs $\{\mathrm{TEM}_{m_o n_o}, \mathrm{TEM}_{m_e n_e}\}$ by evaluating $|\Gamma^{\max}_{00 m_o n_o m_e n_e}|^2$. In the following computations we used for each length the value of the tilt angles given by Eqs. (1) and (3) and the waists of the three cavity modes obtained from the cavity parameters considered in Section 2.

We found that the minimum threshold is obtained for simultaneous operation on a high-order ordinary mode ($m_o \neq 0, n_o = 0$) and on a fundamental extraordinary mode ($m_e = n_e = 0$) when the cavity is longer than 96 mm. Furthermore, the structure of the ordinary signal spreads along the x–z plane (i.e., the plane inside which double refraction occurs) and remains a fundamental Gaussian mode in the orthogonal ($y - z$) direction. This result follows qualitatively the experimental observations made in Subsection 2.C.

A typical result obtained for $L = 104$ mm is represented in Fig. 6, where we have plotted the values of the inverse threshold $|\Gamma^{\max}_{00 m_o n_o m_e n_e}|^2$ versus m_o and m_e (with $n_o = n_e = 0$). We can see that the optimum value corresponds to a TEM_{00} mode for the extraordinary beam and to a high-order mode ($\mathrm{TEM}_{21\ 0}$) for the ordinary beam. This selection is in good agreement with experimental results, as this set of modes is predicted for $L = 104$ mm and was experimentally observed for a cavity length of $L = 103 \pm 0.5$ mm.

To test the theoretical approach quantitatively, we also plotted ordinary mode order m_o versus cavity length L selected experimentally, together with the theoretical prediction. We performed this calculation as before (Fig. 6) by finding the mode order m_o that leads to the largest value of $|\Gamma^{\max}_{00 m_o 000}|^2$. We found good agreement along the

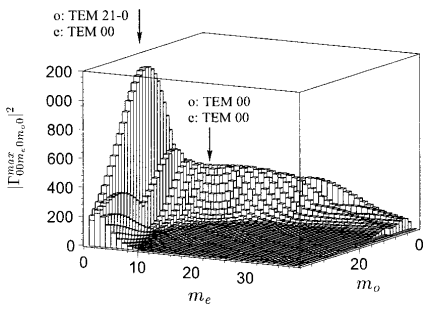

Fig. 6. Values of the threshold inverse computed for transverse-mode pairs TEM_{m_o0} and TEM_{m_e0} on the ordinary and extraordinary signals. The pump is TEM_{00} and the cavity length is $L = 104$ mm, as in Fig. 4. The selected set of transverse modes is the one with maximum value of $|\Gamma^{\max}_{00m_on_om_en_e}|^2$ (i.e., the lowest threshold). Here, it corresponds to the simultaneous selection of a TEM_{00} and a $TEM_{21\ 0}$ mode on the extraordinary and the ordinary beams, respectively. Note the poor efficiency of TEM_{00} operation on both signal and idler: $|\Gamma^{\max}_{000000}|^2 = 0.087$ (point hidden beyond the surface).

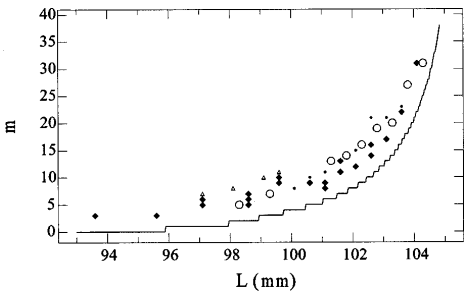

Fig. 7. Order m_o of the ordinary TEM_{0m_e} beam versus cavity length L for the KTP OPO. We tested the reproducibility by making the experimental measurements several times: Each type of point corresponds to a different experiment made after unmounting–remounting and readjustment of the cavity. Solid curve, the numerical prediction with the value of m_o associated with the lowest threshold. The extraordinary and pump beams are TEM_{00}.

whole range of accessible lengths (Fig. 7). In particular, we observed that the effect appears to be correlated with the increase in the beam-tilt angles (Fig. 1) that appear at important lengths.

A slight difference between experimental observation and theoretical prediction consists in a systematic shift of the order of 1 mm of the cavity length along the abscissa of the figure (Fig. 7). A possible origin of the difference is the presence of the thermal lens, that was not included in the theoretical calculation but was always present experimentally because high pump powers are required for obtaining stable operation near the concentric limit. Indeed, experimentally we found that the selected order of the transverse modes decreased when the pump power was decreased. This result is consistent with the fact that the predicted transverse mode order depends significantly on the values of the beam waists.

4. INTERPRETATION IN FOURIER SPACE

Because the theoretical approach is validated by the experiment, we are now in a position to use the numerical results to understand how the transverse wave-vector mismatches (which are due to the beam-tilt angles) are linked with the present pattern selection. We show that, in response to the transverse wave-vector mismatch caused by double refraction, the OPO develops a transverse mode with intense transverse wave-vector components that restore the phase-matching conditions.

Consider a transverse section of the three fields ψ_p, ψ_o, and ψ_e at a given position z inside the crystal (here we take $z = 0$ without loss of generality), and examine their profiles in transverse Fourier space $[|\hat{\psi}_p(k_x, k_y)|^2$, $|\hat{\psi}_o(k_x, k_y)|^2$, and $|\hat{\psi}_e(k_x, k_y)|^2]$. With this representation, the angles α_p^c, α_o^c, and α_e^c associated with each wave-vector direction are directly proportional to the center positions (k_{px}, k_{ox}, and k_{ex}) of the associated spatial spectra (see Fig. 8 for application to TEM_{00} modes). Thus the transverse wave-vector mismatch is directly visualized in Fourier space. In particular (Fig. 8), it clearly appears that the locations (k_{px}, k_{ox}, k_{ex}) of maximum power do not satisfy the phase-matching condition:

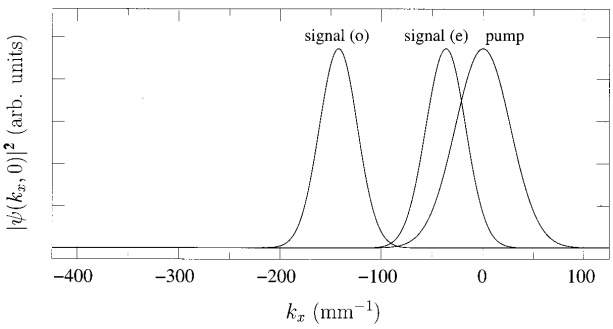

Fig. 8. Transverse Fourier transform of the field profiles in $z = 0$ for TEM_{00} operation on pump, signal, and idler. The origin of the poor efficiency is interpreted as the impossibility for large components (typically near the maxima) to satisfy the wave-vector-matching relation. Note that the center position of each beam is proportional to the beam-tilt angle [Eqs. (1)–(3)].

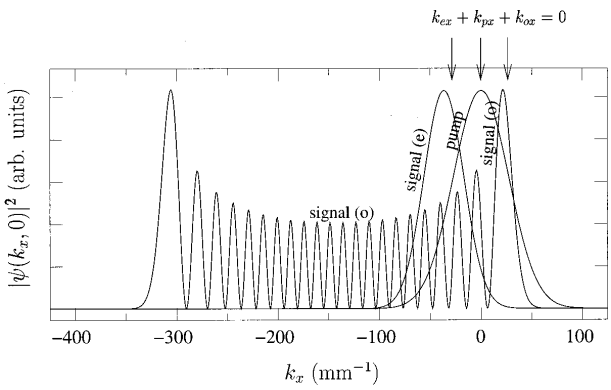

Fig. 9. Interpretation of the transverse-mode selection process. The OPO develops a high-order mode for the ordinary signal, whose main spectral components restore the transverse wave-vector-matching relation. For illustration, three important components that are phase matched are represented (arrows). This situation is to be contrasted with that of TEM_{00} operation, in which no important components can be phase matched (Fig. 8). For clarity, the ordinary signal has been rescaled vertically.

$k_{px} - k_{ox} - k_{ex} = |\Delta k_\perp| \neq 0$. Phase-matching conditions are satisfied only by low-power-density components in the Gaussian wings.

For high-order Hermite–Gaussian modes or order m_o, however, the maximum power-density component $k_{ox}^{\max}$ is located at a finite distance of the axis (Fig. 9), in both real and Fourier space (this distance can be arbitrarily large[21]). Hence there exist high-order modes whose strongest components can approximately satisfy the phase-matching relations, and we can conjecture that the set of modes actually selected will satisfy this condition. Such is what was actually observed for all high-order mode operation. For instance, in Fig. 9 we have plotted the selected set of modes (i.e., with lowest threshold) for the same conditions as in Fig. 6: a TEM_{00} pump, a TEM_{00} extraordinary signal, and a $TEM_{21\ 0}$ ordinary signal. It appears that values of components k_{px}, $k_{ox}^{\max}$, and k_{ex} with high spectral densities now satisfy the phase-matching relation $k_{px} - k_{ex} - k_{ox} = 0$.

5. CONSEQUENCES OF WAVE-VECTOR MISMATCH ON THRESHOLD

Wave-vector mismatch can dramatically increase OPO threshold, and this side effect is unfortunately most important near the concentric situation, i.e., precisely where one would expect good efficiency because of the small waist values. To illustrate the fact that a calculation of optimum threshold should not neglect consideration of a transverse wave-vector mismatch, it is worth comparing the inverse thresholds computed with and without the transverse wave-vector mismatch. To this end we compared the real threshold value, using Eq. (15), and the threshold obtained by setting $\alpha_p^c = \alpha_o^c = \alpha_e^c = 0$ (i.e., $\Delta k_\perp = \mathbf{0}$) in Eq. (15).

For a given set of transverse modes, pump power P_{th} at threshold[20] is directly linked to overlap integral $\Gamma^{\max}_{m_p n_p m_o n_o m_e n_e}$ defined in Eq. (15):

$$P_{\text{th}} = \frac{1}{4}\,\frac{\epsilon_0 c^3 n_p^2 n_e n_o}{128}\left[\frac{(1-R_p)(1-R_e)(1-R_o)}{d_{\text{eff}}^2\omega_e\omega_o}\right] \times \frac{1}{|\Gamma^{\max}_{m_p n_p m_o n_o m_e n_e}|^2}, \tag{16}$$

where R_p and $R_e = R_o$ are the effective reflection coefficients of the mirrors at the wavelengths of the pump and the signal–idler, respectively, ϵ_0 and c are the dielectric constant and the speed of light in vacuum, respectively, and d_{eff} is the second-harmonic generation nonlinear coefficient ($d_{\text{eff}} = 3.2$ pm/V for the KTP crystal considered here[8]). For simplicity we have neglected here the effect of the phase shift between the forward and backward waves induced by propagation between the crystal and the mirrors in the Fabry–Perot cavity: Under this assumption, the threshold of the Fabry–Perot cavity is

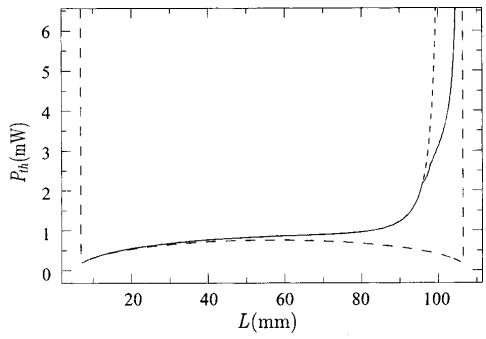

Fig. 10. Comparison of the OPO threshold with (solid curve) and without (long-dashed curve) wave-vector mismatch. Note that, with wave-vector mismatch, high-order modes are selected beyond $L = 96$ mm. For comparison, the exact calculation (including wave-vector mismatch) for TEM_{00} operation is plotted (short-dashed curve).

equal to one quarter of the threshold for a ring cavity (see, e.g., Ref. 5 for the effects of these phase shifts on the Fabry–Perot cavity).

In Fig. 10 the threshold of the OPO is plotted as a function of the length of the cavity in three cases: (i) exact threshold, with transverse mismatch $\Delta\mathbf{k}_\perp$ taken into account and corresponding to the optimum transverse mode of the ordinary signal (solid curve), (ii) the threshold computed after setting $\alpha_p^c = \alpha_o^c = \alpha_e^c = 0$ and thus $\Delta k_\perp = \mathbf{0}$ in Eq. (15) (i.e., the threshold calculated with the usual Boyd–Kleinman theory) (long-dashed curve), and (iii) the threshold with the transverse mismatch taken into account for a set of three TEM_{00} transverse modes (short-dashed curve).

We can see that ignoring the wave-vector mismatch would lead to the erroneous conclusion that the optimal situation corresponds to long cavities (with small waists, close to concentric), as currently expected from qualitative reasoning. In contrast, the complete calculation reveals a dramatic loss of efficiency in the near-concentric region.

Note that in our experiments we indeed observed a clear threshold increase with the length of the cavity. However, a precise measurement of the threshold could not easily be made: First, the low power operation is highly unstable close to the concentric geometry, and second, and more important, a meaningful measurement of the threshold would require a different adaptation of the input pump beam size for each cavity length.

Therefore, when low thresholds are required, large wave-vector mismatches should be avoided. It is hence preferable either to use noncritical phase-matching or—when critical phase matching is required—to use a cavity design without wave-vector mismatch. This can be done with either a hemispheric cavity (with a highly reflecting coating on one face of the crystal) or a walk-off-compensated crystal and two spherical mirrors. In these two cases, because $\alpha_p^c = \alpha_o^c = \alpha_e^c = 0$ and the wave-vector mismatch vanishes, TEM_{00} operation with a low threshold is expected for both signal and idler.

6. REMARKS ON THE DOUBLE-PASS OPTICAL PARAMETRIC OSCILLATOR WITH CRITICAL PHASE MATCHING

The problem of wave-vector mismatch can also appear in doubly resonant OPOs (DROPOs) when a double-pass pump is used, i.e., with a highly reflecting output mirror and a low-reflectance input mirror at pump wavelength. Let us recall that this configuration is largely used in DROPOs because it significantly increases the OPO efficiency. The problem is that, without the second pass of the pump, the backward signal and the idler would generate a field at the sum frequency. In contrast, with the double pass, parametric generation occurs for both forward and backward waves. The threshold can then be reduced by a factor of 4, and the maximal parametric efficiency can be increased from 50% to 100% as a result of the double pass of the pump (see Refs. 9, 23, and 24 for details). However, it is easy to see that this configuration requires proper alignment of the pump, a geometric constraint similar to that of pump resonance for the triply resonant OPO (Fig. 1).

Thus the benefit of the double pass can be strongly affected by the phenomenon discussed in the previous sections. We do not present a quantitative study, which would necessitate a complete work in itself, but it is important to discuss qualitatively how the problem appears.

As above, two important effects that adversely affect efficiency, pump misalignment and transverse wave-vector mismatch, cannot be suppressed simultaneously. However, what significantly complicates the optimization of the DROPO is that, unlike for a triply resonant OPO, for which the resonance condition is stringent, it is not obvious which of the two problems is more important and how the proper balance should be determined. Thus one expects that there will be an additional degree of freedom (the pump direction) for optimizing the OPO operation and that, depending on the particular configuration of the DROPO, the optimum might be reached by perfect alignment, by wave-vector matching or in intermediate situations. In any case, however, the incompatibility between wave-vector mismatch and beam alignment discussed here limits the OPO efficiency.

The preliminary experiments that we made with a DROPO seem to confirm this idea. The experimental setup is similar to the one described in Subsection 2.B, except that we have replaced the input mirror by a one with low reflection (less than 15%) at the pump wavelength. We have observed OPO behavior several millimeters from the concentric limit. Depending on the cavity alignment, we can indeed obtain TEM_{00} emission on both signals as well as the effect described above (a high-order mode on one of the parametrically generated signals only).

7. CONCLUSIONS

In conclusion, the geometric constraints imposed by a cavity can have important side effects on the efficiency of parametric interaction. When critical phase matching and a resonant (or double-pass) pump are used, the relative angles imposed by the cavity resonance conditions

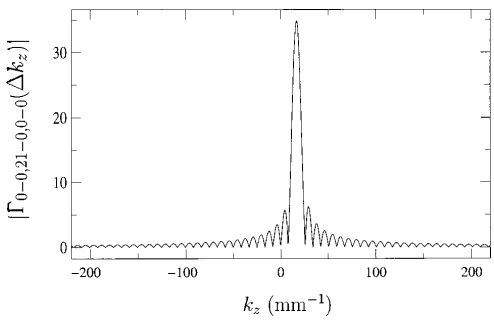

Fig. 11. Typical example of the function $|\Gamma_{m_p n_p m_o n_o m_e n_e}(\Delta k_z)|$ whose maximum must be computed. $L = 104$ mm, the pump and extraordinary signal are TEM_{00}, and the ordinary signal is $TEM_{21\,0}$.

lead to a transverse wave-vector mismatch. As a consequence, the threshold for TEM_{00} is increased, and higher-order modes can be selected by the system. A precise treatment requires extension of the Boyd–Kleinman theory (Section 3) to cavities with possible transverse wave-vector mismatch. However, in a given OPO, one can test the possibility of transverse mismatch by simply finding the relative beam angles (Section 2). Problematic situations appear with a resonant (or double-pass) pump, critical phase matching, and two spherical mirrors. Note that the problem is all the more dramatic as the cavity length is increased, although the small beam waists thus obtained would have suggested a more-efficient parametric interaction. In contrast, favorable situations will be obtained when the transverse mismatch is absent, e.g., with noncritical phase matching, as well as with critical phase matching by use of a hemispheric cavity or a compensated crystal. In these cases one can decrease the beam waists for optimum interaction without being limited by a transverse wave-vector mismatch.

APPENDIX A: COMPUTATION OF THE OVERLAP INTEGRAL

The main point of the numerical work consists of computing the triple integral [Eq. (15)] and its maximal value $|\Gamma^{\max}_{m_p n_p m_o n_o m_e n_e}|$. Whereas quadratures can easily be obtained by use of usual reliable libraries, the search for the maximum $\Gamma^{\max}_{m_p n_p m_o n_o m_e n_e}$ requires a careful-strategy because $|\Gamma_{m_p n_p m_o n_o m_e n_e}(\Delta k_z)|^2$ typically presents many secondary maxima (Fig. 11). A naïve approach that consists of computing triple integral $\Gamma_{m_p n_p m_o n_o m_e n_e}(\Delta k_z)$ directly for many values of Δk_z and then taking the maximum value would thus be a considerably time-consuming method for obtaining a reliable result.

Here we take advantage of the fact that the variable Δk_z appears in Eq. (15) only as an $\exp(i\Delta k_z z)$ factor in the integrand, which leads to considerable simplification in the search for the maximum $|\Gamma^{\max}_{m_p n_p m_o n_o m_e n_e}|$ because we can now consider the integral in Eq. (15) as a Fourier transform.

The only costly calculation is hence the integration over x and y of the integrand of Eq. (15). It is made easily by use of an n-dimensional adaptive-step-size quadrature algorithm, such as DCUHRE,[25] which was used here. If we define

$$S(z) = \int_{-\infty}^{+\infty}\int_{-\infty}^{+\infty} g^{p}_{mn}(x - \rho_p z, y, z) g^{e*}_{mn} \times [x - (\rho_e + \alpha^c_e)z, y, z + \alpha^c_e x] g^{o*}_{mn} \times (x - \ + \alpha^c_o z, y, z + \alpha^c_o x)[\exp i(\Delta k_\perp r)]\mathrm{d}x\mathrm{d}y, \tag{A1}$$

with

$$-\frac{l_c}{2} < z < \frac{l_c}{2} \tag{A2}$$

and

$$S(z) = 0 \quad \text{elsewhere}, \tag{A3}$$

we can say that the function $\Gamma_{m_p n_p m_o n_o m_e n_e}(\Delta k_z)$ is the inverse Fourier transform of $S(z)$:

$$\Gamma_{m_p n_p m_o n_o m_e n_e}(\Delta k_z) = \int_{-\infty}^{+\infty} S(z)\exp^{(igDk_z z)}\mathrm{d}z. \tag{A4}$$

The main idea is the following: As we need the maximal value of $|\Gamma_{m_p n_p m_o n_o m_e n_e}(\Delta k_z)|$, (i) we compute $\Gamma_{m_p n_p m_o n_o m_e n_e}(\Delta k_z)$ at a sufficiently dense set of points, and (ii) we interpolate these data to obtain a good approximation of the maximum, using a classical Shannon interpolation procedure.

Numerically, these two actions are not separated. First we compute $S(z)$ at a sufficient[26] number N of equally spaced points z_i between $-l_c$ and $+l_c$. To obtain the Shannon interpolation of $\Gamma_{m_p n_p m_o n_o m_e n_e}(\Delta k_z)$ directly, we place the data S_i in an overdimensioned[27] array of size pN: $S_i = S(z_i)$ for $i = 1...N$ and $S_i = 0$ elsewhere. Then we compute the backward fast Fourier transform $\hat{S}_i$ of the data S_i. The result gives the desired function, $\Gamma_{m_p n_p m_o n_o m_e n_e}(\Delta k_z)$, interpolated at pN equally spaced points, from which it is easy to determine the maximum of $|\Gamma_{m_p n_p m_o n_o m_e n_e}(\Delta k_z)|$.

The main advantage of this procedure is obtaining the maximum $|\Gamma^{\max}_{m_p n_p m_o n_o m_e n_e}|$ requires only N costly evaluations of the function $S(z_i)$ (and one no-cost fast Fourier transform).

ACKNOWLEDGMENTS

The Centre d'Études et de Recherches Lasers et Applications is supported by the Ministère Chargé de la Recherche, the Région Nord-Pas de Calais, and the Fonds Européen de Développement Économique des Régions (France).

S. Bielawski's e-mail address is serge.bielawski@univ-lille1.fr.

REFERENCES AND NOTES

1. D. Hanna, "Introduction to $\chi^{(2)}$ processes," Quantum Semiclassic. Opt. **9**, 131–138 (1997).
2. G. Boyd and D. Kleinman, "Parametric interaction of focused Gaussian light beams," J. Appl. Phys. **39**, 3597–3639 (1968).
3. J. Zondy, "Comparative theory of walkoff -limited type-II versus type-I second harmonic generation with Gaussian beams," Opt. Commun. **81**, 427–440 (1991).
4. J. Zondy, "The effects of focusing in type-I and type-II difference-frequency generations," Opt. Commun. **149**, 181–206 (1998).
5. S. Schiller, K. Schneider, and J. Mlynek, "Theory of an optical parametric oscillator with resonant pump and signal," J. Opt. Soc. Am. B **16**, 1512–1523 (1999).
6. A. Yariv and P. Yeh, *Optical Waves in Crystals* (Wiley-Interscience, New York, 1984).
7. Note that the choice of normal incidence of the pump upon the crystal is made for convenience. However, the following results are independent of this choice, provided that the three angles remain small (paraxial approximation). Note also that the angular dependence of refractive indices does not appear at this order of the expansion.
8. R. Eckardt, H. Masuda, Y. Fan, and R. Byer, "Absolute and relative nonlinear optical coefficients of KDP, KD*P,

BaB_2O_4, $LiIO_3$, MgO: $LiNbO_3$, and KTP measured by phase-matched second-harmonic generation," IEEE J. Quantum Electron. **26**, 922–933 (1990).
9. R. Smith, "A study of factors affecting the performance of a continuously pumped doubly resonant optical parametric oscillator," IEEE J. Quantum Electron. **QE-9**, 530–541 (1973).
10. S. Yang, R. Eckardt, and R. Byer, "Power and spectral characteristics of continuous-wave oscillators: the doubly to triply resonant transition," J. Opt. Soc. Am. B **10**, 1684–1695 (1993).
11. D. Lee and N. Wong, "Stabilization and tuning of a doubly resonant optical parametric oscillator," J. Opt. Soc. Am. B **10**, 1659–1667 (1993).
12. P. Hansen and P. Buchhave, "Thermal self-frequency locking of a doubly resonant optical parametric oscillator," Opt. Lett. **22**, 1074–1076 (1997).
13. F. Zumsteg, J. Bierlein, and T. Gier, "$K_xR_{1-x}TiOPO_4$: a new nonlinear optical material," J. Appl. Phys. **47**, 4980–4985 (1976).
14. K. Asaumi, "Second-Harmonic power of $KTiOPO_4$ with double refraction," Appl. Phys. B **54**, 265–270 (1992).
15. V. Dmitriev, G. Gurzadyan, and D. Nikogosyan, *Handbook of Nonlinear Optical Crystals*, Vol. 64 of Springer Series in Optical Sciences (Springer-Verlag, Berlin, 1997).
16. G. Oppo, M. Brambilla, D. Camesasca, A. Gatti, and L. A. Lugiato, "Spatiotemporal dynamics of optical parametric oscillators," J. Mod. Opt. **41**, 1151–1162 (1994).
17. K. Staliunas, "Transverse pattern formation in optical parametric oscillators," J. Mod. Opt. **42**, 1261–1269 (1995).
18. S. Longhi, "Traveling-wave states and secondary instabilities in optical parametric oscillators," Phys. Rev. A **53**, 4488–4499 (1996).
19. M. Taki, M. San Miguel, and M. Santagiustina, "Order parameter description of walk-off effect on pattern selection in degenerate optical parametric oscillators," Phys. Rev. E **61**, 2133–2136 (2000).
20. A. Yariv and W. Louisell, "Theory of the optical parametric oscillator," IEEE J. Quantum Electron. **QE-2**, 418–424 (1966).
21. A. E. Siegman, *Lasers* (University Science, Mill Valley, Calif., 1986).
22. More precisely, it cannot be optimized because small variations of the wavelength would only induce small variation of k_0 and of the refractive indices (and hence of α_o and α_p). In consequence a spontaneous change of wavelength would induce a small wave-vector-mismatch variation $\delta(\mathbf{\Delta k}_\perp) \ll \mathbf{\Delta k}_\perp$.
23. J. Bjorkholm, A. Ashkin, and R. Smith, "Improvement of optical parametric oscillators by nonresonant pump reflection," IEEE J. Quantum Electron. **QE-6**, 797–799 (1970).
24. G. Breitenbach, S. Schiller, and J. Mlynek, "81% conversion efficiency in frequency-stable continuous-wave parametric oscillation," J. Opt. Soc. Am. B **12**, 2095–2101 (1995).
25. J. Berntsen, T. O. Espelid, and A. Genz, "Algorithm 698: DCUHRE: an adaptive multidimensional integration routine for a vector of integrals," ACM Trans. Math. Software **17**, 452–456 (1991).
26. We consider that N is sufficiently large when the fast Fourier transform of $S(z_i)$ presents small high-frequency components. Each time this criterion is not satisfied, we decrease the step size by a factor of 2 by keeping alreadycomputed points and evaluating only the intermediate points.
27. Working with this overdimensioned array is useful for obtaining an interpolated set of values of $|\Gamma_{m_p n_p m_o n_o m_e n_e}(\Delta k_z)|$ directly after the backward fast Fourier transform. This interpolation is necessary for obtaining an accurate value of the desired maximum.

"Fast oscillations in an optical parametric oscillator"

P. Suret, M. Lefranc, D. Derozier, J. Zemmouri, and S. Bielawski

Opt. Commun. **200**, 369–379 (2001)

ELSEVIER

15 December 2001

Optics Communications 200 (2001) 369–379

OPTICS COMMUNICATIONS

www.elsevier.com/locate/optcom

Fast oscillations in an optical parametric oscillator

Pierre Suret, Marc Lefranc*, Dominique Derozier, Jaouad Zemmouri, Serge Bielawski

Laboratoire de Physique des Lasers, Atomes, Molécules, UMR CNRS 8523, Centre de Recherches Lasers et Applications, UFR de Physique, Bât. P5, Université des Sciences et Technologies de Lille, F-59655 Villeneuve d'Ascq, France

Received 27 April 2001; accepted 11 October 2001

Abstract

We report on the observation of fast oscillations at frequencies of a few MHz in a triply resonant optical parametric oscillator. These oscillations can appear alone, or superimposed on slow oscillations due to thermo-optical instabilities, and display a great variety of waveforms. The analysis of the regimes observed experimentally leads us to conjecture that the mechanism responsible for this instability is not the Hopf bifurcation of the single-mode mean-field model, but that it is based on the interaction of two signal fields oscillating in cavity modes with neighboring frequencies. This interpretation is supported by numerical simulations of the mean-field model with two coupled modes, which reproduce well the behaviors observed experimentally. We also find chaotic solutions of this model, which unveils another possible scenario leading to deterministic chaos in this system. © 2001 Elsevier Science B.V. All rights reserved.

PACS: 42.65.Yj; 42.65.Sf

Keywords: Optical parametric oscillators; Optical instabilities; Thermo-optical effects; Optical chaos

1. Introduction

Optical parametric oscillators (OPO) are promising sources of coherent light which are based on a nonlinear optical process, namely parametric down-conversion, coupling a "pump" field to two other fields, the "signal" and the "idler". Accordingly, the simplest set of equations describing the time evolution of the fields that are resonant in the OPO cavity, the so-called "mean-field model", is highly nonlinear and thus is susceptible to display instabilities and deterministic chaos. Indeed, it was shown several years ago in the triply resonant, single-mode case that this model can display a transition from stationary to periodic behavior through a Hopf bifurcation [1–3], and that the limit cycle born in this bifurcation can undergo a cascade of period-doubling bifurcations leading to deterministic chaos [3].

With powerful pump lasers becoming increasingly available, OPO can be operated well above oscillation threshold, thereby increasing the probability of observing experimentally the Hopf

* Corresponding author. Tel.: +33-320-336450; fax: +33-320-436825.
E-mail address: marc.lefranc@univ-lille1.fr (M. Lefranc).

0030-4018/01/$ - see front matter
PII: S0030-4018(01)01606-6

instability predicted theoretically. To the best of our knowledge, however, no clear evidence of this instability in an OPO has been reported so far, although fast oscillations at a frequency of about 0.8 MHz, superimposed on much slower ones, have been described by Richy et al. [4]. Unfortunately, the mechanism responsible for these high-frequency oscillations could not be ascertained, while a plausible explanation of the low-frequency ones is based on an thermo-optical instability as shown recently by our group [5,6].

In fact, there is another possible interpretation of the observation of Richy et al. [4], as it was recently shown [7,8] that another phenomenon can lead to periodic behavior in the mean-field model of the OPO. It occurs when two different pairs of signal–idler cavity modes have resonance frequencies that are sufficiently close. Under this condition, a pump photon can be converted into a signal photon of pair 1 and an idler photon of pair 2 without violating energy conservation. This introduces in the mean-field model a cross-coupling between the two pairs, which significantly modifies the dynamical behavior [7,8]. In particular, the two pairs of modes can oscillate simultaneously and periodic behavior can be observed when the fields are detuned with respect to the cavity resonances [7,8].

In this work, we report on the experimental observation in a triply resonant type-II OPO of fast oscillations at frequencies typically between 1 and 10 MHz. These oscillations are easily obtained at the high pump parameters that can be reached with our pump laser (typically several hundred times the threshold power). By modifying a single control parameter such as cavity length, a number of qualitatively different waveforms are observed, including regimes extremely similar to those described by Richy et al. [4]. As will be discussed below, the analysis of the different behaviors observed seems to favor the hypothesis of two coupled modes over that of the Hopf bifurcation predicted theoretically, although we do not have definitive evidence of this at this stage. Furthermore, this conjecture is supported by numerical simulations of the two-mode mean-field model, which reproduce well the experimental behaviors.

2. Experimental observations

The experimental setup is similar to the one described in Ref. [5]. The nonlinear crystal is a 15-mm-long KTP crystal, cut for type-II phase matching. It is contained in a Fabry–Perot cavity of length $L = 45$ mm, made of two identical mirrors with a radius of curvature $R = 3$ cm. The cavity is resonant at 532 nm, the frequency of the Nd:YVO_4 pump laser (coherent Verdi, maximum power 5 W), with a finesse of 45 and highly resonant at the first subharmonic at 1064 nm, with a finesse of 550 (finesses are estimated from the mirror reflectivities and the crystal absorption coefficients) [5]. Under these conditions, the threshold of parametric oscillation is reached at pump powers of the order of 5–8 mW, well under the maximum power of the pump laser. Because we are interested in the dynamics of the OPO, the cavity length is not stabilized by an external device.

In previous works [5,6], we have described in this system thermo-optical instabilities leading to slow oscillations at frequencies of the order of 10 kHz, and which involve a single [5] or several [6] signal–idler mode pairs. The mechanism of these instabilities is based on a feedback loop linking crystal temperature and the optical fields: the heating of the crystal resulting from absorption of the optical fields induces an increase in the refractive indices of the crystal and modifies the optical length of the cavity, and hence the cavity detunings of the fields and their intensities.

For pump powers of several hundred times the threshold (about 2 W and above in our configuration of lowest threshold), oscillations at a higher frequency (typically in the 1–10 MHz range) can also be observed in certain parameter ranges. This is illustrated in Figs. 1–3, which collect typical examples of the waveforms that can be observed. Typically, one can switch from one waveform to another by simply varying a control parameter such as cavity length (with a PZT).

Fig. 1 shows the simplest type of oscillation, which consists of a modulation of the pump and signal intensities at a frequency of about 2.5 MHz. The periodic behavior is stable and persists over time intervals several orders of magnitude larger than the period.

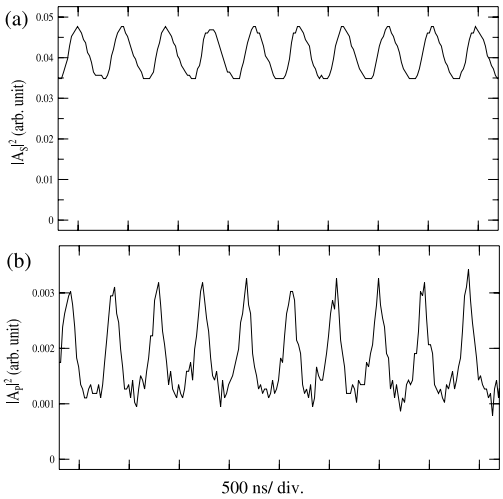

Fig. 1. Fast oscillations observed in the experiments. Pumping rate: 275 times the threshold. (a) Signal intensity (the idler behaves similarly). (b) Pump intensity.

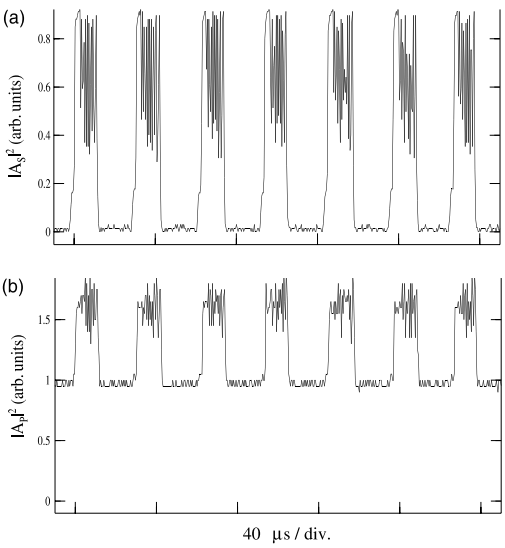

Fig. 2. Fast oscillations combined with slow ones in the experiments. The signal intensity goes periodically down to zero. Pumping rate: 450 times the threshold. (a) Signal intensity (the idler behaves similarly). (b) Pump evolution.

As can be seen in Figs. 2 and 3, the fast oscillations are often superimposed on much slower ones, that are in principle due to the thermo-optical instability mentioned above [5,6]. The main difference between these two regimes is the behavior between two bursts: in Fig. 2, the signal intensity goes back to zero whereas the system keeps emitting signal in Fig. 3. In both cases, the slow period consists of two clearly distinct phases, between which the system switches abruptly.

What is extremely interesting in regimes combining fast and slow oscillations is that, because the thermal instability causes the cavity length to be swept [5,6], more information about the underlying dynamical behavior can be extracted than from the simple modulation of Fig. 1. In particular, we had shown previously (in the absence of fast oscillations) that the two types of behaviors (signal intensity going back to zero or not) are linked to two qualitatively different regimes [5,6]. In the cases similar to Fig. 2, the system was oscillating around the (bistable) resonance curve of a single mode [5], whereas regimes resembling that of Fig. 3 corresponded to mode hopping between two different signal–idler mode pairs [6].

To check whether this was also the case here, we carried out a spectral analysis of the output signal field with an external Fabry–Perot analyzer, as in Ref. [6]. This gave a surprising result: regardless of whether we were studying a regime similar to Fig. 2 or to Fig. 3, we never observed more than a single resonance in the output of the Fabry–Perot analyzer.

Yet, we cannot deduce from this observation that the system is operating in a single-mode regime. Let us first consider the case of Fig. 2, and assume that the monomode hypothesis is correct. Then, the slow oscillations must take place around the bistability cycle formed by the resonance curve of the involved mode [5]. But this immediately rules out the possibility that the fast oscillations stem from the Hopf bifurcation of the monomode mean field. Indeed, it is known that the latter can only occur if the normalized detunings σ_p and σ_s of the pump and the signal verify $\sigma_p\sigma_s < -1$ (see Appendix A), while bistability necessarily implies $\sigma_p\sigma_s > 1$ [3]. The Hopf bifurcation and bistability

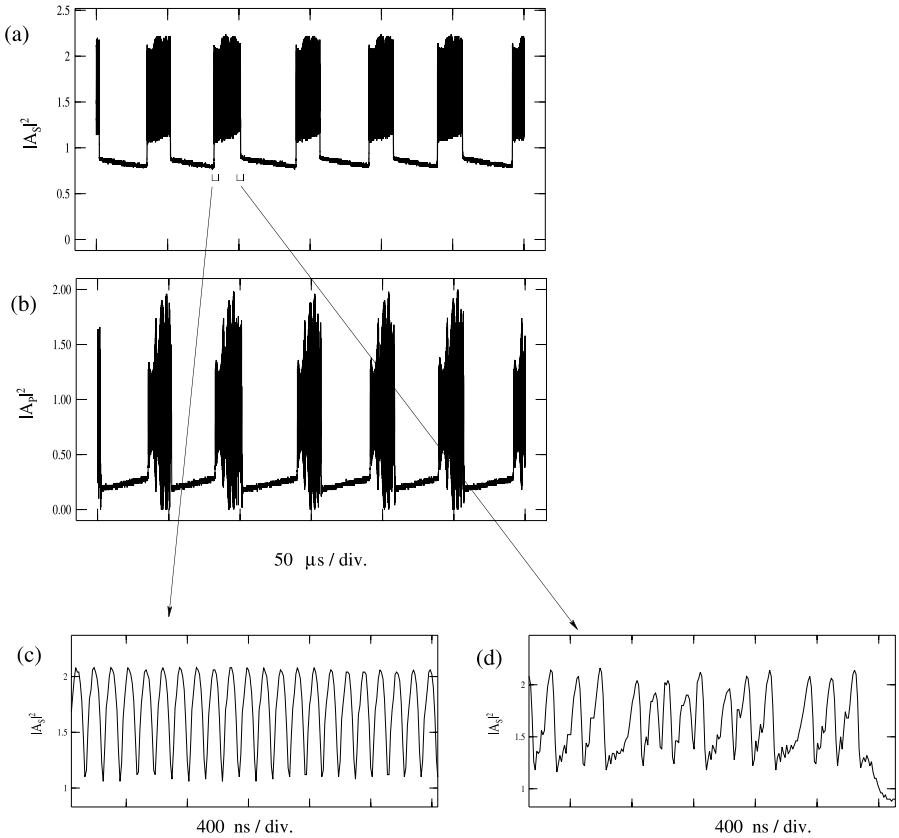

Fig. 3. Alternation between fast oscillations and slow evolution in the experiments. Pumping rate: 440 times the threshold. (a) Signal intensity (the idler behaves similarly). (b) Pump intensity. (c, d) Enlarged views of parts of figure (a): note the change of the shape between the beginning and the end of the fast oscillations.

are thus mutually exclusive [3]. However, because the Hopf bifurcation is the only possible transition from stationary to periodic behavior in the monomode mean-field model, the regimes observed experimentally would be in contradiction with this model.

Regarding the behavior shown in Fig. 3, it is also incompatible with monomode behavior. Indeed, if we assume that the slow oscillations remain close to the branches of asymptotic solutions of the mean-field model [5,6], the two parts separated by sudden jumps that can be seen in Fig. 3 cannot belong to the same nonzero solution branch, which again is in contradiction with a monomode behavior.

In conclusion, both behaviors seem to imply that at least two modes are involved in the dynamics, yet a single optical frequency is apparent in the spectral analysis. The most plausible explanation of the fast oscillations in Figs. 2 and 3 is thus that of two interacting fields oscillating in neighboring cavity modes, as proposed by Marte et al. [7] and Schwob et al. [8].

Since the three regimes shown in Figs. 1–3 are extremely close in parameter space, it is natural to conjecture that the same mechanism is responsible

for the simple modulation displayed in Fig. 1. This is all the more convincing as the frequency of the modulation shown in Fig. 1 is about 2.5 MHz, while that predicted for the Hopf instability has a lower bound of 9.5 MHz under our experimental conditions, as detailed in Appendix A. Although not a formal proof, this seriously decreases the plausibility of the single-mode Hopf instability hypothesis. To provide further support for the two-mode hypothesis, we now carry out numerical simulations of the relevant model and show that it reproduces well the experimental regimes.

3. Theoretical analysis

We assume now that the experimental behaviors described in this paper involve two signal–idler mode pairs. In normal OPO operation, conversion of a pump photon produces a signal photon and an idler photon of the same pair. If the frequencies of two cavity modes of the signal field are identical or sufficiently close so that their resonance curves overlap, a pump photon can also be converted into a signal photon of one pair and an idler photon of the other pair. This introduces a cross-coupling between the two pairs, and leads to new dynamical behaviors [7,8]. In particular, simultaneous emission in the two signal modes can occur whereas usually only the mode of lowest threshold oscillates. Note that in such a stationary regime, energy conservation requires that the two signal fields have exactly the same frequency. Indeed, one has simultaneously $\omega_p = \omega_{s,1} + \omega_{i,1} = \omega_{s,2} + \omega_{i,2} = \omega_{s,1} + \omega_{i,2} = \omega_{s,2} + \omega_{i,1}$, where ω_p is the frequency of the pump, and $\omega_{s,k}$ ($\omega_{i,k}$) is the frequency of the signal (idler) of pair k. This implies that $\omega_{s,1} = \omega_{s,2}$ and $\omega_{i,1} = \omega_{i,2}$, which corresponds to phase locking of the two signal (idler) fields. Note that equality of oscillation frequencies does not require perfect coincidence of the cavity mode resonances in which the two signal fields oscillate: the two fields can be detuned with respect to the corresponding cavity modes. This is illustrated in Fig. 4. When the detunings are nonzero, periodic behavior can also be observed [8].

Because this mode interaction is obviously stronger when two cavity modes have neighboring

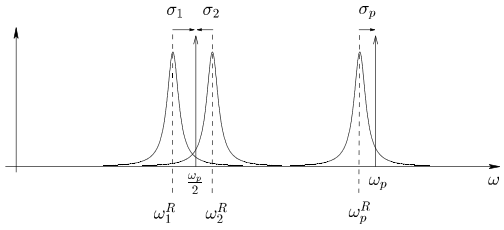

Fig. 4. Graphical illustration of the frequencies involved in the problem, assuming for simplicity that the signal and the idler are the same field. The horizontal axis corresponds to the optical frequency ω. The vertical arrows indicate two important reference frequencies: ω_p, the oscillation frequency of the external pump laser, and $\omega_s = \omega_p/2$ which is the oscillation frequency of the signal fields in the case of a stationary regime. These frequencies will be used to define the rotating frames in model (1a)–(1c). The three curves symbolize the resonance curves of the cavity modes in which the pump field and the two signal fields oscillate. The center frequencies of these resonances, denoted ω_1^R and ω_2^R for signal, and ω_p^R for the pump, are usually not equal to the oscillation frequencies. The difference between the latter and the former is measured (in units of the resonance half-width) by normalized detunings $\sigma_{1,2}$ and σ_p.

resonance frequencies, let us first recall under which conditions frequency degeneracy occurs. Cavity modes can be identified by a longitudinal index m and two transverse indices. When the cavity has axial symmetry there is a natural degeneracy and mode frequencies depend on the transverse indices only through a combination of these indices, which we denote l in the following. Let the frequency of a transverse mode with indices m and l be given by $\nu(m,l) = m\Delta\nu_L + (l+1)\Delta\nu_T$ [9], where $\Delta\nu_L$ and $\Delta\nu_T$ are respectively the longitudinal and transverse mode spacings. We are interested in accidental degeneracies that occur whenever the two spacings are commensurate, i.e., when $\Delta\nu_T = (p/q)\Delta\nu_L$ with p and q two integers: in this case, one has $\nu(m, l+nq) = \nu(m+np, l)$ for any integer n. It is important to note that such coincidences occur not only in the classical degenerate geometries such as the flat ($p/q = 0$), confocal ($p/q = 1/2$) or concentric ($p/q = 1$) configurations, but in principle at the countable set of cavity lengths corresponding to rational mode spacing ratios.

In practice, the effect of mode coupling is more important when the denominator q is not too

large, i.e., when some transverse modes of moderate order are degenerate with a TEM_{00} mode (which has $l = 0$). Simultaneous oscillation is expected to occur not only at exact degeneracies but also across whole intervals around them [8]. As we shall see later, these intervals can be quite large: in numerical simulations, oscillations are observed with cavity modes separated by several half-widths of their resonance curves. Thus, there is potentially a large number of cavity configurations where the effect under study can occur.

We now describe the theoretical model. As in the work of Schwob et al. [8], we assume that the signal and idler fields are degenerate, i.e., they correspond to the same field. This is not completely realistic because not all types of cross-coupling between pairs 1 and 2 can be described. Nevertheless, this will allow us to underline the basic phenomena that appear because of the cross-coupling. For simplicity, we also assume here that the losses of the two pairs are equal and that perfect phase matching is realized. Under these assumptions, the model describing the dynamics of the OPO is [7,8]:

$$\dot{A}_p = \gamma\left[-(1+i\sigma_p)A_p - A_1^2 - \chi A_2^2 - 2\chi_{12}A_1A_2 + E\right] \tag{1a}$$

$$\dot{A}_1 = -(1+i\sigma_1)A_1 + A_pA_1^* + \chi_{12}A_pA_2^* \tag{1b}$$

$$\dot{A}_2 = -(1+i\sigma_2)A_2 + \chi A_pA_2^* + \chi_{12}A_pA_1^* \tag{1c}$$

where A_p and the A_i are the slowly varying field envelopes of the pump field $E_p(t) = A_p(t) \times \exp(i\omega_p t - k_p z)$ and of the signal fields $E_j(t) = A_j(t)\exp(i\omega_p t/2 - k_p z/2)$. Note that the carrier frequencies of the signal fields satisfy $\omega_{s,1} = \omega_{s,2} = \omega_p/2$, as discussed above. The time unit is $\tau_s = 1/\gamma_s$ where γ_s is the cavity damping time at the signal wavelength, $\gamma = \gamma_p/\gamma_s$ is the damping rate of the pump field in reduced time units. In the following, all numerical simulations are carried out with $\gamma = 10$.

The parameters σ_p, σ_1 and σ_2 are the normalized cavity detunings of the A_p, A_1 and A_2 fields. More precisely, $\sigma_p = (\omega_p - \omega_p^R)/\gamma_j$ and $\sigma_j = (\omega_j - \omega_j^R)/\gamma_s$, with the $\omega_{p,i}^R$ being the frequencies of the closest mode resonances and $\omega_1 = \omega_2 = \omega_p/2$ (Fig. 4). Note that if $\Delta\omega_s^R = \omega_2^R - \omega_1^R$ denotes the difference of the frequencies of the two signal modes, then the two signal detunings are linked by the relation $\Delta\omega_s^R = \gamma_s(\sigma_1 - \sigma_2)$. Thus, Eqs. (1a)–(1c) allows one to study the transition that occurs when two mode resonances are progressively separated, by simply varying $\sigma_1 - \sigma_2$.

The parameter $\chi = \chi_2^{(2)}/\chi_1^{(2)}$ is the ratio of the effective nonlinear coefficients characterizing parametric generation for the pairs 2 and 1. In general, $\chi \neq 1$ because modes 1 and 2 do not correspond to the same transverse mode and thus do not have the same parametric efficiency [7]. Here, we assume that the two modes are labeled so that $\chi < 1$. The cross-coupling coefficient χ_{12} allows conversion of a pump photon into a photon of the signal mode 1 and a photon of the signal mode 2. It is related to the overlap integral between the three fields [8]. Finally, E is the pumping rate normalized so that $E = 1$ at threshold of mode 1.

The experimentally measured quantities are the pump intensity I_p and the signal intensity I_s. Before we can compare numerical simulations of model (1a)–(1c) with the experimental observations, we have to determine how the numerical I_s should be expressed as a function of the two mode amplitudes A_1 and A_2. Since these two amplitudes correspond to the same rotating frame (the carrier frequencies are identical), the signal intensity should a priori be proportional to $|A_1 + A_2|^2$ (with the possible beat frequency given by $\Delta\omega = d(\phi_2 - \phi_1)/dt$ where ϕ_1 and ϕ_2 are the phases of A_1 and A_2).

However, the two modes A_1 and A_2 typically correspond to different transverse modes. If we assume that the whole beam is focused on the detector, this implies that no beating should in principle be observed, because the overlap integral of two transverse modes is zero (transverse modes form an orthonormal basis). While this obviously cannot be rigorously verified, we will assume in the following that at least it holds approximately, and use $I_s = |A_1|^2 + |A_2|^2$ in our comparisons.

For $\chi_{12} \neq 0$, the model (1a)–(1c) can display periodic behavior, as described in Ref. [8]. This is illustrated by Fig. 5, which displays a numerical solution of model (1a)–(1c): the two signal modes coexist, with their intensities oscillating periodi-

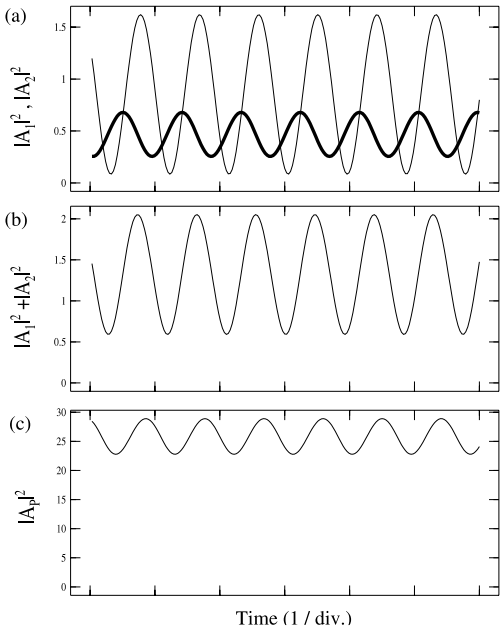

Fig. 5. Numerical integration of model (1a)–(1c). Parameters: $E = 17.4$, $\chi = 0.8$, $\chi_{12} = 0.5$, $\sigma_p = -3.3$, $\sigma_1 = -5$, $\sigma_2 = 7$. (a) Intensities of mode 1 (thin line) and mode 2 (thick line). (b) Total signal intensity. (c) Pump intensity. This numerical regime is comparable to the experimental one displayed in Fig. 1.

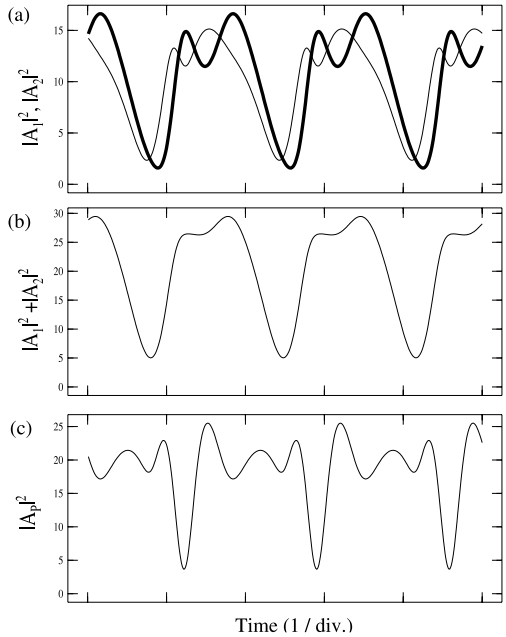

Fig. 6. Numerical integration of model (1a)–(1c). The values of the parameters are similar to the ones used for Fig. 5 except for the detunings: $\sigma_p = -3.6$, $\sigma_1 = -5$, $\sigma_2 = 3$. (a) Intensities of mode 1 (thin line) and mode 2 (thick line). (b) Total signal intensity. (c) Pump intensity.

cally. This numerical instability is similar to the simple modulation observed experimentally (Fig. 1). We observe that $|\sigma_1 - \sigma_2| = 12$ is quite large in this numerical example, as well as in the following ones, showing that even very weakly overlapping resonances can interact significantly. This is because the exact value of the detunings σ_i is meaningful only in an empty cavity: their effect is strongly modified by the nonlinear interaction, which can enhance phase locking. Thus, the dynamical effects described here are expected to occur more easily at high pump power.

It should be noted that the waveforms of the solutions of model (1a)–(1c) depend sensitively on parameters, and especially on detunings. For example, the nonsinusoidal oscillations shown in Fig. 6 differ from the regime shown in Fig. 5 only by the values of the detunings σ_p, σ_1 and σ_2. This explains the great diversity of waveforms observed in the experiments. In particular, the precise shape of the fast oscillations generally changes significantly between the beginning and the end of a burst (see, e.g., the enlarged views in Fig. 3). This variation is in fact natural if we recall that the slow oscillations are related to oscillations of the crystal temperature and of the cavity detunings. Hence, the waveforms at the beginning and the end of a burst differ only because they correspond to different detunings.

To complete our demonstration, however, we still have to show that the regimes combining fast and slow oscillations such as shown in Figs. 2 and 3 can be reproduced qualitatively by extending the model (1a)–(1c) to take into account thermal effects, following the same approach as in our previous works [5,6].

To do so, the main ingredient added to the model is a slow variable θ that describes changes in

the optical length of the crystal due to thermal effects [5,6], and which the detunings depend on. We choose θ so that, to first order in θ, the variation of the detunings $\sigma_j(\theta)$ with temperature is described by

$$\sigma_p(\theta) = \Delta_p - 2\theta/\gamma \tag{2}$$

$$\sigma_1(\theta) = \Delta_1 - \theta \tag{3}$$

$$\sigma_2(\theta) = \Delta_2 - \theta \tag{4}$$

where Δ_p, Δ_1 and Δ_2 are the detunings for the pump, mode 1 and mode 2 of the signal in the "cold" cavity (when crystal temperature is equal to room temperature).

As previously [5,6], the dynamics of θ is described by

$$\dot{\theta} = \epsilon\left[-\theta + \alpha|A_p|^2 + \beta|A_1 + A_2|^2\right] \tag{5}$$

where ϵ^{-1} is the typical thermal time scale and α (resp. β) is proportional to the absorption coefficient of the crystal at the wavelength of the pump (resp. signal).

Figs. 7 and 8 show numerical solutions of the thermo-optical model (1a)–(1c) and (4) for two different sets of parameters. The values of parameters ϵ, γ and E are typical values of the experimental parameters. Since the values of the detunings are not available experimentally, the "cold cavity" detunings Δ_j are adjusted. Similarly, it is difficult to determine experimentally which transverse modes the signal is emitted in. Thus, the exact values of χ and χ_{12} are not known and are arbitrarily chosen to obtain simultaneous emission. Since we had shown previously that it is the absorption of the signal, and not of the pump, which is responsible of the different thermo-optical instabilities [5], we have set $\alpha = 0$ and $\beta = 4$ for the sake of simplicity. In any case, our goal at this stage is not to reproduce exactly the waveforms, but their most important qualitative features.

In this respect, there is a good agreement between the numerical solutions in Figs. 7 and 8 and the experimental regimes in Figs. 2 and 3. In both cases, we observe two distinct time scales, with an alternation of bursts of fast oscillations and of intervals of slow evolution. As can be seen in Figs. 7c and 8c for the thermo-optical model, this corresponds to a slow evolution of temperature. The coupling of the latter with the optical fields is illustrated for example in Fig. 7: when the signal intensity displays fast oscillations (resp. is zero), the variable θ increases (resp. decreases).

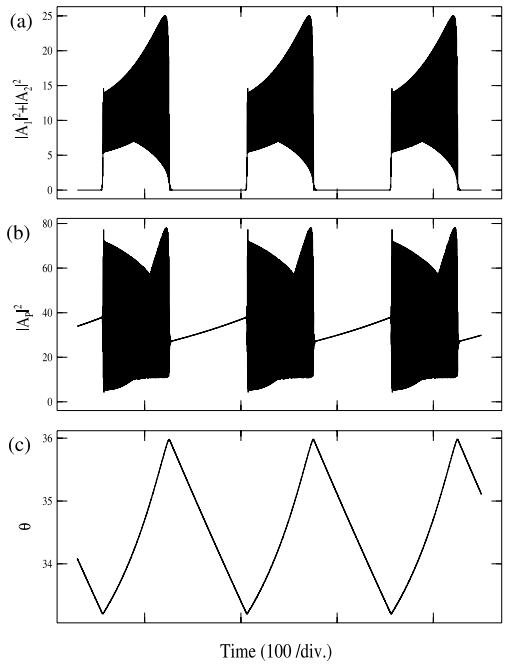

Fig. 7. Numerical integration of model (1a)–(5). Parameters: $E = 17.4$, $\chi = 0.8$, $\chi_{12} = 0.5$, $\Delta_p = 4$, $\Delta_1 = 24$, $\Delta_2 = 40$. (a) Signal intensity. (b) Pump intensity. (c) θ. This numerical regime is comparable to the experimental one displayed in Fig. 2 (alternation of zero signal intensity and fast oscillations).

Because the optical and thermal time scales are very different, the variable θ can be considered as a swept parameter of the purely optical model (1a)–(1c) with the dependence of detunings on θ given by Eqs. (2)–(4). As in our previous studies of thermal effects [5,6], this greatly simplifies the understanding of the observed behaviors.

As temperature (and θ) vary, different types of asymptotic regimes of the optical model corresponding to different values of θ (and hence of the detunings) are observed. For the model with two coupled modes ($\chi_{12} \neq 0$), these asymptotic regimes include: the zero signal intensity state, steady

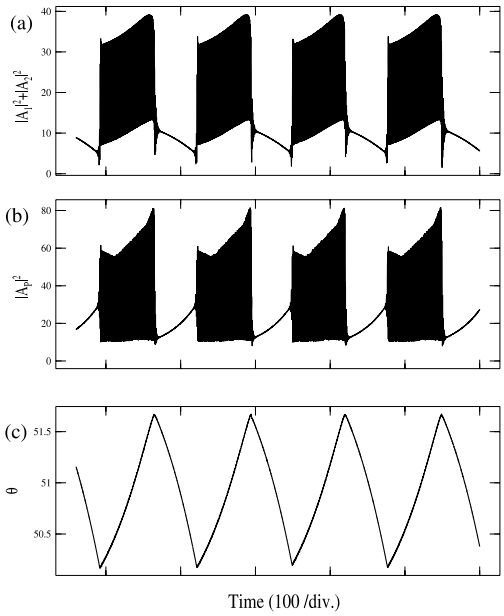

Fig. 8. Numerical integration of model (1a)–(5). Parameters: $E = 17.4$, $\chi = 0.8$, $\chi_{12} = 0.5$, $\Delta_p = 7.6$, $\Delta_1 = 42$, $\Delta_2 = 54$. (a) Signal intensity. (b) Pump intensity. (c) θ. This numerical regime is comparable to the experimental one displayed in Fig. 3 (alternation of slow nonzero evolution and fast oscillations).

states with emission in the two modes, and periodic behavior corresponding to the bursts of fast oscillations [7,8]. Inside these bursts, the gradual evolution of the waveforms is explained by the slow variation of θ. When θ crosses a bifurcation point where a branch of solutions of the optical model disappears, a sudden jump of the field intensities is observed.

In this framework, the difference between regimes where the signal displays intervals of zero intensity and those where it does not is easily understood. In the first case, the OPO completely stops emitting signal between bursts, while in the second case, the two modes always stay above zero and alternate between stationary and periodic behavior. In some cases, one of the modes has an extremely small intensity during the stationary phase, but becomes comparable to the other mode during the oscillating phase.

In the numerical simulations we have performed, we have observed a great diversity of behaviors. For example, we have also found regimes where the three dynamic components (fast oscillations, stationary emission, zero intensity) occur sequentially, as shown in Fig. 9. This example is particularly interesting as it reproduces qualitatively the regimes observed experimentally by Richy et al. [4] (we have also observed such regimes in our experiments). It is thus tempting to conjecture that the mechanism detailed here was also involved in this first observation of fast oscillations in an OPO.

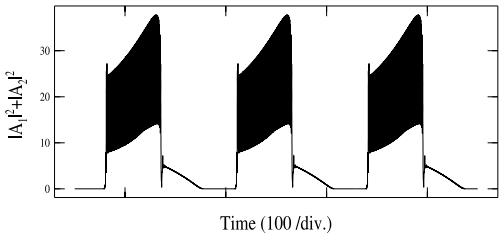

Fig. 9. Signal intensity of a numerical solution of model (1a)–(1c), displaying a sequence of fast oscillations, stationary emission, and zero intensity. $E = 17.4$, $\chi = 0.8$, $\chi_{12} = 0.5$, $\sigma_p = 4$, $\sigma_1 = 24$, $\sigma_2 = 38$.

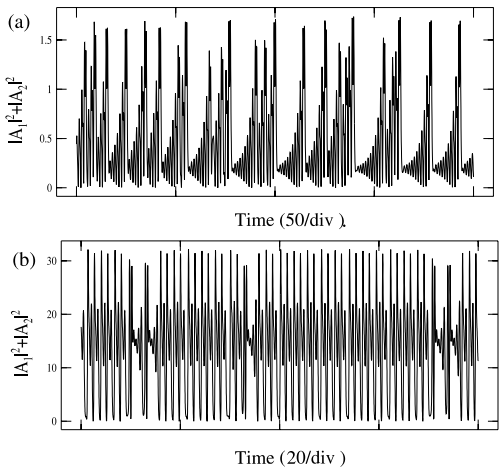

Fig. 10. Chaotic solutions of model (1a)–(1c). (a) Signal intensity for $E = 20.5$, $\chi = 0.6$, $\chi_{12} = 0.34$, $\sigma_p = 3.2$, $\sigma_1 = -4.5$, $\sigma_2 = 6$. (b) Signal intensity for $E = 18.9$, $\chi = 0.69$, $\chi_{12} = 0.38$, $\sigma_p = -0.64$, $\sigma_1 = -14.7$, $\sigma_2 = 6.3$.

In fact, we are certainly far from having exhausted the list of possible behaviors in this system, and further investigations are definitely needed. In particular, we have found examples of chaotic regimes in the purely optical model (1a)–(1c), shown in Fig. 10. The clear qualitative difference between these two regimes (note also the difference in time scales) illustrates well the diversity of regimes that can be found in the OPO with two coupled signal modes. What is interesting in this observation is that unveils a new possible route to deterministic chaos in OPOs. As recalled in Section 1, the only scenario known so far was the one occurring via the Hopf bifurcation of the monomode mean-field model which, however, has not yet been observed experimentally. It remains to be seen if chaotic regimes of the type shown in Fig. 10 will be easier to find in the experiments.

4. Conclusion

In conclusion, we have observed fast oscillations in a triply resonant OPO, at frequencies typically between 1 and 10 MHz. These solutions appear under very different aspects, from a simple quasi-sinusoidal modulation to complex regimes combining fast and slow oscillations. Contrary to what may have been expected a priori, the most probable cause of this instability is not the Hopf bifurcation predicted theoretically in the single-mode mean field [3], but originates in the interaction of two signal modes with neighboring frequencies [7,8]. This is supported not only by an analysis of the complex regimes, but also by the fact that numerical simulations of the mean-field model with two coupled modes reproduces well the regimes observed experimentally, as well as those observed earlier by Richy et al. [4]. This system displays a great variety of dynamical behaviors, including chaotic regimes, and certainly deserves further theoretical and experimental investigations.

Acknowledgements

The Laboratoire de Physique des Lasers, Atomes et Molécules is Unité Mixte de Recherche du CNRS. The Centre d'Études et de Recherches Lasers et Applications is supported by the Ministère chargé de la Recherche, the Région Nord-Pas de Calais and the Fonds Européen de Développement Économique des Régions.

Appendix A. Hopf frequency of the monomode mean-field model

We give here the formula for the frequency of the periodic solution created in the Hopf bifurcation of the monomode mean-field model, and provide a lower bound on it. This allows us to compare it with the frequency of the periodic behaviors observed experimentally.

The mean-field model for a degenerate single-mode OPO reads [3]:

$$\dot{A}_\mathrm{p} = \tau_\mathrm{p}^{-1}\left[-\left(1+\mathrm{i}\sigma_\mathrm{p}\right)A_\mathrm{p} - A_\mathrm{s}^2 + E\right] \tag{A.1}$$

$$\dot{A}_\mathrm{s} = \tau_\mathrm{s}^{-1}\left[-(1+\mathrm{i}\sigma_\mathrm{s})A_\mathrm{s} + A_\mathrm{p}A_\mathrm{s}^*\right] \tag{A.2}$$

which is identical to Eqs. (1a)–(1c) with only one signal mode, except that time has not been renormalized. The variables A_p and A_s are normalized complex amplitudes for the pump and signal field, respectively, E is the amplitude of the input pump, and τ_s (resp., τ_s) is the cavity damping time of the pump (resp., signal) field. The parameters σ_p and σ_s are the normalized detunings of the two fields: $\sigma_j = \tau_j \Delta\omega_j$, where $\Delta\omega_j$ is the difference of the pulsation of the optical field with that of the nearest cavity resonance.

It is known that this model displays under certain conditions a Hopf bifurcation leading from stationary to periodic behavior [1–3]. It was shown in Ref. [3] that, provided the detunings verify

$$\sigma_\mathrm{p}\sigma_\mathrm{s} < -\left[1 + \frac{1+\sigma_\mathrm{p}^2}{2\rho}\right] \tag{A.3}$$

where $\rho = \tau_\mathrm{p}/\tau_\mathrm{s}$, oscillatory behavior is observed when

$$|A_\mathrm{s}|^2 > P_\mathrm{s}^\mathrm{H} = \frac{-(1+\sigma_\mathrm{p}^2)[1+\sigma_\mathrm{p}^2+4\rho(1+\rho)]}{2(1+\rho)^2[1+\sigma_\mathrm{p}^2+2\rho(1+\sigma_\mathrm{p}\sigma_\mathrm{s})]} \tag{A.4}$$

Note that the two conditions above are much more difficult to satisfy in the case of small ρ, as is the case in our experiments ($\rho \approx 0.1$).

To the best of our knowledge, the expression of the pulsation of the periodic solution emerging at the Hopf bifurcation has not been given in previous work. We have thus carried out the calculation of the Hopf bifurcation, and obtained the following expression:

$$\omega_{\mathrm{H}} = \left(\tau_{\mathrm{p}} + \tau_{\mathrm{s}}\right)^{-1} \times \sqrt{\frac{\left(\sigma_{\mathrm{p}}^2\tau_{\mathrm{s}} + 2\sigma_{\mathrm{p}}\sigma_{\mathrm{s}}\tau_{\mathrm{p}} + 2\sigma_{\mathrm{p}}\sigma_{\mathrm{s}}\tau_{\mathrm{s}} - \tau_{\mathrm{s}} - 2\tau_{\mathrm{p}}\right)\left(\sigma_{\mathrm{p}}^2 + 1\right)}{\tau_{\mathrm{s}} + 2\tau_{\mathrm{p}} + \sigma_{\mathrm{p}}^2\tau_{\mathrm{s}} + 2\sigma_{\mathrm{p}}\sigma_{\mathrm{s}}\tau_{\mathrm{p}}}} \tag{A.5}$$

Note that the above expression tends to infinity when condition (A.3) becomes an equality. Since the detunings $\sigma_{\mathrm{p,s}}$ are not easily measurable experimentally, it useful to provide an absolute lower bound to ω_{H} that does not depend on detunings. It is obtained by first letting $\sigma_{\mathrm{s}} \to \infty$, then $\sigma_{\mathrm{p}} \to 0$:

$$\omega_{\mathrm{H}} > \omega_{\mathrm{L}} = \frac{1}{\sqrt{\tau_{\mathrm{p}}\left(\tau_{\mathrm{p}} + \tau_{\mathrm{s}}\right)}} \tag{A.6}$$

The lower bound so obtained can only be approached in the limit of infinite pump power (because of the $\sigma_{\mathrm{s}} \to \infty$ limit), and thus is rather conservative.

In the case of our experiment, with $\tau_{\mathrm{s}} \approx 58$ ns and $\tau_{\mathrm{p}} \approx 4.5$ ns, this gives us a lower bound on the Hopf frequency of $\nu_{\mathrm{L}} = \omega_{\mathrm{L}}/2\pi \approx 9.5$ MHz.

References

[1] K. McNeil, P. Drummond, D. Walls, Self pulsing in second harmonic generation, Opt. Commun. 27 (2) (1978) 292–294.

[2] P. Drummond, K. McNeil, D. Walls, Non-equilibrium transitions in sub/second harmonic generation I. Semiclassical theory, Opt. Acta 27 (3) (1980) 321–335.

[3] L.A. Lugiato, C. Oldano, C. Fabre, E. Giacobino, R.J. Horowicz, Bistability, self-pulsing and chaos in optical parametric oscillators, Il Nuovo Cimento D 10 (8) (1988) 959–976.

[4] C. Richy, K.I. Petsas, E. Giacobino, C. Fabre, L. Lugiato, Observation of bistability and delayed bifurcation in a triply resonant optical parametric oscillator, J. Opt. Soc. Am. B 12 (3) (1995) 456–461.

[5] P. Suret, D. Derozier, M. Lefranc, J. Zemmouri, S. Bielawski, Self-pulsing instabilities in an optical parametric oscillator: experimental observation and modeling of the mechanism, Phys. Rev. A 61 (2000) 021805(R).

[6] P. Suret, M. Lefranc, D. Derozier, J. Zemmouri, S. Bielawski, Periodic mode hopping induced by thermo-optic effects in continuous-wave optical parametric oscillators, Opt. Lett. 26 (2001) 1415–1417.

[7] M. Marte, H. Ritsch, L. Lugiato, C. Fabre, Simultaneous multimode optical parametric oscillation in a triply resonant cavity, Acta Physica Slovaca 47 (3/4) (1997) 233.

[8] C. Schwob, P. Cohadon, C. Fabre, M. Marte, H. Ritsch, A. Gatti, L. Lugiato, Transverse effects and mode couplings in OPOs, Appl. Phys. B 66 (1998) 685–699.

[9] A.E. Siegman, Lasers, University Science Books, 1986.

"Periodic mode hopping induced by thermo-optic effects in continuous-wave optical parametric oscillators"

P. Suret, M. Lefranc, D. Derozier, J. Zemmouri, and S. Bielawski

Opt. Lett. **26**, 1415–1417 (2001)

September 15, 2001 / Vol. 26, No. 18 / OPTICS LETTERS 1415

Periodic mode hopping induced by thermo-optic effects in continuous-wave optical parametric oscillators

Pierre Suret, Marc Lefranc, Dominique Derozier, Jaouad Zemmouri, and Serge Bielawski

Laboratoire de Physique des Lasers, Atomes, Molécules, Unité Mixte de Recherche du 8523 Centre National de la Recherche Scientifique, Centre d'Etudes et de Recherches Lasers et Applications, Université des Sciences et Technologies de Lille, F-59655 Villeneuve d'Ascq, France

Received June 27, 2001

We show that thermal effects can lead to periodic mode hopping in cw optical parametric oscillators (OPOs). This mode hopping may occur as soon as two modes have different intensities at the point where they exchange their stability; this condition is easily fulfilled in OPOs that are triply resonant, or doubly resonant with a weakly resonant pump. We have observed such oscillations experimentally in a type II OPO in both configurations. A simple thermo-optic multimode model reproduces well the experimental regimes. We expect that multimode instabilities based on this mechanism can be observed with various aspects in many experimental setups at high pumping rate. © 2001 Optical Society of America

OCIS codes: 190.4970, 190.3100, 190.4870.

Because of their wide tunability, optical parametric oscillators (OPOs) are promising sources of coherent optical radiation. To lower the oscillation threshold of cw OPOs, researchers commonly set them up as doubly resonant oscillators (DROs) or triply resonant oscillators (TROs), with the signal and idler fields resonant in the cavity.[1] Because of the multiple resonance conditions, however, such configurations are known to suffer from mode and cluster hopping when a control parameter is varied or randomly fluctuates.[2,3]

In this Letter we show that thermo-optic effects can lead to periodic mode hopping in cw OPOs: We have observed thermally induced oscillations at a few kilohertz between two different longitudinal modes in type II OPOs, in both the DRO and the TRO configuration. At high pump power, this instability occurs over wide ranges of detunings, thus severely affecting tunability.

As shown below, this phenomenon can be understood in the same framework as a recently described monomode self-pulsing instability[4]: It involves a feedback loop linking the fast optical fields and the crystal temperature. Unlike in the monomode case, however, the mechanism of oscillations observed does not rely on the presence of a bistability cycle. Thus, the phenomenon occurs over a much larger parameter region than for the monomode case and can be observed even if the pump is only weakly resonant, as in many configurations generally considered as DRO. For brevity, we focus here on the TRO case, which is the natural context for the theoretical analysis, but we also present examples of instabilities observed in our DRO.

The experimental setup is a TRO similar to that previously described.[4] The TRO is based on a KTP crystal cut for type II phase matching. Crystals of length $l_c = 7$ or $l_c = 15$ mm have been used, with similar results. The 5-cm-long Fabry–Perot cavity consists of two mirrors with a radius of curvature of 3 cm and is resonant at the frequencies of the Nd:YVO_4 pump laser (Coherent Verdi; maximum power, 5 W, operating at 532 nm) and of its subharmonic, so that the signal and idler wavelengths are close to 1064 nm. The mirrors have maximal reflectivity, except at 532 nm for the input mirror ($R = 90\%$) and at 1064 nm for the output mirror ($R = 99\%$), and correspond to a finesse of 45 for the pump and 550 for the signal and idler fields, taking into account absorption by the crystal.[4] Under these conditions, the pump power at threshold is ~20 mW. The three fields oscillate in the TEM_{00} mode. The signal and idler display similar time evolution. The DRO is identical to the TRO, except that (i) the input mirror has $R = 15\%$ at 532 nm, corresponding to a finesse of 3 for the pump; (ii) mirrors with a radius of curvature of 5 cm were used; and (iii) only the 15-mm-long crystal was used, with a threshold of ~180 mW. We used no active stabilization to avoid interfering with the intrinsic dynamics of the OPO.

Figure 1 shows typical examples of the regimes studied in this Letter, observed in a TRO and a DRO. These oscillations can be stably observed for up to a few minutes. They are similar to the periodic regimes presented previously[4]: The oscillation period (270 μs) is of the order of the estimated thermal-diffusion time scale,[5] i.e., $\tau_{th} \simeq 230$ μs, and depends markedly on cavity detunings; and the time signals display intervals of slow evolution, separated by sudden jumps in the pump and signal intensities. Yet the present instability cannot be interpreted as

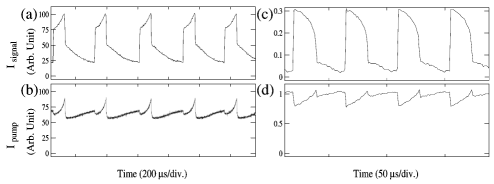

Fig. 1. Experimental self-pulsing regimes: (a) signal and (b) pump intensity in a TRO ($l_c = 7$ mm, $P_{pump} = 1.5$ W) and (c) signal and (d) pump intensity in a DRO ($l_c = 15$ mm, $P_{pump} = 3.6$ W).

0146-9592/01/181415-03$15.00/0

1416 OPTICS LETTERS / Vol. 26, No. 18 / September 15, 2001

oscillations around the bistability cycle of a single mode, because the signal intensity never goes to zero. In fact, the system is exploring the resonance curves of two different longitudinal modes, as we show below.

The output of a confocal Fabry–Perot spectrum analyzer for a typical regime is shown in Fig. 2. The spectrum analyzer was purposely misaligned so that the broadened resonance curve for a given longitudinal mode of the OPO would be swept in a time that is long compared with the oscillation period of the instability.

Two series of peaks, corresponding to two resonances, can easily be seen in Fig. 2. The two resonances are separated by 3 GHz, which is exactly the frequency difference between two adjacent longitudinal modes of the OPO: This clearly confirms the two-mode hypothesis. Moreover, if we look closely at the first resonance and compare the input of the Fabry–Perot analyzer [Fig. 2(b)] with its output [Fig. 2(c)], we can see that mode 1 oscillates only during the first phase of the period and completely vanishes during the second phase. Similarly, mode 2 oscillates only during the second phase (not shown) and thus is in antiphase with mode 1.

This result clearly shows that the instability consists of periodic hopping between two longitudinal modes of the OPO, which is consistent with the fact that two modes with different frequencies cannot oscillate simultaneously in a cw OPO.[6] The same analysis was carried out for the DRO instabilities and led to the same conclusion.

Accordingly, we extended the simple thermo-optic model described previously[4] to multimode operation. The extension is based on the usual two-mode mean-field model of a degenerate TRO[6]:

$$\dot{A}_p = \gamma\{-[1 + i\sigma_p(\theta)]A_p - A_1{}^2 - A_2{}^2 + E\}, \quad (1)$$

$$\dot{A}_1 = -[1 + i\sigma_1(\theta)]A_1 + A_p A_1{}^* + \eta, \quad (2)$$

$$\dot{A}_2 = -[1 + i\sigma_2(\theta)]A_2 + A_p A_2{}^* + \eta, \quad (3)$$

where A_p, A_1, and A_2 are the complex amplitudes of the pump and the two subharmonic modes. The frequencies of the subharmonic modes are assumed to be well separated so that there is no cross coupling between A_1 and A_2.[6] The time unit is the cavity decay time of the signal, γ is the cavity decay rate of the pump, and E is the input pump. The small constant η is an artificial source term that mimics parametric fluorescence.

The core ingredient in our model is that the cavity detunings σ_p, σ_1, and σ_2 of the three fields depend on a slow variable θ, which describes changes in the optical length of the crystal as a result of thermal effects.[4] We choose θ so that, to first order, the cavity detunings are given by $\sigma_{1,2}(\theta) = \Delta_{1,2} - \theta$ and $\sigma_p(\theta) = \Delta_p - 2\theta/\gamma$, where $\Delta_{1,2}$ and Δ_p are the detunings of the fields in the cold cavity (at $\theta = 0$). Conversely, the influence of the optical fields on the dynamics of θ is described by the following equation[4]:

$$\dot{\theta} = \epsilon[-\theta + \alpha|A_p|^2 + \beta(|A_1|^2 + |A_2|^2)], \quad (4)$$

where ϵ^{-1} is an effective thermal time scale ($\epsilon \ll 1$) that we choose here to be equal to τ_{th} and α and β quantify absorption by the crystal at the pump and signal wavelength, respectively.

The model (1)–(4) reproduces the experimental waveforms extremely well, with the two modes alternating with each other as in the experiments (Fig. 3). We did not attempt to recover the exact experimental period, as it depends sensitively on detunings and noise, which are difficult to measure.

The slowly varying (on optical time scale) θ can be considered a parameter of Eqs. (1)–(3) that is swept back and forth. Thus the phase-space trajectory mostly follows the branches of the stationary states of Eqs. (1)–(3), corresponding to monomode operation on modes 1 and 2 (Fig. 4).

In this representation the instability mechanism is easily understood. Recall that the stable mode is the one with the lowest threshold,[6] i.e., the one with smallest $\sigma_i(\theta)^2$. Oscillations take place about the point where the two modes exchange their stabilities, which is given by $\sigma_1(\theta_c) = -\sigma_2(\theta_c)$. In Fig. 4, the effective temperature θ increases (decreases) with time on branch 1 (2). When the stability exchange point is crossed, the system stays near the now weakly unstable branch for some time before switching abruptly to the other branch (which is now stable). The trajectory then proceeds in the reverse direction, and so on. Because the system oscillates around a singular point, calculation of dynamic properties such as the

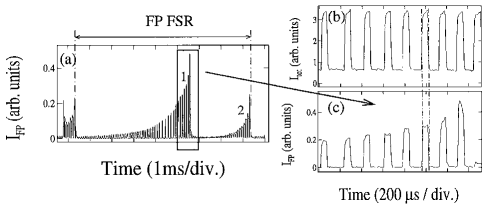

Fig. 2. Spectral analysis: (a) output of the Fabry–Perot analyzer as its length is swept over one free spectral range (10 GHz); (b), (c) details of the resonance of mode 1. (b) Signal intensity fed to the Fabry–Perot analyzer, (c) output of the Fabry–Perot analyzer.

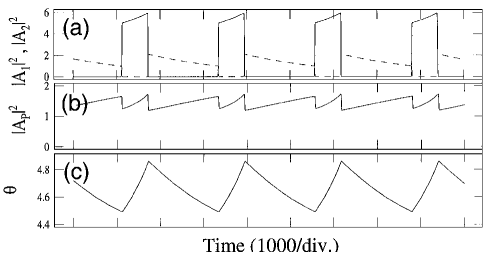

Fig. 3. Numerical integration of Eqs. (1)–(4). (a) $|A_1|^2$ (solid line) and $|A_2|^2$ (dashed line), (b) $|A_p|^2$. $E = 6$, $\Delta_p = -3$, $\Delta_1 = 4$, $\Delta_2 = 5.3$, $\alpha = 2$, $\beta = 0.7$, $\gamma = 10$, $\epsilon = 3 \times 10^{-4}$, and $\eta = 10^{-40}$. One time unit corresponds to 70 ns.

September 15, 2001 / Vol. 26, No. 18 / OPTICS LETTERS 1417

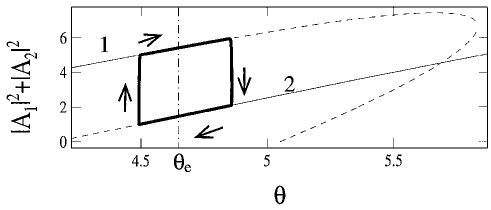

Fig. 4. Phase portrait $(\theta, |A_1|^2 + |A_2|^2)$. Thick box, trajectory associated with the regime of Fig. 3. Solid (dashed) curves, stable (unstable) stationary states of model (1)–(4). The stable solution for $\theta < \theta_c$ $(\theta > \theta_e)$ is mode 1 (mode 2).

period and the amplitude in θ is not straightforward and requires a singular perturbation analysis.

It is easy to see that self-pulsing can appear near the stability exchange as soon as the two modes have different intensities at the point where they exchange their stabilities, so $\dot{\theta}$ has opposite signs on the two branches. In the case of two longitudinal modes discussed here, it suffices that both the pump and the signal modes are slightly detuned $[\sigma_p(\theta_e)\sigma_1(\theta_e) \neq 0]$.[7] The larger the intensity difference, the larger the region in which instability will occur: In some configurations operated at a high pumping rate, we have observed oscillations for approximately half the detuning range.

Although this qualitative description is similar to that of the monomode instability described in Ref. 4, the condition obtained above is much less stringent: It does not depend on the presence of a bistability cycle, which requires that $\sigma_p(\theta_c)\sigma_1(\theta_e) > 1$. This explains why the bimode instability can easily be observed in an OPO in which the pump is weakly resonant [Fig. 1(b)], provided that the pump detuning, even when small, is nonzero. A nonzero pump detuning is possible as soon as the pump is at least double pass,[7] which is the case in many configurations that are classified as doubly resonant.

This conclusion has been confirmed by numerical simulations of the model (1)–(4) in the limit $\gamma \gg 1$ for small values of Δ_p. Another very important result of our simulations is that instability can occur at pump rates as small as twice the threshold (e.g., for $E = 1.5$, $\Delta_p = -0.6$, $\Delta_1 = 2$, $\Delta_2 = 2.9$, $\alpha = 0$, $\beta = 12$, $\gamma = 40$,huey $\eta = 10^{-40}$), which indicates that the range of operating conditions that can be affected by the instability is large.

The mechanism discussed here seems very general. For example, it can also induce oscillations between two transverse modes. In this case the fields need not be detuned, as the intensity difference at the exchange of stability is ensured by the difference in the effective nonlinear coefficients. We have also observed oscillations among three modes or more, as well as fast oscillations superimposed on the thermally induced ones, similar to those reported by Richy *et al.*[8] Finally, we have found numerical solutions of our model with smooth waveforms. Thus the present instability cannot be ruled out when no sudden jump is observed.

These observations lead us to believe that the instability presented here should be observable in many cw DROs or TROs, especially as high-power pump lasers become increasingly available. In particular, it might explain the slow periodic behaviors observed in different cw OPOs by Richy *et al.*[8] and Douillet *et al.*[5] This Letter certainly provides motivation for further study of multimode instabilities, both from a dynamic point of view and with a view to achieving stable operation of cw OPOs at high pump power.

The Centre d'Etudes et de Recherches Lasers is supported by the French Ministère Chargé de la Recherche, the Région Nord-Pas de Calais, and the Fond Européen de Développement Économique des Régions. M. Lefranc's e-mail address is marc.lefranc@univ-lille1.fr.

References

1. C. Fabre, P. F. Cohadon, and C. Schwob, J. Opt. B **9,** 165 (1997).
2. R. Smith, IEEE J. Quantum Electron. **QE-9,** 530 (1973).
3. G. Agarwal and S. Gupta, J. Opt. Soc. Am. B **14,** 2174 (1997).
4. P. Suret, D. Derozier, M. Lefranc, J. Zemmouri, and S. Bielawski, Phys. Rev. A **61,** 021805(R) (2000).
5. A. Douillet, J.-J. Zondy, A. Yelisseyev, S. Lobanov, and L. Isaenko, J. Opt. Soc. Am. B **16,** 1481 (1999).
6. C. Schwob, P. Cohadon, C. Fabre, M. Marte, H. Ritsch, A. Gatti, and L. Lugiato, Appl. Phys. B **66,** 685 (1998).
7. L. Lugiato, C. Oldano, C. Fabre, E. Giacobino, and R. Horowicz, Nuovo Cimento D **10,** 959 (1988).
8. C. Richy, K. Petsas, E. Giacobino, C. Fabre, and L. Lugiato, J. Opt. Soc. Am. B **12,** 456 (1995).

"Self-pulsing instabilities in an optical parametric oscillator: experimental observation and modeling of the mechanism"

P. Suret, D. Derozier, M. Lefranc, J. Zemmouri, and S. Bielawski

Phys. Rev. A **61**, 021805(R) (2000)

RAPID COMMUNICATIONS

PHYSICAL REVIEW A, VOLUME 61, 021805(R)

Self-pulsing instabilities in an optical parametric oscillator: Experimental observation and modeling of the mechanism

Pierre Suret, Dominique Derozier, Marc Lefranc, Jaouad Zemmouri, and Serge Bielawski
Laboratoire de Physique des Lasers, Atomes et Molécules, UMR CNRS, Centre d'Etudes et de Recherches Lasers et Applications, Université des Sciences et Technologies de Lille, F-59655 Villeneuve d'Ascq Cedex, France
(Received 16 February 1999; published 14 January 2000)

We have observed sustained self-pulsing in a continuously pumped, triply resonant, optical parametric oscillator. From the analysis of our experimental data, we conclude that the instability mechanism is different from the Hopf bifurcation predicted by the classical model of parametric interaction. Self-pulsing results from the interplay of a slow variable (temperature) and the optical bistability cycle, leading to a *singularly perturbed system*. From simple arguments, we propose a minimal dynamical model that reproduces well the observed behaviors.

PACS number(s): 42.65.Yj, 42.65.Sf

Continuous-wave optical parametric oscillators (OPOs) have recently received increased interest both experimentally and theoretically. Due to their tunability and to their quantum properties, OPOs are promising sources of coherent light. They have applications in high-resolution spectroscopy [1], implementation of reference standards [2], and can be used to generate squeezed states of light [3].

It is thus important to understand the instabilities that cw OPOs may display, especially as they have been recognized as a system of choice for the study of complex nonlinear dynamics. In particular, theoretical studies have shown that OPOs are good candidates for the observation of various fundamental phenomena, such as transition to chaos [4], spatiotemporal dynamics [5], including localized structures and topological defects [6], as well as quantum images [7].

Yet, such a simple dynamical phenomenon as the self-pulsing instability observed in a triply resonant OPO [8] has not so far been given a clear interpretation. On the one hand, theoretical studies of the classical mean-field model of parametric interaction have predicted the existence of periodic behaviors originating in a Hopf bifurcation [4,9]. On the other hand, the first experimental observation of a self-pulsing regime suggested that a different mechanism might be involved [8]: transverse, thermal, and/or multimode effects possibly have to be taken into account. The nature of the self-pulsing instability thus remains an open and important question, especially as a good understanding of the temporal dynamics of OPOs is a first step towards investigating more sophisticated phenomena such as spatiotemporal dynamics.

In this paper, we identify a generic instability mechanism leading to self-pulsing behaviors, which differs from the Hopf bifurcation of the parametric model, and can result from several physical effects. The main ingredient is the *interplay between the dynamics of a slow variable and the hysteresis cycle of a fast variable*. Slow dynamics can be due to, e.g., thermal [10] or photorefractive effects [11], which are generally ignored in the modeling of OPOs.

Such instabilities are classical in perturbation theory [12,13]: adding a slow variable with a small relaxation rate ϵ is known to lead to a *singularly perturbed system*, which can display a dynamical instability not present in the $\epsilon=0$ case, even for small ϵ. Examples of such instabilities are found in various fields, a classical one being the Van der Pol oscillator in the singular limit [12].

First we present the experimental observations that motivate the present work. We conclude (i) that the observed instability differs from the Hopf bifurcation predicted in Ref. [4] and (ii) that the model of the OPO must involve a variable that is much slower than the optical ones. In the second part, we propose and analyze a minimal model that reproduces the observed dynamical behaviors. We show that the peculiar shape of the regimes can be explained by a mechanism of *periodic bursting*, where the slow variable oscillates around the bistability cycle linked to the fast optical variables.

Our experiments have been carried out with a classical triply resonant OPO (i.e., resonant for the pump and parametrically generated signals) [8]. Because we are mainly interested in studying dynamical effects, the cavity length is not stabilized by a feedback loop. However, thanks to a careful design of the mechanical properties of the cavity and probably to thermal self-locking, as in Refs. [10,14], stationary or periodic regimes can be stably obtained for several minutes at fixed, uncontrolled, cavity length.

The experimental setup is displayed in Fig. 1. The nonlinear crystal is a 7-mm-long KTP crystal (Crystal Laser) cut for type-II phase matching. To avoid transverse effects, the cavity is kept far from the stability limit (even in the presence of thermal lensing) by choosing a length $L=5$ cm and

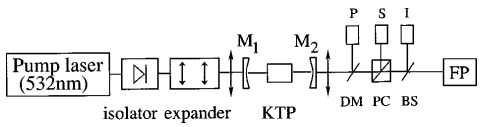

FIG. 1. Experimental setup. Notation used: M_1, input mirror (R_{max} at 1.06 μm, $R=90\%$ at 532 nm); M_2, output mirror ($R=99\%$ at 1.06 μm, R_{max} at 532 nm); DM, dichroic mirror (R_{max} at 532 nm and T_{max} at 1.06 μm); PC, polarizing cube; BS, beam splitter; FP, Fabry-Perot spectrum analyzer; P, S, and I are the photodiodes monitoring the pump, signal, and idler intensities, respectively.

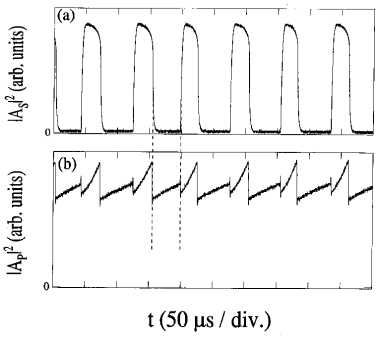

FIG. 2. Typical periodic regime observed experimentally with a pump power of 450 mW. (a) Signal; (b) pump. The pump evolution when the signal is off (as between dashed lines) implies that a parameter of the purely parametric model is in fact a dynamical variable. Note also the pump discontinuities associated with signal switching.

mirrors with a curvature radius of 3 cm. Mirror coatings are such that the cavity is resonant at frequencies of the pump and of its first subharmonic (reflection coefficients are given in the caption of Fig. 1). Taking into account the vendor-specified absorption coefficients of the crystal (2.5% cm^{-1} at 532 nm and 0.1% cm^{-1} at 1064 nm), the cavity finesses are estimated to be 45 for the pump and 550 for the signal and idler fields. The pump is provided by a monomode frequency-doubled Nd:YVO_4 laser (Coherent Verdi, 5 W of maximum power). Threshold power is less than 25 mW, and either stable or self-pulsing operation can be obtained depending on the cavity length and pump power. In order to extract the core of the mechanism leading to self-pulsing, we focus here on regimes involving only a single longitudinal and transverse mode, as was checked with an external Fabry-Perot analyzer.

The output intensities at 532 nm and 1.064 μm are detected by silicium and InGaAs photodiodes, respectively. Because the time evolutions of the signal and idler fields appear to be identical, only the former will be represented here. However, as we will see below, monitoring the time evolution of the pump provides key information on the ingredients to include in the modeling of the OPO.

The observed self-pulsing regimes, such as the typical one displayed in Fig. 2, are found to differ significantly from those predicted from the purely parametric model: (i) time scales ($\sim 10^{-4}$ s) are a few orders of magnitude slower than cavity lifetime ($\sim 10^{-7}$ s); (ii) signal and pump display discontinuities, whereas smooth waveforms would be expected; (iii) during the periods of vanishing signal, the pump continues to evolve on a slow time scale, whereas it should remain constant after a short transient of a few microseconds.

These discrepancies clearly show that a more complete modeling is required. Fortunately, the last observation clearly reveals how to proceed. When the signal is off, the intracavity pump power should depend on the cavity detuning only, as the cavity then behaves as a mere Fabry-Perot interferometer. The unexpected slow evolution thus indicates that the effective cavity length is no longer a parameter, but is slaved to a *new dynamical variable, which relaxes on a slow time scale*. This slow variable can reflect changes in crystal temperature in the case here and in the experiments of Hansen and Buchhave [10], and probably in the experiments of Richy *et al.* [8], but can also be potentially due to a range of effects such as photorefractive changes in the index of refraction [11].

During self-oscillation, no mode hop occurs for the signal and idler fields. Due to the frequency-tuning properties of type-II OPOs [15], this gives an upper bound on the maximum variation $\delta\mathcal{L}$ of the cavity round-trip length. Indeed, one should observe mode hops in our configuration as soon as $\delta\mathcal{L}/\lambda_p \approx 2\times 10^{-2}$, where λ_p is the pump wavelength (i.e., $\delta\mathcal{L} \approx$ 10 nm). That such a tiny effect induces a large variation in the output powers clearly calls for a dynamical interpretation.

In order to show that such a slow dynamics can indeed induce self-pulsing regimes, we consider the simplest OPO model [4,9] (mean-field approximation, degenerate case, and without transverse effects) coupled to a slow variable θ as follows: (i) cavity detunings are assumed to be functions of θ, as discussed above; (ii) the time evolution of θ is driven by pump and signal intensities, as in, e.g., thermal effects (this should, however, be a generic coupling for a scalar variable). Since the cavity is far from degeneracy and given the high cavity finesses, the effect of variations of the cavity geometry (such as induced by a change in the focal length of a thermal lens) is orders of magnitude below the effect of the path length change. Thus, we neglect the influence of θ on other model parameters, such as the input pump power.

If we set A_p and A_s the complex amplitudes of the pump and subharmonic, respectively, the corresponding normalized evolution equations read

$$\dot{A}_p = \gamma\{E - [1 + i\sigma_p(\theta)]A_p - A_s^2\}, \tag{1a}$$

$$\dot{A}_s = -[1 + i\sigma_s(\theta)]A_s + A_p A_s^*, \tag{1b}$$

$$\dot{\theta} = \epsilon f(\theta, |A_p|^2, |A_s|^2), \tag{1c}$$

where the time unit is the cavity decay time τ of the signal field ($\tau \approx 4[L]/cT_s$, with $[L]$ the optical cavity length and T_s the transmission coefficient of the output mirror), γ is the cavity decay rate for the pump, E is the input pump, $\sigma_p(\theta)$ and $\sigma_s(\theta)$ are the normalized detunings associated with the pump and signal, respectively, and ϵ is the relaxation rate of the slow variable θ ($\epsilon \ll 1, \gamma$).

We have seen above that θ should describe changes in the cavity effective length (such as those caused by the dependence of refraction indexes on temperature). For definiteness, we choose θ to be the variation of the signal detuning: $\sigma_s(\theta) = \Delta_s - \theta$. To first order, the pump detuning is then given by $\sigma_p(\theta) = \Delta_p - 2\theta/\gamma$ [16], and the simplest expression for f is obtained by assuming that for fixed field intensities, θ relaxes exponentially to an equilibrium value depending linearly on these intensities:

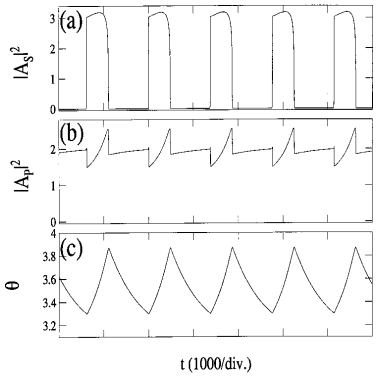

FIG. 3. Numerical integration of (1) with $E=4$, $\gamma=10$, $\epsilon=10^{-3}$, $\Delta_p=-2$, $\Delta_s=2.6$, $\alpha=1.5$, and $\beta=0.6$. (a) Signal; (b) pump; (c) the θ variable.

$$f=-\theta+\alpha|A_p|^2+\beta|A_s|^2, \tag{2}$$

where α and β characterize pump and signal absorption by the crystal. Note that the feedback loop resulting from the coupling to θ naturally accounts for the self-locking observed in our experiments, and also reported in Ref. [10].

As expected, introduction of the singular perturbation (1c) leads to self-pulsing. What is more striking is that numerical integration of this model reproduces extremely well the waveforms observed experimentally. As an example, Fig. 3 shows a typical regime that closely matches the experimental one in Fig. 2 for similar values of the accessible parameters ($\gamma=10$ and $E=4$). Taking into account the normalization of the fields [4], the ratio $\gamma\alpha/\beta$ should be close to the ratio of the absorption coefficients of the crystal, and has thus been fixed at 25. The remaining free parameters α and ϵ have been chosen so that the correct time scale is obtained and the waveforms qualitatively reproduce those observed experimentally. With $\epsilon=10^{-3}$, the thermal time scale is $\tau/\epsilon \approx 70$ μs, which gives the correct order of magnitude of the instability period (experimental and numerical periods are close to 90 μs).

To identify the mechanism and explain the particularities of the self-pulsing regimes, we take into account the large ratio of the two time scales, i.e., the smallness of ϵ. This allows us to use our knowledge of the unperturbed system [4,9] for $\epsilon=0$ to explain the properties of the actual system.

The variable θ is a parameter for the unperturbed system of Eqs. (1a) and (1b), whose stable stationary solutions will be noted $\tilde{A}_p(\theta)$ and $\tilde{A}_s(\theta)$. In first approximation, assume that in the complete model (1), the optical fast variables (A_p, A_s) adiabatically follow the slow one θ. The dynamics is then reduced to

$$\dot{\theta}=\epsilon f\,(\theta,|\tilde{A}_p(\theta)|^2,|\tilde{A}_s(\theta)|^2). \tag{3}$$

It is readily seen that, if $\tilde{A}_p(\theta)$ and $\tilde{A}_s(\theta)$ are smooth functions of θ, the system (3) is purely one-dimensional and can only have fixed points. Thus the key ingredient for the self-pulsing instability is the existence for some parameter range of a bistability cycle associated with $\tilde{A}_p(\theta)$ and $\tilde{A}_s(\theta)$ [4,9]. Periodic behavior then occurs when the dynamics described by Eq. (3) make the system oscillate around the bistability cycle, essentially as if the parameter θ of the unperturbed model of Eqs. (1a) and (1b) were swept back and forth over the bistability region.

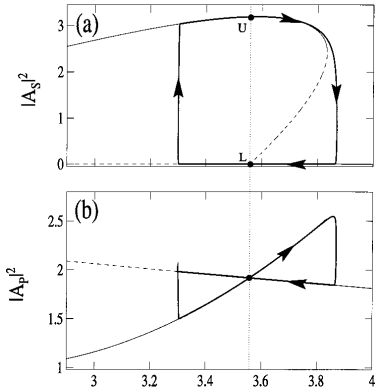

FIG. 4. Phase portrait of the periodic regimes. Thick line: trajectory associated with the regime presented in Fig. 3. The bifurcation diagram of Eqs. (1a) and (1b) with θ as a parameter ($\epsilon=0$) is also shown with full (dashed) lines representing stable (unstable) stationary states.

This is illustrated by Fig. 4 where phase portraits $(\theta(t),|A_s(t)|^2)$ and $(\theta(t),|A_p(t)|^2)$ of a self-pulsing regime of model (1) are plotted with the bistability cycle of the unperturbed system. Figure 4 clearly shows that the dynamics involves slow evolutions (on the thermal time scale) on the branches, interrupted by two fast jumps (on the optical time scale) between the branches. This is the reason for the apparent discontinuities observed on experimental recordings of the pump and signal intensities (Fig. 2). Note that the switch to the upper branch in Fig. 4(a) occurs well after the bifurcation point L has been crossed because the system stays on the unstable off state during a significant amount of time.

Such a mechanism is robust in that it would clearly persist if the model were modified, e.g., to describe more accurately thermal lensing effects. It appears to be similar to those that have been described for a nonlinear Fabry-Perot interferometer [17] and for cold atoms trapped in a cavity [18]. Unlike in other optothermal instabilities such as those reported in Refs. [19,20], the bistability cycle exists here independently of thermal effects.

The identification of the mechanism gives a necessary condition for the appearance of a periodic cycle: the derivative of θ [given by Eqs. (2) and (3)] must be strictly negative on the lower branch and strictly positive on the upper one (which precludes that a fixed point of the complete model be located on the branch segments visited by the cycle).

Without any calculation, this leads at once to the surpris-

ing conclusion that the crucial role in the instability is played by signal absorption, even if weaker than pump absorption. Indeed, we know that $|\tilde{A}_p^{\mathrm{off}}(\theta)|=|\tilde{A}_p^{\mathrm{on}}(\theta)|$ at the bifurcation point L of the bistability cycle [Fig. 4(b)]. Hence, the derivatives of θ at points L and U on the lower and upper branches verify $f_U=f_L+\beta|\tilde{A}_s^{\mathrm{on}}(\theta)|^2$. Since we must have $f_L<0$ and $f_U>0$, this clearly shows that $\beta>0$ is a necessary condition for the appearance of the instability. On the other hand, we have observed that self-pulsing regimes still occur if we set $\alpha=0$. Pump absorption, even if significant, thus cannot lead alone to the instability.

In conclusion, we have identified an instability mechanism for the OPO that differs from the Hopf bifurcation predicted by the parametric model. It is generic in that the main ingredients are (i) the bistability cycle known to exist in triply resonant OPOs and (ii) a slow variable whose existence can be due to several physical effects, the most common one being thermal variations of the crystal refraction indexes.

This result calls for further investigations in several directions. First, a complete bifurcation study of the model is needed, especially to determine which conditions the crystal absorption coefficients α and β must verify for the instability to occur. Second, the straightforward extension of our model to operation on two longitudinal modes is promising as it reproduces well the bimode regimes that we have also observed experimentally. Last, but not least, it is important to reconsider the study of transverse dynamics in connection with the present mechanism. For instance, our preliminary experimental observation near the cavity stability limit suggests the existence of thermally induced transverse variations of refractive indices. To describe this phenomenon, the model should be extended by including transverse effects and a heat diffusion equation.

Note added. We recently became aware of a work by Douillet *et al.* describing an instability in their $AgGaS_2$ OPO that seems very similar to that described in this work [21].

We thank J.-J. Zondy for communicating Ref. [21] prior to publication. We are most grateful to C. Fabre and A. Maître for stimulating discussions and very helpful advice. They introduced one of us (P.S.) to the experimental aspects of OPOs during a two-month stay at the Laboratoire Kastler-Brossel (Ecole Normale Supérieure and Université de Paris VI). This work was funded for the most part by the Centre d'Études et de Recherches Lasers et Applications. The Laboratoire de Physique des Lasers, Atomes et Molécules is Unité Mixte de Recherche du CNRS. The Centre d'Études et de Recherches Lasers et Applications is supported by the Ministère chargé de la Recherche, the Région Nord–Pas de Çalais, and the Fonds Européen de Développement Économique des Régions.

[1] P. H. S. Ribeiro, C. Schwob, A. Matre, and C. Fabre, Opt. Lett. **22**, 1893 (1997), and references therein.
[2] D. Lee and N. C. Wong, Opt. Lett. **17**, 13 (1992).
[3] D. F. Walls and G. J. Milburn, *Quantum Optics* (Springer, Berlin, 1994).
[4] L. Lugiato *et al.*, Nuovo Cimento D **10**, 959 (1988).
[5] G. L. Oppo, M. Brambilla, and L. A. Lugiato, Phys. Rev. A **49**, 2028 (1994).
[6] K. Staliunas and V. J. Sanchez-Morcillo, Phys. Rev. A **57**, 1454 (1998).
[7] A. Gatti *et al.*, Phys. Rev. A **56**, 877 (1997).
[8] C. Richy, K. I. Petsas, E. Giacobino, and C. Fabre, J. Opt. Soc. Am. B **12**, 456 (1995).
[9] K. J. McNeil, P. D. Drummond, and D. F. Walls, Opt. Commun. **27**, 292 (1978).
[10] P. L. Hansen and P. Buchhave, Opt. Lett. **22**, 1074 (1997).
[11] F. Jermann and J. Otten, J. Opt. Soc. Am. B **10**, 2085 (1993).
[12] A. H. Nayfey and D. T. Mook, *Nonlinear Oscillations* (Wiley, New York, 1995).
[13] A. H. Nayfey, *Perturbation Methods* (Wiley, New York, 1973).
[14] A. Douillet and J.-J. Zondy, Opt. Lett. **23**, 1259 (1998).
[15] T. Debuisschert, A. Sizmann, E. Giacobino, and C. Fabre, J. Opt. Soc. Am. B **10**, 1668 (1993).
[16] We take this form for simplicity. More generally, if the derivatives of the refraction indexes of pump and signal with respect to temperature are different, $\sigma_p=\Delta_p-2\eta\theta/\gamma$ with $\eta\neq 1$.
[17] S. L. McCall, Appl. Phys. Lett. **32**, 284 (1978).
[18] A. Lambrecht, E. Giacobino, and J.-M. Courty, Opt. Commun. **115**, 199 (1995).
[19] R. Herrero *et al.*, Opt. Commun. **113**, 324 (1994).
[20] J. I. Rosell *et al.*, Physica D **85**, 509 (1995).
[21] A. Douillet *et al.*, J. Opt. Soc. Am. B **16**, 1481 (1999).

Appendice G
Articles de vulgarisation scientifique

“Radiographie du Chaos”

Marc Lefranc

in Alain Renk, « Construire la Ville Complexe? » (Jean-Michel Place, Paris, 2002)

Les mots sont souvent trompeurs. Entre les bouches des uns et les oreilles des autres s'opèrent parfois de surprenantes transpositions. Elles sont parfois éclairantes, mais peuvent aussi se révéler traîtresses. Dans un article paru il y a presque trente ans, deux mathématiciens américains, T.-Y. Li et J. A. Yorke, forgèrent le terme de « chaos » et l'utilisèrent pour qualifier la structure de l'ensemble des solutions du modèle mathématique qu'ils étudiaient. Avouaient-il ainsi que ce système était à ce point désordonné qu'il échappât à tout entendement? Qu'il se situait de l'autre côté d'une barrière infranchissable au-delà de laquelle tout pouvait arriver?

Non, bien au contraire, puisque leur article se concluait par un théorème. Qui montrait que dans certaines conditions, des systèmes dynamiques (c'est-à-dire qui évoluent dans le temps en suivant des équations bien déterminées) très simples peuvent avoir une infinité d'histoires différentes. Lorsqu'un système se comporte de manière stationnaire ou répète le même motif de manière périodique, nous le décrivons volontiers comme organisé. Un régime « chaotique » au sens du théorème a ceci de particulier qu'il est composé d'une infinité de régimes périodiques entrelacés : on pourrait dire qu'il est infiniment organisé. Aucun de ces cycles ne pouvant attirer le système de manière stable, ils sont parcourus tour à tour, donnant ainsi une impression d'irrégularité alors même que leur organisation obéit à des règles tout à fait rigoureuses. Dans ce type de régime, dont la fumée de cigarette tourbillonnante ou un tube au néon erratique fournissent d'assez bons exemples, « ordre » et « désordre » sont intimement liés.

Cette observation n'était pas neuve - on la doit au mathématicien français Henri Poincaré, il y a plus d'un siècle - mais le terme si suggestif de « chaos », ou plutôt « chaos déterministe » si l'on veut être précis, allait rester pour toujours dans le jargon de ce domaine, jusqu'à donner son nom à une rubrique des journaux de physique. Il allait même déborder largement ce cadre, pour devenir dans le grand public le nom d'une discipline qui, dans l'esprit de beaucoup, se propose de déterminer si un papillon new-yorkais peut provoquer une tempête en mer de Chine.

A chaque fois que je me suis retrouvé à expliquer en quoi consistait mon travail, j'ai ainsi souvent eu à dissiper des malentendus. Pour la plupart, ils prenaient racine dans les images engendrées par ce mot provocateur : « chaos ». Non, il ne s'agit pas d'états parfaitement désordonnés, mais au contraire de régimes dynamiques à l'organisation extrêmement complexe, mais tout à fait analysable si l'on sait choisir ses outils. Oui, ils sont imprédictibles à long terme, mais par contre parfaitement déterministes aux échelles de temps courtes. La nature aime à être simple, mais être simpliste empêche de la comprendre.

Plus rarement, j'ai la troublante sensation de recevoir un écho immédiat de mes explications. Comme si dans des domaines a priori étrangers à la physique, d'autres avaient déjà intériorisé ce mélange surprenant de complexité et de simplicité dont font preuve les régimes chaotiques auxquels je m'intéresse, ainsi que tout ce que l'on peut extraire de leurs propriétés paradoxales. C'est en particulier ce dont j'ai pris l'habitude dans mes conversations avec mon ami Alain Renk. Je ne sais s'il s'agit du phénomène de transposition que j'évoquais en introduction, mais autant j'ai à chaque fois l'impression de stimuler son imagination par mes descriptions, autant ce qu'il m'expose de ses projets architecturaux évoque invariablement en moi des images qui naquirent d'abord au contact du chaos.

Comme par exemple lorsqu'il exige « de travailler les territoires comme des processus en cours ». Bien sûr, puisqu'il les reconnaît comme des écosystèmes, une des sources les plus fécondes de modèles dynamiques. Ou lorsqu'il évoque « la matière fluide des réservoirs

d'incertitude des territoires ». Car un système chaotique est en principe déterministe : si sa position de départ pouvait être déterminée de façon absolue, c'est toute son histoire future qui serait tracée. Mais il est sensible à la moindre perturbation extérieure et la déviation introduite par cette dernière croît exponentiellement avec le temps : s'il faut un certain intervalle de temps pour qu'elle soit multipliée par deux, elle aura à nouveau doublé au bout du même intervalle de temps. C'est le « réservoir d'incertitude » constitué par ces perturbations, amplifiées inexorablement par la dynamique chaotique, qui aiguille le système chaotique sur telle ou telle de ses histoire possibles, passant de l'une à l'autre au gré des fluctuations. La complexité apparente des chemins empruntés n'étant que la conséquence de leur nombre infini.

Les physiciens ont la manie de vouloir tirer parti d'un phénomène dès qu'ils l'ont appréhendé. Ainsi, certains ont montré comment faire suivre à un système chaotique une trajectoire arbitraire en lui appliquant d'infimes perturbations non plus aléatoires mais judicieusement choisies, un peu à la manière d'un jongleur qui tient une perche en équilibre sur son front. Ces signaux de correction sont recalculés à chaque instant en fonction de l'itinéraire effectivement suivi et des consignes en vigueur. Même pour un système de taille imposante, ces perturbations peuvent être si petites que l'on songe naturellement au fameux levier qui permettrait de soulever le monde : c'est en fait la fameuse « sensibilité aux conditions initiales » qui est domestiquée. Cette méthode ne fait-elle qu'imiter la nature ? Certains ont par exemple avancé l'idée que c'est une dynamique légèrement chaotique qui permet aux battements cardiaques de s'adapter facilement à des conditions très variées et de passer rapidement du repos à l'effort.

Aussi, lorsque je lis que la démarche consiste à « se glisser par effraction dans la machine aléatoire pour en orienter certains aspects et rester attentif », je ne peux m'empêcher d'y voir un écho de la technique évoquée plus haut et que les physiciens appellent le « contrôle du chaos ». Les phrases suivantes pourraient elles aussi passer d'un domaine à l'autre presque sans changement : « Le territoire ne plie pas, il accepte de modifier son évolution en consommant les amorces disposées par les hommes à l'écoute. Ces modifications sont difficiles à contrôler mais il est possible à tout moment d'influer sur les évolutions en cours en déplaçant les amorces ou en réglant leur force d'attraction ».

Bien sûr, il faut se garder de prendre les mots...à la lettre. Il n'en reste pas moins qu'il m'est difficile de croire que cette conjonction des discours soit vide de sens. Il y a un avantage certain à piloter un système chaotique plutôt qu'un dispositif optimisé pour un contexte unique. Ce dernier est difficilement adaptable : lorsqu'on le perturbe, il tend à revenir à son régime de référence, le seul qui soit stable. Au contraire, le système chaotique peut passer sans effort d'un comportement à un autre puisqu'en l'absence du signal de contrôle, chaque régime pris individuellement est instable. Commuter et prendre un autre cap n'exige donc pas de forcer le système : c'est sa dynamique naturelle qui l'amène dans le nouvel état, abstraction faite des corrections infinitésimales. Cela me semble très proche de l'idée d'Alain Renk : laisser au territoire la possibilité d'évoluer - d'être un système dynamique - et tirer parti de cette évolution, de cette capacité au changement, pour influer sur lui et guider son histoire, en lui laissant accomplir l'essentiel du travail. Procéder ainsi peut certes se révéler plus long qu'une démarche plus autoritaire, mais permet de faire beaucoup avec très peu et, surtout, exclut naturellement les fonctionnements incompatibles avec les règles qui gouvernent la dynamique interne du système.

Encouragé par l'exhortation à « procéder à des aller-et-retours permanents entre analyse du réel, extrapolation en un modèle théorique et création d'un nouveau réel », je me surprends à rêver et à tenter de filer la métaphore. Une des propriétés fascinantes d'un attracteur chaotique (c'est-à-dire la représentation géométrique de l'histoire d'un système chaotique) est d'être fractal : en examinant une de ses parties, on peut retrouver son organisation globale. On comprendra donc que je sois troublé lorsque j'entends Alain parler de ville fractale. Je crois comprendre qu'il s'agit de pouvoir adapter cette dernière à des communautés de tailles très variables, mais le physicien que je suis ne peut s'empêcher de se demander quel pourrait être le mécanisme qui produirait naturellement cette structure fractale. Un arbre ou des poumons sont (approximativement) fractals car cela leur permet d'optimiser leurs échanges avec le monde extérieur (lumière, air). Un attracteur chaotique l'est car les processus géométriques qui le façonnent s'apparentent à la recette de la pâte feuilletée. A chaque cycle, l'attracteur est étiré, puis replié sur lui-même, comme un rectangle serait transformé en fer à cheval. De même qu'une noisette de beurre déposée sur la pâte finit par se répartir dans toute sa masse, il n'est pas possible de prévoir trop longtemps à l'avance où exactement à l'intérieur de son attracteur se trouvera un système chaotique. Ce mécanisme d'étirement et de repliement donne à l'attracteur chaotique une structure infiniment feuilletée caractéristique. Un peu comme si on pétrissait le plan d'une ville de manière à ce que chaque partie se retrouve en interaction avec tout l'espace, une configuration invariante (c'est-à-dire se reproduisant d'une itération sur l'autre) étant finalement obtenue lorsque dans chaque voisinage se retrouve un germe de la cité tout entière.

Je ne sais à quel point il faut prendre cela au sérieux, mais il est en tout cas amusant de noter que l'on semble retrouver cette notion de processus itératifs connectant un niveau hiérarchique à ceux immédiatement supérieur et inférieur - qui rendent l'attracteur chaotique fractal - dans l'idée « d'univers génératifs », de « matrices théoriques », qui engendrent des mondes plus détaillés sous l'action de transformations, mais sont elle-mêmes modifiées par leurs produits dans une une boucle de rétro-action. L'architecte devient alors lui-même partie d'un réseau de régulation.

En y réfléchissant un peu plus longuement, je me demande si je ne devine pas une explication aux résonances entre la géométrie du chaos et les propositions d'Alain Renk. Elles trouvent peut-être leur source dans la nature, dans le fonctionnement du vivant. Devant s'adapter à moindre coût à des environnements variés, celui-ci fait abondamment usage de systèmes en interaction mutuelle composant des réseaux de régulation complexes, capables de réagir à des variations infimes de leur environnement mais devant également pouvoir amortir tout changement brutal. Par exemple, on se rend progressivement que pour comprendre les processus génétiques, il faut non seulement étudier la structure du génome, mais également le réseau complexe d'interactions et de régulations que tissent les gènes et les protéines.

Être agile tout en étant robuste, cela n'est pas un mince défi. De même, un comportement chaotique trouve fréquemment son origine dans l'existence de boucles de rétroaction entre les différentes variables caractérisant l'état d'un système. Une fois en action, un système chaotique reste de manière stable sur son attracteur tout en amplifiant les perturbations à l'intérieur de celui-ci. En permettant de conjuguer la stabilité nécessaire à la survie et l'instabilité exigée par l'adaptabilité, les comportements chaotiques, ou tout au moins non linéaires, pourraient bien être des ingrédients essentiels de la vie.

Est-il permis d'étendre cette métaphore à l'architecture et à la ville ? De croire que les mots ne sont pas tout à fait trompeurs ? D'espérer que certaines des recettes puisées dans la nature puissent être une source d'inspiration ? Il est difficile de le dire aujourd'hui, mais pourquoi pas ? A condition probablement de ne pas se figer, et de faire rentrer les images et les concepts eux-mêmes dans un processus d'interaction, dans une...boucle de régulation.

Comme le montre l'exemple du génome, un des grands enjeux actuels est de comprendre la complexité sans la mutiler. Le vingt-et-unième siècle sera-t-il celui de d'ingénierie de la complexité ? Dans les sciences, mais peut-être aussi en architecture ?

“Caractérisation Topologique et Contrôle du Chaos”

Marc Lefranc, Serge Bielawski, Dominique Derozier, and Pierre Glorieux

Images de la Physique 1997, 53–60 (C.N.R.S./S.P.M.,)

Chaos

Caractérisation topologique et contrôle du chaos

Après une phase d'excitation où les scientifiques cherchaient et trouvaient du chaos (presque) partout, dans les réactions chimiques, en hydrodynamique, dans les systèmes optiques ou biologiques, on a cru que leur engouement allait retomber. En fait, c'est un champ nouveau d'investigation qui s'ouvrait en même temps qu'une nouvelle manière d'appréhender des effets parfois (mé)connus depuis longtemps.

Outre l'éclairage nouveau qu'elle apporte sur ces phénomènes, la dynamique non linéaire possède sa problématique propre ; la caractérisation topologique du chaos et les techniques qui permettent de le contrôler illustrent bien l'ouverture de ce nouveau champ thématique.

Le terme de « chaos » est associé dans la plupart des esprits à une situation erratique, dont la complexité dépasse l'entendement. A ce sens commun, il est maintenant devenu classique d'opposer, au moins dans les milieux scientifiques, le « chaos déterministe », évolution irrégulière d'un système simple régi par quelques équations bien établies.

La « sensibilité aux conditions initiales » constitue sans aucun doute la caractéristique essentielle de ce type de comportement dynamique : deux systèmes chaotiques identiques, partant de conditions initiales différentes, si proches soient-elles, voient leurs trajectoires respectives se séparer de manière exponentielle. L'évolution est par conséquent imprédictible à long terme : plutôt que de vouloir suivre une trajectoire individuelle, c'est à la dynamique globale du système qu'il faut s'intéresser.

Dans un système dissipatif, on observe que les trajectoires dans l'espace des phases, après un transitoire plus ou moins long, restent confinées dans une région bien définie : l'« attracteur » (voir encadré 1). Dans le cas simple d'un régime stationnaire ou périodique, celui-ci consiste en un point ou une courbe fermée. Lorsque le régime est chaotique, c'est un objet géométrique complexe qui est observé, un attracteur « étrange », tel celui représenté à la figure 1.

Si les divers scénarios de transition vers le chaos présentent souvent une régularité exemplaire, à l'instar de la célèbre cascade de doublements de période, les attracteurs chaotiques paraissent au premier abord extraordinairement intriqués, ne serait-ce que du fait de leur nature fractale.

En conséquence, les méthodes de caractérisation du chaos ont tout d'abord été basées sur la mesure de propriétés globales de l'attracteur, comme sa dimension fractale ou encore les exposants de Lyapunov, qui mesurent les taux de divergence des trajectoires.

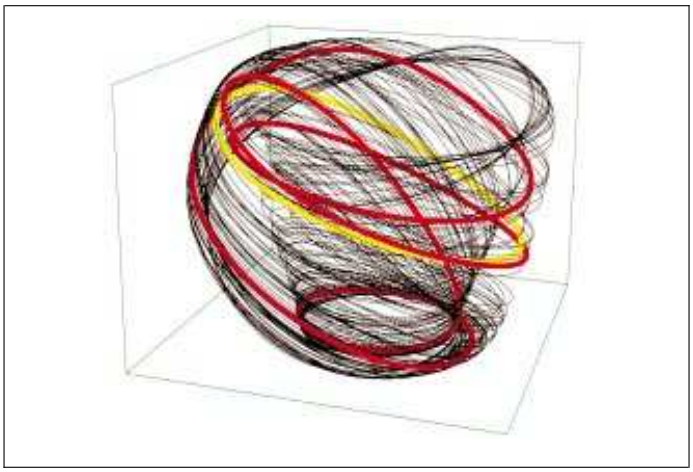

Figure 1 - *Superposition de la reconstruction d'un attracteur chaotique dans un espace des phases à trois dimensions et de deux orbites périodiques instables de périodes T (en jaune) et 4 T (en rouge).*

— Laboratoire de spectroscopie hertzienne, URA CNRS 249, Université Lille 1, 59655 Villeneuve d'Ascq Cedex.

Encadré 1

ESPACE DES PHASES ET SECTION DE POINCARÉ

L'espace des phases est un espace fictif permettant de représenter l'état dynamique d'un système. Il est rapporté à des axes qui correspondent aux différentes grandeurs physiques caractérisant l'état du système. Les différents régimes dynamiques y sont représentés par une courbe, l'« attracteur », qui peut être un point en cas de fonctionnement continu ou un cycle fermé en régime périodique, et devient un attracteur étrange dans le cas d'un comportement chaotique.

La reconstruction d'un attracteur dans l'espace des phases s'avère généralement difficile car certaines variables, comme l'inversion de population pour les lasers, ne sont pas aisément accessibles expérimentalement. Cependant, il est possible de reconstituer la topologie de l'attracteur en prenant comme espace de représentation $X(t)$, $X(t+\tau)$, $X(t+2\tau)$, ... *ou* X, $\dot{X}$, $\ddot{X}$, ... *X étant l'une des variables dynamiques du système et* τ *un délai arbitrairement choisi (voir artible de M. Dubois, Images de la physique, p. 97, 1984). Pratiquement, on choisit pour X la variable la plus facile à mesurer expérimentalement, telle l'intensité émise par le laser.*

Dans le cas des systèmes modulés, la phase $\phi(t)$ *de la modulation est une variable dynamique généralement intéressante à substituer à l'une des variables précédemment considérées. En ce qui concerne le laser* CO_2 *et le laser à fibre, l'attracteur chaotique de dimension inférieure à 3 peut aisément être représenté dans l'espace* $I(t)$, $I(t+\tau)$ *et* $\phi(t)$. *L'espace des phases est topologiquement équivalent à un tore solide construit en combinant le disque et le cercle unités.*

Cette géométrie, naturelle pour les systèmes modulés, permet de réaliser très facilement une section de Poincaré. Celle-ci est constituée des intersections s'effectuant avec un sens prédéfini entre la trajectoire et une hypersurface de l'espace des phases, par exemple un plan si celui-ci est tridimensionnel. Des trajectoires évoluant sur l'attracteur, on ne considère que les intersections s'effectuant dans un sens prédéfini. En réduisant ainsi le nombre de dimensions, on simplifie l'étude de la dynamique, tout en en préservant les propriétés essentielles. Dans le cas des systèmes modulés, une section de Poincaré peut être obtenue expérimentalement au moyen d'un échantillonnage stroboscopique (ϕ = *constante*) *de I et de sa dérivée.*

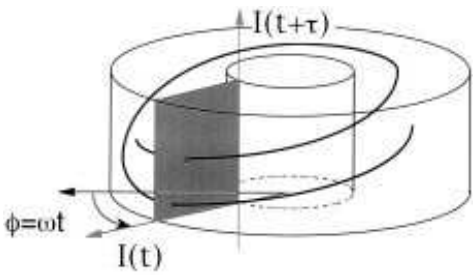

C'est évidemment parce que l'attracteur est laissé invariant par la dynamique chaotique que ces méthodes de caractérisation occupent une place centrale dans l'analyse du chaos. Or, il se trouve que d'autres ensembles de l'espace des phases possèdent également cette propriété d'invariance. Dans un attracteur chaotique sont en effet imbriquées une infinité de solutions périodiques des équations d'évolution : les orbites périodiques instables (OPI).

L'existence de ces orbites est liée à l'ergodicité de la dynamique sur l'attracteur, c'est-à-dire au fait qu'une trajectoire issue d'un point typique de l'attracteur passe, si l'on attend suffisamment longtemps, arbitrairement près de tout point de l'attracteur, y compris du point de départ. Les équations d'évolution étant continues, on peut en général, dans le voisinage d'une trajectoire revenant très près de sa condition initiale, en trouver une autre qui se referme exactement et qui corresponde par conséquent à une orbite périodique.

De même, les orbites périodiques sont denses dans l'attracteur : tout morceau de trajectoire chaotique peut être approché avec une précision arbitraire par un fragment d'orbite périodique, de la même manière que tout nombre réel est la limite d'une suite de nombres rationnels. Les orbites périodiques incluses dans l'attracteur étant instables, une trajectoire passant dans le voisinage de l'une d'entre elles y séjournera un court instant avant de s'en éloigner pour visiter d'autres régions de l'attracteur. La figure 1 montre deux exemples d'orbites périodiques plongées dans un attracteur chaotique.

Les orbites périodiques ne sont toutefois pas qu'un concept abstrait. On sait qu'elles jouent un rôle important dans de nombreux scénarios de transition vers le chaos. Ainsi, dans le cas de la cascade de doublements de période, la variation d'un

paramètre de contrôle fait passer le système par une suite de « bifurcations », chacune correspondant à l'apparition d'une orbite de période double de la précédente, qui devient alors instable. La suite infinie des valeurs du paramètre de contrôle correspondant à ces bifurcations converge de manière géométrique vers une valeur critique au-delà de laquelle peuvent être observés des régimes chaotiques, qui n'apparaissent donc que lorsque un nombre infini d'orbites périodiques ont été créées. De plus, en explorant les zones de paramètres au-delà de la transition, on observe en général une alternance de zones chaotiques et de « fenêtres périodiques » où le système suit un comportement régulier. Ces différentes solutions périodiques ne disparaissent pas lorsque l'on revient à un comportement chaotique : devenues instables, ces orbites restent présentes dans l'attracteur ou dans son voisinage.

Mais surtout, les orbites périodiques instables sont directement accessibles à l'expérience. Dans le cas d'un système à petit nombre de degrés de liberté, l'examen des signaux chaotiques qu'il délivre révèle facilement l'existence de récurrences : au milieu d'une évolution apparemment irrégulière, des bouffées de comportement quasiment périodique apparaissent par intervalles.

La figure 2 présente deux séquences de ce type observées dans le régime chaotique d'un laser CO_2 à pertes modulées (cf. *Images de la physique* 1988). Entre 40 et 70 μs, le système reproduit quasiment à l'identique un comportement 4 T-périodique (T étant la période de modulation, voisine ici de 3 μs), qu'il quitte ensuite pour retrouver une évolution approximativement T-périodique entre 100 et 120 μs. Chacune de ces séquences signale le passage du système au voisinage d'une orbite périodique instable contenue dans l'attracteur. En recherchant de manière systématique ces événements dans les signaux

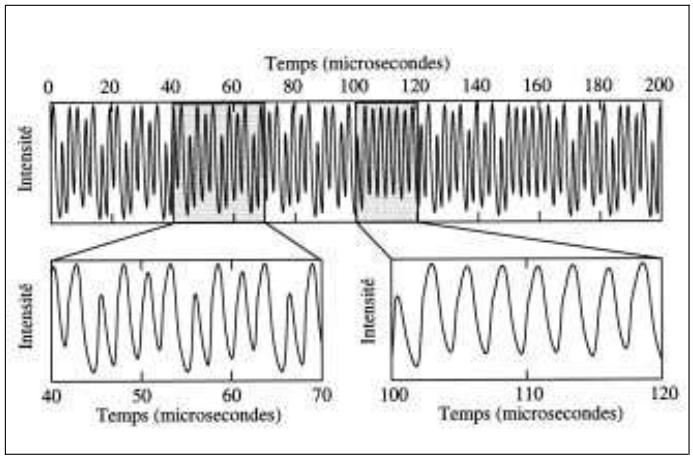

Figure 2 - *Exemples de bouffées de comportement périodique incluses dans un signal chaotique. Ici, un laser CO_2 dont les pertes sont modulées à la période $T \approx 3\,\mu s$ explore entre 40 et 70 μs le voisinage d'une orbite instable de période 4T, et celui de l'orbite périodique de période T entre 100 et 120 μs.*

chaotiques, on a pu repérer dans le laser CO_2 jusqu'à quelques dizaines de comportements périodiques différents, correspondant aux OPI de plus petites périodes.

On notera cependant que le temps nécessaire pour revenir dans le voisinage d'une orbite périodique donnée dépend de manière exponentielle du nombre de degrés de liberté du système. Si un dispositif simple comme le laser CO_2 monomode révèle de nombreuses orbites périodiques instables, il est par contre illusoire de vouloir en repérer dans un système où le nombre de degrés de liberté approche le nombre d'Avogadro !

LES OPI RÉVÉLATRICES DE L'ORGANISATION DU CHAOS

Les orbites périodiques sont déterminées par les mêmes équations d'évolution que l'attracteur. Plutôt que d'aborder de front la complexité de ce dernier, il peut être donc judicieux de s'intéresser aux objets géométriques beaucoup plus simples que sont les OPI. Dans l'espace des phases, ces dernières sont en effet représentées par de simples courbes fermées. Certes, la complexité de leur enchevêtrement est à la mesure de celle de l'attracteur chaotique, mais nous allons voir que leur organisation suit des règles extrêmement rigoureuses.

La théorie des nœuds fournit, sous la forme d'invariants topologiques, des outils permettant d'analyser la manière dont les différentes orbites sont nouées et entrelacées dans l'espace des phases. Par exemple, l'invariant topologique le plus simple est le nombre d'entrelacements d'un couple d'orbites périodiques, qui mesure le nombre de révolutions qu'une orbite effectue autour de l'autre. Ces grandeurs sont invariantes vis-à-vis des déformations continues dans l'espace et constituent en fait une véritable signature de chaque trajectoire.

Ce sont des surfaces à plusieurs branches, appelées gabarits, qui permettent de démêler l'écheveau formé par les OPI. Ces surfaces, dont la figure 3 fournit un exemple, présentent en effet une propriété remarquable : il est possible par des déformations continues d'y amener l'ensemble de toutes les orbites pé-

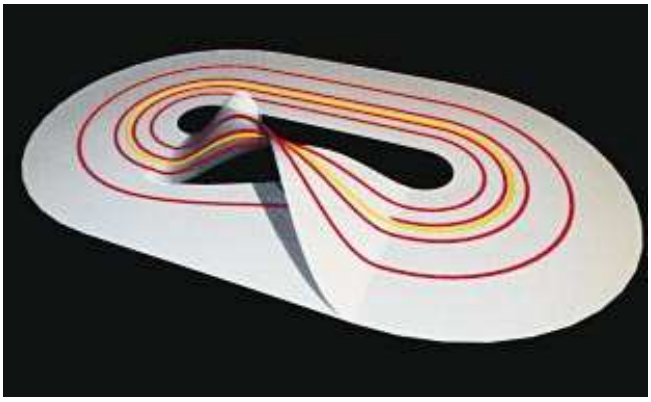

Figure 3 - *Un gabarit est une surface constituée d'un ruban en forme de stade se divisant à un certain endroit en plusieurs branches. Ces dernières se recollent plus loin sur toute la largeur du ruban principal tout en se superposant les unes aux autres. La structure du gabarit (nombre de branches, nombre de torsades de celles-ci, nombre de tours qu'une branche effectue autour d'une autre, ordre dans lequel elles se superposent) détermine les invariants topologiques des courbes fermées qui peuvent être inscrites sur le gabarit, et que l'analyse topologique cherche à mettre en correspondance avec les orbites périodiques détectées expérimentalement.*
Le gabarit représenté ici décrit l'organisation topologique globale des régimes chaotiques observés dans un laser CO_2. Les deux orbites de période T (en jaune) et 4T (en rouge) ont dans cette disposition exactement les mêmes invariants topologiques que dans l'attracteur de la figure 1.

riodiques incluses dans l'attracteur, sans modifier aucun de leurs invariants. La structure topologique du gabarit décrit donc de manière concise l'organisation topologique *globale* de l'attracteur.

La structure du gabarit permet de calculer les invariants topologiques de toutes les orbites qui y sont inscrites. Inversement – et c'est ainsi que l'on procède expérimentalement – il se trouve que les invariants de seules quelques orbites, trois dans les cas les plus simples, suffisent à déterminer sans ambiguïté l'unique gabarit pouvant les porter. Grâce à cette méthode, plusieurs équipes ont pu déterminer l'organisation topologique de divers dispositifs expérimentaux chaotiques. On compte parmi ceux-ci aussi bien des réactions chimiques, comme celle de Belousov-Zhabotinskii ou l'électrodissolution du cuivre, qu'un oscillateur à résonance magnétique nucléaire, ou encore des systèmes optiques comme le laser CO_2 à absorbant saturable ou à modulation de pertes. De manière remarquable, quasiment tous ces systèmes ont révélé le même schéma d'organisation topologique, celui décrit par le gabarit présenté à la figure 3, à l'exception de régimes plus complexes observés dans un laser à fibre ou une réaction catalytique.

On notera enfin qu'outre une caractérisation globale de l'attracteur l'analyse topologique permet une étude détaillée de sa structure fine. En déterminant à chaque période de modulation laquelle des deux branches est visitée par la projection d'une trajectoire chaotique donnée, celle-ci peut être représentée par une suite de 0 et de 1. L'analyse statistique des sous-chaînes extraites de cette séquence donne alors accès à toute une hiérarchie de grandeurs, comme le plus grand exposant de Lyapunov.

CONTRÔLER LE CHAOS GRÂCE AUX ORBITES PÉRIODIQUES INSTABLES

L'existence des OPI peut par ailleurs être mise à profit pour « contrôler » le chaos. La méthode originale a été proposée par Ott, Grebogi et Yorke (OGY), de l'Université du Maryland. Elle a connu un succès immédiat et différentes variantes ont été élaborées grâce auxquelles l'information requise est basée sur des données expérimentales et ne dépend pas d'une modélisation mathématique du système étudié.

Le principe du contrôle du chaos est relativement simple : il suffit d'abord d'attendre que la trajectoire passe au voisinage de l'OPI visée. A ce moment, de très faibles corrections, infinitésimales à la limite, permettent de maintenir le système quasiment sur cette orbite périodique, en tirant avantage autant que possible de la dynamique intrinsèque du système.

Pour comprendre plus précisément comment ces corrections sont appliquées, il est utile de travailler dans une section de Poincaré (voir encadré 1). Chaque trajectoire est alors uniquement représentée par ses intersections avec la section de Poincaré. Une orbite périodique est évidemment constituée d'un nombre fini de points visités de manière cyclique. Quel que soit $\mathbf{X}_F$ l'un de ces points, l'écart d'une trajectoire quelconque à l'orbite périodique visée peut être mesuré par la distance $\xi_k = \mathbf{X}_k - \mathbf{X}_F$ entre le point fixe $\mathbf{X}_F$ et le point d'intersection $\mathbf{X}_k$ de la trajectoire après k périodes de l'orbite.

On notera, et cela aura une importance cruciale dans la suite, qu'une petite variation $\delta\mu$ d'un paramètre de contrôle μ entraîne en général un petit déplacement

$\delta \mathbf{X}_F$ du point fixe dans le plan de section :
$\mathbf{X}_F(\mu + \delta\mu) = \mathbf{X}_F(\mu) + \delta \mathbf{X}_F$.

Pour stabiliser l'OPI, seule importe la dynamique dans un petit voisinage de l'orbite périodique. Dans celui-ci, l'évolution des écarts ξ_k peut être décrite de manière linéaire par $\xi_{k+1} = \Lambda_F \xi_k$, la matrice Λ_F et ses valeurs propres portant le nom de matrice et multiplicateurs de Floquet. Si l'espace des phases est de dimension trois et l'OPI incluse dans l'attracteur, les deux multiplicateurs sont réels. Le module supérieur à 1 de l'un d'entre eux (λ_u) reflète l'instabilité de l'orbite, tandis que la dissipation entraîne que celui du deuxième (λ_s) soit plus petit que 1.

Les directions propres associées à λ_s et λ_u, que nous noterons s et u, sont dénommées respectivement directions stable et instable. Une trajectoire typique explorant le voisinage de l'orbite périodique s'approche de $\mathbf{X}_F$ selon la direction stable tout en s'en éloignant le long de la direction instable (fig. 4a), car les composantes de ξ_k selon les deux directions vérifient : $\xi^u_{k+1} = \lambda_u \xi^u_k$ et $\xi^s_{k+1} = \lambda_s \xi^s_k$.

Manifestement, c'est la dynamique selon u qui fait obstacle à la stabilité recherchée et il faudrait pouvoir contraindre ξ^u à tendre vers zéro, tandis que c'est le sort naturel de ξ^s. Cependant, dans bon nombre de systèmes, comme les lasers, il est délicat, voire impossible, de modifier directement certaines variables dynamiques telles l'intensité du rayonnement ou l'inversion de population. Il faut alors, en tirant profit de la dynamique intrinsèque du système, agir indirectement sur ce dernier par le biais d'une variation judicieuse d'un paramètre de contrôle, par exemple la puissance de pompe ou la longueur de la cavité laser.

L'art du jongleur qui maintient une perche en équilibre sur son front fournit la solution de ce problème : c'est en déplaçant la base de la perche, c'est-à-dire la position du point d'équilibre qu'il arrive à la ramener en position verticale. De même, en déplaçant judicieusement à chaque période le point fixe $\mathbf{X}_F$ en un nouveau point $\mathbf{X}'_F$, on peut s'arranger pour que les points d'intersection suivants convergent de façon exponentielle vers le point fixe $\mathbf{X}_F$.

La méthode de contrôle proposée par Ott, Grebogi et Yorke bénéficie d'une interprétation géométrique aisée. Lorsque la trajectoire passe dans le voisinage du point fixe $\mathbf{X}_F(\mu)$, le paramètre de contrôle μ est modifié de manière à ce que la dynamique par rapport au nouveau point fixe $\mathbf{X}_F(\mu + \delta\mu)$ conduise l'intersection suivante sur la direction stable de $\mathbf{X}_F(\mu)$ (figure 4). Tout écart selon la direction instable est donc rapidement réduit, tandis que celui selon la direction stable tend naturellement vers zéro : on a repoussé la trajectoire vers l'orbite périodique.

Cette stratégie est réalisée en appliquant à un paramètre de contrôle, pendant le temps de vol entre deux intersections, une correction proportionnelle à l'écart selon la direction instable : $\delta\mu_k = \alpha \xi^u_k$. La valeur adéquate du coefficient α dépend de la matrice de Floquet Λ_F et de $\mathrm{d}\mathbf{X}_F/\mathrm{d}\mu$ qui caractérise l'influence du paramètre de contrôle sur la position du point fixe.

Une telle forme de correction présente un double intérêt. D'une part, l'orbite stabilisée coïncide avec celle du système non perturbé : la correction tend en effet vers zéro en même temps que l'écart à l'orbite visée. D'autre part, il n'est pas nécessaire de connaître *a priori* les équations du système, car les caractéristiques de l'OPI (position, direction instable et multiplicateurs de Floquet) intervenant dans la correction peuvent être déterminées entièrement expérimentalement, en analysant l'évolution d'une variable quelconque.

Bien que la méthode OGY soit très générale, d'autres méthodes de contrôle basées sur les mêmes idées sont parfois préférées. On s'est tout d'abord aperçu que l'on pouvait, dans certains cas, se contenter de mesurer l'écart à l'orbite périodique ξ_k d'une variable dynamique quelconque sans avoir à déterminer exactement sa composante selon la direction instable. La perturbation parasite alors introduite selon la direction stable ne compromet pas la stabilisation, à condition que les multiplicateurs de Floquet associés aux directions stables soient suffisamment petits et/ou que la perturbation déplace le point fixe $\mathbf{X}_F$ essentiellement selon la direction instable.

De nombreuses expériences ont également utilisé des méthodes qui,

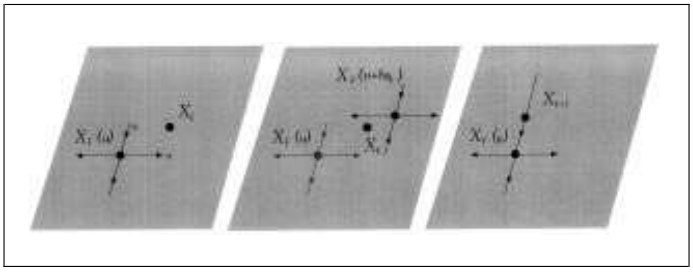

Figure 4 - *Principe de la méthode OGY : à un certain instant, la trajectoire traverse le plan de section en $\mathbf{X}_k$, au voisinage de l'orbite périodique non perturbée $\mathbf{X}_F(\mu)$, dont les directions stable et instable sont repérées par des flèches convergeant vers ou divergeant de l'orbite. On applique alors à un paramètre de contrôle une correction $\delta\mu_k$, qui déplace l'orbite en un point $\mathbf{X}_F(\mu + \delta\mu_k)$. Celui-ci est choisi de manière à ce que la prochaine intersection de la trajectoire se produise en un point $\mathbf{X}_{k+1}$, situé le long de la direction stable de $\mathbf{X}_F(\mu)$.*

tout en satisfaisant aux deux critères mentionnés plus haut (la correction tend vers zéro et il est inutile de connaître les équations du système), ne font pas intervenir explicitement l'écart à l'orbite périodique visée. Un exemple particulièrement intéressant est celui qui consiste à appliquer une correction du type $\delta\mu_k = \alpha(\mathbf{X}_k - \mathbf{X}_{k-1})$, qui, comme dans les autres exemples, tend vers zéro lorsque l'on s'approche de l'orbite périodique. Il faut en général prendre la précaution de n'appliquer la correction qu'une période sur deux, de manière à ne baser son calcul que sur l'évolution du système libre. Cette méthode ne dépend pas de la position de l'orbite et présente l'immense avantage de pouvoir stabiliser une OPI sans avoir à la localiser préalablement.

Elle offre par conséquent la possibilité de « suivre à la trace » une OPI quand on fait varier continûment l'un ou l'autre des paramètres de contrôle du système. On peut ainsi déterminer son domaine d'existence et en particulier l'endroit où elle prend naissance. C'est ce qui est illustré à la figure 5, où après avoir stabilisé un laser chaotique sur son OPI 2 T, un paramètre de contrôle du laser (ici la puissance de pompe) a été progressivement modifié (voir encadré 2). L'OPI reste stabilisée sur tout son domaine d'existence et ce, même en dehors de la zone de comportement chaotique, jusqu'à la bifurcation 2T-4T (doublement de période) où l'orbite devient stable.

Les OPI ne sont pas les seuls états instables d'un système chaotique. Bien souvent, les régimes périodiques ou chaotiques apparaissent après déstabilisation d'un état stationnaire. En utilisant des méthodes semblables à celles évoquées dans le cas des OPI, le système étudié peut être stabilisé sur cet état stationnaire instable (ESI). Outre l'intérêt fondamental, l'impact pratique est considérable. Si, jusqu'ici, les concepteurs de systèmes évitaient soigneusement les zones de paramètres menant à un comportement oscillant ou chaotique, ils peuvent désormais, grâce aux techniques de contrôle, élargir les domaines d'applications à des zones bien souvent plus intéressantes. Ainsi, certains lasers qui fonctionnent de manière continue au voisinage du seuil deviennent chaotiques lorsqu'ils sont fortement excités, c'est-à-dire dans la région où ils fournissent en général le maximum de puissance.

La méthode de contrôle d'un état stationnaire instable diffère de celle présentée précédemment mais le

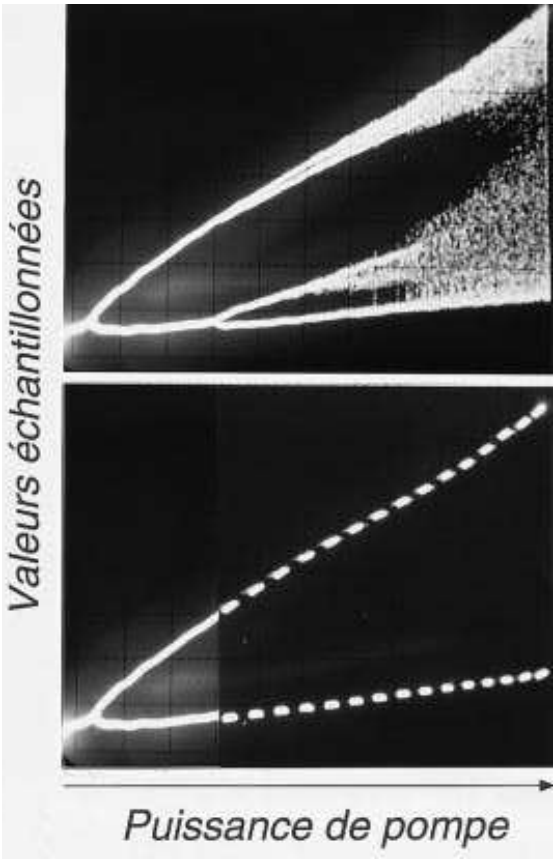

Figure 5 - *Diagramme de bifurcation du laser à fibre optique dopée Nd^{3+}. Le diagramme de bifurcation est obtenu en échantillonnant l'intensité I émise par le laser à la période de modulation ; une unique valeur est obtenue pour un signal T-périodique, deux valeurs différentes lorsque le signal est 2 T-périodique et un ensemble diffus de valeurs lorsque le régime est chaotique.*
(a) Diagramme en l'absence de contrôle : quand la puissance de pompe augmente, le laser évolue vers le chaos par une cascade de doublements de période.
(b) Il demeure sur l'OPI 2T quand celle-ci est stabilisée par la méthode de contrôle du chaos. Le laser a d'abord été amené dans la zone de forte puissance où le laser est chaotique, puis l'orbite 2T a été stabilisée, enfin on réduit la puissance de pompe : le laser reste dans un régime 2T-périodique tant que le contrôle est maintenu. La trace en pointillés représente l'orbite stabilisée, tandis que celle en trait plein est extraite de la partie du diagramme (a) correspondant au domaine de stabilité de cette orbite.

Encadré 2

DISPOSITIF EXPÉRIMENTAL UTILISÉ POUR LE CONTRÔLE DU CHAOS

Le système chaotique est un laser à fibre dopée au néodyme (NDFL) pompé par une diode laser (DL) dont on module à la période T la puissance de sortie. La stabilisation du laser est obtenue en contrôlant celui-ci sur une orbite périodique instable de période nT par la technique de contre-réaction suivante.

A chaque période de l'orbite considérée, on échantillonne le signal de sortie I_k et on mémorise sa valeur précédente I_{k-1}, au moyen des deux échantillonneurs ECH1 et ECH2 (la valeur de I_k peut être considérée comme une coordonnée dans la section de Poincaré). On applique à un paramètre de contrôle (ici la puissance de pompe) une impulsion d'amplitude $\delta\mu_k$ proportionnelle à $I_k - I_{k-1}$. En choisissant correctement la forme de l'impulsion et le gain total de la contre-réaction, le laser se stabilise sur une orbite périodique. Il est également possible de stabiliser le laser sur son état stationnaire instable en remplaçant le dispositif de contrôle par un simple dérivateur analogique.

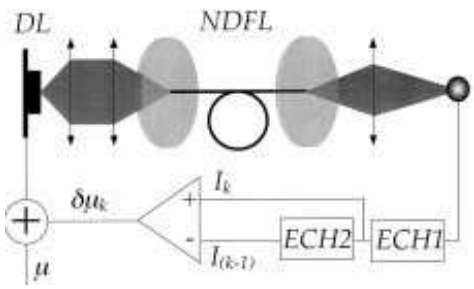

principe reste inchangé : appliquer un signal de contre-réaction à un paramètre de contrôle pour maintenir le système sur l'ESI. Puisqu'un tel état est par définition un point fixe $\mathbf{X}_F(\mu)$ des équations d'évolution, le recours à la section de Poincaré n'est pas ici nécessaire. Pour la même raison, les corrections peuvent être appliquées de manière continue plutôt que périodiquement comme dans le cas des OPI.

Cette méthode s'avère très robuste et comme précédemment, il est possible de simplifier l'expérience en utilisant simplement une variable dynamique plutôt que sa composante selon les directions instables. Ainsi, le laser à fibre utilisé pour le contrôle des OPI a été stabilisé sur son ESI en considérant l'intensité I du laser comme variable dynamique et la puissance de pompe comme paramètre de contrôle (figure 6). Une correction proportionnelle à la dérivée de l'intensité s'est avérée suffisante, permettant ici aussi de s'affranchir de la détermination du point fixe I_F. Expérimentalement, il suffit simplement de remplacer le dispositif précédemment utilisé pour le contrôle des OPI, par un dérivateur suivi

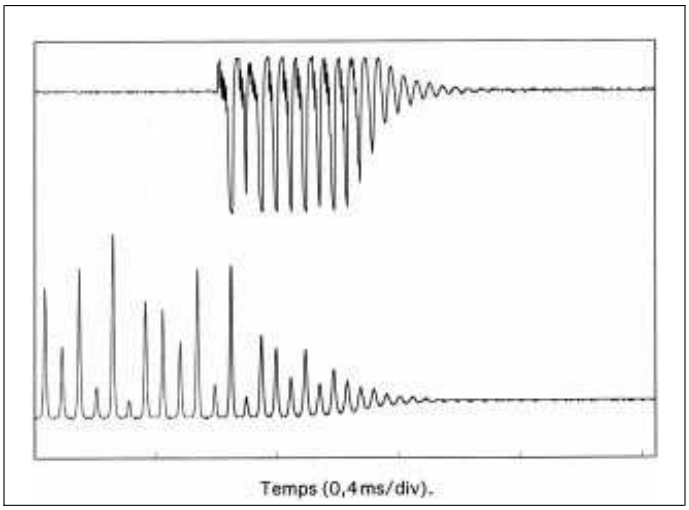

Figure 6 - *Evolution de l'intensité émise par le laser à fibre lorsque l'on active le contrôle en vue de le stabiliser sur son état stationnaire instable. La trace du haut représente la correction activée à t = 0.6 ms, et la trace du bas l'évolution de l'intensité du laser. Avant application de la correction, le laser est chaotique. Après un transitoire durant environ 0.8 ms, l'intensité devient stationnaire. On remarquera que l'amplitude de la correction tend bien vers zéro et qu'à la limite elle ne corrige plus que les fluctuations autour de l'ESI, introduites par le bruit expérimental.*

d'un amplificateur à gain variable. En choisissant un gain suffisamment grand, le laser a pu être stabilisé dans tout le domaine où il avait précédemment un comportement oscillant ou chaotique.

On le voit, le contrôle du chaos peut avoir un impact technologique considérable, évident dans le cas des ESI, mais également indéniable en ce qui concerne les OPI, où il permet de tirer parti à la fois de l'ordre et du chaos. Un attracteur contenant une infinité d'orbites périodiques, il est en effet possible, par d'infimes variations des paramètres, de commuter d'une orbite à une autre, et de tirer ainsi d'un système chaotique toute une harmonie de signaux périodiques différents, là où un système régulier aurait un comportement fixé une fois pour toutes.

Il importe évidemment de généraliser les méthodes actuelles, notamment pour stabiliser les orbites les plus instables, ou, si l'on désire contrôler des systèmes à grand nombre de degrés de liberté, les orbites à plusieurs directions instables. Il est même possible d'aller plus loin : il a été récemment montré que l'on pouvait forcer un système à suivre n'importe quelle trajectoire chaotique choisie à l'avance dans un attracteur.

En conclusion, les orbites périodiques instables ouvrent la porte à une approche différente de l'« ordre dans le chaos ». Considéré dans sa globalité, un attracteur chaotique ne révèle en toute rigueur cet ordre que dans la limite d'un temps infini. En le décomposant en OPI, c'est un ordre local, à court terme, qui devient accessible.

Paradoxalement, la manière la plus simple de comprendre un attracteur chaotique à petit nombre de degrés de liberté semble être maintenant de se le représenter comme un « sac de nœuds ». L'analyse topologique en démonte la complexité, les méthodes de contrôle permettent d'en tirer le meilleur parti.

POUR EN SAVOIR PLUS

Tufillaro (N.B.), Abbott (T.A.) and Reilly (J.P.), *An experimental approach to nonlinear dynamics and chaos.* Addison Wesley, Reading, Mass., 1992.

Lefranc (M.) et Glorieux (P.), « Des nœuds dans le chaos », *Pour La Science*, dossier hors-série « Le Chaos », 58-63 (Janvier 1995).

Mindlin (G.B.), Solari (H.G.), Natiello (M.A.), Gilmore (R.) and Hou (X.J.), « Topological analysis of chaotic time series data from Belousov-Zhabotinski reaction », *J. Nonlinear Sci.* **1,** 147-173 (1991).

Lefranc (M.), Glorieux (P.), Papoff (F.), Molesti (F.) and Arimondo (E.), « Combining topological analysis and symbolic dynamics to describe a strange attractor and its crises », *Phys. Rev. Lett.* **73,** 1364-1367 (1994).

Ott (E.), Grebogi (C.) and Yorke (J.A.), « Controlling chaos », *Phys. Rev. Lett.* **64,** 1196-1199 (1990).

Bielawski (S.), Derozier (D.) and Glorieux (P.), « Experimental characterization of unstable periodic orbits by controlling chaos », *Phys. Rev. A* **47,** R2492-2495 (1993).

Bielawski (S.), Bouazaoui (M.), Derozier (D.) and Glorieux (P.), « Stabilization and characterization of unstable steady states in a laser », *Phys. Rev. A* **47,** 3276-3279 (1993).

Hayes (S.), Grebogi (C.) and Ott (E.), « Communicating with chaos », *Phys. Rev. Lett.* **70,** 3031-3034 (1993).

Article proposé par : Marc Lefranc, Serge Bielawski, Dominique Derozier et Pierre Glorieux

“Dénouement dans le Chaos”

Marc Lefranc, and Pierre Glorieux

Hors-Série « La Science des Noeuds », 92–96 (Pour La Science, Avril 1997)

Dénouement dans le chaos

Marc LEFRANC et Pierre GLORIEUX

Les composantes périodiques d'une évolution chaotique peuvent être associées à des courbes fermées dont l'enchevêtrement, démêlé grâce à la théorie des nœuds et des tresses, suit un modèle d'organisation simple.

L'image mythologique de la complexité est celle du fameux nœud gordien, qui prédisait la domination sur le monde à celui qui réussirait à le démêler. Alexandre le Grand trancha dans le vif en détruisant ce nœud d'un coup d'épée.

C'est une manœuvre un peu plus délicate que choisit le physicien qui dissèque le chaos. Outre la difficulté commune de ces deux entreprises, il existe une parenté plus profonde entre l'analyse du chaos et le démêlage de nœuds compliqués : l'attracteur d'un système chaotique s'enroule autour d'orbites périodiques qui forment des nœuds. Qu'est-ce qu'un attracteur chaotique? Qu'est-ce qu'une orbite périodique? Avant tout, rappelons ce que le physicien de la fin des années 1990 entend par chaos, et plus précisément par «chaos déterministe» (voir *Le chaos*, dossier hors série de Pour la science).

Depuis les travaux d'Henri Poincaré et, plus récemment, du météorologiste américain E. Lorenz, on sait que certains systèmes, mathématiques, chimiques ou même biologiques, possèdent une «sensibilité aux conditions initiales» : deux systèmes identiques, placés dans des conditions initiales voisines, suivent d'abord des évolutions très semblables, puis leurs différences augmentent avec le temps (de manière exponentielle). Quelle que soit la différence des conditions initiales, aussi minime soit-elle, elle finit par devenir macroscopique. Il est donc impossible de prédire à long terme le comportement de tels systèmes, qui sont pourtant régis par des lois déterministes. Ainsi la complexité des interactions atmosphériques fait que le battement d'aile d'un papillon au Brésil pourrait influer sur le déclenchement d'un ouragan au Japon.

La fabrication de la pâte feuilletée, par succession d'étirements et de repliements, illustre la sensibilité aux conditions initiales : dans le film *L'aile ou la cuisse*, un pâtissier laisse tomber la cendre de son mégot dans la pâte feuilletée qu'il prépare. Renonçant à en extraire la tache de cendres, il continue à allonger et à replier sa pâte. La cendre initialement localisée se répartit peu à peu dans toute la pâte.

Des trajectoires alambiquées

Les tours et détours d'une trajectoire individuelle ne révèlent pas les mécanismes à l'œuvre. Pour démêler le sac de nœuds du chaos, il faut prendre du recul et embrasser d'un coup d'œil toute l'histoire du système. C'est ce qu'a fait Poincaré, en élaborant une description géométrique de la dynamique.

L'état d'un système est caractérisé par les valeurs de quelques variables, telles que la température, la densité ou la vitesse d'écoulement en tout point d'un fluide, ou encore la position et la vitesse angulaire d'un pendule pesant. La connaissance de ces variables à un instant donné permet de déterminer l'évolution future du système. Pour visualiser l'évolution temporelle du système, on fabrique un espace de dimension suffisante *(ad hoc)*, dont les coordonnées sont les variables représentatives du système ; l'état du système à un instant donné est alors représenté par un point unique de cet espace des états, ou «espace des phases». Lorsque le système évolue, le point représentatif se déplace dans l'espace des phases suivant une trajectoire exactement déterminée par les lois physiques. Le déterminisme interdit donc à deux trajectoires de se couper, car le point d'intersection aurait alors deux futurs possibles.

Dans le cas d'un système au repos, la trajectoire se limite à un «point fixe». La trajectoire d'un système dont l'évolution est périodique comme une horloge se reproduit à l'identique à intervalles réguliers ; c'est une courbe fermée, un «cycle». Si la dynamique fait intervenir deux phénomènes périodiques de fréquences incommensurables, la trajectoire s'enroule sur un tore (la surface d'une chambre à air, engendrée par deux cercles : un petit cercle qui tourne sur un grand cercle). La trajectoire d'un système chaotique est nettement plus complexe. Elle parcourt un domaine de l'espace des phases qui n'est ni un cycle (de dimension un), ni une surface (de dimension deux), ni un volume (de dimension trois), mais une structure intermédiaire feuilletée et fractale, un «attracteur étrange», de dimension non entière, et ce sans jamais revenir à son point de départ *(voir la figure 1)*.

Cette représentation géométrique de l'évolution temporelle dans l'espace des phases retrace en une seule figure l'histoire d'un système et permet de comprendre les mécanismes engendrant le chaos. Adoptons un moment la méthode d'Alexandre et découpons l'attracteur étrange en tranches, traditionnellement dénommées «sections de Poincaré». Choisissons un plan de section et examinons comment évoluent les trajectoires issues d'une moitié de l'attracteur *(indiquée en mauve dans la première section de la figure 2b)*. Dans un premier temps, cette région s'étire, puis elle se replie et les points se répartissent entre les deux moitiés de l'attracteur.

Après un tour sur l'attracteur, on retrouve l'autre région *(la blanche)* à la place occupée initialement par la mauve : au tour suivant, elle reproduira le comportement de cette dernière.

La dernière section de la figure 2*b* montre que la région mauve, qui paraissait uniforme dans le premier carré, est composée de deux parties provenant des deux moitiés de l'attracteur, et qui s'écrasent l'une contre l'autre jusqu'à devenir indiscernables. Comme ce processus se répète à chaque tour, ce sont en fait une infinité de couches qui se sont juxtaposées dans cette région. Cela nous rappelle la recette de la pâte feuilletée! Cette succession d'étirements et de repliements de la trajectoire est aussi appelée «fer à cheval de Smale», du nom du mathématicien américain qui l'a analysé. Ainsi, partant d'une condition initiale donnée, un point représentatif de l'état du système voyage au bout d'un certain temps dans n'importe quelle région de l'attracteur. Comme nous allons le voir, c'est le même mécanisme qui noue les «nœuds du chaos».

Un chaos organisé autour des cycles

En pratique, les études expérimentales ne nous permettent pas de reconstituer le véritable espace des phases : la plupart des expériences ne donnent accès qu'à quelques variables, voire une seule. C'est comme si nous cherchions un objet d'après sa photographie réduite à une ligne! Fort heureusement, on peut construire une «photographie» équivalente, en accolant des «lignes photographiques» prises à des instants régulièrement espacés : la mesure à intervalles réguliers d'une seule variable permet de se passer de toute information sur les autres. Ces mesures décalées dans le temps peuvent être prises comme coordonnées dans un nouvel espace où la trajectoire du système a les mêmes propriétés que dans l'espace des phases de départ.

Comme on ne sait pas *a priori* combien de dimensions sont nécessaires à la description du système, on augmente le nombre de dimensions jusqu'à ce que la trajectoire reconstituée ne se coupe jamais : à cette seule condition, le déterminisme est respecté. Pour de nombreux systèmes chaotiques, trois dimensions suffisent. Dans ce cas, l'attracteur étrange équivaut à une courbe sans point d'intersection, plongée dans un espace à trois dimensions : cette des-

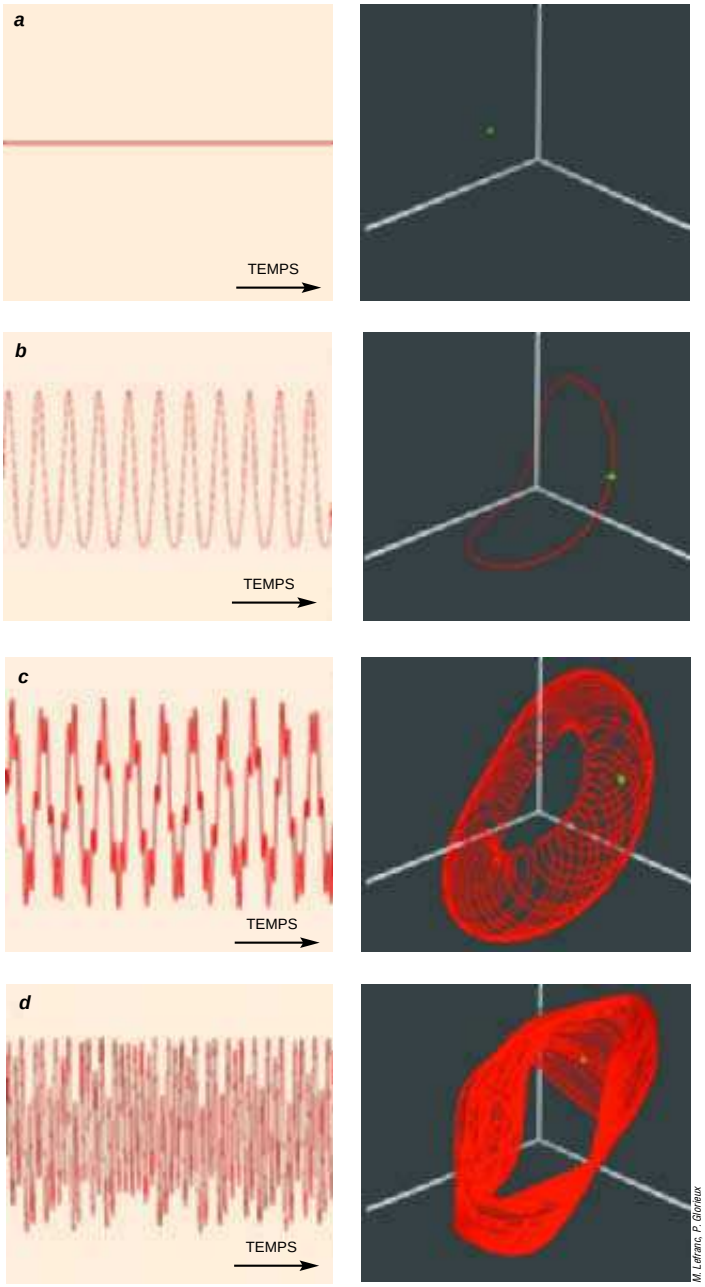

1. Évolutions temporelles et attracteurs associés dans l'espace des phases. Les figures de gauche montrent l'évolution d'un signal en fonction du temps : stationnaire *(a)*, périodique *(b)*, formé de deux oscillations indépendantes *(c)* et chaotiques *(d)*. Dans l'espace des phases *(figures de droite)*, on porte sur des axes les grandeurs représentatives de l'état du système : un point *(représenté en vert)* correspond à l'état du système à un instant donné, et ce point se déplace au cours du temps ; sa trajectoire *(en rouge)* possède une géométrie caractéristique de la dynamique observée : un point fixe *(a)*, une courbe fermée *(b)*, un tore *(c)*, un attracteur étrange *(d)*.

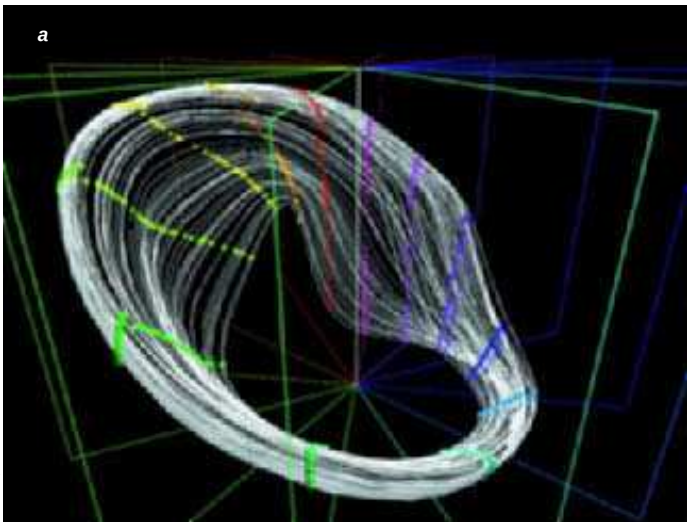

M. Lefranc, P. Glorieux

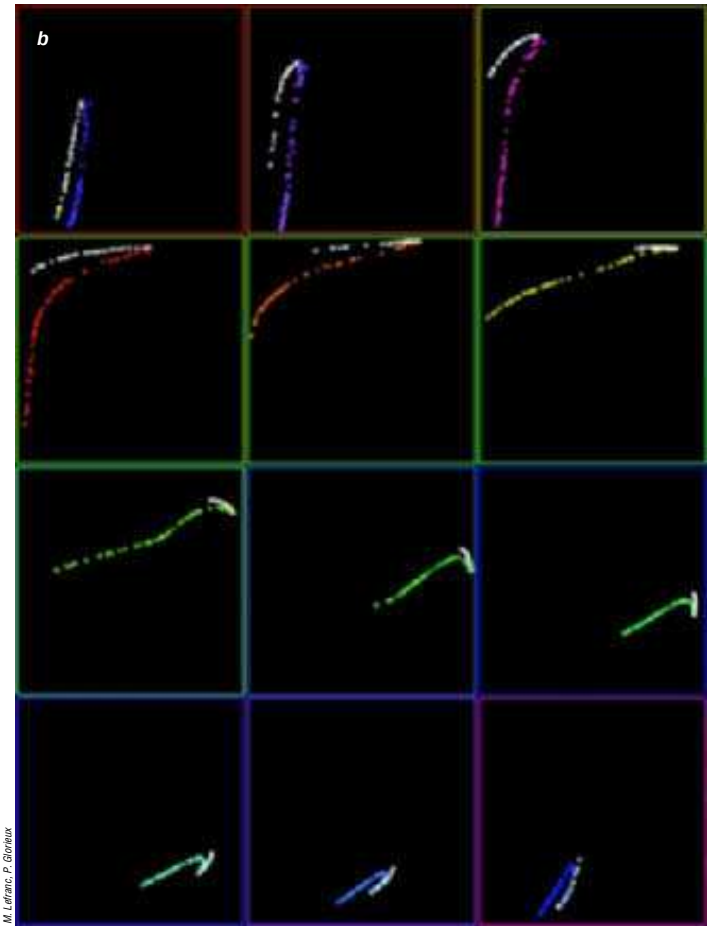

M. Lefranc, P. Glorieux

cription ressemble à celle d'un nœud! Toutefois les nœuds dont traite la théorie des nœuds sont des courbes fermées, tandis qu'une trajectoire chaotique ne se referme jamais (sinon on aurait un système périodique). Comment alors la théorie des nœuds permet-elle de démêler le chaos?

La réponse réside dans un phénomène flagrant pour celui qui examine directement les signaux chaotiques. Dans ces signaux apparaissent des bouffées de comportement presque périodiques *(voir la figure 3)* : l'évolution du système se répète quelque temps, puis reprend un cours imprévisible. Les périodes de ces tronçons périodiques, c'est-à-dire le nombre d'oscillations qu'ils comportent, sont comprises entre un et six. Un examen ici approfondi de signaux s'étalant sur une durée plus longue révélerait l'existence d'une multitude de telles séquences, de périodes arbitrairement élevées ; le nombre de séquences distinctes ayant une période donnée augmente de manière exponentielle avec la valeur de cette période.

Ainsi l'attracteur chaotique contient une infinité de trajectoires périodiques. La trajectoire chaotique ne suit pas exactement ces orbites, mais elle s'en approche à plusieurs reprises au cours de son évolution sur l'attracteur. Autrement dit, l'attracteur étrange s'enroule autour de ces orbites périodiques, qui forment ainsi son ossature. À chacune des orbites périodiques, on associe une courbe fermée dans l'espace des phases. Grâce à la théorie des nœuds, on étudie leur organisation dans l'espace, glanant ainsi des renseignements précieux sur le système chaotique.

2. Les sections de Poincaré renseignent sur la structure de l'attracteur étrange. Les intersections de l'attracteur de la figure *(a)* avec 12 plans de coupe sont reproduites dans la figure *(b)*. En effectuant un tour sur l'attracteur, on obtient différentes coupes montrant la succession des phases d'étirement, qui sont responsables de la sensibilité aux conditions initiales, et des phases de repliement, qui maintiennent la trajectoire dans un volume fini. Dans la première section, on a distingué deux régions de l'attracteur : l'une est tracée en mauve, l'autre en blanc. Les trajectoires mauves s'étirent, puis se replient en deux bandes, tandis que les trajectoires blanches passent de l'autre côté de l'attracteur en se repliant sur les mauves. Dans la dernière section, la plupart des trajectoires sont passées d'une région à une autre.

La dissection des cycles

Pour étudier les cycles autour desquels s'organise le chaos, nous reprenons, une fois encore, la méthode d'Alexandre : nous tranchons le nœud représentant un cycle, et nous déplions la tresse obtenue. La figure 4 montre deux cycles qui ont été «mis à plat» de cette manière : ils composent une tresse à cinq brins entrelacés, formée des tresses associées aux deux orbites. La tresse de l'orbite de période 1 *(en jaune)* se réduit à un simple brin, tandis que celle de l'orbite de période 4 *(en rouge)* comporte quatre brins : elle présente une structure non triviale.

Dans cette représentation, chaque orbite apparaît comme une tresse à *p* brins, où *p* est la période de l'orbite. L'ensemble des orbites de l'attracteur forme un amas de tresses imbriquées les unes dans les autres. Cette description à l'aide de tresses facilite l'analyse des orbites. Chacun sait former une tresse avec des brins de ficelle ordinaire : il suffit d'échanger deux brins adjacents, et de répéter cette opération autant de fois que nécessaire. En combinant ces croisements simples entre brins voisins, on engendre n'importe quel type de tresse. Inversement, pour analyser la structure d'une tresse formée d'un ou plusieurs cycles, il suffit, de relever entre quels brins et dans quel ordre s'effectuent les croisements (voir *L'art de tresser*, par Patrick Dehornoy, dans ce dossier).

Bien sûr, la configuration des croisements dépend de la manière dont on regarde la tresse : en changeant l'angle de vue de la tresse de la figure 4, on fait apparaître ou disparaître certains croisements, ou encore on inverse l'ordre de deux croisements consécutifs. Heureusement la théorie des nœuds et des tresses nous enseigne que ces incohérences apparentes ne modifient pas les propriétés topologiques de ces objets : la structure de la tresse décrite de cette manière ne dépend pas de la perspective choisie. Par exemple, le nombre de croisements entre les tresses jaune et rouge de la figure 4, égal à quatre, indique que la tresse rouge entoure deux fois la tresse jaune. Ce nombre est le plus simple des invariants topologiques de tresse (on le nomme le nombre d'entrelacements des deux orbites).

Une orbite périodique n'est pas tressée arbitrairement. Ce sont les mécanismes d'étirement et de repliement qui, en enroulant les brins de l'orbite les uns autour des autres, engendrent un nœud particulier. Dans un comportement de type «fer à cheval», les brins d'une orbite donnée se répartissent en deux groupes : ceux qui passent par la branche blanche du premier carré de la figure 2, et ceux qui passent par la branche mauve (c'est-à-dire ceux qui se replient sur les autres). Associons à ces deux groupes les symboles *B* (pour blanc) et *M* (pour mauve). Lorsqu'on parcourt les brins de l'orbite, on établit une séquence de symboles caractéristiques des brins rencontrés, telle que *BMMM*. Cette séquence, et c'est une des propriétés fondamentales de la dynamique chaotique, identifie de manière unique l'orbite périodique entre toutes les autres. Or, cette séquence fournit la «recette» du tressage des brins : par exemple, tous les brins *M* doivent se croiser au cours de la phase de repliement. Autrement dit, deux cycles différents ont en général des types de tresse différents, et le type de tresse caractérise l'orbite. Dans la discussion précédente, la partition de l'attracteur en deux régions *(B et M)* est naturelle, car les sections de Poincaré comportent des points serrés, assimilables à des branches. Dans d'autres situations expérimentales, la dilatation et le repli sont bien plus difficiles à mettre en évidence, et il est alors délicat de construire un codage symbolique similaire à la partition en points blancs et mauves. Il faut dans ce cas mesurer les invariants topologiques des orbites pour déterminer le type de nœud et remonter à la séquence symbolique associée à chaque orbite. L'extraction de ces séquences donne ensuite accès à des mesures quantitatives du degré de chaos, qui complètent l'information qualitative fournie par l'analyse topologique.

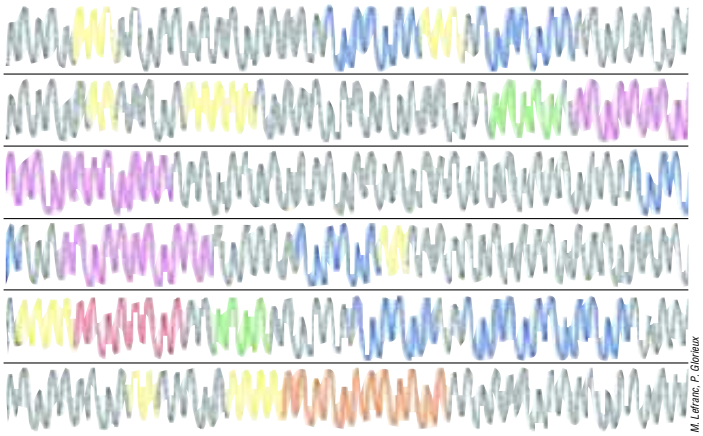

3. Signal chaotique composé de bouffées presque périodiques. On a tracé en fonction du temps l'intensité du rayonnement émis par un laser à gaz carbonique, auquel on applique une modulation sinusoïdale de période T. Les bouffées périodiques (en couleurs) sont des multiples de T, allant de 1 à 6 (respectivement jaune, vert, bleu, rouge, violet et orange). Ces bouffées indiquent que le système visite le voisinage d'orbites périodiques instables, associées à des courbes fermées dans l'espace des phases. Ces courbes forment l'ossature de l'attracteur, et on analyse leur organisation par la théorie des nœuds.

Le gabarit

Une fois que l'on a identifié plusieurs cycles d'un attracteur (par la tresse associée), on les regroupe dans une représentation unique, le gabarit. Le gabarit est une surface sur laquelle on peut déposer l'ensemble des cycles, en les déformant, sans modifier les nœuds qu'ils portent, c'est-à-dire sans couper aucune courbe *(voir la figure 5)*. Chaque attracteur chaotique possède un gabarit unique, l'objet géométrique le plus simple qui puisse contenir les nœuds présents dans l'attracteur. La structure du gabarit rassemble toutes les propriétés topologiques des orbites qu'il supporte, et son étude révèle les effets d'étirement et de repliement caractéristiques du système chaotique.

La mesure des invariants de quelques orbites périodiques détectées dans un signal expérimental chaotique permet de déterminer la structure du gabarit associé à l'attracteur du système et de décrire l'organisation topologique globale de ce dernier. Cette méthode de caractérisation du chaos est extrêmement robuste : un

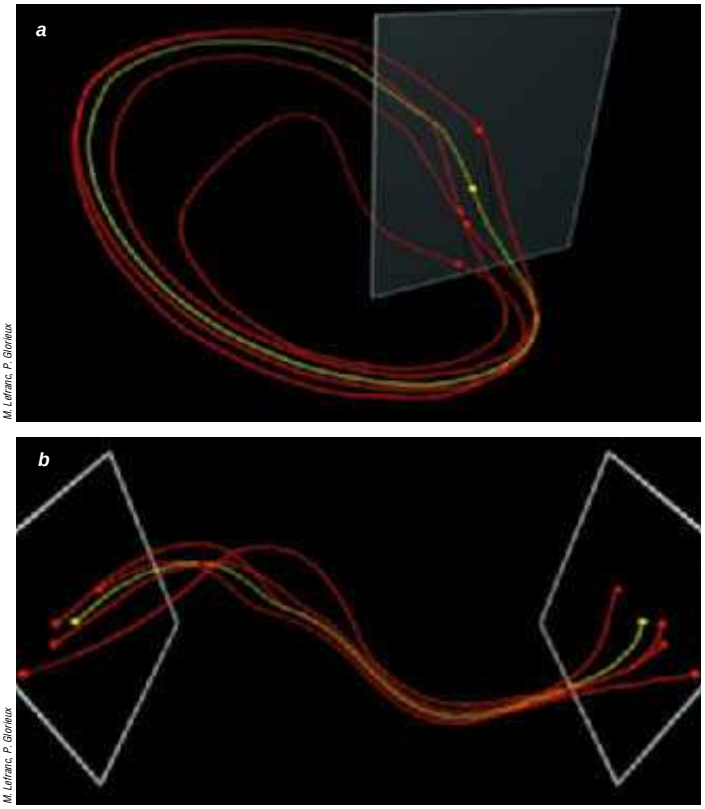

M. Lefranc, P. Glorieux

M. Lefranc, P. Glorieux

4. Deux orbites périodiques, de périodes 1 et 4 *(a)*, ont été extraites de l'attracteur de la figure 2, et correspondent aux bouffées de mêmes couleurs de la figure 3 : l'une est une boucle triviale, l'autre forme un nœud de trèfle, le plus simple des nœuds. Au cours du temps, ces trajectoires tournent toutes dans le même sens sur l'attracteur. Autrement dit, lorsqu'on les coupe le long d'un plan de section et quand on les déplie *(b)*, ces orbites ont une orientation unique, correspondant à la flèche du temps : elles forment des tresses. L'ordre et le sens des croisements, déterminés par l'étirement et le repliement des trajectoires, fournissent des invariants topologiques, qui simplifient l'analyse de l'attracteur. En pratique, on observe directement une projection de ces tresses en visualisant les signaux sur un écran d'oscilloscope, et en synchronisant ce dernier sur la période T de modulation.

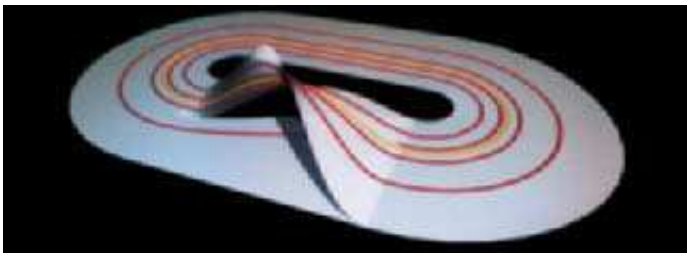

M. Lefranc, P. Glorieux

5. Dépôt sur une surface à deux branches, le gabarit, des orbites de la figure 4. Le gabarit peut porter toutes les orbites périodiques de l'attracteur, sans modifier leurs invariants topologiques. Sa structure est elle-même décrite par une tresse fermée, non pas de simples brins, mais de rubans, dont la torsion reproduit les effets de repliement. Ainsi on classe les gabarits des systèmes chaotiques, par des méthodes similaires à la classification des nœuds. La majorité des attracteurs observés expérimentalement est associée au gabarit à deux branches représenté ici.

niveau de bruit modéré ne modifie pas les invariants topologiques. En outre, contrairement à d'autres méthodes, elle teste efficacement les modèles théoriques : lorsqu'un modèle théorique prédit un gabarit différent de celui observé expérimentalement, on conclut évidemment qu'il est inadapté et qu'il doit subir une révision importante.

En principe, selon la valeur de ses paramètres de fonctionnement, un système donné possède un grand nombre d'attracteurs différents, donc plusieurs gabarits. On peut approfondir l'épreuve expérimentale d'un modèle théorique par l'exploration et la comparaison de l'organisation des régimes chaotiques du système qu'il décrit. La plupart des systèmes expérimentaux analysés jusqu'ici (lasers, réactions chimiques, cordes vibrantes, ou encore expériences d'hydrodynamique) appartiennent à la même classe topologique, celle du gabarit de la figure 5. Celui-ci comporte deux branches : la première subit une simple dilatation tandis que la deuxième subit une torsion d'un demi-tour avant de se replier sur l'autre. Nous retrouvons ici une modélisation simple des mécanismes d'étirement et de repliement que nous avons vus à l'œuvre dans la figure 4. Toutefois nous avons observé récemment, dans un laser, les premiers exemples d'une organisation différente. Ces nouveaux gabarits se distinguent notamment par le nombre de leurs branches et par leurs torsions.

La théorie des nœuds fournit des outils efficaces pour l'étude systématique de la dynamique chaotique. Elle paraît cependant limitée : elle ne s'applique que dans un espace à trois dimensions, laissant les physiciens désemparés lorsque la reconstruction de l'attracteur nécessite quatre dimensions ou plus. Il reste donc à découvrir comment généraliser cette approche et quel pourrait être l'analogue du gabarit dans ce cas. Sans doute faut-il encore une fois s'inspirer de la pensée d'Henri Poincaré qui écrivait, il y a près d'un siècle :

«*Ce qui nous rend ces solutions périodiques si précieuses, c'est qu'elles sont pour ainsi dire la seule brèche par où nous puissions pénétrer dans une place réputée jusqu'ici inabordable*».

Pierre Glorieux dirige le Laboratoire de spectroscopie hertzienne de l'Université des sciences et techniques de Lille. Marc Lefranc est chargé de recherche dans ce laboratoire.

“Des Noeuds dans le Chaos”

Marc Lefranc, and Pierre Glorieux

Hors-Série « Le Chaos », 58–63 (Pour La Science, Janvier 1995)

Des nœuds dans le chaos

Marc Lefranc et Pierre Glorieux

Avec la théorie des nœuds, on caractérise les orbites noyées dans un attracteur étrange. Cette analyse topologique des attracteurs révèle le degré d'organisation d'un système chaotique.

Les nœuds que l'on réalise avec un bout de ficelle sont des objets usuels, mais le mélange de simplicité et de complexité qui émane d'eux fascine aussi bien les jeunes enfants que les mathématiciens les plus chevronnés, voire même les psychanalystes. En physique, la théorie des nœuds a joué un rôle crucial dans des domaines variés, tels que la physique statistique, la théorie des supercordes *(sic)* ou les théories de jauge topologiques.

C'est maintenant le domaine du chaos déterministe que les physiciens essaient de démêler grâce aux nœuds. S'il est somme toute naturel de comparer l'évolution complexe d'un système chaotique à un sac de nœuds, cette métaphore prise à la lettre a mené récemment à une méthode puissante d'analyse topologique des phénomènes chaotiques. Cette méthode est utile pour analyser aussi bien les modèles théoriques que les systèmes réels, comme nous l'illustrerons à l'aide de données expérimentales provenant d'un laser à gaz carbonique dont on module les pertes.

C'est une approche géométrique des systèmes dynamiques qui révèle le lien qui unit nœuds et chaos. A la suite d'Henri Poincaré, les physiciens représentent l'état d'un système dynamique à un instant donné par un point situé dans l'espace des phases (ou espace des états) : les coordonnées de cet espace fictif correspondent aux différentes variables du système, par exemple la position et la vitesse angulaire dans le cas d'un pendule (*voir la figure 1*). Si l'état du système est stationnaire, le point représentatif reste fixe ; si le système évolue dans le temps, le point parcourt une trajectoire dans l'espace des phases : par exemple, si l'évolution du système est périodique, la trajectoire correspondante dans l'espace des phases est une courbe fermée.

Cette approche prend tout son intérêt lorsqu'elle est appliquée à des systèmes chaotiques. Au premier abord le comportement de ces systèmes semble erratique, sans aucun ordre. C'est en considérant l'évolution du système dans l'espace des phases que l'on s'aperçoit que la dynamique chaotique n'est pas aléatoire, mais bien déterminée : la trajectoire du point représentatif s'enroule sur un objet géométrique fractal, un «attracteur étrange», dont la figure 2 fournit un exemple observé dans un laser à gaz carbonique. Ce type de laser constitue un dispositif de choix pour observer le chaos.

Le chaos mis en lumière

Le laser à gaz carbonique émet une lumière infrarouge (de longueur d'onde égale à dix micromètres environ). Un modulateur de fréquence réglable est placé dans la cavité du laser. Comme il transmet et absorbe alternativement la lumière émise, il induit des «pertes» périodiques pour le rayonnement dans la cavité laser. Lorsque l'amplitude de la modulation de pertes est faible, l'intensité du laser diminue, puis augmente avec

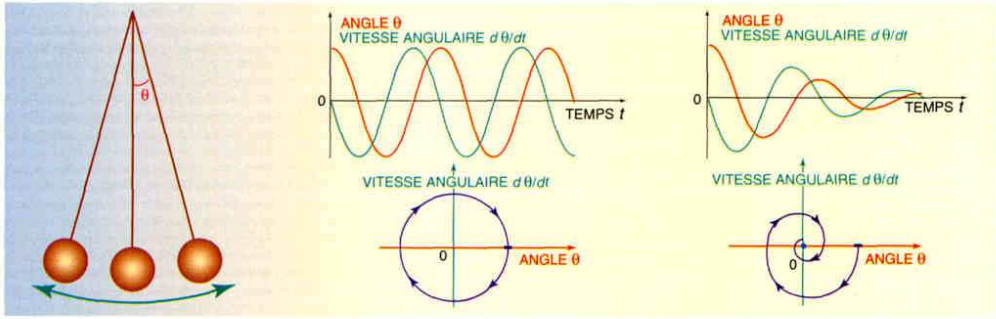

1. Le pendule non amorti est un système périodique. ***Pour des battements de faible amplitude, l'angle du pendule par rapport à la verticale varie dans le temps suivant une sinusoïde (au milieu). Pour un pendule libre, l'espace des phases est à deux dimensions. Le point représentatif de ce système a pour coordonnées l'angle et la vitesse angulaire du pendule. Quand le pendule oscille sans amortissement, le point représentatif décrit une boucle, ou orbite périodique : le système repasse périodiquement par les mêmes états. Quand le pendule est amorti (à droite), la trajectoire du point représentatif dans l'espace des phases tend vers un point unique, à l'origine des deux axes : ce point, ou attracteur ponctuel, correspond à l'état final du pendule amorti, lorsqu'il est immobile.***

la même période que la modulation. Quand on augmente l'amplitude de la modulation, la période du signal devient deux fois, quatre fois, huit fois plus longue que celle du modulateur, jusqu'à ce que toute périodicité disparaisse (la période est infinie) : c'est la cascade de de dédoublements de période, caractéristique d'une transition vers le chaos.

Les avantages expérimentaux du laser sont multiples : d'abord le nombre de ses variables caractéristiques est petit ; ensuite les phénomènes physiques y sont rapides (autour d'une microseconde), ce qui permet d'enregistrer de longues séries temporelles.

Nous avons observé un laser à gaz carbonique en régime chaotique et recherché l'existence d'une structure ordonnée dans le chaos. A tout instant t, nous mesurons deux variables du système : l'intensité du rayonnement émis par le laser et la phase de la modulation. Comme nous voulons construire un attracteur dans un espace à trois dimensions (l'espace naturel d'un nœud), nous avons besoin d'une troisième variable ; nous la choisissons, dans l'esprit de la méthode du délai temporel, égale à l'intensité du rayonnement émis un instant plus tard $t + \Delta t$. Le décalage temporel Δt est choisi de manière empirique : si Δt est trop court, les valeurs mesurées à l'instant t et $t + \Delta t$ sont presque identiques ; si Δt est trop long, ces valeurs sont décorrélées, et les coordonnées du point représentatif du système semblent erratiques. Nous avons choisi un décalage égal au cinquième environ de la période de modulation.

Ainsi que les mathématiciens David Ruelle et Floris Takens l'ont montré, nous obtenons, par cette méthode du délai temporel, une courbe à trois dimensions qui possède les mêmes propriétés que l'attracteur correspondant à trois variables distinctes : en régime périodique, l'attracteur est une courbe fermée ; en régime chaotique, l'attracteur est une courbe fractale.

Les orbites périodiques instables

Comment étudier de tels attracteurs ? Plutôt que d'aborder de front la complexité d'un attracteur étrange, certains physiciens analysent la topologie d'objets géométriques simples : les orbites périodiques instables contenues dans l'attracteur.

Que sont ces orbites ? Dans un signal chaotique, il existe un grand nombre de séquences de courtes durées pendant lesquelles le système chaotique évolue de

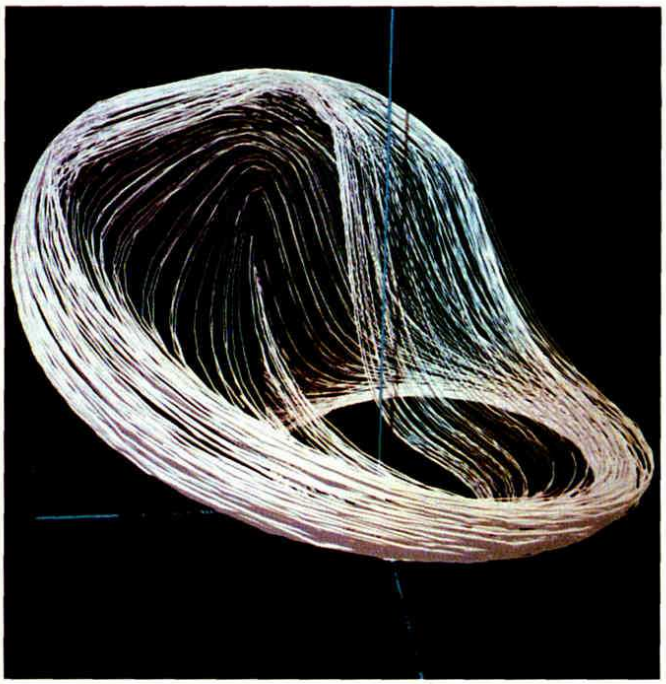

2. L'ATTRACTEUR ÉTRANGE correspondant au comportement d'un laser à gaz carbonique à pertes modulées, reconstruit à partir de la série temporelle de la figure 3. L'état du laser à un instant t est représenté, dans cet espace des phases, par un point dont les coordonnées sont : la valeur du logarithme de l'intensité du rayonnement émis par le laser à cet instant t, la valeur de cette quantité à un instant décalé t + Δt, et la phase de la modulation.

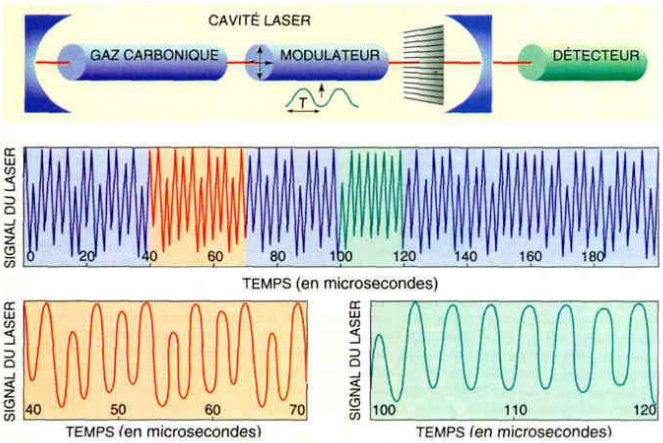

3. UN LASER À DIOXYDE DE CARBONE délivre un signal chaotique. La cavité laser (en haut) comporte le milieu actif (le gaz carbonique), un modulateur qui change la polarisation périodiquement (avec une période T = 2,61 microsecondes) et un discriminateur de polarisation. Le signal détecté (en bas) révèle l'existence de séquences pendant lesquelles le système est presque périodique. Dans un système modulé, les périodes de ces séquences sont des multiples de la période de modulation T. On observe ainsi une séquence de périodicité 4T entre 40 microsecondes et 70 microsecondes, et une de périodicité T entre 100 et 120 microsecondes.

La caractérisation des nœuds

C'est parce qu'on peut assimiler une courbe fermée de l'espace (sans point d'intersection) à un nœud mathématique qu'il existe un lien entre la théorie des nœuds et les orbites périodiques instables des systèmes chaotiques.

L'objet de la théorie des nœuds, celui de l'étude des orbites périodiques instables et, à partir de là, des attracteurs étranges, est la recherche des invariants du système, c'est-à-dire des caractéristiques propres aux systèmes étudiés. Pour cela, on associe à chaque nœud ou courbe fermée une quantité qui reste constante quelles que soient les déformations continues que l'on fait subir au nœud ou à l'orbite, donc quelle que soit sa représentation dans un espace euclidien pour le nœud et dans l'espace des phases pour l'orbite. Ensuite on identifie le nœud à la réunion d'un ensemble de nœuds premiers, de la même façon qu'un nombre est décomposé en produits de nombres premiers. Cette décomposition est unique, et s'appuie sur une classification des nœuds premiers.

Les problèmes de la classification des nœuds premiers naquirent de la représentation à deux dimensions des nœuds qui sont plongés dans l'espace habituel à trois dimensions. Le principal problème était de déterminer si deux représentations apparemment différentes correspondaient à deux nœuds différents ou n'étaient que des projections d'un même nœud. Le terme mathématique consacré est isotope : deux nœuds sont isotopes si on peut passer de l'un à l'autre par des transformations continues sans couper la courbe. Dans ces transformations continues, on fait passer une boucle dans une autre ou sur une autre, on tord ou on étire un brin pour le démêler, mais on ne rompt jamais la ficelle. La question est : étant donné deux nœuds, comment être sûr qu'ils ne sont pas isotopes ?

On caractérise un nœud, ou une orbite périodique, à l'aide d'«invariants» mathématiques de plus en plus complexes. Les plus connus sont au nombre de quatre.

L'invariant le plus simple est le nombre minimum d'enlacements (l'ordre du nœud) : on l'obtient après avoir éliminé toutes les boucles et tous les enroulements inutiles. Cet invariant a été utilisé dès le début de la théorie des nœuds, par les physiciens anglais Tait et Little, à la fin du XIXe siècle. Ils ont ainsi construit une table des nœuds premiers contenant jusqu'à dix enlacements, mais n'ont pas su prouver la non-isotopie des nœuds à plus de quatre enlacements.

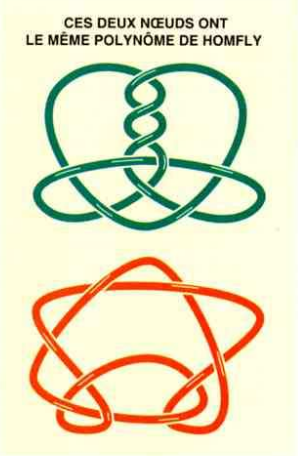

On montre en effet que les nœuds à un et deux enlacements sont isotopes à un nœud sans enlacement, la circonférence ou nœud trivial. Le premier nœud non trivial contient trois enlacements : c'est le nœud de trèfle. Pour quatre enlacements, on n'obtient encore qu'un seul nœud (d'ordre quatre), appelé le nœud en huit. En revanche, à partir de cinq enlacements, plusieurs types de nœuds sont du même ordre. Par conséquent, il fallait un autre invariant pour les distinguer.

Le polynôme d'Alexander, découvert en 1926, est le second invariant connu. Il est égal au déterminant de la matrice du nœud, un tableau de chiffres à *n* lignes et *n* colonnes (*n* est le nombre d'enlacements du nœud), construit en numérotant chaque enlacement le long du nœud et en lui associant un signe qui dépend du sens de parcours *(voir l'encadré de la page ci-contre)*. Le polynôme d'Alexander établit la non-isotopie des nœuds premiers jusqu'à l'ordre huit. A partir de l'ordre neuf, il existe des nœuds premiers non isotopes, qui ont le même polynôme d'Alexander. Nous devons alors faire appel à un troisième invariant.

Le polynôme de Jones, découvert par Vaughan Jones en 1984, ressemble beaucoup au polynôme d'Alexander, mais il est plus efficace. Des chercheurs l'ont encore généralisé en un polynôme à deux variables, nommé HOMFLY ; cet invariant permet notamment de distinguer un nœud de son image dans un miroir. Malheureusement, même ce polynôme ne caractérise pas totalement un nœud !

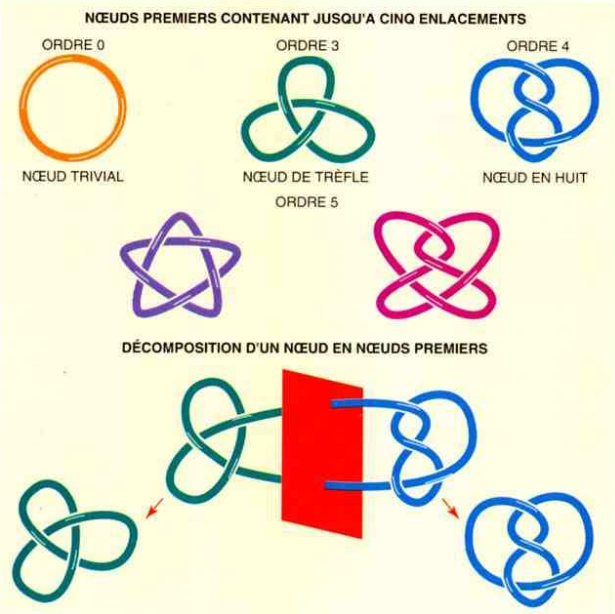

façon presque périodique avant de reprendre un comportement chaotique *(voir la figure 3)*.

Un attracteur étrange s'enroule en effet autour d'une infinité d'orbites périodiques, correspondant à des trajectoires fermées (des boucles) dans l'espace des phases : tout segment d'une trajectoire chaotique peut être approché aussi près que l'on veut par un fragment d'orbite périodique, de la même manière que tout nombre réel est la limite d'une suite de rationnels. Cette propriété est illustrée par la figure 4, qui montre les orbites périodiques extraites des signaux expérimentaux correspondant à l'attracteur de la figure 2 et reconstruites dans le même espace des phases.

Ces orbites périodiques sont instables : une trajectoire dont le point de départ est situé exactement sur l'une d'entre elles parcourra celle-ci indéfiniment, mais s'en éloignera rapidement à la moindre perturbation. Une trajectoire chaotique typique explorant tout l'attracteur visite successivement le voisinage de chacune des orbites périodiques, y demeurant d'autant plus longtemps qu'elle s'en sera approchée.

C'est lorsqu'un système chaotique évolue dans l'ombre d'une orbite de période assez petite que l'on observe les séquences de comportement périodique évoquées plus haut. La recherche de ces séquences permet de recenser une partie des orbites périodiques contenues dans l'attracteur, et de connaître leurs trajectoires approchées. L'observation de tels phénomènes répétitifs suggère que le système chaotique étudié obéit à des lois déterministes mettant en jeu un petit nombre de degrés de liberté : il est en effet très improbable qu'un système purement aléatoire, ou même à grand nombre de degrés de liberté, retourne si vite dans le voisinage d'un état occupé antérieurement.

Notons qu'il est possible de tirer parti des orbites périodiques instables pour contrôler un système chaotique : de même qu'un jongleur parvient, par des corrections infimes mais judicieuses, à tenir une perche en équilibre sur son front, on peut, en corrigeant légèrement ses paramètres à tout instant, maintenir un système chaotique au voisinage de l'orbite périodique instable qu'il vient de visiter, et le stabiliser sur l'un de ses nombreux régimes périodiques. Dans le cas d'applications pratiques exigeant un comportement régulier, on élargit ainsi la plage de paramètres utilisables (voir *La maîtrise du chaos*, par William Ditto et Louis Pecora, dans ce dossier). Ce domaine d'étude est en plein développement, si l'on en croit le nombre de publications parues (plus de 200 durant les trois dernières années).

La construction du polynôme d'Alexander

Comment obtient-on le polynôme d'Alexander d'un nœud ? Dans un croisement, un brin passe sous un autre : nommons «tunnel» le premier brin et «pont» le second. Partant d'un point sur le nœud, on numérote tous les tunnels rencontrés le long de la boucle. Un tunnel est de signe + si la circulation du pont qui le surplombe va de la gauche vers la droite, de signe – dans le cas contraire. Chaque pont est associé à un numéro, celui du tunnel auquel il aboutit.

Maintenant construisons la matrice du nœud, un tableau de chiffres contenant n lignes et n colonnes, n étant le nombre de croisements du nœud : si le nœud numéro k est une boucle inutile, c'est-à-dire du type *(1)* à *(4)*, on écrit la ligne k :

	1	…	$k-1$	k	$k+1$	…
k	0	…	0	-1	1	0

Si le tunnel k est du type *(5)*, la ligne k de la matrice s'écrit :

	1	…	$k-1$	k	$k+1$	…	j	…
k	0	…	0	1	$-t$	0	$t-1$	0

Si le tunnel k est du type *(6)*, la ligne k s'écrit :

	1	…	$k-1$	k	$k+1$	…	j	…
k	0	…	0	$-t$	1	0	$t-1$	0

Lorsque toutes les cases de la matrice sont remplies, on supprime une ligne et une colonne, et on calcule le déterminant résultant. On obtient un polynôme en t ; autrement dit, une somme de puissances de t.

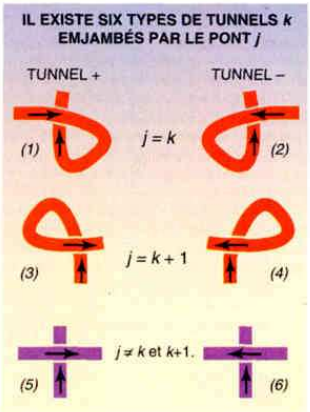

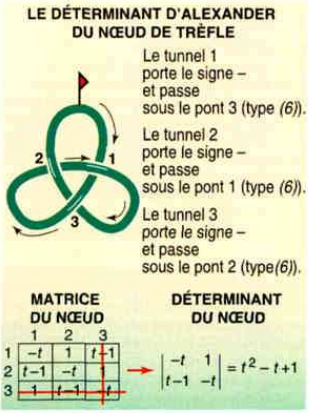

Les invariants topologiques

L'enchevêtrement des orbites périodiques instables reflète la complexité de l'attracteur étrange *(voir la figure 4)*. Lorsqu'un attracteur est contenu dans un espace des phases à trois dimensions, ce qui est le cas des systèmes chaotiques les plus simples (à trois variables), il existe des outils pour caractériser cet enchevêtrement : une boucle dans un espace à trois dimensions n'est rien d'autre qu'un nœud, objet topologique largement étudié par les mathématiciens.

On décrit l'organisation des orbites périodiques instables (de même que la structure des nœuds) au moyen d'invariants topologiques, tels que le nombre d'enlacements de deux orbites, ou des quantités plus abstraites comme les polynômes de nœud *(voir l'encadré ci-dessus)* ; ces grandeurs restent inchangées lorsqu'on déforme une boucle de manière continue (sans la couper). Par conséquent, les trajectoires approchées des orbites périodiques instables obtenues expérimentalement possèdent exactement les mêmes invariants que les orbites elles-mêmes.

Pour la même raison, les invariants d'une orbite périodique ne dépendent pas des paramètres du système et lui sont propres (ils constituent une sorte de «patrimoine génétique» de l'orbite). Cette propriété est caractéristique d'un système déterministe : par un point de l'espace des phases ne passe qu'une seule trajectoire, celle fixée par les lois d'évo-

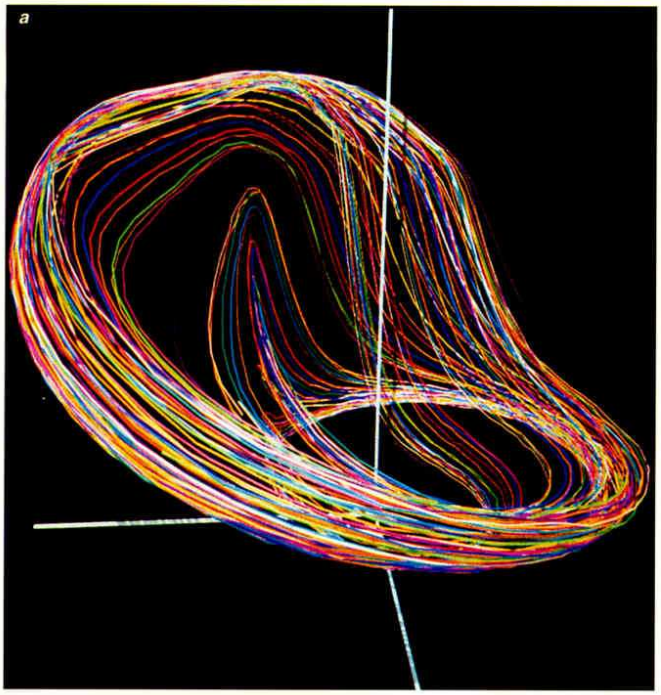

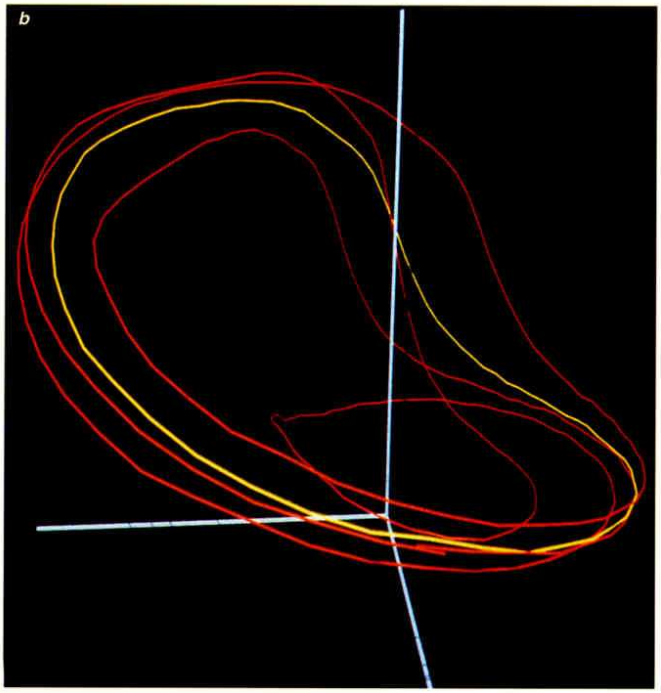

lution (si deux trajectoires passaient par le même point, cela signifierait que le système possède deux avenirs possibles, ce qui contredit l'hypothèse d'une évolution déterministe) ; une orbite ne se croise donc jamais elle-même, ni ne croise une autre orbite, ce qui serait le seul moyen de modifier ses invariants.

Par conséquent les invariants sont le reflet de l'organisation topologique globale des orbites périodiques instables. Ils apportent une information essentielle : on a ainsi montré que des orbites périodiques formant certains types de nœuds n'existent que dans des systèmes présentant du chaos déterministe.

Toutefois le calcul des invariants topologiques ne servirait qu'à remplir de longs tableaux de chiffres, s'il n'existait pas un ordre caché dans le chaos. Pour révéler cet ordre caché, il faut mettre à plat et démêler l'enchevêtrement des orbites périodiques instables. C'est ce que l'on fait à l'aide de surfaces particulières, appelées «gabarits» *(voir la figure 5)*.

Le gabarit de l'attracteur

Il existe, pour tout attracteur étrange inclus dans un espace tridimensionnel, une surface unique sur laquelle toutes les orbites périodiques instables peuvent être amenées continûment *sans modifier leurs invariants*. Cette surface constitue le gabarit de l'attracteur étrange.

Le gabarit détermine de façon remarquable l'organisation globale de l'attracteur étrange : si les orbites périodiques constituent le squelette de l'attracteur, le gabarit en est l'épine dorsale. Il indique la classe topologique, non seulement de l'attracteur, mais aussi du système étudié : le spectre des orbites périodiques varie avec les paramètres de contrôle, tandis que le schéma d'organisation

***4. Les orbites périodiques instables** correspondant à l'attracteur étrange du laser à gaz carbonique sont reconstituées dans l'espace des phases, chacune avec une couleur différente (a). Il est difficile de distinguer à l'œil nu la structure de cet ensemble de celle de l'attracteur. Nous avons isolé deux de ces orbites (b) : la première, de période T (en jaune), forme un nœud trivial (une circonférence) ; la seconde, de période 4T (en rouge), dessine le plus simple des nœuds non triviaux, le «nœud de trèfle». Un invariant topologique élémentaire pour ce couple d'orbites périodiques instables est le nombre d'enlacements des deux orbites, c'est-à-dire le nombre de tours que fait la seconde autour de la première : ce nombre est ici égal à deux.*

indiqué par le gabarit demeure en général inchangé.

L'équipe du théoricien américain Robert Gilmore a montré comment adapter ces concepts (introduits par les mathématiciens Joan Birman et Robert Williams) à l'analyse de données expérimentales. Les invariants de quelques orbites de petite période (trois orbites dans le cas du laser à gaz carbonique modulé) suffisent à définir la structure complète du gabarit. On vérifie alors que les autres orbites périodiques détectées s'inscrivent exactement sur le gabarit déterminé. On s'assure ainsi que le gabarit décrit correctement la structure topologique du régime chaotique étudié, et que la dynamique observée possède un degré d'organisation tel qu'elle ne peut obéir qu'à des lois déterministes.

Quatre systèmes expérimentaux différents ont été analysés par cette méthode : la réaction chimique de Belousov-Zhabotinsky, un oscillateur à résonance magnétique nucléaire, et deux lasers à gaz carbonique, l'un à absorbant saturable, l'autre à pertes modulées (présenté dans cet article). Ces quatre systèmes ont révélé la même organisation topologique. En outre, pour les trois derniers, l'organisation observée avait été prévue par les modèles théoriques.

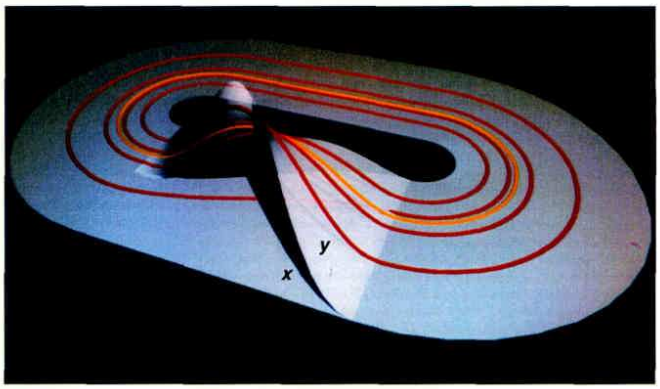

***5. Le gabarit** décrit la structure topologique d'un attracteur étrange : toutes les orbites périodiques de l'attracteur s'y disposent. Il se compose d'un ruban principal qui se scinde en plusieurs branches ; ces branches se recouvrent ensuite sur la largeur du ruban principal. Les propriétés du gabarit peuvent être résumées par des nombres entiers (obtenus à partir des invariants des orbites de plus faible période) : le nombre de branches qu'il comporte, le nombre de torsades des branches, le nombre de tours qu'une branche effectue autour d'une autre et l'ordre suivant lequel les branches se superposent lorsqu'elles se recollent. Ce gabarit-ci (celui du laser à gaz carbonique modulé) est dénommé «fer à cheval» : les deux branches se replient l'une sur l'autre à la manière d'un fer à cheval. Une branche rejoint le ruban principal sans changer son orientation (la branche x), tandis que l'autre subit une torsion d'un demi-tour (la branche y). Nous avons projeté sur ce gabarit les deux orbites de la figure 4b : l'orbite de période T (en jaune) est appelée symboliquement y, car elle passe par la branche y, et l'orbite de période 4T (en rouge) est appelée xyyy, car elle passe une fois par la branche x et trois fois par la branche y.*

La dynamique symbolique

L'analyse topologique du gabarit et la projection des orbites périodiques sur ce gabarit nous ont menés vers la découverte d'un ordre inhérent au chaos. On a vu que l'ensemble des invariants topologiques apporte bien plus d'informations qu'il n'est nécessaire pour déterminer la structure du gabarit. Nous avons organisé ces informations au moyen de ce que l'on appelle la «dynamique symbolique». Cette méthode consiste ici à attribuer à chaque orbite inscrite sur le gabarit un nom symbolique énumérant les branches par lesquelles elle passe successivement : si l'on nomme x la branche non torsadée et y la branche torsadée du gabarit de la figure 5, les deux orbites qui y sont représentées sont symbolisées y *(en jaune)* et $xyyy$ (= xy^3) *(en rouge)*. Il s'avère que chaque mot formé à partir des lettres x et y, à la condition de ne pas être la simple répétition d'un motif plus court (comme yy), correspond à une orbite différente.

De manière générale, seules quelques projections sur le gabarit respectent les invariants topologiques d'une orbite expérimentale donnée. Pour la plupart des orbites de faible périodicité, cette projection est même unique, et il est alors naturel de désigner l'orbite par le nom symbolique correspondant à cette projection.

La liste des noms symboliques associés aux différentes orbites constituant un attracteur est riche d'enseignements. Dans un attracteur expérimental, le chaos n'est pas complètement «développé» : certaines séquences de symboles sont absentes, car toutes les orbites périodiques autorisées par la structure topologique du gabarit n'ont pas encore été créées. La liste des noms symboliques fournit une mesure du degré de chaos.

Le laser à gaz carbonique modulé produit une série de «crises» correspondant à un changement de régime chaotique : à la suite d'une collision avec une orbite périodique, un attracteur étrange s'étend brusquement dans l'espace des phases, ou bien disparaît pour laisser la place à un autre attracteur. L'analyse topologique et symbolique des régimes observés de part et d'autre de ces crises révèle des mécanismes intéressants.

Ainsi les orbites périodiques avec lesquelles les attracteurs entrent en collision sont-elles associées à des noms symboliques particuliers, de la forme $x^n y^2$. En outre, avant la première crise, les noms des orbites périodiques instables détectées, tels que xy^2xy^3, $xyxy^2$, ne contiennent jamais deux x consécutifs. La crise ne survient que lorsque toutes les orbites vérifiant cette règle ont été créées, et ce n'est qu'immédiatement après la crise que des orbites comportent la séquence x^2, interdite jusque là. Les dynamiques symboliques correspondant aux régimes précédant et suivant la crise se distinguent donc nettement, les différentes crises observées étant accompagnées des apparitions successives des séquences x^n. La simplicité des règles de sélection indique que l'organisation des crises est gouvernée par la topologie de l'attracteur, et elle encourage les chercheurs à poursuivre les recherches dans cette voie.

On a souvent tendance à considérer un comportement périodique comme plus ordonné qu'un régime chaotique. L'analyse topologique met en lumière la stricte organisation de l'infinité d'orbites périodiques contenues dans les attracteurs étranges. Fondée sur la mesure de propriétés robustes – les invariants topologiques des orbites périodiques instables –, l'analyse topologique fournit des informations essentielles à la compréhension des phénomènes chaotiques, et montre que le régime le plus ordonné n'est pas forcément celui qu'on croit.

References

1. G. B. Mindlin, X.-J. Hou, H. G. Solari, R. Gilmore, and N. B. Tufillaro. Classification of strange attractors by integers. *Phys. Rev. Lett.*, 64(20):2350–2353, 1990.
2. G. B. Mindlin, H. G. Solari, M. A. Natiello, R. Gilmore, and X.-J. Hou. Topological analysis of chaotic time series data from Belousov–Zhabotinski reaction. *J. Nonlinear Sci.*, 1:147–173, 1991.
3. R. Gilmore. Topological analysis of chaotic dynamical systems. *Rev. Mod. Phys.*, 70:1455–1530, 1998.
4. R. Gilmore and M. Lefranc. *The Topology of Chaos*. Wiley, New York, 2002.
5. M. Lefranc and P. Glorieux. Topological analysis of chaotic signals from a CO_2 laser with modulated losses. *Int. J. Bifurcation Chaos Appl. Sci. Eng.*, 3:643–649, 1993.
6. G. Boulant, S. Bielawski, D. Derozier, and M. Lefranc. Experimental observation of a chaotic attractor with a reverse horsehoe topological structure. *Phys. Rev. E*, 55(4):R3801–3804, 1997.
7. G. Boulant, M. Lefranc, S. Bielawski, and D. Derozier. Horseshoe templates with global torsion in a driven laser. *Phys. Rev. E*, 55(5):5082–5091, 1997.
8. G. Boulant, J. Plumecoq, S. Bielawski, D. Derozier, and M. Lefranc. Model validation and symbolic dynamics of chaotic lasers using template analysis. In M. Dong, W. Ditto, L. Pecora, M. Spano, and S. Vohra, editors, *Proceedings of the 4th Experimental Chaos Conference*, pages 121–126, Singapore, 1998. World Scientific.
9. G. Boulant, M. Lefranc, S. Bielawski, and D. Derozier. A non-horseshoe template in a chaotic laser model. *Int. J. Birfurcation Chaos Appl. Sci. Eng.*, 8(5):965–975, 1998.
10. M. Lefranc, P. Glorieux, F. Papoff, F. Molesti, and E. Arimondo. Combining topological analysis and symbolic dynamics to describe a strange attractor and its crises. *Phys. Rev. Lett.*, 73:1364–1367, 1994.
11. Jérôme Plumecoq and Marc Lefranc. From template analysis to generating partitions I: Periodic orbits, knots and symbolic encodings. *Physica D*, 144:231–258, 2000.

12. Jérôme Plumecoq and Marc Lefranc. From template analysis to generating partitions II: Characterization of the symbolic encodings. *Physica D*, 144:259–278, 2000.
13. J. W. L. McCallum and R. Gilmore. A geometric model for the Duffing oscillator. *Int. J. Bifurcation Chaos Appl. Sci. Eng.*, 3(3):685–691, 1993.
14. R. Gilmore and J. W. L. McCallum. Structure in the bifurcation diagram of the Duffing oscillator. *Phys. Rev. E*, 51:935–956, 1995.
15. Axelle Amon and Marc Lefranc. Topological signature of deterministic chaos in short nonstationary signals from an optical parametric oscillator. *Phys. Rev. Lett.*, 92:094101, 2004.
16. Marc Lefranc. Alternative determinism principle for topological analysis of chaos. *Phys. Rev. E*, 74(3):035202, Sep 2006.
17. Christophe Szwaj, Serge Bielawski, and Dominique Derozier. Propagation of waves in the spectrum of a multimode laser. *Phys. Rev. Lett.*, 77(22):4540–4543, Nov 1996.
18. Christophe Szwaj, Serge Bielawski, Dominique Derozier, and Thomas Erneux. Faraday instability in a multimode laser. *Phys. Rev. Lett.*, 80(18):3968–3971, May 1998.
19. T. W. Carr, T. Erneux, C. Szwaj, M. Lefranc, D. Derozier, and S. Bielawski. Cascade of parametric instabilities in a multimode laser. *Phys. Rev. A*, 64(5):053808, Oct 2001.
20. Jérôme Plumecoq, Christophe Szwaj, Dominique Derozier, Marc Lefranc, and Serge Bielawski. Eckhaus instability induced by nonuniformities in a laser. *Phys. Rev. A*, 64(6):061801, Nov 2001.
21. E. Louvergneaux. Pattern-dislocation-type dynamical instability in 1d optical feedback kerr media with gaussian transverse pumping. *Phys. Rev. Lett.*, 87(24):244501, Nov 2001.
22. J.A. Giordmaine and R.C. Miller. Tunable coherent parametric oscillation in $LiNbO_3$ at optical frequencies. *Phys. Rev. Lett.*, 14(24):973, 1965.
23. A. Yariv and W.H. Louisell. Theory of the optical parametric oscillator. *IEEE J. Quantum Electron.*, QE-2(9):418, 1966.
24. J. Opt. Soc. Am. B. *Special issue on optical parametric devices*, volume 11, 1995. (11) p. 2084-2322.
25. C. Fabre, P. F. Cohadon, and C. Schwob. Cw optical parametric oscillators: single mode operation and frequency tuning properties. *J. Opt. B: Quantum Semiclass. Opt.*, 9(2):165–172, 1997.
26. G.L. Oppo, M. Brambilla, and L.A. Lugiato. Formation and evolution of rolls patterns in optical parametric oscillators. *Physical review A*, 49(3):2028, 1994.
27. G.L. Oppo, M. Brambilla, D. Camesasca, A. Gatti, and L.A. Lugiato. Spatiotemporal dynamics of optical parametric oscillators. *Journal of modern optics*, 41(6):1151, 1994.
28. K. Staliunas. Transverse pattern formation in optical parametric oscillators. *Journal of modern optics*, 42(6):1261, 1995.
29. S. Longhi and A. Geraci. Swift-Hohenberg equation for optical parametric oscillator. *Phys. Rev. A*, 54(5):4581, 1996.
30. G.J. Valcárcel, K. Staliunas, E. Roldan, and V.J. Sánchez-Morcillo. Transverse patterns in degenerate optical parametric oscillation and degenerate four-wave mixing. *Phys. Rev. A*, 54(2):1609, 1996.

31. K. Staliunas and V.J. Sánchez-Morcillo. Localized structures in degenerate optical parametric oscillators. *Opt. Commun.*, 139:306, 1997.
32. L. A. Lugiato, C. Oldano, C. Fabre, E. Giacobino, and R. J. Horowicz. Bistability, self-pulsing and chaos in optical parametric oscillators. *Il Nuovo Cimento*, 10D(8):959–976, 1988.
33. P. Suret, D. Derozier, M. Lefranc, J. Zemmouri, and S. Bielawski. Self-pulsing instabilities in an optical parametric oscillator: experimental observation and modeling of the mechanism. *Phys. Rev. A*, 61:021805(R), January 2000.
34. P. Suret, M. Lefranc, D. Derozier, J. Zemmouri, and S. Bielawski. Periodic mode hopping induced by thermo-optic effects in continuous-wave optical parametric oscillators. *Opt. Lett.*, 26:1415–1417, 2001.
35. P. Suret, M. Lefranc, D. Derozier, J. Zemmouri, and S. Bielawski. Fast oscillations in an optical parametric oscillator. *Opt. Commun.*, 200:369–379, 2001.
36. A. Amon, M. Nizette, M. Lefranc, and T. Erneux. Bursting oscillations in optical parametric oscillators. *Phys. Rev. A*, 68:023801, 2003.
37. Axelle Amon, Marc Lefranc, Serge Bielawski, and Dominique Derozier. Multimode behavior of optical parametric oscillators. en cours de rédaction.
38. J. Hasty, D. McMillen, F. ISaacs, and J.J. Collins. Computational studies of gene regulatory networks: in numero molecular biology. *Nat. Rev. Genet.*, 2:268–279, 2001.
39. J. Hasty, F. Isaacs, M. Dolnik, D. McMillen, and J.J. Collins. Designer gene networks: Towards fundamental cellular control. *Chaos*, 11:207–220, 2001.
40. J. Hasty, D. McMillen, and J.J. Collins. Engineered gene circuits. *Nature*, 420:224, 2002.
41. A. Goldbeter, D. Gonze, G. Houart, J.-C. Leloup, J. Halloy, and G. Dupont. From simple to complex oscillatory behavior in metabolic and genetic control networks. *Chaos*, 11:247–260, 2001.
42. A. Goldbeter. *Biochemical Oscillations and Cellular Rhythms: The molecular bases of periodic and chaotic behaviour*. Cambridge University Press, Cambridge, 1996.
43. B Alberts, A. Johnson, J. Lewis, M. Raff, K. Roberts, and P. Walte. *Molecular Biology of the Cell*. Garland Publishing, 2002.
44. J. Craig Venter *et al.* The Sequence of the Human Genome. *Science*, 291(5507):1304–1351, 2001.
45. J.C. Dunlap. Molecular bases for circadian clocks. *Cell*, 96(2):271–290, 1999.
46. M.W. Young and S.A. Kay. Time zones: a comparative genetics of circadian clocks. *Nat. Rev. Genet.*, 2(9):702–715, 2001.
47. H. Poincaré. *Les Methodes nouvelle de la mécanique céleste*. Gauthier-Villars, Paris, 1892.
48. E.N. Lorenz. *The essence of Chaos*. University of Washington Press, 1996.
49. E. Ott. *Chaos in Dynamical Systems*. Cambridge University Press, Cambridge, 1993.
50. N. H. Packard, J. P. Crutchfield, J. D. Farmer, and R. S. Shaw. Geometry from a time series. *Phys. Rev. Lett.*, 45(9):712–715, 1980.
51. Peter Grassberger and Itamar Procaccia. Characterization of strange attractors. *Phys. Rev. Lett.*, 50(5):346–349, Jan 1983.

52. J.-P. Eckmann and D. Ruelle. Ergodic theory of chaos and strange attractors. *Rev. Mod. Phys.*, 57(3):617–656, 1985.
53. Thomas C. Halsey, Mogens H. Jensen, Leo P. Kadanoff, Itamar Procaccia, and Boris I. Shraiman. Fractal measures and their singularities: The characterization of strange sets. *Phys. Rev. A*, 33(2):1141–1151, Feb 1986.
54. E.A. Jackson. *Perspectives of nonlinear dynamics*. Cambridge University Press, 1989.
55. S. Smale. Differentiable dynamical systems. *Bull. Am. Math. Soc.*, 73:747–817, 1967.
56. G. Iooss and D. D. Joseph. *Elementary Stability and Bifurcation Theory*. Springer-Verlag, Berlin, 1980.
57. J. Guckenheimer and P. H. Holmes. *Nonlinear Oscillators, Dynamical Systems and Bifurcations of Vector Fields*. Springer-Verlag, New York, 1986.
58. S. Wiggins. *Introduction to Applied Nonlinear Dynamical Systems and Chaos*. Springer-Verlag, New York, 1990.
59. Sylvain Crovisier. Birth of homoclinic intersections: a model for the central dynamics of partially hyperbolic systems, 2006. http://www.citebase.org/abstract?id=oai:arXiv.org:math/0605387.
60. A. Katok and B. Hasselblatt. *Introduction to the Modern Theory of Dynamical Systems*. Cambridge University Press, Cambridge, 1995.
61. L.P. Shilnikov. A case of the existence of a countable number of periodic motions. *Sov. Math. Dokl.*, 6:163–166, 1965.
62. L.P. Shilnikov. A contribution to the problem of the structure of an extended neighborhood of a rough equilibrium state of saddle focus type. *Math USSR Sbornik*, 10:91–102, 1970.
63. F. Argoul, A. Arnéodo, and P. Richetti. Experimental evidence for homoclinic chaos in the belousov-zhabotinskii reaction. *Phys. Lett. A*, 120:269–275, 1987.
64. F. Argoul, A. Arnéodo, and P. Richetti. Dynamique symbolique dans la réaction de belousov-zhabotinskii : une illustration expérimentale de la théorie de shil'nikov des orbites homoclines. *J. Chim. Phys.*, 84:1367–1385, 1987.
65. T. Braun, R. R. B. Correira, and N. Altmann. Topological model of homoclinic chaos in a glow discharge. *Phys. Rev. E*, 51:4165–4168, 1995.
66. F.T. Arecchi, A. Lapucci, R. Meucci, J.A. Roversi, and P.H. Coullet. Experimental characterization of shil'nikov chaos by statistics of return times. *Europhys. Lett.*, 6:677–682, 1988.
67. D. Dangoisse, A. Bekkali, F. Papoff, and P. Glorieux. Shilnikov dynamics in a passive Q-switching laser. *Europhysics Letters*, 6:335–+, June 1988.
68. C. Letellier, P. Dutertre, and B. Maheu. Unstable periodic orbits and templates of the Rössler system: toward a systematic topological characterization. *Chaos*, 5:271–282, 1995.
69. J. Theiler. Estimating fractal dimension. *Journal of the Optical Society of America A*, 7:1055–1073, June 1990.
70. E. A. Jackson. *Perspectives in Nonlinear Dynamics*. Cambridge University Press, Cambridge, 1990.
71. J. S. Birman and R. F. Williams. Knotted periodic orbits in dynamical systems I: Lorenz's equations. *Topology*, 22:47–82, 1983.

72. J. Birman and R. Williams. Knotted periodic orbits in dynamical systems II: knot holders for fibered knots. *Cont. Math.*, 20:1–60, 1983.
73. D. Auerbach, P. Cvitanović, J.-P. Eckmann, G. Gunaratne, and I. Procaccia. Exploring chaotic motion through periodic orbits. *Phys. Rev. Lett.*, 58:2387–2389, 1987.
74. P. Cvitanović. Invariant measures of strange sets in terms of cycles. *Phys. Rev. Lett.*, 61:2729–2732, 1988.
75. R. Badii, E. Brun, M. Finardi, L. Flepp, R. Holzner, J. Parisi, C. Reyl, and J. Simonet. Progress in the analysis of experimental chaos through periodic orbits. *Rev. Mod. Phys.*, 66:1389–1415, 1994.
76. D. Rolfsen. *Knots and Links*. Publish or Perish, Berkeley, CA, 1976.
77. L. H. Kaufmann. *Knots and Physics*. World Scientific, Singapore, 1991.
78. J. Used, J.-C. Martín, and M. Lefranc. unpublished.
79. Hao Bai-Lin. *Elementary symbolic dynamics and chaos in dissipative systems*. World Scientific, 1989.
80. G. B. Mindlin, R. Lopez-Ruiz, H. G. Solari, and R. Gilmore. Horseshoe implications. *Phys. Rev. E*, 48(6):4297–4304, 1993.
81. T. Hall. Weak universality in two-dimensional transitions to chaos. *Phys. Rev. Lett.*, 71(1):58–61, 1993.
82. T. Hall. The creation of horseshoes. *Nonlinearity*, 7:861–924, 1994.
83. A. de Carvalho and T. Hall. How to prune a horseshoe. *Nonlinearity*, 15:R19–R68, 2002.
84. A. de Carvalho and T. Hall. The forcing relation for horseshoe braid types. *Experiment. Math.*, 11:271–288, 2002.
85. P. Boyland. Topological methods in surface dynamics. *Topology Appl.*, 58:223–298, 1994.
86. E. Yao, M. Lefranc, and F. Papoff. Unstable periodic orbits in the presence of spatio-temporal chaos. *Journal of Optics B: Quantum and Semiclassical Optics*, 2:382–385, June 2000.
87. M. Lefranc. Alternate determinism principle for topological analysis of chaos. ArXiv preprint nlin.CD/050305, 2005.
88. F. Papoff, A. Fioretti, E. Arimondo, G. B. Mindlin, H. G. Solari, and R. Gilmore. Structure of chaos in the laser with a saturable absorber. *Phys. Rev. Lett.*, 68:1128–1131, 1992.
89. N. B. Tufillaro, R. Holzner, L. Flepp, R. Brun, M. Finardi, and R. Badii. Template analysis for a chaotic NMR laser. *Phys. Rev. A*, 44(8):R4786–R4788, 1991.
90. C. Letellier, L. Le Sceller, P. Dutertre, G. Gouesbet, Z. Fei, and J. L. Hudson. Topological characterization and global vector field reconstruction of an experimental electrochemical system. *J. Phys. Chem.*, 99:7016–7027, 1995.
91. N. B. Tufillaro, P. Wyckoff, R. Brown, T. Schreiber, and T. Molteno. Topological time series analysis of a string experiment and its synchronized model. *Phys. Rev. E*, 51(3):164–174, 1995.
92. N. B. Abraham, P. Mandel, and L. M. Narducci. Dynamical instabilities and pulsations in lasers. In E. Wolf, editor, *Progress in Optics XXV*, pages 1–190, Amsterdam, 1988. North-Holland.

93. L. M. Narducci and N. B. Abraham. *Laser Physics and Laser Instabilities*. World Scientific, Singapore, 1988.
94. C. Scheffczyk, U. Parlitz, T. Kurz, W. Knop, and W. Lauterborn. Comparison of bifurcation structures of driven dissipative nonlinear oscillators. *Phys. Rev. A*, 43(12):6495–6502, Jun 1991.
95. P. Walters. *An introduction to ergodic theory*. Springer-Verlag, Berlin, 1982.
96. P. Grassberger and H. Kantz. Generating partitions for the dissipative Hénon map. *Phys. Lett. A*, 113(5):235–238, 1985.
97. M. Finardi, L. Flepp, J. Parisi, R. Holzner, R. Badii, and E. Brun. Topological and metric analysis of heteroclinic crisis in laser chaos. *Phys. Rev. Lett.*, 68(20):2989–2991, 1992.
98. R. L. Davidchack, Y.-C. Lai, E. M. Bollt, and M. Dhamala. Estimating generating partitions of chaotic systems by unstable periodic orbits. *Phys. Rev. E*, 61(2):1353–1356, 2000.
99. M. B. Kennel and M. Buhl. Estimating good discrete partitions from observed data: symbolic false nearest neighbors. *Phys. Rev. Lett.*, 91:084102, 2003.
100. Y. Hirata, K. Judd, and D. Kilminster. Estimating a generating partition from observed time series: symbolic shadowing. *Phys. Rev. E*, 70:016215, 2004.
101. P. Cvitanović, G. H. Gunaratne, and I. Procaccia. Topological and metric properties of Hénon-type strange attractors. *Phys. Rev. A*, 38:1503–1520, 1988.
102. P. Boyland. Topological methods in surface dynamics. *Topology and its Applications*, 58:223–298, 1994.
103. T.-Y. Li and J. A. Yorke. Period three implies chaos. *Am. Math. Mon.*, 82(12):985–992, 1975.
104. M. Bestvina and M. Handel. Train-tracks for surface homeomorphisms. *Topology*, 34:109–140, 1995.
105. H. D. I. Abarbanel. *Analysis of Observed Chaotic Data*. Springer-Verlag, New York, 1996.
106. E. Yao, F. Papoff, and G.-L. Oppo. Characterisation of spatio-temporal complexity in optical experiments. *Optics Communications*, 155:73–78, October 1998.
107. Eric Yao, Francesco Papoff, and Gian-Luca Oppo. Statistics and scaling behavior of chaotic domains in a liquid crystal light valve with rotated feedback. *Phys. Rev. E*, 59(3):2918–2926, Mar 1999.
108. M.A. Vorontsov and W.B. Miller, editors. *Self-organization in optical systems and applications in information technology*. Springer, 1995.
109. C. Richy, K. I. Petsas, E. Giacobino, C. Fabre, and L. Lugiato. Observation of bistability and delayed bifurcation in a triply resonant optical parametric oscillator. *J. Opt. Soc. Am. B*, 12(3):456–461, 1995.
110. M. Vaupel, A. Maître, and C. Fabre. Observation of pattern formation in optical parametric oscillator. *Phys. Rev. Lett.*, 83(25):5278, 1999.
111. A. Yariv. *Quantum Electronics*. CBS College Publishing, 1985.
112. Journal of the European Optical Society. *Special issue on $\chi^{(2)}$ second order nonlinear optics: from fundamentals to applications*, Quantum and semiclassical Optics, 1997. (2).

113. K.J McNeil, P.D. Drummond, and D.F. Walls. Self pulsing in second harmonic generation. *Opt. Commun.*, 27(2):292–294, 1978.
114. P.D. Drummond, K.J. McNeil, and D.F. Walls. Non-equilibrium transitions in sub/second harmonic generation I. semiclassical theory. *Optica Acta*, 27(3):321–335, 1980.
115. N. B. Abraham and W. J. Firth. Overview of transverse effects in nonlinear-optical systems. *Journal of the Optical Society of America B Optical Physics*, 7:951–962, June 1990.
116. P. Mandel and M. Tlidi. REVIEW ARTICLE: Transverse dynamics in cavity nonlinear optics (2000 2003). *Journal of Optics B: Quantum and Semiclassical Optics*, 6:60–+, September 2004.
117. A.H. Nayfeh and D.T. Mook. *Nonlinear oscillation*. New York. Wiley interscience publication, 1979.
118. S.L. McCall. Instability and regenerative pulsation phenomena in fabry-perot nonlinear optic media devices. *Appl. Phys. Lett.*, 32(5):284, 1978.
119. A. Lambrecht, E. Giacobino, and J.-M. Courty. *Opt. Commun.*, 115:199, 1995.
120. S. Barland, O. Piro, M. Giudici, J. R. Tredicce, and S. Balle. Experimental evidence of van der Pol–Fitzhugh–Nagumo dynamics in semiconductor optical amplifiers. *Phys. Rev. E*, 68(3):036209, 2003.
121. C. Fabre, M. Vaupel, N. Treps, P.-F. Cohadon, C. Schwob, and A. Maître. C.w. optical parametric oscillators: single mode or multimode? *C. R. Acad. Sci. Paris*, 1 IV(5):553–559, 2000.
122. E.M. Izhikevich. Neural excitability, spiking and bursting. *Int. J. Bifurc. Chaos*, 10:1171–1266, 2000.
123. M. Marte, H. Ritsch, L. Lugiato, and C. Fabre. Simultaneous multimode optical parametric oscillation in a triply resonant cavity. *Acta Physica Slovaca*, 47(3/4):233, 1997.
124. J. Keener and J. Sneyd. *Mathematical Physiology*, volume 8 of *Interdiscplinary Appl. Mathematics*. Springer, Berlin, 1998.
125. Eugene M. Izhikevich. Synchronization of elliptic bursters. *SIAM Review*, 43(2):315–344, 2001.
126. R.C. Eckardt, C.D. Nabors, W.J. Koslovsky, and R.L. Byer. optical parametric oscillator frequency tuning and control. *J. Opt. Soc. Am. B*, 8(3):646, 1991.
127. T. Debuisschert, A. Sizmann, E. Giacobino, and C. Fabre. Type-II continuous-wave optical parametric oscillators: oscillation and frequency-tuning characteristics. *J. Opt. Soc. Am. B*, 10(9):1668, 1993.
128. C. Schwob, P.F. Cohadon, C. Fabre, M.A.M. Marte, H. Ritsch, A. Gatti, and L. Lugiato. Transverse effects and mode couplings in OPOs. *Appl. Phys. B*, 66:685–699, 1998.
129. K. W. Kohn. Molecular interaction map of the mammalian cell cycle control and dna repair systems. *Mol. Biol. Cell*, 10:2703–2734, 1999.
130. A. Goldbeter. *Biochemical oscillations and cellular rythms*. Cambridge University Press, Cambridge, 1996.
131. M. A. Savageau. Design principles for elementary gene circuits: Elements, methods and examples. *Chaos*, 11:142–159, 2001.

132. A. Becksei, B. Séraphin, and L. Serrano. Positive feedback in eukaryotic gene networks: celle differentiation by graded to binary response conversion. *EMBO J.*, 20:2528–2535, 2001.
133. R. Thomas and M. Kaufman. Multistationarity, the basis of cell differentiation and memory. i. structural conditions of multistationarity and other nontrivial behavior. *Chaos*, 11:170–179, 2001.
134. J.J. Tyson, K. Chen, and B. Novak. Network dynamics and cell physiology. *Nature Rev. Mol. Cell Biol.*, 2:908, 2001.
135. Hiromi Hirata, Shigeki Yoshiura, Toshiyuki Ohtsuka, Yasumasa Bessho, Takahiro Harada, Kenichi Yoshikawa, and Ryoichiro Kageyama. Oscillatory expression of the bHLH factor Hes1 regulated by a negative feedback loop. *Science*, 298:840–843, 2002.
136. J. S. Griffith. Mathematics of cellular control processes i. negative feedback to one gene. *J. Theor. Biol.*, 20:202–208, 1968.
137. M.B. Elowitz and S. Leibler. A synthetic oscillatory network of transcriptional regulators. *Nature*, 403:335–338, 2000.
138. N. Barkai and S. Leibler. Circadian clocks limited by noise. *Nature*, 403:267–268, 2000.
139. T. Roenneberg and M. Merrow. The network of time: Understanding the molecular circadian system. *Curr. Biol.*, 13:R198, 2003.
140. M.C. Moore-Ede, F.M. Sulzman, and C.A. Fuller. *The clocks that time us: physiology of the circadian timing system*. Harvard University Press, 1982.
141. Evelyne Derelle, Conchita Ferraz, Stephane Rombauts, Pierre Rouze, Alexandra Z. Worden, Steven Robbens, Frederic Partensky, Sven Degroeve, Sophie Echeynie, Richard Cooke, Yvan Saeys, Jan Wuyts, Kamel Jabbari, Chris Bowler, Olivier Panaud, Benoit Piegu, Steven G. Ball, Jean-Philippe Ral, Francois-Yves Bouget, Gwenael Piganeau, Bernard De Baets, Andre Picard, Michel Delseny, Jacques Demaille, Yves Van de Peer, and Herve Moreau. From the Cover: Genome analysis of the smallest free-living eukaryote Ostreococcus tauri unveils many unique features. *PNAS*, 103(31):11647–11652, 2006.
142. C. A. Strayer and S. A. Kay. The ins and outs of circadian regulated gene expresion. *Curr. Opin. Plant. Biol.*, 2:114, 1999.
143. T. Matsuo, S. Yamaguchi, S. Mitsui, A. Emi, F. Shimoda, and H. Okamura. Control mechanism of the circadian clock for timing of cell division in vivo. *Science*, 302:255, 2003.
144. B. C. Goodwin. Oscillatory behavior of enzymatic control processes. *Adv. Enzyme Regul.*, 3:425–439, 1965.
145. J. S. Griffith. Mathematics of cellular control processes ii. positive feedback to one gene. *J. Theor. Biol.*, 20:209–216, 1968.
146. M. H. Jensen, K. Sneppen, and G. Tiana. Sustained oscillations and time delays in gene expression of protein hes1. *FEBS Lett.*, 541:176–177, 2003.
147. J. Lewis. Autoinhibition with transcriptional delay: a simple mechanism for the zebrafish somitogenesis oscillator. *Curr. Biol.*, 13:1398–1408, 2003.
148. N. A. M. Monk. Oscilatory expression of hes1, p53 and nk-κb driven by transcriptional time delays. *Curr. Biol.*, 13:1409–1413, 2003.

149. M.C. Mackey and L. Glass. Oscillations and chaos in physiological control systems. *Science*, 197:287–289, 1977.
150. A. Goldbeter. A model for circadian oscillations in the Drosophila period protein (per). *Proc. R. Soc. Lond. B*, 261:319–324, 1995.
151. Jean-Christophe Leloup, Didier Gonze, and Albert Goldbeter. Limit cycle models for circadian rhythms based on transcriptional regulation in Drosophila and Neurospora. *J. Biol. Rhythms*, 14:433–448, 1999.
152. V. Lemaire, C. F. Lee, J. Lei, R. Métivier, and L. Glass. Sequential recruitement and combinatorial assembling of multiprotein complexes in transcriptional activation. *Phys. Rev. Lett.*, 96:198102, 2006.
153. P. François and V. Hakim. Core genetic module: the mixed feedback loop. *Phys. Rev. E*, 72:031908, 2005.

